Investigating Climate Change and Carbon Cycling during the Latest Cretaceous to Paleogene (~67–52 million years ago); new geochemical records from the South Atlantic and Indian oceans

Submitted by James Stewart Kinmond Barnet to the University of Exeter

as a thesis for the degree of

Doctor of Philosophy in Geology

September 2018

I certify that all material in this thesis which is not my own work has been identified and that no material has previously been submitted and approved for the award of a degree by this or any other University.

Signature: ……..

ABSTRACT

The Late Cretaceous–early Paleogene is the most recent period of Earth history with a dynamic carbon cycle that experienced sustained global greenhouse warmth and can offer a valuable insight into our anthropogenically-warmer future world. Yet, knowledge of ambient climate conditions and evolution of the carbon cycle at this time, along with their relation to forcing mechanisms, are still poorly constrained. In this thesis, I examine marine sediments recovered from the South Atlantic Walvis Ridge (ODP Site 1262) and Indian Ocean Ninetyeast Ridge (IODP Site U1443 and ODP Site 758), to shed new light on the evolution of the climate and carbon cycle from the Late Maastrichtian through to the Early Eocene (~67.10–52.35 Ma). The overarching aims of this thesis are: 1) to identify the long-term trends and principle forcing mechanisms driving the climate and carbon cycle during this time period, through construction of 14.75 million-year-long, orbital-resolution (~1.5–4 kyr), stratigraphically complete, benthic stable carbon ($\delta^{13}C_{benthic}$) and oxygen ($\delta^{18}O_{benthic}$) isotope records; 2) to investigate in more detail the climatic and carbon-cycle perturbations of the Early–Middle Paleocene (e.g., the Dan-C2 event, Latest Danian Event and the Danian/Selandian Transition Event) and place these in their proper (orbital) temporal context; 3) to investigate the Late Maastrichtian warming event and its relationship to the eruption of the Deccan Traps Large Igneous Province, as well as its role (if any) in the subsequent Cretaceous/Paleogene (K/Pg) mass extinction; 4) to provide the first orbital-resolution estimates of temperature and carbonate chemistry variability from the low latitude Indian Ocean spanning the Late Paleocene–Early Eocene, through analysis of trace element and stable isotope data from multiple foraminiferal species. Taken together, the results presented in this thesis provide a critical new insight into the dynamic evolution of the climate and carbon cycle during the greenhouse world of the early Paleogene, and shed light on the potential forcing mechanisms driving the climate and carbon cycle during this time.

ACKNOWLEDGEMENTS

Firstly, I would like to extend a huge thank you to my supervisors, Kate Littler and Dick Kroon. I would like to thank Kate for ensuring my PhD studentship was viable from the start. Throughout my PhD, Kate offered superb and pro-active guidance, innovative ideas for financial support, thought-provoking discussions, and was always generous with her time when I needed to chat about aspects of my project at short notice, for which I am truly thankful. I would like to thank Dick for allowing me to use his pre-washed samples from ODP Site 1262, for accompanying me on a very busy sampling trip to the Bremen Core Repository, and for insightful and thoughtful discussions on the ODP Site 1262 benthic records. I would also like to thank Ian Bailey for stepping in as first supervisor in Kate's absence during my thesis write up, for very generously taking the time to read through the whole of my thesis, and for offering many valuable comments and suggestions which helped to improve the readability and science.

I was fortunate enough to work with a variety of international collaborators during my PhD studentship. In particular, I would like to thank Jim Zachos, Dustin Harper and Tali Babila for hosting me in the trace metal lab at the University of California Santa Cruz (UCSC) in April–May 2016. I would have been lost in the UCSC lab and with the subsequent interpretation of my data without their support, and they made me feel welcome during my stay at UCSC. Special thanks also go to Melanie Leng and Hilary Sloane (NERC Isotope Geosciences Facility) for funding and supervising the generation of the new benthic stable carbon and oxygen isotope data for my Site 1262 record, as without their financial and technical support, this project would not have been possible.

I thank Michael Henehan (GFZ Potsdam) for generously funding and analysing my extra samples from ODP Site 758 for trace metals in the Yale Metal Geochemistry Centre, and Thomas Westerhold (MARUM) for generating the age model for my Site 1262 core and for insightful discussions regarding spectral analysis techniques for orbitally-tuned stable isotope records. I would also like to thank Kirsty Edgar (University of Birmingham) for teaching me how to differentiate between the key Paleogene planktic *Morozovella* and *Subbotina* foraminifera species, Gabriela de Jesús Arreguín Rodríguez (University of Zaragoza) for

allowing me to use her raw Site 1262 benthic foraminifera assemblage data in my discussion of the Dan-C2 event, Leah LeVay (Texas A&M) for performing the high-resolution calcareous nannofossil biostratigraphy for my Indian Ocean sites, and Rehemat Bhatia (UCL) for insightful chats over Facebook messenger on the interpretation of my Mg/Ca data.

Thank you to my examiners, Sev Kender and Caroline Lear, for taking the time to read my thesis.

I also had the privilege of working with some great academics within our “Deep Time Global Change” group and also within the broader Camborne School of Mines at the University of Exeter. I would in particular like to thank Clemens Ullmann for setting up the stable isotope facility on campus and generating my bulk carbonate stable carbon isotope data, without whom this data generation would not have been possible. I would also like to thank Gavyn Rollinson and Calum Beeson for their technical support and for allowing me to pick foraminifera for long hours on the Wild-Heerbrugg microscope in the microscopy lab over the course of two years, as well as for talking to me, keeping me sane and reassuring me that it would all be worth it when I have data to interpret and write about. I’m pleased to say that they were right.

Last but by no means least, I would like to thank my partner, Jenna Hunt, and my parents, Shirley Barnet and Douglas Barnet, for their unwavering support during the long and stressful months of my thesis write up and for always picking me up when I was feeling down.

TABLE OF CONTENTS

LIST OF FIGURES

LIST OF TABLES

1.0. INTRODUCTION

1.1. MOTIVATION AND THESIS OUTLINE

The Late Cretaceous–early Paleogene (~67–50 Ma) is the most recent period of Earth's history that experienced sustained global greenhouse warmth and was characterised by a dynamic carbon cycle. This interval of Earth's history was punctuated by massive upheavals in both the geosphere and biosphere due to a bolide impact ~66.02 Ma at the end of the Cretaceous (Schulte et al., 2010), Large Igneous Province (LIP) volcanism in the Deccan Traps, India (~66 Ma; Renne et al., 2015; Schoene et al., 2015) and North Atlantic Igneous Province (NAIP; ~63–60 and ~57–54 Ma; Sinton & Duncan, 1998), and transient global warming events termed "hyperthermals", which had profound and long-lasting impacts on Earth's biota, carbon cycle, and climate. This enigmatic period of time has therefore become the subject of heightened interest in recent decades due to the insights it may offer on the nature of an anthropogenically-warmer future world.

Sediment cores recovered from the deep sea by the International Ocean Discovery Program (IODP) and its predecessors, the Integrated Ocean Drilling Program (IODP), Ocean Drilling Program (ODP), and Deep Sea Drilling Project (DSDP), offer the best insights into environmental change in the deep past due to their stratigraphic completeness and (often) well preserved organic and inorganic proxies (e.g., fossil foraminifera). In this thesis, I present new geochemical results from sediments recovered during: ODP Site 1262, drilled on Walvis Ridge in the South Atlantic during Expedition 208 (Shipboard Scientific Party, 2004a); ODP Site 758, drilled on Ninetyeast Ridge in the Indian Ocean during Expedition 121 (Shipboard Scientific Party, 1989); and IODP Site U1443, a redrill of ODP Site 758 recovered during Expedition 353 (Shipboard Scientific Party, 2016).

ODP Site 1262, which is located in a perched basin near the base of the NW flank of Walvis Ridge, recovered an expanded and stratigraphically complete succession of Late Maastrichtian–Early Eocene (~67–52 Ma) clayey nannofossil ooze, making it an ideal site to investigate changes to Earth's climate and carbon

cycle at orbital-resolution during the early Paleogene greenhouse world (Kroon et al., 2007; Zachos et al., 2010). Located at a palaeo-depth of ~3000–3500 m during the early Paleogene, this site can also be used to monitor fluctuations in the depth of the lysocline and calcite compensation depth (CCD) during hyperthermal events (e.g., Zachos et al., 2005). The shallow palaeo-depth of sediment deposition at ODP Site 758 and IODP Site U1443 in the Indian Ocean during the early Paleogene (~1500 m) resulted in generally good preservation of planktic foraminifera, which makes these sites ideal for investigating the palaeoceanography of the understudied Indian Ocean using isotopic and trace metal proxies (Shipboard Scientific Party, 1989; 2016).

There are 7 chapters in this thesis, including four data chapters and a synthesis chapter. Chapter 1 contains a thesis overview and a literature review, which describes in detail the state-of-the-art with regards to Paleocene-Eocene palaeoclimate science and the outstanding questions that remain. Chapter 2 contains the detailed lithostratigraphy of the sampled sites, sampling strategy, as well as the sedimentological and geochemical methods used throughout this thesis.

In Chapter 3, ["*Climate and carbon cycling during the Late Maastrichtian to Early Eocene (~67.1–52.4 million years ago)*"], I present analysis of ~14.75 million year long, orbital-resolution (~1.5–4 kyr), stratigraphically complete, benthic stable carbon ($\delta^{13}C_{benthic}$) and oxygen ($\delta^{18}O_{benthic}$) isotope records spanning the Late Maastrichtian–Early Eocene (~67.10–52.35 Ma) from ODP Site 1262. This dataset is a compilation of both data that I have generated (Late Maastrichtian–Middle Paleocene) and previously published records (Late Paleocene–Early Eocene; McCarren et al., 2008; Stap et al., 2010; Littler et al., 2014; Lauretano et al., 2015). These new compilations have been placed onto an updated orbitally-tuned age model for this site, which allows us to identify the long-term trends in climate and the carbon cycle as well as place all known climatic and carbon-cycle events into their proper temporal context. I use this record to examine the principle forcing mechanisms driving the climate and carbon cycle at orbital resolution during the early Paleogene, and examine the phasing relationship between climate (oxygen isotopes) and carbon cycle (carbon isotopes), which can offer clues on the nature of carbon stores and

modes of release during carbon-cycle perturbations. The stratigraphic completeness and resolution of the new $\delta^{13}C_{benthic}$ and $\delta^{18}O_{benthic}$ records from ODP Site 1262 also allow us to shed new light on some of the critical and poorly studied events of the Early Paleocene, including the Latest Danian Event (LDE) and the Danian/Selandian Transition Event (D/STE).

In Chapter 4, ("*What caused the Late Maastrichtian warming event and could this event have contributed to the severity of the K/Pg mass extinction?*"), I use the Late Maastrichtian portion of the new benthic stable isotope records from ODP Site 1262 to provide a new orbital-resolution chronology for the Late Maastrichtian warming event (LMWE; ~66.2 Ma). I then use this record, in combination with new absolute ages for Deccan Traps LIP volcanism, to elucidate the relationship between the LIP and this important pre-K/Pg boundary climate perturbation. I also present the most complete compilation of (recalibrated) pCO_2 proxy data, a synthesis of published palaeoclimate proxy data, and the most up-to-date compilation of published biotic data, to further interrogate the likely role of LIP volcanism in the genesis of the LMWE, the magnitude and scale of environmental change during the LMWE, and elucidate whether it contributed to the severity of the subsequent K/Pg mass extinction. This work is published as a first author manuscript in *Geology* (Barnet et al., 2017; **Appendix 2**).

In Chapter 5, ("*Can the Dan-C2 event be classified as a global "hyperthermal" event?*"), I focus on the early Danian (earliest Paleocene) portion of the new benthic stable isotope records from ODP Site 1262 and combine these with a synthesis of published palaeoclimate proxy records across the Dan-C2 event (~65.9–65.7 Ma). I provide a new orbital-resolution chronology of the event and critically evaluate the nature and scale of environmental change during Dan-C2. I identify whether there was any deep-sea warming in the bottom waters of the South Atlantic during Dan-C2, and hence if it fits the criteria for a true hyperthermal. By integrating a new high-resolution benthic foraminiferal assemblage study across the event from ODP Site 1262 (Arreguín-Rodríguez, pers. comm.), I critically assess whether the Dan-C2 event was also characterised by significant biotic turnover in the deep South Atlantic.

In Chapter 6, ("*The coupled evolution of ocean temperatures and carbonate chemistry in the northern Indian Ocean during the Paleocene–Eocene*"), I have addressed the paucity of early Paleogene data from the Indian Ocean by generating new high-resolution geochemical records from the southern Bay of Bengal. I present the first long-term trace metal (Mg/Ca & B/Ca) foraminiferal records for the Late Paleocene–Early Eocene from Ninetyeast Ridge IODP Site U1443 and ODP Site 758. I use these records to determine the magnitude of long-term temperature and carbonate chemistry (related to pH) change across a depth transect through the water column of the low-latitude Indian Ocean during the Late Paleocene–Early Eocene, as well as attempt to identify the magnitude of temperature and carbonate chemistry change during larger 405-kyr and 100-kyr eccentricity cycles of this time. I then compare these data to published temperature proxy data to determine if the thermal properties of the surface ocean and intermediate waters of the low latitude Indian Ocean are characteristic of low latitude surface waters and intermediate-deep water masses globally. My record also captures a portion of the PETM, providing a critical minimum constraint on the magnitude of warming which occurred in the surface to deep low-latitude Indian Ocean during this hyperthermal event. This data will provide an invaluable contribution to the ongoing NERC-funded "DeepMIP" project, which aims to provide robust palaeoclimate data to compare to new modelling simulations of Paleocene–Eocene climates (https://deepmip.org/).

1.2. SETTING THE SCENE: LATE MAASTRICHTIAN TO EARLY PALEOGENE CLIMATE AND CARBON CYCLING

1.2.1. LONG-TERM EVOLUTION OF CLIMATE AND THE CARBON CYCLE DURING THE LATE MAASTRICHTIAN–EARLY PALEOGENE

A broad insight into the overarching climate of the Late Maastrichtian–early Paleogene can be gained from macro- and microfossil records. Fossil evidence for sub-tropical forests on Antarctica, incursion of the sub-tropical dinoflagellate cyst *Apectodinium augustum* into the Arctic Ocean, and fossilised remains of alligators and turtles in the Canadian Arctic, provide evidence for temperate-subtropical (essentially frost-free) climates in the polar latitudes during this time period (e.g., Sluijs et al., 2006; Pross et al., 2012; Eberle et al., 2014). These occurrences support the assertion that the Cretaceous and early Paleogene were characterised by long-term global greenhouse climates.

For a more quantitative and detailed insight into climate and carbon cycle dynamics, high-fidelity geochemical proxy (e.g., benthic stable isotope or trace metal) records are required. The current basis of our knowledge on the long-term evolution of the carbon cycle and climate during the Late Maastrichtian–early Paleogene is based on the study of benthic foraminiferal stable isotope ($\delta^{13}C_{benthic}$ and $\delta^{18}O_{benthic}$) records, spliced together or stacked from multiple sites (e.g., Zachos et al., 2001; 2008; Cramer et al., 2009; Figure 1). These composite records are supplemented across certain discrete time intervals by higher resolution single-site benthic records (e.g., Westerhold et al., 2011; 2018; Sexton et al., 2011; Littler et al., 2014; Figure 2; Figure 3), and across specific "hyperthermal" events such as the PETM and Eocene Thermal Maximum 2 (ETM-2) by high-resolution trace metal (Mg/Ca and B/Ca) and organic palaeothermometer ($\mathrm{TEX}_{86}^{\mathrm{H}}$) records (e.g., Zachos et al., 2003; Sluijs et al., 2007a; Penman et al., 2014; Babila et al., 2016, 2018; Frieling et al., 2017; Harper et al., 2018). However, to date, no single-site stratigraphically complete deep-sea benthic stable isotope record exists which spans the whole of this important time interval at ~1.5–4 kyr resolution from the Atlantic Ocean. Similarly, to date, no longer term Mg/Ca and B/Ca records have been generated at orbital-resolution during this time interval, with a complete absence of any trace metal data from

the early Paleogene of the poorly studied Indian Ocean. Thus, our ability to deconvolve the interactions between the carbon cycle and climate at orbital resolution, and in multiple ocean basins, is hampered, leaving many outstanding questions remaining.

Examination of the existing benthic stable isotope records suggests generally warm global temperatures from the Late Maastrichtian–early Paleogene as compared to the Neogene, with both temporal (long-term and orbital-scale) and spatial variability in temperature trends. Following the relatively cool climate of the Late Maastrichtian (with bottom water temperatures of ~7–8°C), the first few million years of the Paleocene were characterised by a gradual warming trend which peaked ~63 Ma (Westerhold et al., 2011, 2018). This Early Paleocene warming was subsequently interrupted by a long-term cooling trend that reached temperatures comparable to the Late Maastrichtian by the start of the Late Paleocene, ~59 Ma (Zachos et al., 2001; 2008; Cramer et al., 2009; Westerhold et al., 2011; 2018; Figure 1; Figure 2a). This cooling coincided with a long-term rise to the most positive oceanic carbon isotope values of the Cenozoic known as the “Paleocene Carbon Isotope Maximum” (PCIM; ~58–57 Ma; Zachos et al., 2001; Cramer et al., 2009; Westerhold et al., 2011, 2018; Littler et al., 2014; Figure 2b; Figure 3a,b). The PCIM represents the massive sequestration of reduced carbon in either biogenic CH_4 hydrates beneath the continental shelves, low latitude peat deposits, marine black shales, or high-latitude permafrost, at the termination of Middle Paleocene cooling (e.g., Corfield, 1994). Based on the low rates of pyrite sulphur burial during this time, Kurtz et al. (2003) argued that a significant portion of this organic carbon (C_{org}) burial took place in terrestrial coal swamps, rather than in marine anoxic environments. The extensive lateral distribution of lignite and coal of Late Paleocene age across North America and Eurasia support this interpretation (Kurtz et al., 2003). Significant temperature- and climate-sensitive carbon reservoirs were therefore primed to be released as the ambient climate warmed and precipitation patterns shifted during the Late Paleocene to Early Eocene (Figure 1; Figure 3c). A resultant increase in reconstructed atmospheric pCO_2 (Royer, 2014) is accompanied by an increasingly light $\delta^{13}C$ signature in marine carbonates, which peaked during the Early Eocene Climatic Optimum (EECO; ~52–50 Ma; Zachos et al., 2001, 2008; Cramer et al., 2009; Littler et al., 2014; Westerhold et al., 2018; Figure 3a,b).

Following this event, the Middle–Late Eocene (~50–34 Ma) was characterised by a long-term cooling trend, which crossed a critical threshold at the Eocene/Oligocene boundary (~34 Ma), resulting in the first permanent widespread glaciation of Antarctica (Zachos et al., 2001, 2008; Cramer et al., 2009; Figure 1).

All else being equal, rising CO_2 levels in the ocean-atmosphere system over short timescales should lead to a shoaling of the global ocean lysocline and calcite compensation depth (CCD), since CO_2 uptake by the oceans lowers pH (e.g., Zachos et al., 2005). Despite evidence for rising ambient CO_2 levels in the ocean-atmosphere system from the Late Paleocene to Early Eocene, proxy data from both the Indian Ocean (Slotnick et al., 2015) and South Atlantic (Westerhold et al., 2007, 2008; Figure 3e), along with modelling studies of the Atlantic and Pacific (Komar et al., 2013), suggest that the CCD deepened in the global ocean up until ~52 Ma, before shoaling during EECO (~52–50 Ma). The deepening of the CCD prior to EECO is likely caused by increased chemical weathering rates and delivery of solutes to the global ocean, raising alkalinity during the increasingly warm and humid greenhouse conditions of the Late Paleocene to Early Eocene, which outcompeted the effects of a long-term rise in CO_2 levels (Hilting et al., 2008).

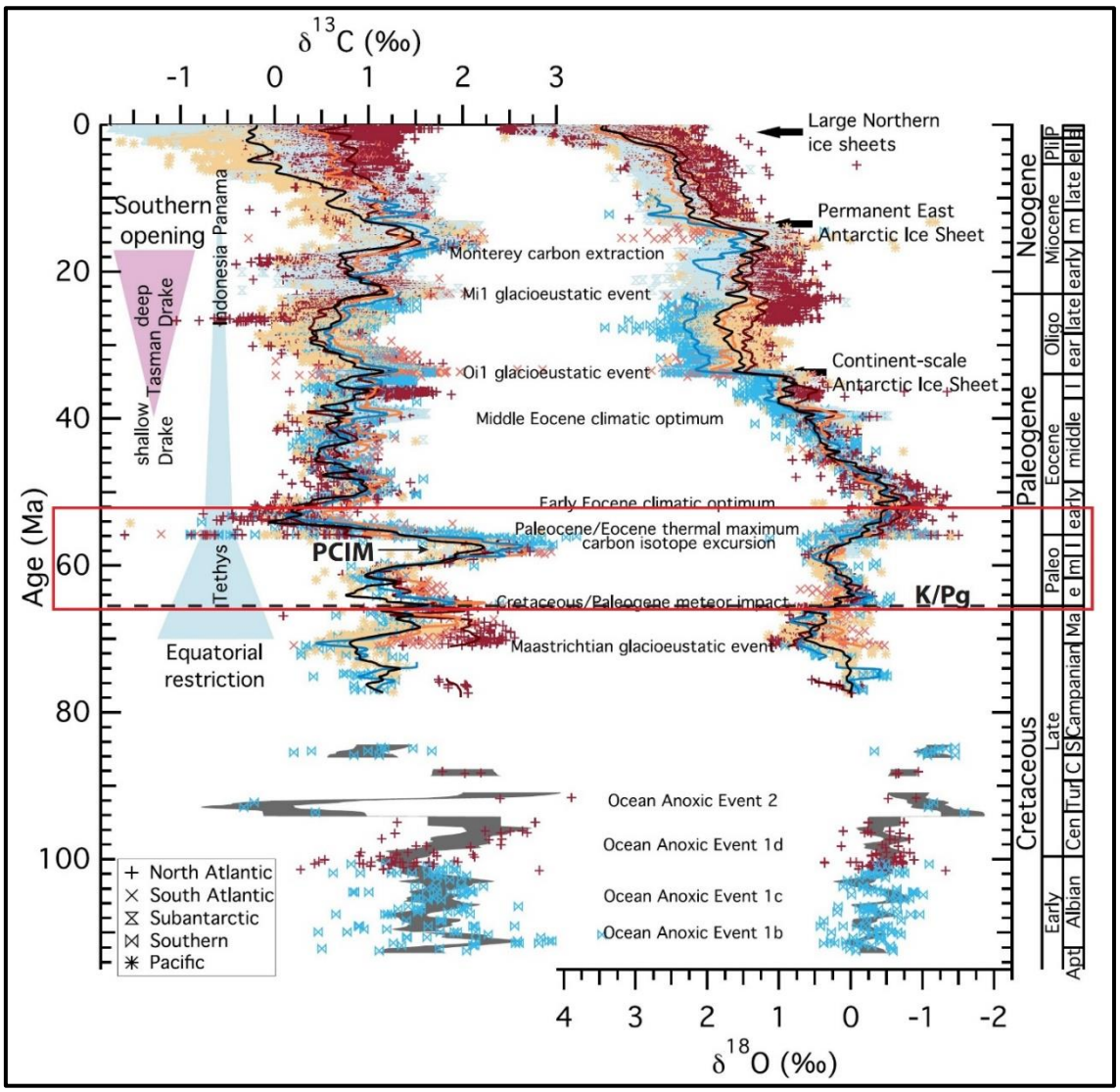

Figure 1. The spliced/stacked benthic stable carbon ($\delta^{13}C_{benthic}$) and benthic stable oxygen ($\delta^{18}O_{benthic}$) isotope records forming the basis for our understanding of Late Maastrichtian–early Paleogene carbon cycle and climate evolution to date (from Cramer et al., 2009). The Late Maastrichtian–Early Eocene, forming the focus for this thesis, is highlighted by the red box. Stratigraphic positions of the Cretaceous/Paleogene (K/Pg) boundary, Paleocene Carbon Isotope Maximum (PCIM), Paleocene-Eocene Thermal Maximum (PETM), and Early Eocene Climatic Optimum (EECO) are shown.

Superimposed on these longer-term variations were short-term orbitally-paced variations in climate and the carbon cycle, resulting in so-called transient "hyperthermal" events and smaller climatic perturbations. Paleogene hyperthermals were characterised by the release of massive quantities of greenhouse gases (either carbon dioxide or methane) over a geologically brief time period of 10's of thousands of years, rapid global warming at both the surface of the Earth and in the deep ocean, as well as ocean acidification and consequent

dissolution of deep-sea carbonates (e.g., Cramer et al., 2003; Zachos et al., 2005, 2010; McInerney & Wing, 2011). Recent studies have shown that these hyperthermals were a regular feature punctuating a dynamic early Paleogene climate and carbon cycle, with a defined periodicity paced by orbital forcing (e.g., Cramer et al., 2003; Lourens et al., 2005; Zachos et al., 2010; Littler et al., 2014; Figure 3a,b,c). Since they may represent the closest geological analogue for future anthropogenic climate change, the largest climatic events of the Early Eocene, such as the PETM and ETM-2, have been the focus for many palaeo-proxy (e.g., Zachos et al., 2003, 2005; Tripati & Elderfield, 2004, 2005; Sluijs et al., 2007a; McCarren et al., 2008; Stap et al., 2009, 2010; Penman et al., 2014; Babila et al., 2016, 2018; Gutjahr et al., 2017; Frieling et al., 2017; Harper et al., 2018) and modelling (e.g., Panchuk et al., 2008; Zeebe et al., 2009; DeConto et al., 2012; Sagoo et al., 2013; Bowen et al., 2015; Frieling et al., 2017; Carmichael et al., 2017; Cui & Schubert, 2017; Zeebe et al., 2017) studies.

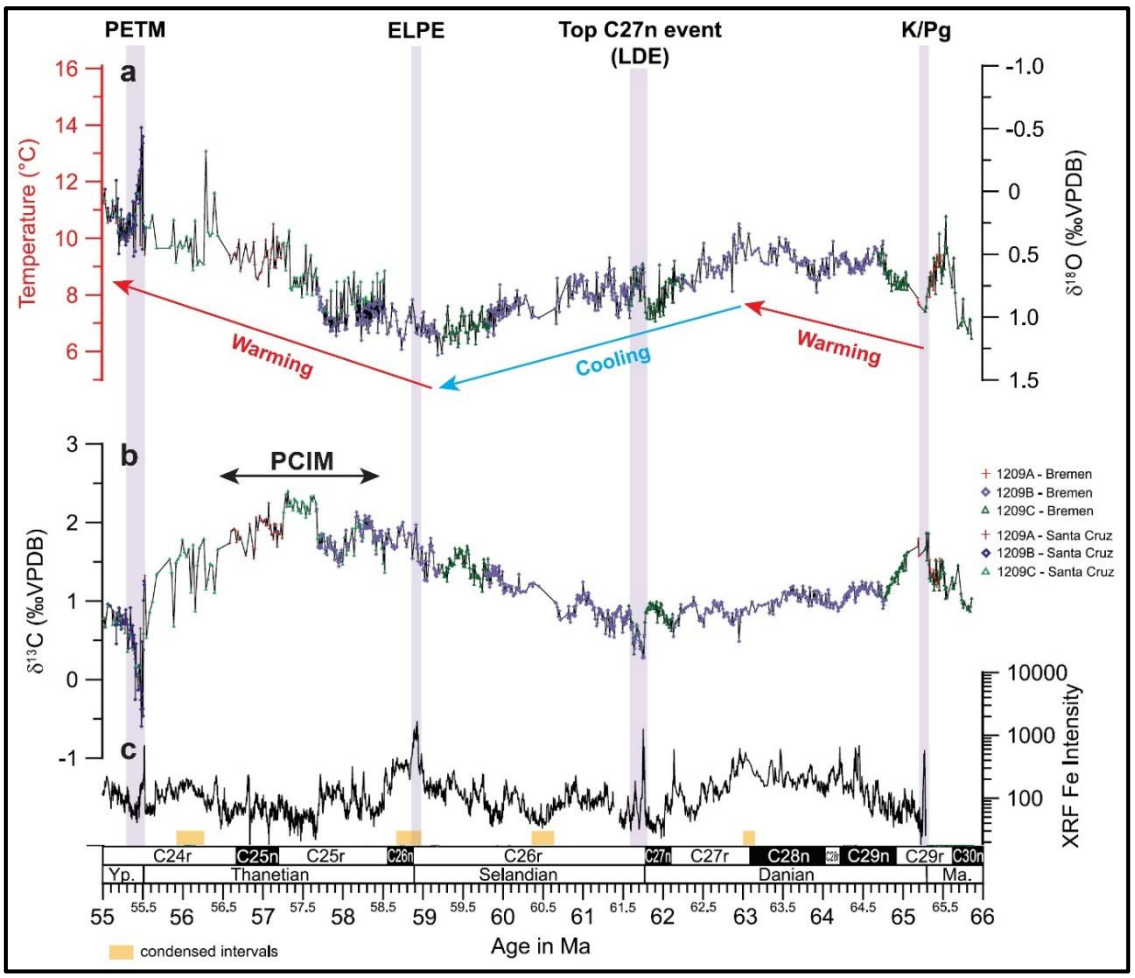

*Figure 2. Single-site benthic stable isotope and Fe intensity records spanning the Paleocene Epoch from equatorial Pacific ODP Site 1209 (figure modified from Westerhold et al., 2011): (**a**) benthic stable oxygen isotope ($\delta^{18}O_{benthic}$) record, with long-term climate trends indicated by coloured arrows; (**b**) benthic stable carbon isotope ($\delta^{13}C_{benthic}$) record, with position of the Paleocene Carbon Isotope Maximum (PCIM) indicated; (**c**) high-fidelity x-ray fluorescence (XRF)-core scanner derived Fe intensity record. Hiatuses and condensed intervals can be clearly seen in the benthic stable isotope records and are also indicated by orange bars at the base of the figure. Stratigraphic positions of the Cretaceous/Paleogene (K/Pg) boundary, Latest Danian Event (LDE), Early Late Paleocene Event (ELPE) and Paleocene-Eocene Thermal Maximum (PETM) are also shown.*

1.2.2. THE EVOLUTION OF PALEOGENE CYCLOSTRATIGRAPHIC STUDIES

The methodologies, techniques and orbital chronologies developed from Paleogene cyclostratigraphic studies have been refined significantly over the past 15 years. The orbital target curves (astronomical solutions) forming the basis for the development of these orbital chronologies from high-resolution sedimentary

successions have also evolved significantly over this time. Early studies were tuned to the La2004 orbital solution (Laskar et al., 2004), however more recent studies have been tuned to the significantly revised La2010(a-d) or La2011 solutions (Laskar et al., 2011a,b), whereby the integration of high-fidelity geological data such as benthic stable isotope or Fe intensity records are required to discrimate between the different orbital solutions beyond ~50 Ma (i.e., during the time interval considered in this thesis).

Early cyclostratigraphic studies focused specifically on the Late Paleocene–Early Eocene using spliced or stacked bulk carbonate carbon isotope ($\delta^{13}C_{bulk}$), colour reflectance, magnetic susceptibility, or Fe intensity records from multiple deep-sea cores (e.g., Cramer et al., 2003; Lourens et al., 2005; Westerhold et al., 2007). Whilst these studies identified orbital eccentricity (i.e., 100 and 400 kyr cycles) as the dominant pacemaker of climate and the carbon cycle during this time, undetected stratigraphic gaps and splicing errors created a number of inconsistencies between the resultant orbital chronologies. These inconsistencies were subsequently partially reconciled by the generation of single-site $\delta^{13}C_{bulk}$ and higher-fidelity X-ray fluorescence (XRF)-core scanner-derived Fe intensity and magnetic susceptibility records from stratigraphically complete Late Paleocene–Early Eocene successions from the South Atlantic (Walvis Ridge), equatorial Pacific (Shatsky Rise), and the North Atlantic margin at Zumaia, Spain (e.g., Westerhold et al., 2008; Zachos et al., 2010; Dinarès-Turell et al., 2014; Figure 2c; Figure 3e). These proxy records nevertheless have their associated limitations for constraining orbital-scale carbon cycle variability.

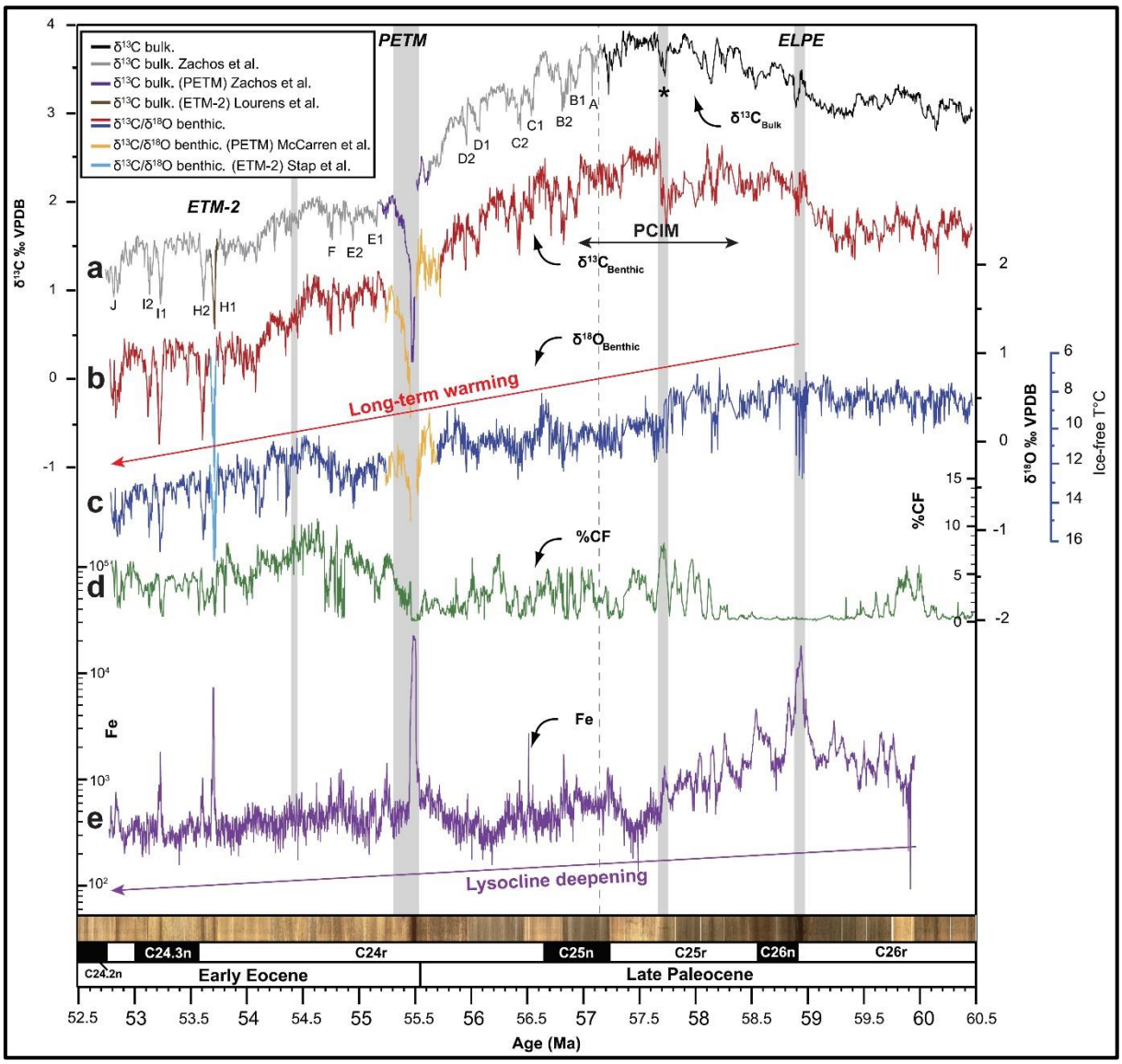

*Figure 3. Single-site high-resolution stable isotope and dissolution proxy records from South Atlantic ODP Site 1262 (figure modified from Littler et al., 2014): (**a**) bulk carbonate stable carbon isotope ($\delta^{13}C_{bulk}$) record; (**b**) benthic foraminiferal stable carbon isotope ($\delta^{13}C_{benthic}$) record, with position of the Paleocene Carbon Isotope Maximum (PCIM) indicated; (**c**) benthic foraminiferal stable oxygen isotope ($\delta^{18}O_{benthic}$) record, with the long-term Late Paleocene–Early Eocene warming trend shown; (**d**) % coarse fraction (% CF; >63 μm), largely composed of planktic foraminifera at this site; (**e**) x-ray fluorescence (XRF)-core scanner derived Fe intensity record, with the deepening Late Paleocene–Early Eocene lysocline trend illustrated (data from Westerhold et al., 2007, 2008). Sources of the raw stable isotope data are indicated in the box in the top left hand corner. Stratigraphic positions of the Early Late Paleocene Event (ELPE), Paleocene-Eocene Thermal Maximum (PETM), and Eocene Thermal Maximum 2 (ETM-2) are also indicated. The benthic stable isotope records from ODP Site 1262 are of much higher resolution and more stratigraphically complete compared to the temporally equivalent benthic records from equatorial Pacific ODP Site 1209 (Westerhold et al., 2011, 2018; Figure 2).*

XRF-derived Fe intensity, magnetic susceptibility, and colour reflectance records represent proxies for the concentration of terrigenous clays in marine cores, as these clays are relatively rich in Fe and magnetic minerals compared to biogenic oozes. Sediments deposited at low-mid latitude deep-sea sites above the CCD were dominated by calcareous biogenic oozes during the Paleogene, composed of the carbonate tests of foraminifera and calcareous nannoplankton. Cyclic increases in the relative abundance of terrigenous clays in these deep-sea sediments can therefore be used as a proxy for carbonate dissolution at the seafloor due to orbitally-paced shoaling of the lysocline and CCD. This lysocline and CCD shoaling could result from periodic increases in export productivity of C_{org} from the surface to deep ocean, and/or the transient release of isotopically light carbon from climate- or temperature-sensitive carbon reservoirs, in association with orbitally-induced variations in seasonal insolation (e.g., Westerhold et al., 2008). However, the relative abundance of clays in deep-sea sediments is also controlled by surface ocean biogenic carbonate productivity and/or shifts in the flux (riverine or aeolian) of terrigenous clays to the site of deposition. These competing variables can therefore significantly modify the relative abundance of clays in deep-sea sediments in the absence of carbonate dissolution, especially across major biotic events such as the K/Pg mass extinction, hampering interpretations of the shifting depth of the palaeo-lysocline and CCD using these XRF-derived proxies alone.

Similarly, interpretations of bulk carbonate stable isotope ($\delta^{13}C_{bulk}$ and $\delta^{18}O_{bulk}$) records can also produce an incoherent picture of changes to the global carbon cycle and climate. The composition of bulk carbonate contains a variety of different carbonate components, each carrying their own distinct stable isotope signal (due to differing species-specific vital effects or precipitation of carbonate tests at varying depths in the water column). Bulk carbonate records are therefore prone to containing some inherent “noise”, which may mask the amplitude or character of true global changes to the exogenic carbon cycle and climate. This is particularly exacerbated in long-term (multi-million year) records by the fact that these carbonate components often change temporally through the record, as a result of species extinctions, radiations, or selective dissolution of certain thinner-walled components (such as surface-dwelling nannofossils) during ocean acidification events associated with hyperthermals. Furthermore, $\delta^{18}O_{bulk}$ data in

particular can also be significantly biased by crystallisation of secondary diagenetic carbonate, either on the seafloor or during post-burial diagenesis, which has the potential to obliterate the primary stable isotope signal and limit the utility of $\delta^{18}O_{bulk}$ records for understanding the evolution of past climates. It is also not possible to obtain reliable palaeotemperature estimates from $\delta^{18}O_{bulk}$ records due to the mix of (multi-species) foraminifera and inorganic calcite in the bulk rock, thus further hampering our understanding of carbon-cycle–climate interactions using bulk carbonate geochemical proxies.

To overcome the limitations presented by examining long, composite, orbital-scale, stable isotope records generated from bulk sediments from the Paleogene, single-site, single-species benthic stable isotope records are required. Such records offer a much more accurate insight into the time-averaged magnitude and character of cyclic perturbations to the global carbon cycle and climate, without having to consider artefacts induced by changing carbonate components, vital effects, local surface water variability, and (to a certain extent) diagenesis. The first orbital-scale benthic stable isotope records for the entire Paleocene were constructed from equatorial Pacific ODP Site 1209 (Westerhold et al., 2011), which were subsequently extended into the Eocene up to ~45 Ma by Westerhold et al. (2018). These records offered hitherto unparalled insights into the orbital pacing of Paleocene climate and carbon-cycling, however, it became apparent that these cores also contain a number of hiatuses and condensed intervals (Figure 2a,b). Furthermore, with scant high-resolution benthic stable isotope data from the other major ocean basins, there is little basis to confirm whether the climate and carbon-cycle trends identified from the equatorial Pacific are indeed global in scale. As a consequence, attention turned to ODP Site 1262, where early Paleogene sedimentation rates on the Walvis Ridge were much higher (~0.4–1.4 cm/kyr; Shipboard Scientific Party, 2004a) than at ODP Site 1209 (~0.1–0.5 cm/kyr; Shipboard Scientific Party, 2002a). The utility of ODP Site 1262 for orbital-resolution benthic stable isotope cyclostratigraphic studies was demonstrated by Littler et al. (2014), which presented a high-resolution (2–4 kyr) benthic stable isotope record for the Late Paleocene–Early Eocene (Figure 3b,c).

Whilst the majority of Paleogene cyclostratigraphic studies have focused on the time period containing the largest and most frequent hyperthermal events, the enigmatic Late Paleocene–Early Eocene (e.g., Westerhold et al., 2007; Zachos et al., 2010; Kirtland Turner et al., 2014; Littler et al., 2014; Figure 3b,c), comparatively few studies have focused on the preceding Early–Middle Paleocene or Late Maastrichtian. Scant knowledge therefore also exists on ambient climate evolution between the K/Pg mass extinction and the well-studied hyperthermals of the Late Paleocene–Early Eocene, during the build-up to peak greenhouse conditions of the Paleogene achieved during EECO (52–50 Ma; Zachos et al., 2001, 2008; Cramer et al., 2009; Figure 1). Without a sound knowledge of their context with respect to ambient long-term (multi-million year) climate and carbon-cycle variability of the time, it is therefore difficult to assess how appropriate an analogue the well-studied hyperthermal events of the Late Paleocene–Early Eocene are for future anthropogenic climate change.

2. MATERIALS AND METHODS

This chapter describes in detail the sample locations, lithostratigraphy of the sampled sites, nature of samples and sampling strategy used in this thesis, as well as the sedimentological and geochemical methods applied to these samples. Methodology pertaining to data processing (e.g., spectral analysis) and calibration (e.g., to temperature or carbonate chemistry) is outlined in the results sections of the respective chapters where the data are presented. Where collaborators have assisted with data generation or the supervision of labwork, this has been acknowledged.

2.1. SITES AND SITE LOCATIONS

Core samples were taken from three sites for use in this project, two from the Ocean Drilling Program (ODP) and one from its successor, the International Ocean Discovery Program (IODP). The locations of these sites are illustrated in Figure 4. The past and present characteristics for each site are listed in Table 1.

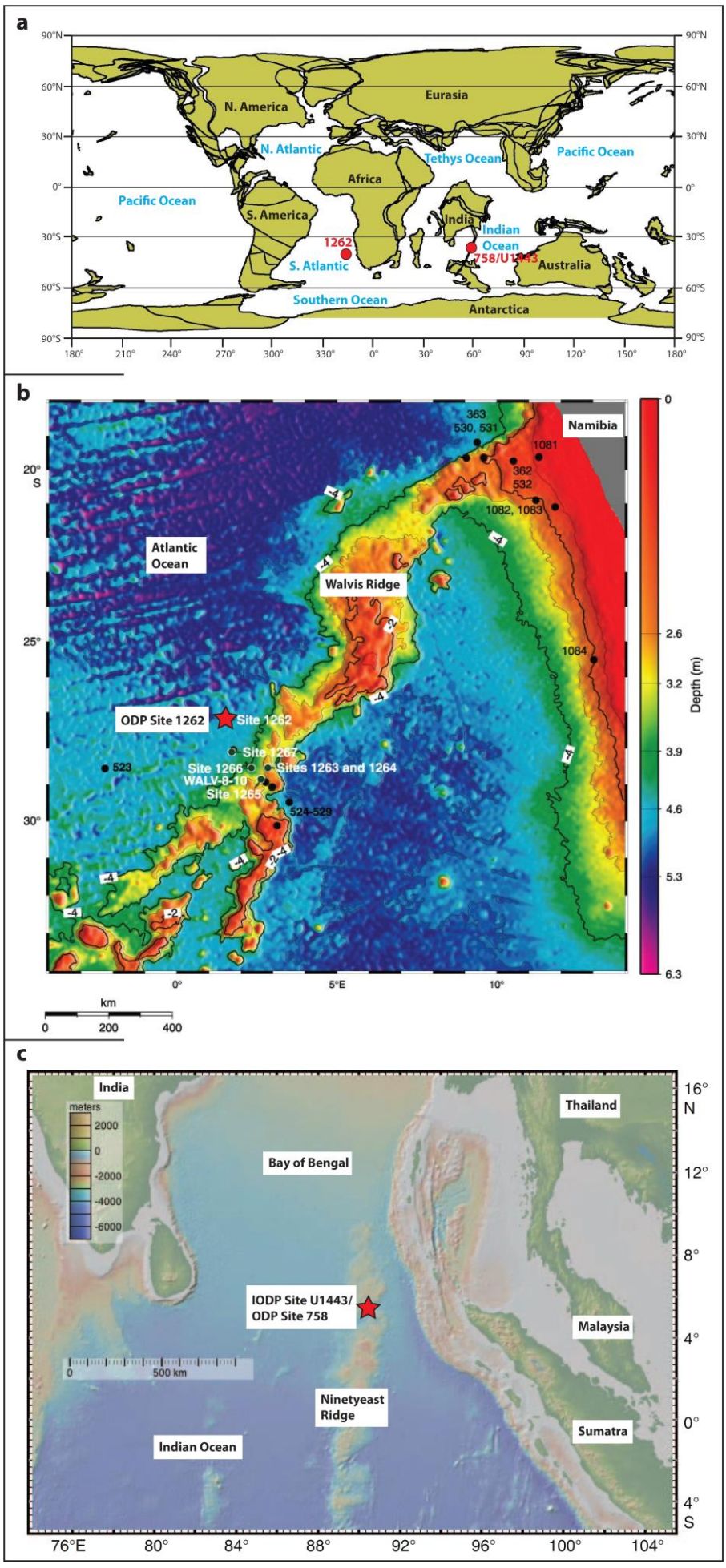
a
N. America
Eurasia
N. Atlantic
Tethys Ocean
Pacific Ocean
Africa
Pacific Ocean
S. America
India
Indian Ocean
1262
S. Atlantic
758/U1443
Australia
Southern Ocean
Antarctica
b
363
530, 531
Namibia
1081
362
532
1082, 1083
Atlantic Ocean
Walvis Ridge
1084
ODP Site 1262
Site 1262
Site 1267
Site 1266
Sites 1263 and 1264
WALV-8-10
Site 1265
523
524-529
Depth (m)
km
c
India
meters
Thailand
Bay of Bengal
IODP Site U1443/
ODP Site 758
Malaysia
500 km
Ninetyeast Ridge
Sumatra
Indian Ocean

*Figure 4 (previous page). Locations of ODP Site 1262, ODP Site 758 and IODP Site U1443; the sites used in this study. (**a**) Palaeogeographic reconstruction for the Cretaceous/Paleogene (K/Pg) boundary (66 Ma) with the locations of sites used in this study. Adapted from the Ocean Drilling Stratigraphic Network (ODSN) Paleomap Project (http://www.odsn.de/odsn/services/paleomap/paleomap.html). (**b**) Location of ODP Site 1262 on a zoomed in present-day bathymetric map of the south-east Atlantic (from Shipboard Scientific Party, 2004b). (**c**) Locations of ODP Site 758 and IODP Site U1443 on a present-day bathymetric map of the northern Indian Ocean and surrounding landmasses (from Shipboard Scientific Party, 2016).*

Table 1

Site	Lat.	Long.	Palaeo-lat at K/Pg boundary (~66 Ma)	Palaeo-lat at PETM (~56 Ma)	Water depth (m)	Palaeo-water depth (m)	Geochemical techniques	Studied interval & no. of samples
ODP Site 1262	27.2°S	1.6°E	40.3°S	40.6°S	4759	3000–3500	$\delta^{13}C_{benthic}$ $\delta^{18}O_{benthic}$ $\delta^{13}C_{planktic}$ $\delta^{18}O_{planktic}$ % coarse fraction	Late Maastrichtian–Early Eocene (~67.1–52.35 Ma) 1,599 samples
ODP Site 758	5.4°N	90.4°E	43.6°S	28.6°S	2923.6	1500	$\delta^{13}C_{bulk}$ $\delta^{13}C_{planktic}$ $\delta^{18}O_{planktic}$ Mg/Ca B/Ca	Late Paleocene (~57.3–56.4 Ma) 85 samples
IODP Site U1443	5.4°N	90.4°E	43.6°S	28.6°S	2929.4	1500	$\delta^{13}C_{bulk}$ $\delta^{13}C_{planktic}$ $\delta^{18}O_{planktic}$ Mg/Ca B/Ca	Late Paleocene–Early Eocene (~59–53 Ma) 216 samples

Site summaries. Present-day latitudes, longitudes, water depths, and palaeo-water depths during the Late Maastrichtian–early Paleogene are from the initial scientific reports for each site (Shipboard Scientific Party, 2004a, 1989, and 2016). Palaeo-latitudes for each site at the Cretaceous/Paleogene (K/Pg) boundary (~66 Ma) and Paleocene-Eocene Thermal Maximum (PETM; ~56 Ma) were computed relative to the palaeomagnetic reference frame of Torsvik et al. (2012) using Version 2.1 of the model from paleolatitude.org (van Hinsbergen et al., 2015). The geochemical techniques applied to samples from these cores during this study are listed in the right-hand column.

2.1.1. ODP SITE 1262

Samples used to generate the high-resolution benthic stable carbon isotope ($\delta^{13}C_{benthic}$) and benthic stable oxygen isotope ($\delta^{18}O_{benthic}$) records in this

thesis were taken from ODP Site 1262, the deepest of six sites drilled during a depth transect across the South Atlantic Walvis Ridge during ODP Leg 208 (Shipboard Scientific Party, 2004a; Figure 4b). ODP Site 1262 is located in the Angola Basin near the base of the north-western flank of Walvis Ridge, at a present-day water depth of 4759 m (Table 1; Figure 4b). The palaeo-water depth of the site deepened from ~3000 m during the Late Maastrichtian to ~3500 m during the Early Eocene (Shipboard Scientific Party, 2004a; Table 1), making the site a useful recorder for fluctuations in the latest Cretaceous to early Paleogene lysocline and CCD in the South Atlantic. The principle objective of the site was to recover a complete stratigraphic section across the Cretaceous-Paleogene (K/Pg) boundary and through the transient warming events ("hyperthermals") of the early Paleogene, including the PETM. Based on seismic data and the neighbouring older DSDP Sites 527 and 523, the site was positioned in a perched basin where an expanded sequence of Late Maastrichtian–Early Eocene calcareous marine sediments was predicted beneath a condensed (~100 m-thick) Neogene cover. Three holes were drilled using the Advanced Piston Corer (APC) method (1262A, 1262B, and 1262C), with a stratigraphically complete Late Maastrichtian–Early Eocene splice generated that incorporates the three holes. The expanded and stratigraphically complete sedimentary record from ODP Site 1262 therefore represents a valuable opportunity to examine the biotic and climatic response to critical events of the Late Cretaceous–early Paleogene in the deep South Atlantic at orbital-resolution.

2.1.2. ODP SITE 758 AND IODP SITE U1443

Samples used to generate the Late Paleocene–Early Eocene trace metal proxy (Mg/Ca and B/Ca) records presented in this thesis were taken from ODP Site 758 and IODP Site U1443. IODP Site U1443 (IODP Expedition 353; Shipboard Scientific Party, 2016) is a redrill of ODP Site 758 (ODP Expedition 121; Shipboard Scientific Party, 1989) and is located ~100 m to the south-east on the crest of the Ninetyeast Ridge (Figure 4c). The sites were drilled at a present-day water depth of ~2924–2929 m, but were located at a palaeo-water depth of ~1500 m during the early Paleogene (Table 1; Figure 4c). Planktic foraminifera were therefore deposited well above the Paleogene CCD in this region (~4,000 m depth; Slotnick et al., 2015). The generally good preservation

of planktic foraminifera relative to other deep ocean sites makes these sites ideal for applying trace metal proxies to reconstruct absolute temperature estimates and changes in carbonate chemistry (related to pH) during the early Paleogene. Previous work has produced only low-resolution foraminiferal stable isotope data from this site, and only from a limited number of foraminifera species (Zachos et al., 1992).

Although ODP Site 758 is a key Neogene site, being one of only two Indian Ocean sites in the "LR04 stack" (Lisiecki and Raymo, 2005), the Paleogene strata at this site was found to be stratigraphically incomplete with a number of unconformities and condensed intervals. Only three holes in total from both sites penetrated to the Paleocene (758A, U1443A, and U1443B). The Extended Core Barrel (XCB) method was used to penetrate the Paleogene at both sites, generating a biscuited core and further hampering the recovery of complete Paleogene stratigraphies from both sites.

2.2. LITHOSTRATIGRAPHY

2.2.1. ODP SITE 1262

The three holes at ODP Site 1262 penetrated an expanded ~140 m-thick Maastrichtian–Early Eocene section of nannofossil ooze and clayey nannofossil ooze, overlain by a more condensed ~100 m of Middle Eocene–Pleistocene clays, nannofossil clays and nannofossil oozes (Shipboard Scientific Party, 2004a). The expanded Late Maastrichian–Early Eocene interval can be subdivided into a more clay-rich Maastrichtian–Late Paleocene section and a purer nannofossil ooze within the Late Paleocene–Early Eocene. A complete K/Pg boundary section was recovered and correlated between Holes 1262B and 1262C, where the boundary represents a sharp contact between an expanded sequence of carbonate-rich, clay-bearing nannofossil ooze with foraminifers below, to more condensed nannofossil- and foraminifera-bearing clays above (Figure 5). Clay content generally decreases upward through the Paleocene section within the ODP Site 1262 cores, becoming a pure nannofossil ooze by the Late Paleocene (Shipboard Scientific Party, 2004a). Due to the relatively deep palaeo-depth of the site (deepening from ~3000 m during the Late

Maastrichtian to ~3500 m by the Early Eocene), sediments were at times deposited below the lysocline, as well as close to or below the CCD during the largest hyperthermal events such as the PETM (Shipboard Scientific Party, 2004a; Zachos et al., 2005; Kroon et al., 2007). The site is therefore a particularly sensitive recorder of the transient shoaling of the lysocline and CCD during early Paleogene hyperthermal events. For example, the Paleocene/Eocene boundary is marked by a sharp contact between nannofossil ooze below and red haematitic and ash-bearing clay above, deposited in response to severe carbonate dissolution at the site during the PETM (Zachos et al., 2005; Figure 6).

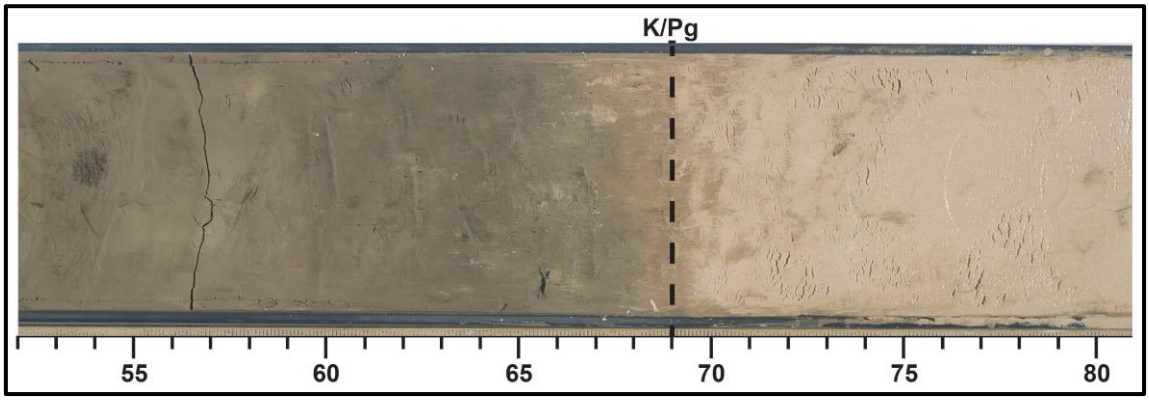

Figure 5. Photograph of the lithological change across the Cretaceous/Paleogene (K/Pg) boundary preserved at 69 cm depth in Core 1262-C-13-H-2, illustrating the abrupt transition from pale grey Late Maastrichtian clay-bearing nannofossil ooze below (to the right) to brown nannofossil- and foraminifera-bearing clays above (to the left) at ODP Site 1262. Scale bar indicates depth within the core section in cm. Photograph from Shipboard Scientific Party (2004a).

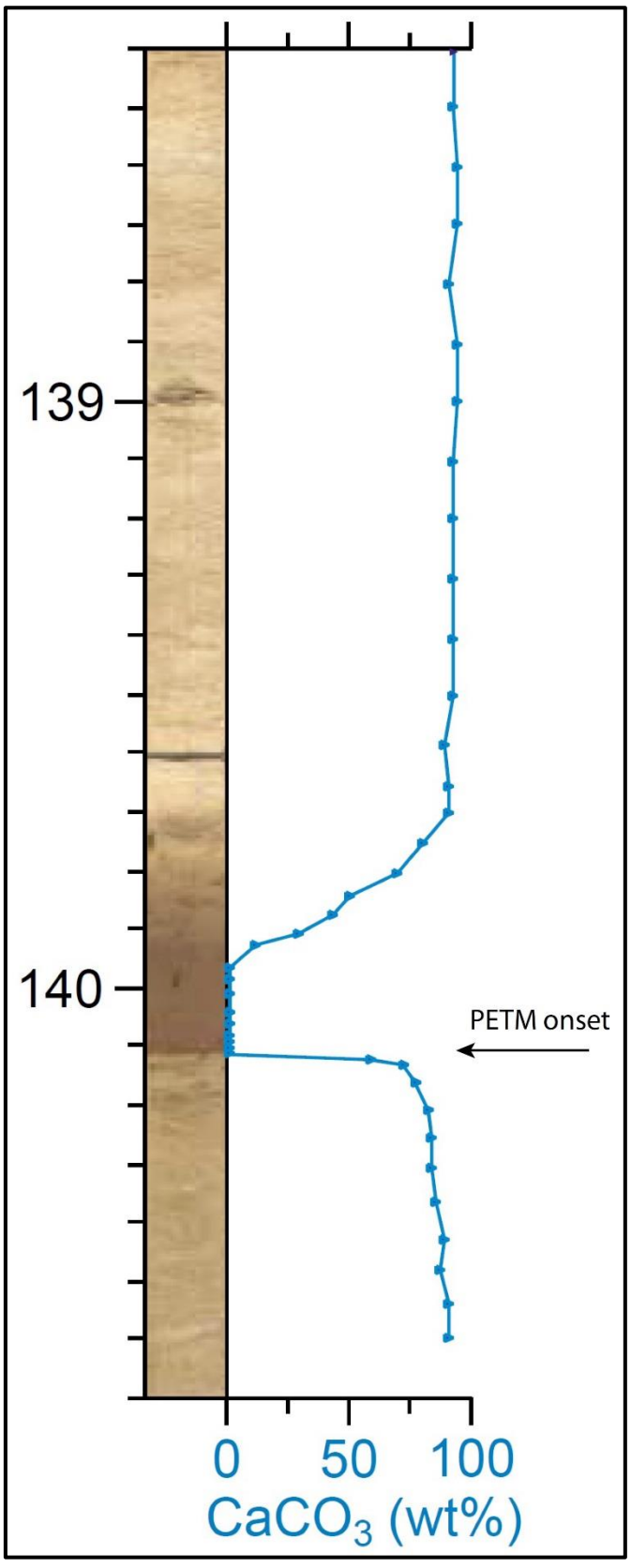

Figure 6. Core photograph and carbonate dissolution proxy data (% calcium carbonate; $CaCO_3$) across the Paleocene-Eocene Thermal Maximum (PETM) at ODP Site 1262, illustrating the transition from nannofossil ooze below to red haematitic clay almost devoid of carbonate during the event (Zachos et al., 2005).

2.2.2. ODP SITE 758 AND IODP SITE U1443

At both ODP Site 758 and IODP Site U1443, the lithostratigraphy consists of Campanian–Maastrichtian glauconitic marlstone, Late Maastrichtian–Late Oligocene calcareous and nannofossil chalk, and Late Oligocene–Recent nannofossil ooze, all overlying Late Cretaceous basaltic basement (Shipboard Scientific Party, 1989, 2016; Figure 7). Clay content generally increases upwards and is highest within the Plio-Pleistocene succession.

At IODP Site U1443, the Early, Middle and Late Paleocene are represented by a ~40 m-thick sequence of nannofossil chalk, but with significant gaps in recovery between Cores 35X, 36X and 37X in IODP Hole U1443A, and stratigraphically equivalent Cores 33X and 34X in IODP Hole U1443B, leading to some missing sections of Late Paleocene stratigraphy which were not recovered at IODP Site U1443 (Figure 7). This missing stratigraphy, however, does appear to have been recovered within Core 28X at ODP Hole 758A, based on shipboard biostratigraphy (Shipboard Scientific Party, 1989). By contrast, based on the preliminary shipboard biostratigraphy, the Eocene stratigraphy is extremely condensed at both sites and comprises a total stratigraphic thickness of only ~1.2 m (Figure 7). A K/Pg boundary section was recovered within Core U1443A-39X, however, is highly bioturbated and is considered to be incomplete (Shipboard Scientific Party, 2016).

The Late Paleocene–Early Eocene chalk occurs as 2–12 cm-long discrete drilling biscuits surrounded by 1–10 cm of drilling slurry. The biscuits can be differentiated from the slurry by their generally paler colour, more lithified texture, and rounded outline (Figure 8). According to the initial scientific reports for each site, planktic foraminifera are well-preserved throughout the Paleocene sequence, whilst calcareous nannofossils are moderate- to well-preserved (Shipboard Scientific Party, 1989, 2016).

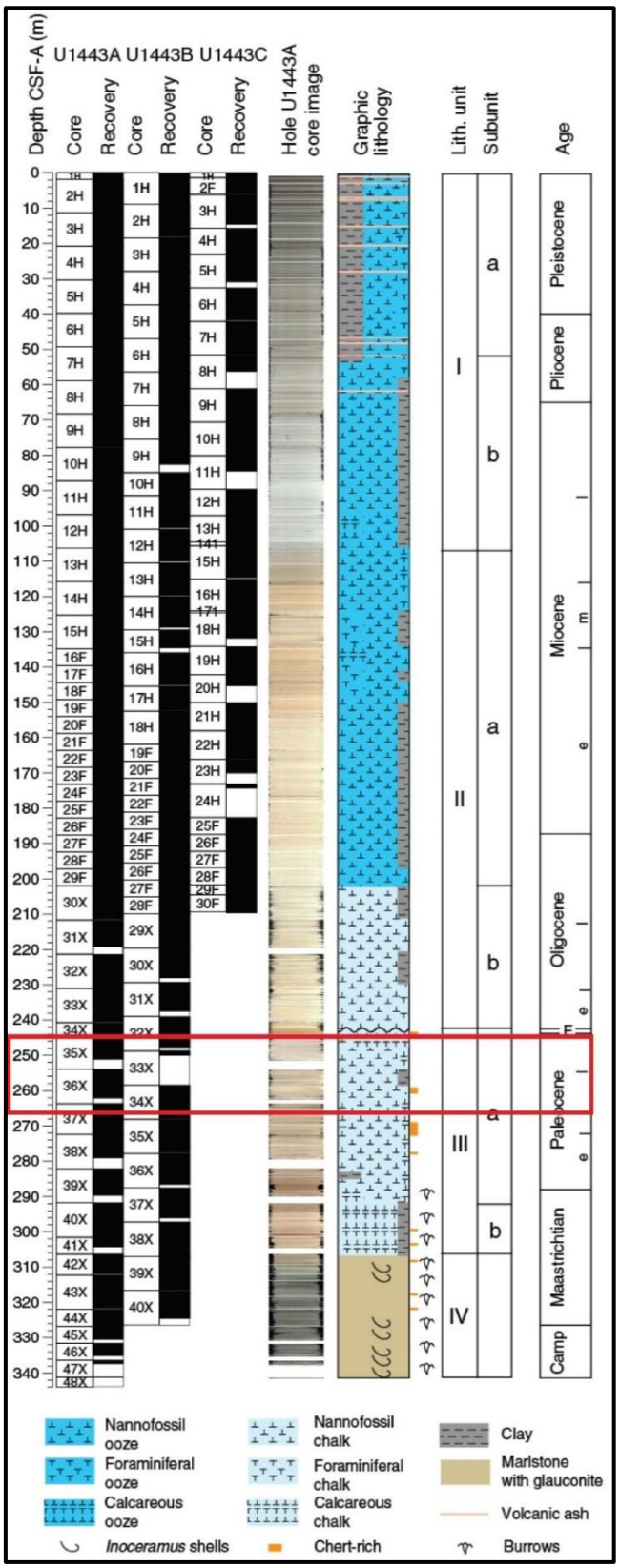

Figure 7. Lithostratigraphy of Indian Ocean Ninetyeast Ridge IODP Site U1443 and core recovery from U1443A, U1443B and U1443C (black shading indicates recovered core sections). The study interval is framed by a red box. Note the core gap between 35X and 36X in IODP Hole U1443A, which is encompassed within a larger section of missing stratigraphy in IODP Hole U1443B. Figure from Shipboard Scientific Party (2016).

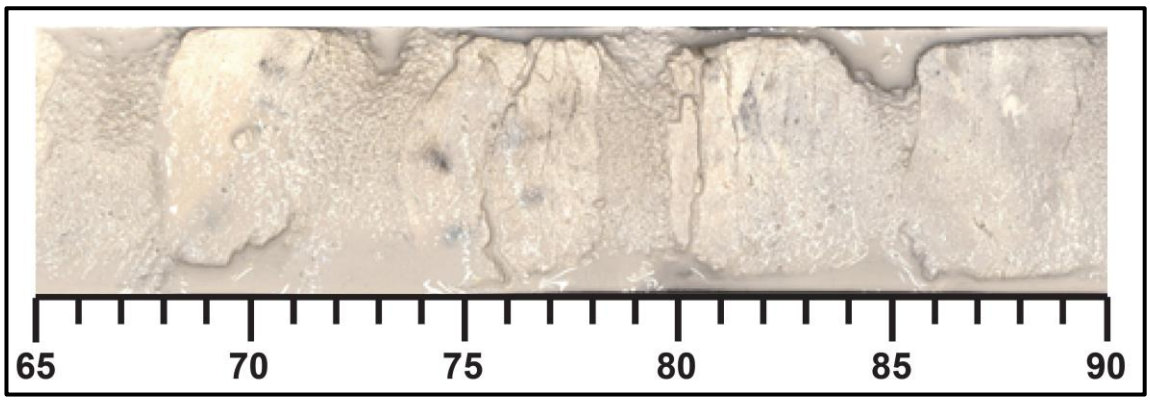

Figure 8. Photograph of a section of Core U1443A-35X-1 (65–90 cm), illustrating the biscuited nature of the cores from ODP/IODP Holes 758A and U1443A. Core biscuits are distinguished by their paler colour, rounded outline and more lithified texture, and are surrounded by drilling slurry. Scale at the bottom of the figure represents the depth in core (in cm). Photograph taken from the LIMS Online Report (LORE) portal website: http://web.iodp.tamu.edu/LORE/.

2.3. SAMPLES

2.3.1. ODP SITE 1262

The bulk of the core samples from ODP Site 1262 were taken by Prof. Kroon from the primary splice during the initial sample party at the Bremen Core Repository (BCR) in 2004, then subsequently washed and sieved by Prof. Kroon, with the >63 µm coarse fraction stored at the University of Edinburgh. I collected these coarse fraction samples from the University of Edinburgh at the start of my PhD studentship in September 2014. Prof. Kroon and I made a further trip to the BCR in June 2015 to resample sections of core from which samples in the initial set had been depleted for other analyses, in particular focusing on the Early Paleocene section immediately post-dating the K/Pg boundary.

1,599 samples, each with a volume of ~10 cubic centimetres (cc), were taken for benthic stable isotope analysis from the ODP Site 1262 splice. These samples span ODP Holes 1262B (Core 19H–23H) and 1262C (Core 10H–14H) between 184.865 and 236.075 metres composite depth (mcd), and correspond to the Late Maastrichtian to Middle Paleocene. Samples were taken at 3 cm intervals from 184.865 to 214.54 mcd (Early–Middle Paleocene) and 216.73-236.07 mcd (Late Maastrichtian), but the resolution was increased to 1 cm

spacing within the condensed, clay-rich earliest Paleocene interval immediately post-dating the K/Pg boundary (214.54–216.73 mcd). This sampling procedure yields a temporal resolution of ~1.5–4 kyr throughout the record (based on the orbitally-tuned age model generated during this study; **Chapter 3**), sufficient to reliably resolve down to 21-kyr precession cyclicity. Despite condensed intervals within parts of the Late Maastrichtian–Middle Paleocene record, there is no clear evidence of significant bioturbation (i.e., mottling or burrow structures) within the ODP Site 1262 cores sampled during this study (Figure 5). However, the possibility for bioturbation cannot be excluded from the condensed dark clay-rich interval immediately post-dating the K/Pg boundary. Due to deposition at lower bathyal water depths (~3000–3500 m) during the Late Maastrichtian–early Paleogene, trace fossils within the ODP Site 1262 cores would be dominated by the *Zoophycos* ichnofacies, characterised predominantly by horizontal patterned feeding traces with limited vertical penetration (Seilacher, 1967). As a result, the impact of bioturbation on sample resolution at the centimetre scale is expected to be negligible.

2.3.2. IODP SITE U1443

216 samples, each with a volume of ~15 cc, were taken from Cores U1443A-35X, U1443A-36X and Sections 1–2 of Core U1443A-37X, corresponding to 244.945–265.595 metres core depth below sea floor (CSF-A). These samples encompass the Late Paleocene–Early Eocene based on shipboard biostratigraphy data (Shipboard Scientific Party, 2016). Samples were requested from each easily identifiable core biscuit at ~5–10 cm intervals, and care was taken to avoid sampling the drilling slurry. With a mean Maastrichtian–early Paleogene sedimentation rate of ~0.36 cm/kyr (Shipboard Scientific Party, 2016), this sampling procedure yields a temporal resolution of ~14–28 kyr, sufficient to resolve short (100-kyr) and long (405-kyr) eccentricity cycles within the record if present, but not precession (~21 kyr). These samples were requested online by myself, then sampled by Dr. Littler and other members of the shipboard scientific party at the Kochi Core Center (KCC) in October 2015.

2.3.3. ODP SITE 758

Due to a coring gap between IODP Cores U1443A-35X and U1443A-36X, and a larger coring gap encompassing this stratigraphic interval in IODP Hole U1443B (see Figure 7), 85 samples, each with a volume of ~15 cc, were taken from ODP Core 758A-28X Sections 1–7 between 257.05–266.04 metres below sea floor (mbsf) and corresponding to the Late Paleocene, to splice in to fill the gap in the IODP Site U1443A record. The sampling interval was chosen following the calcareous nannofossil biostratigraphy as described in Shipboard Scientific Party (1989), and the low-resolution carbon isotope stratigraphy previously generated for this site (Zachos et al., 1992). Samples were taken from each easily identifiable core biscuit at ~5–15 cm intervals, typically identified by their lighter colour and more lithified texture. Assuming a mean Maastrichtian–early Paleogene sedimentation rate of ~0.36 cm/kyr (Shipboard Scientific Party, 2016), this sampling procedure yields a temporal resolution of ~14–42 kyr, sufficient to resolve short (100-kyr) and long (405-kyr) eccentricity cycles within the record. These samples were requested from the KCC online by myself, sampled by KCC staff, and despatched by post.

2.4. SEDIMENTOLOGICAL, PALAEONTOLOGICAL AND GEOCHEMICAL METHODS FOR ODP SITE 1262 SAMPLES

2.4.1. SAMPLE PREPARATION

Samples were firstly oven-dried at 50°C for 2–3 days and then weighed to obtain a bulk dry weight for each sample. Samples were then soaked in a cold Calgon [buffered sodium hexametaphosphate; $(NaPO_3)_6$] solution for 12–24 hours to disaggregate, followed by sieving through a 63 μm sieve to remove fine clay particles and nannofossils. The sieved sample was then soaked in cold Calgon solution for a second time and placed on a shaker table for 2 hours at 200 rpm to remove any further fine particles attached to the foraminifera tests, followed by further sieving through a 63 μm sieve. Samples were then dried on filter paper at room temperature and weighed again to obtain a weight of the dried >63 μm coarse fraction. Following weighing, the coarse fractions were decanted into labeled glass vials.

2.4.2. BENTHIC FORAMINIFERA PICKING AND PREPARATION

Specimens of the cosmopolitan epifaunal benthic foraminifera species *Nuttallides truempyi* were picked from the >150 μm size fraction using a wet paintbrush under a Wild Heerbrugg binocular microscope at the University of Exeter. *N. truempyi* was picked because it is long-ranging, is often the most abundant epifaunal benthic species in the assemblage, and allows easy merging of the new Late Maastrichtian–Middle Paleocene benthic stable isotope data, generated during this study, with the existing Late Paleocene–Early Eocene records from ODP Site 1262 which also use *N. truempyi* (e.g., Littler et al., 2014). *N. truempyi* is considered to be in stable isotopic equilibrium with ocean bottom waters and therefore record time-averaged global variations in the carbon cycle ($\delta^{13}C$) and bottom water temperature ($\delta^{18}O$), removed from the effects of local and short-term fluctuations ("noise") recorded by surface water (planktic) foraminiferal data (Shackleton et al., 1984).

Tests of *N. truempyi* were picked in a sufficient number (n = 5–13) to yield 40–70 μg of material. Preference was given to using a larger number of smaller specimens from the 150–212 μm fraction, to homogenise any anomalous isotopic values from individual specimens. As far as possible, only complete specimens with unbroken chambers and lacking any obvious diagenetic overgrowths under optical light microscopy were selected for stable isotope analysis. A subset of *N. truempyi* specimens from three stratigraphic intervals (196.9, 215.19 and 235.5 mcd), corresponding to the Early Paleocene (~62.32 Ma), earliest Paleocene (~65.72 Ma) and Late Maastrichtian (~67.06 Ma), respectively, were selected for imaging using a Field Emission Gun Scanning Electron Microscope (FEG-SEM), to assess the preservation of primary benthic foraminiferal calcite across the record (Figure 9). Both whole specimens and test walls on crushed specimens were imaged to assess the degree of diagenetic recrystallisation of test surfaces and test walls. Whilst preservation is generally good for benthic foraminifera of this age, samples from ODP Site 1262 do exhibit some incipient recrystallisation of test surfaces, pores and primary wall structures. Recent studies (e.g., Edgar et al., 2013) have shown that such recrystallisation of benthic foraminiferal calcite has a negligible effect on primary $\delta^{13}C$ and $\delta^{18}O$ values due to recrystallisation at shallow burial depths (<100 m) in a very similar environment to that in which the

primary calcite was precipitated. The primary isotopic signature of these foraminifera has not therefore been significantly biased by burial diagenesis.

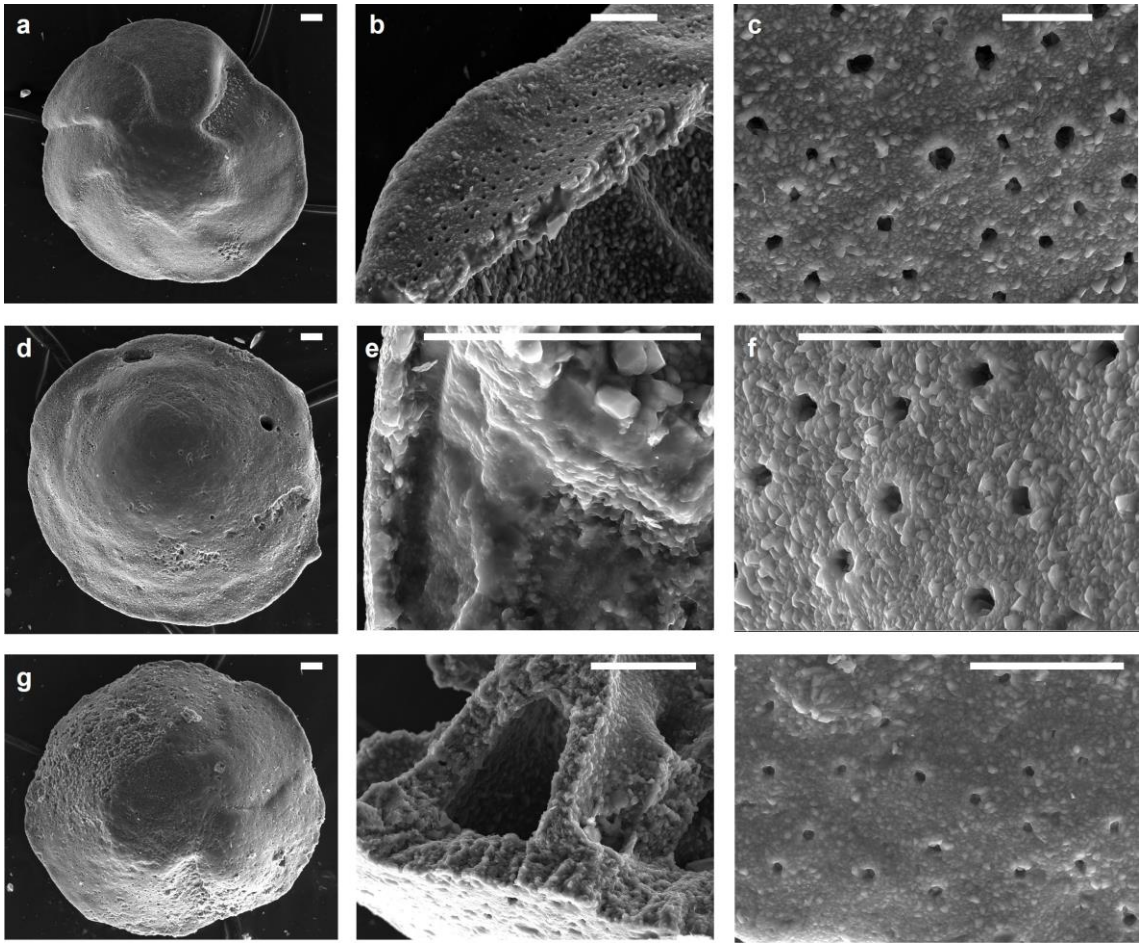

*Figure 9. Scanning Electron Microscope (SEM) images of Nuttallides truempyi from ODP Site 1262: (**a–c**) Late Danian [196.9 metres composite depth (mcd); ~62.32 Ma] tests illustrating whole specimen umbilical view (**a**); cross section of test wall (**b**); and pore structure (**c**); (**d–f**) earliest Danian (215.19 mcd; ~65.72 Ma) tests illustrating whole specimen spiral side (**d**); cross section of test wall (**e**); and pore structure (**f**); (**g–i**) Late Maastrichtian (235.5 mcd; ~67.06 Ma) tests illustrating whole specimen umbilical view (**g**); cross section of test wall (**h**); and pore structure (**i**). The white scale bar on each image represents 20 µm.*

2.4.3. GENERATION OF LATE MAASTRICHTIAN–MIDDLE PALEOCENE BENTHIC STABLE ISOTOPE DATA FROM ODP SITE 1262

Stable isotope data were generated at the Natural Environment Research Council (NERC) Isotope Geosciences Facility (NIGF) under the supervision of Prof. Melanie Leng and Hilary Sloane. Data were generated using an IsoPrime 100 Gas Source Isotope Ratio Mass Spectrometer in dual inlet mode equipped

with a Multiprep device. Samples were reacted with anhydrous phosphoric acid at 90°C, with isotopic measurements made on the cryogenically cleaned CO_2 gas produced. Replicate runs were performed on roughly every 1 in 10 samples (dependent on the sample being of sufficient size to run replicate analyses), to check for consistency, with the mean value from the replicate runs included in the final results. Samples that were "lost" during the first run (e.g., did not produce useable data) were re-run at a later date if sufficient sample was still available. Long-term analytical error (1σ) for the complete Late Maastrichtian–Middle Paleocene data set was 0.03 ‰ for $\delta^{13}C$ and 0.05 ‰ for $\delta^{18}O$. An internal standard, Keyworth Carrara Marble (KCM), calibrated against the international standard NBS-19, was used to place data on the Vienna Pee Dee Belemnite (VPDB) scale. These data are presented in their entirety in **Chapter 3**, with a focus on the Late Maastrichtian portion in **Chapter 4**, and the early Danian (Early Paleocene) section in **Chapter 5**.

2.4.4. PLANKTIC STABLE ISOTOPE DATA ACROSS THE DANIAN/SELANDIAN TRANSITION EVENT FROM ODP SITE 1262

To identify possible temperature and carbon cycle perturbations within the mixed layer above South Atlantic ODP Site 1262 during the Danian/Selandian Transition Event (D/STE), 30 stratigraphic horizons previously analysed for benthic stable isotopes were selected for planktic stable isotope analysis between 186.60 and 189.24 mcd (Core 1262C-10-H-3–5). These data are presented in **Chapter 3 Section 3.6.6**. Within this planktic stable isotope data set, sample resolution was increased from 15–20 cm before and after the event to 3–6 cm within the core of the isotope excursion, identified within the new benthic stable isotope data generated from this site during this study. The planktic foraminifera species *Morozovella conicotruncata* was picked for analysis. This species is amongst the most common in the sample set, and based on comparable relationships between $\delta^{13}C$, $\delta^{18}O$, and test size to modern photosymbiotic species and its better-studied ancestor *M. velascoensis*, is believed to have hosted algal symbionts and therefore must have been restricted to the photic zone (e.g., Olsson et al., 1999). Typically 6–8 specimens (~100 µg) were picked from the narrow 250–300 µm size fraction, to minimise the impact of size-related ontogenetic vital effects on our stable isotope data (e.g., Friedrich et

al., 2012). SEM images of representative samples across the D/STE (Figure 10) illustrate some diagenetic recrystallisation of test surfaces, pores and primary wall structures. However, as the degree of recrystallisation does not vary significantly across the sample set, the overall trends exhibited by the planktic isotope records are considered reliable.

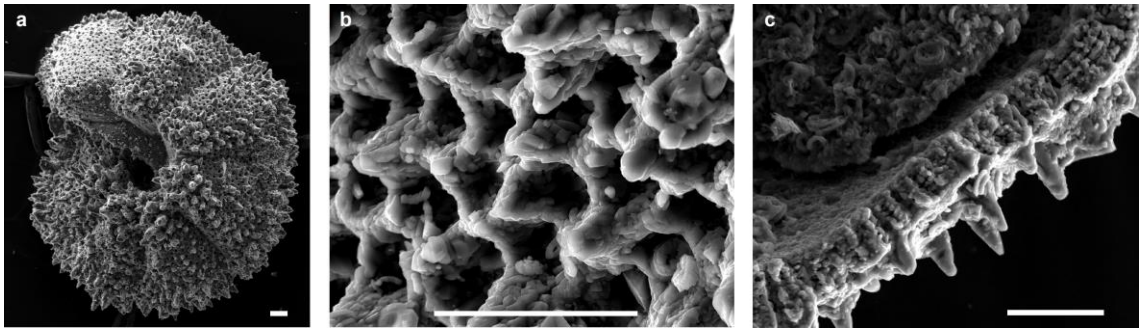

*Figure 10. Scanning Electron Microscope (SEM) images of Morozovella conicotruncata from South Atlantic ODP Site 1262: (**a**) Whole specimen spiral side (187.14 mcd; ~61.15 Ma); (**b**) pore structure (187.80 mcd; ~61.23 mcd); (**c**) cross section of test wall (187.14 mcd; ~61.15 Ma). The white scale bar on each image represents 20 µm.*

Planktic stable isotope data were generated on a Thermo Electron Delta+ Advantage Isotope Ratio Mass Spectrometer at the Wolfson Laboratory, School of Geosciences, University of Edinburgh. Samples were reacted with 100% orthophosphoric acid at 75°C in a Kiel Carbonate III preparation device, with isotopic measurements made on the CO_2 gas produced. Analytical error (1σ) for a powdered coral laboratory standard run on the day of analysis was 0.04 ‰ for both $\delta^{13}C$ and $\delta^{18}O$. Data are reported relative to the VPDB scale.

2.4.5. BENTHIC FORAMINIFERA ASSEMBLAGE ANALYSIS

Benthic foraminiferal assemblage analysis across the Dan-C2 event was performed by Dr. Gabriela de Jesús Arreguín-Rodríguez at the University of Zaragoza. Benthic foraminifera were analysed in 39 samples from 216.55–214.03 mcd (~66.01–65.46 Ma) at ODP Site 1262, incorporating 14 samples studied previously by Alegret & Thomas (2007). Sample resolution ranged from typically ~5–12 cm across the peak of the event to up to ~20 cm spacing within the recovery interval. Approximately 300 benthic foraminifera specimens were picked from the >63 µm fraction of each sample and identified following the

schemes of Van Morkhoven et al. (1986), Tappan & Loeblich (1988), Tjalsma and Lohmann (1983), and Alegret and Thomas (2001). For each sample, the relative abundance of each taxa, diversity (Fisher-α index), heterogeneity (Shannon-Weaver Index), agglutinated-calcareous ratio, infaunal-epifaunal ratio, and percentage of low-oxygen tolerant buliminids *sensu lato* were calculated (Van Morkhoven et al., 1986; Tappan & Loeblich, 1988; Tjalsma and Lohmann, 1983; Sen Gupta and Machain-Castillo, 1993; Alegret and Thomas, 2001).

The Shannon-Weaver Index for heterogeneity within a sample is defined as follows (Shannon & Weaver, 1949):

$$H = -\sum_s Ps * \log(Ps) \qquad \textit{[Eq. 1]}$$

where *H* is heterogeneity, *Ps* is the relative abundance of species *s* in the sample, and the summation is over the number of species in the sample. These data are presented in **Chapter 5**.

2.4.6. PERCENTAGE COARSE FRACTION

Percentage coarse fraction is a useful tracer for the shifting depth of the lysocline and CCD in pelagic sites, but the data are produced as a by-product of the sediment washing process. Weights (in grams) were routinely obtained for the dried bulk sample, prior to disaggregation in Calgon ($Bulk_w$), and the dried >63 μm coarse fraction sieved after disaggregation (CF_w). Percentage coarse fraction (*% CF*) was then calculated using the following formula:

$$\%\ CF = (CF_w/Bulk_w)*100 \qquad \textit{[Eq. 2]}$$

Percentage coarse fraction data across the Early Paleocene hyperthermal events and smaller climatic perturbations are presented in **Chapters 3** and **5**.

2.5. SEDIMENTOLOGICAL AND GEOCHEMICAL METHODS FOR IODP SITE U1443 AND ODP SITE 758 SAMPLES

2.5.1. BULK CARBONATE STABLE CARBON ISOTOPE ANALYSES AND PRELIMINARY CORRELATION BETWEEN IODP HOLE U1443A AND ODP HOLE 758A

To constrain the orbital and carbon isotope stratigraphy of the Late Paleocene–Early Eocene sample set from IODP Hole U1443A and ODP Hole 758A, firstly bulk carbonate stable carbon isotope ($\delta^{13}C_{bulk}$) data were generated for all samples between 244.945–258.655 m (CSF-A) from IODP Hole U1443A. Prior to analysis, samples were freeze-dried for 24–36 hours depending on their moisture content, then 30 mg of each sample was gently ground into a fine powder using a mortar and pestle. This first batch of $\delta^{13}C_{bulk}$ data were generated on a VG Optima Dual Inlet Mass Spectrometer at the NERC Isotope Geosciences Facility under the supervision of Prof. Melanie Leng, with technical support from Hilary Sloane. Powdered sample equivalent to 10 mg of pure calcite was reacted with anhydrous phosphoric acid at 25.2°C for 16 hours, with isotopic measurements made on the cryogenically cleaned CO_2 gas produced. Analytical error (1σ) for this sample set was 0.03 ‰ for $\delta^{13}C$. Replicate runs were performed on roughly every 1 in 10–15 samples and for apparent outliers, to check for consistency, with the mean value from the replicate runs included in the final results.

To fill the stratigraphic gap between Cores U1443A-35X and U1443A-36X (see Figure 7), $\delta^{13}C_{bulk}$ data were generated for all samples from ODP Hole 758A (257.045–266.035 mbsf) on a Sercon 20-22 Isotope Ratio Mass Spectrometer at the University of Exeter, with the assistance of Dr. Clemens Ullmann. For analysis on the Sercon 20-22, ~500–650 µg of sample was gently ground into a fine powder using a mortar and pestle then reacted with anhydrous phosphoric acid, with isotopic measurements made on the CO_2 gas produced. Average analytical error (2σ) for this sample set was 0.06 ‰ for $\delta^{13}C$.

A preliminary correlation between IODP Hole U1443A and ODP Hole 758A could then be performed based on bulk carbonate carbon isotope

stratigraphy. To confirm that the peak of the PCIM had been resolved within the $\delta^{13}C_{bulk}$ record, lower resolution $\delta^{13}C_{bulk}$ data (~5–24 cm) were also generated from 258.735–265.595 m (CSF-A) in IODP Hole U1443A at the University of Exeter on the Sercon 20-22, following the same procedure as described above. All $\delta^{13}C_{bulk}$ data from IODP Site U1443 and ODP Site 758 are presented in **Chapter 6** of this thesis.

2.5.2. CALCAREOUS NANNOPLANKTON AND PLANKTIC FORAMINIFERA BIOSTRATIGRAPHY

To refine and add confidence to the preliminary correlation between IODP Hole U1443A and ODP Hole 758A based on carbon isotope stratigraphy, as well as to correlate to the stratigraphically complete reference $\delta^{13}C_{bulk}$ record from ODP Site 1262 (Zachos et al., 2010; Littler et al., 2014; Chapter 3), high-resolution (~10–20 cm) calcareous nannoplankton biostratigraphy was performed by Dr. Leah LeVay (Texas A&M University) on samples washed and prepared by myself from both sites. Small toothpick samples were selected and split from existing larger samples and sent to Dr. LeVay. The calcareous nannoplankton zonal scheme of Agnini et al. (2007), generated from ODP Site 1262, was employed, which allowed zones NP6/CP5 to NP12/CP10 to be assigned. The age constraints provided by the calcareous nannofossils were supplemented with lower resolution (~12–100 cm) planktic foraminifera biostratigraphy for IODP Hole U1443A, performed by Dr. Kirsty Edgar (University of Birmingham), based on samples washed and prepared by myself. The zonal scheme of Wade et al. (2011) was applied, which allowed zones P4c to E4 to be assigned.

2.5.3. SAMPLE SELECTION AND PREPARATION FOR TRACE METAL (MG/CA AND B/CA) ANALYSIS

For trace metal (Mg/Ca and B/Ca) analysis, samples were selected from the peak and trough of each identifiable short (100-kyr) eccentricity cycle, as seen in the $\delta^{13}C_{bulk}$ data, from the peak of the PCIM (~58 Ma) to the Early Eocene (~53 Ma), thereby giving a temporal resolution within the trace metal records of ~50 kyr. These samples were disaggregated in cold Calgon solution and sieved

through a 63 µm sieve, following the same procedure as described above for the ODP Site 1262 samples in **Section 2.4.1.**

2.5.4. FORAMINIFERA PICKING AT IODP SITE U1443 AND ODP SITE 758

In order to examine temperature and carbonate chemistry (related to pH) variations in a depth transect through the water column above the Ninetyeast Ridge IODP/ODP Sites U1443 and 758, surface and thermocline-dwelling planktic foraminifera and benthic foraminifera were picked for trace metal analysis to record the properties of the mixed layer (<30 m), thermocline (~50–200 m), and intermediate waters on the crest of the Ninetyeast Ridge (palaeo-depth ~1500 m; Shipboard Scientific Party, 1989, 2016), respectively. These foraminifera were picked with a wet paintbrush using a Wild Heerbrugg binocular microscope. Mixed layer and subsurface (thermocline-dwelling) planktic foraminifera were picked from a narrow size range (≤50 µm), to minimise ontogenetic vital effects related to test size (e.g., Elderfield et al., 2002; Friedrich et al., 2012).

The following foraminifera species were picked for trace metal analysis:

- *Morozovella velascoensis* and *M. subbotinae-marginodentata plexus* were picked from the 250–300 µm fraction for mixed layer trace metal (Mg/Ca & B/Ca) data. Tests were picked in a sufficient number (n = 40–60) to yield 550–800 µg of material where possible, and permit two analyses per sample.

- *Subbotina velascoensis* and *S. hornibrooki* were picked from the 212–250 µm fraction for thermocline trace metal (Mg/Ca & B/Ca) data. Tests were picked in a sufficient number (n = 40–60) to yield 300–550 µg of material and permit one analysis per sample.

- The cosmopolitan epifaunal benthic species *Nuttallides truempyi* was picked from the >150 µm fraction to generate intermediate water B/Ca

data. A sufficient number of tests (n = 40–70) were picked to yield ~400–700 µg of material, where possible.

- The shallow infaunal benthic species *Oridorsalis umbonatus* was picked from the >150 µm fraction for intermediate water Mg/Ca data. A sufficient number of tests (n = 30–40) were picked where possible to yield ~300–400 µg of material to analyse for Mg/Ca. Where *O. umbonatus* was scarce within the older Late Paleocene portion of the sample set, 2–4 closely spaced samples were combined to yield sufficient material for analysis.

The rationale behind the choice of species is outlined in **Chapter 6 Section 6.4.2**. SEM photos of planktic foraminifera specimens, illustrating the preservation of primary calcite at the microscale, are included for three stratigraphic levels within the Late Paleocene–Early Eocene of the Indian Ocean cores in **Chapter 6 Section 6.6.2**.

2.5.5. GENERATION OF PLANKTIC STABLE ISOTOPE DATA FROM IODP/ODP SITES U1443/758

To more reliably correlate variations in planktic B/Ca to carbon cycle perturbations and estimate changes in salinity within the surface mixed layer, planktic stable carbon isotope ($\delta^{13}C_{planktic}$) and oxygen isotope ($\delta^{18}O_{planktic}$) data were also generated for each of the samples analysed for trace metals, respectively. Typically 6–8 specimens (~100–150 µg) of *M. velascoensis/M. subbotinae-marginodentata plexus* were picked from the narrow 250–300 µm size fraction, to minimise the impact of size-related ontogenetic vital effects on the stable isotope data (e.g., Friedrich et al., 2012). Planktic stable isotope data were generated on a Thermo Finnigan MAT 253 Isotope Ratio Mass Spectrometer equipped with a Kiel IV Carbonate Preparation Device at Cardiff University, with long-term analytical precision of 0.02 ‰ for $\delta^{13}C$ and 0.03 ‰ for $\delta^{18}O$ (1σ).

2.5.6. CRUSHING AND CLEANING OF IODP SITE U1443 AND ODP SITE 758 FORAMINIFERAL SAMPLES AT THE UNIVERSITY OF CALIFORNIA SANTA CRUZ

A strict crushing and cleaning protocol was carried out in the trace metal clean lab at the Department of Earth and Planetary Sciences, University of California Santa Cruz (UCSC), by myself under the supervision of Mr. Dustin Harper and Prof. James Zachos. The specific cleaning protocol employed at UCSC follows a modified version of the Boyle & Keigwin (1985/86) method, and is outlined below:

- Foraminifera were gently crushed between two clean glass plates, sufficient to crack open and expose all chambers to the cleaning fluids.

- Samples were firstly cleaned ultrasonically three times in boron-clean Milli-Q water, followed by two times in methanol, then another three times in distilled water, syphoning the solution off each time between rinses. This process removes clays and fine-grained carbonate particles attached to the tests.

- Surface ferromanganese oxide contaminants were removed from the test walls by a reductive cleaning procedure, involving 30 minutes in 100 µl of a hot, but sub-boiling, hydrazine/ammonium citrate solution, comprised of 0.25 mol citric acid, 16 mol ammonia, and 1 mol hydrazine, with sonication every 3 minutes for up to 30 seconds.

- Surface organics were removed from test walls by an oxidative cleaning procedure, involving 10 minutes in 250 µl of a hot (80–90°C) hydrogen peroxide (H_2O_2) solution, with sonication every 4 minutes for up to 30 seconds.

- A final heating rinse was then performed for 5 minutes in hot boron-clean Milli-Q water, before samples were syphoned into acid-leached 0.5 ml polypropylene centrifuge tubes.

- Samples were then completely dissolved in 350 µl of nitric acid (HNO_3).

2.5.7. GENERATION OF TRACE METAL DATA FOR IODP SITE U1443 AND ODP SITE 758 FORAMINIFERAL SAMPLES AT THE UNIVERSITY OF CALIFORNIA SANTA CRUZ

Samples were run on a Thermo Finnigan Element XR Inductively-Coupled Plasma-Mass Spectrometer (ICP-MS) at UCSC, following the methods of Brown et al. (2011). Larger *Morozovella sp*. samples (>600 µg) were divided into two and replicate runs were performed. The masses analysed for B/Ca were ^{11}B and ^{43}Ca, and for Mg/Ca were ^{24}Mg, ^{25}Mg, and ^{43}Ca. Samples containing <40 ppm calcium were considered to contain an insufficient mass of sample and were excluded from the final results. Similarly, samples with Mn/Ca & Fe/Ca ratios of >100 µmol/mol and Ti/Ca & Zn/Ca ratios of >50 µmol/mol were also excluded, due to the likelihood of contamination from adsorbed clays, overgrowths, or laboratory gloves. Solution standards with known elemental composition and blanks were routinely run between samples to check instrument precision, accuracy and consistency. Long-term reproducibility of consistency standards indicates inter-run precision for Mg/Ca of <3% (2σ) and for B/Ca of <5% (2σ). In order to account for possible Ca matrix effects, 6 standards with a range in [Ca] from 40 ppm to 320 ppm were analysed. If element/Ca ratios showed a dependence on [Ca], values were adjusted using a linear matrix effect correction. Thus, sample values derived from solutions with [Ca] either higher or lower than the target concentration of 160 ppm were appropriately adjusted to account for any matrix effects.

2.5.8. CRUSHING AND CLEANING OF ODP SITE 758 FORAMINIFERAL SAMPLES AT YALE UNIVERSITY

A subset of Late Paleocene samples from ODP Site 758 were firstly analysed for trace metals at Yale University. However, following the identification of a potential laboratory offset between samples analysed from IODP Site U1443 at UCSC and samples analysed from ODP Site 758 at Yale University, duplicate samples from ODP Site 758 were also analysed at UCSC using the same cleaning and analytical protocols as for the IODP Site U1443 samples (described

above). The data from each lab are clearly distinguished in **Chapter 6**. Foraminifera crushing and cleaning at Yale University were carried out by Dr. Michael Henehan, following the procedure outlined in Henehan et al. (2016a). This procedure includes:

- 4–7 clay cleaning steps, depending on sample size and cleanliness. Each of these cleaning steps involved ultrasonication in boron-free Milli-Q water for 30 seconds, followed by a Milli-Q rinse.

- Surface organics were removed from test walls by an oxidative cleaning procedure. 250 µl of 1% hydrogen peroxide (H_2O_2) buffered in 0.1 mol ammonium hydroxide (NH_4OH) solution was added to the sample, then samples were placed in a hot water bath at 80˚C for 15 minutes, with ultrasonication for 15 seconds after every 5 minutes. Samples were rinsed off 3 times and transferred to acid-leached Teflon centrifuge tubes. The reductive cleaning step, performed at UCSC for the IODP Site U1443 foraminiferal samples, was omitted.

- 250 µl of 0.0005 mol nitric acid (HNO_3) was added to each sample and left for 30 seconds to remove re-adsorbed contaminants. Samples were then rinsed with two Milli-Q rinses.

- The sample was then dissolved in a solution of 200 µl of boron-clean Milli-Q water and 0.5 mol nitric acid (HNO_3), followed by 5 minutes of centrifugation.

2.5.9. GENERATION OF TRACE METAL DATA AT YALE UNIVERSITY

Samples for trace metal analysis were analysed on a Thermo Element XR ICP-MS at the Yale Metal Geochemistry Centre (YMGC) by Dr. Michael Henehan, following the methods outlined by Rae et al. (2011). A Teflon barrel spray chamber with ammonia gas was used to improve boron washout. In-house standards were routinely run to measure accuracy and consistency. Long-term reproducibility of in-house standards is typically better than 3% (2σ uncertainty) for Mg/Ca and 5% (2σ uncertainty) for B/Ca.

3. CLIMATE AND CARBON CYCLING DURING THE LATE MAASTRICHTIAN TO EARLY EOCENE (~67.1–52.4 MILLION YEARS AGO)

3.1. ABSTRACT

This chapter presents the complete ~14.75 myr-long Late Maastrichtian–Early Eocene benthic stable carbon and oxygen isotope records from the South Atlantic ODP Site 1262. These records, based on a compilation of new Late Maastrichtian–Middle Paleocene data (1,599 samples) and previously published Late Paleocene–Early Eocene records (from 2,446 samples), combined with a compilation of recalibrated atmospheric pCO_2 estimates (373 data points), provide new insights into the principle forcing mechanisms of, and phasing between, the carbon cycle and climate at this time. Spectral analysis of the benthic stable isotope records documents long (405-kyr) and short (100-kyr) eccentricity as the dominant pacemakers of the climate and carbon cycle dynamics during this time, through modulation of precession. Perturbations to the global carbon cycle lag changes to global climate, suggesting that temperature-sensitive light carbon was released as a positive feedback to an initial warming induced by changes in orbital configuration. In addition, I also present new ODP Site 1262 planktic stable isotope data and a synthesis of published palaeoclimate proxy data from other sites, to evaluate whether the Latest Danian Event (LDE), Lower Chron 26r (L. C26r) event, and Danian/Selandian Transition Event (D/STE) can be classified as global hyperthermals. The new data and synthesis identify the LDE as an orbitally-paced double-spiked hyperthermal of around half the magnitude of ETM-2/H2 and the Lower C26r event as a smaller climatic perturbation with a global response, but question the D/STE as a global hyperthermal due to the absence of a bottom water temperature response at the equatorial Pacific ODP Site 1209.

3.2. INTRODUCTION

Orbital cyclicity of varying frequencies from 10’s to 100’s of thousands of years (kyr) has been shown to act as the pacemaker of Earth’s climate system and carbon cycle since the Mesozoic (e.g., Huang et al., 2010; Sexton et al., 2011; Kirtland Turner et al., 2014; Liebrand et al., 2016). Most previous

cyclostratigraphic studies covering the early Paleogene have focused specifically on the Late Paleocene–Early Eocene using bulk carbonate carbon isotope records ($\delta^{13}C_{bulk}$; Cramer et al., 2003; Zachos et al., 2010; Kirtland Turner et al., 2014), colour reflectance, magnetic susceptibility and Fe intensity records (Lourens et al., 2005; Westerhold et al., 2007; Westerhold & Röhl, 2009), and more recently, single-species benthic foraminiferal stable isotope records (Sexton et al., 2011; Littler et al., 2014; Westerhold et al., 2011, 2018). The highest resolution Late Paleocene–Early Eocene benthic isotope records to date were generated from ODP Site 1262 by Littler et al. (2014), which identified eccentricity as the dominant pacemaker of the climate and carbon cycle during the Late Paleocene–Early Eocene, through the modulation of precession. Littler et al. (2014) also used their benthic records to identify that changes in the carbon cycle lagged climate during long and short eccentricity cycles of this time, suggesting that greenhouse gases were released as a positive feedback to an initial warming induced by orbital forcing, therefore offering suggestions for the carbon stores involved and modes of release during hyperthermals. By contrast, much of the preceding Paleocene has been comparatively neglected, with only lower resolution semi-continuous single-site benthic records (e.g., Westerhold et al., 2011; 2018) and stacked benthic records from multiple sites (e.g., Zachos et al., 2001, 2008; Cramer et al., 2009) spanning this time interval.

A number of other potential hyperthermal events and smaller climatic perturbations have recently been proposed during the Late Maastrichtian–Middle Paleocene, including the Late Maastrichtian warming event (LMWE; ~66.2 Ma; Li & Keller, 1998; Tobin et al., 2012; Barnet et al., 2017; **Chapter 4**), Dan-C2 event (~65.9–65.7 Ma; Quillévéré et al., 2008; Coccioni et al., 2010; Gilmour et al., 2013; **Chapter 5**), Latest Danian Event (LDE; ~62.1–62.0 Ma; Bornemann et al., 2009; Deprez et al., 2017; **Section 3.6.6.**), Lower Chron 26r event (L. C26r event; ~61.73 Ma; Coccioni et al., 2012; **Section 3.6.6.**), and Danian/Selandian Transition Event (D/STE; ~61.4–61.2 Ma; Arenillas et al., 2008; **Section 3.6.6.**), amongst others. There is currently little evidence for a deep-sea temperature response associated with some of these events, such as the Dan-C2 and D/STE, as they have predominantly been described from continental shelf settings and bulk carbonate stable isotope data (e.g., Arenillas et al., 2008; Coccioni et al., 2010). Establishing these and other events as global in scale, and placing them

in the context of background orbital scale variability, is essential for ultimately understanding their origin and/or impacts.

3.3. AIMS AND OBJECTIVES

The overarching goal of this chapter is to identify the principle orbital periodicities that pace the interconnected climate and carbon cycle of the Late Maastrichtian to Early Eocene (~67.10–52.35 Ma), and to critically examine the understudied Early Paleocene hyperthermals and smaller climatic perturbations.

Specific questions to be addressed are:

- What are the principle forcing mechanisms driving the climate and carbon cycle during this time interval?

- Is there any temporal evolution in the relative power of these principle orbital periodicities through this time interval?

- What is the phasing between the carbon cycle and climate at the principle orbital frequencies during this period, and what does this tell us about the underlying mechanisms driving these cycles?

- How did ocean circulation pathways between the Pacific and Atlantic evolve during this interval?

- Can the Latest Danian Event (LDE), Lower Chron 26r (L. C26r) event, and Danian/Selandian Transition Event (D/STE) be classified as global hyperthermals?

- Are all hyperthermals and smaller climatic perturbations of this time period paced by orbital forcing, or is there a significant role for non-orbital forcing mechanisms (e.g., LIP volcanism)?

These questions will be addressed through examination of new high-resolution (~1.5–4 kyr), stratigraphically complete, single-species, benthic

foraminiferal stable carbon ($\delta^{13}C_{benthic}$) and oxygen ($\delta^{18}O_{benthic}$) isotope records from ODP Site 1262, calibrated to an updated orbitally-tuned age model. In addition, a synthesis of published geochemical records across the Early Paleocene understudied hyperthermals will also be incorporated and discussed.

3.4. METHODS

3.4.1. DATA SOURCES

Location of sites, lithostratigraphy, sample strategy, and all sedimentological and geochemical method information is presented in **Chapter 2, Sections 2.1–2.4**. The locations of ODP Site 1262 and other sites discussed in this chapter are illustrated in Figure 11. Further details about these sites, along with the types of data and literature sources used, are listed in Table 2.

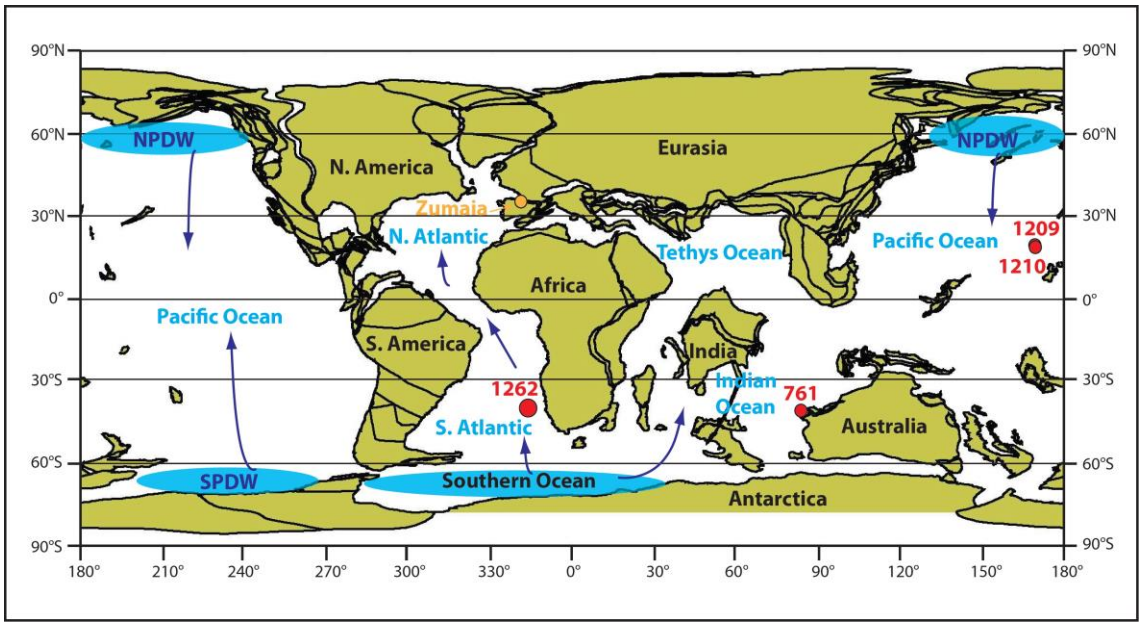

Figure 11. Cretaceous/Paleogene (K/Pg) boundary time (~66 Ma) palaeogeographic reconstruction, with locations of deep-sea sites (in red) and onshore sites (in orange) discussed in this chapter (also see Table 2). Locations of the principle areas of deep water formation are indicated in blue shading with the following abbreviations: NPDW = North Pacific Deep Water. SPDW = South Pacific Deep Water (Thomas et al., 2003, 2008). The predicted movement of deep water masses is indicated by dark blue arrows. Adapted from Ocean Drilling Stratigraphic Network (ODSN) Paleomap Project (http://www.odsn.de/odsn/services/paleomap/paleomap.html).

Table 2

Site	Current Lat.	Current Long.	Palaeo-lat at K/Pg (66 Ma)	Palaeo-lat at PETM (56 Ma)	Current water depth (m)	Palaeo-water depth (m)	Data type	Data sources
ODP Site 1262	27.2°S	1.6°E	40.3°S	40.6°S	4759	3000–3500	$\delta^{13}C_{benthic}$ $\delta^{18}O_{benthic}$ $\delta^{13}C_{bulk}$ Fe intensity $\delta^{13}C_{planktic}$ $\delta^{18}O_{planktic}$ % CF	Listed in **Section 3.4.2.** Listed in **Section 3.4.2.** Listed in **Section 3.4.3.** Westerhold et al. (2007, 2008) This study This study Kroon et al. (2007)
ODP Site 1209	32.7°N	158.5°E	22.8°N	27.5°N	2387	~2500	$\delta^{13}C_{benthic}$ $\delta^{18}O_{benthic}$ Fe intensity	Westerhold et al. (2011) Westerhold et al. (2011) Westerhold et al. (2008)
ODP Site 1210	32.2°N	158.3°E	22.3°N	27.0°N	2574	~2700	$\delta^{13}C_{planktic}$ $\delta^{18}O_{planktic}$	Jehle et al. (2015) Jehle et al. (2015)
ODP Site 761	16.7°S	115.5°E	42.6°S	39.4°S	2168	<2000	$\delta^{13}C_{benthic}$ $\delta^{18}O_{benthic}$	Quillévéré et al. (2002) Quillévéré et al. (2002)
Zumaia, Spain	43.3°N	2.3°W	32.1°N	31.9°N	Subaerial	900–1100	$\delta^{13}C_{bulk}$	Dinarès-Turell et al. (2014)

Present-day latitudes, longitudes, water depths and palaeo-water depths are from the initial scientific reports for each deep-sea site (Shipboard Scientific Party, 2004a, 2002a, 2002b & 1990). Onshore site longitudes and latitudes for Zumaia are from Dinarès-Turell et al. (2014), with palaeo-water depth data from Arenillas et al. (2008). Palaeo-latitudes for each site at the Cretaceous/Paleogene (K/Pg) boundary (~66 Ma) and Paleocene-Eocene Thermal Maximum (PETM; ~56 Ma) were computed relative to the palaeomagnetic reference frame of Torsvik et al. (2012), using Version 2.1 of the model from paleolatitude.org (van Hinsbergen et al., 2015). The geochemical datasets used from each site and sources of this data are listed in the two right-hand columns.

3.4.2. COMPILATION OF THE COMPLETE LATE MAASTRICHTIAN–EARLY EOCENE BENTHIC STABLE ISOTOPE RECORDS FROM ODP SITE 1262

To produce the composite ~14.75 million year-long Late Maastrichtian–Early Eocene benthic stable isotope records from ODP Site 1262, the new Late Maastrichtian–Middle Paleocene $\delta^{13}C_{benthic}$ and $\delta^{18}O_{benthic}$ records generated during this study were combined with the Late Paleocene–Early Eocene (Littler et al., 2014), PETM (McCarren et al., 2008), ETM-2 (Stap et al., 2010), and Early Eocene (Lauretano et al., 2015) records previously published for this site. A full breakdown of stable isotope data by literature source is plotted against metres composite depth in **Appendix 31**.

The stable isotope data published for the Late Paleocene from ODP Site 1262 (Littler et al., 2014) were generated in MARUM, Bremen, on a Thermo-Finnigan MAT 251 Isotope Ratio Mass Spectrometer interfaced with a Kiel Device. To check for inter-lab consistency, *N. truempyi* specimens picked from the oldest four stratigraphic intervals published by Littler et al. (2014) were also analysed for $\delta^{13}C$ and $\delta^{18}O$ at the NERC Isotope Geosciences Facility during this study. The existence of a negligible offset, largely within error between laboratories (Table 3), highlights that no correction needs to be applied to the new data generated during this study to generate the complete Late Maastrichtian–Early Eocene record.

Table 3

Depth (mcd)	**$\delta^{13}C$ (this study)**	**$\delta^{18}O$ (this study)**	**$\delta^{13}C$ (Littler et al., 2014)**	**$\delta^{18}O$ (Littler et al., 2014)**	**$\delta^{13}C$ difference**	**$\delta^{18}O$ difference**
184.865	1.59	0.52	1.65	0.46	–0.06	+0.06
184.895	1.60	0.50	1.76	0.56	–0.16	–0.06
184.955	1.65	0.51	1.68	0.44	–0.03	+0.07
184.985	1.52	0.39	1.72	0.42	–0.20	–0.03
Mean					**–0.11**	**+0.01**

Inter-laboratory comparison of South Atlantic ODP Site 1262 benthic stable isotope data. Overlapping samples were run at the NERC Isotope Geosciences Facility (IsoPrime 100 Gas Source Isotope Ratio Mass Spectrometer; this study) and at MARUM, Bremen (Thermo-Finnigan MAT 251 Isotope Ratio Mass Spectrometer interfaced with a Kiel Device; Littler et al., 2014).

3.4.3. APPROXIMATING THE SHALLOW-TO-DEEP CARBON ISOTOPE GRADIENT

The gradient between published bulk sediment carbon isotope data ($\delta^{13}C_{bulk}$; Lourens et al., 2005; Zachos et al., 2005, 2010; Kroon et al., 2007; Littler et al., 2014) and our benthic data ($\delta^{13}C_{bulk}$–$\delta^{13}C_{benthic}$ gradient) is used as an approximation for the surface-to-deep carbon isotope gradient and hence relative shifts in surface ocean dissolved inorganic carbon (DIC) $\delta^{13}C$, since the majority of the carbonate component of sediments from this site ($\delta^{13}C_{bulk}$) is composed of calcareous nannofossils and planktic foraminifera. However, such carbonate components are also the most prone to diagenetic overprinting, therefore, there

is also the potential for this gradient to be modified by diagenesis in certain parts of the record.

3.4.4. CONVERSION OF BENTHIC $\delta^{18}O$ TO TEMPERATURE

Since it is generally agreed that there was an absence of significant polar continental ice sheets during the early Paleogene (e.g., Zachos et al., 2008; Pross et al., 2012), $\delta^{18}O_{benthic}$ data can be converted directly to bottom water temperatures. The raw *N. truempyi* $\delta^{18}O$ data ($\delta^{18}O_{Nutt}$) were first converted to *Cibicidoides* values ($\delta^{18}O_{Cib}$) following Katz et al. (2003):

$$\delta^{18}O_{Cib}\ (‰) = (\delta^{18}O_{Nutt} + 0.10)/0.89 \qquad [Eq.\ 3]$$

This conversion was applied as the $\delta^{18}O$-Temperature relationships in Bemis et al. (1998) provide a good fit to benthic *Cibicidoides* data (Bemis et al., 1998). The temperature calibration of Kim & O'Neil (1997) for inorganic calcite, modified by Bemis et al. (1998; Equation 1), was used to convert $\delta^{18}O_{benthic}$ data to temperature:

$$T\ (°C) = 16.1 - 4.64(\delta^{18}O_c - \delta^{18}O_{sw}) + 0.09(\delta^{18}O_c - \delta^{18}O_{sw})^2 \qquad [Eq.\ 4]$$

where T is temperature in °C, $\delta^{18}O_c$ is the oxygen isotopic value of foraminiferal calcite ($\delta^{18}O_{Cib}$) in ‰ VPDB, and $\delta^{18}O_{sw}$ is the oxygen isotopic value of ambient ocean water (modelled as –1.27 ‰ VSMOW; assuming an ice-free world, consistent with Westerhold et al., 2011 and Littler et al., 2014). Note that Cramer et al. (2011) propose an alternative $\delta^{18}O_{sw}$ value for ocean water in an ice-free world of –0.89 ‰ VSMOW, which would offset calculated deep ocean temperatures to ~+1.7°C warmer if used in Eq. 4.

3.4.5. AGE MODEL

An updated orbitally-tuned age model spanning the Late Maastrichtian–Early Eocene (~67.10–52.35 Ma) was generated for ODP Site 1262 by Dr. Thomas Westerhold (University of Bremen), based on the samples I processed and analysed during this project. This age model was constructed by recognition

and counting of the stable long (405-kyr) eccentricity cycles in the new $\delta^{13}C_{benthic}$ record generated and compiled from ODP Site 1262 during this study. The age model was tuned to the La2010b orbital solution of Laskar et al. (2011a) and anchored to absolute astronomical ages of 66.0225 Ma for the K/Pg boundary (Dinarès-Turell et al., 2014) and 55.93 Ma for the onset of the PETM (Westerhold et al., 2007). This age model represents a refinement of the Westerhold et al. (2008) age model, tuned to the older La2004 astronomical solution (Laskar et al., 2004), and the Dinarès-Turell et al. (2014) age model for this site, tuned to the La2010d and La2011 astronomical solutions (Laskar et al., 2011a; Laskar et al., 2011b). The Westerhold et al. (2008) age model was based on high-resolution XRF core scanner-derived Fe intensity data from the South Atlantic, equatorial Pacific and North Atlantic, however, difficulties were encountered with interpreting the number of 405-kyr cycles within condensed intervals of the Early Paleocene, post-dating the K/Pg boundary. This earlier age model was refined by Dinarès-Turell et al. (2014), who incorporated additional $\delta^{13}C_{bulk}$ and magnetostratigraphic data to solve earlier uncertainties in the number of 405-kyr cycles during the Early Paleocene. The premise for identifying eccentricity cycles using these geochemical proxies is based on the response of marine productivity along with temperature- and climate-sensitive carbon reservoirs to periodic insolation changes induced by orbital forcing. During eccentricity maxima, enhanced seasonal insolation contrasts can result in increased productivity in the surface ocean, accompanied by increased remineralisation of C_{org} at depth, along with the transient release of isotopically light carbon from climate- and temperature-sensitive carbon reservoirs, resulting in a transient shoaling of the lysocline and CCD. The new high-resolution single-species $\delta^{13}C_{benthic}$ record generated during this study represents a much higher fidelity record of orbitally-induced perturbations to the carbon cycle, however, single-species $\delta^{13}C_{benthic}$ records can still be biased by significant changes in export productivity, which can modify the isotopic composition of deep ocean DIC (see **Chapter 5**). Fe intensity records can be biased by significant changes in biogenic carbonate productivity following extinction events, such as in the aftermath of the K/Pg boundary, along with variations in the flux of Fe-rich dust to the site. Similarly, the magnitude of eccentricity cycles within $\delta^{13}C_{bulk}$ data can be biased by competing inter-species vital effects, selective extinction or evolutionary events, and diagenesis.

Uncertainties associated with the age model include error associated with absolute ages of key tie points (i.e., the K/Pg boundary and the PETM), errors involved with the identification and counting of 405-kyr eccentricity cycles, and differences in absolute ages of 405-kyr cycles between the various orbital solutions used as the tuning target, where the different solutions diverge beyond ~50 Ma (Laskar et al., 2011a). The development of high-precision radiometric dating methods (e.g., U/Pb and Ar/Ar) has significantly reduced uncertainties associated with absolute ages of volcanic and volcaniclastic rocks to typically <100 kyr (e.g., Renne et al., 2015; Schoene et al., 2015). Misidentification of the number of 405-kyr cycles represented one of the principle uncertainties in earlier orbitally-tuned age models and could offset the age model by multiples of 405 kyr, depending on how many cycles are omitted. Since a consistent correlation of the number of 405-kyr cycles has been achieved at multiple sites in the Pacific, South Atlantic and North Atlantic, based on a variety of different geochemical proxies (Westerhold et al., 2008; Dinarès-Turell et al., 2014), it is considered unlikely that any cycles have been omitted in this new age model. Lastly, Westerhold et al. (2017) have recently shown that La2010b represents the optimal astronomical solution for orbital tuning of deep-sea sediment cores older than ~50 Ma, based on the modulation of short (100-kyr) eccentricity cycles by long (405-kyr) eccentricity, evident in Fe intensity records from multiple sites on Walvis Ridge. The La2010b solution is therefore considered the most reliable tuning target for sediment cores of Late Maastrichtian–Early Eocene age. The age tie points used to create this updated age model are listed in **Appendix 3**.

3.4.6. SPECTRAL ANALYSIS

3.4.6.1. DATA PREPARATION

In order to perform spectral analysis of the complete Late Maastrichtian–Early Eocene $\delta^{13}C_{benthic}$ and $\delta^{18}O_{benthic}$ datasets from ODP Site 1262, the data were first pre-processed in the following ways. To circumvent the distorting effects that large transient climatic events such as hyperthermals can have on the results of spectral analysis, the data that record the main body and majority of the recovery of the PETM excursion were removed and replaced by a linear interpolation. The complete Late Maastrichtian–Early Eocene datasets were then

graphically detrended in KaleidaGraph 4.0 using a 15 % running mean to remove long-term (>1 million year) trends. The detrended $\delta^{13}C_{benthic}$ data < –0.6‰ and > +0.4‰ and detrended $\delta^{18}O_{benthic}$ data < –0.4‰ and > +0.3‰ were then cropped to dampen the effects of large amplitude variability in the isotopic record. Finally, the complete datasets were linearly resampled at 3 kyr resolution in Astrochron 0.6.5 (Meyers, 2014).

3.4.6.2. BAND PASS FILTERING

To illustrate temporal variations in the amplitude of Milankovitch periodicities across the records, the graphically detrended $\delta^{13}C_{benthic}$ and $\delta^{18}O_{benthic}$ datasets were firstly band pass filtered using AnalySeries 2.0 (Paillard et al., 1996) for the long eccentricity (~405-kyr) cycle at 0.002467 ± 0.000700 cycles/kyr (i.e., 316–565 kyr), the short eccentricity (~100-kyr) cycle at 0.010 ± 0.003 cycles/kyr (i.e., 77–143 kyr), and ~21-kyr precession at 0.0476 ± 0.0143 cycles/kyr (i.e., 16–30 kyr).

3.4.6.3. MULTI-TAPER METHOD POWER SPECTRA

To identify the dominant forcing mechanisms driving the palaeoclimate ($\delta^{18}O_{benthic}$) and carbon cycle ($\delta^{13}C_{benthic}$) through the Late Maastrichtian to Early Eocene, Multi-Taper Method (MTM) power spectra were generated for the complete ODP Site 1262 $\delta^{18}O_{benthic}$ and $\delta^{13}C_{benthic}$ records using the mtmML96 code in Astrochron 0.6.5 (Meyers, 2014). Background estimate and confidence levels (99%, 95%, 90%) are based on a robust red noise estimation (Meyers, 2012).

To examine for temporal changes in dominant periodicities over time, MTM power spectra were also generated for the following 5 discrete time windows, defined based on palaeoclimatic (i.e., long-term warming or cooling) trends:

- Window 1 – Late Maastrichtian–Early Paleocene (67.1–64.0 Ma)
- Window 2 – Early Paleocene (64.0–61.25 Ma)
- Window 3 – Middle Paleocene (61.25–58.75 Ma)
- Window 4 – Late Paleocene (58.75–55.93 Ma)

- Window 5 – Early Eocene (55.83–52.35 Ma)

3.4.6.4. EVOLUTIONARY WAVELET SPECTRA

To further visualise the evolution of spectral power in the carbon cycle and climate from the Late Maastrichtian to Early Eocene, evolutionary wavelet spectra were generated by Dr. Thomas Westerhold from the graphically detrended, cropped and linearly resampled ODP Site 1262 $\delta^{13}C_{benthic}$ and $\delta^{18}O_{benthic}$ datasets in Matlab, using the free software and code provided by C. Torrence and G. Compo (http://paos.colorado.edu/research/wavelets/).

3.4.6.5. CROSS SPECTRAL ANALYSIS

To determine the coherency and phasing between $\delta^{13}C_{benthic}$ (carbon cycle) and $\delta^{18}O_{benthic}$ (climate) during the Late Maastrichtian–Early Eocene, cross-spectral analysis was performed on the complete ODP Site 1262 $\delta^{13}C_{benthic}$ and $\delta^{18}O_{benthic}$ datasets using the Blackman-Tukey method in AnalySeries 2.0 (Paillard et al., 1996).

To examine for temporal changes in phasing with time, cross spectral analysis was also performed for each of the 5 discrete time windows defined in **Section 3.4.6.3.**

3.4.7. COMPILATION OF ATMOSPHERIC pCO_2 ESTIMATES

The compilation of published pCO_2 proxy data by Royer (2014) formed the basis for the compilation of published pCO_2 data presented in this chapter, and has been supplemented with additional recently generated data (Steinthorsdottir et al., 2016; Anagnostou et al., 2016; Gehler et al., 2016; Cui & Schubert, 2016, 2017). The compilation consists of proxy data based on pedogenic carbonates, stomatal indices, boron isotopes, oxygen isotopes, phytoplankton, C3 plants, and liverworts. All pCO_2 proxy data were migrated onto the updated ODP Site 1262 age model by temporally shifting the age of the K/Pg boundary and/or the PETM in the published datasets to 66.0225 Ma and 55.93 Ma, respectively. Pedogenic carbonate proxy estimates were recalibrated during this study, with the method

described in detail below. The recalibrated pedogenic carbonate pCO_2 proxy data are included in **Appendix 5** and published raw pCO_2 estimates from the other proxies in **Appendix 6**.

3.4.7.1. RECALIBRATION OF pCO_2 ESTIMATES BASED ON THE PEDOGENIC CARBONATE PROXY

Published pedogenic carbonate atmospheric pCO_2 estimates were recalculated using a revised and updated S_z (soil-respired CO_2) concentration in the Cerling palaeobarometer (Cerling, 1999):

$$C_a = S_z \frac{[\delta^{13}C_s - 1.0044\,\delta^{13}C_r - 4.4]}{\delta^{13}C_a - \delta^{13}C_s} \qquad \textit{[Eq. 5]}$$

where C_a is atmospheric CO_2 concentration (ppmV), and $\delta^{13}C_s$, $\delta^{13}C_r$, and $\delta^{13}C_a$ are isotopic compositions of soil CO_2, soil-respired CO_2, and atmospheric CO_2, respectively. Atmospheric pCO_2 estimates were recalculated using the original published values for $\delta^{13}C_s$, $\delta^{13}C_r$, and $\delta^{13}C_a$, but using a revised and updated S_z value of 2500 ppmV for sub-humid temperate and tropical soils (Breecker et al., 2010; Hong & Lee, 2012). The final estimates of pCO_2 scale with the value of S_z. Earlier studies used significantly higher S_z values of 4000–7000 ppmV (e.g., Nordt et al., 2002, 2003), assuming that pedogenic carbonates formed under mean growing season soil conditions when S_z concentrations were at their maximum. Making this assumption resulted in atmospheric pCO_2 estimates significantly higher than other proxies (Royer et al., 2006), and brought into question this model parameter (Breecker et al., 2010). Breecker et al. (2010) identified that pedogenic carbonates form instead under seasonally warm and very dry conditions, when S_z values are significantly lower than mean growing season soil conditions. Such values have been determined to be typically ~2500 ppmV in sub-humid temperate and tropical soils and ~1000 ppmV in desert soils. Since the palaeoenvironments of the palaeosols under consideration here were characterised by sub-humid climates, a revised S_z value of 2500 ppmV has been used. Our conclusions are not dependent on the choice of 2500 ppmV for S_z, as we have estimated error based on a realistic range of S_z from 1500 to 3500 ppmV, taking in the range of minimum annual S_z values for sub-humid temperate and

tropical soils collated in Table 1 of Breecker et al. (2010). These error bars are therefore conservative values, as only one parameter was varied in their construction.

3.4.8. INTEGRATION OF OTHER PUBLISHED PALAEOCLIMATE PROXY DATA

All other published Early–Middle Paleocene palaeoclimate proxy data presented in this chapter have been calibrated in the time domain to our orbitally-tuned age model developed from ODP Site 1262. Datasets were first aligned based on the easily identifiable expression of the Latest Danian Event (LDE) within the stable isotope or carbonate dissolution proxy data. Mean sedimentation rates for the Early Paleocene at each site (Table 4) were then used to estimate ages above and below the LDE for the available published data. For equatorial Pacific ODP Site 1210, data were aligned with the ODP Site 1262 age model based on the isotopic expression of the LDE, as above, with the age model presented in the original literature source employed.

Table 4

Site	Early Paleocene sedimentation rate (cm/kyr)	Literature source
ODP Site 1262	0.5–1	This study (orbitally-tuned age model)
ODP Site 1209	0.4–0.6	Westerhold et al. (2011)
ODP Site 761	1–2	Quillévéré et al. (2002)
Zumaia	1.3–1.6	Dinarès-Turell et al. (2014); independent orbitally tuned age model

Mean Early Paleocene sedimentation rates used to recalibrate the age models for the deep-sea sites used in this study.

3.5. DATA ATTRIBUTION

I picked all of the benthic foraminifera analysed for the Late Maastrichtian–Middle Paleocene part of the ODP Site 1262 record (1,599 samples; 184.865–236.075 mcd; ~67.10–60.91 Ma), planktic foraminifera across the D/STE (30 samples; 186.60–189.24 mcd; ~61.40–61.09 Ma), and prepared all foraminifera

tests for stable isotope analysis. I compiled all of the published benthic foraminiferal stable isotope records spanning the Late Paleocene–Early Eocene from ODP Site 1262 (an additional 2,446 paired benthic carbon and oxygen isotope data points), to produce the composite Late Maastrichtian–Early Eocene record forming the basis of this chapter. I converted the benthic stable isotope data to bottom water temperatures, prepared the records for spectral analysis, and generated the Multi-Taper Method power spectra, coherence and phasing plots. I also compiled and recalibrated all published Early–Middle Paleocene palaeoclimate proxy and Late Maastrichtian–Early Eocene atmospheric pCO_2 data from the literature. Prof. Dick Kroon (University of Edinburgh) and I carried out sample collection from the Bremen Core Repository for the Late Maastrichtian–Middle Paleocene part of the record, along with sample disaggregation, sieving, and calculation of % coarse fraction. The new Late Maastrichtian–Middle Paleocene benthic stable isotope data were funded and generated by the NERC Isotope Geosciences Facility (grant number IP-1581-1115), under the supervision of Prof. Melanie Leng, and are included in **Appendix 4**. The new planktic stable isotope data across the D/STE were generated at the Wolfson Laboratory, University of Edinburgh, funded by Prof. Dick Kroon, and are included in **Appendix 7**. The updated orbitally-tuned age model for ODP Site 1262 used in this study, along with the evolutionary wavelet spectra, were generated by Dr. Thomas Westerhold (MARUM, Bremen) using samples and data generated and prepared by myself.

3.6. RESULTS AND DISCUSSION

3.6.1. EVOLUTION OF THE CLIMATE AND CARBON CYCLE DURING THE LATE MAASTRICHTIAN–EARLY EOCENE

The complete compiled Late Maastrichtian–Early Eocene stable carbon and oxygen isotope records for ODP Site 1262 are shown in Figure 12, alongside the Fe intensity record for this site (Westerhold et al., 2007, 2008), recalibrated proxy data for atmospheric pCO_2, and sedimentation rates. An overall long-term warming of ~+5.5°C (decrease in $\delta^{18}O_{benthic}$ from +0.6 ‰ to –0.5 ‰) is observed from the Late Maastrichtian through to the Early Eocene (Figure 12e). This is accompanied by an overall decrease of ~–1.2 ‰ in $\delta^{13}C_{benthic}$ (Figure 12c) and ~–

1.8 ‰ in $\delta^{13}C_{bulk}$ (Figure 12b), consistent with increased injection of isotopically light carbon (i.e., greenhouse gases) into the exogenic carbon cycle, and/or a shift in the relative fluxes of carbon between reservoirs (Komar et al., 2013). Atmospheric pCO_2 values rise from ~100–500 ppm during the earliest Paleocene to ~100–750 ppm during the Late Paleocene–Early Eocene (Figure 12a), suggesting an overall increase in greenhouse gas levels during this time. Elemental Fe concentrations in sediments deposited at ODP Site 1262 also decreased markedly from the Early Paleocene through to the Early Eocene (Figure 12f), whilst sedimentation rates markedly increased (from ~0.2 to ~1.7 cm/kyr) over the same time interval (Figure 12g). This pattern could be interpreted to reflect increased $CaCO_3$ preservation at ODP Site 1262 as a result of a progressively deepening lysocline, and a corresponding dilution of the terrestrially-derived Fe content. Assuming the CCD exhibits a similar trend, this pattern would be consistent with proxy data from the Indian Ocean (Hancock et al., 2006; Slotnick et al., 2015), and modelling studies of the Atlantic and Pacific (Komar et al., 2013). As a result of the gradual rise of background atmospheric pCO_2, lysocline deepening is likely related to a rise in alkalinity due to increased chemical weathering and delivery of solutes to the global ocean, under increasingly warm and humid greenhouse conditions during the Late Paleocene to Early Eocene (Hilting et al., 2008). However, some of the Early Paleocene–Early Eocene elemental Fe intensity and sedimentation rate patterns could be explained by shifts in biogenic carbonate productivity and/or variations in the flux of wind-blown aeolian dust from the African continent, without invoking dissolution of calcium carbonate. This is particularly true for the first 1–2 million years of the Paleocene, when biogenic carbonate productivity was likely to have been significantly reduced following the K/Pg mass extinction, resulting in the highest elemental Fe intensities and lowest sedimentation rates (~0.2–0.5 cm/kyr) of the early Paleogene at ODP Site 1262 (Figure 12f,g).

Superimposed on Late Maastrichtian to Early Eocene warming were shorter-term shifts in Earth's climate and biosphere. At ODP Site 1262, the mass extinction within marine biota across the K/Pg boundary is accompanied by a reversal of the surface-to-deep carbon isotope gradient ($\delta^{13}C_{bulk}$ shifts by > –2.5 ‰ whereas $\delta^{13}C_{benthic}$ changes by only ~–0.8 ‰; Figure 12b,c,d). Although this apparent reversal could in part be explained by extreme vital effects within the

very small opportunistic planktic foraminifera species which evolved in the immediate aftermath of the K/Pg boundary (Birch et al., 2012, 2013), it is also thought to record partial collapse of the biological pump following the K/Pg mass extinction, resulting in reduced surface water primary productivity and decreased remineralisation of isotopically more negative C_{org} at depth (Kump, 1991; Birch et al., 2016; see **Chapter 5** for further discussion). The pre-K/Pg $\delta^{13}C_{bulk}$–$\delta^{13}C_{benthic}$ isotope ($\Delta^{13}C$) gradient was not completely restored until the Danian/Selandian Transition Event (D/STE), over 4.5 million years after the K/Pg mass extinction (Figure 12d). A similar but smaller reduction in the $\Delta^{13}C$ gradient is also observed for ~1.5 million years directly following the PETM (Figure 12d). These are the two largest climatic and biotic events preserved in the ODP Site 1262 benthic stable isotope records and clearly had long-term effects on the marine biological pump. These events potentially crossed a threshold leading to significant changes in structure of mixed layer calcifying communities, which was not surpassed during smaller hyperthermals such as ETM-2 (Stap et al., 2009, 2010).

The coolest conditions of the Paleocene occurred between ~61–58 Ma (Figure 12e), when ODP Site 1262 was characterised by bottom water temperatures of ~7°C and by increasingly positive $\delta^{13}C_{bulk}$ and $\delta^{13}C_{benthic}$ values, peaking at a Cenozoic high during the PCIM (Figure 12b,c). Cooler global temperatures at this time were likely facilitated by the burial of significant volumes of carbon in either biogenic CH_4 hydrates beneath the continental shelves (e.g., Dickens, 2003, 2011), low-latitude peat deposits (e.g., Kurtz et al., 2003), or high-latitude permafrost (DeConto et al., 2012), to produce the observed positive carbon isotope signature of the ocean-atmosphere system. The extensive lateral distribution of lignite and coal of Late Paleocene age across North America and Eurasia suggest that low-latitude peat deposits may have been the largest carbon reservoir during this time (Kurtz et al., 2003). Significant temperature- and climate-sensitive carbon reservoirs were therefore primed to be episodically released as ambient climate warmed and periodically crossed critical thresholds, resulting in pulsed release during the hyperthermals and smaller climatic perturbations of the Late Paleocene to Early Eocene (Zachos et al., 2010; Lunt et al., 2011; Kirtland Turner et al., 2014; Figure 12b,c).

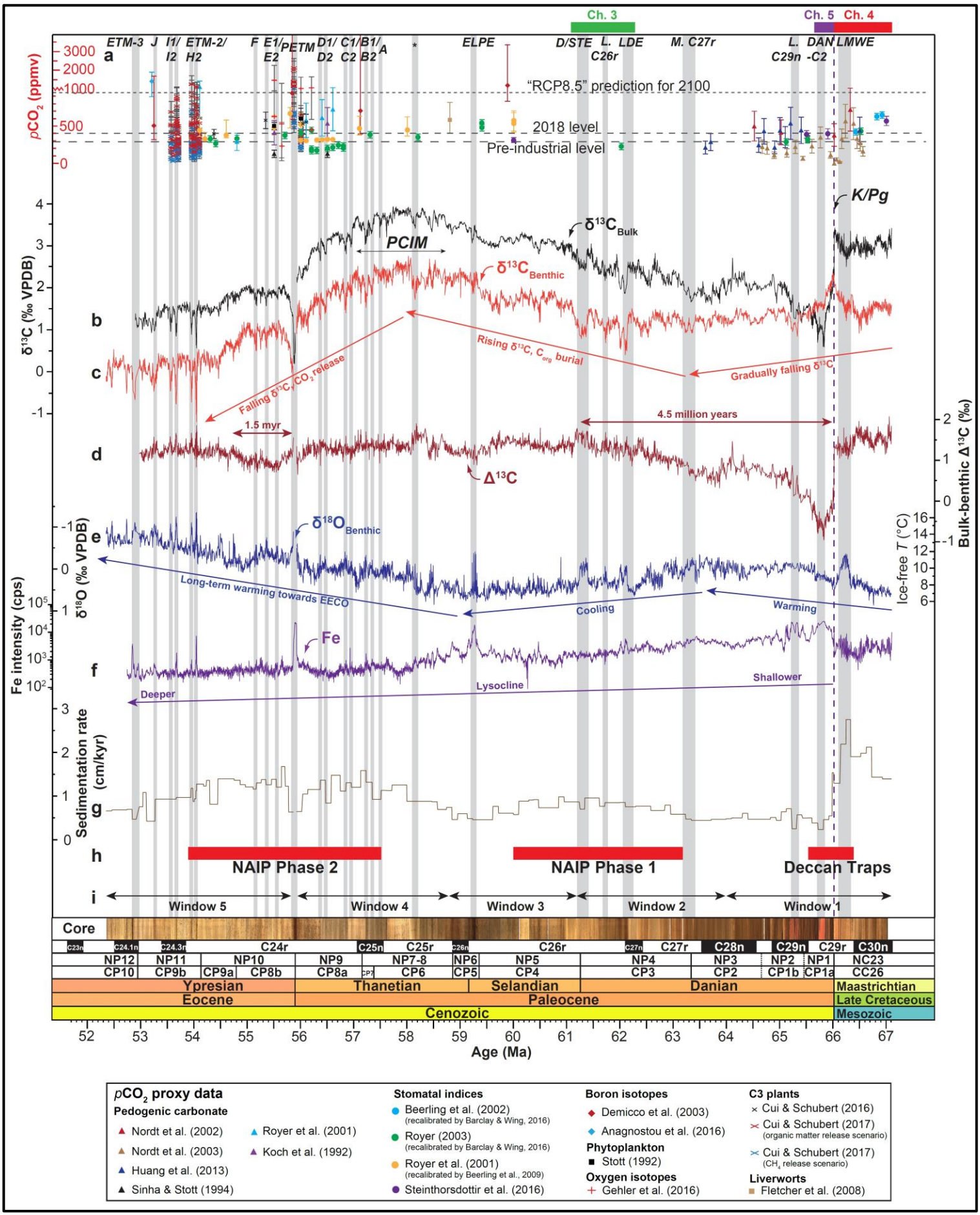
Ch. 3
Ch. 5
Ch. 4
ETM-3
J
I1/ I2
ETM-2/ H2
F
E1/ E2
PETM
D1/ D2
C1/ C2
B1/ B2
A
ELPE
D/STE
L. C26r
LDE
M. C27r
L. C29n
DAN
-C2
LMWE
K/Pg
pCO2 (ppmv)
3000
2000
1000
500
0
"RCP8.5" prediction for 2100
2018 level
Pre-industrial level
a
δ13C (‰ VPDB)
δ13CBulk
PCIM
δ13CBenthic
b
c
Rising δ13C, Corg burial
Gradually falling δ13C
Falling δ13C, CO2 release
1.5 myr
4.5 million years
d
Δ13C
Bulk-benthic Δ13C (‰)
δ18O (‰ VPDB)
δ18OBenthic
e
Long-term warming towards EECO
Cooling
Warming
Ice-free T (°C)
Fe intensity (cps)
Fe
f
Lysocline
Shallower
Deeper
Sedimentation rate (cm/kyr)
g
h
NAIP Phase 2
NAIP Phase 1
Deccan Traps
i
Window 5
Window 4
Window 3
Window 2
Window 1
Core
C23n
C24.1n
C24.3r
C24r
C25n
C25r
C26n
C26r
C27n
C27r
C28n
C29n
C29r
C30n
NP12
NP11
NP10
NP9
NP7-8
NP6
NP5
NP4
NP3
NP2
NP1
NC23
CP10
CP9b
CP9a
CP8b
CP8a
CP7
CP6
CP5
CP4
CP3
CP2
CP1b
CP1a
CC26
Ypresian
Thanetian
Selandian
Danian
Maastrichtian
Eocene
Paleocene
Late Cretaceous
Cenozoic
Mesozoic
52
53
54
55
56
57
58
59
60
61
62
63
64
65
66
67
Age (Ma)
pCO2 proxy data
Pedogenic carbonate
Nordt et al. (2002)
Nordt et al. (2003)
Huang et al. (2013)
Sinha & Stott (1994)
Royer et al. (2001)
Koch et al. (1992)
Stomatal indices
Beerling et al. (2002) (recalibrated by Barclay & Wing, 2016)
Royer (2003) (recalibrated by Barclay & Wing, 2016)
Royer et al. (2001) (recalibrated by Beerling et al., 2009)
Steinthorsdottir et al. (2016)
Boron isotopes
Demicco et al. (2003)
Anagnostou et al. (2016)
Phytoplankton
Stott (1992)
Oxygen isotopes
Gehler et al. (2016)
C3 plants
Cui & Schubert (2016)
Cui & Schubert (2017) (organic matter release scenario)
Cui & Schubert (2017) (CH4 release scenario)
Liverworts
Fletcher et al. (2008)

*Figure 12 (previous page). Recalibrated proxies for atmospheric pCO_2, along with stable carbon and oxygen isotope records, elemental Fe intensities and sedimentation rates from South Atlantic ODP Site 1262 (palaeo-depth ~3000–3500 m), calibrated against an updated orbitally-tuned age model: (**a**) Recalibrated atmospheric pCO_2 data. Labelled dashed lines indicate pre-industrial and 2018 levels, along with the most pessimistic prediction (RCP8.5) for the year 2100 (from Cubasch et al., 2013). A legend is included at the bottom of the figure. The recalibrated and raw pCO_2 data are included in **Appendix 5** and **Appendix 6** respectively. (**b**) Bulk carbonate stable carbon isotope data ($\delta^{13}C_{bulk}$; Lourens et al., 2005; Zachos et al., 2005, 2010; Kroon et al., 2007; Littler et al., 2014); (**c**) benthic foraminiferal carbon isotope data ($\delta^{13}C_{benthic}$; McCarren et al., 2008; Stap et al., 2010; Littler et al., 2014; Lauretano et al., 2015; this study); (**d**) $\delta^{13}C_{bulk}$– $\delta^{13}C_{benthic}$ ($\Delta^{13}C$) gradient; (**e**) benthic foraminiferal oxygen isotope data ($\delta^{18}O_{benthic}$; McCarren et al., 2008; Stap et al., 2010; Littler et al., 2014; Lauretano et al., 2015; this study); (**f**) Fe intensity data (Westerhold et al., 2007, 2008); (**g**) sedimentation rate (cm/kyr) based on the tie points used to create the updated orbitally-tuned age model presented in this thesis (**Appendix 3**); (**h**) radiometric ages of large igneous province volcanism (Deccan Traps; Renne et al., 2015; Schoene et al., 2015 and North Atlantic Igneous Province [NAIP]; Sinton & Duncan, 1998). (**i**) temporal distribution of discrete time windows used in Figure 16 and Figure 19. The windows are defined as follows. Window 1: Late Maastrichtian–Early Paleocene warming, including Deccan Traps volcanism and main $\Delta^{13}C$ gradient recovery phase after the K/Pg boundary. Window 2: Early Paleocene cooling, including the LDE, L. C26r, and D/STE events, as well as complete recovery of the $\Delta^{13}C$ gradient. Window 3: Middle Paleocene cooling, including rising $\delta^{13}C_{benthic}$ values to the PCIM. Window 4: Late Paleocene warming, including rapidly decreasing $\delta^{13}C_{benthic}$ values after the PCIM. Window 5: Early Eocene warming, post-PETM. A full breakdown of data sources for the stable isotope and Fe intensity data is illustrated in **Appendix 25.** Magnetozones are from Bowles (2006), with calcareous nannofossil biozones from Agnini et al. (2007), Monechi et al. (2013), and Shipboard Scientific Party (2004a). Coloured arrows and annotations indicate broad long-term trends observed within the records. PCIM – Paleocene Carbon Isotope Maximum. Hyperthermals and smaller climatic perturbations are illustrated by labelled grey vertical bars, with the following abbreviations: LMWE – Late Maastrichtian warming event; Dan-C2 – Dan-C2 event; L. C29n – Lower Chron 29n event; M. C27r – Middle Chron 27r event; LDE – Latest Danian Event; L. C26r – Lower Chron 26r event; D/STE – Danian/Selandian Transition Event; ELPE – Early Late Paleocene Event; PETM – Paleocene-Eocene Thermal Maximum; ETM-2 – Eocene Thermal Maximum 2; ETM-3 – Eocene Thermal Maximum 3. Coloured bars above the figure indicate portions of the record discussed in greater detail later in this chapter and in subsequent chapters.*

3.6.2. COMPARISON BETWEEN THE SOUTH ATLANTIC AND EQUATORIAL PACIFIC RECORDS

A comparison between the new Late Maastrichtian–Early Eocene benthic stable isotope records from ODP Site 1262 and the published records across the

same time interval from equatorial Pacific ODP Site 1209 (Westerhold et al., 2011, 2018), is illustrated in Figure 13. This comparison clearly highlights the higher resolution of the new benthic stable isotope records generated from ODP Site 1262 (~1.5–4 kyr) compared to the benthic records from ODP Site 1209 (~4–5 kyr), as well as the superior stratigraphic completeness of the South Atlantic record. The new ODP Site 1262 record therefore permits an analysis of the coupled evolution of climate and carbon cycle at unprecedented resolution during the Late Maastichtian–Early Eocene.

The long-term trends exhibited by the carbon cycle and climate are broadly synchronous between both ocean basins, indicating a similar evolution of carbon cycle and deep ocean temperature during this time interval in both the Atlantic and Pacific. However, the ODP Site 1209 $\delta^{13}C_{benthic}$ data are generally offset from the ODP Site 1262 data towards more negative isotopic values, typically by ~–0.2–0.4 ‰, suggestive of an older deep-water mass (characterised by a lighter carbon isotope signature) bathing the equatorial Pacific site. This is broadly consistent with independent evidence for early Paleogene ocean circulation patterns provided by neodymium isotope data, which suggest a bi-modal source of deep-water formation from North Pacific Deep Water (NPDW) and South Pacific Deep Water (SPDW) sources in the Pacific, but a single source from the Southern Ocean in the Atlantic (e.g., Thomas et al., 2003, 2008; Dameron et al., 2017; Figure 11). Based on the palaeo-latitudes of ODP Site 1262 and ODP Site 1209 during the early Paleogene (Figure 11, Table 2), ODP Site 1262 would have been located significantly closer to deep-water formation in the Southern Ocean than ODP Site 1209 would have been to deep water production in the South Pacific. However, deep water sourced from NPDW may be of a comparable age at ODP Site 1209 to deep water sourced from the Southern Ocean at ODP Site 1262 (Figure 11).

The Atlantic-Pacific offset in $\delta^{13}C_{benthic}$ is not stable throughout the study interval, however, as a collapse of the gradient in the aftermath of the K/Pg boundary, a decoupling between the records during the latest Maastrichtian, and a reduction in the gradient following the PETM are clear from the data. In general, a collapse in the $\delta^{13}C_{benthic}$ gradient between the ocean basins could be explained by a global collapse in primary productivity, which would control the volume of

pelagic rainout of more isotopically negative surface ocean organic carbon and would therefore modify the isotopic composition of deep ocean DIC everywhere. An alternative, and perhaps more parsimonious, explanation for the collapse in the interbasin $\delta^{13}C_{benthic}$ gradient could be changes in the source of deep water formation in one or both basins, due to changes in thermohaline circulation pathways. The collapse in surface ocean primary productivity following the K/Pg mass extinction is likely to be the primary explanation for the collapse in the Atlantic-Pacific gradient at the start of the Paleocene, which would have resulted in less negative $\delta^{13}C_{benthic}$ values in the oldest deep ocean water masses globally. However, there is also evidence for transient shifts in the predominance of NPDW and SPDW sources in the equatorial Pacifc during the Late Maastrichtian based on neodymium isotopes (Dameron et al., 2017). These include an influx of older and more corrosive SPDW during the LMWE, and a reversal to younger less corrosive predominantly NPDW as the climate cooled during the LMWE recovery (Dameron et al., 2017). The incursion of an older water mass during the LMWE may explain the transient decoupling between the carbon isotope records across this event, although this could alternatively be an artefact of age model inconsistencies between the two sites. Meanwhile, the incursion of younger NPDW immediately prior to the K/Pg boundary may also account for a portion of the collapse in the carbon isotope gradient immediately before and following the K/Pg boundary, as the water masses at ODP Site 1262 and ODP Site 1209 during this time may have been of a comparable age. Although strong evidence for significant changes in thermohaline circulation do not exist for the PETM (e.g., Thomas et al., 2003), a reduction in the volume of deep-water production in the Southern Ocean may have occurred due to polar amplification of surface ocean warming in the high latitudes (Lunt et al., 2010; see **Chapter 6** for further discussion). A change to a more slugglish thermohaline circulation during this time may have decreased ventilation of deep ocean bottom waters and initiated the benthic foraminiferal extinction event (e.g., Thomas, 2003), as well as partially homogenised differences in age of the deep water masses between the Atlantic and Pacific. Biotic turnover during the PETM may also have played a role in reducing the increasingly negative carbon isotope signature of deep ocean DIC with increasing age of the deep water mass, similar to during the aftermath of the K/Pg mass extinction.

Many of the larger hyperthermal events and smaller climatic perturbations of the Late Paleocene–Early Eocene (e.g., the LMWE, LDE, PETM, ETM-2/H2, I1/I2, J, and ETM-3) have a pronounced expression in the $\delta^{13}C_{benthic}$ and $\delta^{18}O_{benthic}$ records from both ODP Site 1262 and ODP Site 1209, confirming a global carbon cycle and climate response within two discrete ocean basins during these events. However, there appears to be a differential response between the two ocean basins during some of the smaller climatic events of the Early–Middle Paleocene, such as the D/STE. The evidence for a global climate and carbon cycle response associated with the LDE and D/STE is discussed in further detail later in this chapter (**Section 3.6.6**).

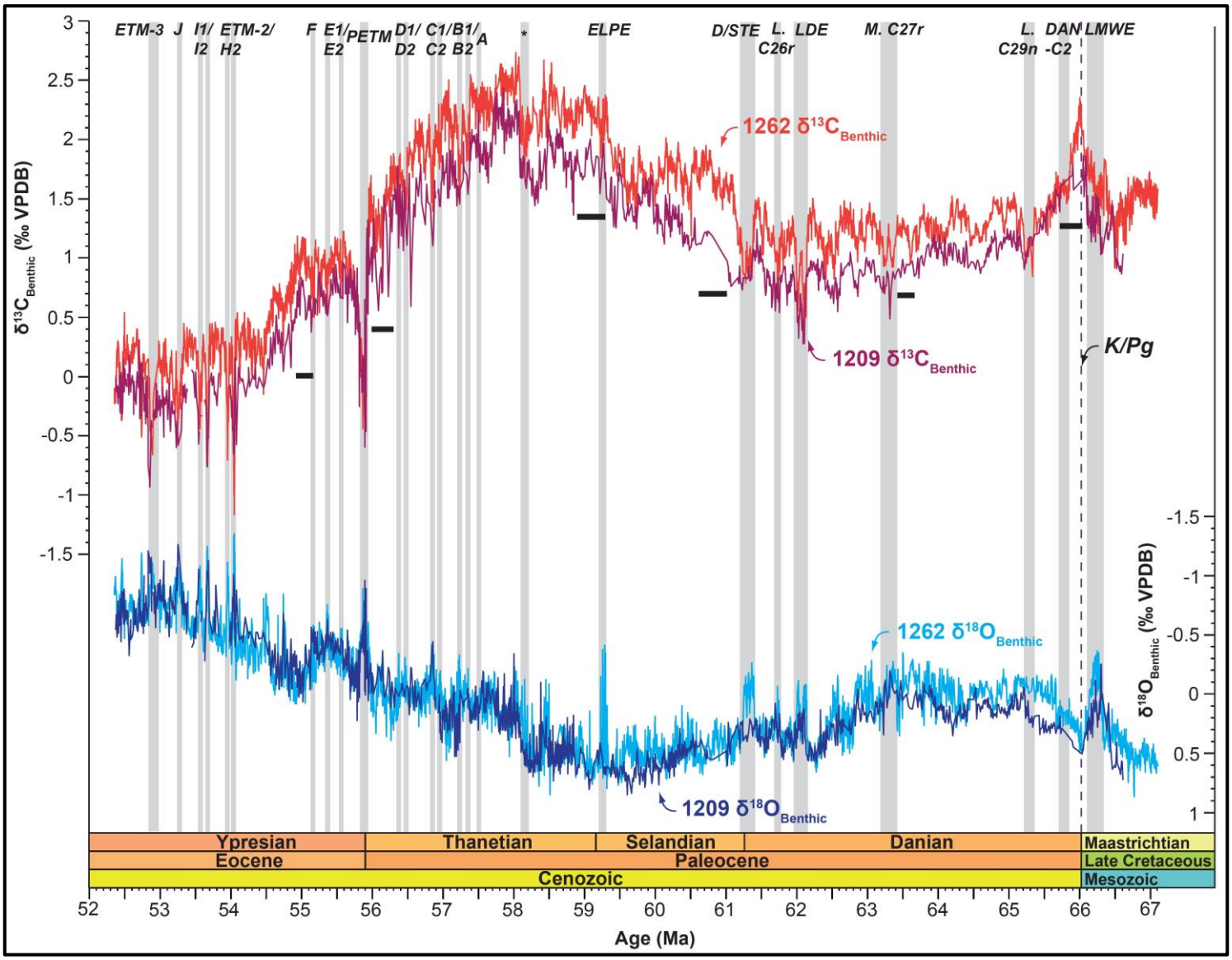

Figure 13 (previous page). Benthic stable carbon isotope ($\delta^{13}C_{benthic}$) data and benthic stable oxygen isotope ($\delta^{18}O_{benthic}$) data from South Atlantic Walvis Ridge ODP Site 1262 and equatorial Pacific Shatsky Rise ODP Site 1209 (Westerhold et al., 2011, 2018), spanning the Late Maastrichtian–Early Eocene. Condensed intervals at ODP Site 1209 are highlighted beneath the $\delta^{13}C_{benthic}$ record by black bars. This comparison highlights the higher resolution and greater stratigraphic completeness of the new ODP Site 1262 records generated and compiled during this study, compared to the published ODP Site 1209 record. Hyperthermals and smaller climatic perturbations are illustrated by labelled grey vertical bars, with the following abbreviations: LMWE – Late Maastrichtian warming event; Dan-C2 – Dan-C2 event; L. C29n – Lower Chron 29n event; M. C27r – Middle Chron 27r event; LDE – Latest Danian Event; L. C26r – Lowr Chron 26r event; D/STE – Danian/Selandian Transition Event; ELPE – Early Late Paleocene Event; PETM – Paleocene-Eocene Thermal Maximum; ETM-2 – Eocene Thermal Maximum 2; ETM-3 – Eocene Thermal Maximum 3. K/Pg = Cretaceous/Paleogene boundary.

3.6.3. ORBITAL PACING OF LATE MAASTRICHTIAN–EARLY EOCENE CHANGES IN CLIMATE AND THE CARBON CYCLE

Similar to the findings of other studies of the Mesozoic and Paleogene (e.g., Huang et al., 2010; Westerhold et al., 2009, 2011; Husson et al., 2011; Liebrand et al., 2016), the Late Maastrichtian–Early Eocene benthic stable isotope ($\delta^{13}C_{benthic}$ & $\delta^{18}O_{benthic}$) records from ODP Site 1262 are characterised by the existence of a strong imprint of orbital cyclicity (Figure 14). The presence of peaks of spectral power at the long (405-kyr) and short (100-kyr) eccentricity bands, as well as ~19–23 kyr (precession), in both the $\delta^{13}C_{benthic}$ (Figure 14a) and $\delta^{18}O_{benthic}$ (Figure 14b) data, suggests that changes in both climate and the carbon cycle were paced predominantly by an eccentricity beat through modulation of precession throughout this time. The weakness of high-latitude forcing in this warm greenhouse world, as suggested previously (Littler et al., 2014; Zeebe et al., 2017), is confirmed by the weak expression of 41 kyr-paced obliquity in both records (Figure 14a,b). This conclusion is consistent with our estimates of generally warm ocean bottom water temperatures of ~7–14°C (Figure 12e), suggesting warm surface waters in high latitude regions of deep-water formation.

To examine temporal changes in dominant periodicities over time, the $\delta^{13}C_{benthic}$ & $\delta^{18}O_{benthic}$ data were firstly band pass filtered at 405-kyr, 100-kyr, and 21-kyr frequencies to identify the varying amplitude of eccentricity and precession

cycles through the record (Figure 15). The isotope records were further divided into 5 discrete time windows (illustrated in Figure 12i and Figure 15g) based on palaeoclimatic and carbon cycle trends (i.e., periods characterised by long-term warming or cooling trends), and MTM power spectra were generated for each time window (Figure 16). Lastly, evolutionary wavelet spectra were generated for the complete $\delta^{13}C_{benthic}$ and $\delta^{18}O_{benthic}$ records (Figure 17).

Long and short eccentricity have the greatest concentration of spectral power within the Early Paleocene (64–61.25 Ma) and Late Paleocene–Early Eocene (58.75–52.35 Ma) time slices (Figure 16b,d,e; Figure 17a,b), which may be expected given larger amplitude variations within the 400-kyr (Figure 15c) and 100-kyr (Figure 15d) filters corresponding to larger hyperthermal events within the ODP Site 1262 records. By contrast, more significant power is concentrated in the $\delta^{13}C_{benthic}$ record at 19–23 kyr frequencies during the Late Maastrichtian–Early Paleocene time slice (Figure 16a). The 21-kyr filter (Figure 15e) and wavelet spectrum (Figure 17a) show that this amplified precession cyclicity occurs exclusively during the Late Maastrichtian, with an abrupt decrease in power across the K/Pg boundary. This feature is also picked out in the elemental Fe record, especially during the LMWE (Figure 12f), suggesting amplified carbon cycle sensitivity to orbital precession during this Late Maastrichtian greenhouse event (see **Chapter 4, Sections 4.6.5. and 4.6.6.** for further discussion). Interestingly, and in contrast to most of the record, there are also peaks in spectral power close to the 41-kyr obliquity band in the oldest Late Maastrichtian–Early Paleocene portion of the record (Figure 16a,b), which may indicate a more significant role of high-latitude insolation forcing on global climate during this period characterised by the coolest climates within the record. Based on comparable $\delta^{18}O$-derived Southern Ocean temperatures between the Maastrichtian and the threshold triggering the onset of Antarctic ice sheet growth during the Late Eocene, Huber et al. (2018) suggested the possible buildup of small ephemeral ice sheets on Antarctica during the Maastrichtian. However, the development of ice sheets during the Cretaceous remains a controversial topic and direct evidence for glaciation (e.g., unequivocal ice rafted debris) from this time period is yet to be found.

An apparent concentration of spectral power corresponding to the long-obliquity (1200 kyr) band on the MTM plots (Figure 14a,b) and evolutionary wavelet spectra (Figure 17a,b) may suggest some long-obliquity climate and carbon cycle modulation during this time, although power at this frequency could be an artefact as it is a multiple of the 405-kyr eccentricity cycle. Furthermore, caution should be emphasised when interpreting the significance of longer-term (>1 million year) cycles, due to the possible introduction of bias when the records were detrended prior to performing spectral analysis (see **Section 3.4.6.**).

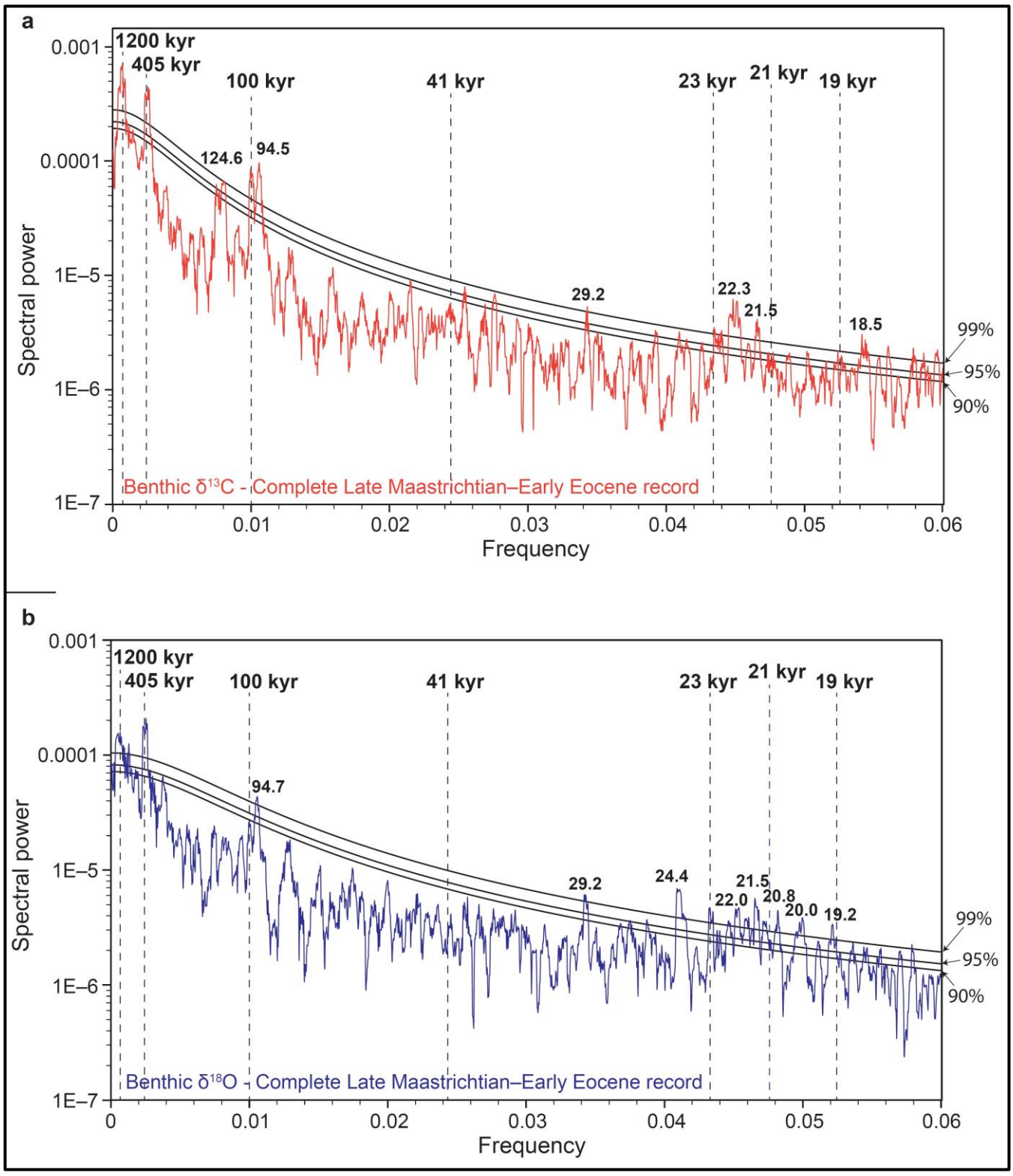

*Figure 14. Multi-Taper Method (MTM) power spectra for the complete Late Maastrichtian–Early Eocene (67.10–52.35 Ma) benthic stable isotope records from South Atlantic ODP Site 1262: (**a**) $\delta^{13}C_{benthic}$ record. The resolution of the record enables the split eccentricity peaks at ~125 and ~95 kyr to be clearly resolved. (**b**) $\delta^{18}O_{benthic}$ record. Vertical dashed lines indicate Milankovitch frequencies. 99%, 95% and 90% confidence levels are indicated by labelled black lines.*

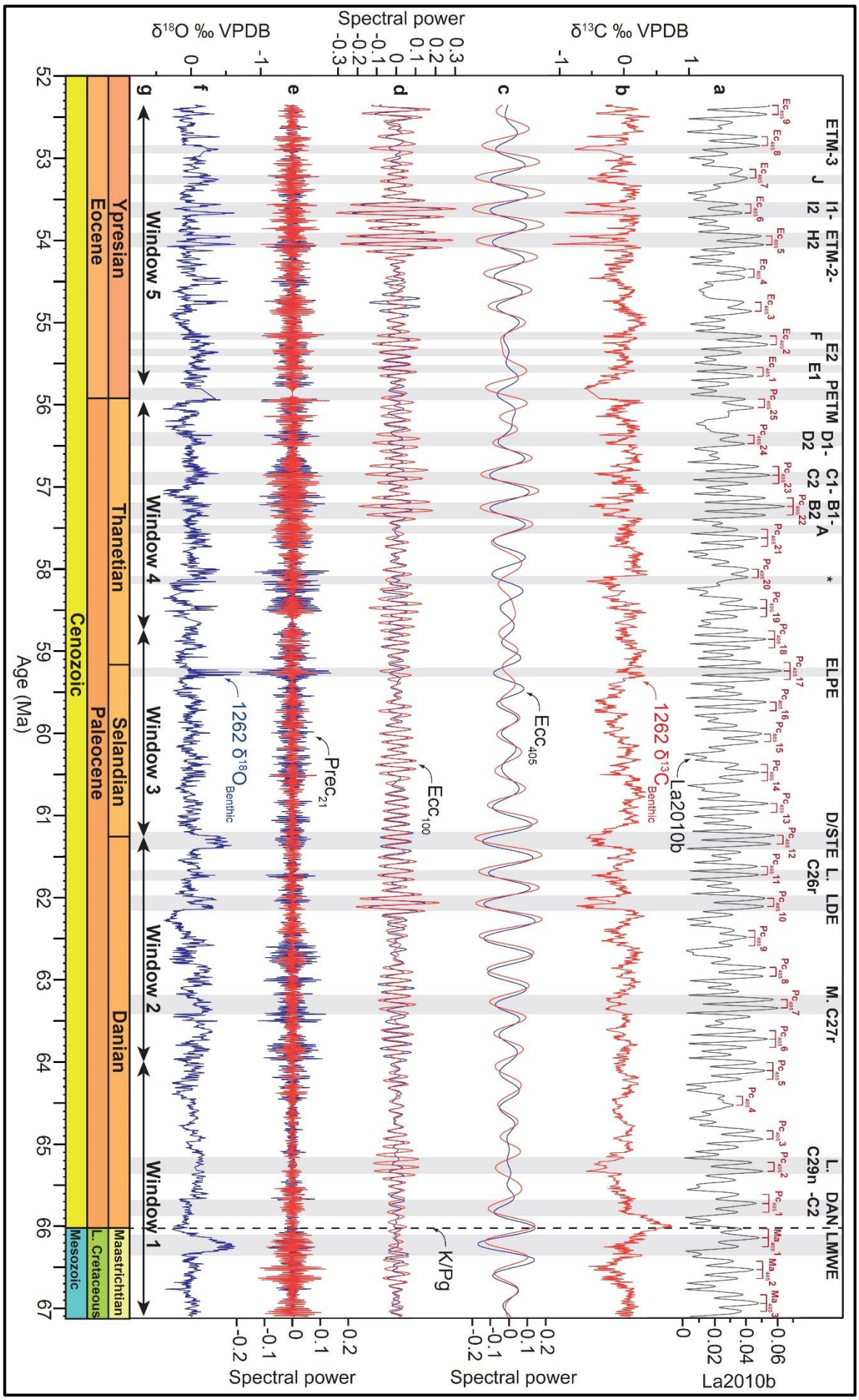
δ18O ‰ VPDB
Spectral power
δ13C ‰ VPDB
ETM-3
J
I1-
I2
ETM-2-
H2
F
E2
E1
PETM
D1-
D2
C1-
C2
B1-
B2
A
*
ELPE
D/STE
L. C26r
LDE
M. C27r
L. C29n
DAN
-C2
LMWE
a
b
c
d
e
f
g
Window 5
Window 4
Window 3
Window 2
Window 1
Ypresian
Thanetian
Selandian
Danian
Eocene
Paleocene
Cenozoic
Maastrichtian
L. Cretaceous
Mesozoic
Age (Ma)
1262 δ18OBenthic
Prec21
Ecc405
Ecc100
1262 δ13CBenthic
La2010b
K/Pg
Spectral power
Spectral power
La2010b

*Figure 15 (previous page). Data filters at the principle Milankovitch frequencies for the benthic stable carbon isotope ($\delta^{13}C_{benthic}$) record in red and benthic stable oxygen isotope ($\delta^{18}O_{benthic}$) record in blue from South Atlantic ODP Site 1262: (**a**) La2010b orbital solution (Laskar et al., 2011a). Long eccentricity (405-kyr) maxima are labelled in red following the nomenclature of Husson et al. (2011) for the Maastrichtian, Dinarès-Turell et al. (2014) for the Paleocene, and Westerhold & Röhl (2009) for the Eocene. (**b**) Detrended $\delta^{13}C_{benthic}$ data; (**c**) long eccentricity (405-kyr) filter (Ecc_{405}); (**d**) short eccentricity (100-kyr) filter (Ecc_{100}); (**e**) precession (21-kyr) filter ($Prec_{21}$); (**f**) detrended $\delta^{18}O_{benthic}$ data; (**g**) temporal distribution of discrete time windows used in Figure 16 and Figure 19. Hyperthermals and smaller climatic perturbations are illustrated by labelled grey vertical bars, with the following abbreviations: LMWE – Late Maastrichtian warming event, K/Pg – Cretaceous/Paleogene boundary, Dan-C2 – Dan-C2 event, L. C29n – Lower Chron 29n event, M. C27r – Middle Chron 27r event, LDE – Latest Danian Event, L. C26r – Lower Chron 26r event, D/STE – Danian/Selandian Transition Event, ELPE – Early Late Paleocene Event, PETM – Paleocene-Eocene Thermal Maximum, ETM-2 – Eocene Thermal Maximum 2, ETM-3 – Eocene Thermal Maximum 3.*

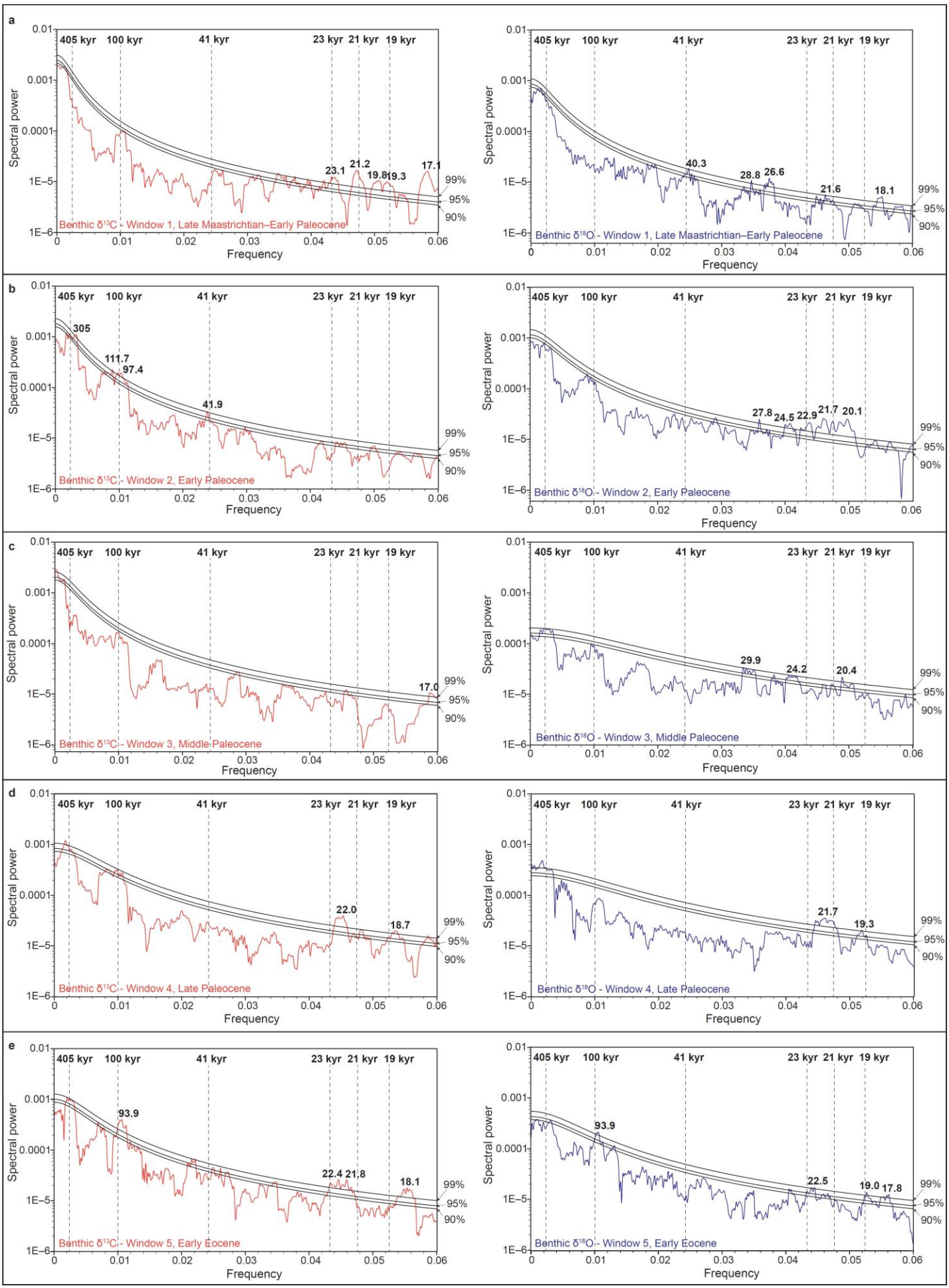
a
405 kyr 100 kyr 41 kyr 23 kyr 21 kyr 19 kyr
Spectral power
Frequency
23.1 21.2 19.8 19.3 17.1
Benthic δ13C - Window 1, Late Maastrichtian–Early Paleocene
40.3 28.8 26.6 21.6 18.1
Benthic δ18O - Window 1, Late Maastrichtian–Early Paleocene
99%
95%
90%
b
305 111.7 97.4 41.9
Benthic δ13C - Window 2, Early Paleocene
27.8 24.5 22.9 21.7 20.1
Benthic δ18O - Window 2, Early Paleocene
c
17.0
Benthic δ13C - Window 3, Middle Paleocene
29.9 24.2 20.4
Benthic δ18O - Window 3, Middle Paleocene
d
22.0 18.7
Benthic δ13C - Window 4, Late Paleocene
21.7 19.3
Benthic δ18O - Window 4, Late Paleocene
e
93.9 22.4 21.8 18.1
Benthic δ13C - Window 5, Early Eocene
93.9 22.5 19.0 17.8
Benthic δ18O - Window 5, Early Eocene

*Figure 16 (previous page). Multi-Taper Method (MTM) power spectra for the benthic stable carbon isotope ($\delta^{13}C_{benthic}$) record in red and benthic stable oxygen isotope ($\delta^{18}O_{benthic}$) record in blue from South Atlantic ODP Site 1262, for the following 5 discrete time windows (identified in Figure 12i and Figure 15g): (**a**) Window 1, Late Maastrichtian–Early Paleocene (67.1–64.0 Ma); (**b**) Window 2, Early Paleocene (64.0–61.25 Ma); (**c**) Window 3, Middle Paleocene (61.25–58.75 Ma); (**d**) Window 4, Late Paleocene (58.75–55.93 Ma); (**e**) Window 5, Early Eocene (55.83–52.35 Ma). Labelled vertical dashed lines indicate Milankovitch cycle frequencies. 99%, 95% and 90% confidence levels are indicated by labelled black lines.*

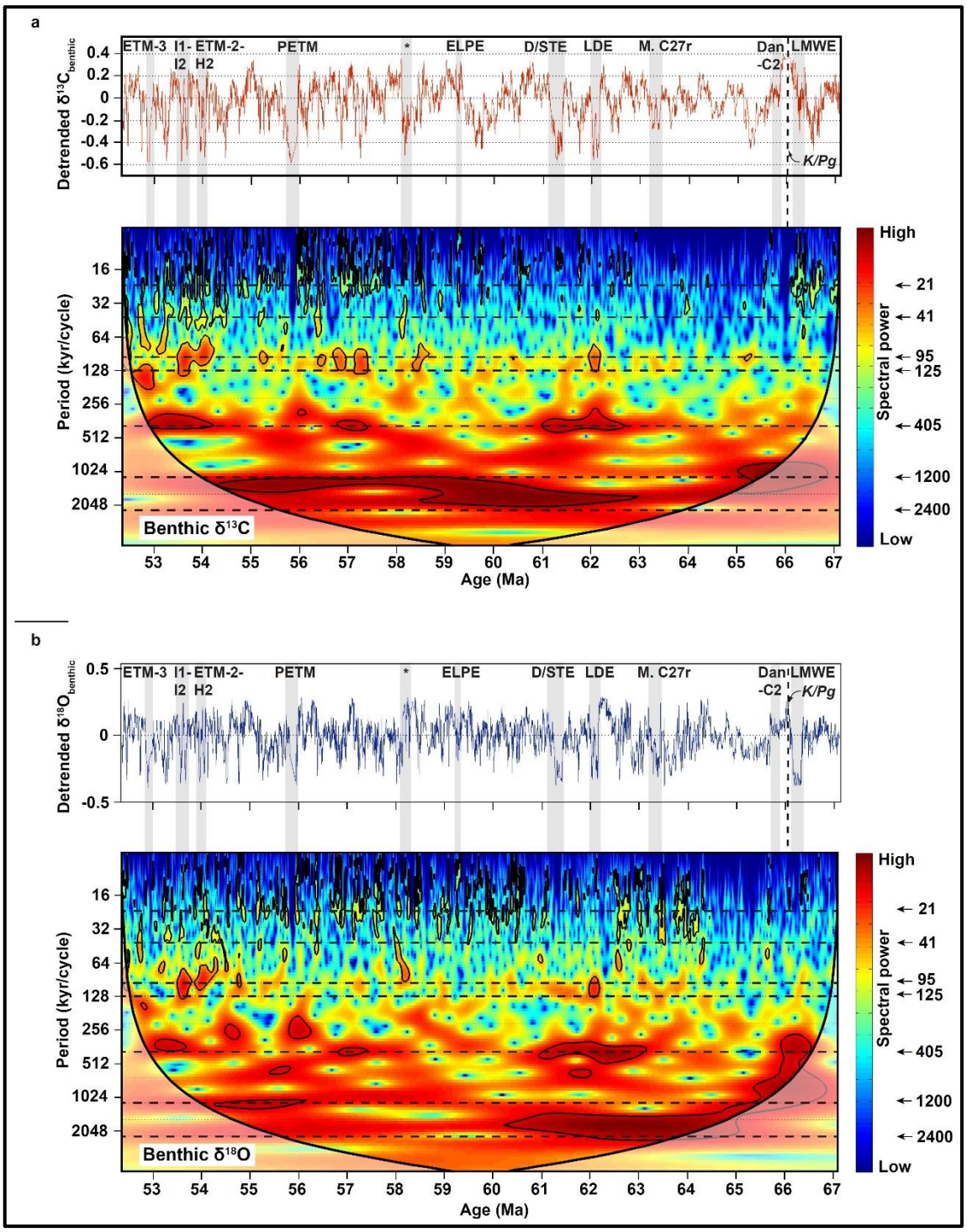

*Figure 17. Evolutionary wavelet spectra for the complete Late Maastrichtian–Early Eocene (67.10–52.35 Ma) benthic stable isotope records from South Atlantic ODP Site 1262: (**a**) $\delta^{13}C_{benthic}$ record; (**b**) $\delta^{18}O_{benthic}$ record. Milankovitch cycles (in kyr) are indicated by dashed lines across the spectra and labelled with arrows along the right-hand margin. Key hyperthermals and smaller climatic perturbations are illustrated by labelled grey vertical bars, with the following abbreviations: LMWE – Late Maastrichtian warming event, Dan-C2 – Dan-C2 event, M. C27r – Middle Chron 27r event, LDE – Latest Danian Event, D/STE – Danian/Selandian Transition Event, ELPE – Early Late Paleocene Event, PETM – Paleocene-Eocene Thermal Maximum, ETM-2 – Eocene Thermal Maximum 2, ETM-3 – Eocene Thermal Maximum 3.*

3.6.4. PHASING BETWEEN THE CHANGES IN CLIMATE AND THE CARBON CYCLE

Cross spectral analysis of the complete Late Maastrichtian–Early Eocene $\delta^{18}O_{benthic}$ and $\delta^{13}C_{benthic}$ records (Figure 18), and of their five discrete time windows (Figure 19), allows us to examine phasing between changes in climate and the carbon cycle at Milankovitch frequencies during the Late Maastrichtian–Early Eocene. If the whole record is considered, changes in the carbon cycle ($\delta^{13}C_{benthic}$) lag changes in climate ($\delta^{18}O_{benthic}$) by ~22.8 ±5.7 kyr at the 405-kyr band, ~4.5 ± 2.2 kyr at the 125-kyr band, and ~3 ± 0.7 kyr at the 95-kyr band, but within error, are almost in phase at precession frequencies (19–23 kyr; Figure 18). These observations suggest that changes in orbital configuration, namely eccentricity modulation of precession, were sufficient to induce at least minor deep-sea warming. This initial warming was further amplified via a positive feedback by the release of isotopically-light carbon from temperature-sensitive (e.g., biogenic CH_4 or high-latitude permafrost), or climate-sensitive (e.g., low-latitude peat), stocks.

A comparable lag ($\delta^{13}C_{benthic}$ lagging $\delta^{18}O_{benthic}$) is observed at the 405-kyr frequency within the Late Maastrichtian–Early Paleocene (~23.0 ± 11.5 kyr; Window 1; Figure 19a), Early Paleocene (~22.0 ± 4.8 kyr; Window 2; Figure 19b) and Early Eocene (~25.1 ± 5.0 kyr; Window 5; Figure 19e) time slices, with smaller lags of 0.7–5.3 ± 0.7–5.4 kyr within the 100-kyr band (Figure 19a-e). An apparent 7.3 ± 14.6 kyr lag of $\delta^{18}O_{benthic}$ behind $\delta^{13}C_{benthic}$ is dismissed in the Late Paleocene Window 4 (Figure 19d), since phasing at the 405-kyr frequency is less coherent (coherence of 0.81) and uncertainty is much greater (± 14.6 kyr) within that window compared to the other time slices. The lower level of coherency during Window 4 may be related to the temporary decoupling between the carbon and oxygen isotope records at the 405-kyr frequency within the older portion of this time window at ~58.5 Ma (Figure 15c). The similar lags observed during both the warmest climate within the record, the Early Eocene, and the coolest, the Late Maastrichtian, suggests a lack of sensitivity of phasing to ambient climate state, at least within the climatic range defined within this time interval.

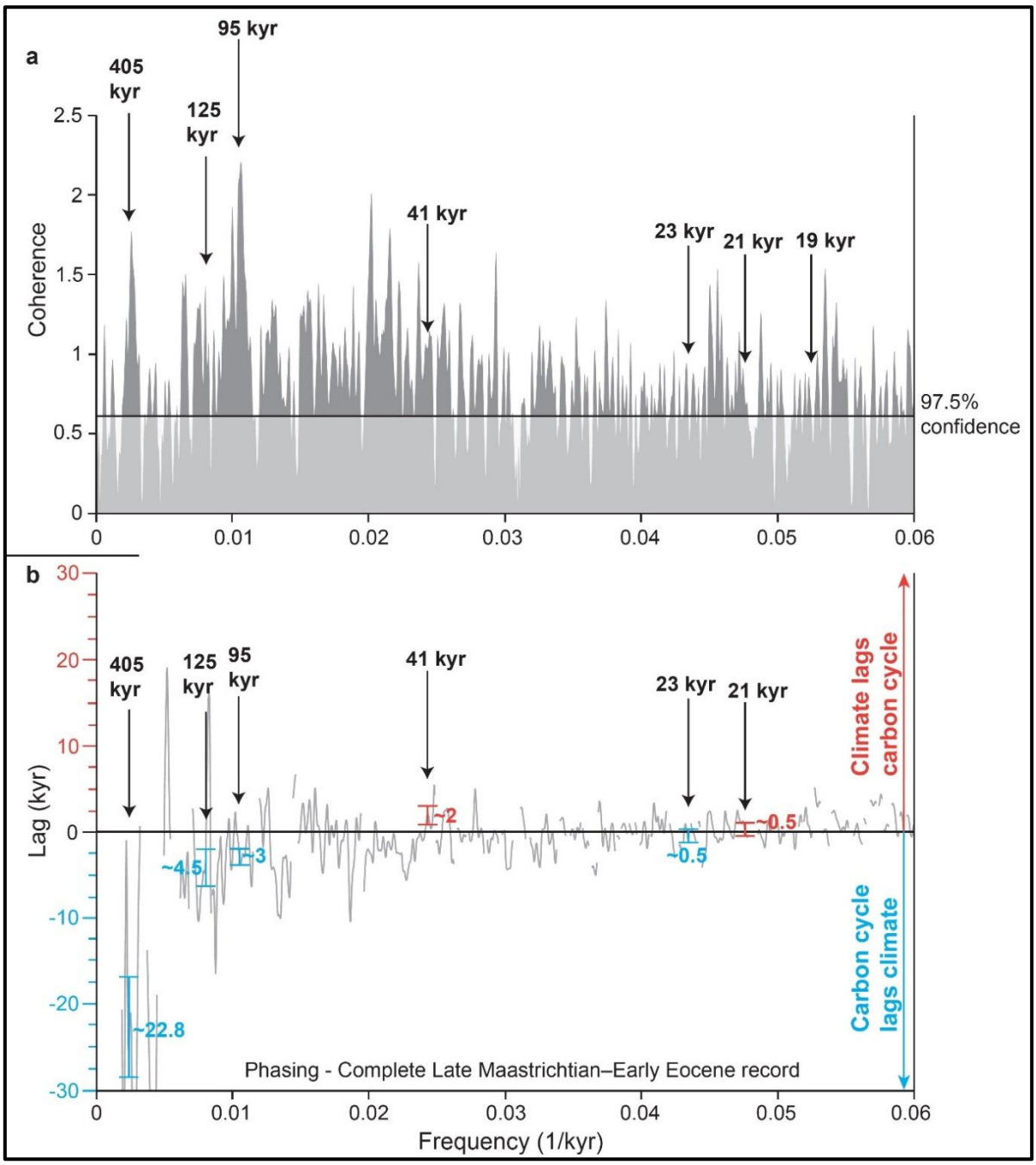

*Figure 18. Coherence (**a**) and phasing (**b**) between the benthic stable carbon isotope ($\delta^{13}C_{benthic}$) record and benthic stable oxygen isotope ($\delta^{18}O_{benthic}$) record from South Atlantic ODP Site 1262. On the coherence spectra, frequencies above the 97.5% confidence level are considered coherent, for which the phasing between $\delta^{13}C_{benthic}$ and $\delta^{18}O_{benthic}$ was calculated. Negative values for the phasing (lag) in blue indicate that $\delta^{13}C_{benthic}$ lags $\delta^{18}O_{benthic}$ (i.e., carbon cycle lags climate), whilst positive values in red indicate $\delta^{18}O_{benthic}$ lags $\delta^{13}C_{benthic}$ (i.e., climate lags carbon cycle). Values for the mean lag (in kyr) are indicated, with the range of values at the 97.5% confidence level indicated by error bars.*

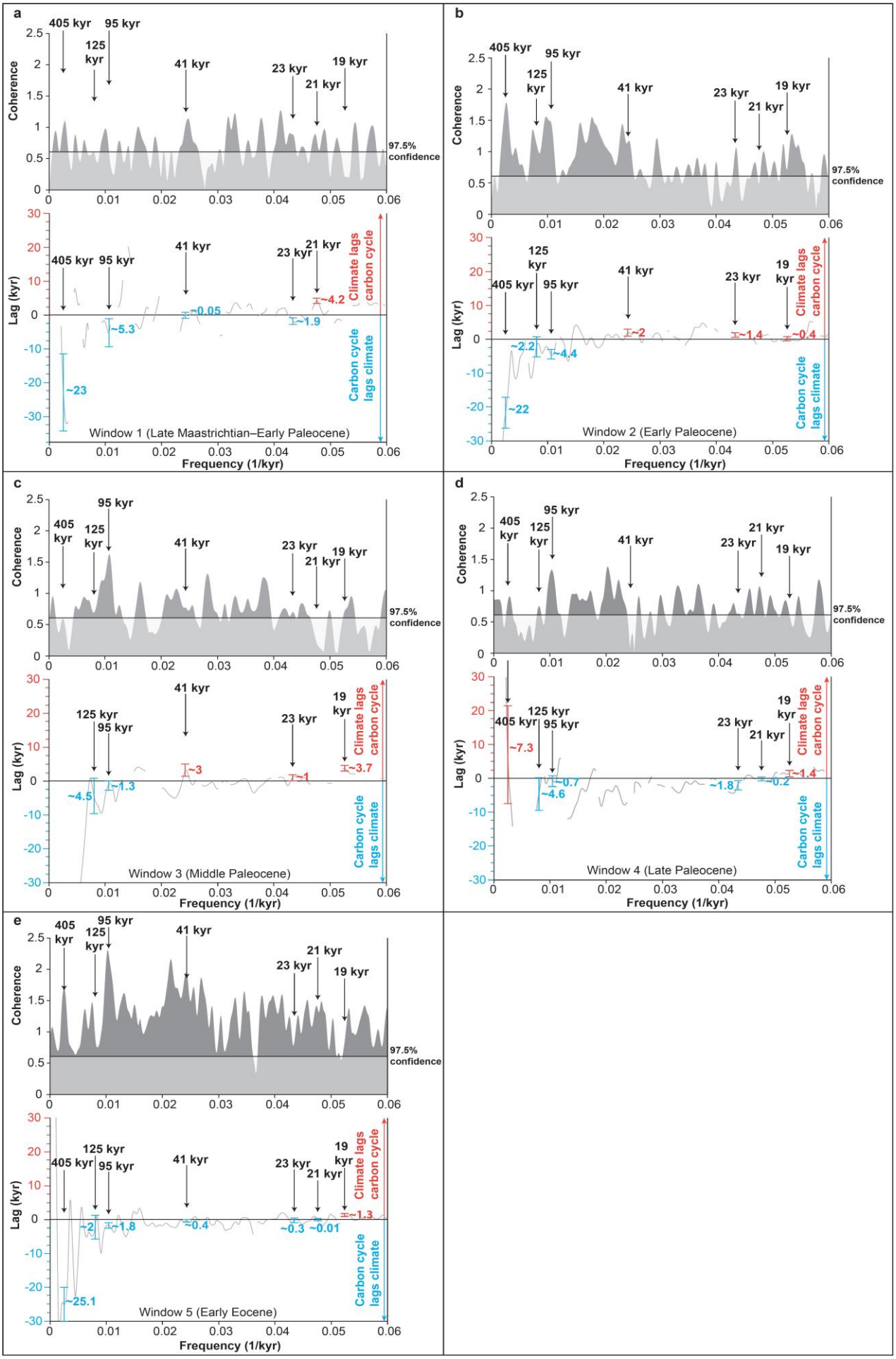
a
405 kyr
95 kyr
125 kyr
41 kyr
23 kyr
21 kyr
19 kyr
Coherence
97.5% confidence
Lag (kyr)
Climate lags carbon cycle
Carbon cycle lags climate
~0.05
~4.2
~1.9
~5.3
~23
Window 1 (Late Maastrichtian–Early Paleocene)
Frequency (1/kyr)
b
~2
~1.4
~0.4
~2.2
~4.4
~22
Window 2 (Early Paleocene)
c
~3
~3.7
~1
~4.5
~1.3
Window 3 (Middle Paleocene)
d
~7.3
~0.7
~4.6
~1.8
~0.2
~1.4
Window 4 (Late Paleocene)
e
~0.4
~1.3
~0.3
~0.01
~2
~1.8
~25.1
Window 5 (Early Eocene)

*Figure 19 (previous page). Coherence and phasing between the benthic stable carbon isotope ($\delta^{13}C_{benthic}$) and benthic stable oxygen isotope ($\delta^{18}O_{benthic}$) records from South Atlantic ODP Site 1262, for the following 5 discrete time windows (defined in Figure 12i and Figure 15g): (**a**) Window 1, Late Maastrichtian–Early Paleocene (67.1–64.0 Ma); (**b**) Window 2, Early Paleocene (64.0–61.25 Ma); (**c**) Window 3, Middle Paleocene (61.25–58.75 Ma); (**d**) Window 4, Late Paleocene (58.75–55.93 Ma); (**e**) Window 5, Early Eocene (55.83–52.35 Ma). On the coherence spectra, frequencies above the 97.5% confidence level are considered coherent, for which the phasing between $\delta^{13}C_{benthic}$ and $\delta^{18}O_{benthic}$ was calculated. Negative values for the phasing (lag) in blue indicate that $\delta^{13}C_{benthic}$ lags $\delta^{18}O_{benthic}$ (i.e., carbon cycle lags climate), whilst positive values in red indicate $\delta^{18}O_{benthic}$ lags $\delta^{13}C_{benthic}$ (i.e., climate lags carbon cycle). Values for the mean lag (in kyr) are indicated, with the range of values at the 97.5% confidence level indicated by error bars.*

3.6.5. PLACING THE DISCRETE HYPERTHERMAL EVENTS INTO AN ORBITAL CYCLOSTRATIGRAPHIC FRAMEWORK

The new orbitally-tuned age model allows us to place all hyperthermals and smaller climatic perturbations of this time period into a robust cyclostratigraphic framework for the first time from the South Atlantic. Since the age model was tuned to 405-kyr eccentricity cycles based on the response of the carbon cycle to orbitally-induced changes in insolation, identified using the $\delta^{13}C_{benthic}$ record and correlated to dissolution proxy records (i.e., Fe intensity, magnetic susceptibility and colour reflectance), the correlation of climatic events (such as hyperthermals) to orbital forcing mechanisms can be achieved using the independent $\delta^{18}O_{benthic}$ record.

The majority of Paleogene hyperthermals and smaller climatic perturbations occur during maxima in the 405-kyr eccentricity cycle (Figure 15a), when Earth's orbit around the Sun was most elliptical, leading to an enhanced expression of two 100-kyr cycles. The majority of the climatic perturbations during the Paleocene–Eocene are therefore characteristically double-spiked, such as ETM2-H2 and I1-I2 of the Early Eocene, or the LDE and Middle C27r events of the Early Paleocene (Figure 15b,f). Variations in orbital eccentricity have little effect on the total amount of solar radiation received by Earth's surface, but these cycles do modify the difference between perihelion temperatures (when Earth passes closest to the Sun) and aphelion temperatures (when Earth is farthest from the Sun), which will be greatest during eccentricity maxima (Laskar et al., 2011a). Precession cycles can therefore be significantly amplified during

eccentricity maxima, leading to enhanced seasonal contrasts and thus potentially destabilising temperature- or climate-sensitive carbon reservoirs over a critical threshold leading to their catastrophic release. The double-spiked nature of many hyperthermals suggests that either the carbon source was not completely depleted during the first event, or alternatively, significant recharge of the carbon source took place over the ~100 kyr between events, in order to generate the second typically slightly smaller event ~100 kyr later.

The LMWE and PETM represent notable exceptions, however, as their inceptions do not occur during 405-kyr eccentricity maxima and they lack the characteristic orbitally-paced double spike of most other hyperthermals (Figure 15b,f). Even though the peak of these events may be in phase with a 100-kyr maxima in eccentricity (e.g., Zachos et al., 2010; Figure 15a), their initiations may not be purely orbitally-paced (see **Chapter 4** for further discussion of the origin of the LMWE). Deccan Traps volcanism (Renne et al., 2015; Schoene et al., 2015) and the second phase of NAIP volcanism (Sinton & Duncan, 1998; Gutjahr et al., 2017) likely represent important non-orbital triggers for the LMWE and PETM, respectively (Figure 12h). The potential release of significant quantities of thermogenic methane during extrusion of NAIP volcanism subaqueously into marine organic-rich shales may also help to explain the significantly greater magnitude of the PETM (Svensen et al., 2004; Gutjahr et al., 2017), compared to other early Paleogene hyperthermals.

3.6.6. THE EXPRESSION OF THE LATEST DANIAN EVENT, LOWER CHRON 26R EVENT, AND DANIAN/SELANDIAN TRANSITION EVENT AT ODP SITE 1262

The new high-resolution ODP Site 1262 benthic stable isotope records presented here also shed light on the poorly studied events of the Late Maastrichtian and Early–Middle Paleocene. This section focuses on the Latest Danian Event (LDE), Lower Chron 26r (L. C26r) event, and Danian/Selandian Transition Event (D/STE). The new ODP Site 1262 planktic stable isotope data generated across the D/STE during this study are presented here and discussed in **Section 3.6.6.1**. The Late Maastrichtian warming event (LMWE) and Dan-C2 event are discussed in **Chapters 4 and 5**, respectively.

The new $\delta^{13}C_{benthic}$ and $\delta^{18}O_{benthic}$ data from ODP Site 1262 spanning ~62.45–61.0 Ma are presented in Figure 20. The updated orbitally-tuned age model used in this study for these data highlights that the LDE, Lower C26r event and D/STE represent three orbitally-paced perturbations to the climate and carbon cycle during three consecutive 405-kyr eccentricity maxima: $Pc_{405}10$, $Pc_{405}11$ and $Pc_{405}12$, respectively (Figure 20a).

The LDE is the largest of the three events and is characterised by pronounced double-spiked negative excursions in $\delta^{13}C_{benthic}$ and $\delta^{18}O_{benthic}$, spaced ~100 kyr apart (Figure 20b). The oldest of these excursions, named LDE1 after Deprez et al. (2017), commences ~62.16 Ma and is characterised by decreases of ~–0.9‰ in $\delta^{13}C_{benthic}$ and ~–0.6‰ in $\delta^{18}O_{benthic}$ over ~20 kyr. The excursion in $\delta^{18}O_{benthic}$ records a temperature increase of ~+2.5°C in the bottom waters bathing ODP Site 1262. Peak warmth during LDE1 lasts for ~40 kyr and is characterised by bottom water temperatures of ~10°C. This is then followed by positive excursions of ~+0.5‰ in $\delta^{13}C_{benthic}$ and ~+0.3‰ in $\delta^{18}O_{benthic}$ over ~30 kyr, representing partial recovery towards pre-LDE1 conditions between the two ~100 kyr-paced excursions. The second and slightly smaller excursion, named LDE2 (Deprez et al., 2017), is characterised by decreases of ~–0.5‰ in $\delta^{13}C_{benthic}$ and ~–0.4‰ in $\delta^{18}O_{benthic}$ over ~40 kyr. The excursion in $\delta^{18}O_{benthic}$ represents a second temperature rise of ~+2.0°C at ODP Site 1262 to peak temperatures of ~10°C, comparable to those observed for LDE1. The peak of LDE2 lasts for a duration of ~20 kyr, followed by recovery to pre-excursion conditions by ~61.95 Ma. The LDE therefore lasts for a total duration of ~200 kyr and encompasses the magnified expression of two short (100-kyr) eccentricity cycles during the $Pc_{405}10$ long (405-kyr) eccentricity maximum.

The Lower C26r event occurred ~61.73 Ma and is characterised by single transient excursions of ~–0.5‰ in $\delta^{13}C_{benthic}$ and $\delta^{18}O_{benthic}$, lasting a total duration of ~100 kyr (Figure 20b). Whilst changes in bottom water temperature during this event are of comparable magnitude to the second ~100-kyr-paced excursion of the LDE (LDE2) at ODP Site 1262, this event lacks its characteristic double-spiked nature. The Lower C26r event represents the amplification of the first short (100-kyr) eccentricity maximum during the $Pc_{405}11$ long (405-kyr) eccentricity maximum. The second amplified 100-kyr maximum during $Pc_{405}11$ in the

La2010b orbital solution has a comparatively muted response of ~–0.2‰ in $\delta^{18}O_{benthic}$ and negligible response in $\delta^{13}C_{benthic}$ at ODP Site 1262, suggesting a bottom water warming of only ~+0.75°C.

The onset of the D/STE occurred at ~61.4 Ma and is characterised by excursions of ~–0.6‰ in $\delta^{13}C_{benthic}$ and ~–0.4‰ in $\delta^{18}O_{benthic}$ over ~20–40 kyr (Figure 20b). The D/STE encompasses two amplified short (100-kyr) eccentricity maxima during the $Pc_{405}12$ long (405-kyr) eccentricity maximum, however, there is a muted recovery interval between the two amplified 100-kyr maxima compared to the LDE. Peak warmth during this event (of ~10–11°C) lasts ~140 kyr. Superimposed on this long-lasting broad warming trend are two transient positive excursions of ~+0.3‰ in $\delta^{13}C_{benthic}$ and $\delta^{18}O_{benthic}$. A total duration of the event of ~200 kyr is comparable to the duration of the LDE.

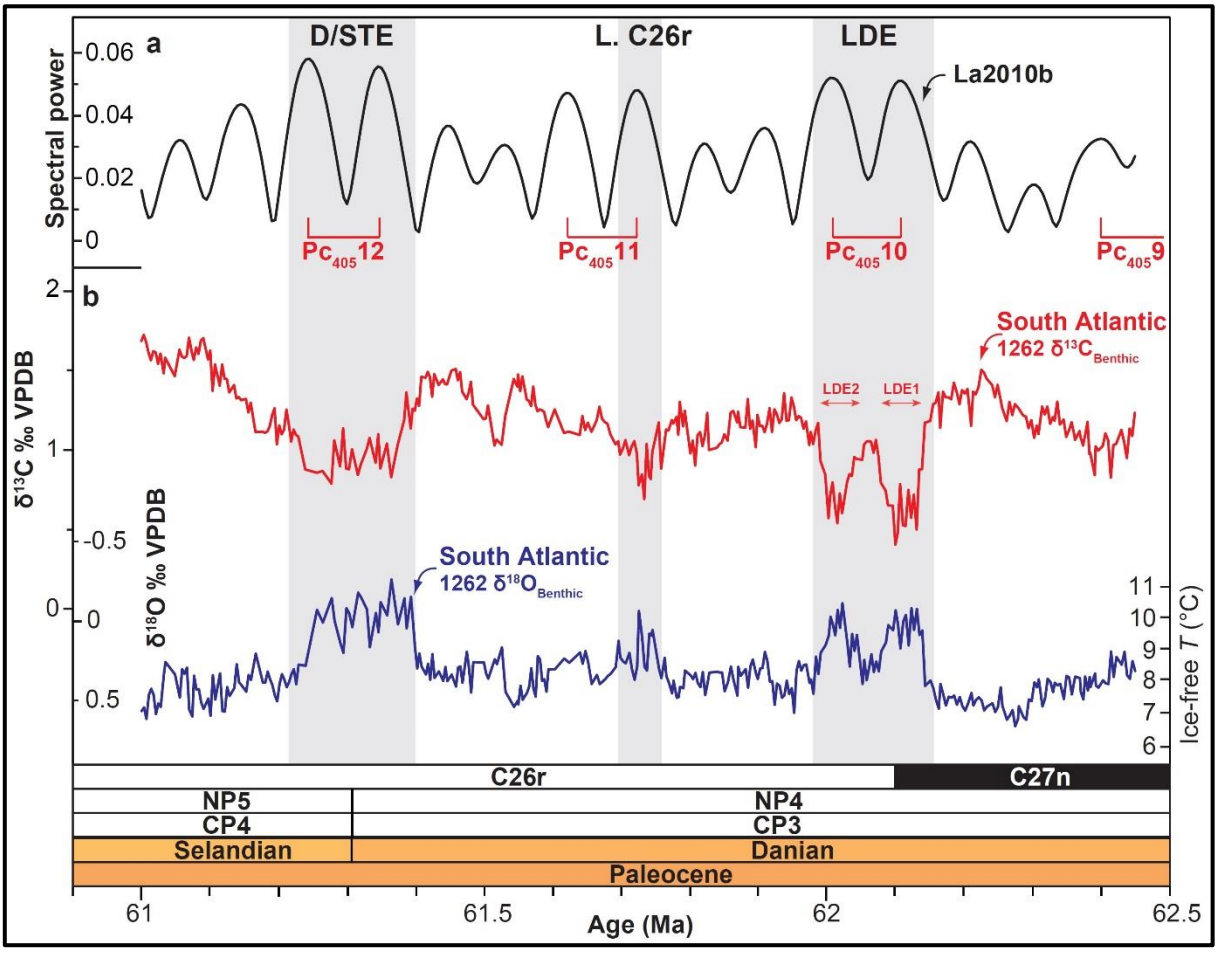

*Figure 20. Late Danian–early Selandian benthic foraminiferal stable isotope data from South Atlantic ODP Site 1262 (palaeo-depth ~3000 m): (**a**) La2010b orbital solution (Laskar et al., 2011a). Long (405-kyr) eccentricity maxima are labelled following the nomenclature of Dinarès-*

*Turell et al. (2014). (**b**) Benthic stable isotope data (this study), illustrating the expressions of the Latest Danian Event (LDE), Lower Chron 26r event (L. C26r), and Danian/Selandian Transition Event (D/STE). The oldest and youngest of the LDE carbon cycle perturbations have been named LDE1 and LDE2 respectively, after Deprez et al. (2017). Magnetozones are from Bowles (2006) and nannoplankton zones from Monechi et al. (2013).*

3.6.6.1. COMPARISON BETWEEN THE NEW STABLE ISOTOPE DATA FROM ODP SITE 1262 WITH PUBLISHED STABLE ISOTOPE DATA FOR THE EARLY PALEOCENE

A comparison of the new benthic data from ODP Site 1262 with published datasets from equatorial Pacific ODP Site 1209 (Westerhold et al., 2011) and Indian Ocean ODP Site 761 (Quillévéré et al., 2002) between ~62.6–61 Ma confirms the global nature of the LDE (Figure 21). Whilst the double-spiked nature of the LDE is not resolved in the lower resolution benthic stable isotope data from the Indian Ocean, the LDE is characterised by pronounced ~100 kyr paced double-spiked negative excursions in $\delta^{13}C_{benthic}$ and $\delta^{18}O_{benthic}$ in both the South Atlantic and equatorial Pacific. The magnitude of warming of bottom waters at equatorial Pacific ODP Site 1209 (~+2°C) is slightly lower compared to the South Atlantic (~+2.5°C).

The Lower C26r event is also characterised by negative excursions in $\delta^{13}C_{benthic}$ and $\delta^{18}O_{benthic}$ of a comparable magnitude in the South Atlantic and equatorial Pacific, suggesting that a comparable warming of ~+2°C took place in the deep waters bathing ODP Sites 1262 and 1209 during the event. Unlike the South Atlantic, the Lower C26r excursion in the equatorial Pacific takes the form of a double-spiked excursion, analogous to, but of a smaller magnitude than, the LDE.

An even more significant discrepancy exists between the isotopic responses of the D/STE in the South Atlantic and Pacific Oceans. Whilst the D/STE is characterised by broad negative excursions in $\delta^{13}C_{benthic}$ and $\delta^{18}O_{benthic}$ and a warming of ~+2°C at ODP Site 1262, it appears to have no transient expression in benthic isotope data from equatorial Pacific ODP Site 1209.

A comparison of published bulk carbonate, surface planktic, and subsurface planktic (thermocline) stable isotope data from the South Atlantic, North Atlantic, and equatorial Pacific between ~62.5–61 Ma confirms that the LDE is associated with global changes in (near) surface $\delta^{13}C$ and $\delta^{18}O$ (Figure 22). Negative excursions in $\delta^{13}C$ and $\delta^{18}O$ confirm a carbon cycle perturbation and suggest a potential coeval warming of the mixed layer and thermocline waters in the equatorial Pacific during the LDE. The double spiked excursion in $\delta^{13}C$ is also observed in bulk carbonate data from both the North and South Atlantic. Although the data is at a lower resolution, there is also evidence for a negative $\delta^{13}C$ perturbation and potential surface warming within planktic data from the equatorial Pacific, especially at thermocline depths, during the Lower C26r event. The D/STE is characterised by a broad negative excursion of ~–0.3‰ in $\delta^{18}O_{planktic}$ from ODP Site 1262, suggesting a potential broad temperature increase of ~+1.5°C in the mixed layer in the South Atlantic during the event.

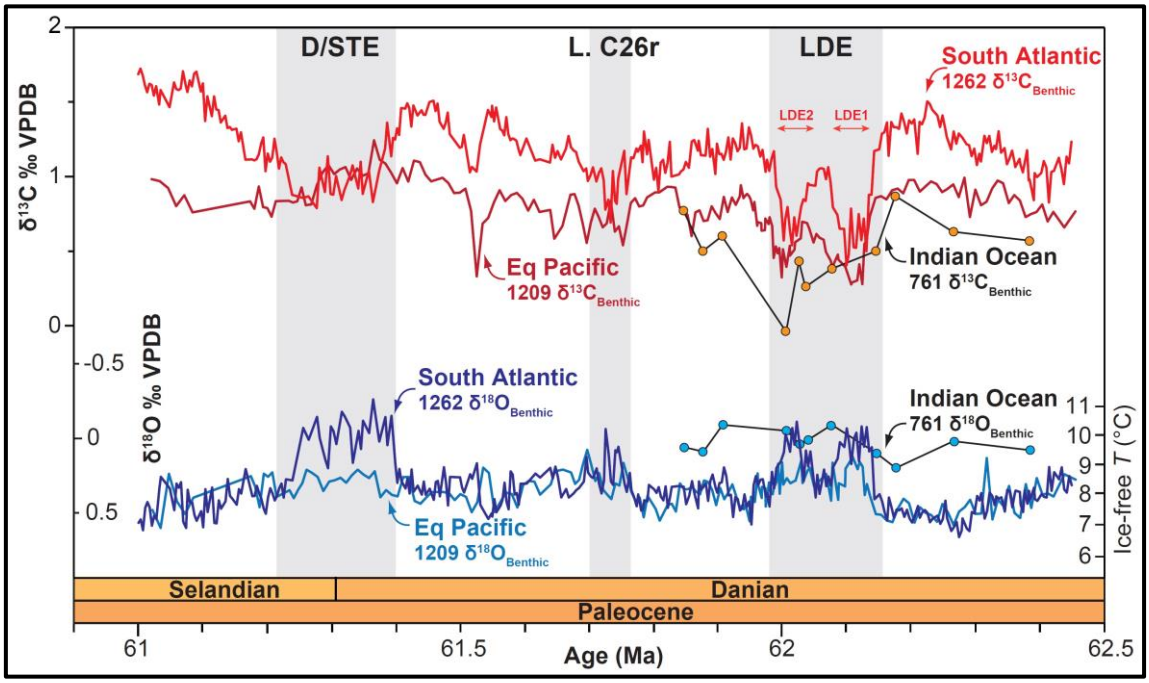

Figure 21. Comparison between the benthic stable carbon isotope ($\delta^{13}C_{benthic}$) and benthic stable oxygen isotope ($\delta^{18}O_{benthic}$) data from South Atlantic ODP Site 1262 (palaeo-depth ~3000 m; this study), equatorial Pacific ODP Site 1209 (palaeo-depth ~2000–2500 m; Westerhold et al., 2011), and SE Indian Ocean ODP Site 761 (palaeo-depth <2000 m ; Quillévéré et al., 2002), across the Latest Danian Event (LDE), Lower Chron 26r event (L. C26r), and Danian/Selandian Transition Event (D/STE). The oldest and youngest of the LDE carbon cycle perturbations have been named LDE1 and LDE2 respectively, after Deprez et al. (2017).

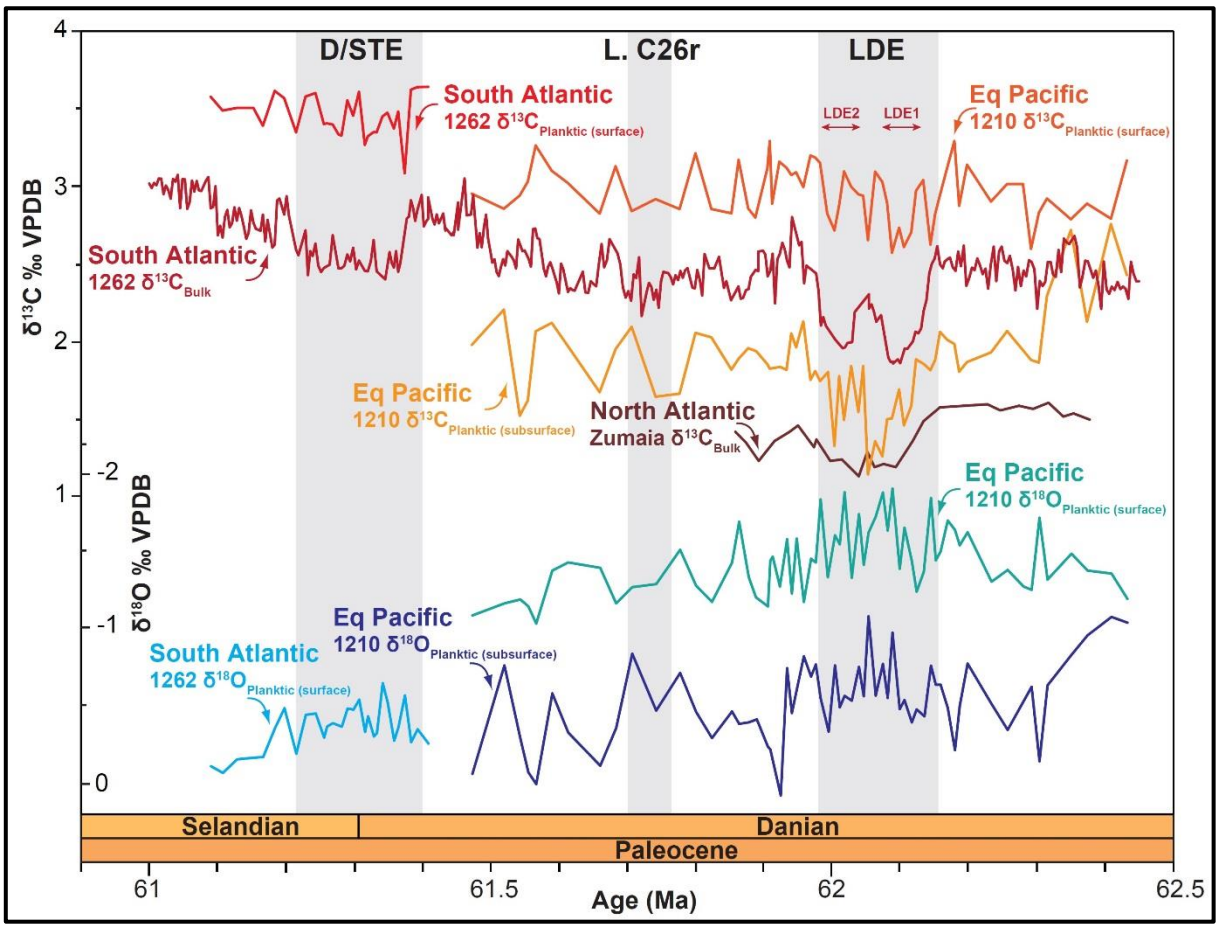

Figure 22. Compilation of mixed layer planktic stable isotope ($\delta^{13}C_{Planktic\ (surface)}$ & $\delta^{18}O_{Planktic\ (surface)}$), subsurface (thermocline) planktic stable isotope ($\delta^{13}C_{Planktic\ (subsurface)}$ & $\delta^{18}O_{Planktic\ (subsurface)}$), and bulk carbonate stable isotope ($\delta^{13}C_{Bulk}$ & $\delta^{18}O_{Bulk}$) data across the Latest Danian Event (LDE), Lower Chron 26r event (L. C26r), and Danian/Selandian Transition Event (D/STE). The compilation includes data from South Atlantic ODP Site 1262 (palaeo-latitude ~40°N; bulk carbonate data from Kroon et al., 2007; planktic data from this study), equatorial Pacific ODP Site 1210 (palaeo-latitude ~25°N; Jehle et al., 2015), and Zumaia, Spain (palaeo-latitude ~32°N; Dinarès-Turell et al., 2014). The oldest and youngest of the LDE carbon cycle perturbations have been named LDE1 and LDE2 respectively, after Deprez et al. (2017).

3.6.6.2. DISSOLUTION PROXY DATA ACROSS THE LDE, LOWER C26R EVENT AND D/STE

The transient release of CO_2 into the atmosphere, regardless of its isotopic composition, will lower the pH of the oceans as they equilibrate with the atmosphere. If the CO_2 is released at a sufficient rate such that the riverine flux of carbonate ion (CO_3^{2-}) from continental weathering cannot keep pace with the fall in pH, such as during transient hyperthermal events, ocean acidification occurs. This ocean acidification is compensated, via a negative feedback, by

shoaling of the lysocline and CCD, leading to dissolution of deep-sea carbonates. Proxies for carbonate dissolution, including % coarse fraction and Fe intensity data from South Atlantic ODP Site 1262 (Kroon et al., 2007; Westerhold et al., 2008) and Fe intensity data from equatorial Pacific ODP Site 1209 (Westerhold et al., 2008), are shown in Figure 23.

The LDE is characterised by prominent double-spiked peaks in Fe intensity in both the South Atlantic and equatorial Pacific, confirming the occurrence of significant carbonate dissolution associated with LDE1 and LDE2. In agreement with the stable isotope data, the greatest magnitude excursion in Fe intensity is associated with LDE1, which also has the greatest expression in the % coarse fraction data, confirming that it was the larger of the two events.

By contrast, there appears to be little change in the carbonate dissolution proxies above background variability during the Lower C26r event and D/STE at ODP Site 1262, although spikes in Fe intensity at ODP Site 1209 may be indicative of some carbonate dissolution. The new benthic stable isotope data from ODP Site 1262 suggest that these were smaller events, likely to be associated with smaller shifts in depth of the lysocline and CCD, which may not have risen above the depth of ODP Site 1262 in the South Atlantic.

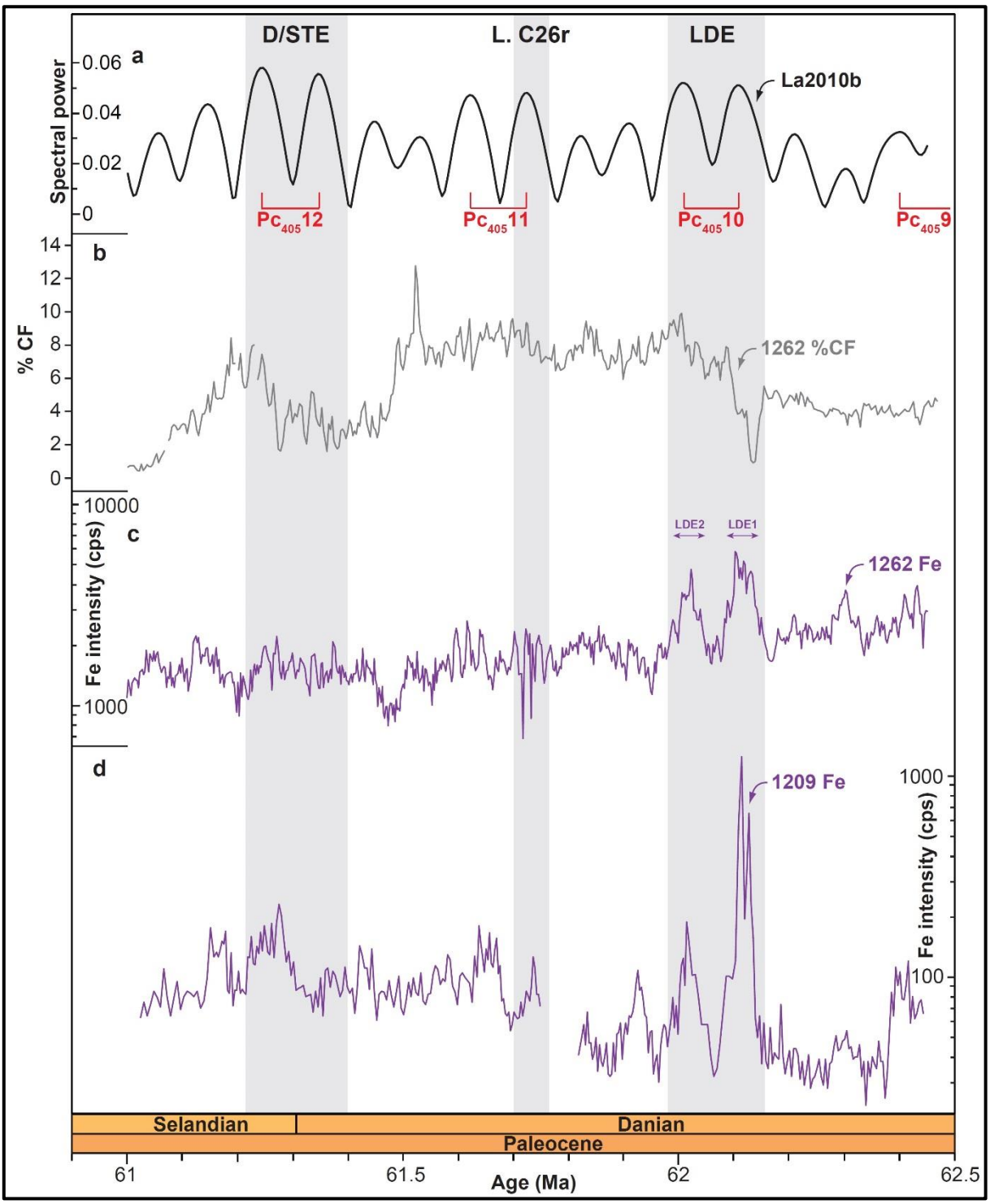

*Figure 23. Orbital pacing of carbonate dissolution proxy data across the Latest Danian Event (LDE), Lower Chron 26r event (L. C26r), and Danian/Selandian Transition Event (D/STE): (**a**) La2010b orbital solution (Laskar et al., 2011a). Long (405-kyr) eccentricity maxima are named following the nomenclature of Dinarès-Turell et al. (2014). (**b**) South Atlantic ODP Site 1262 % coarse fraction data (% CF; >63 µm; Kroon et al., 2007); (**c**) South Atlantic ODP Site 1262 Fe intensity data (palaeo-depth ~3000 m; Westerhold et al., 2008); (**d**) equatorial Pacific ODP Site 1209 Fe intensity data (palaeo-depth ~2000–2500 m; Westerhold et al., 2008). The oldest and youngest of the LDE perturbations have been named LDE1 and LDE2 respectively, after Deprez et al. (2017).*

3.6.6.3. SHOULD THE LDE, LOWER C26R EVENT AND D/STE BE CLASSIFIED AS GLOBAL HYPERTHERMALS?

Based on the available data, the LDE can be classified as an orbitally-paced hyperthermal analogous to the comparatively better-studied double-spiked hyperthermals of the Late Paleocene–Early Eocene such as ETM-2/H2 (Figure 12c,e,f), albeit with a bottom water warming of about half the magnitude. The Lower C26r event also appears to be orbitally-paced and have a global temperature response in ocean bottom waters, but is clearly a much smaller climatic perturbation than the LDE without a pronounced dissolution event in the deep South Atlantic and equatorial Pacific. An interpretation of the D/STE is more problematic, however. The event is clearly orbitally-paced with a pronounced bottom water temperature response in the South Atlantic, however, the lack of a bottom water temperature response in the equatorial Pacific and lack of significant carbonate dissolution question whether the D/STE can be classified as a global hyperthermal. Further palaeoclimate proxy studies are required to elucidate the nature of global environmental change associated with the D/STE.

The LDE, L. C26r and D/STE are the largest orbitally-paced excursions in the carbon cycle and climate of the Early Paleocene in the new benthic foraminiferal records from ODP Site 1262. Whilst these three events appear to be orbitally-paced, their timing coincides with the first phase of volcanism within the NAIP, from ~63–60 Ma (Sinton & Duncan, 1998; Figure 12h). This volcanism may play a role in explaining the greater magnitude of these events compared to others of the Early Paleocene, due to elevated background global temperatures and increased sensitivity to orbital forcing (see **Chapter 4** for evidence of this from the LMWE). However, the current paucity of atmospheric pCO_2 proxy data for the Early–Middle Paleocene severely hampers our understanding of the evolution of atmospheric pCO_2 in relation to NAIP volcanism and orbital forcing mechanisms during this time interval at present (Figure 12a).

3.7. CONCLUSIONS

In this chapter, I have generated and compiled new orbital-resolution $\delta^{13}C_{benthic}$ and $\delta^{18}O_{benthic}$ records spanning the Late Maastrichtian–Early Eocene

from South Atlantic Walvis Ridge ODP Site 1262 (palaeo-depth ~3000–3500 m), calibrated to an updated orbitally-tuned age model. I have used these records to elucidate the principle forcing mechanisms driving the carbon cycle and climate during this time, as well as identify the phasing relationship between carbon cycle and climate. I have placed all 26 transient “hyperthermals” and smaller climatic perturbations of this time period into an orbital cyclostratigraphic framework, and integrated the new Early–Middle Paleocene data generated during this study with published palaeoclimate proxy data to shed light on the poorly studied events of the Early Paleocene, namely the LDE, Lower C26r event, and D/STE. The main conclusions of this chapter are as follows:

- Long-term trends in the carbon cycle and deep sea temperature evolution are comparable between the South Atlantic ODP Site 1262 and equatorial Pacific ODP Site 1209, suggesting that these trends are global in nature. ODP Site 1209 $\delta^{13}C_{benthic}$ data are offset to lighter values compared to data from ODP Site 1262 throughout much of the record, consistent with an older deep water mass bathing the equatorial Pacific site. A transient decoupling in this gradient during the latest Maastrichtian may be related to shifts in the predominance of North and South Pacific deep water sources in the equatorial Pacific, a collapse after the K/Pg boundary due to a collapse in primary productivity within both ocean basins following the mass extinction, and a reduction following the PETM due to a reduction in high-latitude deep-water production coupled with biotic turnover.

- Long (405-kyr) and short (100-kyr) eccentricity are the dominant pacemakers of the climate and carbon cycle during the Late Maastrichtian–Early Eocene period as a whole, through modulation of precession.

- Power within the obliquity (41-kyr) band is generally weak throughout the Late Maastrichtian–Early Eocene, however peaks in spectral power during the Late Maastrichtian–Early Paleocene may indicate a more significant role during the coolest climates of the time period.

- Perturbations to the global carbon cycle lag changes to global climate by ~23 kyr within the 405-kyr band and ~3–4.5 kyr within the ~100-kyr band during this time period, suggesting that light carbon was released from temperature- or climate-sensitive reservoirs as a positive feedback to an initial warming induced by orbital forcing.

- All known hyperthermals of this time period occur during maxima in the long (405-kyr) eccentricity cycle and therefore appear to be orbitally-paced, with the exception of the PETM and LMWE, which are likely to have been triggered or augmented by LIP volcanism.

- The LDE can be classified as an orbitally-paced double-spiked hyperthermal of around half the magnitude of ETM-2/H2, whilst the Lower C26r event can be classed as a smaller climatic perturbation with a global response.

- The D/STE cannot be classified as a global hyperthermal event due to the absence of a bottom water temperature response in the equatorial Pacific.

4. WHAT CAUSED THE LATE MAASTRICHTIAN WARMING EVENT AND COULD THIS EVENT HAVE CONTRIBUTED TO THE SEVERITY OF THE K/PG MASS EXTINCTION?

4.1. ABSTRACT

This chapter expands upon a manuscript published in Geology (Geological Society of America), entitled: "*A new high-resolution chronology for the late Maastrichtian warming event: Establishing robust temporal links with the onset of Deccan volcanism*" (Barnet et al., 2017). This published manuscript is included in **Appendix 2**. This chapter provides a new orbital-resolution chronology of the Late Maastrichtian warming event (LMWE), based on new $\delta^{13}C_{benthic}$ and $\delta^{18}O_{benthic}$ records generated during this study, calibrated to an update of the orbitally-tuned age model for ODP Site 1262. This revised chronology points to the synchronous onset of the main phase of Deccan Traps volcanism (Kalsubai sub-group) with climatic warming, strongly suggesting a causal link. A volcanogenic CO_2 trigger for this event is further supported by the inception of warming during a minimum in the 405-kyr eccentricity cycle, as well as evidence for a muted global carbon isotope response at this time. A synthesis of published palaeoclimate and biotic data are also reviewed to elucidate the magnitude and nature of the global environmental change that occurred during the LMWE, as well as to evaluate if the event played a role in the subsequent K/Pg mass extinction. The lack of evidence for major extinctions of a global scale within marine or terrestrial biota suggests that bolide impact should still be regarded as the primary driver of the K/Pg mass extinction. However, Deccan-induced environmental change, in particular rapid cooling over the final 200-kyr of the Maastrichtian, along with acid rain and/or the emission of toxic aerosols, may have played an ancillary role in making certain environmentally-sensitive communities more susceptible to extinction during bolide impact at the K/Pg boundary (~66 Ma).

4.2. INTRODUCTION

The LMWE is defined as a transient global warming in the marine realm of ~2.5–4°C based on benthic oxygen isotopes (e.g., Li & Keller, 1998; Westerhold

et al., 2011) and TEX_{86}^{H} sea surface temperature data (Vellekoop et al., 2016; Woelders et al., 2017), and as a 5–8°C warming in the terrestrial realm based on pedogenic carbonate $\delta^{18}O$ (Nordt et al., 2003), clumped isotopes (Δ_{47}; Zhang et al., 2018), and analyses of leaf margins in woody dicot plants (Wilf et al., 2003; Figure 24). This event is characterised by a breakdown of thermal stratification and a consequent reduction in the marine surface to deep temperature gradient at mid–low latitudes (Li & Keller, 1998, 1999; Barrera & Savin, 1999; Figure 25). Limited evidence also exists for a global eustatic sea level rise at this time (Stüben et al., 2003), and for transient changes in thermohaline circulation, including an influx of older and more corrosive South Pacific Deep Water into the equatorial Pacific (Dameron et al., 2017), and a speculative transient switch in the source of deep water formation in the South Atlantic from the Southern Ocean to warm saline outflow from the low latitude Tethys (Li & Keller, 1998, 1999).

Warming during the Late Maastrichtian has long been linked to a major pulse of Deccan Traps volcanism (e.g., Li & Keller, 1998; Tobin et al., 2012; Punekar et al., 2014a; Keller et al., 2016). Until recently, however, the large uncertainty (typically ± 0.5 to >1 million years at 1σ) associated with radiogenic dating methods (e.g., Courtillot et al., 1988; Courtillot et al., 2000; Hofmann et al., 2000; Chenet et al., 2007) has prevented a definitive evaluation of cause and effect. This evaluation has also been hampered by the absence of sufficient high-resolution stratigraphically complete sedimentary sequences on robust orbitally-tuned age models, which has also precluded the generation of a complete high-resolution chronology of this event (Figure 24).

A benthic stable isotope record across the LMWE from the Walvis Ridge, South Atlantic, already exists based on data from DSDP Site 525 (Li & Keller, 1998), located at a relatively shallow palaeo-depth of ~1000–1500 m (Shipboard Scientific Party, 1984a). However, this record is incomplete as there is a coring gap (spanning ~100 kyr prior to the onset of the event), the sample resolution is fairly low at ~10 kyr, and it has not been calibrated to an up-to-date orbitally-tuned age model. As a result, developing an orbital-resolution chronology of the event and correlating to discrete episodes of Deccan Traps volcanism cannot be achieved with this existing record. Furthermore, this record was also based on a species of benthic foraminifera (*Anomalinoides acuta*) which is less routinely

employed in more recent benthic foraminiferal stable isotope studies focused on this time period, which use *Nuttallides truempyi* (e.g., Littler et al., 2014; Westerhold et al., 2011; 2018), therefore temperature calibrations for *Anomalinoides acuta* may be less robust. The relatively shallow palaeo-depth of the DSDP Site 525 record also implies that it records variations in temperature of an intermediate depth water mass, which may not be fully representative of bottom water masses in the South Atlantic. A stratigraphically complete high-fidelity Late Maastrichtian record with orbital-resolution age control is therefore urgently required to definitively temporally correlate the LMWE with Deccan Traps volcanism. A stratigraphically complete and expanded Late Maastrichtian and K/Pg boundary sequence of foraminifera-bearing, carbonate-rich nannofossil ooze was deposited at ODP Site 1262 at ~3000 m palaeo-depth (Shipboard Scientific Party, 2004a; **Chapter 3**, Figure 12g), and has a mean sedimentation rate of ~1.3–2.8 cm/kyr. This sedimentary archive permits orbital-resolution studies of the LMWE to be conducted and various outstanding research questions concerning the LMWE to be addressed.

In addition to the issue of the role of Deccan Traps volcanism, the second major outstanding and heavily debated question concerning the LMWE is the biotic impact that environmental change at this time had on the severity of the K/Pg mass extinction. Some studies have presented evidence that minor precursor extinction events affected primarily benthic marine invertebrate species in the high-latitudes (Tobin et al., 2012), thermocline-dwelling foraminifera in the global oceans (Keller, 2001; Abramovich & Keller, 2002; Keller & Abramovich, 2009), and lacustrine ostracodes and charophytes in the terrestrial realm (Zhang et al., 2018). Yet many marine and terrestrial biota appear to exhibit no appreciable decline in species abundance or diversity prior to K/Pg boundary time (e.g., Bown et al., 2004; Brusatte et al., 2015; Witts et al., 2015). As a result, the relationship, if any, between the LMWE and the K/Pg mass extinction remains unclear to date.

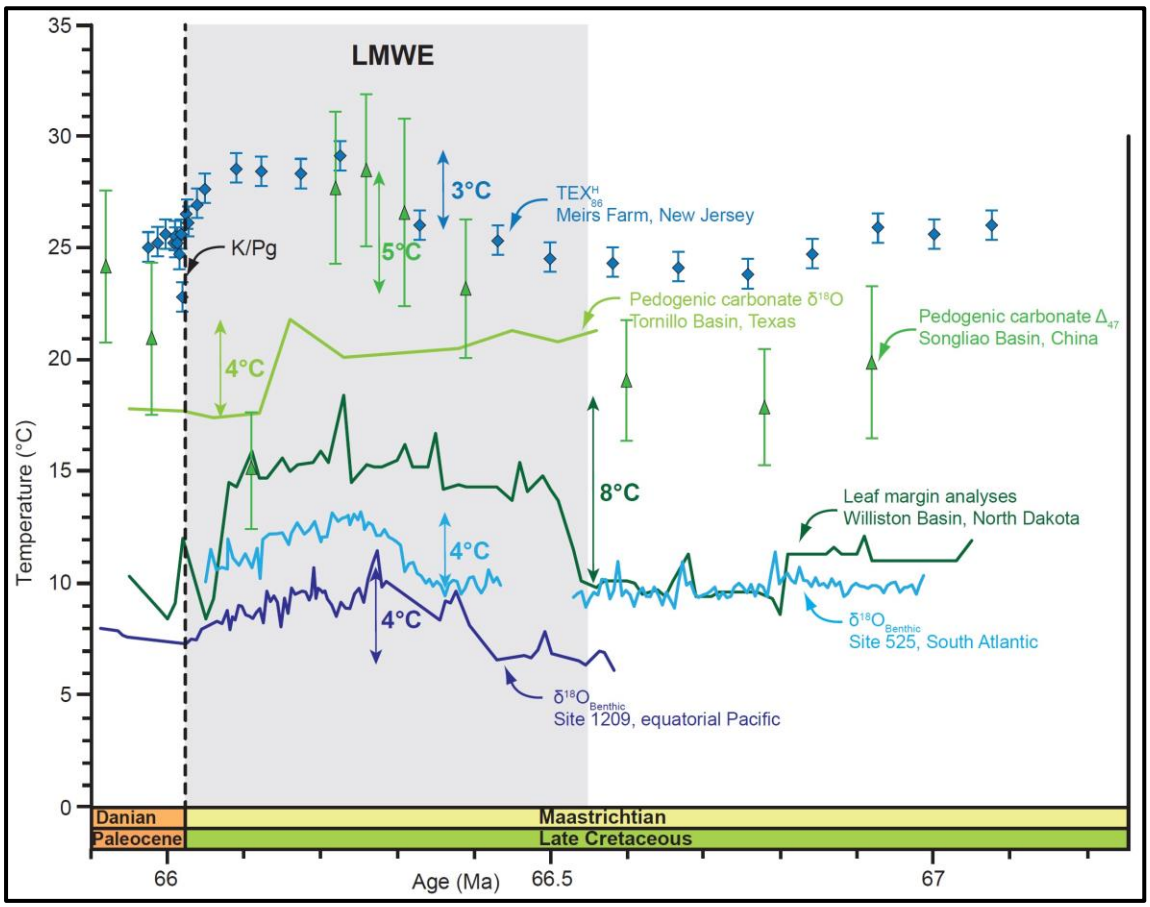

Figure 24. Magnitude of the Late Maastrichtian warming event (LMWE) in terrestrial (green curves & symbols) and marine (blue curves & symbols) sediment archives, including pedogenic carbonate $\delta^{18}O$ data from Tornillo Basin, Texas, USA (Nordt et al., 2003), leaf margin analyses from Williston Basin, North Dakota, USA (Wilf et al., 2003), pedogenic carbonate clumped isotopes (Δ_{47}) from Songliao Basin, China (Zhang et al., 2018), $\delta^{18}O_{benthic}$ data from DSDP Site 525, South Atlantic (Li & Keller, 1998) and ODP Site 1209, equatorial Pacific (Westerhold et al., 2011), and TEX_{86}^{H} sea surface temperature data from Meirs Farm, New Jersey, USA (Vellekoop et al., 2016). All datasets have been temporally aligned to a Cretaceous/Paleogene (K/Pg) boundary age of 66.0225 Ma (consistent with this study) for correlation. Discrepancies in the onset and duration of warming are likely related to age model inconsistencies between studies and sites, which have hampered the development of a robust chronology for the event to date. Only data shown from ODP Site 1209 are calibrated to an independent orbitally-tuned age model (Westerhold et al., 2011).

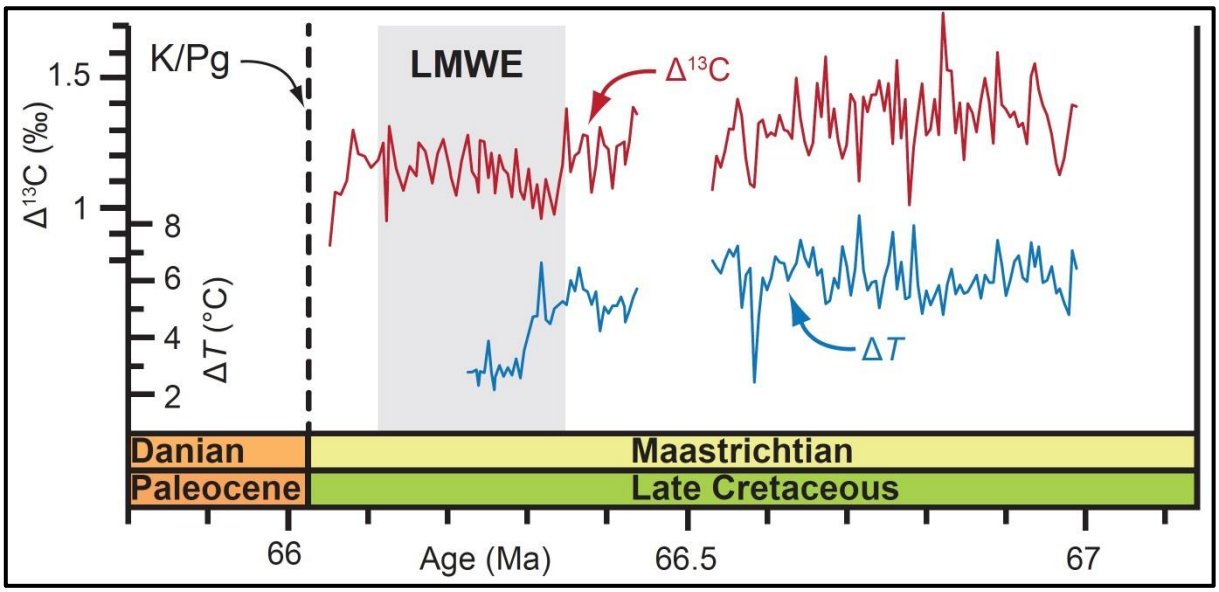

Figure 25. Shallow-to-deep carbon isotope ($\Delta^{13}C$) and temperature (ΔT) gradients during the Late Maastrichtian and across the Late Maastrichtian warming event (LMWE) at South Atlantic Walvis Ridge DSDP Site 525 (palaeo-depth 1000–1500 m; data from Li & Keller, 1998). The surface-to-deep carbon isotope and temperature gradients were calculated from the difference between isotopic values derived from the planktic foraminifera Rugoglobigerina rugosa and the benthic foraminifera Anomalinoides acuta (Li & Keller, 1998). Palaeotemperatures were calculated using the calibration of Kim & O'Neil (1997), modified by Bemis et al. (1998; Equation 1). See ***Chapter 3 Section 3.4.4*** *for methods. K/Pg = Cretaceous/Paleogene boundary.*

4.3. AIMS AND OBJECTIVES

The overarching goal of this chapter is to establish a more robust temporal link with the main phase of Deccan Traps volcanism on the Indian sub-continent and to evaluate whether this anomalous climate event played a role in the subsequent K/Pg mass extinction. Specific questions to be addressed are:

- Did the onset of the main phase of Deccan Traps LIP volcanism initiate the LMWE?

- What was the global nature and magnitude of environmental change during the LMWE, and did this vary spatially or by latitude?

- Did orbital forcing play a role in the inception, duration and timing of the LMWE?

- How does the LMWE compare to the archetypal hyperthermals of the early Paleogene, such as the PETM, in terms of magnitude of environmental change, rate of change, duration, and causal mechanisms?

- What was the biotic response within the marine and terrestrial realms during the LMWE, and could this event, therefore, have acted as a primer or contributed to the severity of the K/Pg mass extinction ~66 Ma?

These questions will be addressed by the development of an orbital-resolution chronology of the LMWE based on the Late Maastrichtian portion of the new ODP Site 1262 $\delta^{13}C_{benthic}$ and $\delta^{18}O_{benthic}$ records generated during this study, calibrated to an updated orbitally-tuned age model. This will be integrated with a synthesis of published palaeoclimate proxy (e.g., *p*CO_2, stable carbon and oxygen isotope, Fe intensity, % $CaCO_3$, organic palaeothermometer [TEX_{86}^{H}] and clumped isotope [Δ_{47}]) and biotic data across this time interval.

4.4. METHODS

4.4.1. DATA SOURCES AND PROCESSING

Location of sites, lithostratigraphy, sample strategy, and all sedimentological and geochemical method information are presented in **Chapter 2 Sections 2.1–2.4**. Methods employed for spectral analysis of the ODP Site 1262 benthic stable isotope datasets are described in detail in **Chapter 3 Section 3.4.6** and for recalibration of atmospheric *p*CO_2 estimates based on the pedogenic carbonate proxy in **Chapter 3 Section 3.4.7**. The locations of ODP Site 1262 and other sites discussed in this chapter are illustrated in Figure 26. Further details about these sites, along with the types of data and literature sources used, are listed in Table 5.

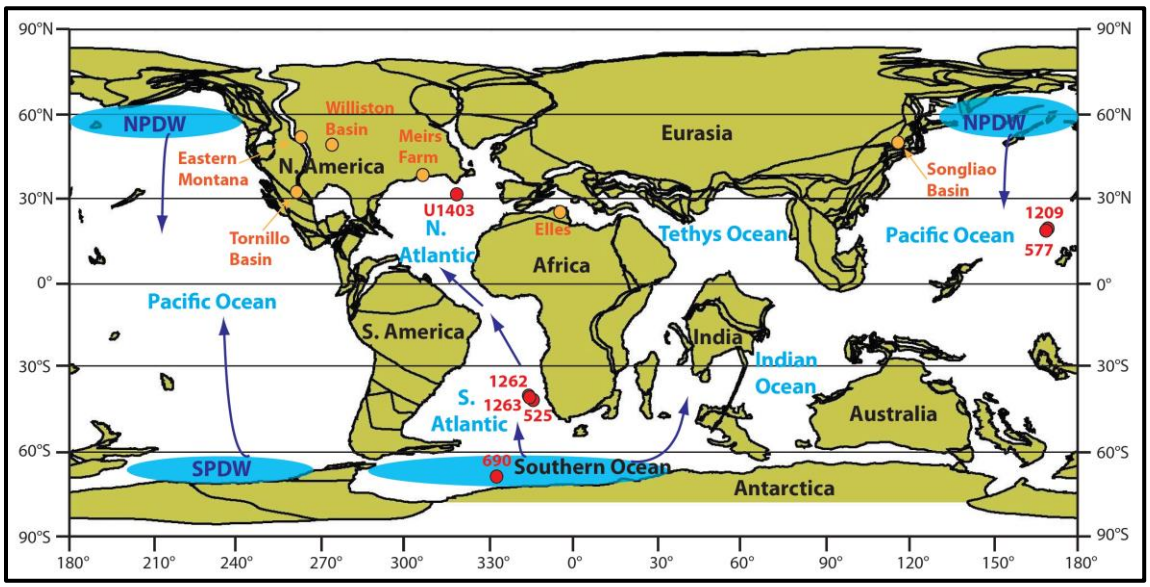

Figure 26. Cretaceous/Paleogene (K/Pg) boundary (66 Ma) palaeogeographic reconstruction with locations of deep-sea sites (in red) and onshore sites (in orange) used in this chapter (also see Table 5). Locations of the principle areas of deep water formation are indicated by blue shading with the following abbreviations: NPDW = North Pacific Deep Water. SPDW = South Pacific Deep Water (Thomas et al., 2003, 2008). The predicted movement of deep water masses is indicated by dark blue arrows. Adapted from the Ocean Drilling Stratigraphic Network (ODSN) Paleomap Project (http://www.odsn.de/odsn/services/paleomap/paleomap.html).

Table 5

Site	Current Lat.	Current Long.	Palaeo-lat.	Current water depth (m)	Palaeo-water depth (m)	Data type	Source of data
ODP Site 1262	27.2°S	1.6°E	40.3°S	4759	3000	$\delta^{13}C_{benthic}$ $\delta^{18}O_{benthic}$ Fe intensity $\%CaCO_3$	This study This study Westerhold et al. (2008) Kroon et al. (2007)
ODP Site 1263	28.5°S	2.8°E	42.0°S	2717	1500	$\delta^{13}C_{benthic}$	McCarren et al. (2008)
ODP Site 1209	32.7°N	158.5°E	22.8°N	2387	2000–2500	$\delta^{13}C_{benthic}$ $\delta^{18}O_{benthic}$	Westerhold et al. (2011)
DSDP Site 577	32.4°N	157.7°E	22.7°N	2675	2000–2500	$\delta^{13}C_{fine\ fraction}$ $\delta^{18}O_{fine\ fraction}$	Zachos et al. (1985)
DSDP Site 525	29.1°S	3.0°E	42.5°S	2467	1000–1500	$\delta^{13}C_{planktic}$ $\delta^{18}O_{planktic}$ $\delta^{13}C_{benthic}$ $\delta^{18}O_{benthic}$ $\Delta^{13}C$ gradient T gradient	Li & Keller (1998)
ODP Site 690	65.2°S	1.2°E	70.4°S	2914	1000–2000	$\delta^{13}C_{planktic}$ $\delta^{18}O_{planktic}$	Stott & Kennett (1990)
IODP Site U1403	39.9°N	51.8°W	31.0°N	4949	4000	$\delta^{18}O_{bulk}$	Batenburg et al. (2017)
Elles, Tunisia	35.9°N	9.2°E	20°N	Subaerial	100-150	$\delta^{18}O_{benthic}$	Stüben et al. (2003)
Meirs Farm, USA	40.1°N	74.5°W	37°N	Subaerial	<35m	TEX_{86}^{H}	Vellekoop et al. (2016)
Williston Basin, USA	46.3°N	103.9°W	49°N	Subaerial	Terrestrial	Leaf margin analyses	Wilf et al. (2003)
Tornillo Basin, USA	29.3°N	103.5°W	32°N	Subaerial	Terrestrial	Pedogenic carbonate $\delta^{18}O$ & pCO_2	Nordt et al. (2003)
Songliao Basin, China	44.2°N	124.3°E	51°N	Subaerial	Terrestrial	Clumped isotopes (Δ_{47})	Zhang et al. (2018)
Eastern Montana, USA	47.5°N	107°W	52.6°N	Subaerial	Terrestrial	Bivalve clumped isotopes	Tobin et al. (2014)

Details of drilling sites from which data have been included in this study. Present-day latitudes, longitudes, water depths and palaeo-water depths are from the initial scientific reports for each deep-sea site (Shipboard Scientific Party, 2004a, 2004c, 2002a, 1985, 1984a, 1988b, 2014), and from Esmeray-Senlet et al. (2015) for Meirs Farm and Stüben et al. (2003) for Elles. Palaeo-latitudes for each site at the Cretaceous/Paleogene (K/Pg) boundary (66 Ma) were computed relative to the palaeomagnetic reference frame of Torsvik et al. (2012), using Version 2.1 of the model from paleolatitude.org (van Hinsbergen et al., 2015).

4.4.2. INTEGRATION OF PUBLISHED PALAEOCLIMATE PROXY DATA

All other published data presented in this chapter have been calibrated in the time domain to our orbitally-tuned age model developed from ODP Site 1262. A significant hurdle with correlating datasets from older literature arises from the variety of absolute ages historically assigned to the K/Pg boundary, including 65.0 Ma (Cande & Kent, 1995), 65.5 ±0.3 Ma (Gradstein et al., 2004), 66.0225 ±0.004 Ma (Dinarès-Turell et al., 2014), and 66.043 ±0.043 Ma (Renne et al., 2013, 2015). The preferred astronomical age of 66.0225 Ma (Dinarès-Turell et al., 2014) has been adopted in our orbitally-tuned age model, therefore, we first aligned the stratigraphy of all published datasets with this age for the K/Pg boundary. Mean sedimentation rates for the Late Maastrichtian at each deep-sea site (Table 6) were then used to estimate ages relative to the K/Pg boundary for the available published data. Datasets for which mean sedimentation rate information was not available were aligned to an astronomical K/Pg boundary age of 66.0225 Ma, as above, with the age model presented in the original literature source employed.

Table 6

Site	Late Maastrichtian sedimentation rate (cm/kyr)	Literature source
ODP Site 1262	1.5–2	This study (orbitally-tuned age model)
ODP Site 1209	0.5	Westerhold et al. (2011)
DSDP Site 577	1	Shipboard Scientific Party (1985)
DSDP Site 525	1.9	Gerta Keller (pers. comm.)
ODP Site 690	1	Shipboard Scientific Party (1988b)
IODP Site U1403	0.96–1.04	Batenburg et al. (2017)

Mean Late Maastrichtian sedimentation rates used to recalibrate the age models for the deep-sea sites used in this study.

4.4.3. CALCULATION OF DECCAN TRAPS FORMATION VOLUMES

To compare the magnitude and scale of discrete outpourings of the Deccan Traps, and understand how the size of the eruptions varied temporally during K/Pg boundary time, eruption volumes for each of the basaltic formations comprising the Deccan Traps were calculated by both equal area and variable area methods. For the equal area method, formation thicknesses published by Jay & Widdowson (2008) were multiplied by a constant base flow radius of 600

km for each formation, which represents the maximum present-day aerial extent of the Deccan Traps basalts (Jay & Widdowson, 2008). For the variable area method, formation volumes were calculated using the same formation thicknesses from Jay & Widdowson (2008) as above, but by varying the base flow radius from 600 km for the Poladpur, Wai and Mahabaleshwar formations, to 250 km for all other formations. These varying radiuses represent putative estimates of present-day formation aerial extents and are therefore considered to produce more reliable estimates for eruption volumes (Jay & Widdowson, 2008).

4.5. DATA ATTRIBUTION

I picked all of the benthic foraminifera and prepared them for stable isotope analysis, converted the stable isotope data to bottom water temperatures, performed the spectral analysis, and compiled and recalibrated all previously published data from the literature. Sample collection from the Bremen Core Repository, along with sample disaggregation and sieving, were carried out by both Prof. Dick Kroon (University of Edinburgh) and myself. The new benthic stable isotope data were funded and generated by the NERC Isotope Geosciences Facility (grant number IP-1581-1115), under the supervision of Prof. Melanie Leng, and are included as part of **Appendix 4**. The updated orbitally-tuned age model for ODP Site 1262 used in this study was generated by Dr. Thomas Westerhold (MARUM, Bremen) from samples prepared and analysed by myself.

4.6. RESULTS AND DISCUSSION

4.6.1. NEW ORBITAL-RESOLUTION CHRONOLOGY OF THE LMWE FROM ODP SITE 1262

New $\delta^{13}C_{benthic}$ and $\delta^{18}O_{benthic}$ records from ODP Site 1262 spanning ~67.1–65.9 Ma, calibrated to an updated orbitally-tuned age model correlated to the La2010b orbital solution of Laskar et al. (2011a), are presented in Figure 27. Prior to the onset of the LMWE, $\delta^{18}O_{benthic}$ remained relatively stable, oscillating around ~+0.5‰ from ~67.1–66.8 Ma, followed by a decrease of ~–0.25‰ from

~66.8–66.5 Ma. A second period of relative stability then ensued between ~66.5–66.34 Ma, with $\delta^{18}O_{benthic}$ values of ~–0.3‰. The LMWE initiated at ~66.34 Ma, immediately after the C30n/C29r magnetozone boundary (Bowles, 2006), and is characterised at ODP Site 1262 by a negative excursion in $\delta^{18}O_{benthic}$ of ~–0.9‰ over ~80 kyr. The core of the warming during this event, which is characterised by the most negative $\delta^{18}O_{benthic}$ values of ~–0.3–0.36‰ in our record, occurred for ~60 kyr from ~66.27–66.21 Ma. Recovery of the event in $\delta^{18}O_{benthic}$ between ~66.21–66.03 Ma occurred in three stages characterised by increases of ~+0.3‰, separated by brief periods of relative stability from ~66.18–66.14 Ma and ~66.11–66.08 Ma. A decrease in $\delta^{18}O_{benthic}$ started at ~66.03 Ma, ~10 kyr before K/Pg boundary time and spans the boundary.

When converted to bottom water temperatures, the ODP Site 1262 $\delta^{18}O_{benthic}$ dataset reveals that relatively stable and cool temperatures (~7–8°C) persisted from ~67.1–66.8 Ma in the South Atlantic during the late Maastrichtian, followed by a gradual warming trend of ~+1°C from ~66.8 to ~66.5 Ma. A second period of relative stability of bottom water temperatures at ~8–9°C occurred from ~66.5–66.34 Ma. The initiation of the LMWE was characterised by a deep water warming of ~+4°C at ODP Site 1262 over a time period of ~80 kyr, with maximum bottom water temperatures of ~11.5–12°C persisting for ~60 kyr during the core of the event between ~66.27–66.21 Ma. A longer-term cooling to pre-excursion conditions then took place over ~200 kyr, terminating ~10 kyr before K/Pg boundary time. This cooling occurred in three stages of ~–1.5°C, separated by brief periods of relative stability between ~66.18–66.14 Ma and ~66.11–66.08 Ma. Bottom waters at ODP Site 1262 started to warm again ~10 kyr before the end of the Maastrichtian by ~+1.0°C for ~20 kyr, with warming continuing across K/Pg boundary time, followed by a more gradual longer-term warming into the early Danian. There is no evidence for any transient cooling at ~66 Ma in association with the “impact winter” immediately following the bolide impact, but the lower resolution of our record across the K-Pg boundary interval (~5–7 kyr) may alias such a signal.

The evolution of the carbon cycle during the Late Maastrichtian can be elucidated from the $\delta^{13}C_{benthic}$ data. A stable plateau at ~1.6‰ in $\delta^{13}C_{benthic}$ occurred from ~67.1–66.8 Ma, followed by a decrease of ~–0.6‰ to the lightest

values within the Late Maastrichtian part of the record (~1.0‰) at ~66.5 Ma. This decrease could result from an increase in export productivity of C_{org} from the surface to deep ocean, followed by burial. Somewhat counterintuitively, Kump and Arthur (1999) have shown that the $\delta^{13}C$ of marine carbonates can actually decrease during a major C_{org} burial event, as the $\delta^{13}C$ signature of organic matter becomes increasingly heavier as CO_2 concentrations fall, due to increasing photosynthetic fractionation. Such a C_{org} burial event and fall in CO_2 should result in a decrease in global temperature. However, the parallel +1°C warming inferred from the $\delta^{18}O_{benthic}$ record suggests that the decreasing $\delta^{13}C_{benthic}$ values are more likely to result from the release of small amounts of isotopically light carbon (i.e., greenhouse gases) into the exogenic carbon cycle over ~300 kyr from ~66.8–66.5 Ma. These greenhouse gases may have been released from temperature- or climate-sensitive reservoirs in response to orbitally-induced changes in insolation or climate.

$\delta^{13}C_{benthic}$ values then rose towards and above pre-excursion values between ~66.5–66.34 Ma, peaking at ~1.8‰ at ~66.34 Ma, immediately prior to the onset of the LMWE. This rise in $\delta^{13}C_{benthic}$ may suggest partial sequestration of the isotopically light carbon released during the preceding 300 kyr or a decrease in export productivity, and corresponds to a stabilisation of bottom water temperatures. The response in $\delta^{13}C_{benthic}$ is comparatively muted during the LMWE, with a decrease of ~–0.6‰ for ~80 kyr, suggesting that isotopically light carbon stocks (e.g., biogenic methane) were not released in significant quantities during the event. The lightest $\delta^{13}C_{benthic}$ values of ~1.3‰ occur almost synchronously with peak greenhouse conditions, as identified in the $\delta^{18}O_{benthic}$ data. $\delta^{13}C_{benthic}$ data then exhibit a longer-term step-wise rise of ~+1.1‰ during the recovery and across K/Pg boundary time between ~66.21–66.0 Ma, with periods of relative stability coinciding with those in the $\delta^{18}O_{benthic}$ data during the periods ~66.18–66.14 Ma and ~66.11–66.08 Ma. These rising values may suggest that sequestration of isotopically light carbon took place into marine and/or continental reservoirs, or that a reduction in export productivity took place over the final 200 kyr of the Maastrichtian prior to the K/Pg mass extinction. $\delta^{13}C_{benthic}$ values peak at ~2.3‰, ~10 kyr after the K/Pg boundary, followed by the onset of a more rapid decline into the early Danian.

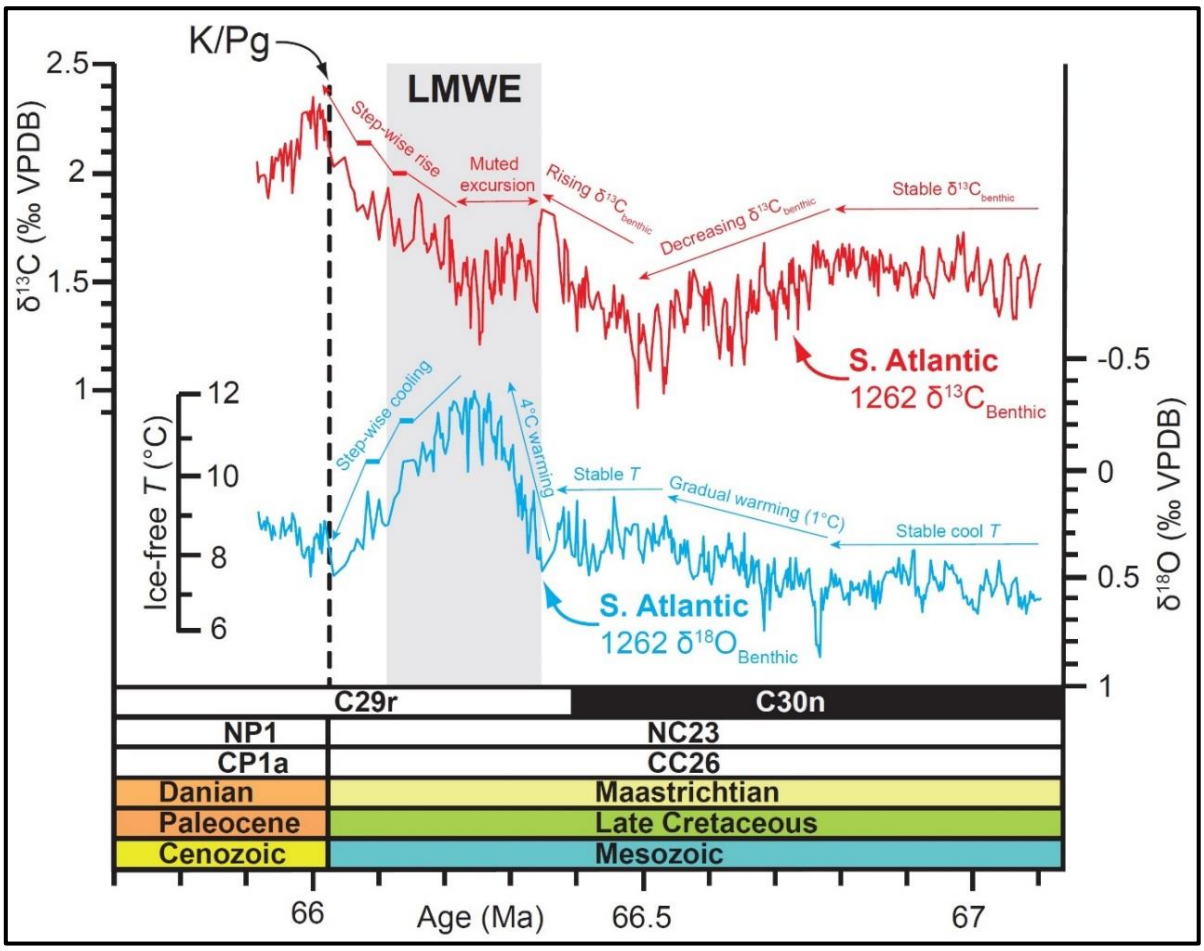

Figure 27. Late Maastrichtian–Cretaceous/Paleogene (K/Pg) boundary benthic foraminiferal stable isotope data from South Atlantic ODP Site 1262 (palaeo-depth ~3000 m), illustrating the nature of the Late Maastrichtian warming event (LMWE). Magnetozones are from Bowles (2006) and nannoplankton zones from Shipboard Scientific Party (2004a). Arrows and annotations indicate broad trends in temperature and the carbon cycle described in the main text.

4.6.2. COMPARISON BETWEEN THE NEW $\delta^{13}C_{BENTHIC}$ AND $\delta^{18}O_{BENTHIC}$ DATA FROM ODP SITE 1262 WITH PUBLISHED STABLE ISOTOPE DATA FOR THE LATE MAASTRICHTIAN

A comparison of the new benthic data from ODP Site 1262 (palaeo-depth ~3000 m) with previously published benthic data from DSDP Site 525 (palaeo-depth ~1000–1500 m; Li & Keller, 1998), also on Walvis Ridge, permits an evaluation of the extent of warming at deep to intermediate depths of the South Atlantic (Figure 28). The similarity of the magnitude and character of the excursions in $\delta^{13}C_{benthic}$ and $\delta^{18}O_{benthic}$ at both sites, suggests that a similar magnitude of warming occurred in deep and intermediate waters of the South Atlantic during the LMWE. Benthic isotope data from the deep equatorial Pacific

also show a coeval warming pulse of ~+3–4°C ($\delta^{18}O_{benthic}$ decrease of ~–0.6–0.8‰), and a similar muted excursion in $\delta^{13}C_{benthic}$ of ~–0.4‰ (Westerhold et al., 2011; Figure 29). The similarity between the $\delta^{13}C_{benthic}$ and $\delta^{18}O_{benthic}$ records across the LMWE from the South Atlantic and equatorial Pacific confirms that the characteristics of the event recorded in the South Atlantic are global in scale.

A compilation of planktic foraminiferal and bulk sediment stable isotope datasets (Figure 30) reveals that these records are also characterised by a muted response in $\delta^{13}C$ during the LMWE, with a negative excursion of ~–0.3–0.4‰ over ~40 kyr. However, the magnitude of change in $\delta^{18}O_{planktic}$ during this time varies significantly between records. At equatorial Pacific DSDP Site 577, negligible change is recorded in bulk fine fraction (<63µm) $\delta^{18}O$ data (Zachos et al., 1985), whilst a noisy excursion of up to ~–0.4‰ from the mid-latitude DSDP Site 525 may be biased by diagenesis (Li & Keller, 1998). $\mathrm{TEX}_{86}^{\mathrm{H}}$ data from the mid latitude New Jersey margin record a warming of ~+3°C in surface waters that is similar to, but slightly less than, the magnitude of deep-sea warming observed at ODP Site 1262 (Vellekoop et al., 2016; Figure 24). In the high-latitude Southern Ocean at ODP Site 690, $\delta^{18}O_{planktic}$ decreases by ~–0.5‰ (Kennett & Stott, 1991), suggesting a surface water warming of ~+2°C. Taken together, these data hint at the possibility of polar amplification of surface water warming during the LMWE. However, additional single-species planktic foraminiferal stable isotope and other proxy records (e.g., planktic foraminiferal Mg/Ca or $\mathrm{TEX}_{86}^{\mathrm{H}}$) from a greater range of latitudes are required to evaluate this suggestion more fully.

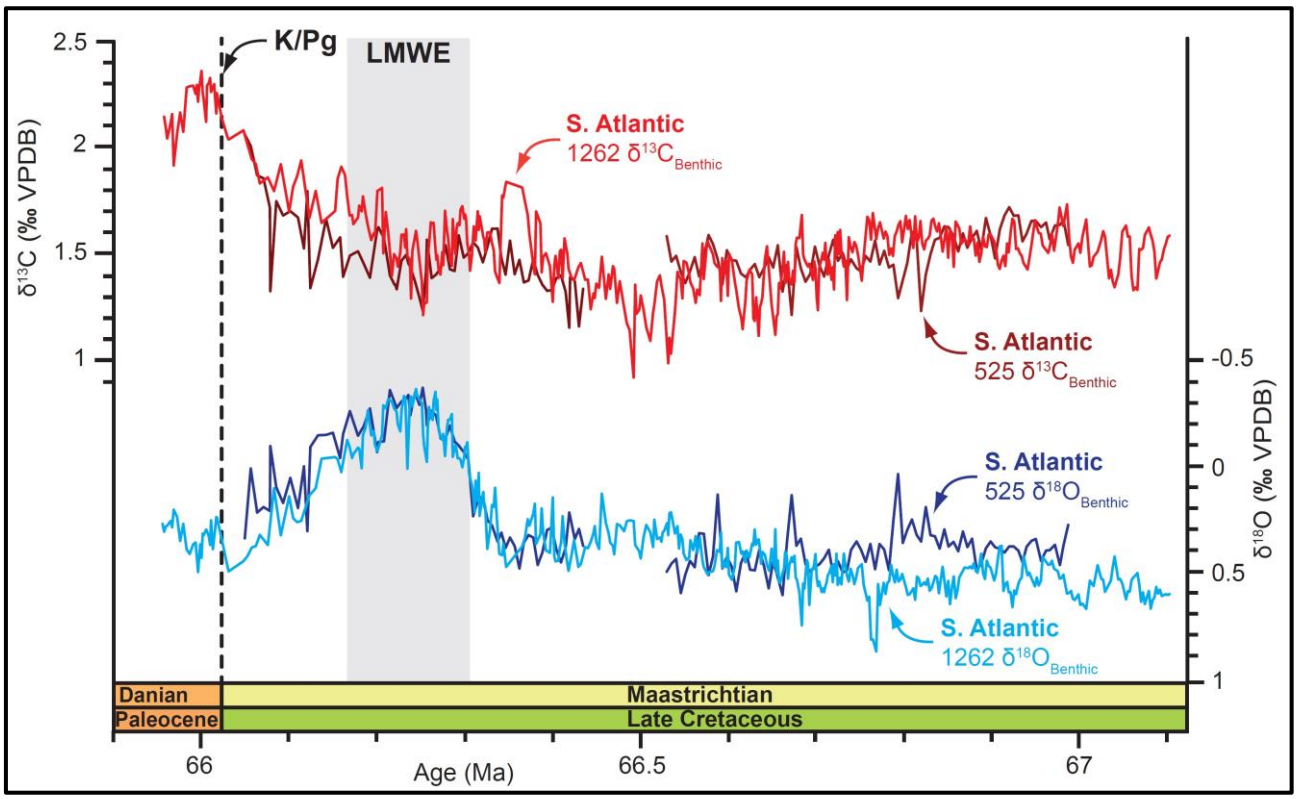

Figure 28. Comparison of the benthic stable carbon isotope ($\delta^{13}C_{benthic}$) and benthic stable oxygen isotope ($\delta^{18}O_{benthic}$) data from South Atlantic Walvis Ridge ODP Site 1262 (palaeo-depth ~3000 m; this study) and DSDP Site 525 (palaeo-depth ~1000–1500 m; Li & Keller, 1998) across the Late Maastrichtian, Late Maastrichtian warming event (LMWE) and Cretaceous/Paleogene (K/Pg) boundary. Note the superior resolution and greater stratigraphic completeness of the ODP Site 1262 benthic stable isotope records compared to the records from DSDP Site 525.

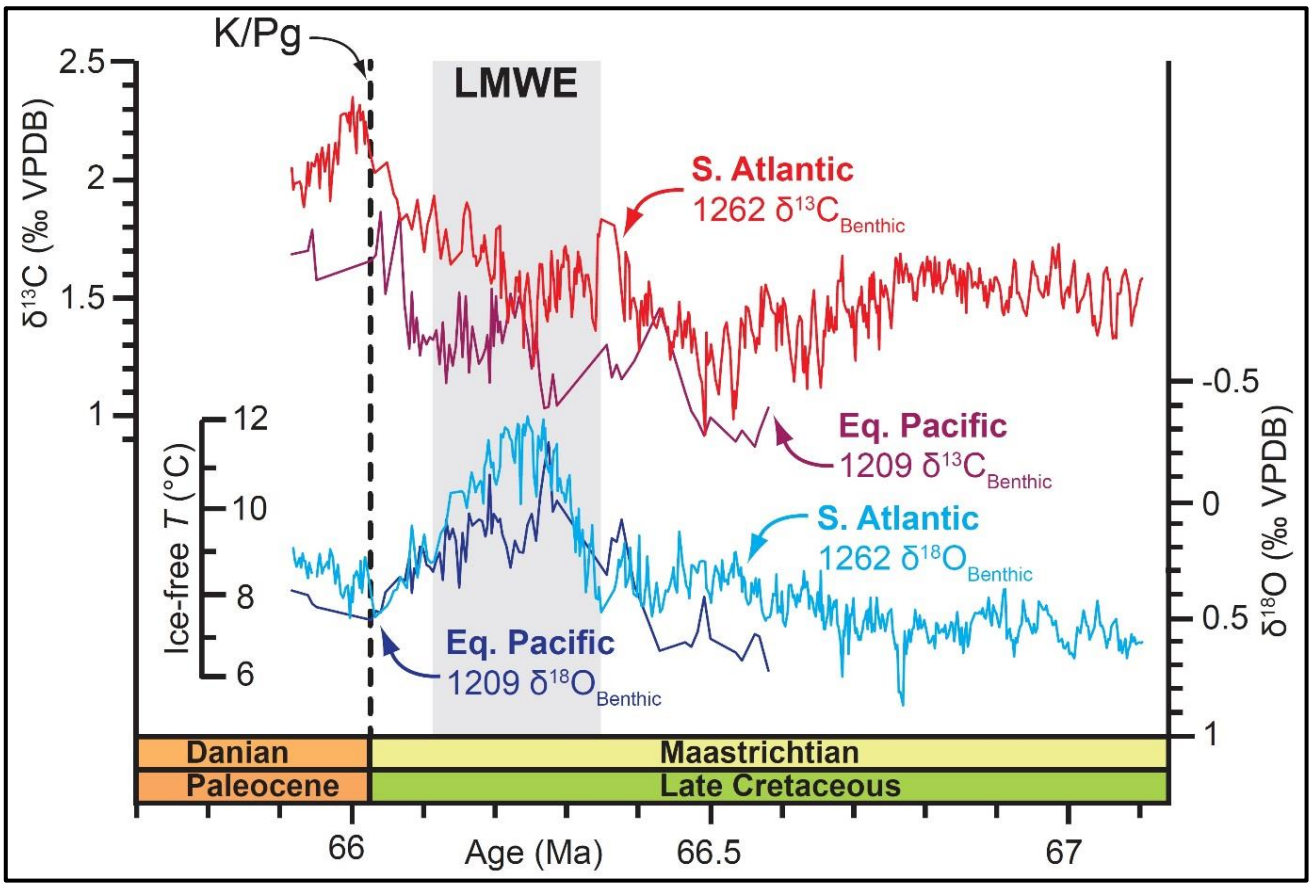

Figure 29. Comparison of the benthic stable carbon isotope ($\delta^{13}C_{benthic}$) and benthic stable oxygen isotope ($\delta^{18}O_{benthic}$) data from South Atlantic Walvis Ridge ODP Site 1262 (palaeo-depth ~3000 m; this study) and equatorial Pacific ODP Site 1209 (palaeo-depth ~2000–2500 m; Westerhold et al., 2011) across the Late Maastrichtian, Late Maastrichtian warming event (LMWE) and Cretaceous/Paleogene (K/Pg) boundary. Note the superior resolution and larger portion of the Late Maastrichtian captured by the benthic stable isotope records from ODP Site 1262 compared to the records from ODP Site 1209.

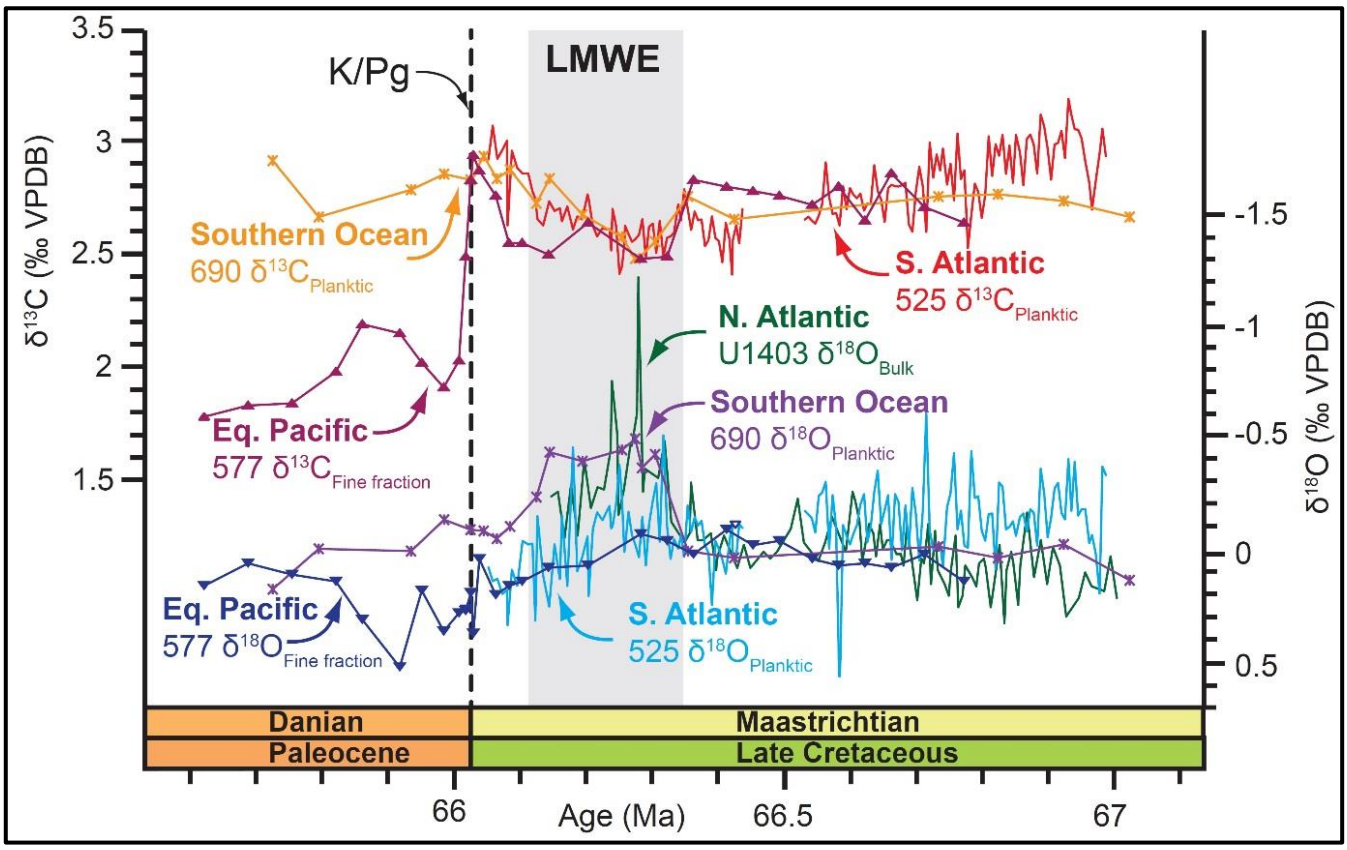

Figure 30. Compilation of planktic stable isotope ($\delta^{13}C_{Planktic}$ & $\delta^{18}O_{Planktic}$), bulk fine fraction (<63 μm) carbonate stable isotope ($\delta^{13}C_{Fine\ fraction}$ & $\delta^{18}O_{Fine\ fraction}$), and bulk carbonate stable isotope ($\delta^{13}C_{Bulk}$ & $\delta^{18}O_{Bulk}$) data across the Late Maastrichtian warming event (LMWE) and Cretaceous/Paleogene (K/Pg) boundary. Data are from equatorial Pacific DSDP Site 577 (palaeo-latitude ~22.7°N; Zachos et al., 1985), NW Atlantic IODP Site U1403 (palaeo-latitude ~31.0°N; Batenburg et al., 2017), South Atlantic DSDP Site 525 (palaeo-latitude ~42.5°S; Li & Keller, 1998), and Southern Ocean ODP Site 690 (palaeo-latitude ~70.4°S; Stott & Kennett, 1990). To compare the magnitude of the LMWE excursion in $\delta^{18}O$ by latitude, $\delta^{18}O$ data have been normalised to a baseline of 0 ‰ for pre-event conditions.

4.6.3. COMPARISON BETWEEN THE DEEP MARINE, SHALLOW MARINE, AND TERRESTRIAL REALMS

The climatic evolution prior to, during, and following the LMWE in the deep South Atlantic, surface waters of the New Jersey margin, and in the mid-latitude terrestrial realms of China and the USA, is shown in Figure 31. Prior to the onset of the LMWE (~67.1–66.34 Ma), the pattern of temperature change in the deep ocean, mid-latitude surface waters, and mid-latitude terrestrial realm appears to covary. This period is characterised by stable cool temperatures or a gradual cooling from ~67.1–66.8 Ma (Figure 31; Phase 1), followed by a gradual precursor warming of ~+1–1.5°C for ~400 kyr prior to onset of the LWME (Figure

31; Phase 2). During the LMWE onset, the greatest apparent magnitude of warming occurs in the terrestrial realm (>+5°C), and the least (~+3°C) in surface waters of the New Jersey margin (Figure 31; Phase 3). It should be noted that the terrestrial clumped isotope proxies record the variation in peak summer temperatures, rather than mean annual temperatures, therefore the greater magnitude of warming observed in these terrestrial proxies could also be biased by increased seasonality within the mid-latitude terrestrial realm across this time interval (Zhang et al., 2018). The terrestrial temperature estimates are also characterised by significantly larger uncertainties (±3–4°C) than the marine proxies (±1°C), which may bias the apparent magnitude of warming observed in the terrestrial realm based on the sparse proxy datasets presented here.

Whilst the pattern of temperature change in the oceanic and terrestrial realms prior to the LMWE appears to be comparable, its recovery phase tells a different story. Whilst South Atlantic records suggest that the deep sea cooled gradually and in a step-wise fashion by ~–4°C towards pre-excursion temperatures just prior to K/Pg boundary time, a dramatic cooling of ~–12.5°C occurred over ~100 kyr between 66.2–66.1 Ma in northern China and ~–8–10°C in the USA (Figure 31; Phase 4), although the influence of poorer age model control on the terrestrial sequences and the larger uncertainties associated with the terrestrial temperature estimates should also be considered. Mid-latitude surface waters of the New Jersey margin, however, are characterised by a longer duration of warmer temperatures, with a cooling towards pre-excursion conditions only during the final ~100 kyr of the Maastrichtian (Figure 31; Phase 4). Therefore, whilst the magnitude of warming and subsequent cooling in the marine realm during the Late Maastrichtian appears to have been relatively modest (~3–4°C), evidence exists for transient temperature fluctuations of a significantly greater rate and magnitude in the terrestrial realm during the final 300–400 kyr of the Maastrichtian. A portion of this apparently significant mid-latitude terrestrial cooling could also be explained by a reduction in seasonality (hence significantly cooler summer temperatures), however, therefore may not reflect the true magnitude of change in mean annual temperature (e.g., Zhang et al., 2018).

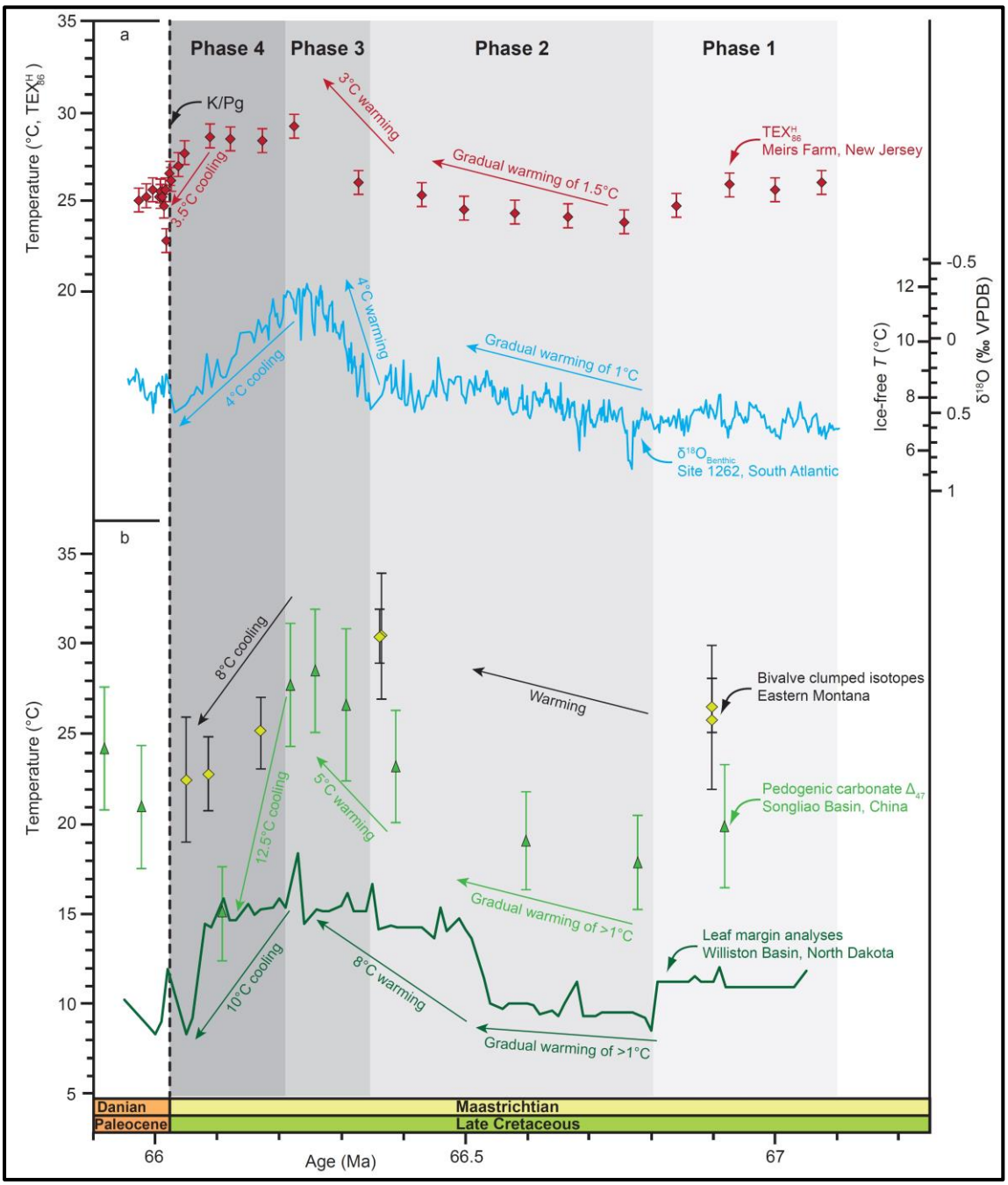

*Figure 31. Comparison of the magnitude and pattern of Late Maastrichtian climate change in the shallow to deep marine and terrestrial realms: (**a**) Marine realm, with mid-latitude sea surface (TEX_{86}^{H}) temperature data from New Jersey, USA (palaeo-latitude ~37°N; Vellekoop et al., 2016) and bottom water ($\delta^{18}O_{benthic}$) temperature data South Atlantic ODP Site 1262 (palaeo-latitude ~40.3°S; palaeo-depth ~3000m; this study). (b) Mid-latitude terrestrial realm, with bivalve clumped isotope data from eastern Montana, USA (palaeo-latitude ~52.6°N; Tobin et al., 2014), pedogenic carbonate clumped isotope [Δ_{47}] data from Songliao Basin, China (palaeo-latitude ~51°N; Zhang et al., 2018), and leaf margin temperature data from North Dakota, USA (palaeo-latitude ~49°N; Wilf et al., 2003). Shading and phase numbers correspond to periods of climatic evolution referred to in **Section 4.6.3**.*

4.6.4. EVOLUTION OF ATMOSPHERIC *p*CO_2

Recalibrated estimates for atmospheric *p*CO_2 levels during the Late Maastrichtian and K/Pg boundary time are compared to the new benthic stable isotope data from ODP Site 1262 in Figure 32. Although of low temporal resolution (~100 kyr), recalibrated estimates based on the pedogenic carbonate proxy record a significant rise in *p*CO_2 broadly correlating with the LMWE, whilst estimates based on the stomatal index proxy appear to generally fall outside of the LMWE and are therefore likely to be more representative of ambient conditions (Figure 32a).

Estimates of atmospheric *p*CO_2 based on the pedogenic carbonate proxy record a rise from pre-event values of ~200 ppm up to values of ~500–700 ppm during the peak of the LMWE, before falling again during the recovery phase (Nordt et al., 2002, 2003; Figure 32a). Assuming maximum positive error, CO_2 concentrations may have peaked as high as 1000 ppm during the event. Although absolute proxy estimates of atmospheric *p*CO_2 are associated with significant uncertainty, the trend of rising *p*CO_2 from pre-excursion to peak event is well beyond error and is therefore considered significant.

Evidence for increasing atmospheric *p*CO_2 during the event, along with the muted global carbon isotope response within marine carbonates (Figure 27; Figure 28; Figure 29; Figure 30), supports a primary contribution of an isotopically heavier source of CO_2 (such as mantle-derived CO_2) as the trigger for the LMWE. The onset of the rise in CO_2 appears to pre-date the onset of warming as recorded by the ODP Site 1262 $\delta^{18}O_{benthic}$ record by ~200 kyr, however this is likely to be an artefact of the comparatively poorer age control on the terrestrial sequences in Alberta and Texas (Nordt et al., 2002, 2003). Further higher resolution *p*CO_2 proxy data, with tighter age control, are required to confirm the timing of the rise in atmospheric CO_2 and to further support the correlation to global climate change at this time.

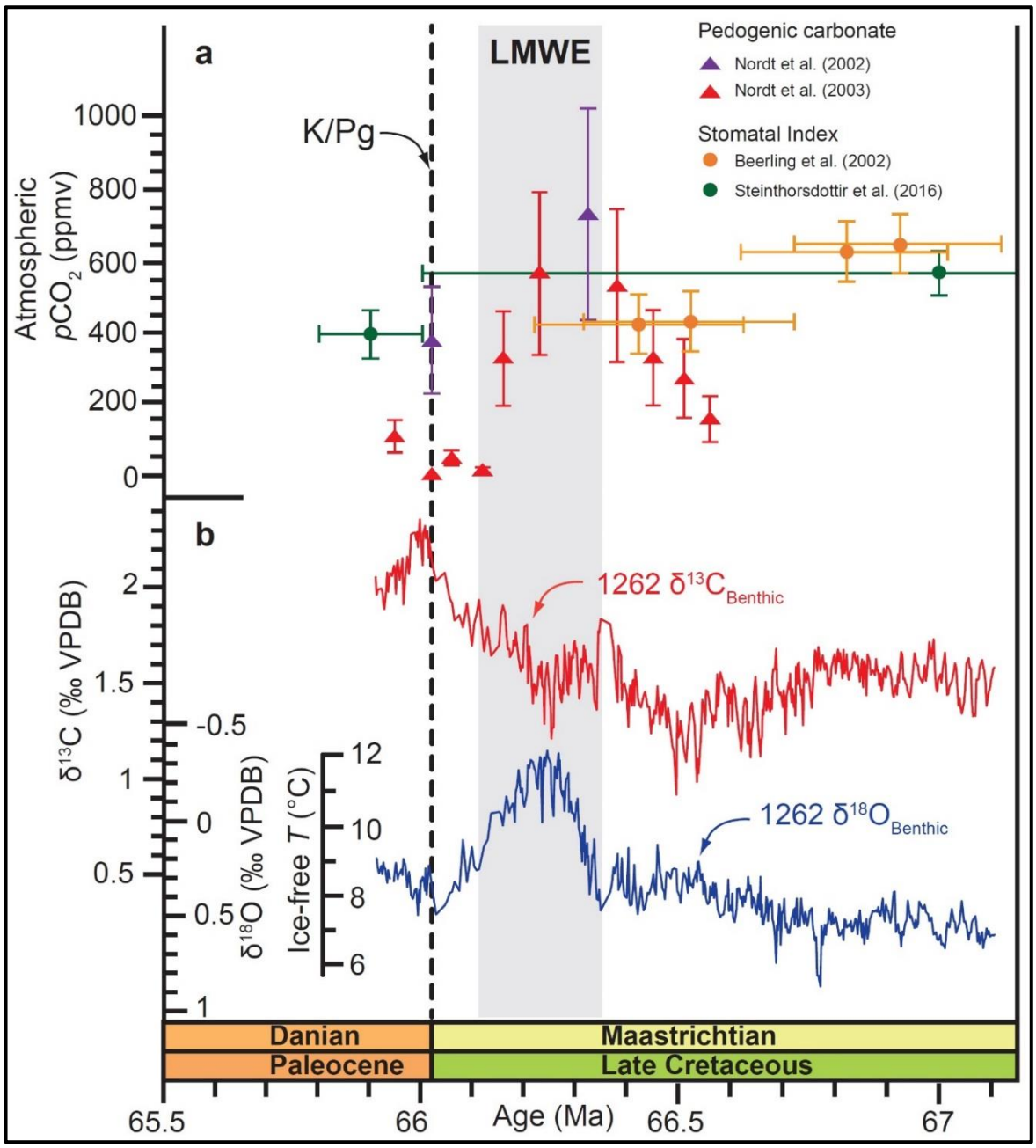

*Figure 32. Recalibrated proxy data for atmospheric pCO_2 across the Late Maastrichtian warming event (LMWE): (**a**) Recalibrated atmospheric pCO_2 data. Data based on the pedogenic carbonate proxy are indicated by triangles (purple triangles from Nordt et al., 2002, recalibrated during this study; red triangles from Nordt et al., 2003, recalibrated during this study), and estimates based on the stomatal index proxy by circles (orange circles from Beerling et al., 2002, recalibrated by Barclay & Wing, 2016; green circles from Steinthorsdottir et al., 2016); (**b**) South Atlantic ODP Site 1262 benthic stable isotope data (this study).*

4.6.5. DISSOLUTION PROXIES

The transient release of CO_2 into the atmosphere, regardless of its isotopic composition, will lower the pH of the oceans as they equilibrate with the

atmosphere. If the CO_2 is released at a sufficiently high rate such that the riverine flux of carbonate ion (CO_3^{2-}) from continental weathering cannot keep pace with the fall in pH, such as during transient hyperthermal events, ocean acidification occurs. This ocean acidification is compensated, via a negative feedback, by shoaling of the lysocline (calcite saturation horizon) and CCD (depth below which carbonates are not preserved), leading to dissolution of deep-sea carbonates. There is, however, a lack of evidence for significant prolonged carbonate dissolution (as inferred from records of ODP Site 1262 Fe intensity and % $CaCO_3$) associated with the LMWE on the Walvis Ridge (Figure 33). This interval of the Late Maastrichtian is also characterised by the highest sedimentation rates of the entire Late Maastrichtian–Early Eocene (~2.2–2.8 cm/kyr), further suggesting that this event was not characterised by significant carbonate dissolution at ODP Site 1262 (Figure 12g; Figure 33d).

Nonetheless, strong evidence does exist suggesting that changes in deep-sea dissolution were strongly amplified on precessional timescales during the LMWE. Peaks in dissolution on such timescales at ODP Site 1262 correlate with minima in $\delta^{13}C_{benthic}$, but often with maxima in $\delta^{18}O_{benthic}$ (compare Figure 33b-c). This observation suggests that these dissolution cycles and accompanying negative $\delta^{13}C_{benthic}$ excursions are unlikely to result from the transient release of isotopically light carbon into the ocean-atmosphere system, as a corresponding increase in temperature (decrease in $\delta^{18}O_{benthic}$) would be expected. A more parsimonious explanation is that carbonate dissolution and the carbon cycle are responding to precession-forced changes in surface ocean productivity related to changes in seasonal insolation, which were amplified during the LMWE. A periodic increase in export productivity, and resulting increase in C_{org} remineralisation at depth, would result in periodically more corrosive bottom waters. An increase in export productivity accompanied by C_{org} burial would also result in CO_2 drawdown, providing a mechanism for the accompanying cooling as observed in the $\delta^{18}O_{benthic}$ record, whilst a negative $\delta^{13}C_{benthic}$ excursion would still be expected in marine carbonates due to increasing photosynthetic fractionation within the organic matter (Kump and Arthur, 1999). The LMWE is characterised by the highest sedimentation rates of the entire Late Maastrichtian–Early Eocene (~2.2–2.8 cm/kyr), supporting a scenario of increased export productivity during this time (Figure 12g; Figure 33d). The most amplified

precession cycles in % $CaCO_3$, Fe intensity and $\delta^{13}C_{benthic}$ occur during peak greenhouse conditions of the LMWE, as well as the $Ma_{405}2$ long (405-kyr) eccentricity maximum (compare Figure 33a to Figure 33b-c). These amplified cycles are characterised by paired excursions of ~–0.3–0.4‰ in $\delta^{13}C_{benthic}$ (Figure 33c) and a fall of 30–40% $CaCO_3$ (Figure 33b). These perturbations represent fairly sizeable orbitally-paced excursions to the carbon cycle, accounting for around two thirds of the magnitude of the negative $\delta^{13}C_{benthic}$ excursion (~–0.6 ‰) associated with the LMWE (Figure 33c). In contrast to the LMWE, however, precession-forced dissolution cycles and minima in $\delta^{13}C_{benthic}$ during the $Ma_{405}2$ and $Ma_{405}3$ eccentricity maxima do generally correlate with minima in $\delta^{18}O_{benthic}$ (implying coeval warming), suggesting that the release of climate- or temperature-sensitive carbon stores may have played a more important role in the amplitude of precession cycles prior to the LMWE. Precession cyclicity appears to exert a strong control over variability within the dissolution proxies during 100-kyr eccentricity maxima across the Late Maastrichtian portion of the record as a whole. There is, however, a dramatic decrease in power within the precession band across the K/Pg boundary, with an apparent switch to variability controlled by 100-kyr eccentricity during the early Danian (Figure 33b; see **Chapter 5**, **Section 5.6.7.** for further discussion of the Early Paleocene).

4.6.6. SPECTRAL ANALYSIS

Based on our updated orbitally-tuned age model, the onset of the Late Maastrichtian warming event occurs during a 405-kyr eccentricity minimum, with the peak of the event in phase with a 100-kyr eccentricity maximum but prior to a 405-kyr maximum (Figure 34). The subsequent 405-kyr eccentricity maximum coincides with the first “plateau” in $\delta^{18}O_{benthic}$ during the recovery phase from the LMWE at ~66.14 Ma. It is also associated with a transient decrease in $\delta^{13}C_{benthic}$ of ~–0.2‰ during a longer term trend of increasing $\delta^{13}C_{benthic}$ up to the K/Pg boundary (Figure 34a,c).

The amplification of precession cyclicity during 100-kyr eccentricity maxima, and during the LMWE as a whole, can be clearly seen in the 21-kyr filter for $\delta^{13}C_{benthic}$ (Figure 34b). The greatest amplification of precession cyclicity correlates with larger amplitude variations in the 100-kyr $\delta^{13}C_{benthic}$ filter,

illustrating the clear modulation of precession amplitude by eccentricity (Figure 34b). The amplification of both $\delta^{13}C_{benthic}$ and $\delta^{18}O_{benthic}$ 21-kyr cycles during the LMWE suggests the climate system and carbon cycle were both at their most sensitive to changes in precession during Late Maastrichtian greenhouse warming, due to pronounced cycles in export productivity (see **Section 4.6.5**). The clear antiphase behaviour between $\delta^{13}C_{benthic}$ and $\delta^{18}O_{benthic}$ within the 21-kyr band (and 100-kyr band) during the LMWE, supports the scenario of periodic increases in export productivity on precessional timescales during this greenhouse event (see **Section 4.6.5**; Figure 34b). However, $\delta^{13}C_{benthic}$ and $\delta^{18}O_{benthic}$ are generally in phase at the 21-kyr band during 405-kyr eccentricity maxima earlier in the Maastrichtian, confirming a more important role of transient episodes of greenhouse gas release from climate- or temperature-sensitive carbon stores on precessional timescales during this time (Figure 34b). An abrupt switch in power from the 21-kyr precession band to the 100-kyr eccentricity band across the K/Pg boundary can be clearly seen in the 100-kyr and 21-kyr filters, especially for $\delta^{13}C_{benthic}$ (see **Chapter 5**, **Section 5.6.7.** for further discussion of the Early Paleocene).

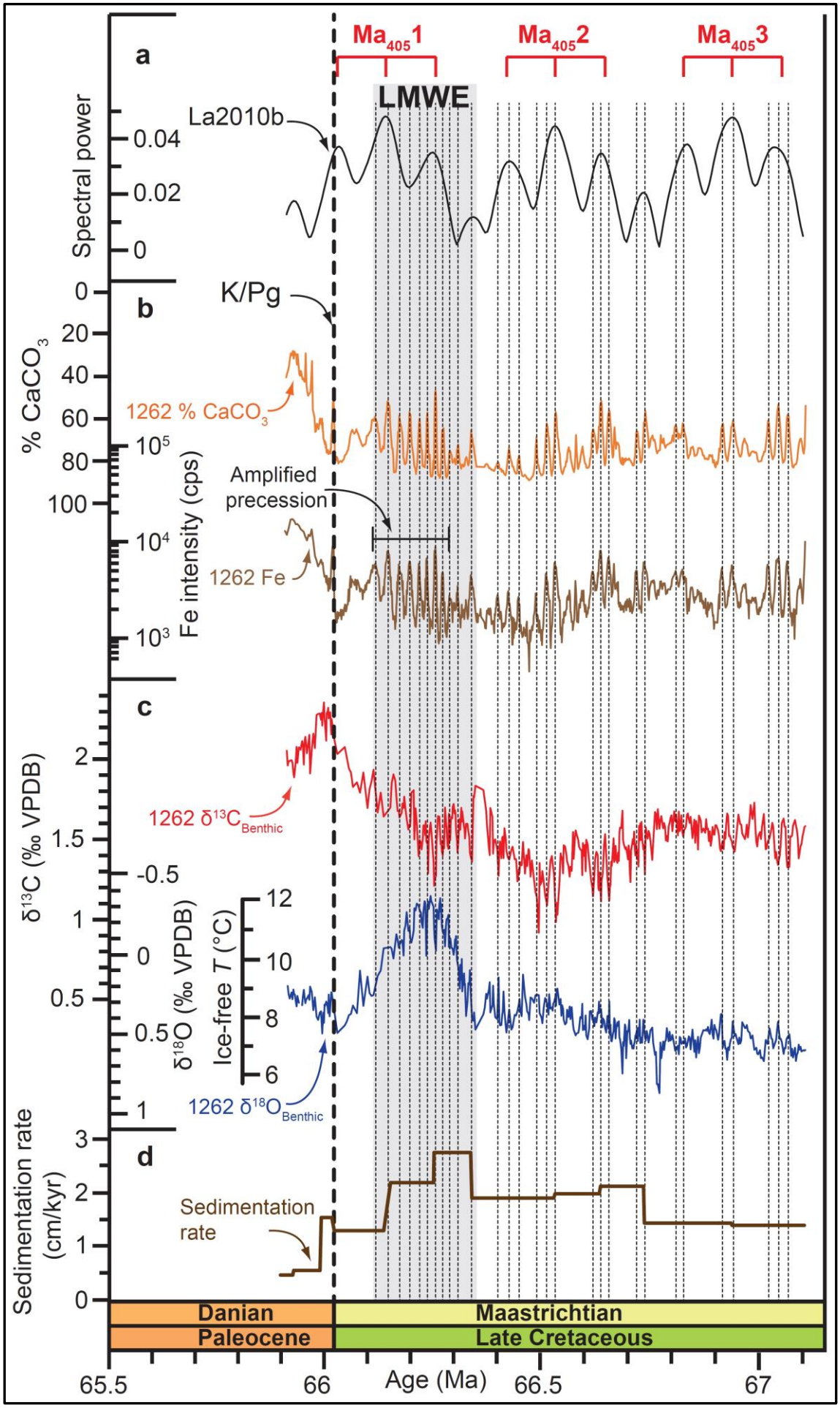
Ma405 1
Ma405 2
Ma405 3
LMWE
a
Spectral power
0.04
0.02
0
La2010b
K/Pg
b
% CaCO3
20
40
60
80
100
1262 % CaCO3
Amplified precession
Fe intensity (cps)
10^5
10^4
10^3
1262 Fe
c
δ13C (‰ VPDB)
2
1.5
1
0.5
1262 δ13CBenthic
δ18O (‰ VPDB)
-0.5
0
0.5
1
Ice-free T (°C)
12
10
8
6
1262 δ18OBenthic
d
Sedimentation rate (cm/kyr)
3
2
1
0
Sedimentation rate
Danian
Paleocene
Maastrichtian
Late Cretaceous
65.5
66
Age (Ma)
66.5
67

*Figure 33 (previous page). Orbital pacing of carbonate dissolution proxy and benthic stable isotope data from ODP Site 1262: (**a**) La2010b orbital solution (Laskar et al., 2011a); (**b**) proxy data for carbonate dissolution, including % $CaCO_3$ (Kroon et al., 2007) and Fe intensity (Westerhold et al., 2008); (**c**) benthic stable isotope data (this study); (**d**) sedimentation rate based on the tie points used to create the orbitally-tuned age model generated during this study (**Appendix 3**). Long (405-kyr) eccentricity maxima are named following the nomenclature of Husson et al. (2011). Dashed lines indicate precession-forced carbonate dissolution events correlated between the geochemical proxies, which are amplified during 100-kyr eccentricity maxima and throughout the Late Maastrichtian warming event (LMWE).*

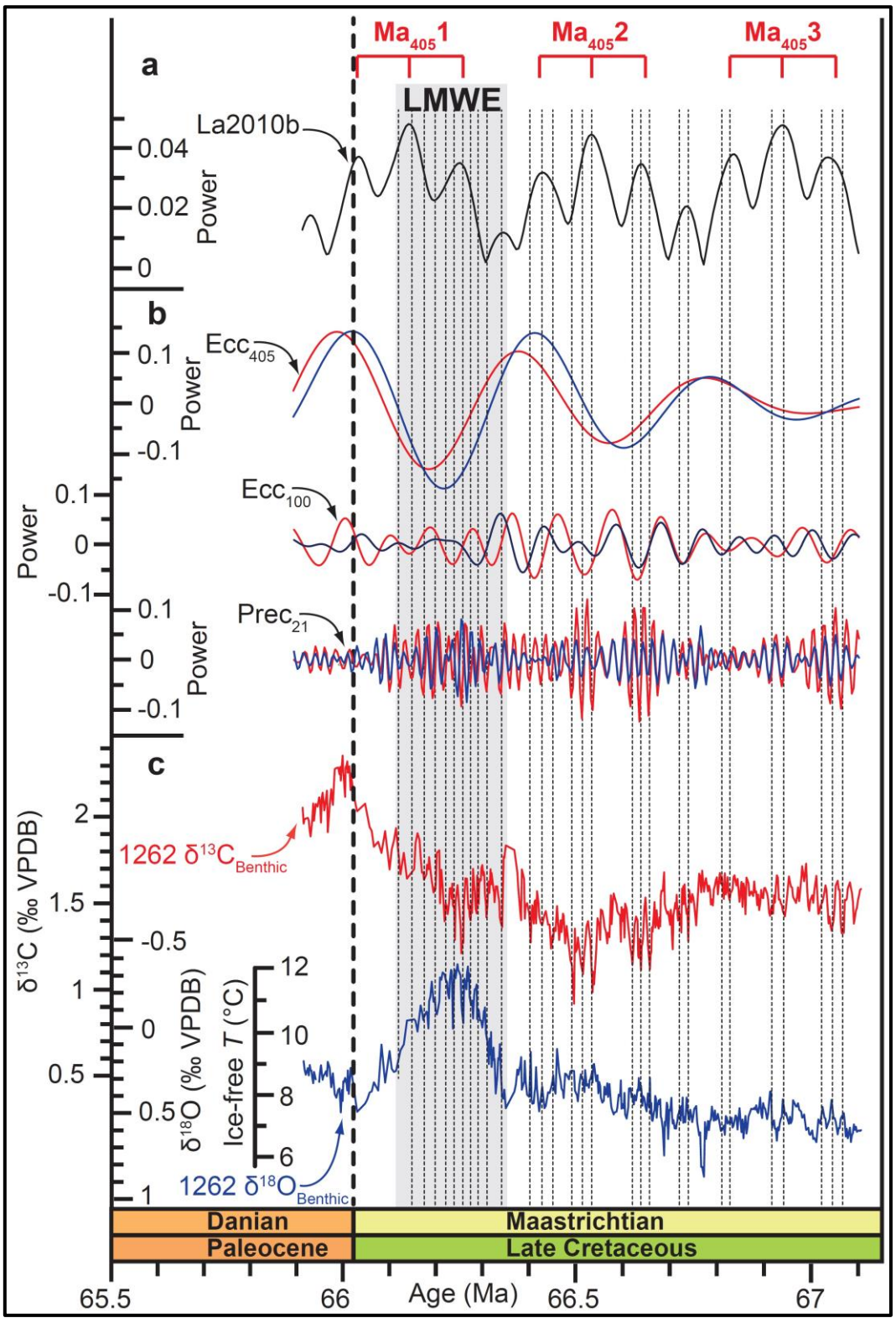

*Figure 34. Spectral analysis of the new Late Maastrichtian and K/Pg boundary $\delta^{13}C_{benthic}$ and $\delta^{18}O_{benthic}$ records from South Atlantic ODP Site 1262: (**a**) La2010b orbital solution (Laskar et al., 2011a); (**b**) filters at the long (405-kyr) eccentricity frequency (Ecc_{405}), short (100-kyr) eccentricity frequency (Ecc_{100}), and precession (21-kyr) frequency ($Prec_{21}$), for $\delta^{13}C_{benthic}$ in red and $\delta^{18}O_{benthic}$ in blue (this study); (**c**) benthic stable isotope data (this study). Dashed lines indicate the precession-forced release of isotopically light carbon, amplified during 100-kyr eccentricity maxima and during the Late Maastrichtian warming event (LMWE).*

4.6.7. CORRELATION TO DECCAN TRAPS VOLCANISM

Owing to a close temporal association with the K/Pg boundary mass extinction, Deccan Traps volcanism has long been argued as a potential causal factor in the severity of the mass extinction (e.g., Keller et al., 2016). The Deccan Traps LIP was erupted predominantly subaerially across the Indian sub-continent, although an unknown volume was also erupted offshore, such as within the Krishna Godavari Basin (Keller et al., 2012). Based on the latest radiogenic dates (Renne et al., 2015; Schoene et al., 2015), the main phase of Deccan Traps volcanism commenced ~250–350 kyr before the K/Pg boundary and ceased ~500 kyr after the K/Pg boundary, spanning a total duration of <1 million years (Table 7). The basalts of the Deccan Traps have been subdivided into 3 sub-groups, including the pre-K/Pg Kalsubai sub-group (~66.4–66.2 Ma), the K/Pg boundary spanning Lonovala sub-group (~66 Ma), and the post-K/Pg Wai sub-group (~65.9–65.5 Ma; Table 7). The pre-K/Pg Kalsubai sub-group, of greatest interest for correlating to the LMWE, has been further subdivided into the Jawhar, Igatpuri, Neral, Thakurvadi, and Bhimashankar formations (from oldest to youngest, Table 7). Based on the thicknesses and aerial extents of the preserved basalt flows, the most voluminous outpourings of the Deccan Traps occurred within the post-K/Pg Wai sub-group (Table 7).

Radiometric ages for discrete formations within the Deccan Traps are listed in Table 7 and correlated to the LMWE in Figure 35. The within-error overlap in radiometric Ar/Ar and U/Pb ages for volcanics of the Deccan Traps Kalsubai sub-group and the duration of the LMWE (~66.38 ±0.05–66.20 ±0.13 Ma; Table 7; Figure 35a,b), as defined by our orbitally-tuned age model, strongly suggests a causal link. The oldest Jawhar Formation has been dated as 66.38 ±0.05 Ma (based on the Ar/Ar method; Renne et al., 2015) or 66.288 ± 0.027 Ma (based on U/Pb dating; Schoene et al., 2015), correlating very closely temporally with the onset of the LMWE (~66.34 Ma). Both of these radiometric ages were measured on flows close to the centre of the Jawhar Formation, therefore may be considered as minimum estimates for the absolute age of the onset of extrusive volcanism.

Formation volumes calculated by both the equal area and variable area methods are listed in Table 7 and correlated to the LMWE in Figure 35b. Volumes calculated using the variable area method, calculated by varying the base flow radius for each formation based on putative estimates of present-day aerial extents of each sub-group across the Indian sub-continent, are considered the most accurate. The Jawhar and Thakurvadi formations represent the most voluminous stratigraphic units within the Kalsubai sub-group, comprising volumes of 36,000 and 43,000 km^3 respectively (variable area method; Table 7, Figure 35b). Ar/Ar ages for 3 distinct flows within the Thakurvadi Formation of 66.27 ± 0.07 Ma, 66.24 ± 0.08 Ma and 66.20 ± 0.13 Ma (Renne et al., 2015) place the most voluminous outpourings of this formation synchronous in time with peak greenhouse conditions during the LMWE (~66.27–66.21 Ma; Figure 35a,b).

Table 7

Sub-group	Formation name	Radiometric age (Ar/Ar method; Ma)	Radiometric age (U/Pb method; Ma)	Volume (km^3; equal area method)	Volume (km^3; variable area method)
Kalsubai	Jawhar	66.38±0.05	66.288±0.027	194,000	36,000
	Igatpuri	66.35±0.07	-	52,000	9,000
	Neral	66.28±0.05	-	50,000	9,000
	Thakurvadi	66.27±0.07 66.24±0.08 66.20±0.13	-	232,000	43,000
	Bhimashankar	66.21±0.07	-	46,000	9,000
Lonovala	Khandala	-	-	67,000	12,000
	Bushe	-	-	121,000	22,000
Wai	Poladpur	65.92±0.3	-	139,000	147,000
	Ambenali	65.62±0.08	65.661±0.087	180,000	190,000
	Mahabaleshwar	-	65.552±0.026 65.545±0.026 65.535±0.027	96,000	102,000
	Panhala	-	-	67,000	12,000
	Desur	-	-	57,000	10,000

Radiometric ages and volumes calculated by both equal area and variable area methods for the formations of the Deccan Traps, India. For the equal area method, formation thicknesses published by Jay & Widdowson (2008) were multiplied by a constant base flow radius of 600 km for each formation, which represents the maximum present-day aerial extent of the Deccan Traps basalts (Jay & Widdowson, 2008). For the variable area method, formation volumes were calculated using the same formation thicknesses from Jay & Widdowson (2008), but by varying the base flow radius from 600 km for the Poladpur, Wai and Mahabaleshwar formations, to 250 km for all other formations. These varying radiuses represent putative estimates of present-day sub-group aerial extents (Jay & Widdowson, 2008). Ar/Ar ages are from Renne et al. (2015) and U/Pb ages from Schoene et al. (2015). Analytical uncertainty stated at 1σ.

The suggestion that Deccan volcanogenic CO_2 emissions are the leading candidate for the primary climate driver of the LWME over 100-kyr timescales, is supported by both the relatively long duration of the LMWE (~300 kyr from initial onset to complete recovery; Figure 35a), evidence for a rise in atmospheric pCO_2 during the event from pedogenic carbonate proxy data but accompanied by a globally muted response in $\delta^{13}C$ (Figure 32), and its initiation during a minimum in the 405-kyr eccentricity cycle (Figure 34a,c). These characteristics suggest that a primary control by orbital forcing is unlikely. Nonetheless, a modulatory role of orbital forcing during the event is evident given the strongly amplified precession cyclicity within both the carbon cycle (Figure 34b), climate (Figure 34b) and dissolution proxies (Figure 33b) from ODP Site 1262 during greenhouse warming. Furthermore, the $Ma_{405}1$ long (405-kyr) eccentricity cycle appears to exert a control on the step-wise recovery from the event (Figure 34a,c), and the peak of the event occurs during a 100-kyr eccentricity maximum (Figure 34a).

The volumes of the post-K/Pg Poladpur and Ambenali formations (147,000 and 190,000 km^3, respectively, variable area method; Table 7; Figure 35b) extruded as part of the Wai sub-group, are significantly greater than formations of the pre-K/Pg Kalsubai sub-group. The Wai sub-group is, however, characterised by 20 weathering horizons (or red boles), a significantly greater number (17 more) than that recorded for the pre-K/Pg Kalsubai sub-group. This suggests that while peak greenhouse gas emissions associated with Deccan Traps volcanism may have been higher in the earliest Paleogene than during the LMWE, volcanic eruptions in the Danian were characterised by longer periods of quiescence, providing more time for atmospheric CO_2 sequestration via silicate weathering and/or organic carbon burial between eruption events (Renne et al., 2015). By contrast, more frequent, albeit smaller magnitude, episodes of Deccan Traps volcanism during the LMWE could have resulted in a larger cumulative increase in atmospheric pCO_2 than during the earliest Danian (Renne et al., 2015; Schoene et al., 2015).

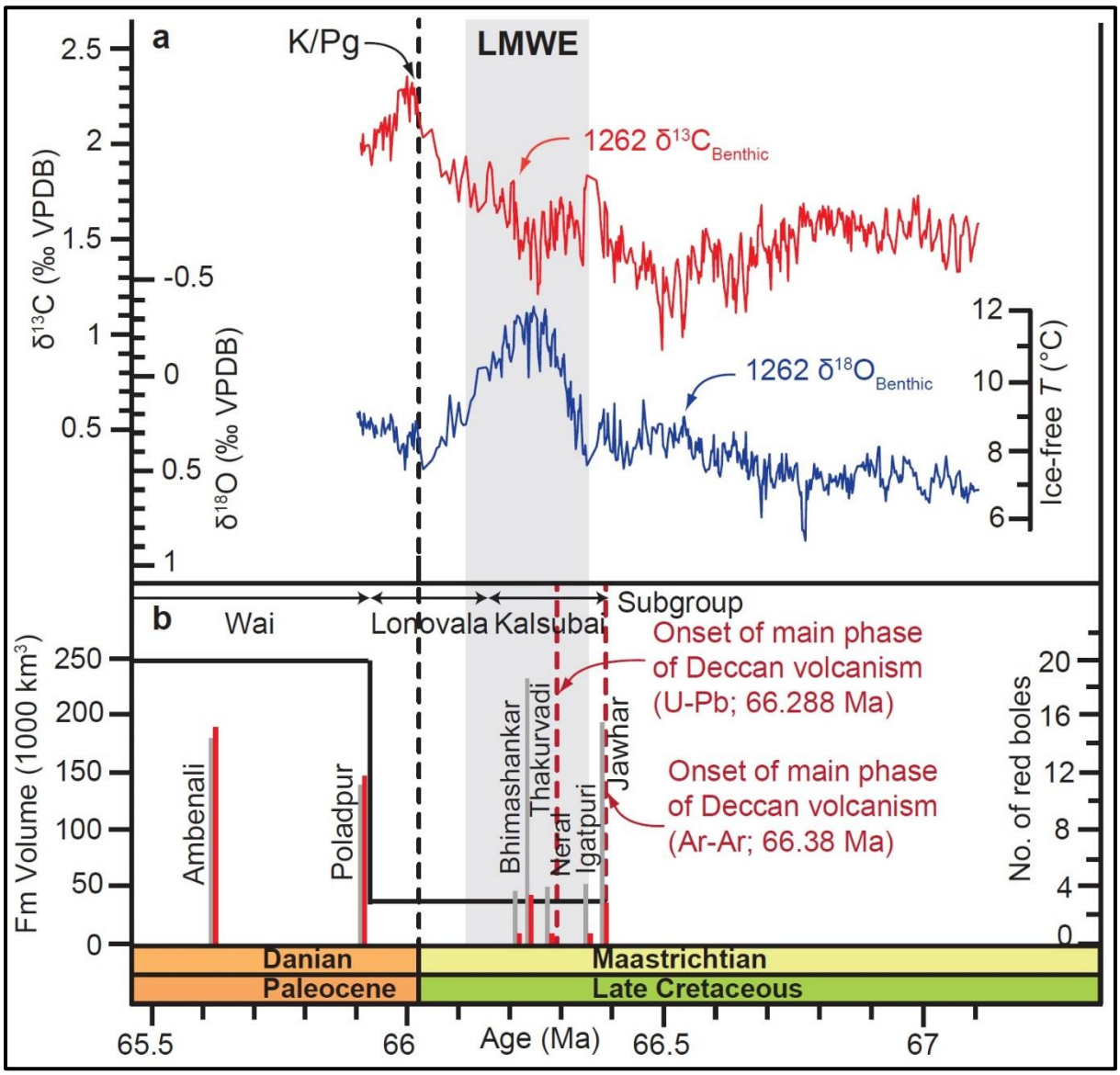

*Figure 35. Correlation of the Late Maastrichtian warming event (LMWE) to Deccan Traps volcanism: (**a**) South Atlantic ODP Site 1262 benthic stable isotope data (this study); (**b**) radiometric ages and formation volumes for the Deccan Traps. Ar-Ar ages for the discrete Deccan Traps formations are from Renne et al. (2015), with the U-Pb age for the onset of volcanism (Jawhar Formation) also shown (Schoene et al., 2015). Vertical grey bars indicate formation volumes calculated by the equal area method, whilst vertical red bars indicate formation volumes calculated by the variable area method. The total number of red boles per sub-group is indicated by the black line (data from Renne et al., 2015).*

4.6.8. MUTED CARBON ISOTOPE EXCURSION AND CARBONATE DISSOLUTION

Despite strong evidence for climatic warming and some evidence for elevated atmospheric pCO_2 during the LMWE (Figure 32a), the muted excursion

in benthic (~–0.6‰; Figure 29) and planktic (~–0.3–0.4‰; Figure 30) carbon isotopes for this time imply that this warming event was characterised by a relatively minor perturbation to the isotopic composition of the global carbon pool. By contrast, the benthic carbon isotope excursion recorded by marine carbonates during the Paleocene–Eocene Thermal Maximum (PETM), which was characterised by a slightly greater magnitude of bottom water warming of ~+5°C, is typically significantly larger, at ~–2.5–3.5‰ (McInerney & Wing, 2011; Figure 36a). Both the PETM and LMWE coincided with large igneous province volcanism. A significant portion of North Atlantic Igneous Province (NAIP) volcanism was extruded subaqueously into marine organic-rich shales during the PETM (Svensen et al., 2004; Gutjahr et al., 2017), and while an unknown volume of Deccan Traps volcanism was erupted offshore in the Krishna-Godavari Basin, most of it was erupted subaerially on the Indian sub-continent (e.g., Keller et al., 2012). The muted $\delta^{13}C$ excursion implies that sources of isotopically light carbon commonly invoked to explain the magnitude of the PETM excursion, such as biogenic methane ($\delta^{13}C$ of ~–60‰; Kvenvolden, 1993; Milkov, 2005), thermogenic methane released during intrusion of NAIP volcanism into organic-rich shales ($\delta^{13}C$ of ~–35 to –50‰; Hunt, 1996), or the oxidation of organic matter ($\delta^{13}C$ of ~–25‰; Higgins & Schrag, 2006), were not released in significant quantities during the LMWE. The muted carbon isotope response during the LMWE is therefore consistent with the release of predominantly isotopically heavier mantle-derived carbon during Deccan Traps volcanism, with a typical $\delta^{13}C$ value of ~–5 to –7‰ (e.g., Higgins & Schrag, 2006), being the primary driver of changes in atmospheric pCO_2 and global warming at this time.

A second characteristic of the LMWE, which sets it apart from typical Paleogene hyperthermals, is the lack of evidence for significant carbonate dissolution seen in marine proxies (e.g., Fe intensity) and sedimentation rates at ODP Site 1262 (Figure 33b,d). Many of the early Paleogene hyperthermals such as the PETM (Figure 36b) or Latest Danian Event (Figure 37c; see **Chapter 3**, **Section 3.6.6.**) are characterised by prominent peaks in Fe intensity in ODP Site 1262 sediments deposited during the onset and core of their carbon isotope excursions, which correspond to sharp increases in terrigenous clay content as a result of carbonate dissolution (Westerhold et al., 2007, 2008). This discrepancy may be related to the rate of greenhouse gas emission, which occurred relatively

slowly over ~80 kyr during the LMWE, but was much more rapid, on the order of ~10–40 kyr, during Paleogene hyperthermals (McInerney and Wing, 2011; Zeebe et al., 2017; Figure 36a; Figure 37a).

Despite the lack of evidence for significant dissolution at ODP Site 1262 during the LMWE, evidence for enhanced deep-sea dissolution at this time has been described from the high latitudes in % $CaCO_3$ records from ODP Site 690 (Henehan et al., 2016b), and in orbitally-tuned Fe intensity and magnetic susceptibility data from IODP Site U1403 (Batenburg et al., 2017). These marine sites may have been particularly sensitive to smaller carbon cycle perturbations during this time. ODP Site 690 was located in the principle region of deep-water formation in the Southern Ocean and IODP Site U1403, at a palaeo-depth of ~4 km on the Newfoundland margin, would have been more sensitive to smaller fluctuations in depth of the CCD during the Maastrichtian than the shallower ODP Site 1262 (Henehan et al., 2016b; Figure 26). Carbonate dissolution associated with the LMWE has also been described from the equatorial Pacific Shatsky Rise in planktic foraminiferal fragmentation data, however this dissolution event may also be explained by a transient influx of older more corrosive South Pacific Deep Water during the LMWE in the equatorial Pacific (Dameron et al., 2017; Figure 26). The significantly amplified sensitivity to precession within the $\delta^{13}C_{benthic}$, Fe intensity, and % $CaCO_3$ records from ODP Site 1262 during the LMWE, suggests that transient shoaling of the lysocline and CCD took place during this time primarily in response to periodic precession-forced increases in export productivity (Figure 36a,b; Figure 37a,c; see **Section 4.6.5**).

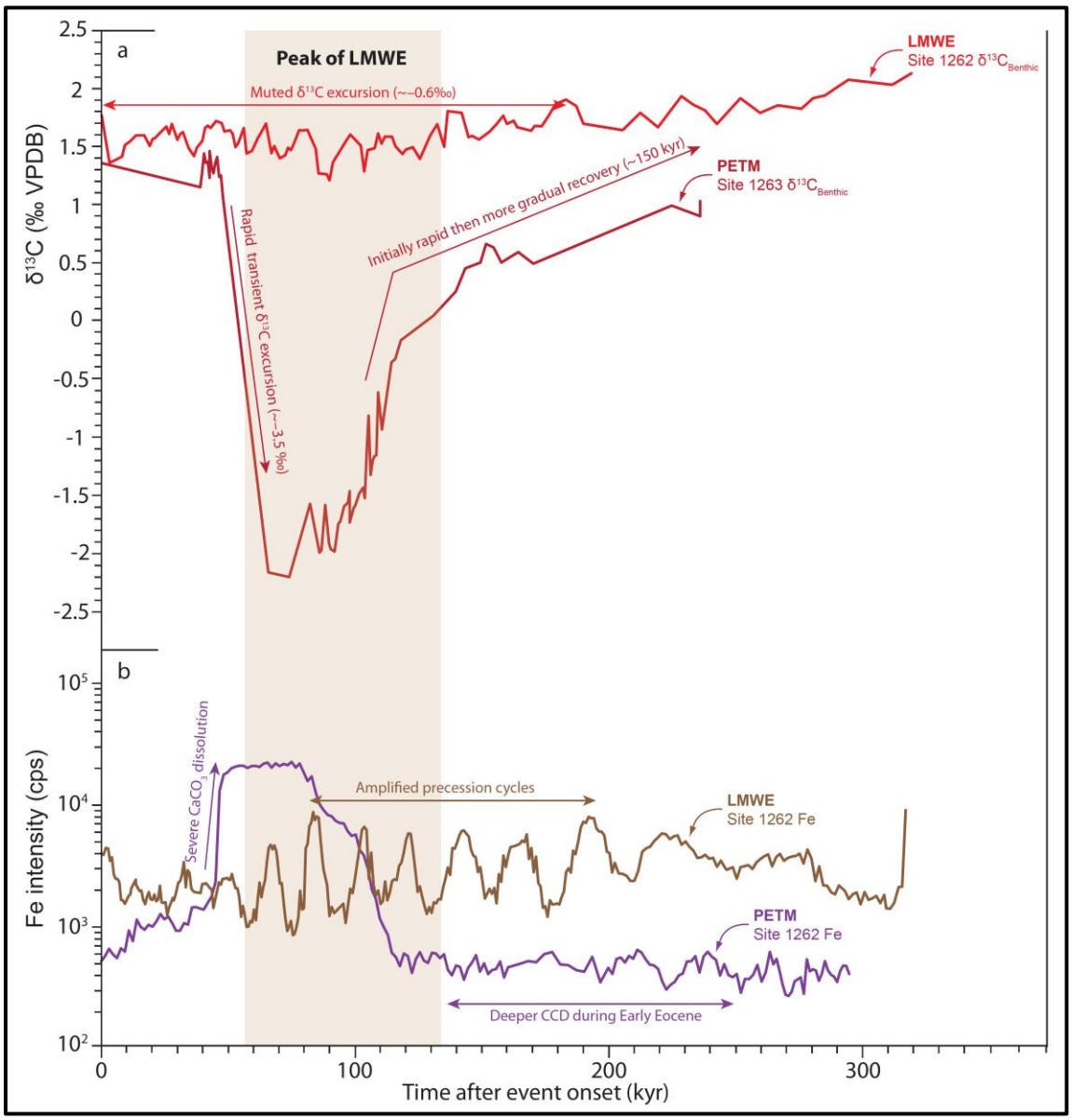

*Figure 36. Comparison between the geochemical characteristics of the Late Maastrichtian warming event (LMWE) and Paleocene–Eocene Thermal Maximum (PETM) from the South Atlantic Walvis Ridge, plotted relative to time since onset of the respective events: (**a**) $\delta^{13}C_{benthic}$, with data for the LMWE from ODP Site 1262 (~3000 m palaeo-depth; this study) and data for the PETM from ODP Site 1263 (~1500 m palaeodepth; McCarren et al., 2008), since the PETM record at the deeper ODP Site 1262 has been severely truncated by carbonate dissolution. (**b**) Fe intensity data from ODP Site 1262, with data for the LMWE from Westerhold et al. (2008) and for the PETM from Westerhold et al. (2007).*

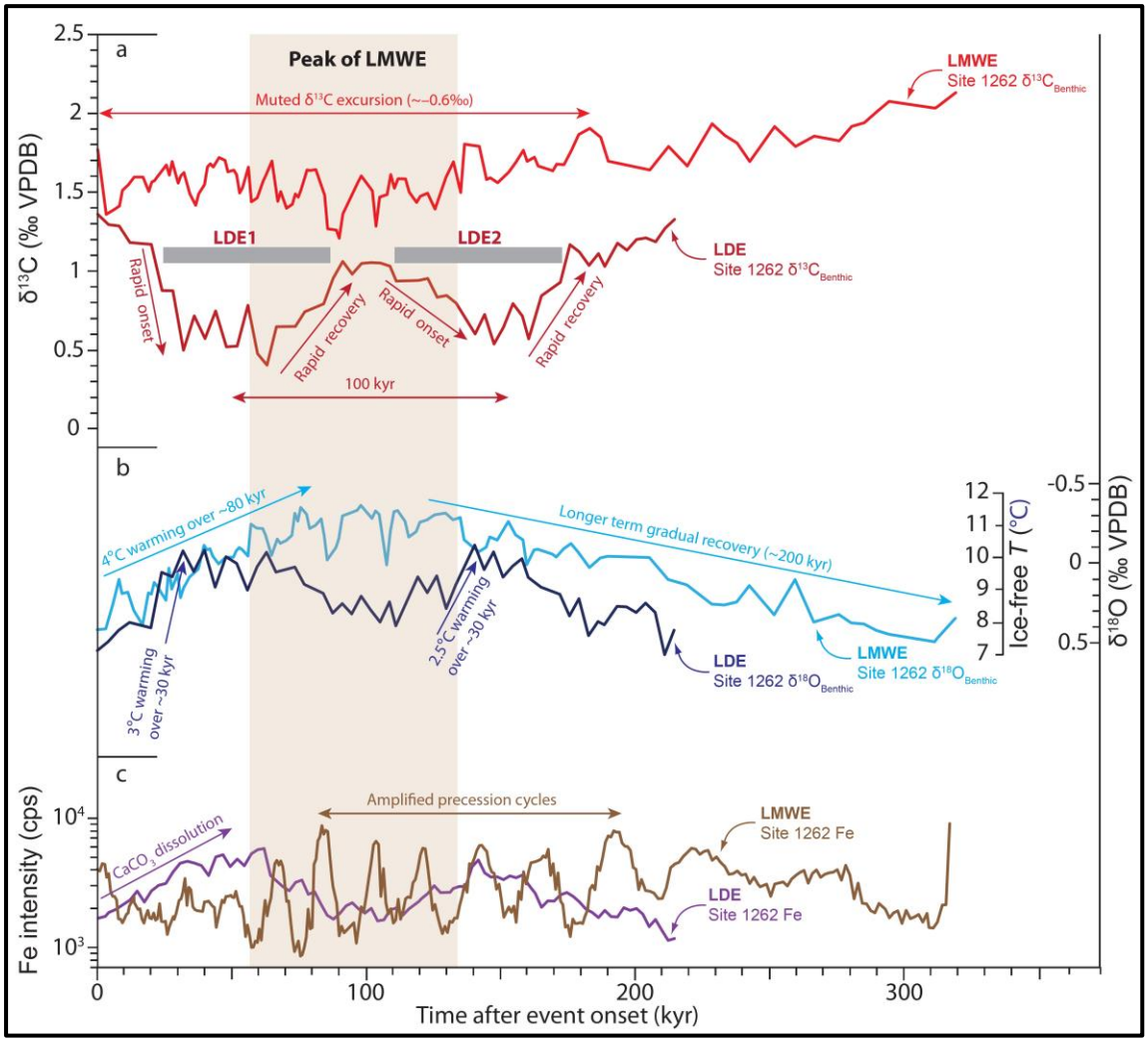

*Figure 37. Comparison between the geochemical characteristics of the Late Maastrichtian warming event (LMWE) and Latest Danian Event (LDE) at South Atlantic Walvis Ridge ODP Site 1262 (~3000 m palaeo-depth), plotted relative to time since onset of the respective events: (**a**) $\delta^{13}C_{benthic}$ data (this study). (**b**) $\delta^{18}O_{benthic}$ data (this study). (**c**) Fe intensity data (Westerhold et al., 2008). The oldest and youngest of the paired LDE excursions have been named LDE1 and LDE2 respectively, after Deprez et al. (2017). See **Chapter 3**, **Section 3.6.6.** for further discussion of the LDE.*

4.6.9. BIOTIC CHANGE DURING THE LATE MAASTRICHTIAN WARMING EVENT

Available fossil records suggest that the pronounced changes to climate documented during the latest Maastrichtian were also accompanied by a significant biotic response, particularly in (near) surface-dwelling marine organisms such as coccolithophorids and planktic foraminifera (Figure 38). However, most of these assemblage changes appear to be transient in nature, and did not result in large turnovers or extinction events during the LMWE.

There is strong evidence for transient shifts in calcareous nannoplankton communities during the LMWE in response to global warming and changes in nutrient availability (Thibault & Gardin, 2007; Sheldon et al., 2010; do Monte Guerra et al., 2016). In the mid southern latitudes (DSDP Site 525, Walvis Ridge), the LMWE is characterised by increased abundances of the thermophilic nannofossil species *Micula murus* and low-fertility species *Watznaueria barnesiae*, along with a corresponding decline in the high-fertility species *Biscutum constans* (Thibault & Gardin, 2007; Figure 38). An increase in abundance of *Watznaueria barnesiae* has also been described from sediments from the mid-northern latitudes (Danish Basin), where it is also interpreted as a warm-water indicator (Sheldon et al., 2010). A number of thermophilic calcareous nannoplankton evolutionary events occurred firstly in the low latitudes and subsequently within the mid-latitudes during the latest Maastrichtian (including *Micula murus*, *Ceratolithoides kamptneri* and *Micula prinsii*), their migration to the mid-latitudes roughly coincident with the LMWE, confirming the poleward migration of a number of warm water nannofossil taxa in response to global warming (do Monte Guerra et al., 2016).

Evidence also exists for significant changes in the composition and morphology of planktic foraminiferal communities during the LMWE. The records recording these changes are characterised by blooms of the opportunistic planktic foraminifera genus *Guembelitria* in continental shelf and slope settings of the southern Tethys (Abramovich & Keller, 2002; Keller et al., 2002; Abramovich et al., 2010; Punekar et al., 2014a), Indian Ocean (Tantawy et al., 2009), North Atlantic (Font et al., 2018), eastern Tethys and Texas (Keller et al., 2016; Figure 38). Furthermore, there is evidence for dwarfing of various planktic foraminifera species, which may be due to high reproduction rates as opposed to growth (Abramovich & Keller, 2003; Keller & Abramovich, 2009; Tantawy et al., 2009; Figure 38), and a significant reduction in photosymbiotic activity potentially due to surface water eutrophication, or the crossing of a temperature threshold (Abramovich & Keller, 2003). Poleward migration of the warm-water planktic foraminifera *Pseudotextularia elegans* was described by Olsson et al. (2001) during the event, along with the appearance of the tropical morphotype of the planktic foraminifera genus *Rosita* at mid latitudes (Kucera & Malmgren, 1998). Vertical migration of certain temperature sensitive species, such as

Pseudoguembelina hariaensis to deeper water depths, has also been observed from DSDP Site 525 (Abramovich & Keller, 2003). The response between different planktic foraminifera genera, however, varies spatially, with some tropical–sub-tropical species such as *Pseudoguembelina costulata*, *Rugoglobigerina rugosa*, *Pseudoguembelina kempensis,* and *Planoglobulina multicamerata* declining in abundance or becoming absent within the warm interval at mid-latitude sites such as DSDP Site 525. Conversely, abundances of some mid-latitude species such as *Pseudoguembelina hariaensis* and *Globotruncana arca* appear to remain constant throughout the warming event and were not displaced as might be expected during an influx of tropical species (Abramovich & Keller, 2003).

Whilst there is strong evidence for transient shifting planktic communities in association with the LMWE, evidence for global species-level extinction at this time is rather more limited and contradictory. There is evidence for a decline in species diversity and minor extinctions amongst thermocline-dwelling foraminifera, whose ecological niches were shifted the most by the dramatic reduction in the surface to deep temperature gradient (Keller, 2001; Abramovich & Keller, 2002; Keller & Abramovich, 2009). Tobin et al. (2012) also present evidence for a minor precursor extinction event mainly affecting benthic marine invertebrates from the high southern latitudes (Seymour Island, Antarctica), but this occurred ~150 kyr before the K/Pg boundary and is roughly coincident with the onset of the recovery from peak warming in our orbitally-tuned age model (Figure 38b,c). However, subsequent studies on Seymour Island contradicted the earlier interpretations of Tobin et al. (2012), concluding that there was no appreciable decline in ammonite faunas during the Late Maastrichtian prior to bolide impact (Witts et al., 2015). Many of the large global compilations of species radiations and extinctions through time also lack evidence for significant extinctions during the event. Albeit relatively low resolution, the global nannoplankton compilations of Bown et al. (2004) and Bown (2005) suggest a small drop in diversity and a minor increase in extinction rate during the Late Maastrichtian, but that no major extinctions occurred until K/Pg boundary time. The lack of significant global extinctions during the LMWE is also confirmed by the fact that global biostratigraphic datums of nannoplankton and planktic foraminifera do not exist for the latest Maastrichtian (Martini, 1971; Romein, 1979;

do Monte Guerra, 2016; Figure 38). The LMWE appears to have had little impact on benthic foraminiferal communities, with no evidence for extinctions or an appreciable decline in diversity prior to bolide impact at the K/Pg boundary (Keller, 2001). The lack of evidence for significant global ocean acidification, along with the apparent smaller magnitude of temperature change within ocean bottom waters during the LMWE compared to terrestrial environments, are likely to have contributed to the resilience of benthic foraminifera to latest Maastrichtian environmental change.

In terrestrial sequences with sufficient biostratigraphic age control, shifts in floral and faunal communities appear to mainly correlate temporally with the subsequent cooling phase following peak greenhouse conditions of the LMWE, as opposed to warming. Such changes include precursor extinction events affecting charophytes and ostracodes commencing ~150–200 kyr before the K/Pg boundary in the Songliao Basin (northern China), and a decline in floral species diversity in North Dakota (USA) during the final 100 kyr of the Maastrichtian (Wilf et al., 2003; Zhang et al., 2018; Figure 38b,c). Many terrestrial sequences, however, are typically incomplete, or characterised by poor biostratigraphic age control, hampering both the correlation of any terrestrial floral and faunal events with climate change at 100 kyr timescales, and the identification of any spatial trends associated with these events. As a consequence, there is little evidence for discrete extinction events amongst large terrestrial faunal groups such as non-avian dinosaurs directly associated with the LMWE (Mitchell et al., 2012; Brusatte et al., 2015).

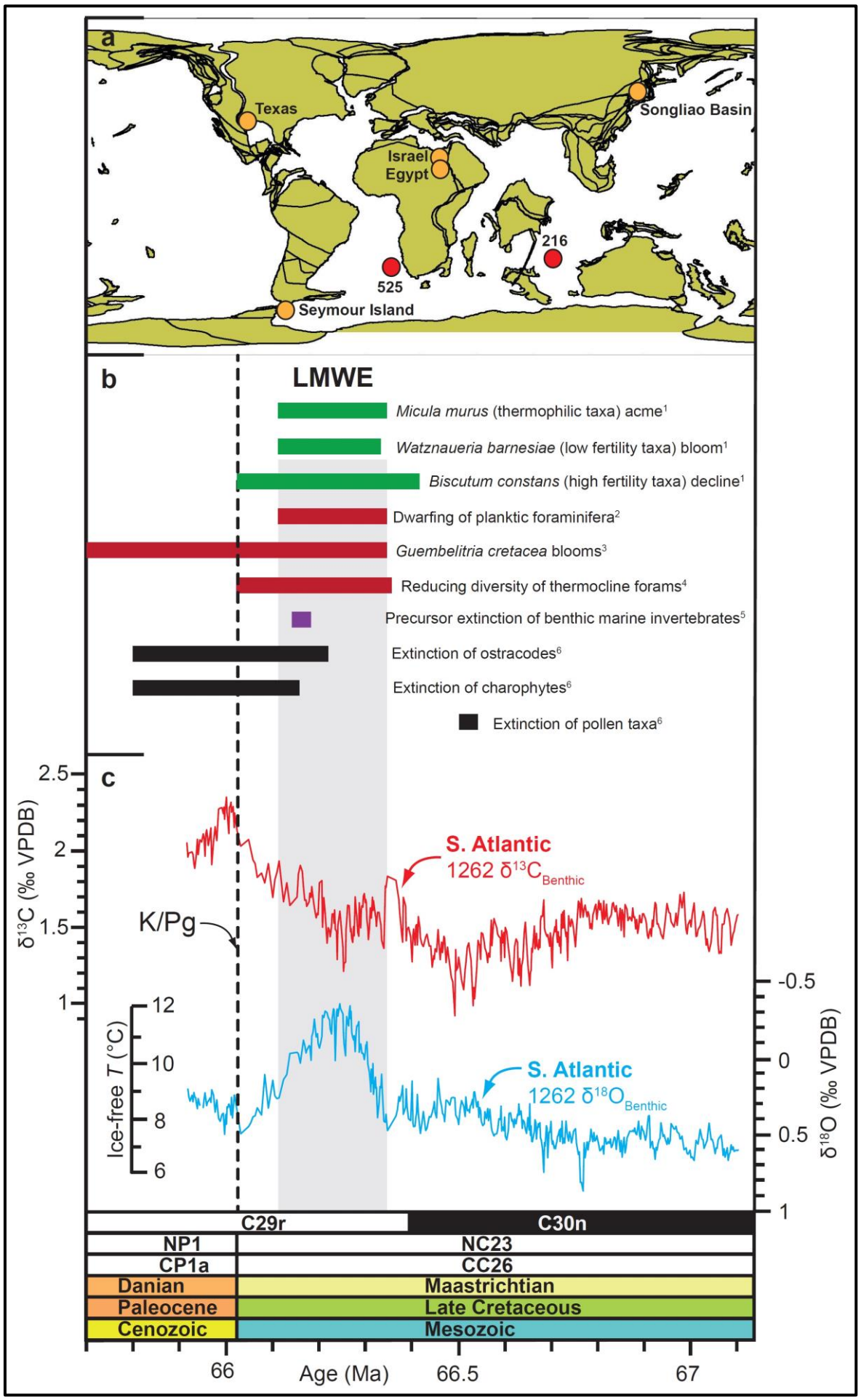
a
Texas
Songliao Basin
Israel
Egypt
216
525
Seymour Island
b
LMWE
Micula murus (thermophilic taxa) acme1
Watznaueria barnesiae (low fertility taxa) bloom1
Biscutum constans (high fertility taxa) decline1
Dwarfing of planktic foraminifera2
Guembelitria cretacea blooms3
Reducing diversity of thermocline forams4
Precursor extinction of benthic marine invertebrates5
Extinction of ostracodes6
Extinction of charophytes6
Extinction of pollen taxa6
c
δ13C (‰ VPDB)
2.5
2
1.5
1
K/Pg
S. Atlantic
1262 δ13CBenthic
Ice-free T (°C)
12
10
8
6
S. Atlantic
1262 δ18OBenthic
-0.5
0
0.5
1
δ18O (‰ VPDB)
C29r
C30n
NP1
NC23
CP1a
CC26
Danian
Maastrichtian
Paleocene
Late Cretaceous
Cenozoic
Mesozoic
66
Age (Ma)
66.5
67

*Figure 38 (previous page). Summary compilation of biotic events during the Late Maastrichtian–earliest Paleocene and Late Maastrichtian warming event (LMWE): (**a**) Location map for sites from which biotic event data have been used in this compilation. Deep sea sites are illustrated by labelled red circles and onshore sites by labelled orange circles. (**b**) Biotic events. Green bars indicate specific events affecting coccolithophorids, red bars indicate events affecting planktic foraminifera, purple bars indicate marine benthic invertebrates, and black bars indicate biotic responses within the terrestrial realm. Literature sources are indicated by superscript numbers. 1. Coccolithophorid data from South Atlantic Walvis Ridge DSDP Site 525 (Thibault & Gardin, 2007). 2. Dwarfing of planktic foraminifera from DSDP Site 525 (Abramovich & Keller, 2003) and Indian Ocean Ninetyeast Ridge DSDP Site 216 (Keller & Abramovich, 2009). 3. Blooms of the opportunistic planktic foraminifera Guembelitria cretacea from eastern Tethys (Israel & Egypt) and Texas, USA (Keller et al., 2016). 4. Decreasing diversity and minor extinctions of thermocline-dwelling planktic foraminifera at DSDP Site 525 (Keller, 2001; Keller & Abramovich, 2009). 5. Precursor minor extinction event of benthic marine invertebrates at Seymour Island, Antarctic Peninsula (Tobin et al., 2012). 6. Biotic response in the terrestrial realm of Songliao Basin, northern China (Zhang et al., 2018). Note that the apparent extinction of pollen-bearing floral taxa ~500 kyr before the K/Pg boundary may be an artefact of preservational bias due to lithological change rather than a global event. (**c**) South Atlantic ODP Site 1262 benthic stable isotope data (this study). Magnetozones are from Bowles (2006) and calcareous nannofossil zones from Shipboard Scientific Party (2004a).*

4.6.10. COULD THE LATE MAASTRICHTIAN WARMING EVENT HAVE BEEN A PRIMER FOR THE K/PG MASS EXTINCTION?

There is little doubt that pronounced changes occurred in the biotic realm during the LMWE. The lack of evidence, however, for major global extinctions at this time raises doubt over whether Deccan-induced climate change played a major role in the severity of the K/Pg mass extinction.

Whilst being a significant warming event, on the same order of magnitude as the PETM, there are several possible reasons why a smaller biotic response is observed for the Late Maastrichtian relative to the PETM. The most important feature that differentiates the LMWE from the PETM concerns the rate of change and the relatively long duration of its onset and its total duration (~80 kyr vs. ~10–20 kyr and ~300 kyr vs. ~120–220 kyr, respectively; Röhl et al., 2007; Murphy et al., 2010; Figure 36a). Such a rapid onset and duration is a characteristic feature of other Paleogene hyperthermals such as the Latest Danian Event (LDE), with the onset and total duration of each of the climatic perturbations associated with

the LDE encompassing ~20 kyr and ~100 kyr respectively (Figure 37a,b). The relatively slow onset of the LMWE could have allowed greater opportunity for adaptation of marine and terrestrial flora and fauna to environmental change, and could have allowed temperature-sensitive species to shift geographic location rather than face extinction. The relatively slow rate of CO_2 emission associated with Deccan Traps volcanism could be invoked to explain the lack of evidence for severe shoaling of the lysocline and CCD, therefore preventing mass extinctions of benthic carbonate communities as observed for benthic foraminifera during the PETM (e.g., Thomas, 1998; Thomas, 2003). The LMWE was preceded by a gradual warming of ~1–1.5°C over the preceding ~400 kyr, which could have allowed for appreciable morphological adaptation and migration (e.g., do Monte Guerra et al., 2016). The profound effect of the rate of environmental change on the magnitudes of extinctions during transient climate events can offer significant learnings for current anthropogenic climate change. Whilst the onset of the PETM was rapid in geological terms (10,000–20,000 years), current anthropogenic climate change is proceeding at rates which are orders of magnitude faster (hundreds of years), which may result in an impact on Earth's marine and terrestrial biota which is orders of magnitude more severe.

The LMWE was not the only longer-term volcanically-induced warming of the Maastrichtian, as it was preceded by ~+2–3°C warming of intermediate waters during the Early Late Maastrichtian warming event between ~69.5–68 Ma (~2–3 million years before the LMWE; Keller et al., 2016). Similar to the LMWE, the Early Late Maastrichtian event was also characterised by blooms of the opportunistic planktic foraminifera *Guembelitria cretacea* and has been attributed to either an early phase of the Deccan Traps or volcanism on the Indian Ocean Ninetyeast Ridge (Keller et al., 2016). Albeit of a smaller magnitude, longer duration and more poorly studied, this warming event is characterised by maximum evolutionary diversity in planktic foraminifera (e.g., Keller et al., 2016), ammonites (e.g., Witts et al., 2015), and is not associated with any major global extinctions (Keller et al., 2016). This lack of faunal response suggests that marine and terrestrial species of the Middle–Late Maastrichtian were apparently able to adapt to volcanically-induced climate change.

A second major problem with invoking the LMWE as a primer for the K/Pg mass extinction is that our data from ODP Site 1262 suggest that global climate had recovered to pre-excursion conditions before the time of the bolide impact at the K/Pg boundary. The warming event therefore appears to be somewhat decoupled from the K/Pg mass extinction, with transient morphological adaptations to profound environmental change, such as dwarfing of foraminifera, ceasing during the cooling over the final 100 kyr of the Maastrichtian (Figure 38b). The more prolonged step-wise recovery from the event over ~200 kyr could have allowed perturbed ecosystems the opportunity to at least partially, if not fully, recover before the bolide impact ~66 Ma. The fact that blooms of opportunistic foraminifera were restricted to ocean margin (continental shelf and slope) environments during the Maastrichtian and did not occur in the open ocean until K/Pg boundary time (Abramovich et al., 2010), further suggests that perturbations to the global environment during bolide impact were far more severe than during Deccan Traps volcanism.

Dating of precursor extinction events of marine benthic invertebrates in the high-latitude oceans (Tobin et al., 2012), of lacustrine ostracodes and charophytes in China (Zhang et al., 2018), and of floral species in North Dakota, USA (Wilf et al., 2003), places them within the cooling recovery phase after peak greenhouse conditions. Whilst the recovery of bottom water temperatures appears to have been rather step-wise and gradual in benthic records from the South Atlantic and equatorial Pacific, evidence exists for profound climatic cooling in the terrestrial realm during the terminal 100–200 kyr of the Maastrichtian (Wilf et al., 2003; Tobin et al., 2014; Zhang et al., 2018). Data from clumped isotopes (Δ_{47}) suggest that the subsequent cooling occurred much faster and was of a far greater magnitude than the prior warming, and therefore is more likely to have pushed terrestrial communities over a critical threshold leading to extinction (Tobin et al., 2014; Zhang et al., 2018). In addition to global climate change, additional environmental changes initiated by Deccan Traps volcanism such as the emission of toxic aerosols (sulphur and chlorine gas) and associated acid rain or ozone depletion, may also have contributed to destabilising ecosystems during this time, in particular for terrestrial floral and faunal communities (Self et al., 2008). Terrestrial communities in closest proximity to the Indian sub-continent should have been most affected by these Deccan-induced

environmental changes, although the spatial distribution and resolution of terrestrial floral and faunal data are currently insufficient to test this hypothesis (Figure 38a). Such environmental changes are likely to have also commenced with the onset of Deccan volcanism and therefore with the onset of global warming, therefore cannot solely explain the occurrence of precursor extinction events ~150 kyr after the initiation of volcanism.

Based on the evidence discussed here, it is challenging to invoke Deccan-induced global warming during the LMWE as a major contributor to the severity of the K/Pg mass extinction. The bolide impact should therefore still be considered as the primary driver of this mass extinction event. Environmental effects of the vaporisation of a vast shallow marine platform composed of carbonate- and sulphate-rich rocks on the present day Yucatan Peninsula, Mexico, include a rapid cooling, extended darkness following the input of vast quantities of aerosols into the atmosphere, and acid rain, during the so-called “impact winter” over the first few decades to centuries following impact (e.g., Vellekoop et al., 2016; Schulte et al., 2010; Stüben et al., 2002, 2003; Figure 39). Some of the highest resolution K/Pg boundary stratigraphic sections from Tunisia (southern Tethyan margin) suggest that an abrupt warming event and marine transgression immediately preceded bolide impact by a few 10’s of kyr (Stüben et al., 2002, 2003). These records, therefore, record a period of major environmental instability leading up to K/Pg boundary time (Figure 39). Such environmental changes proceeded at rates that were orders of magnitude faster than those inferred for the Deccan eruptions. Their effects on terrestrial and marine ecosystems were therefore likely to have been orders of magnitude more severe. If Deccan-induced environmental change did play an ancillary role in the K/Pg mass extinction, it appears that rapid cooling over the final ~200 kyr of the Maastrichtian and acid rain or toxic effusive gases were the more likely candidates for priming biota for extinction during bolide impact, as opposed to greenhouse warming.

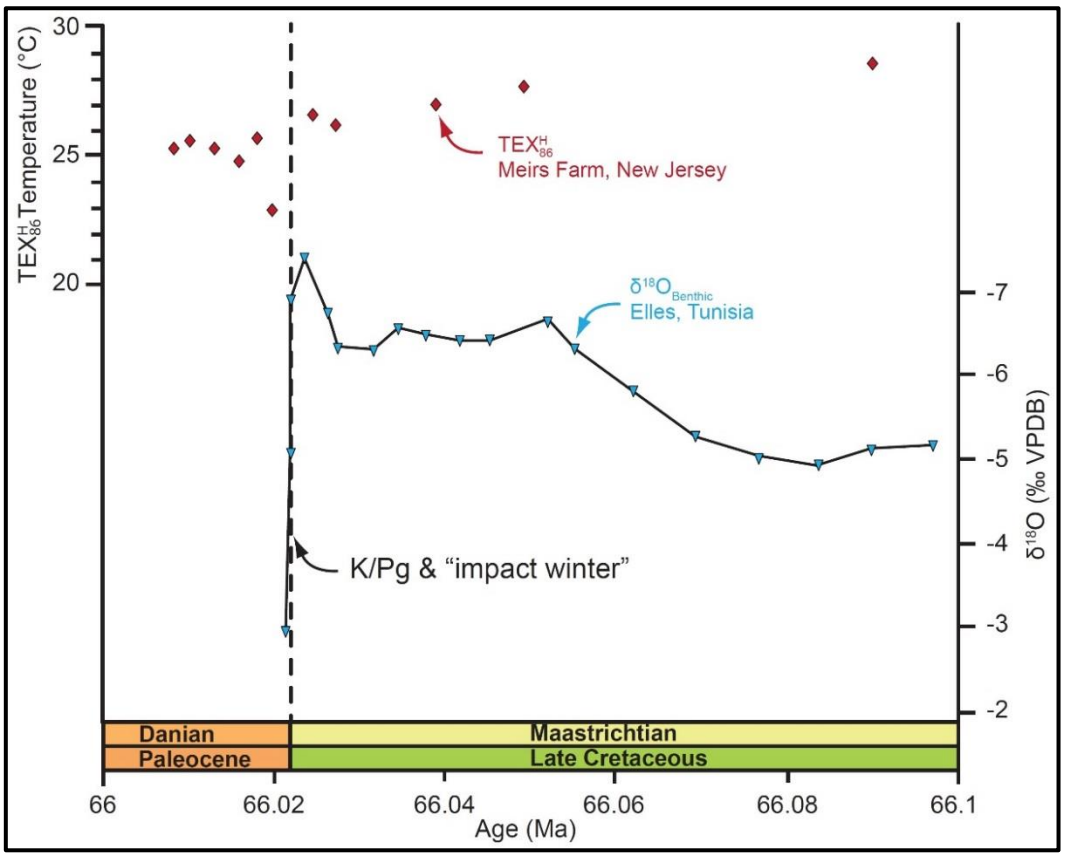

Figure 39. Abrupt climatic changes across the K/Pg boundary, based on TEX^H_{86} data from New Jersey (Vellekoop et al., 2016) and $\delta^{18}O_{benthic}$ data from Elles, Tunisia (Stüben et al., 2003). Pre-boundary warming is illustrated by $\delta^{18}O_{benthic}$, followed by an abrupt cooling at the boundary associated with the "impact winter". Note that due to diagenesis, $\delta^{18}O_{benthic}$ data from Elles cannot be converted into reliable temperature estimates. The magnitude of temperature change cannot therefore be quantified. However, the trends are considered reliable since the magnitude of diagenesis does not vary significantly across the record.

4.7. CONCLUSIONS

In this chapter, I have presented new Late Maastrichtian $\delta^{13}C_{benthic}$ and $\delta^{18}O_{benthic}$ data generated from South Atlantic ODP Site 1262 calibrated to an updated orbitally-tuned age model. I have used these new data to generate an orbital-resolution chronology of the Late Maastrichtian warming event (~66.34–66.03 Ma), enabling the most definitive correlation to date with the onset of Deccan Traps volcanism on the Indian sub-continent. The main conclusions of this chapter are as follows:

- The inception of the LMWE coincides, within analytical uncertainty, with the onset of the main phase of Deccan Traps LIP volcanism, strongly suggesting a causal link.

- The primary role of Deccan Traps volcanism is further supported by the muted carbon isotope excursion recorded in marine carbonates despite evidence for rising atmospheric pCO_2, suggesting that volcanogenic CO_2 (with a $\delta^{13}C$ signature of ~–6‰) was the primary driver of greenhouse warming over 100-kyr timescales.

- A strong role of orbital forcing on the inception of the event is unlikely, since the onset of warming occurs during a minimum in the 405-kyr eccentricity cycle, although amplified carbon cycle sensitivity to precession, resulting from periodic increases in marine export productivity, is evident during greenhouse warming.

- Despite evidence for shifting marine planktic communities during the LMWE, the lack of evidence for global extinction events and comparatively muted biotic response, compared to the PETM, are likely to be associated with a slower rate of warming over a longer timeframe during the LMWE compared to the PETM.

- The lack of evidence for global extinctions within marine and terrestrial biota suggests that bolide impact was the primary driver of the K/Pg mass extinction, although Deccan-induced environmental change may have played an ancillary role in making certain environmentally-sensitive ecosystems more susceptible to extinction.

5. CAN THE DAN-C2 EVENT BE CLASSIFIED AS A GLOBAL "HYPERTHERMAL" EVENT?

5.1. ABSTRACT

This chapter examines in further detail the early Danian (earliest Paleocene) portion of the new $\delta^{13}C_{benthic}$ and $\delta^{18}O_{benthic}$ records generated from South Atlantic ODP Site 1262. This new record is used here to develop an orbital-resolution chronology of the so-called "Dan-C2" event (~65.9–65.7 Ma) and to identify the presence and magnitude of any transient deep-water temperature response in bottom waters of the South Atlantic. This new stable isotope record is integrated with a new high-resolution study of benthic foraminiferal assemblages from our study site and additional published contemporaneous proxy-datasets migrated onto the new ODP Site 1262 age model, to evaluate the nature and magnitude of global environmental change during Dan-C2. Despite sharing some of the characteristics of other early Paleogene hyperthermals, the lack of a transient deep-sea temperature response in both the Atlantic and Pacific suggests that the Dan-C2 event is not a typical hyperthermal. The event is instead interpreted to reflect the magnified expression of the first 405-kyr eccentricity maximum of the Paleocene within shallow marine and terrestrial records, due to partial collapse of the biological pump following the K/Pg mass extinction, extreme vital effects within opportunistic planktic foraminifera taxa which evolved in the immediate aftermath of the mass extinction, and elevated background atmospheric CO_2 levels from ongoing Deccan Traps volcanism. Future work should focus on constraining the geographic variability and magnitude of climatic warming in the terrestrial realm and surface waters, to more fully evaluate the scale of global environmental change that occurred during Dan-C2.

5.2. INTRODUCTION

The Danian–Late Cretaceous (Dan-C2) event was first described in detail from studies of the NW Atlantic ODP Site 1049 on Blake Nose, where it is characterised by two ~100 kyr-paced negative excursions in bulk carbonate $\delta^{13}C$ and $\delta^{18}O$ ($\delta^{13}C_{bulk}$ and $\delta^{18}O_{bulk}$) and planktic $\delta^{13}C$ and $\delta^{18}O$ ($\delta^{13}C_{planktic}$ and $\delta^{18}O_{planktic}$) (Quillévéré et al., 2008). The Dan-C2 event was described from ~300–

350 kyr after the K/Pg boundary at ODP Site 1049, therefore its name is somewhat erroneous as it occurred entirely during the early Danian (Quillévéré et al., 2008). The global nature of these twinned negative carbon isotope excursions (CIEs) is confirmed by $\delta^{13}C_{bulk}$ records (representing predominantly a surface signal) from widely distributed marine sections, including the South Atlantic ODP Site 1262 (Kroon et al., 2007) and DSDP Sites 527 and 528 (Quillévéré et al., 2008), the northern Tethyan margin (Gubbio, Italy; Coccioni et al., 2010, 2012; Galeotti et al., 2015), and the southern Tethyan margin (Egypt; Punekar et al., 2014b). The event is also expressed in a $\delta^{13}C_{bulk}$ record from lacustrine sediments deposited in the Boltysh meteorite crater, Ukraine (Gilmour et al., 2013). The magnitude and character of the Dan-C2 CIEs are, however, very different between marine carbonate and terrestrial sediment archives, raising questions about the origin of this event (e.g., Gilmour et al., 2013; Quillévéré et al., 2008). Whilst the Dan-C2 event is characterised by two 100-kyr paced carbon isotope excursions in marine carbonates, the event is characterised by a single carbon isotope excursion with pronounced onset, main body and recovery phases, as well as of a significantly greater magnitude, in terrestrial sediments.

The Dan-C2 event shares a number of similarities with many of the other double-spiked hyperthermals of the early Paleogene. These similarities include pacing by orbital eccentricity (e.g., Quillévéré et al., 2008), pronounced negative CIEs in both marine carbonate and terrestrial sediment archives (Quillévéré et al., 2008; Gilmour et al., 2013), apparent warming of both ocean surface waters and the terrestrial environment (Quillévéré et al., 2008; Gilmour et al., 2013; Jolley et al., 2015; Zhang et al., 2018), and evidence for deep-sea carbonate dissolution in the South Atlantic (Walvis Ridge; e.g., Westerhold et al., 2008).

Despite these similarities there are also, however, a number of complications with interpretation of the Dan-C2 event as a typical hyperthermal. Most importantly, and partly owing to geographically limited $\delta^{18}O_{benthic}$ datasets from the NW Atlantic (Quillévéré et al., 2008) and equatorial Pacific (Westerhold et al., 2011), no evidence currently exists for transient warming in the deep-sea during this event. In addition, whilst significant peaks in Fe intensity, magnetic susceptibility, and terrigenous mineral content in deep-sea sediments deposited

during Dan-C2 have been attributed to dissolution of marine carbonates (Westerhold et al., 2008; Quillévéré et al., 2008), low resolution benthic foraminiferal assemblage studies have concluded that no appreciable changes in endobenthic communities occurred during this time (Alegret & Thomas, 2005, 2007; Alegret et al., 2012). This lack of change in benthic carbonate communities raises the question as to whether significant carbonate dissolution did occur during the Dan-C2 event.

With the exception of two single-species stable isotope records from the NW Atlantic ODP Site 1049 and the equatorial Pacific ODP Site 1209, the Dan-C2 event has mainly been recognised in the marine realm from bulk carbonate records. Yet bulk oxygen isotope ($\delta^{18}O_{bulk}$) data, in particular, are prone to bias due to the inclusion of diagenetic carbonate, inter-species fractionation effects, and evaporation/precipitation effects, which often amplify or dampen, and sometimes completely mask, temperature signals in such records. Published benthic stable isotope data from the NW Atlantic ODP Site 1049 preserve evidence of temperature variations at intermediate water depths during Dan-C2 (at a palaeo-depth of ~1000–2000 m), but may not be fully representative of bottom water masses in the global ocean. These data have also not been calibrated to an orbitally-tuned age model, hampering a definitive correlation to Paleogene orbital solutions, and therefore, our understanding of the origin of the event and any similarilities to other climate and carbon cycle perturbations of the early Paleogene. A benthic stable isotope dataset from the deeper equatorial Pacific ODP Site 1209 (from a palaeo-depth of ~2000–2500 m) has been placed on an orbitally-tuned age model, however, this site is characterised by a prominent earliest Danian condensed interval encompassing the onset and much of the main body of the Dan-C2 event (see **Chapter 3** Figure 13). Therefore, neither of these existing records can be used to generate a stratigraphically complete orbital-resolution chronology of the Dan-C2 event, nor can they fully constrain the response of the deep ocean during this time.

The early Danian stratigraphy at ODP Site 1262 consists of a complete section of reddish-brown nannofossil-foraminifera-bearing clays deposited at a mean sedimentation rate of ~0.25–0.5 cm/kyr (Shipboard Scientific Party, 2004a; Figure 12g), which was likely deposited at a palaeo-depth of ~3000 m. ODP Site

1262, therefore, represents an excellent opportunity to develop a high-resolution chronology for the Dan-C2 event, and to evaluate the evolution of deep-sea temperature and changes in the deep-sea benthic community during the first hypothesised hyperthermal event of the Paleogene Period at much higher resolution than previous studies.

5.2.1. RECOGNITION OF THE DAN-C2 EVENT IN PUBLISHED RECORDS FROM ODP SITE 1262

The published $\delta^{13}C_{bulk}$ and $\delta^{18}O_{bulk}$ records from ODP Site 1262 (Kroon et al., 2007), calibrated to the updated orbitally-tuned age model correlated to the La2010b orbital solution of Laskar et al. (2011a) presented herein (**Chapter 3**), are shown in Figure 40. The K/Pg boundary is characterised by a rapid, geologically instantaneous drop of ~–1.1‰ in $\delta^{13}C_{bulk}$, followed by a longer term step-wise decline of ~–0.8‰ to the onset of the Dan-C2 event at ~65.87 Ma.

The Dan-C2 event is manifested as prominent double-spiked excursions in $\delta^{13}C_{bulk}$ at ODP Site 1262, separated by a partial recovery phase. The first (oldest) excursion, termed “DC1” herein, occurred ~65.83 Ma and is characterised by a negative excursion of ~–0.8‰ in $\delta^{13}C_{bulk}$. The second (younger) excursion, termed “DC2” in this thesis, is characterised by a smaller decrease of ~–0.4‰ in $\delta^{13}C_{bulk}$ at ~65.71 Ma. These excursions are separated by a partial recovery phase of ~+0.4‰ and spaced ~100 kyr apart in our age model, suggesting a pacing by the short (100 kyr) eccentricity cycle.

The $\delta^{18}O_{bulk}$ record exhibits a noisy negative excursion commencing before the supposed event, with a transient positive excursion suggestive of surface ocean cooling correlating with the larger “DC1” event in the carbon isotope record. The ODP Site 1262 $\delta^{18}O_{bulk}$ record therefore confirms the difficulties of using bulk carbonate data as a proxy for characterising surface ocean temperature change during Dan-C2, emphasising the need for single-species benthic records from this site to better evaluate the magnitude of deep-ocean (global) warming during this event.

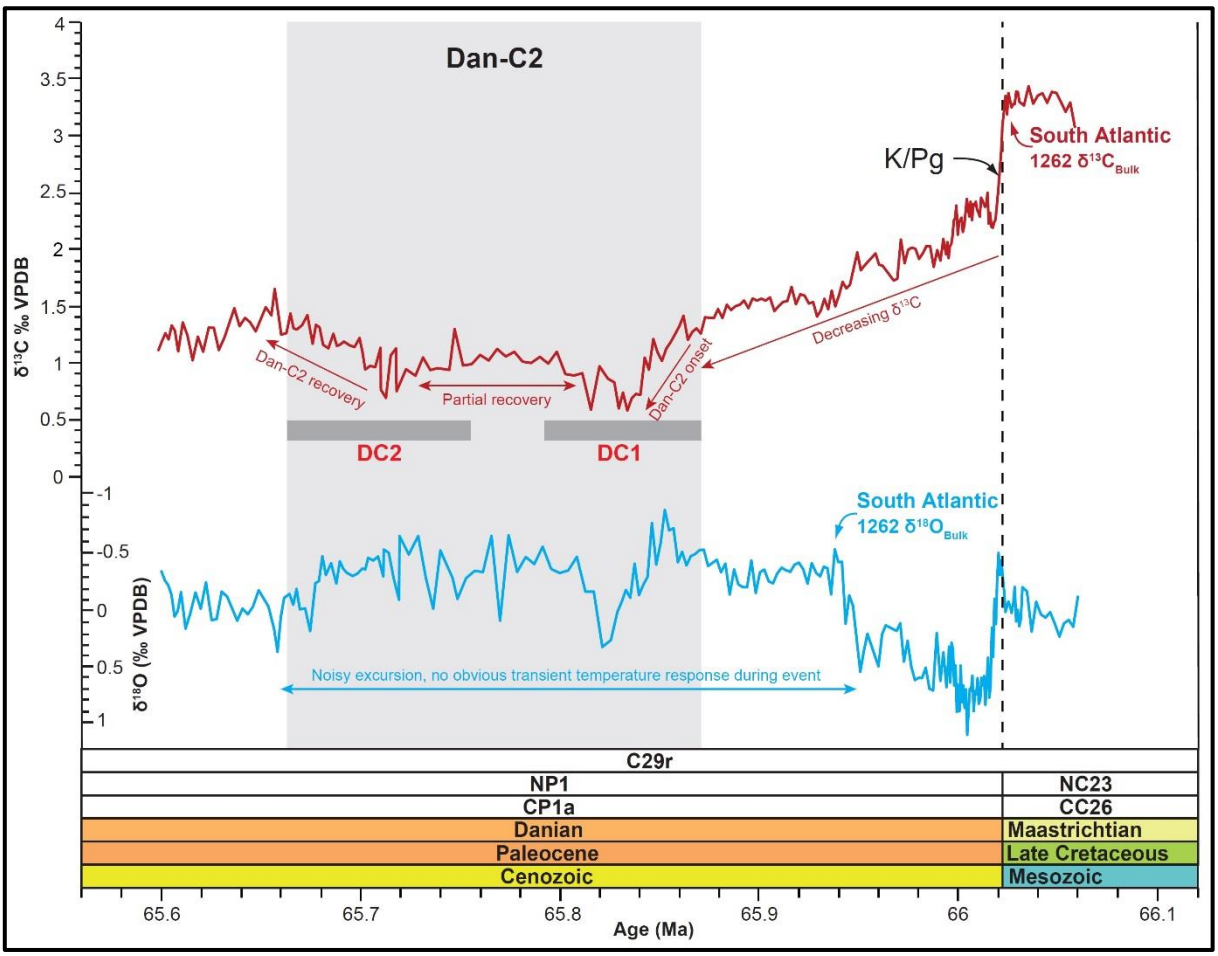

Figure 40. Cretaceous/Paleogene (K/Pg) boundary to early Danian palaeoceanographic data, illustrating the nature of the Dan-C2 event in the bulk carbonate stable isotope records ($\delta^{13}C_{bulk}$ and $\delta^{18}O_{bulk}$; Kroon et al., 2007) from South Atlantic Walvis Ridge ODP Site 1262. Magnetozones are from Bowles (2006). Nannoplankton zones are from Shipboard Scientific Party (2004a).

5.3. AIMS AND OBJECTIVES

The overaching goal of this chapter is to identify the presence and magnitude of any transient deep-water temperature response in bottom waters of the South Atlantic during Dan-C2 (~65.9–65.7 Ma), and to evaluate the nature and magnitude of global environmental change during the event. Specific questions to be addressed are:

- Can the Dan-C2 event be classified as a “typical” hyperthermal event with a pronounced temperature response in the deep-sea?

- What was the nature and magnitude of environmental change within the terrestrial and shallow marine realms during Dan-C2, and are these changes global in scale?

- Was there a global pertubation to the carbon cycle during Dan-C2 associated with the massive injection of greenhouse gases into the exogenic carbon cycle?

- Is the timing, onset, duration and character of the event paced by orbital forcing, or was there an important role for non-orbital forcing mechanisms (i.e., Deccan Traps LIP volcanism)?

These questions will be addressed by the development of an orbital-resolution chronology of the Dan-C2 event based on the early Danian (Early Paleocene) portion of the new ODP Site 1262 $\delta^{13}C_{benthic}$ and $\delta^{18}O_{benthic}$ records, calibrated to an updated orbitally-tuned age model. This new chronology will be integrated with a new high-resolution study of benthic foraminiferal assemblages from ODP Site 1262 (Arreguín-Rodríguez, pers. comm.), and additional published contemporaneous palaeoclimate proxy-datasets migrated onto the new ODP Site 1262 age model.

5.4. METHODS

5.4.1. DATA SOURCES AND PROCESSING

Lithostratigraphy, sample strategy, and all sedimentological and geochemical method information for samples from ODP Site 1262 are presented in **Chapter 2 Sections 2.1–2.4**. Methods employed for spectral analysis of the ODP Site 1262 benthic stable isotope datasets are described in detail in **Chapter 3 Section 3.4.6** and for recalibration of atmospheric pCO_2 estimates based on the pedogenic carbonate proxy in **Chapter 3 Section 3.4.7**. The locations of ODP Site 1262 and other sites discussed in this chapter are illustrated in Figure 41. Further details about these sites, along with the types of data and literature sources used, are listed in Table 8.

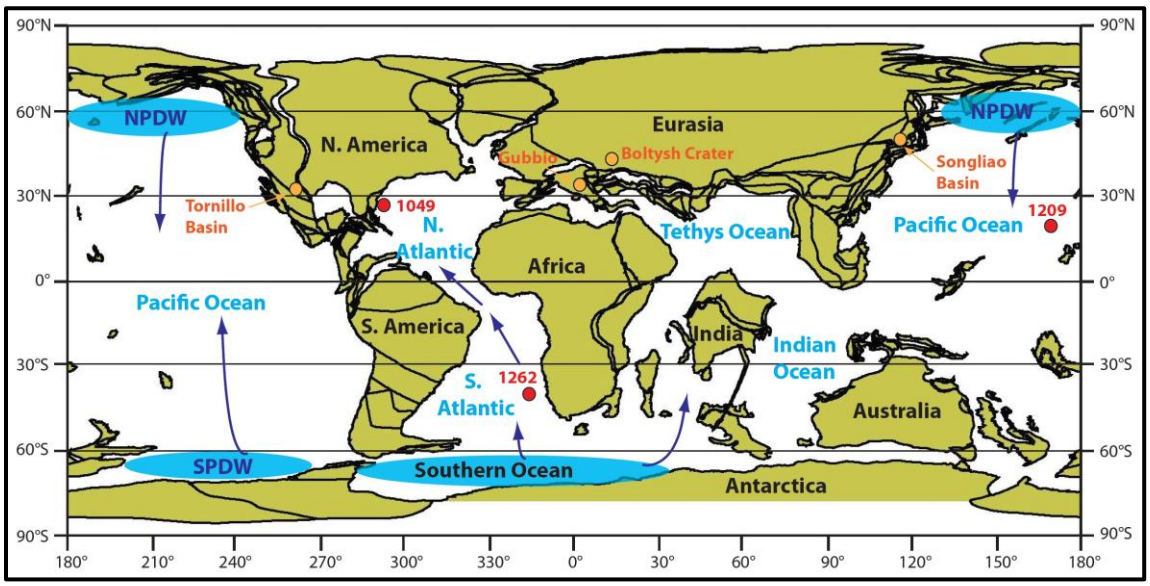

Figure 41. Cretaceous/Paleogene (K/Pg) boundary time (~66 Ma) palaeogeographic reconstruction with locations of the deep-sea sites (in red) and onshore sites (in orange) used in this chapter (also see Table 8). Locations of the principle areas of deep water formation are indicated by blue shading with the following abbreviations: NPDW = North Pacific Deep Water. SPDW = South Pacific Deep Water (Thomas et al., 2003, 2008). The predicted movement of deep water masses is indicated by dark blue arrows. Adapted from the Ocean Drilling Stratigraphic Network (ODSN) Paleomap Project (http://www.odsn.de/odsn/services/paleomap/paleomap.html).

Table 8

Site	Current Lat.	Current Long.	Palaeo-lat.	Current water depth (m)	Palaeo-water depth at K/Pg (m)	Data type	Source of data
ODP Site 1262	27.2°S	1.6°E	40.3°S	4759	~3000	$\delta^{13}C_{bulk}$ $\delta^{18}O_{bulk}$ $\delta^{13}C_{benthic}$ $\delta^{18}O_{benthic}$ % CF Benthic assemblages Fe intensity	Kroon et al. (2007) Kroon et al. (2007) This study This study This study Arreguín Rodríguez (pers. comm.) Westerhold et al. (2008)
ODP Site 1209	32.7°N	158.5°E	22.8°N	2387	~2000–2500	$\delta^{13}C_{benthic}$ $\delta^{18}O_{benthic}$	Westerhold et al. (2011) Westerhold et al. (2011)
ODP Site 1049	30.1°N	76.1°W	27.8°N	2671	~1000–2000	$\delta^{13}C_{bulk}$ $\delta^{13}C_{planktic}$ $\delta^{13}C_{benthic}$ $\delta^{18}O_{bulk}$ $\delta^{18}O_{planktic}$ $\delta^{18}O_{benthic}$	Quillévéré et al. (2008) Quillévéré et al. (2008) Quillévéré et al. (2008) Quillévéré et al. (2008) Quillévéré et al. (2008) Quillévéré et al. (2008)
Gubbio, Italy	43.4°N	13.6°E	35.0°N	Subaerial	~1500–2500	$\delta^{13}C_{bulk}$	Coccioni et al. (2010)
Tornillo Basin, Texas	29.3°N	103.5°W	32°N	Subaerial	Terrestrial	Pedogenic carbonate pCO_2	Nordt et al. (2003)
Boltysh Crater, Ukraine	48.1°N	34.2°E	49°N	Subaerial	Terrestrial (lacustrine)	$\delta^{13}C_{org}$	Gilmour et al. (2013)
Songliao Basin, China	44.2°N	124.3°E	51°N	Subaerial	Terrestrial	Clumped isotopes (Δ_{47})	Zhang et al. (2018)

Details of sites with data included in this study. Present-day latitudes, longitudes, water depths and palaeo-water depths are from the initial scientific reports for each deep-sea site (Shipboard Scientific Party, 2004a, 2002a, 1998). Longitude and latitude for Gubbio, Tornillo Basin, Boltysh Crater and Songliao Basin are from the data reference cited. The palaeo-water depth for Gubbio is from Kuhnt (1990). Palaeo-latitudes for each site at Cretaceous/Paleogene (K/Pg) boundary time (~66 Ma) were computed relative to the palaeomagnetic reference frame of Torsvik et al. (2012), using Version 2.1 of the model from paleolatitude.org (van Hinsbergen et al., 2015). Types of data incorporated from each site, along with data sources, are listed in the two right-hand columns.

5.4.2. INTEGRATION OF OTHER PUBLISHED PALAEOCLIMATE PROXY DATA

All other published data presented in this chapter have been calibrated in the time domain to our orbitally-tuned age model developed from ODP Site 1262 (**Chapter 3**). All published datasets were firstly aligned with the preferred astronomical age of 66.0225 Ma for the K/Pg boundary (Dinarès-Turell et al.,

2014). Mean sedimentation rates for the early Danian from each deep-sea site (Table 9) were then used to estimate ages relative to the K/Pg boundary for the available published data.

For the Boltysh Crater lacustrine sequence, Gilmour et al. (2013) identified a concentration of spectral power at 30 m periodicity within their $\delta^{13}C_{org}$ data and interpreted these cycles to represent variability in the carbon cycle with either 21-kyr precession or 41-kyr obliquity pacing. The cyclicity they identified is interpreted here to represent 41-kyr obliquity, creating an age and duration for the terrestrial isotopic excursion that is consistent with the total duration of the double-spiked Dan-C2 event in our orbitally-tuned isotope data from the South Atlantic. Datasets for which mean sedimentation rate information was not available were aligned to the astronomical K/Pg boundary age of 66.0225 Ma with the age model presented in the original literature source employed.

Table 9

Site	Early Danian sedimentation rate (cm/kyr)	Literature source
ODP Site 1262	~0.25–0.5	This study (orbitally-tuned age model)
ODP Site 1209	~0.6	Westerhold et al. (2011)
ODP Site 1049	~2	Quillévéré et al. (2008)
Boltysh Crater	~73	Gilmour et al. (2013)

Mean Early Danian sedimentation rates used to recalibrate the age models for the sites used in this study.

5.5. DATA ATTRIBUTION

I collected the samples used in this study from the Bremen Core Repository with the help of Prof. Dick Kroon (University of Edinburgh), and we were both responsible for their disaggregation and sieving. I generated the % coarse fraction data across the Dan-C2 event (included in **Appendix 8**), picked all of the benthic foraminifera from these samples and prepared them for stable isotope analysis, converted the resultant stable isotope data to temperature estimates, performed the spectral analysis, and compiled/recalibrated all previously published data from the literature. The new benthic stable isotope data were funded and generated by the NERC Isotope Geosciences Facility (grant

number IP-1581-1115), under the supervision of Prof. Melanie Leng, and are included as part of **Appendix 4**. The updated orbitally-tuned age model for ODP Site 1262 was generated by Dr. Thomas Westerhold (MARUM, Bremen) from samples which I prepared and analysed. The benthic foraminiferal assemblage data used in this study were generated by Dr. Gabriela de Jesús Arreguín Rodríguez (University of Zaragoza) based on samples washed and prepared by myself, forming part of Dr. Arreguín Rodríguez's thesis and provided by personal communication for inclusion in this chapter. The benthic foraminiferal assemblage data and benthic stable isotope data presented in this chapter form the basis for a manuscript currently in preparation, with Dr. Arreguín Rodríguez as first author and myself as second author.

5.6. RESULTS AND DISCUSSION

5.6.1. PRESERVATION OF BENTHIC FORAMINIFERA ACROSS THE DAN-C2 EVENT AT ODP SITE 1262

To assess the preservation of *Nuttallides truempyi* during the peak of the Dan-C2 event, a whole specimen and test wall on a crushed specimen were imaged from a stratigraphic horizon corresponding to the peak of the DC2 isotope excursion using a Field Emission Gun Scanning Electron Microscope (FEG-SEM; Figure 42). Preservation of benthic foraminifera from the peak of the event is generally good for benthic foraminifera of this age, although the sample does exhibit some incipient recrystallisation of test surfaces, pores and primary wall structures. Since the amount of recrystallisation at this stratigraphic horizon is not significantly greater than during the preceding Late Maastrichtian or subsequent late Danian (Figure 9), it can be concluded that the benthic stable isotope data across the Dan-C2 event have not been selectively biased by diagenesis.

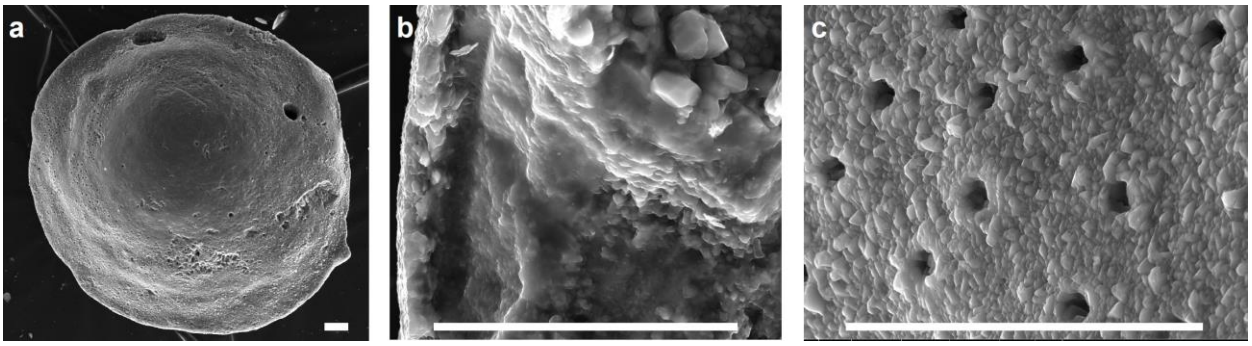

*Figure 42. Scanning Electron Microscope (SEM) images of Nuttallides truempyi specimens from the peak of the DC2 event (215.19 mcd; ~65.72 Ma) at ODP Site 1262, illustrating whole specimen spiral side (**a**); cross section of test wall (**b**); and pore structure (**c**). The white scale bar on each image represents 20 µm.*

5.6.2. CARBON ISOTOPE AND DEEP-WATER TEMPERATURE RESPONSE AT SOUTH ATLANTIC ODP SITE 1262

The new $\delta^{13}C_{benthic}$ and $\delta^{18}O_{benthic}$ records from ODP Site 1262 spanning ~66.06–65.60 Ma are plotted in Figure 43 alongside the corresponding bulk carbonate records on an updated orbitally-tuned age model correlated to the La2010b orbital solution of Laskar et al. (2011a). Whilst there is evidence for a long-term rise in bottom water temperature of ~+1.5–2.0°C ($\delta^{18}O_{benthic}$ decrease of ~–0.45‰) over the 280 kyr following the K/Pg boundary, there is no evidence for any transient orbitally-paced warming in deep waters of the South Atlantic during Dan-C2. Similarly, the excursions in $\delta^{13}C_{benthic}$ are also muted compared to $\delta^{13}C_{bulk}$, with a broad negative excursion of ~–0.5‰ encompassing the DC1 and DC2 excursions, but lacking a clearly resolvable partial recovery phase between them. A significant discrepancy between the magnitude and nature of the excursions in $\delta^{13}C_{benthic}$ and $\delta^{13}C_{bulk}$ at the K/Pg boundary results in a collapse of the bulk–benthic carbon isotope ($\Delta^{13}C$) gradient at the boundary, followed by a reversal of the normal bulk–benthic carbon isotope ($\Delta^{13}C$) gradient during the early Danian, reaching greatest magnitude during the peaks of DC1 (–0.9‰) and DC2 (–0.8‰).

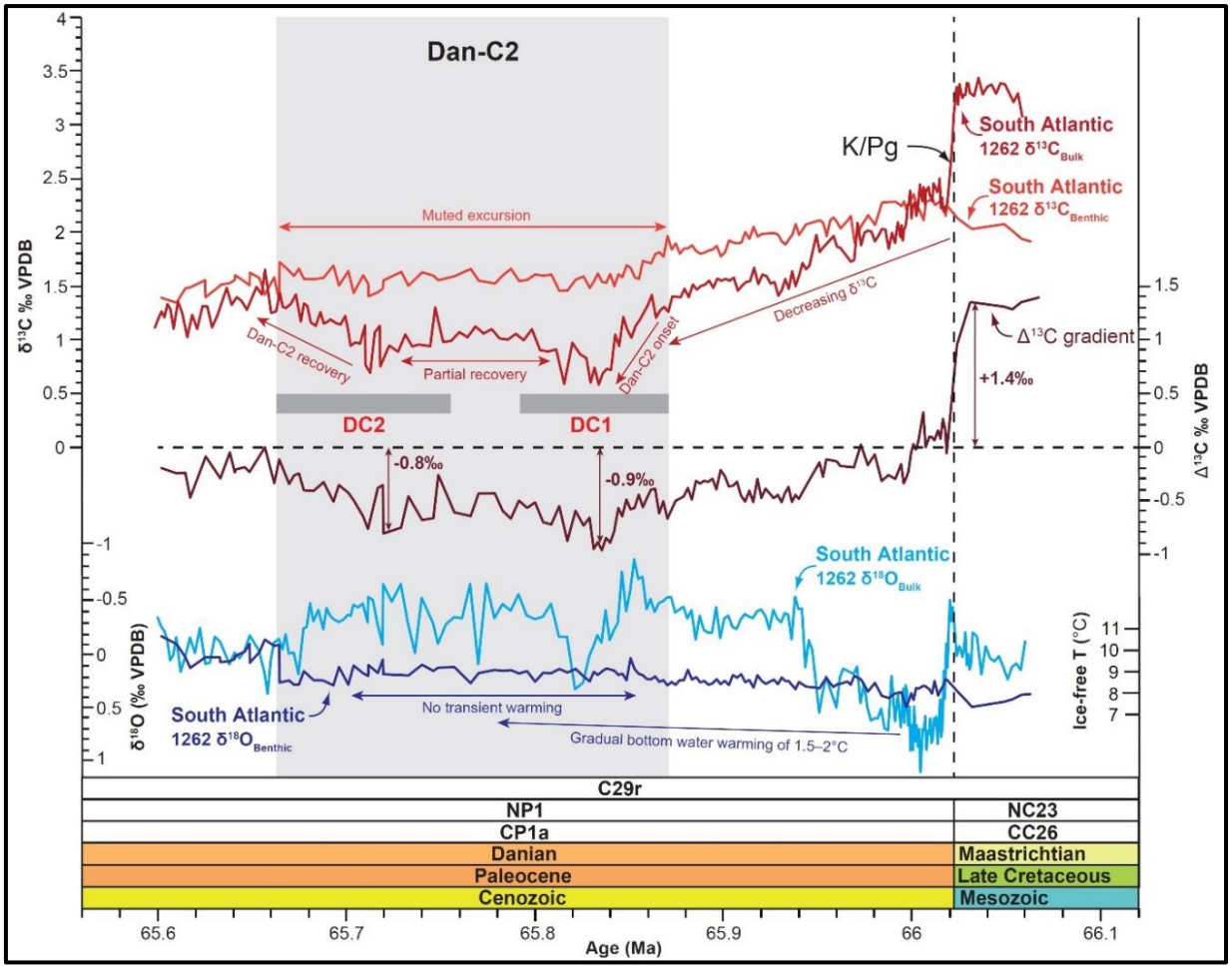

Figure 43. Cretaceous/Paleogene (K/Pg) boundary to early Danian palaeoceanographic data, illustrating the nature of the Dan-C2 event in the stratigraphy of South Atlantic ODP Site 1262. Shown are benthic stable isotope data ($\delta^{13}C_{benthic}$ and $\delta^{18}O_{benthic}$; this study), bulk carbonate stable isotope data ($\delta^{13}C_{bulk}$ and $\delta^{18}O_{bulk}$; Kroon et al., 2007), and the $\delta^{13}C_{bulk}$-$\delta^{13}C_{benthic}$ ($\Delta^{13}C$) gradient. Magnetozones are from Bowles (2006). Nannoplankton zones are from Shipboard Scientific Party (2004a).

5.6.3. COMPARISON BETWEEN NEW BENTHIC STABLE ISOTOPE DATA FROM ODP SITE 1262 AND PUBLISHED BENTHIC STABLE ISOTOPE RECORDS

A comparison of the new ODP Site 1262 benthic stable isotope data to other published (lower resolution and less resolved) benthic records from the NW Atlantic ODP Site 1049 and the equatorial Pacific ODP Site 1209 confirms the lack of a deep water temperature response in global ocean bottom waters during Dan-C2 (Figure 44). Bottom water temperatures from the South Atlantic (~9°C) and the equatorial Pacific (~8.5°C) are comparable during the event. The warmer

temperatures at this time inferred for the NW Atlantic from ODP Site 1049 $\delta^{18}O_{benthic}$ data (by ~+1.5˚C) likely reflect its shallower palaeo-water depth of ~1000–2000 m, compared to the equatorial Pacific (~2500 m) and the South Atlantic (~3000 m) sites (Figure 44). All three sites exhibit a comparable trend of gradual long-term warming through the event by ~+1.5–2°C from K/Pg boundary time to the peak of DC2, but do not record any transient warming associated with the onset of Dan-C2 itself.

In contrast to the ODP Site 1262 $\delta^{13}C_{bulk}$ record, no pronounced negative excursion is recorded in $\delta^{13}C_{benthic}$ data from either the deep South Atlantic or the equatorial Pacific across Dan-C2 (Figure 44). The $\delta^{13}C_{benthic}$ data from the shallower NW Atlantic ODP Site 1049 is, however, characterised by a double-spiked negative excursion of ~–0.9‰ in $\delta^{13}C_{benthic}$ during DC1, and then a negative excursion of ~–0.8‰ during DC2. The shallower palaeo-depth of the NW Atlantic ODP Site 1049 (~1000–2000 m) suggests that $\delta^{13}C_{benthic}$ data from this site record the carbon isotope signature of an intermediate depth water mass. This finding raises the possibility that this intermediate water mass of the NW Atlantic represents a younger water mass sourced from a more proximal location than the deep waters of the Atlantic and Pacific, perhaps from the North Atlantic, however there is currently no other data to test this hypothesis. Therefore, only data from the deeper ODP Sites 1262 and 1209, with their muted $\delta^{13}C_{benthic}$ response, may truly reflect carbon isotopic variations in the bottom water masses of the global ocean at this time.

5.6.4. COMPARISON BETWEEN PUBLISHED PLANKTIC AND BULK CARBONATE STABLE ISOTOPE RECORDS

Although the deep Atlantic does not appear to warm appreciably during Dan-C2, the response in surface waters of the South Atlantic (ODP Site 1262) and the NW Atlantic (ODP Site 1049) appears to be more pronounced (Figure 45). At ODP Site 1049, the Dan-C2 event is manifested as a double-spiked excursion in both $\delta^{18}O_{bulk}$ and $\delta^{18}O_{planktic}$. The older DC1 excursion is characterised by a negative excursion of ~–1.5‰ in $\delta^{18}O_{bulk}$ and a smaller ~–0.9‰ excursion in $\delta^{18}O_{planktic,}$ followed by slightly smaller negative excursions of ~–1.25‰ and ~–0.9‰ in $\delta^{18}O_{bulk}$ and $\delta^{18}O_{planktic}$, respectively, during DC2. Whilst

the excursions in $\delta^{18}O_{bulk}$ cannot reliably be converted into estimates for the magnitude of temperature change, the excursions in $\delta^{18}O_{planktic}$ may be suggestive of two pulses of surface water warming of up to ~+4°C during DC1 and DC2 in the NW Atlantic (Quillévéré et al., 2008). However, excursions in $\delta^{18}O_{planktic}$ can be a function of temperature and/or significant variations in $\delta^{18}O$ of the surface ocean water ($\delta^{18}O_{sw}$), which is primarily controlled by salinity. In the absence of significant volumes of continental ice during this time, two pulses of amplified freshwater runoff (with a negative $\delta^{18}O$ signature) from the adjacent North American landmass could alternatively explain at least a portion of the excursions in $\delta^{18}O_{planktic}$ during Dan-C2. It is therefore challenging to accurately quantify the magnitude of surface water warming during Dan-C2 from a single ocean margin $\delta^{18}O_{planktic}$ dataset, without another independent temperature proxy.

A double-spiked negative excursion is also recognised in $\delta^{13}C_{bulk}$ and $\delta^{13}C_{planktic}$ records from the NW Atlantic ODP Site 1049, as well as within $\delta^{13}C_{bulk}$ records from the northern Tethyan margin and South Atlantic (Figure 45). The largest changes in these records occur during the DC1 excursion, varying in magnitude from ~–1.3 ‰ in $\delta^{13}C_{bulk}$ from the NW Atlantic, to ~–0.8 ‰ in $\delta^{13}C_{planktic}$ data from the NW Atlantic, $\delta^{13}C_{bulk}$ data from the Tethys, and $\delta^{13}C_{bulk}$ from the South Atlantic. The excursion associated with DC2 in these records is typically slightly smaller, ranging between a maximum of ~–1.2 ‰ in $\delta^{13}C_{bulk}$ from the NW Atlantic, ~–0.8 ‰ in $\delta^{13}C_{planktic}$ data from the NW Atlantic and $\delta^{13}C_{bulk}$ data from the Tethys, and ~–0.4 ‰ in $\delta^{13}C_{bulk}$ from the South Atlantic. Large negative excursions in $\delta^{13}C_{bulk}$ and $\delta^{18}O_{bulk}$ have also been identified from Israel, situated along the southern Tethyan margin (Punekar et al., 2014b). The Israeli excursions lack the characteristic double-spiked nature of many other marine records, but this may be an artefact of low sample resolution, stratigraphic hiatuses, or condensation. Therefore, whilst the Dan-C2 event is characterised by a muted excursion in $\delta^{13}C_{benthic}$ from the South Atlantic ODP Site 1262, pronounced excursions in $\delta^{13}C_{planktic}$ are suggestive of an orbitally-paced carbon cycle perturbation within ocean surface waters.

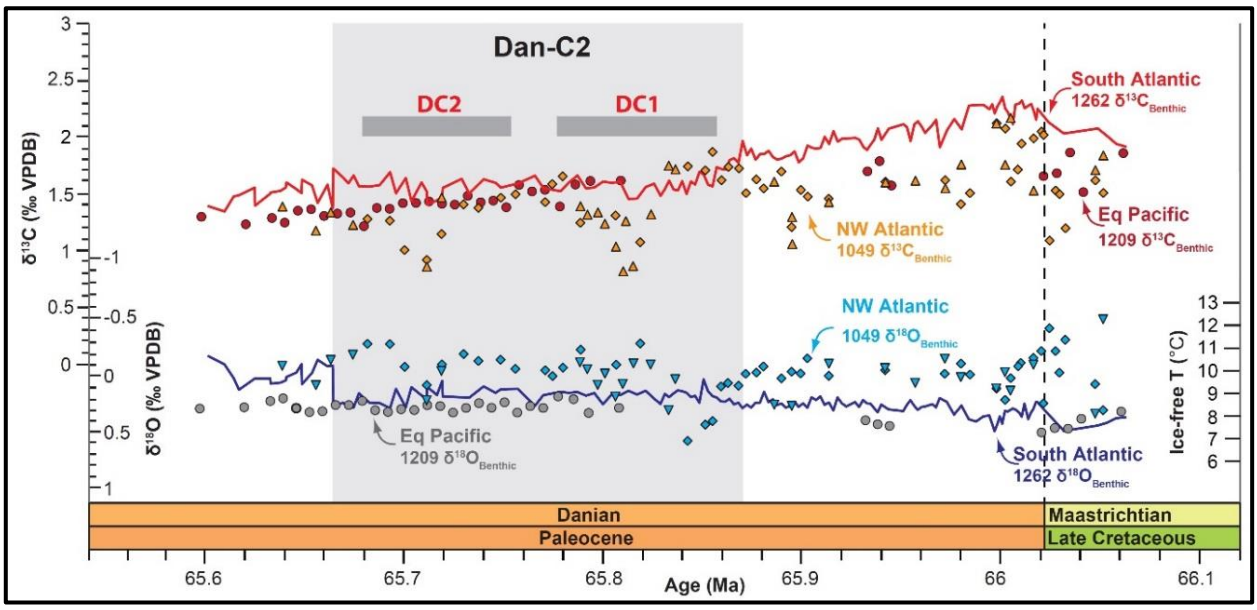

Figure 44. Comparison of the new benthic stable isotope data from South Atlantic ODP Site 1262 (palaeo-depth ~3000 m; this study), with lower resolution benthic data from equatorial Pacific ODP Site 1209 (palaeo-depth ~2000–2500 m; Westerhold et al., 2011) and NW Atlantic Blake Nose ODP Site 1049 (palaeo-depth ~1000–2000 m; Quillévéré et al., 2008). The ODP Site 1049 data are based on analysis of both Nuttallides truempyi (blue diamonds) and Stensioeina beccariiformis (blue triangles). These two datasets are plotted together assuming no isotopic offset exists between these two species (Quillévéré et al., 2008).

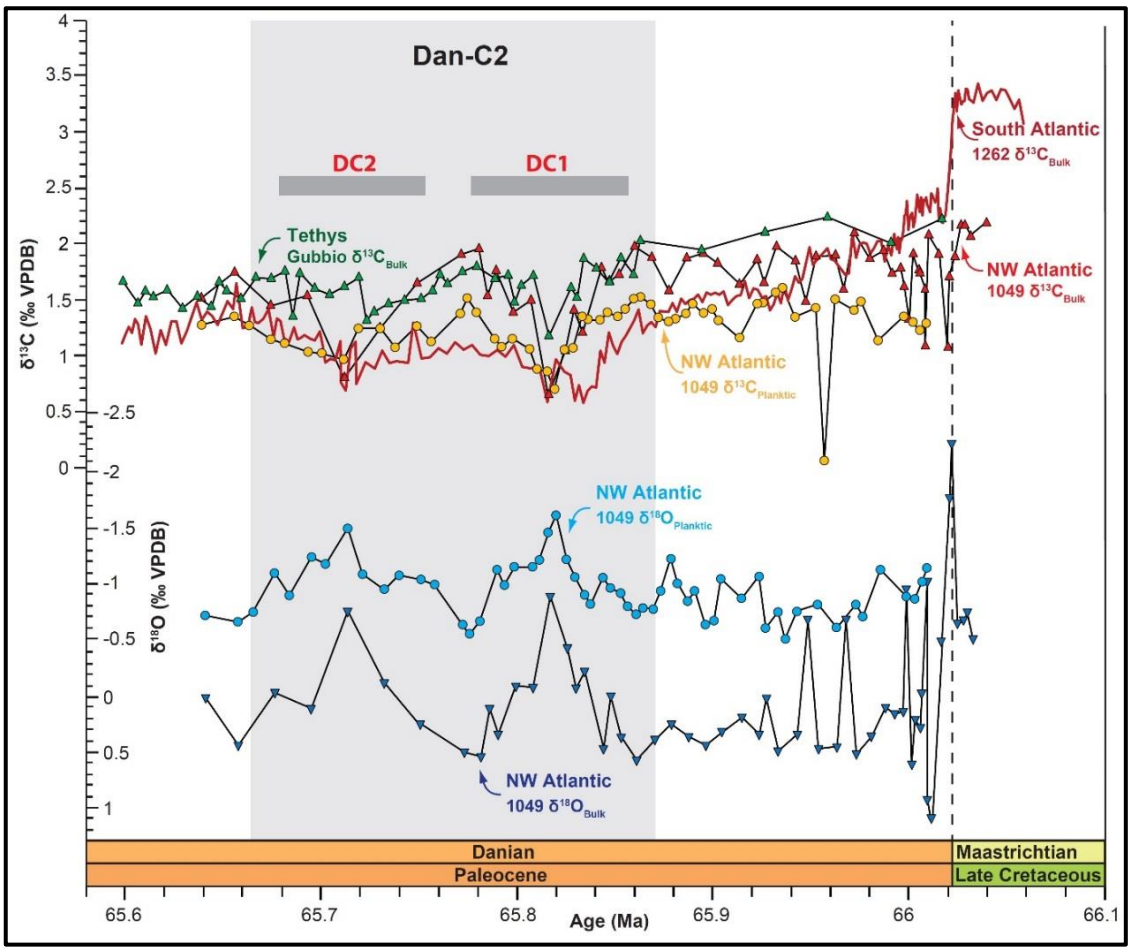

Figure 45. Compilation of planktic stable isotope data ($\delta^{13}C_{planktic}$ & $\delta^{18}O_{planktic}$) and bulk stable isotope data ($\delta^{13}C_{bulk}$ & $\delta^{18}O_{bulk}$) across the Dan-C2 event, including planktic and bulk data from NW Atlantic Blake Nose ODP Site 1049 (palaeo-depth ~1000–2000 m; Quillévéré et al., 2008), bulk data from Gubbio, Italy, northern Tethyan margin (palaeo-depth ~1500–2500 m; Coccioni et al., 2010), and bulk data from South Atlantic Walvis Ridge ODP Site 1262 (palaeo-depth ~3000 m; Kroon et al., 2007).

5.6.5. COMPARISON BETWEEN THE CARBON CYCLE AND CLIMATE RESPONSE OF DAN-C2 IN THE MARINE AND TERRESTRIAL REALMS

The character and magnitude of the Dan-C2 CIE recorded in the terrestrial realm differs significantly from its expression in marine records (Figure 46). A record of $\delta^{13}C_{org}$ across Dan-C2 from the Boltysh Crater in Ukraine represents the most complete and highest resolution terrestrial record of the CIE. As well as having a longer duration than that observed in the marine realm (~260 kyr vs. 200 kyr), the continental CIE lacks the characteristic double-spiked nature of the isotopic excursion typical of marine carbonates. This single excursion is also of a

significantly greater magnitude (~–5‰) than that characterising either DC1 or DC2 in marine carbonates (~–1.3–0.4‰). Whilst the onset of the terrestrial and marine CIEs appears to be comparably rapid (~30–40 kyr), the peak of the continental CIE lasts longer than either of the marine DC1 or DC2 CIEs (~100 kyr vs. ~20–40 kyr), and is characterised by a more prolonged recovery phase to a positive excursion over ~120 kyr. Progressive increases in the abundance of thermophilic *Normapolles* angiosperm pollen in the Boltysh Crater stratigraphy and the disappearance of lacustrine algae and mesic forest species, along with the appearance of brackish species such as *Restionaceae* and gypsum horizons, suggest a change to a warmer and drier climate in Ukraine at this time (Gilmour et al., 2013; Jolley et al., 2015). Changes in the composition of vegetation and precipitation patterns also have the potential to magnify or dampen the magnitude of the CIE in terrestrial organic matter. For example, the proliferation of new opportunistic floral species which evolved in the immediate aftermath of the K/Pg mass extinction may have discriminated between ^{13}C and ^{12}C in a different way during photosynthesis, potentially offering an explanation for the significantly greater magnitude of the excursion in the terrestrial realm compared to the marine realm.

The magnitude of the temperature response between the marine and continental realms also differs significantly (Figure 47). Whilst there is no evidence for transient warming associated with the event in bottom waters of the South Atlantic, there is evidence in pedogenic carbonate clumped isotope (Δ_{47}) data from the Songliao Basin for a significant warming of ~+6°C over ~70 kyr from ~65.88–65.81 Ma in northern China (Zhang et al., 2018). It is important to note that these pedogenic carbonates are interpreted to have formed in China during the summer months, prior to the onset of the monsoon rains (Zhang et al., 2018), and the absolute temperature estimates derived from them are also characterised by significantly uncertainties (±3–4°C). These clumped isotope data therefore only represent estimates of the trends in maximum summer temperatures, which may differ from trends in mean annual temperature. It is therefore not possible to discrimate whether the pedogenic carbonate temperature proxy reflects increased seasonality in the mid-latitude continental realm or warming of the mean annual temperature across this time interval.

Based on the available evidence, it can therefore be tentatively suggested that warming during Dan-C2 may be amplified from the deep ocean (where it is negligible), to surface ocean (~+4˚C), and most significant in the terrestrial realm (~+6˚C). However, further work using a multi-proxy approach (e.g., Mg/Ca, clumped isotope or TEX_{86} data in combination with $\delta^{18}O_{planktic}$ records) is urgently required to better identify the true magnitude and spatial variability of warming in the terrestrial and shallow marine realms during Dan-C2, and discriminate climatic warming from competing variables such as changes in surface ocean salinity or seasonality.

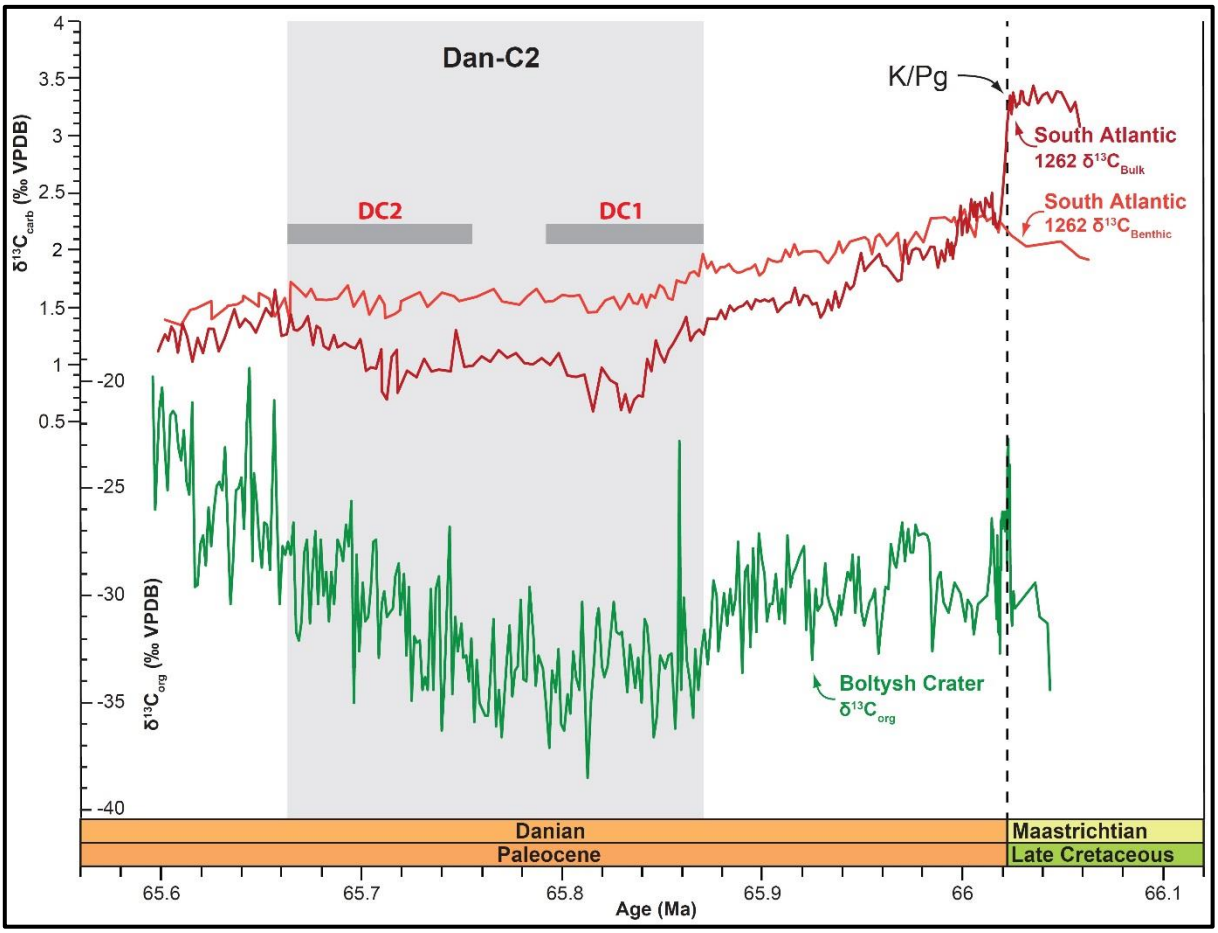

Figure 46. Comparison between the expression of the Dan-C2 carbon isotope excursion in bulk marine carbonate ($\delta^{13}C_{Bulk}$; Kroon et al., 2007) and benthic foraminiferal marine carbonate ($\delta^{13}C_{Benthic}$; this study) from South Atlantic Walvis Ridge ODP Site 1262 (palaeo-depth ~3000 m), and terrestrial organic matter ($\delta^{13}C_{org}$; Gilmour et al., 2013) from Boltysh Crater, Ukraine. Stratigraphic position of the Cretaceous/Paleogene (K/Pg) boundary is indicated.

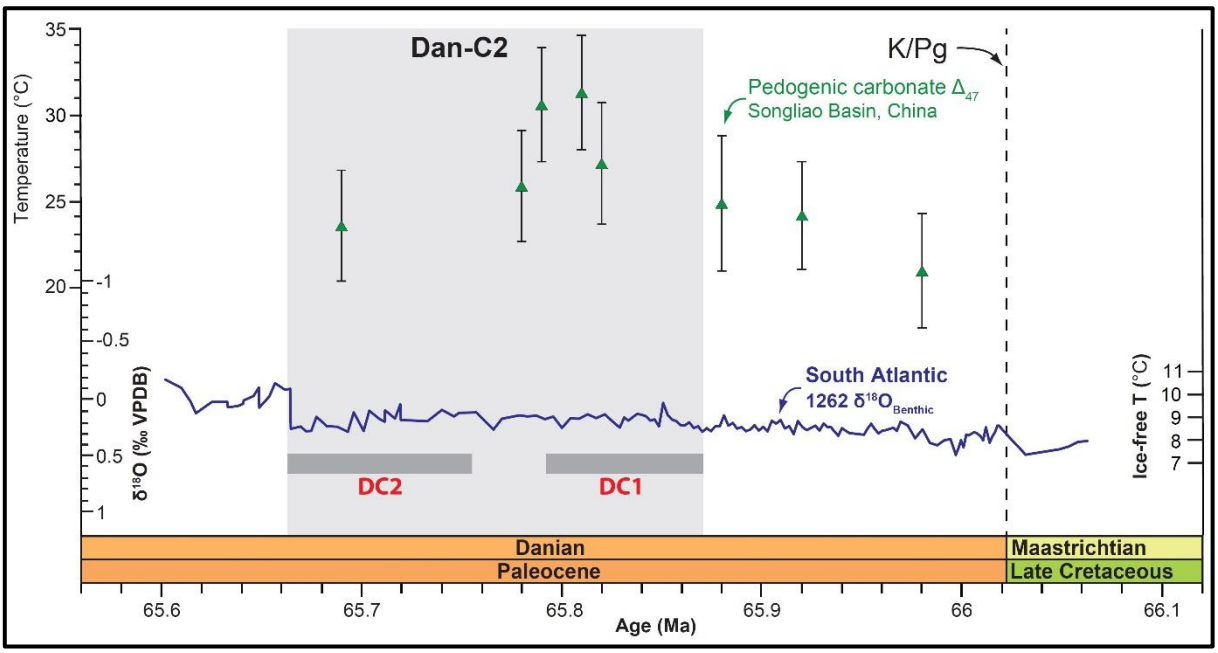

Figure 47. Comparison between the magnitude of warming observed during the Dan-C2 event in ocean bottom waters of the South Atlantic ODP Site 1262 from benthic stable oxygen isotope data ($\delta^{18}O_{benthic}$; palaeo-depth ~3000 m; this study), and in the terrestrial realm from pedogenic carbonate clumped isotope data (Δ_{47}; Songliao Basin, northern China; Zhang et al., 2018).

5.6.6. EVOLUTION OF ATMOSPHERIC pCO_2 AND CARBONATE DISSOLUTION DURING THE EARLY DANIAN

A recalibration of estimates for atmospheric pCO_2 based on pedogenic carbonate (Nordt et al., 2003) across the Dan-C2 event reveals that the event is broadly associated with evidence for increased storage of carbon in the atmosphere (Figure 48a). More high precision pCO_2 data are required to evaluate more fully variations in atmospheric pCO_2 at this time. Nonetheless, the available data suggest that pCO_2 rose by at least ~250 ppm relative to pre-excursion values, peaking at ~350 ±138.5 ppm during the core of the event, and that the recovery phase was associated with a decline in pCO_2 to ~225 ±91 ppm. Although absolute pCO_2 estimates are associated with significant uncertainty, the rise from pre-event to peak CO_2 levels is beyond error and therefore considered significant.

Examination of the % coarse fraction (% CF; this study), Fe intensity (Westerhold et al., 2008), and sedimentation rate records from ODP Site 1262 suggest that the rise in pCO_2 during Dan-C2 may have been associated with

carbonate dissolution in the deep south Atlantic (Figure 48c,d). Two minima in % CF and maxima in Fe intensity are accompanied by the lowest sedimentation rates of the early Paleogene (~0.23 cm/kyr) at ODP Site 1262, suggestive of increased carbonate dissolution corresponding to the DC1 and DC2 carbon cycle perturbations. Based on these data, and on the magnitude of change in $\delta^{13}C_{bulk}$, changes in the depth of the lysocline associated with the Dan-C2 event in the South Atlantic were greatest during DC1.

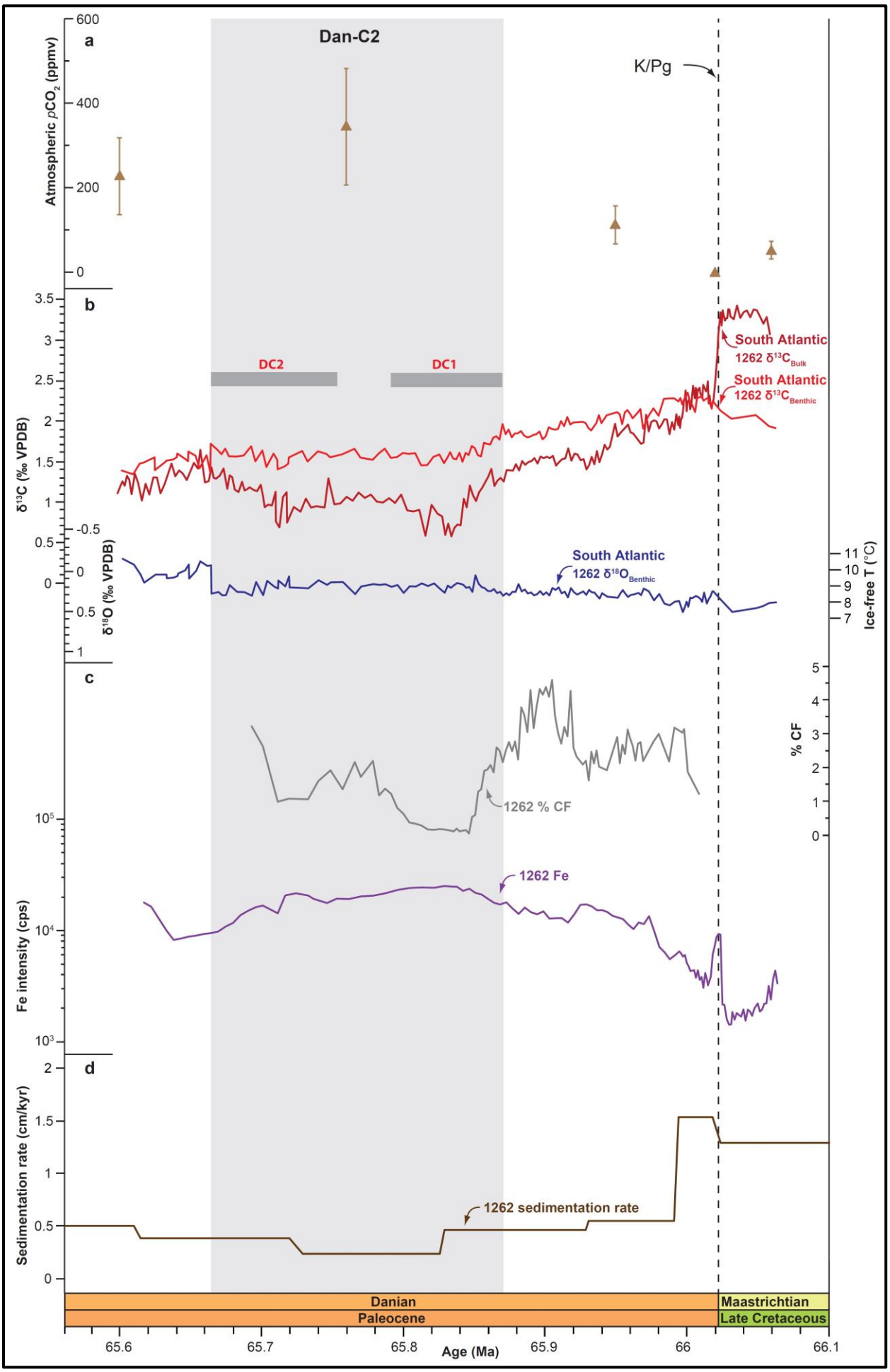
Dan-C2
K/Pg
a
Atmospheric pCO_2 (ppmv)
600
400
200
0
b
$\delta^{13}C$ (‰ VPDB)
3.5
3
2.5
2
1.5
1
0.5
0
DC2
DC1
South Atlantic
1262 $\delta^{13}C_{Bulk}$
South Atlantic
1262 $\delta^{13}C_{Benthic}$
-0.5
0
0.5
1
$\delta^{18}O$ (‰ VPDB)
South Atlantic
1262 $\delta^{18}O_{Benthic}$
11
10
9
8
7
Ice-free T (°C)
c
5
4
3
2
1
0
% CF
1262 % CF
10^5
10^4
10^3
Fe intensity (cps)
1262 Fe
d
2
1.5
1
0.5
0
Sedimentation rate (cm/kyr)
1262 sedimentation rate
Danian
Paleocene
Maastrichtian
Late Cretaceous
65.6
65.7
65.8
Age (Ma)
65.9
66
66.1

*Figure 48 (previous page). Records of environmental change across the Dan-C2 event: (**a**) estimates of atmospheric pCO_2 based on the pedogenic carbonate proxy (raw data from Nordt et al., 2003; recalibrated in this study); (**b**) bulk carbonate stable carbon isotope ($\delta^{13}C_{bulk}$; Kroon et al., 2007) and new benthic stable isotope ($\delta^{13}C_{benthic}$ and $\delta^{18}O_{benthic}$) data from the South Atlantic Walvis Ridge ODP Site 1262 (palaeo depth ~3000 m); (**c**) proxies for carbonate dissolution at ODP Site 1262: % coarse fraction (% CF; >63 µm; this study) and Fe intensity data (Westerhold et al., 2008); (**d**) sedimentation rate at ODP Site 1262 based on the orbitally-tuned age model presented in this thesis.*

5.6.7. SPECTRAL ANALYSIS

Based on our new age model, the Dan-C2 event is associated with the first long (405-kyr) eccentricity maxima of the Paleocene ($Pc_{405}1$; Figure 49). The paired DC1 and DC2 excursions in $\delta^{13}C$ and $\delta^{18}O$ observed in marine carbonates are spaced ~100 kyr apart and correlate to two amplified short (100-kyr) eccentricity maxima during $Pc_{405}1$ (Figure 49a,c).

In contrast to the preceding Late Maastrichtian, the data filters illustrate very low amplitude cyclicity in $\delta^{13}C_{benthic}$ and $\delta^{18}O_{benthic}$ at 21-kyr precession and 100-kyr eccentricity frequencies during Dan-C2 (Figure 49b; compare with **Chapter 4**, Figure 34). The imprint of 100-kyr cyclicity is, however, clearly evident within the dissolution proxies (Figure 50b) and the $\delta^{13}C_{bulk}$ record (Figure 50c) from ODP Site 1262, suggesting that significant orbitally-paced perturbations to the carbon cycle occurred during 100-kyr eccentricity maxima (compare Figure 50a,b,c). Variability in dissolution is nevertheless not amplified on precession timescales (Figure 50b,c) during 100-kyr eccentricity maxima. The dominant periodicity on orbital timescales driving deep sea dissolution in the South Atlantic therefore appears to switch from 21-kyr precession in the Late Maastrichtian to 100-kyr eccentricity during the Early Paleocene (see **Chapter 4**, **Sections 4.6.5 and 4.6.6.** for further discussion on the Late Maastrichtian). The significant decrease in sedimentation rate after K/Pg boundary time (to ~0.25–0.5 cm/kyr) may hamper the recognition of precession cycles within the earliest Paleocene ODP Site 1262 benthic records (Figure 48d), and artificially transfer power into the 100-kyr band (e.g., Zeebe et al., 2017). However, power returns within the 21-kyr filter by ~64–64.5 Ma (see **Chapter 3**, Figure 15e), a time characterised by fairly low sedimentation rates (~0.5 cm/kyr) but situated at the end of the main recovery phase of the bulk-benthic $\delta^{13}C$ gradient after the K/Pg mass extinction

(see **Chapter 3**, Figure 12d,g). Therefore, the transfer in power from 21-kyr precession to 100-kyr eccentricity across the K/Pg boundary may alternatively reflect a changing response of marine productivity to orbital forcing, as surface ocean marine productivity was characterised by the predominance of significantly different low diversity opportunistic species following the mass extinction and partial collapse of the biological pump at the K/Pg boundary (e.g., Birch et al., 2016).

5.6.8. ROLE OF DECCAN TRAPS VOLCANISM

The Dan-C2 event broadly temporally coincides with the most voluminous outpourings of Deccan Traps volcanism comprising the Poladpur and Ambenali formations of the Wai sub-group (see **Chapter 4**, **Section 4.6.7.** for further details on volume estimates). Spot ages and associated error bars for the dated parts of the Poladpur and Ambenali formations are illustrated in Figure 49d and Figure 50d. These ages suggest that the major outpourings of the Poladpur and Ambenali formations occurred before and after the Dan-C2 event respectively, but do not correlate precisely with the event itself. However, these spot ages were defined from one discrete horizon within each formation, therefore it is possible that volcanism continued throughout this time interval.

In contrast to the preceding LMWE, which initiated during a 400-kyr eccentricity minimum, the two negative CIEs associated with the Dan-C2 event appear to be paced by 100-kyr eccentricity and occurred during the $Pc_{405}1$ eccentricity maximum, suggesting a primary role of orbital forcing. Ongoing Deccan Traps volcanism may have played a secondary role however, contributing to generally elevated atmospheric CO_2 levels and a generally warm greenhouse climate during this time. Ongoing Deccan Traps volcanism therefore appears to have played a modulatory role rather than have been a causal factor in the initiation of the Dan-C2 event.

*Figure 49 (next page). Spectral analysis of the new early Danian benthic stable isotope ($\delta^{13}C_{benthic}$ and $\delta^{18}O_{benthic}$) records from the South Atlantic ODP Site 1262: (**a**) La2010b orbital solution (Laskar et al., 2011a). Long (405-kyr) eccentricity cycles are named following the nomenclature of Dinarès-Turell et al. (2014), with short (100-kyr) cycles of the Paleocene numbered sequentially, starting from the Cretaceous/Paleogene (K/Pg) boundary. (**b**) Filters at the long (405-kyr) eccentricity frequency, short (100-kyr) eccentricity frequency, and precession (21-kyr) frequency for $\delta^{13}C_{benthic}$ in red and $\delta^{18}O_{benthic}$ in blue (this study); (**c**) benthic stable isotope data (this study). Grey bands represent correlation of 100-kyr eccentricity maxima across the records. (d) Spot radiometric ages for Deccan volcanism (Ar-Ar ages from Renne et al., 2015; U-Pb ages from Schoene et al., 2015), illustrated by red circles and labelled with formation names. Uncertainty (1σ) on the Deccan age estimates is indicated by red bars.*

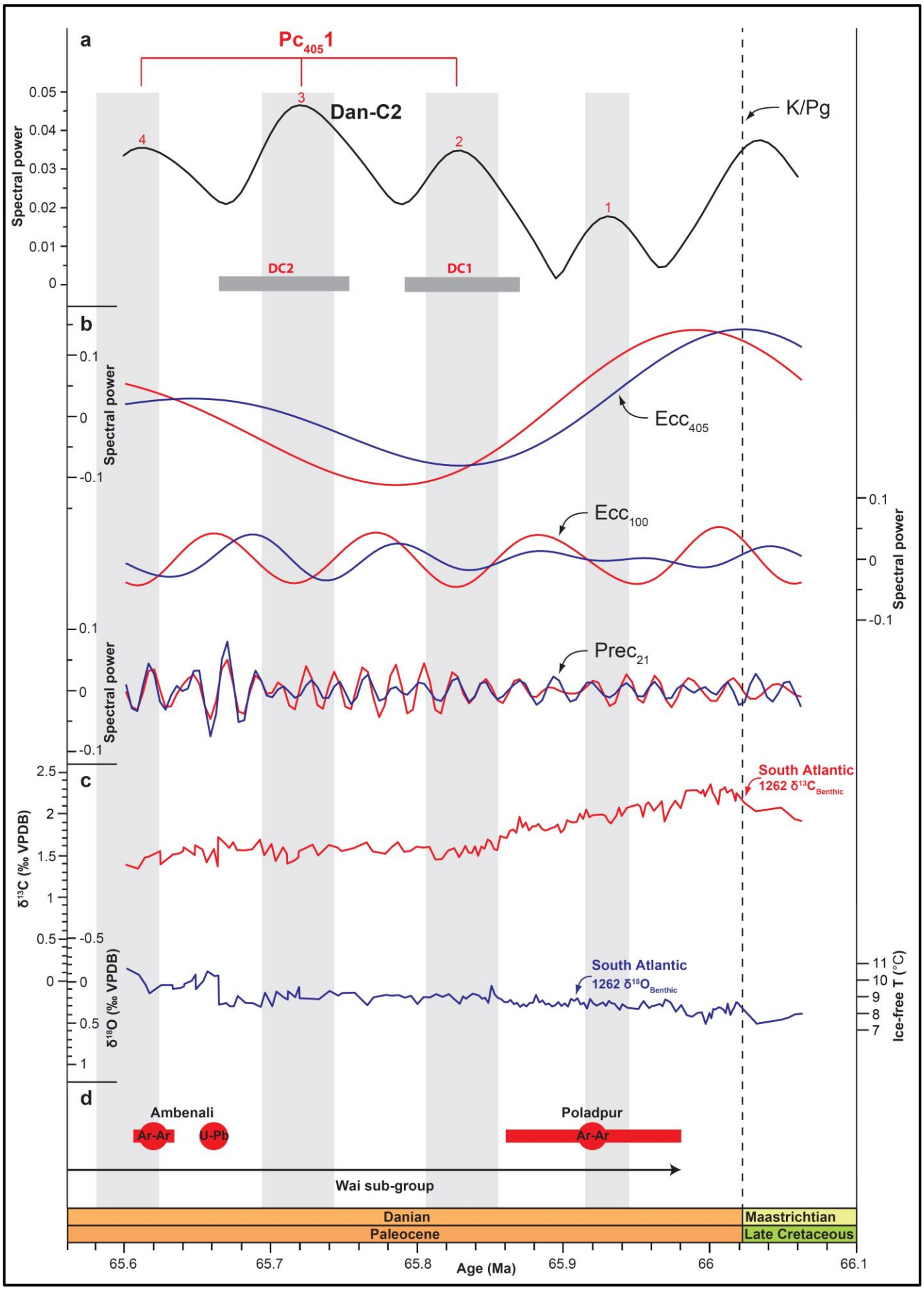
a
Pc405 1
Dan-C2
K/Pg
Spectral power
0.05
0.04
0.03
0.02
0.01
0
4
3
2
1
DC2
DC1
b
Spectral power
0.1
0
-0.1
Ecc405
Ecc100
Prec21
Spectral power
c
δ13C (‰ VPDB)
2.5
2
1.5
1
0.5
0
South Atlantic
1262 δ13CBenthic
δ18O (‰ VPDB)
-0.5
0
0.5
1
South Atlantic
1262 δ18OBenthic
Ice-free T (°C)
11
10
9
8
7
d
Ambenali
Ar-Ar
U-Pb
Poladpur
Ar-Ar
Wai sub-group
Danian
Paleocene
Maastrichtian
Late Cretaceous
65.6
65.7
65.8
Age (Ma)
65.9
66
66.1

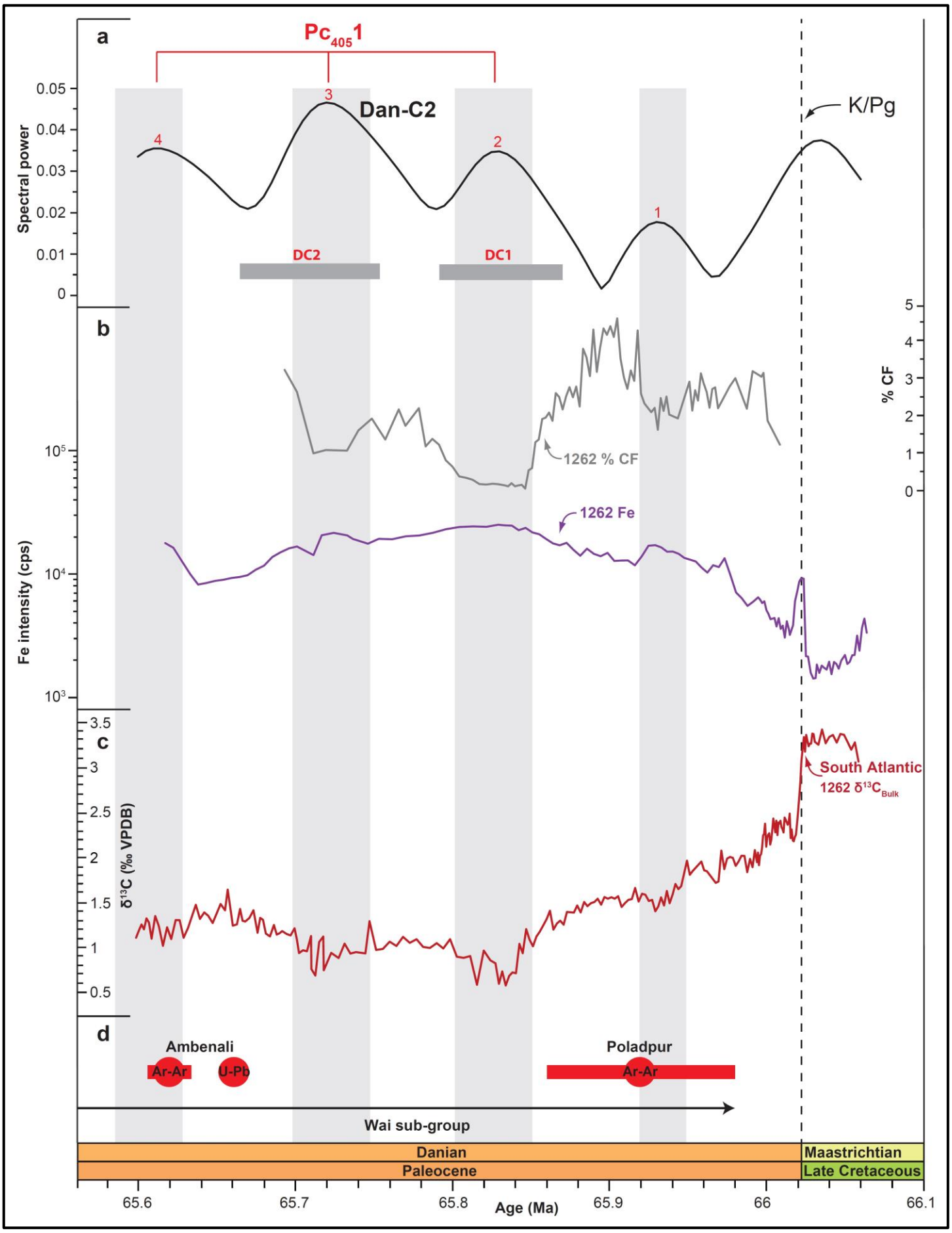
a
Pc405 1
Dan-C2
K/Pg
Spectral power
0.05
0.04
0.03
0.02
0.01
0
4
3
2
1
DC2
DC1
b
1262 % CF
1262 Fe
Fe intensity (cps)
10⁵
10⁴
10³
% CF
5
4
3
2
1
0
c
South Atlantic
1262 δ13CBulk
δ13C (‰ VPDB)
3.5
3
2.5
2
1.5
1
0.5
d
Ambenali
Ar-Ar
U-Pb
Poladpur
Ar-Ar
Wai sub-group
Danian
Paleocene
Maastrichtian
Late Cretaceous
65.6
65.7
65.8
Age (Ma)
65.9
66
66.1

*Figure 50 (previous page). Orbital pacing of carbonate dissolution proxy and bulk carbonate stable carbon isotope ($\delta^{13}C_{bulk}$) records from South Atlantic ODP Site 1262: (**a**) La2010b orbital solution (Laskar et al., 2011a). Long (405-kyr) eccentricity cycles are named following the nomenclature of Dinarès-Turell et al. (2014), with short (100-kyr) cycles numbered sequentially, starting from the Cretaceous/Paleogene (K/Pg) boundary. (**b**) Proxy data for carbonate dissolution including % Coarse Fraction (% CF; >63 μm; this study) and Fe intensity data (Westerhold et al., 2008); (**c**) $\delta^{13}C_{bulk}$ record (Kroon et al., 2007); (**d**) spot radiometric ages for Deccan volcanism (Ar-Ar ages from Renne et al., 2015; U-Pb ages from Schoene et al., 2015), illustrated by red circles and labelled with formation names. Uncertainty (1σ) on the Deccan age estimates is indicated by red bars.*

5.6.9. BENTHIC FORAMINIFERAL ASSEMBLAGE ANALYSIS

The results of benthic foraminiferal assemblage analysis performed by Dr. Gabriela de Jesús Arreguín Rodríguez are presented in Figure 51 and Figure 52. The composition and shifts in the benthic assemblages during the Dan-C2 event do not support a scenario of severe carbonate dissolution at the seafloor, but instead support a significant change in food supply (Thomas, 1998; Thomas et al., 2000; Kaminski and Gradstein, 2005; Alegret and Thomas, 2007, 2009). The assemblage is dominated by calcareous species, however, agglutinated species represent nearly a quarter of the assemblage between DC1 and DC2 (Figure 51f). This peak in agglutinated species is dominated by *Spiroplectammina spectabilis*, since no marked change occurs in the abundance of the other main agglutinated species found in Dan-C2 sediments deposited at ODP Site 1262, *Clavulinoides sp.* (Figure 52). The abundance of agglutinated taxa as a whole are, however, lower during the core of the DC1 and DC2 isotopic events (Figure 51f). Oligotrophic species tolerant of low carbonate saturation states, such as *Nuttallides truempyi*, decrease in abundance across Dan-C2, whilst species tolerant of higher food supply such as *Stensieoina beccariiformis* and *Spiroplectammina spectabilis* increase in abundance (Figure 52; Thomas, 1998; Thomas et al., 2000; Kaminski and Gradstein, 2005). The apparent increase in agglutinated taxa across the central part of the event could therefore be related to higher food supply, as opposed to increasing corrosivity of South Atlantic bottom waters.

Taken as a whole, epifaunal benthic foraminifera slightly dominate the assemblage of the stratigraphy studied, but represent up to ~68% of it during both DC1 and DC2 (since ~32% is composed of infaunal taxa in Figure 51), mirroring the isotopic excursion observed in marine carbonates (Figure 51g). Infaunal taxa including buliminids *s.l.*, uniserial lagenids, stilostomellids, polymorphinids, and unilocular taxa all decrease in abundance during Dan-C2 (Figure 51g-l), whilst *Spiroplectammina spectabilis* is the only infaunal species that increases in abundance (Figure 52). The generally good preservation of benthic foraminifera (Figure 42), along with the dominance of calcareous species within the assemblage, therefore suggests that ODP Site 1262 was situated well above the lysocline and calcite compensation depth during the early Danian and throughout the Dan-C2 event, in contrast to the interpretation of carbonate dissolution during the event based on the Fe intensity and % coarse fraction data.

Diversity (Fisher-α index; Figure 51d) decreases to a minimum value of 13 during DC1, then recovers to pre-excursion values of 21, before a second smaller drop to 17 during DC2. Heterogeneity (Shannon-Weaver index; Figure 51e) exhibits a longer term noisy decline to minimum values of ~3.15 at the end of Dan-C2.

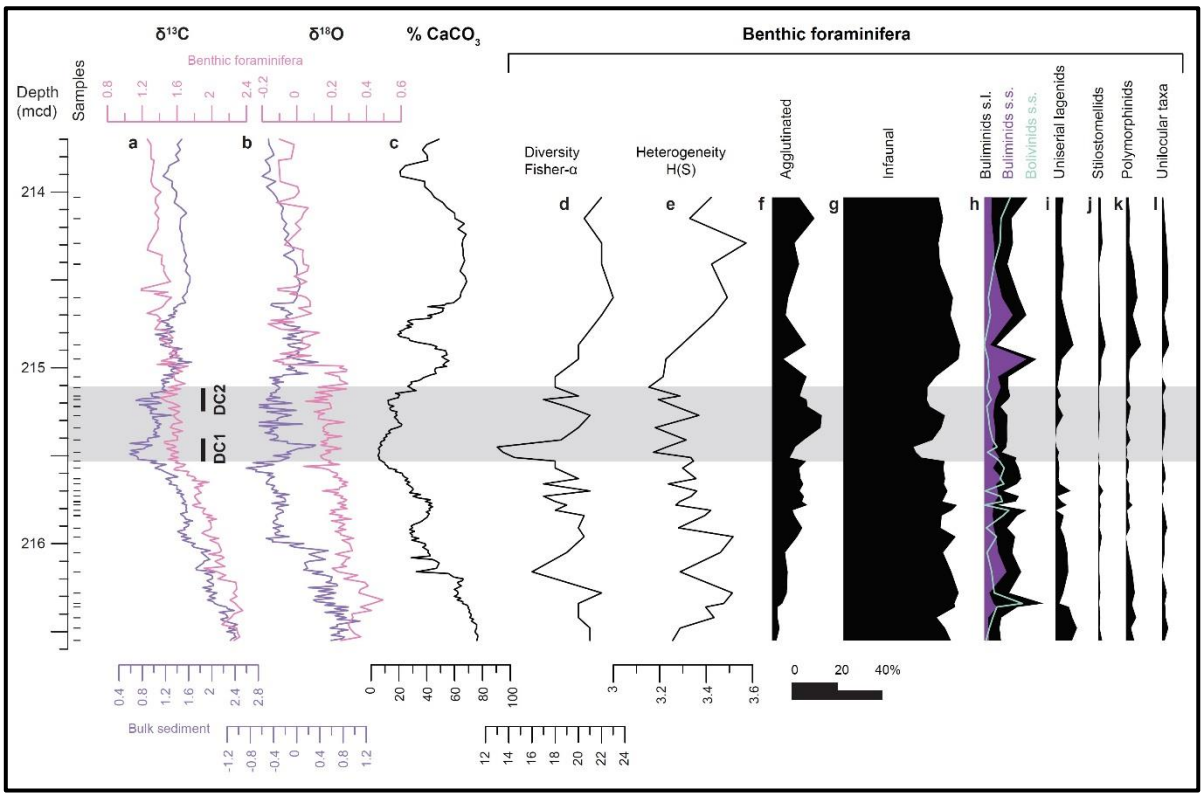

*Figure 51. Benthic foraminifera assemblage analysis across the Dan-C2 event at the South Atlantic ODP Site 1262. Benthic foraminifera species and groups were identified following the schemes of Van Morkhoven et al. (1986), Tappan & Loeblich (1988), Tjalsma and Lohmann (1983), and Alegret and Thomas (2001). (**a**) benthic foraminiferal $\delta^{13}C$ (this study) and bulk carbonate $\delta^{13}C$ (Kroon et al., 2007) records; (**b**) benthic foraminiferal $\delta^{18}O$ (this study) and bulk carbonate $\delta^{18}O$ (Kroon et al., 2007) records; (**c**) % $CaCO_3$ carbonate dissolution proxy record; (**d**) diversity (Fisher-α Index); (**e**) heterogeneity (Shannon-Weaver Index); (**f**) abundance of agglutinated taxa; (**g**) abundance of infaunal taxa; and abundance of specific infaunal taxa groups including Buliminids (**h**); uniserial lagenids (**i**); Stilostomellids (**j**); Polymorphinids (**k**); and unilocular taxa (**l**). Figure modified from Gabriela de Jesús Arreguín Rodríguez (pers. comm.).*

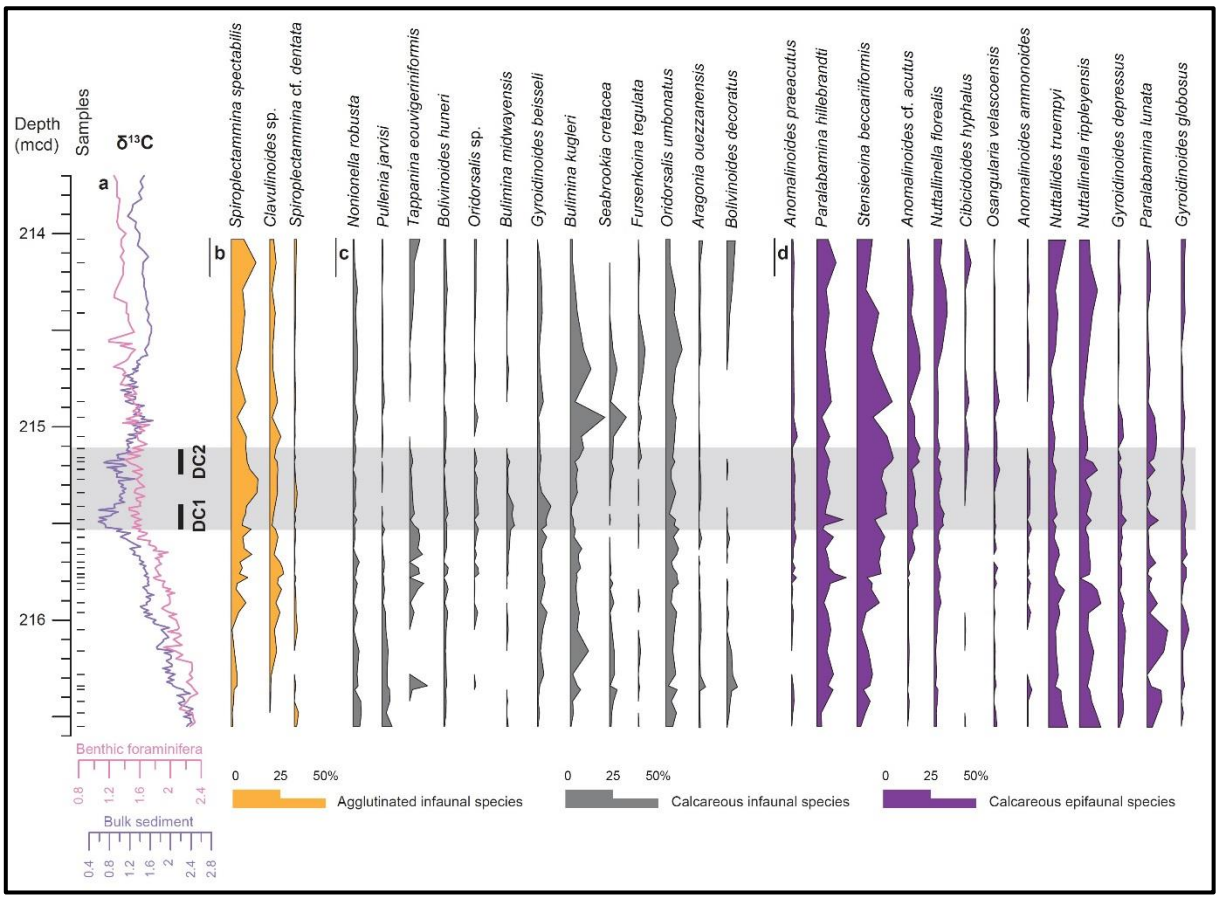

*Figure 52. Benthic foraminifera species abundances across the Dan-C2 event at the South Atlantic ODP Site 1262. Species and groups were identified following the schemes of Van Morkhoven et al. (1986), Tappan & Loeblich (1988), Tjalsma and Lohmann (1983), and Alegret and Thomas (2001). (**a**) ODP Site 1262 benthic foraminiferal $\delta^{13}C$ (this study) and bulk carbonate $\delta^{13}C$ (Kroon et al., 2007) records, highlighting the position of the Dan-C2 event; (**b**) abundance plots of agglutinated infaunal species (in orange); (**c**) abundance plots of calcareous infaunal species (in grey); (**d**) abundance plots of calcareous epifaunal species (in purple). Figure modified from Gabriela de Jesús Arreguín Rodríguez (pers. comm.).*

5.6.10. IS DAN-C2 A TYPICAL PALEOGENE HYPERTHERMAL?

Hyperthermal events of the early Paleogene are typically characterised by the release of massive quantities of greenhouse gases over a geologically brief time period of 10's of thousands of years, rapid global warming at both Earth's surface and in the deep ocean, acidification of the oceans, and a pacing determined by orbital forcing (Zachos et al., 2005; McInerney & Wing, 2011). The Dan-C2 event has been proposed as the first hyperthermal of the Paleogene Period (e.g., Quillévéré et al., 2008; Coccioni et al., 2010; Gilmour et al., 2013).

The new data presented here, however, allow us to question this hypothesis (Figure 53).

The geochemical expression of the Dan-C2 event appears at first glance to share many of the characteristics of typical early Paleogene hyperthermals. There is possible evidence for a significant transient warming event ranging from up to ~+4°C in the surface ocean (assuming no changes in salinity) to ~+6°C in the terrestrial realm (Quillévéré et al., 2008; Zhang et al., 2018), along with a $\delta^{13}C$ excursion ranging from ~–0.8–1.5‰ in bulk and planktic marine carbonates to ~–5‰ in terrestrial organic matter (Quillévéré et al., 2008; Gilmour et al., 2013). Whilst evidence for Dan-C2 is currently limited to mid-latitude records, its expression in $\delta^{13}C$ and $\delta^{18}O$ data from marine and terrestrial sequences across the mid-latitude Northern Hemisphere, from geographically disparate continents and ocean basins, suggest that this event may have been associated with global perturbations to the climate and carbon cycle. The total duration of the event (~200 kyr), and the double-spiked nature of changes in marine $\delta^{13}C$ at this time, are also comparable to the character of other hyperthermals such as the Latest Danian Event (LDE; Figure 53a; see also **Chapter 3**, **Section 3.6.6.**), as is the occurrence of Dan-C2 during the $Pc_{405}1$ eccentricity maximum (Figure 49a). Similar to the other more widely studied hyperthermals (e.g., ETM2/H2; see also **Chapter 3**), Dan-C2 appears to be associated with geochemical and sedimentological characteristics that are suggestive of deep-sea carbonate dissolution (Figure 53c). Dan-C2 may also be associated temporally with the latter stages of Deccan Traps volcanism in India (Figure 49d; Figure 50d; Renne et al., 2015; Schoene et al., 2015; see also **Chapter 4**, **Section 4.6.7.**).

Although the Dan-C2 event is characterised by many sedimentological and geochemical features typical of a Paleogene hyperthermal, the new ODP Site 1262 benthic stable isotope and faunal assemblage data presented here challenge whether this is the case. The lack of any transient negative excursion in the new $\delta^{18}O_{benthic}$ record from the South Atlantic (Figure 53b) is consistent with more poorly resolved and lower resolution records from the NW Atlantic and the equatorial Pacific (Quillévéré et al., 2008; Westerhold et al., 2011; Figure 44), which together suggest that the deep ocean did not warm during Dan-C2. Many hyperthermals of the Paleogene are characterised by a greater magnitude of

warming in the terrestrial realm compared to the deep sea, and by polar amplification of surface temperatures (e.g., Cramwinckel et al., 2018). If polar amplification of surface ocean warming also occurred at this time, we might expect that signal to be transmitted to the deep South Atlantic through deep water formation in the Southern Ocean (e.g., Thomas et al., 2003, 2008; Lunt et al., 2010). For instance, Paleogene hyperthermals such as the LDE (~62.1–62.0 Ma; Figure 53b; see also **Chapter 3**, **Section 3.6.6.**) and the Late Maastrichtian warming event (LMWE; ~66.27–66.21 Ma; see also **Chapter 4**), that occurred both before and after Dan-C2, were characterised by pronounced bottom water warming of ~+2.5–4°C. The fact that apparent surface ocean warming during Dan-C2 was not accompanied by a synchronous temperature perturbation in the deep ocean strongly suggests that it was not a typical early Paleogene hyperthermal.

If high-latitude deep water formation was significantly reduced during Dan-C2, bottom waters could have been isolated from surface warming. While it is thought that Atlantic deep water production predominantly took place in the Southern Ocean and Pacific deep water production from a combination of the Southern Ocean (SPDW) and North Pacific (NPDW) during the early Paleogene based on neodymium isotope data (e.g., Thomas et al., 2003, 2008; Lunt et al., 2010; Figure 41), no studies have focused on specific changes in ocean circulation across the Dan-C2 event. A transient switch in the source of deep water formation from the Southern Ocean to warm saline outflow from the Tethys Ocean or the Northern Hemisphere has been postulated for some of the larger climatic events of the Paleogene, such as the PETM (e.g., Nunes & Norris, 2006; Lunt et al., 2010). Yet such a change in ocean circulation should amplify warming in the deep waters rather than reduce it, due to the sinking of much warmer low-latitude surface waters as opposed to cold high-latitude Southern Ocean surface waters. Such dramatic changes in thermohaline circulation are typically associated with marked turnover or extinctions amongst benthic communities, such as the benthic foraminifera extinction event during the PETM (e.g., Thomas, 1998; Thomas, 2003). The lack of significant changes amongst benthic foraminifera communities (Figure 51; Figure 52), lack of amplified deep water warming (Figure 44), and lack of evidence for a major shift in the composition of

the deep water source during Dan-C2, therefore suggest that major transient changes in ocean circulation did not occur during this event.

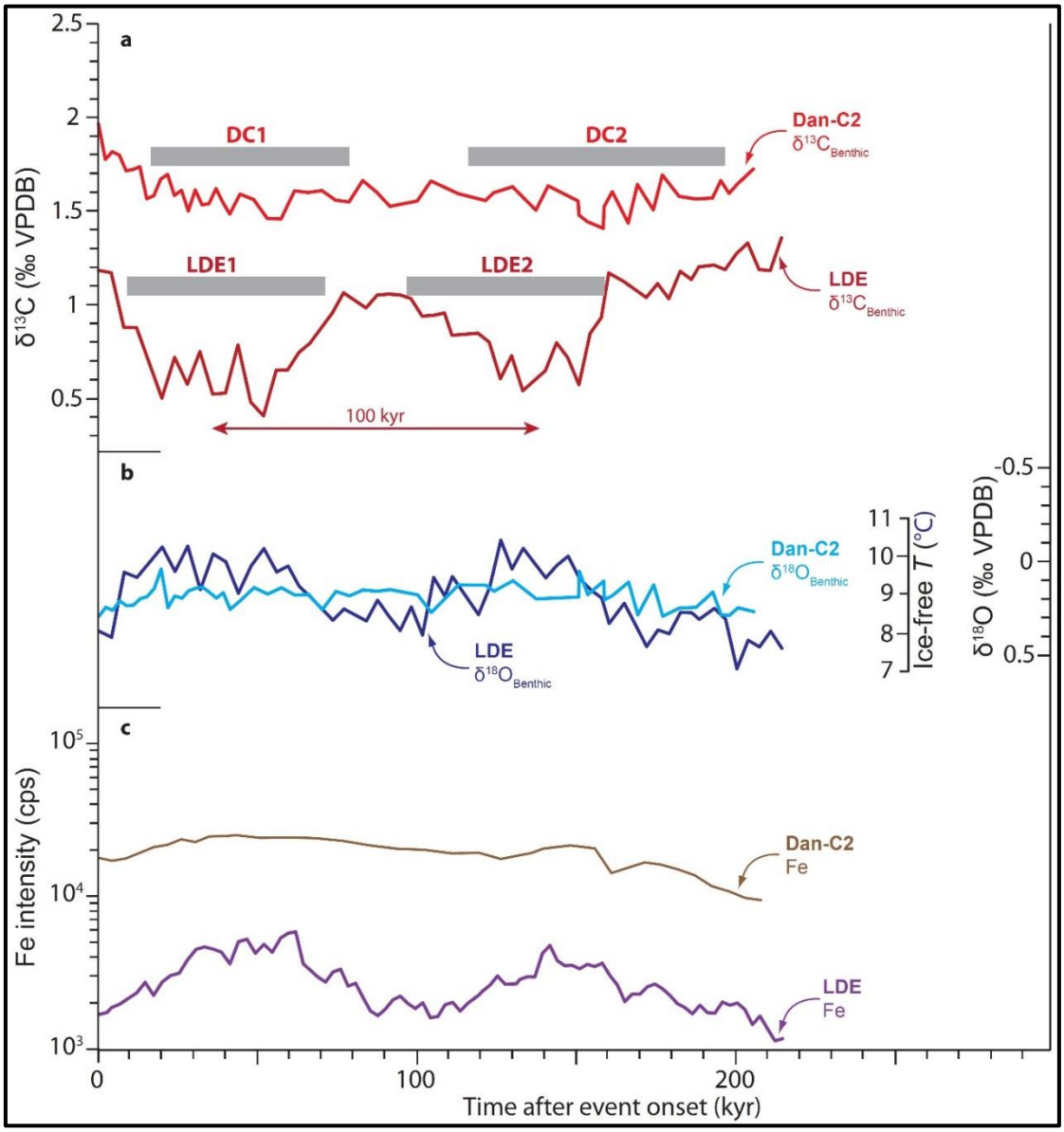

*Figure 53. Comparison between the benthic stable isotope and geochemical expressions of the Dan-C2 event and Latest Danian Event (LDE) at South Atlantic ODP Site 1262, plotted relative to time since onset of the respective events: (**a**) benthic stable carbon isotope ($\delta^{13}C_{benthic}$) records (this study); (**b**) benthic stable oxygen isotope ($\delta^{18}O_{benthic}$) records (this study); (**c**) Fe intensity records (Westerhold et al., 2008). The oldest and youngest of the Dan-C2 carbon isotope excursions have been named DC1 and DC2 respectively (this study). The oldest and youngest of the LDE carbon isotope excursions have been named LDE1 and LDE2 after Deprez et al. (2017). See **Chapter 3**, **Section 3.6.6.** for further discussion of the LDE.*

Whilst orbitally-paced minima in % coarse fraction and high Fe intensities are suggestive of significant carbonate dissolution during Dan-C2, the lack of a

major change in structure of benthic foraminifera communities (Figure 51; Figure 52), along with generally good preservation of benthic foraminifera (Figure 42), suggest, by contrast, that significant carbonate dissolution did not occur during the event. However, drops in diversity and heterogeneity during Dan-C2 support a scenario of strong environmental instability on the seafloor. A switch from the dominance of oligotrophic species to more mesotrophic species during Dan-C2 suggests that this instability may be related to changes in the magnitude and type of food supply, as opposed to transient fluctuations in carbonate saturation state. By contrast, decreasing abundance of *Nuttallides truempyi,* a species tolerant of low carbonate saturation states (Thomas, 1999; Thomas et al., 2000; Kaminski and Gradstein, 2005), during Dan-C2, may actually suggest increasing carbonate saturation state in the deep ocean in response to reduced calcareous nannoplankton and planktic foraminifera productivity following the K/Pg mass extinction (as suggested by Kroon et al., 2007). Furthermore, the immediate aftermath of the K/Pg mass extinction was characterised by the evolution and spread of blooms of opportunistic planktic foraminifera taxa with abnormally small tests <63 µm in diameter (e.g., Birch et al., 2016). These opportunistic planktic foraminifera species may have been more susceptible to dissolution (e.g., Birch et al., 2012, 2013). The apparent orbitally-paced dissolution events in Fe intensity and % coarse fraction may therefore simply reflect the typical 405-kyr and 100-kyr orbital heartbeat of the Paleogene carbon cycle, with a magnified expression in the sedimentary record due to the partial collapse of the biological pump and blooms of unusually small opportunistic planktic foraminifera taxa in the immediate aftermath of the K/Pg mass extinction.

The increased clay content in South Atlantic deep-sea sediments during Dan-C2 could alternatively be explained by a switch in climatic regime in the hinterland. In contrast to most other Paleogene hyperthermal events, which are believed to have been characterised by an intensified hydrological cycle or more seasonally extreme precipitaton events (e.g., Harding et al., 2011; Manners et al., 2013), changes in palynofloras from the Boltysh Crater (in the Ukraine) suggest that Dan-C2 was characterised by a warmer and drier climate (Gilmour et al., 2013; Jolley et al., 2015). Recent modelling studies, however, have suggested that the response of the climate and hydrological cycle to greenhouse warming may have been geographically heterogeneous, with some regions

experiencing a decrease in precipitation (Carmichael et al., 2017). An arid African continent could have increased deflation of aeolian dust to ODP Site 1262 on Walvis Ridge. Both increased aeolian dust deposition and significantly reduced pelagic settling of carbonate material through the water column could therefore help to explain the anomalously high clay contents observed in sediments deposited at our study site during Dan-C2, and the early Danian as a whole, without invoking increased carbonate dissolution. This interpretation is challenged, however, by the fact that sedimentation rates decrease to a minimum of 0.23 cm/kyr during the peak of the Dan-C2 event (Figure 46d), suggesting that reduced settling of pelagic carbonate material through the water column (hence reduced dilution of Fe-rich clays settling to the seafloor) following the K/Pg mass extinction is likely to be the dominant cause for the spike in Fe intensity during the event.

The new ODP Site 1262 $\delta^{13}C_{benthic}$ record allows us to question whether there was indeed a major global perturbation to the carbon cycle during Dan-C2. The magnitudes of the $\delta^{13}C_{benthic}$ excursions from both the deep South Atlantic and the equatorial Pacific during this event are significantly muted compared to the typical magnitude recorded in bulk and planktic carbonate datasets (Figure 43; Figure 44; Figure 45). The $\delta^{13}C_{benthic}$ expression of Dan-C2 is also significantly muted compared to other hyperthermal events recorded in our newly compiled ODP Site 1262 $\delta^{13}C_{benthic}$ record spanning ~67.1–52.35 Ma, such as the LDE (Figure 53a; **Chapter 3**, Figure 12c). The discrepancy between bulk and benthic carbonate records could be explained by the mass extinction of surface-dwelling plankton ~66 Ma. The significantly reduced pelagic rain-out of organic matter from the surface waters would result in significantly reduced volumes of ^{12}C-enriched organic matter remineralisation at depth. Since this process occurred immediately prior to the onset of Dan-C2, it could create a more positive $\delta^{13}C$ signature of bottom water DIC immediately prior to the onset of the event, and could therefore serve to dampen the expression of any negative global $\delta^{13}C$ perturbation in benthic records. This process could therefore explain the muted excursion characterising the Dan-C2 event in the $\delta^{13}C_{benthic}$ record from ODP Site 1262. By contrast, significantly reduced surface water primary productivity would initiate a more negative $\delta^{13}C$ signature of surface mixed layer DIC immediately prior to the onset of the event, therefore the expression of any negative

perturbations to the global carbon cycle (by the release of greenhouse gases into the exogenic carbon cycle) could have been magnified in $\delta^{13}C_{bulk}$ and $\delta^{13}C_{planktic}$ records.

The extremely small tests of the opportunistic planktic foraminifera which evolved in the immediate aftermath of the K/Pg boundary have been shown to exhibit very strong vital effects, with $\delta^{13}C$ test values up to –2‰ lighter than DIC due to the incorporation of a relatively high proportion of respired ^{12}C into their test calcite (Birch et al., 2012, 2013). Their dominance in marine sediments deposited during Dan-C2 could further amplify the apparent magnitude of the excursion in $\delta^{13}C_{bulk}$ and $\delta^{13}C_{planktic}$ records (Birch et al., 2012, 2013). Therefore it is likely that profound biotic changes in the marine realm following the K/Pg boundary mass extinction have significantly biased the apparent magnitude of the Dan-C2 CIE within marine carbonates. The true magnitude of the carbon cycle perturbation may therefore lie somewhere between the upper end member observed in $\delta^{13}C_{bulk}$ records and the lower end member observed in $\delta^{13}C_{benthic}$ records.

Although the event appears to have been orbitally-paced, the role of ongoing Deccan Traps volcanism during this time should also be considered. The preceding globally warm climate of the LMWE, which was primarily forced by Deccan volcanism (see **Chapter 4**), was also characterised by increased carbon cycle sensitivity to 21-kyr precession related to periodically enhanced export productivity. Although increased sensitivity to precession is not observed during the Dan-C2 event, perhaps due to the low sedimentation rates which characterise this time interval at ODP Site 1262 or a different response of surface ocean marine productivity to orbital forcing during this time, it could be possible that carbon cycle sensitivity to 100-kyr eccentricity may have been amplified during this volcanically-induced warm climate period within the bulk and planktic $\delta^{13}C$ records.

Lastly, although there is evidence for warming during Dan-C2 within the terrestrial and shallow marine realms, the apparent magnitude and nature of warming could have been biased by changes in other climate parameters such as precipitation (and hence freshwater runoff) rates or seasonality. The ~+6°C

warming based on pedogenic clumped isotope data from the Songliao Basin is characterised by large uncertainty and only reflects the change in maximum summer temperatures, which could be increasing due to increased seasonality, whilst mean annual temperatures may exhibit little change across this time interval. Due to the paucity of terrestrial temperature data for this event, it is currently not possible to discriminate between increased seasonality in the mid-latitude Northern Hemisphere or a significant warming of mean annual temperature. Similarly, the conversion of $\delta^{18}O_{planktic}$ data to temperature could also be biased by significant changes in freshwater input to ODP Site 1049, which was located in reasonably close proximity to the North American landmass, or by changes in net evaporation from the surface ocean. Without an independent temperature proxy, such as Mg/Ca or $\mathrm{TEX}_{86}^{\mathrm{H}}$, it is not possible to accurately quantify the magnitude of temperature change that took place in the surface waters of the NW Atlantic during Dan-C2 at present. The lack of any global nannoplankton or planktic foraminiferal biostratigraphic datums temporally associated with Dan-C2 (e.g., Figure 43) suggests that the magnitude of temperature change within the surface waters did not cross any thresholds leading to significant biotic turnover, unlike during some hyperthermal events of the Paleocene–Early Eocene (e.g., Figure 12).

5.7. CONCLUSIONS

In this chapter, I present new early Danian $\delta^{13}C_{benthic}$ and $\delta^{18}O_{benthic}$ data generated from the South Atlantic Walvis Ridge ODP Site 1262, calibrated to an updated orbitally-tuned age model. I have used these data to generate an orbital-resolution chronology of the Dan-C2 event and elucidate the evolution of bottom water temperatures in the South Atlantic during this time. By integrating a new high-resolution benthic foraminifera assemblage study performed by Dr. Gabriela de Jesús Arreguín Rodríguez, along with other published stable isotope and geochemical data, I have evaluated whether the Dan-C2 event can be classified as a typical hyperthermal. The main conclusions of this chapter are as follows:

- The lack of transient deep-sea warming in the Atlantic and Pacific, along with a lack of significant change in benthic foraminifera

communities, suggest that the Dan-C2 event is not a typical hyperthermal.

- The Dan-C2 event is interpreted to reflect the first 405-kyr eccentricity maximum of the Paleocene, with a magnified expression within bulk and planktic carbon isotope records due to the peculiar oceanographic conditions (i.e., partial collapse of the biological pump and extreme vital effects within opportunistic planktic foraminifera taxa) following the K/Pg mass extinction, along with ongoing Deccan Traps volcanism.

- An apparently significant magnitude of warming in the terrestrial realm and surface ocean is also difficult to reconcile with the lack of temperature change in the deep waters of the global ocean, although these apparent magnitudes of terrestrial and surface water warming could be biased by changes in seasonality and precipitation (i.e., terrestrial freshwater runoff) patterns during this time interval.

- Future work should focus on constraining the geographic variability and magnitude of climatic warming in the terrestrial realm and surface waters, to evaluate the magnitude and scale of environmental change that occurred during Dan-C2.

6. THE COUPLED EVOLUTION OF OCEAN TEMPERATURES AND CARBONATE CHEMISTRY IN THE NORTHERN INDIAN OCEAN DURING THE PALEOCENE–EOCENE

6.1. ABSTRACT

This chapter focuses on understanding trends in ocean temperature and carbonate chemistry in the understudied northern Indian Ocean during the Late Paleocene–Early Eocene. I present the first high-resolution, trace metal (Mg/Ca and B/Ca) and stable isotope, multi-species foraminiferal records generated from IODP Site U1443 and ODP Site 758 on the Ninetyeast Ridge, spanning ~58–53 Ma at orbital resolution. I use these records to discuss the long-term evolution of marine temperature at different depths in the water column [mixed layer (~0–30 m), thermocline (~50–200 m), and intermediate waters (~1500 m)], the evolution of carbonate chemistry (related to pH and/or DIC concentration) of the mixed layer and thermocline, and relative changes in carbonate saturation state at intermediate water depths. A long-term warming trend can be inferred at all water depths studied in the northern Indian Ocean based on rising Mg/Ca values from the Late Paleocene to Early Eocene, interrupted by a brief cooling phase during the latest Paleocene (~57.4–56.4 Ma). Within the mixed layer, a relative temperature rise of ~+2°C from ~58 Ma to 53 Ma, along with mean absolute temperatures of ~30 (±1.4)°C during the Late Paleocene and ~31 (±1.4)°C during the Early Eocene, are comparable to absolute temperatures and the magnitude of warming within the surface ocean of the equatorial Atlantic and Pacific, suggesting a common thermal evolution across the low latitudes globally at this time. Amplified warming of ~+4°C at thermocline depths, with a particularly pronounced step change to warmer temperatures during the PETM and Early Eocene, may be related to downwelling of increasingly saline warm mixed layer waters as net evaporation exceeded net precipitation within subtropical regions during PETM and Early Eocene greenhouse warming. Amplified warming within intermediate waters of the Indian Ocean (~+3°C) relative to the low latitude surface ocean, as well as within deep ocean waters globally (~+5°C), is likely to be related to polar amplification of Early Eocene greenhouse warming. This warming is accompanied by steadily decreasing mixed layer planktic B/Ca ratios, suggesting falling pH and/or increasing DIC, consistent with proxy data for

increasing atmospheric pCO_2 levels and global warming during this time. The benthic B/Ca record provides evidence for a transient drop in carbonate saturation state during the latest Paleocene followed by recovery to pre-excursion values, before a second rapid decrease commenced during the Early Eocene from ~54.5 Ma, preceding global shoaling of the CCD during EECO by ~2.5 million years. A portion of the PETM recovery phase is also resolved within the trace metal record from IODP Site U1443, suggesting a warming of ~+1.7°C to temperatures of ~31.0 (±1.4)°C within the mixed layer, ~+2.7°C to temperatures of ~30.3 (±1.4)°C within the thermocline, and +3.0°C to temperatures of ~14.2 (±1.8)°C in intermediate waters. These absolute temperatures and magnitudes of change are comparable to those from the recovery phase at equatorial Pacific ODP Site 1209, suggesting that a third to a half of the complete magnitude of the PETM has been captured within the new Indian Ocean record. A decrease in B/Ca values suggests that a fall in pH/increase in DIC occurred at all water depths of the Indian Ocean during the PETM, confirming the global scale of ocean acidification during this hyperthermal event. Absolute B/Ca values suggest a Southern Ocean source for thermocline and mixed layer waters during the PETM, potentially due to upwelling of intermediate-deep waters along the southern margin of Eurasia or India.

6.2. INTRODUCTION

6.2.1. APPLYING THE MG/CA PROXY TO THE EARLY PALEOGENE

The Mg/Ca palaeothermometer is based on the strong temperature dependence on the substitution of Mg^{2+} into biogenic calcite, and has emerged as one of the most promising techniques for determining absolute marine temperatures in the deep past as it requires no prior knowledge on the $\delta^{18}O$ of seawater ($\delta^{18}O_{sw}$) or continental ice volumes (e.g., Elderfield & Ganssen, 2000). An exponential positive relationship between Mg/Ca ratios and calcification temperature in foraminiferal calcite, corresponding to a 7–11% increase in Mg/Ca per °C, has been determined by cultivation experiments on modern mixed layer planktic foraminifera (e.g., (Nürnberg et al., 1996; Lea et al., 1999; Russell et al., 2004; Kisakürek et al., 2008), sediment trap studies on planktic and thermocline-dwelling species (e.g., Delaney et al., 1985; Lea et al., 1999; Anand et al., 2003;

McConnell & Thunell, 2005), and core-top analyses on a suite of modern planktic and benthic foraminifera (e.g., Delaney et al., 1985; Nürnberg, 1995; Rosenthal et al., 1997; Elderfield & Ganssen, 2000; Dekens et al., 2002; Lear et al., 2002; Rathmann et al., 2004; Brown et al., 2011). These studies on modern foraminifera have also revealed important inter-species and inter-genera variations in Mg uptake, highlighting the importance of temperature-controlled physiological processes on the incorporation of Mg into biogenic calcite (Rosenthal et al., 1997; Lea et al., 1999). Such findings underscore the need for species-specific calibration equations, where possible, to more accurately estimate absolute temperatures from Mg/Ca data (e.g., Dekens et al., 2002; Evans & Müller, 2012; Lear et al., 2015; Evans et al., 2016a). However, these calibrations only exist for extant species, so for extinct species one must apply either a calibration for a closely related extant relative, or a multi-species calibration equation such as that presented by Anand et al. (2003).

Although temperature exerts the dominant control on Mg uptake under most naturally occurring environmental conditions, secondary controls are exerted by significant changes in salinity (e.g., Kisakürek et al., 2008; Hönisch et al., 2013), carbonate saturation state and hence pH (Lea et al., 1999; Russell et al., 2004; Kisakürek et al., 2008; Evans et al., 2016a), and variations in the primary Mg/Ca ratio of seawater (Mg/Ca_{sw}) from which the foraminifera calcified (Evans & Müller, 2012; Lear et al., 2015; Evans et al., 2015). Although early Paleogene Mg/Ca_{sw} is generally accepted to have been significantly lower than that of today, and typically between ~1.5–2.5 mol/mol based on proxy and modelling studies (e.g., Stanley & Hardie, 1998; Berner, 2004; Dickson, 2004; Demicco et al., 2005; Coggon et al., 2010; Evans & Müller, 2012; Evans et al., 2018), the temporal evolution of Mg/Ca_{sw} during the Late Paleocene–Early Eocene is poorly constrained. Due to the relatively long residence times of Mg (~13 million years) and Ca (~1 million years) in the oceans (Broecker & Peng, 1982; Li, 1982), Mg/Ca_{sw} can be assumed to be constant over 10,000–100,000 year timescales. However, where it can be quantified, corrections to account for changing Mg/Ca_{sw} with time should be taken into account when constructing long-term (multi-million year) temperature records using the Mg/Ca proxy. Mg/Ca_{sw} proxy estimates for the early Paleogene have been determined by isolating the temperature and biological controls on Mg uptake within foraminiferal carbonate

from the control of changing Mg/Ca_{sw}. This can be achieved, for example, by coupling the Mg/Ca proxy with an independent temperature proxy such as clumped isotopes on the same foraminiferal sample (Evans et al., 2018), or by analysing Mg/Ca ratios within inorganic carbonate veins of a known age (Coggon et al., 2010), and echinoderm fragments which are believed to exhibit a relatively minor discrimination against Mg compared to foraminifera (Dickson, 2002, 2004). Mg/Ca_{sw} proxy data for the early Paleogene (especially the Paleocene) are very sparse, however, hampering our understanding of the evolution of Mg/Ca_{sw} during this enigmatic time interval (e.g., Evans & Müller, 2012).

As well as environmental controls on Mg uptake during growth, post-depositional processes can also significantly modify primary planktic foraminiferal Mg/Ca ratios and therefore absolute temperature estimates. Post-depositional dissolution of carbonate tests below the lysocline preferentially removes the most impure (high-Mg) calcite, therefore biasing Mg/Ca-derived temperature estimates towards cooler values (Rosenthal & Boyle, 1993; Brown & Elderfield, 1996; Rosenthal et al., 2000; Dekens et al., 2002; Regenburg et al., 2006; Regenburg et al., 2014). Due to the higher solubility of Mg-rich calcite, preferential dissolution of this phase can commence at a significantly shallower depth than the saturation horizon and lysocline for low-Mg calcite (Rosenthal et al., 2000). The diagenetic recrystallisation of inorganic calcite can also modify primary Mg/Ca values of planktic foraminifera, however the direction of bias (i.e., to higher or lower values) may be difficult to decipher. Since diagenetic recrystallisation typically takes place on the seafloor or beneath the sediment-water interface, where temperatures are significantly cooler than calcification temperatures within the warm surface waters (e.g., Kozdon et al., 2011, 2013), such recrystallisation could in theory bias Mg/Ca-derived temperature estimates towards cooler values. However, since the Mg distribution coefficient (D_{Mg}) is significantly higher for inorganic calcite compared to biogenic calcite, diagenetic recrystallisation of inorganic calcite, even in a colder environment, could potentially increase primary Mg/Ca ratios in highly recrystallised foraminifera specimens (e.g., Oomori et al., 1987; Erez, 2003; Kozdon et al., 2013). Furthermore, Kozdon et al. (2013) demonstrated that recrystallisation of inorganic calcite derived from dissolution of biogenic calcite can exert a negligible influence on the Mg/Ca ratios of recrystallised specimens. These findings demonstrate that the effects of

diagenetic recrystallisation on primary Mg/Ca ratios in planktic foraminifera is a complex process, and underscore the importance of using well-preserved foraminifera specimens without evidence for significant dissolution or recrystallisation when reconstructing absolute temperature estimates using the Mg/Ca palaeothermometer proxy.

The Mg/Ca proxy has been extensively used to deconvolve the temperature and ice volume components from $\delta^{18}O_{benthic}$ data during Plio-Pleistocene and Quaternary glacial-interglacial cycles (e.g., Mashiotta et al., 1999; Elderfield & Ganssen, 2000; Lea et al., 2000; Lea et al., 2002; Sosdian & Rosenthal, 2009; Elderfield et al., 2012), as well as to isolate changes in temperature and ice volume build-up on Antarctica across the Eocene/Oligocene transition (Wade et al., 2012), and to track long-term Cenozoic trends in climate over the past 50 million years (Lear et al., 2000). During a time period believed to lack a significant build up of polar continental ice sheets, the Mg/Ca proxy can also be employed alongside stable oxygen isotopes ($\delta^{18}O$) to estimate both changes in temperature and changes in $\delta^{18}O_{sw}$ (to identify any major changes in net precipitation/evaporation), during the early Paleogene Period. The few early Paleogene studies to date have mainly focussed on temperature change during larger hyperthermal events such as the PETM (e.g., Zachos et al., 2003; Tripati & Elderfield, 2004, 2005; Bornemann et al., 2014; Hollis et al., 2015; Babila et al., 2016) and ETM-2 (Harper et al., 2018), with only a handful of low-resolution longer-term studies encompassing this time period more broadly (Lear et al., 2000; Tripati et al., 2003; Dutton et al., 2005a; Lear et al., 2015). Furthermore, previous Paleogene studies have mainly been focussed on sites in or bordering the Atlantic and Pacific oceans, with a complete lack of data from the Indian Ocean, hampering our understanding of the temperature evolution in this poorly studied ocean basin during the early Paleogene greenhouse world. Our understanding of the broader low latitude response to greenhouse warming and ability to quantify equator-pole temperature gradients have also been hampered by the paucity of Late Paleocene–Early Eocene marine records comprising suitably well-preserved foraminifera for the generation of reliable Mg/Ca data from the low latitudes and equatorial regions.

The planktic foraminifera from IODP Site U1443 and ODP Site 758 on the crest of the shallow Ninetyeast Ridge, were deposited at a paleo-depth of ~1500 m (Shipboard Scientific Party, 1989, 2016), well above the early Paleogene CCD (~4000 m; Slotnick et al., 2015), and therefore represent an ideal opportunity to generate the first long-term orbital-resolution Mg/Ca-derived temperature record for the Late Paleocene–Early Eocene, and the first record of its kind for this time period from the Indian Ocean and the low-latitudes in general. In addition to unravelling the long-term temperature evolution, the resolution of this Mg/Ca record (~14–42 kyr) also allows us to resolve the magnitude of temperature change across some key hyperthermals (including the PETM), as well as smaller eccentricity-paced climatic events of this time period.

6.2.2. APPLYING THE B/CA PROXY TO THE EARLY PALEOGENE

B/Ca ratios in planktic and benthic foraminiferal carbonate represent a novel method of estimating changes in carbonate chemistry (related to pH) at various depths within the water column of the oceans in the deep past. Empirical studies correlating B/Ca ratios in planktic foraminiferal calcite to pH were carried out by Hemming & Hanson (1992). Boron is present in seawater almost exclusively as either borate [$B(OH)_4^-$] or boric acid [$B(OH)_3$]. Hemming & Hanson (1992) observed that boron isotopic compositions of modern marine carbonates all fall within the range of 22.1‰ (±3‰), which is very similar to the isotopic composition of $B(OH)_4^-$ (19.4–24.1‰) but not $B(OH)_3$ (40.4–45.2‰). They therefore suggested that negatively charged $B(OH)_4^-$ is the predominant form of B incorporated into foraminiferal carbonate, where it substitutes for the carbonate (CO_3^{2-}) ion. Since there is a strong pH control on the relative abundance of $B(OH)_4^-$ versus $B(OH)_3$ in ocean water, whereby $B(OH)_4^-$ is the dominant species at higher pH, these early studies predicted a strong pH control on B incorporation into foraminiferal calcite. As a consequence, B/Ca ratios were interpreted to reflect the relative abundance of $B(OH)_4^-$, or more specifically, the $B(OH)_4^-/HCO_3^-$ ratio, and therefore positively correlate with pH of the ocean waters from which the foraminifera calcified. These early ideas of Hemming & Hansen (1992) have been broadly supported by studies on synthetic carbonates (Hemming et al., 1995; Sanyal et al., 2000; He et al., 2013) and laboratory-controlled culture studies (Henehan et al., 2013, 2015; Allen et al., 2011). More recent studies

suggest that B/Ca is better defined as a proxy for the $B(OH)_4^-$/DIC ratio, as $B(OH)_4^-$ competes with HCO_3^- and potentially also CO_3^{2-} for inclusion in the calcite lattice (Haynes et al., 2017).

However, core-top and sediment trap studies on modern planktic foraminifera from the open ocean have questioned whether pH is the only or dominant control on B incorporation into planktic foraminiferal calcite in the natural environment. Salinity, nutrient (predominantly phosphate; $[PO_4^{3-}]$) concentrations, DIC, B concentration in seawater ($[B]_{sw}$), temperature, test size and growth rate have all been proposed to affect the incorporation of B into biogenic calcite (e.g., Wara et al., 2003; Hönisch & Hemming, 2004; Yu et al., 2007; Allen et al., 2011, 2012, Allen & Hönisch, 2012; Naik & Naidu, 2014; Henehan et al., 2013, 2015; Haynes et al., 2017).

To minimise the competing effects of significant changes in salinity and nutrient concentrations on B/Ca records, an open ocean site far from major locations of upwelling or freshwater runoff must be chosen. However, the calculation of relative surface ocean pH change based on the planktic B/Ca proxy is still complicated in open ocean sites by the negative correlation observed in culture studies between B/Ca ratios and DIC (e.g., Allen et al., 2011; Haynes et al., 2017), as well as a species-specific temperature dependence on the partition coefficient (K_D) of $B(OH)_4^-$ between planktic foraminiferal carbonate and seawater (Yu et al., 2007). Since increasing DIC and decreasing pH will both work in the same direction to lower B/Ca ratios during hyperthermal events (such as the PETM), without a sound understanding of the magnitude of change within the surface ocean DIC reservoir, estimates of relative pH change based on the B/Ca proxy during time periods characterised by a dynamic carbon cycle will be significantly overestimated (Haynes et al., 2017). By contrast, a positive correlation between calcification temperature and B/Ca ratios, determined in modern planktic foraminifera based on core top studies, could serve to partially counteract the effects of decreasing pH on B/Ca ratios during hyperthermal events, and hence result in an underestimation of pH change (Wara et al., 2003; Yu et al., 2007). Furthermore, since there is a positive correlation between $[B]_{sw}$ and B/Ca ratios, corrections to account for varying $[B]_{sw}$ in the geological past must also be taken in account when constructing multi-million year B/Ca records

(e.g., Kender et al., 2014), despite the long residence time (~20 million years) of boron in the oceans (Spivack and Edmond, 1987). Deep time studies, such as during the Paleogene period, are further complicated by the use of planktic foraminifera species that are now extinct. Such studies therefore rely on using calibrations from a closely related extant relative for which modern core top, sediment trap, or culture studies relating changing B/Ca to carbonate system parameters exist, with the added assumption that B incorporation into such fossil species was controlled by the same parameters (e.g., Brown et al., 2011; Evans & Müller, 2012).

In addition to primary environmental controls on B uptake, post-depositional dissolution of planktic foraminiferal carbonate can also preferentially remove B-enriched calcite and therefore lower the primary B/Ca ratio (e.g., Coadic et al., 2013). By contrast, epifaunal benthic foraminifera appear to be a much more robust proxy for carbonate saturation state of bottom waters (e.g., Brown et al., 2011; Rae et al., 2011), and also appear to be unaffected by dissolution (Coadic et al., 2013).

Despite these limitations, the B/Ca proxy has been extensively and successfully applied to elucidate changes in carbonate chemistry (related to relative pH change) during the Holocene and glacial-interglacial cycles (e.g., Yu et al., 2007; Foster, 2008; Yu et al., 2010). However, Paleogene applications of this proxy are very sparse and are entirely focused on the PETM (e.g., Penman et al., 2014; Babila et al., 2016, 2018), with no context from longer-term records. To date, there have been no studies focusing on longer term early Paleogene trends in carbonate chemistry using B/Ca, and certainly none from the Indian Ocean. The shallow palaeo-depth (~1500 m; Shipboard Scientific Party, 1989, 2016) of the open-ocean IODP Site U1443 and ODP Site 758 makes these sites ideal for constructing both planktic and benthic B/Ca records, and for generating the first long-term orbital-resolution records of carbonate chemistry change (related to pH, DIC, and carbonate saturation state) from the Indian Ocean.

6.3. AIMS AND OBJECTIVES

The overaching goal of this chapter is to identify the long-term evolution of temperature and carbonate chemistry (related to pH and DIC concentration) within the mixed layer, thermocline, and intermediate waters of the low latitude Indian Ocean during the Late Paleocene–Early Eocene (~58–53 Ma), and to identify if the characteristics of the low latitude Indian Ocean are typical of the low latitudes globally. In addition, the evolution of temperature and carbonate chemistry during the PETM and larger orbitally-paced climatic events of this time period will be investigated. Specific questions to be addressed are:

- How did marine temperatures in the mixed layer (~0–30 m), thermocline (~50–200 m), and at intermediate depths (~1500 m) above IODP Site U1443 and ODP Site 758 evolve from the peak of the PCIM to the Early Eocene (~58–53 Ma)?

- Are absolute temperatures and the thermal evolution of the mixed layer of the low latitude Indian Ocean during the Late Paleocene–Early Eocene characteristic of the low latitudes globally?

- Are absolute temperatures and the thermal evolution of the intermediate waters of the low latitude Indian Ocean characteristic of global intermediate to deep water masses during this time period, and is there a coupled thermal evolution between the high latitude regions of deep water production and the low latitudes?

- Were there any significant changes in $\delta^{18}O_{sw}$ during this time interval, related to changes in net precipitation or evaporation (hence sea surface salinity) in the low southern latitudes (assuming an ice-free world)?

- How did the temperature gradient between the mixed layer and thermocline, as well as between the mixed layer and intermediate waters, evolve during this time period?

- What was the direction and magnitude of mixed layer carbonate chemistry change above IODP Site U1443 and ODP Site 758 during this time period?

- Were there any relative changes in carbonate saturation state within intermediate waters bathing IODP Site U1443 and ODP Site 758 during this time period?

- Can these trace metal proxies as applied to IODP Site U1443 and ODP Site 758 be used to quantify the magnitude of change in temperature and carbonate chemistry during orbital (400-kyr and 100-kyr) cycles of the Late Paleocene–Early Eocene?

- What portion of the PETM has been captured within the trace metal record from IODP Site U1443 and how does the magnitude of change in temperature and carbonate chemistry within the low latitude Indian Ocean compare to the better studied Atlantic and Pacific oceans?

6.4. METHODS

6.4.1. DATA SOURCES

Lithostratigraphy, sample strategy, and all sedimentological and geochemical method information for samples from ODP Site 758 and IODP Site U1443 is presented in **Chapter 2 Sections 2.1–2.3** and **2.5**. The location of the deep-sea sites used in this chapter is shown in Figure 54. Further details about these sites are listed in Table 10.

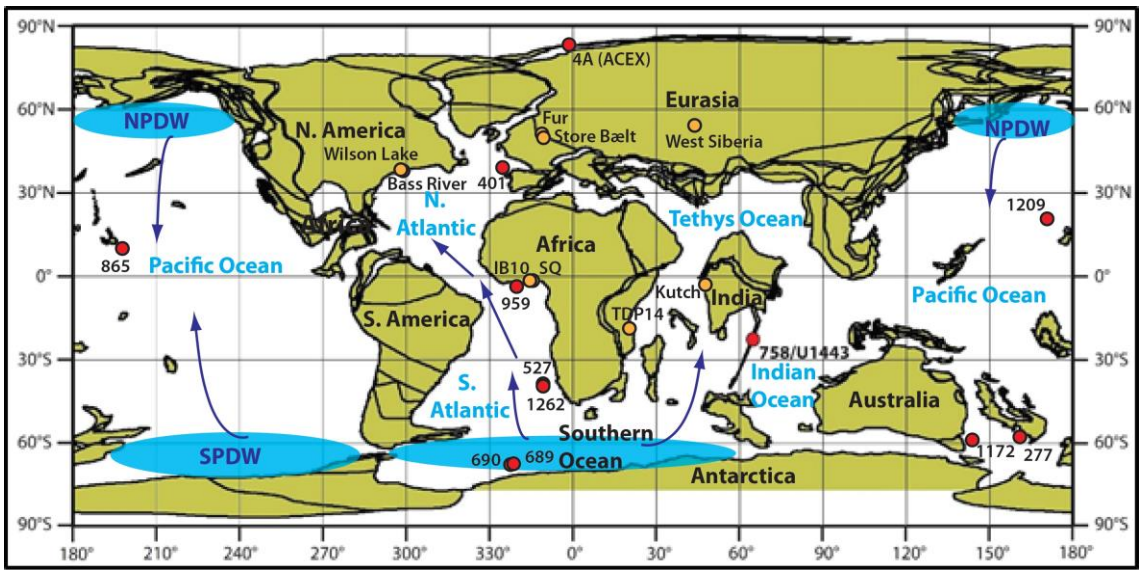

Figure 54. Paleocene/Eocene boundary time (~56 Ma) palaeogeographic reconstruction with locations of the deep-sea sites (in red) and onshore sites (in orange) used in this chapter (also see Table 10). Locations of the principle areas of deep water formation are indicated by blue shading with the following abbreviations: NPDW = North Pacific Deep Water. SPDW = South Pacific Deep Water (Thomas et al., 2003, 2008). The predicted movement of deep water masses is indicated by dark blue arrows. Adapted from the Ocean Drilling Stratigraphic Network (ODSN) Paleomap Project (http://www.odsn.de/odsn/services/paleomap/paleomap.html). SQ = Sagamu Quarry. TDP14 = Tanzania Drilling Project Site 14.

Table 10

Site	Current Lat.	Current Long.	Palaeo-lat. at 56 Ma	Current water depth (m)	Palaeo-water depth (m) at 56 Ma	Data type	Source of data
IODP Site U1443	5.4°N	90.4°E	28.6°S	2929.4	~1500	Mg/Ca B/Ca $\delta^{13}C_{bulk}$ $\delta^{13}C_{planktic}$ $\delta^{18}O_{planktic}$	This study
ODP Site 758	5.4°N	90.4°E	28.6°S	2923.6	~1500	Mg/Ca B/Ca $\delta^{13}C_{bulk}$ $\delta^{13}C_{planktic}$ $\delta^{18}O_{planktic}$	This study
ODP Site 865	18.4°N	179.6°W	10.5°N	1516.2	~1300–1500	Mg/Ca $\delta^{13}C_{planktic}$	Tripati et al. (2003); Tripati & Elderfield (2004, 2005)
ODP Site 1262	27.2°S	1.6°E	40.6°S	4759	~3500	$\delta^{13}C_{benthic}$ $\delta^{18}O_{benthic}$ Mg/Ca	Littler et al. (2014) Lauretano et al. (2015) Littler (pers. comm)
ODP Site 1209	32.7°N	158.5°E	22.8°N	2387	~2000–2500	Mg/Ca B/Ca $\delta^{13}C_{planktic}$ $\delta^{18}O_{benthic}$	Zachos et al. (2003); Penman et al. (2014); Westerhold et al. (2011, 2018); Tripati &

							Elderfield (2005); Dutton et al. (2005a,b)
DSDP Site 527	28.0°S	1.8°E	41.4°S	4428.0	~3400	Mg/Ca $\delta^{13}C_{planktic}$	Tripati & Elderfield (2004, 2005)
ODP Site 959	3.6°N	2.7°W	9.5°S	2090.7	~2500	TEX_{86}^{H}	Frieling et al. (2018); Cramwinckel et al. (2018)
ODP Site 689	64.5°S	3.1°E	71.0°S	2080.3	~1500–2000	B/Ca	Babila et al. (2018)
ODP Site 690	65.2°S	1.2°E	72.8°S	2914	~2500	Mg/Ca B/Ca	Lear et al. (2015) Babila et al. (2018)
IODP 302 Site 4A (ACEX)	87.9°N	136.2°E	76.7°N	1288	~50–100	TEX_{86}^{H}	Sluijs et al. (2006, 2008)
ODP Site 1172	44.0°S	149.9°E	58.5°S	2621.7	~50–100	TEX_{86}^{H}	Bijl et al. (2009); Sluijs et al. (2011)
DSDP Site 277	52.2°S	166.2°E	54.8°S	1214	~1000–2000	Mg/Ca	Hollis et al. (2015)
DSDP Site 401	47.4°N	8.8°W	36.0°N	2495	~1800–2000	Mg/Ca	Bornemann et al. (2014)
D.G.I. 83101, Store Bælt, Denmark	55.4°N	11.1°E	44.7°N	50	~200	TEX_{86}^{H}	Schoon et al. (2015)
IB10B Core, Nigeria	6.9°N	3.0°E	7.1°S	Subaerial	~50–100	Mg/Ca TEX_{86}^{H}	Frieling et al. (2017)
Sagamu Quarry, Nigeria	6.8°N	3.6°E	7.3°S	Subaerial	~50–100	Mg/Ca TEX_{86}^{H} $\delta^{18}O_{planktic}$	Frieling et al. (2017)
Tanzania Drilling Project Site 14	9.3°S	39.5°E	25.0°S	Subaerial	>300	$\delta^{18}O_{planktic}$	Pearson et al. (2007); Aze et al. (2014)
Kutch, India	23.4°N	69.8°E	6.0°S	Subaerial	<50	Clumped isotopes (Δ_{47})	Evans et al. (2018)
Bass River, USA	39.6°N	74.4°W	34.6°N	Subaerial	~80–150	Mg/Ca B/Ca	Babila et al. (2016)
Wilson Lake, USA	39.7°N	75.0°W	34.9°N	Subaerial	~80–150	TEX_{86}^{H}	Zachos et al. (2006)
Fur, Denmark	56.8°N	9.0°E	45.8°N	Subaerial	~100–200	TEX_{86}^{H}	Schoon et al. (2015)
West Siberia	53.5°N	73.5°E	51°N	Subaerial		TEX_{86}^{H}	Frieling et al. (2014)

Details of sites with data included in this study. Present-day latitudes, longitudes, water depths and palaeo-water depths for each deep-sea site are from the initial scientific reports for each site (Shipboard Scientific Party, 1975, 1979, 1984b, 1988a, 1988b, 1989, 1993, 1996, 2001, 2002a, 2004, 2016; Moore et al., 2006), and from the data reference cited for onshore sites. Palaeo-latitudes for the sites at Paleocene/Eocene boundary time (~56 Ma) were computed relative to the palaeomagnetic reference frame of Torsvik et al. (2012), using Version 2.1 of the model from paleolatitude.org (van Hinsbergen et al., 2015). Types of data incorporated from each site, along with data sources, are listed in the two right-hand columns.

6.4.2. FORAMINIFERA SPECIES

This section describes the rationale behind the choice of foraminifera species picked for trace metal analysis, under the supervision of Dr. Kirsty Edgar (University of Birmingham). Specific details related to foraminifera picking (e.g., size fractions and masses of carbonate required) are detailed in **Chapter 2 Section 2.5.4**.

6.4.2.1. SPECIES LIVING IN THE MIXED LAYER

Morozovella velascoensis was picked for Late Paleocene mixed layer trace metal (Mg/Ca & B/Ca) and stable isotope ($\delta^{13}C$ and $\delta^{18}O$) data, as it represents the most abundant and easily identifiable species within the Late Paleocene sample set. Since *M. velascoensis* becomes extinct after the PETM (Pearson et al., 2006), *M. subbotinae-marginodentata plexus* was picked from the Early Eocene samples. *M. subbotinae-marginodentata plexus* represents two species (*Morozovella subbotinae* and *Morozovella marginodentata*) which are almost indistinguishable under the optical microscope and characterised by comparable $\delta^{13}C$ and $\delta^{18}O$ signatures to *M. velascoensis* (D'Hondt et al., 1994), therefore are likely to have inhabited a very similar environmental niche to each other as well as *M. velascoensis*. A comparison between the $\delta^{13}C$ (Table 11) and Mg/Ca data (Table 12) from *M. subbotinae-marginodentata plexus* and *M. velascoensis* analysed during this study confirms a negligible offset in $\delta^{13}C$, and trace metal values that fall within analytical uncertainty. Based on a similar association with low-mid latitude surface waters as modern photosymbiotic foraminifera and comparable trends in $\delta^{13}C$ and $\delta^{18}O$ values with increasing test size, these *Morozovella* species are believed to have harboured algal symbionts and must therefore have been restricted to the mixed layer photic zone throughout their life cycle (D'Hondt et al., 1994). These species of *Morozovella* can therefore record the evolution of temperature and carbonate chemistry of the integrated mixed layer from ~0–30 m below the surface (Frieling et al., 2017).

Table 11

Core sample	Depth (mbsf)	$\delta^{13}C$ (‰) *M. velascoensis*	$\delta^{13}C$ (‰) *M. subbotinae-marginodentata plexus*	$\delta^{13}C$ difference (‰)
U1443A-35X-3, 40.5–41.5 cm	248.31	3.46	3.49	–0.03
U1443A-35X-3, 24–25 cm	248.15	3.39	3.60	–0.21
U1443A-35X-3, 13–14 cm	248.04	3.33	3.44	–0.11
U1443A-35X-3, 10–11 cm	248.01	3.45	3.36	+0.09
Mean				**–0.07**

Comparison of planktic stable carbon isotope ($\delta^{13}C_{planktic}$) data between Morozovella velascoensis and M. subbotinae-marginodentata plexus, confirming a negligible offset in $\delta^{13}C$ between species.

Table 12

Core sample	Depth (mbsf)	Mg/Ca (mmol/mol) *M. velascoensis*	Error (± 3%) *M. velascoensis*	Mg/Ca (mmol/mol) *M. subbotinae-marginodentata plexus*	Error (± 3%) *M. subbotinae-marginodentata plexus*	Mg/Ca difference
U1443A-35X-3, 40.5–41.5 cm	248.31	4.45	±0.13	4.67	±0.14	–0.22
758A-28X-2, 139.5–140.5 cm	259.81	3.49	±0.11	3.49	±0.11	0
758A-28X-3, 30–31 cm	260.22	3.61	±0.11	3.51	±0.11	+0.10
Mean						**–0.04**

Comparison of foraminiferal magnesium/calcium (Mg/Ca) data between Morozovella velascoensis and M. subbotinae-marginodentata plexus, confirming that the trace metal data from both species generally fall within analytical uncertainty (± 3%).

6.4.2.2. SPECIES LIVING IN THE THERMOCLINE

The coarsely cancellate, thermocline-dwelling species *Subbotina velascoensis* was picked for Late Paleocene thermocline trace metal data, as it represents the most abundant and easily identifiable *Subbotina* species within the Late Paleocene sample set. Since *S. velascoensis* becomes extinct during the Early Eocene after the PETM (Pearson et al., 2006), the closely related coarsely cancellate species *S. hornibrooki,* which evolved during the Early

Eocene since the PETM (Pearson et al., 2006), was picked from Early Eocene samples. A comparison between Mg/Ca data suggests that trace metal values fall within analytical uncertainty for both species (Table 13).

Table 13

Core sample	**Depth (mbsf)**	**Mg/Ca (mmol/mol) *S. velascoensis***	**Error (±3%) *S. velascoensis***	**Mg/Ca (mmol/mol) *S. hornibrooki***	**Error (±3%) *S. hornibrooki***	**Mg/Ca difference**
U1443A-35X-3, 40.5–41.5 cm	248.31	4.25	±0.13	4.35	±0.13	–0.10
U1443A-35X-3, 10–11 cm	248.01	4.26	±0.13	4.23	±0.13	0.03
Mean						**–0.04**

Comparison of foraminiferal magnesium/calcium (Mg/Ca) data between Subbotina velascoensis and S. hornibrooki from two earliest Eocene samples immediately post-dating the PETM. The difference in Mg/Ca values between the two species falls well within analytical uncertainty (± 3%).

6.4.2.3. SPECIES LIVING IN THE BOTTOM (INTERMEDIATE) WATERS

The cosmopolitan epifaunal benthic species *Nuttallides truempyi* was picked to generate intermediate water B/Ca data. The use of an epifaunal species is vital for reconstructing intermediate water B/Ca (and hence relative changes in carbonate saturation state), as the B/Ca of infaunal species is buffered by pore water chemistry and, therefore, is unsuitable for reconstructing short-term changes in intermediate water carbonate chemistry (Brown et al., 2011). In addition, benthic B/Ca–carbonate saturation state calibrations exist for the closely related extant relative *Nuttallides umbonifera* (Brown et al., 2011).

The shallow infaunal benthic species *Oridorsalis umbonatus* was picked for intermediate water Mg/Ca data. Since pore waters are relatively buffered against transient changes in carbonate saturation state, the use of a shallow infaunal species minimises the effects of significant changes in pH on Mg/Ca ratios (e.g., Lear et al., 2015). Furthermore, since *O. umbonatus* is an extant species, temperature calibrations have been developed based on modern core-top studies (e.g., Lear et al., 2002; Rathmann et al., 2004; Lear et al., 2015).

6.4.3. CONVERSION OF PLANKTIC MG/CA DATA TO ABSOLUTE TEMPERATURE ESTIMATES

The primary Mg/Ca ratio recorded by foraminiferal tests in the open ocean is not only a function of temperature but also of the pH and Mg/Ca ratio of seawater (Mg/Ca_{sw}) from which the foraminifera calcified (e.g., Evans & Müller, 2012; Evans et al., 2016a). Therefore, an accurate temperature calibration must take into account both a temperature dependency and a component to account for differences in pH and Mg/Ca_{sw} in the deep past relative to the modern. Furthermore, transient decreases in surface ocean pH across specific hyperthermal events (e.g., the PETM) must also be taken into account where they can be constrained (e.g., Penman et al., 2014; Gutjahr et al., 2017), otherwise both absolute temperature estimates and the magnitude of relative temperature changes will be overestimated (e.g., Evans et al., 2016a).

The evolution of ambient seawater pH during the Late Paleocene–Early Eocene is currently poorly constrained. Based on a low-resolution study, Tyrell & Zeebe (2004) suggest an ambient pH of ~7.7 during the early Paleogene. A similar pH value has been adopted for the pre-PETM surface ocean by Penman et al. (2014) and Gutjahr et al. (2017), therefore a value of 7.7 has been adopted for this thesis. However, proxy data based on boron isotopes ($\delta^{11}B$) are available for the PETM, suggesting a drop in pH of 0.3 units (from ~7.7 to ~7.4) in association with a large injection of greenhouse gases into the exogenic carbon cycle (Penman et al., 2014; Gutjahr et al., 2017). Since the magnitude of the PETM excursion in the carbon isotope record from IODP Site U1443 represents approximately a third to a half of the typical magnitude of the PETM carbon isotope excursion at other deep-sea sites (e.g., Zachos et al., 2003; McInerney & Wing, 2011; see **Section 6.6.1.** and **Section 6.7.1.**), a value for PETM pH of 7.6 has been modelled during the portion of the PETM resolved in the new Mg/Ca record presented in this thesis.

Prior to performing temperature calculations, the complete surface and subsurface planktic Mg/Ca dataset was pH-corrected using the following linear correction (Evans et al., 2016a):

$$Mg/Ca_{test} = -0.70 \times pH + 6.7 \quad \textit{[Eq. 6]}$$

where Mg/Ca_{test} is the measured Mg/Ca value in foraminiferal tests, ambient pH is modelled as 7.7, and PETM pH is modelled as 7.6.

Mg/Ca ratios in planktic foraminiferal tests exhibit an exponential dependence on temperature of the seawater from which they calcify, in the form (e.g., Anand et al., 2003):

$$Mg/Ca_{test}^{pH} = B \times exp^{(AT)} \quad \textit{[Eq. 7]}$$

where Mg/Ca_{test}^{pH} is the pH-corrected Mg/Ca value in foraminiferal tests, *B* and *A* are the pre-exponential and exponential constants in the temperature calibration respectively, and *T* is temperature in °C.

Since all early Paleogene planktic foraminifera species are now extinct, species-specific temperature calibrations for the fossil species used in this study do not exist. Therefore, the multi-species temperature calibration of Anand et al. (2003), based on a 6-year culture study involving 10 species of modern planktic foraminifera, has been adopted in this study:

$$Mg/Ca_{test}^{pH} = 0.38(\pm 0.02) \times exp^{[0.090(\pm 0.003) \times T]} \quad \textit{[Eq. 8]}$$

To correct for the difference in early Paleogene Mg/Ca_{sw} compared to the modern, firstly a knowledge of Mg/Ca_{sw} during the time period of interest is required. Proxy data for the early Paleogene are very sparse and characterised by significant uncertainty on absolute values (e.g., Dickson, 2002; Evans et al., 2018). However, modelling studies by Stanley & Hardie (1998) and Demicco et al. (2005), which were consistent with the limited proxy dataset available at the time (within uncertainty), predict a mean Mg/Ca_{sw} of ~1.5 mol/mol during the Late Paleocene–Early Eocene. More recently, Evans et al. (2018) have generated proxy data for the Early Eocene, suggesting Mg/Ca_{sw} of ~2.5 mol/mol. Since the temporal evolution of Mg/Ca_{sw} from the Late Paleocene to Early Eocene cannot be accurately constrained by the currently available sparse proxy dataset, it is not

possible to accurately correct for secular changes in Mg/Ca_{sw} across the Mg/Ca record presented in this thesis. However, to encompass the range of possible values for Late Paleocene–Early Eocene Mg/Ca_{sw}, values of 1.5 mol/mol and 2.5 mol/mol have been used in the temperature calibration to provide a range of plausible estimates for absolute temperature. Temperatures calibrated using a value for Mg/Ca_{sw} of 2.5 mol/mol are considered the most robust, as this value is based on proxy data from the Early Eocene (Evans et al., 2018), whilst the value of 1.5 mol/mol is derived from older modelling outputs constrained by sparse proxy data (Stanley & Hardie, 1998, and Demicco et al., 2005).

Recent work has suggested that the relationship between Mg/Ca_{sw} and Mg/Ca_{test} is best described by a power curve function fit (Ries, 2004; Hasiuk & Lohmann, 2010) in the form:

$$Mg/Ca_{test}^{pH} = \frac{F \times Mg/Ca_{sw}^{t=t^H}}{F \times Mg/Ca_{sw}^{t=0^H}} \qquad \textit{[Eq. 9]}$$

where *F* is the pre-exponential constant (which cancels out in the equation), $Mg/Ca_{sw}^{t=t^H}$ is the Mg/Ca value of seawater during the time period of interest (early Paleogene; modelled as 2.5 mol/mol or 1.5 mol/mol) to the power of a species-specific constant, *H*; and $Mg/Ca_{sw}^{t=0^H}$ is the primary Mg/Ca value of modern day seawater (5.17 mol/mol; Dickson, 2002) to the power of a species-specific constant, *H*. The value of *H* can only be accurately calibrated for extant planktic foraminifera, with a culture study by Delaney et al. (1985) on *Globigerinoides sacculifer* giving a preliminary value for *H* of 0.41, and a more recent culture study by Evans et al. (2016b) on *Globigerinoides ruber* giving a value for *H* of 0.79. Since temperature calibrations using *H* = 0.41 and Mg/Ca_{sw} = 2.5 mol/mol produce absolute mixed layer temperature estimates that are significantly cooler than other proxy and modelling estimates for the low latitudes during the early Paleogene (e.g., Frieling et al., 2017; Evans et al., 2018), I have used *H* = 0.79 and Mg/Ca_{sw} = 2.5 mol/mol for the temperature calibrations presented in this thesis.

Therefore, the complete temperature calibration used to calculate absolute temperature estimates from the mixed layer and thermocline planktic data in this thesis can be described by the following:

$$Mg/Ca_{test}^{pH} = \frac{F \times Mg/Ca_{sw}^{t=t^H}}{F \times Mg/Ca_{sw}^{t=0^H}} \times B \times exp^{(AT)} \qquad \textit{[Eq. 10]}$$

This can then be rearranged to make temperature (*T*) the subject as follows:

$$T = \frac{\ln(Mg/Ca_{test}^{pH} \times \frac{Mg/Ca_{sw}^{t=0^H}}{Mg/Ca_{sw}^{t=t^H}} \times \frac{1}{B})}{A} \qquad \textit{[Eq. 11]}$$

The uncertainty associated with absolute planktic Mg/Ca-derived temperature estimates includes a small component of analytical uncertainty (±0.3°C), based on the ±3% analytical uncertainty on the Mg/Ca measurements, and a larger component of calibration error (±1.13°C; Anand et al., 2003), giving a total uncertainty of ±1.4°C. This uncertainty value is still a conservative one however, as it does not include uncertainty associated with the Late Paleocene–Early Eocene evolution of Mg/Ca_{sw}, pH and salinity.

6.4.4. CALCULATION OF SURFACE OCEAN $\delta^{18}O_{sw}$

Absolute values and the magnitudes of excursions in $\delta^{18}O$ recorded in planktic foraminiferal calcite are a function of both temperature and the oxygen isotope composition of seawater ($\delta^{18}O_{sw}$) from which the foraminifera calcified. Since the light isotope (^{16}O) is preferentially evaporated from the sea surface, $\delta^{18}O_{sw}$ can be used as a proxy for changes in net evaporation/precipitation within the subtropical surface ocean above IODP/ODP Sites U1443/758, assuming an ice-free world during the Late Paleocene to Early Eocene. Since Mg/Ca and $\delta^{18}O_{planktic}$ data were generated for the same mixed layer foraminiferal samples, the temperature component controlling excursions in $\delta^{18}O_{planktic}$ can be removed, allowing estimates of $\delta^{18}O_{sw}$ to be calculated. $\delta^{18}O_{sw}$ was calculated using the following temperature equation from Bemis et al. (1998), based on a culturing study of the modern planktic foraminifera *Orbulina universa* under low light conditions:

$$\delta^{18}O_{sw} = 0.27 + (T\ (°C) - 16.5 + 4.8 * \delta^{18}O_{calcite} / 4.8 \qquad [Eq.\ 12]$$

where *T* is temperature (in °C) and $\delta^{18}O_{calcite}$ is the measured value of $\delta^{18}O$ in planktic foraminiferal calcite (in VPDB). Whilst the absolute calculated values of $\delta^{18}O_{sw}$ are dependent on the temperature value used in the equation, positive or negative shifts in $\delta^{18}O_{sw}$ can be used as a proxy for an increase or decrease in salinity of the surface waters, respectively. Mg/Ca-derived temperature estimates calculated assuming Mg/Ca_{sw} = 2.5 mol/mol were used to estimate $\delta^{18}O_{sw}$, as this value is considered the most robust.

6.4.5. CONVERSION OF BENTHIC MG/CA DATA TO ABSOLUTE TEMPERATURE ESTIMATES

Unlike the extinct planktic species used in this thesis, the benthic foraminifera *Oridorsalis umbonatus* is extant and therefore several linear and exponential species-specific temperature calibrations exist (e.g., Lear et al., 2000; Rathmann et al., 2004; Bryan & Marchitto, 2008; Lear et al., 2010; Lear et al., 2015). I have used the exponential temperature calibration in the following form (modified from Ries, 2004):

$$Mg/Ca_{test} = B \times {Mg/Ca_{sw}}^{H} \times exp^{(A \times BWT)} \qquad [Eq.\ 13]$$

where Mg/Ca_{test} is the measured value of Mg/Ca in foraminiferal tests, *B* is the pre-exponential constant, Mg/Ca_{sw} is the Mg/Ca ratio of Late Paleocene–Early Eocene seawater to the power of a species-specific constant, *H*; *A* is the exponential constant, and *BWT* is bottom water temperature. In this thesis, I have used the temperature calibration of Lear et al. (2015), which has been used to calculate Paleocene–Eocene bottom water temperatures which are consistent with benthic $\delta^{18}O$-derived temperatures from the same site. Since *O. umbonatus* Mg/Ca appears to have a low sensitivity to changing Mg/Ca_{sw}, bottom water temperatures have only been calculated assuming Mg/Ca_{sw} = 2.5 mol/mol in the following equation (Lear et al., 2015):

$$Mg/Ca_{test} = 0.46 \pm 0.05 \times {Mg/Ca_{sw}}^{0.51 \pm 0.07} \times exp^{(0.114 \pm 0.02 \times BWT)} \qquad [Eq.\ 14]$$

This can be rearranged to make bottom water temperature (*BWT*) the subject as follows:

$$BWT = \frac{\ln(\frac{Mg/Ca_{test}}{0.46 \times Mg/Ca_{sw}{}^{0.51}})}{0.114} \qquad \textit{[Eq. 15]}$$

The uncertainty associated with absolute benthic Mg/Ca-derived temperature estimates includes a small component of analytical uncertainty (±0.3°C), based on the ±3% analytical uncertainty on the Mg/Ca measurements, and a larger component of calibration error (±1.5°C), based on the error bars associated with the constants used in the temperature calibration equation (Eq. 14; Lear et al., 2015), giving a total uncertainty of ±1.8°C.

6.4.6. CONVERSION OF MG/CA DATA TO RELATIVE TEMPERATURE CHANGE

Owing to the uncertainties associated with choice of the pre-exponential and exponential constants for determining absolute temperatures from fossil planktic foraminifera species, relative temperature changes across the complete Late Paleocene–Early Eocene Mg/Ca record and during the PETM have also been calculated. This method avoids uncertainties with choice of the pre-exponential constant "*B*" in the following equation (modified from Zachos et al., 2003):

$$\Delta T = \frac{1}{A} \times \ln(\frac{Mg/Ca_{test}^{pH\ b}}{Mg/Ca_{test}^{pH\ a}}) \qquad \textit{[Eq. 16]}$$

where Δ*T* is the relative temperature change in °C between two pH-corrected values of Mg/Ca in foraminiferal tests ($Mg/Ca_{test}^{pH\ a}$ and $Mg/Ca_{test}^{pH\ b}$), and *A* is the exponential constant. A range of values for the exponential constant "*A*" have been modelled, including the mean value of 0.090 from modern planktic foraminifera (Anand et al., 2003), as well as the "most likely" and "lower limit" in the range of modelled values for "*A*" of 0.075 and 0.05 respectively, during the Paleogene with Mg/Ca_{sw} of ~1.5–2.5 mol/mol (Evans et al., 2016a). Since the stable carbon isotope data generated during this study suggest that a third to a half of the total magnitude of the PETM excursion has been captured in the trace

metal records, two values for PETM pH of 7.6 and 7.5 (representing one and two thirds respectively of the total magnitude of PETM pH decrease calculated from boron isotope data; Penman et al., 2014), have been modelled in the reconstruction of relative temperature change during the PETM.

Since Mg/Ca_{test} values for *Oridorsalis umbonatus* appear to be much less sensitive to Mg/Ca_{sw}, changes in bottom water temperatures were calculated using a single value of 0.114 for the exponential constant "*A*" after Lear et al. (2015).

6.4.7. CONVERSION OF PLANKTIC B/CA TO RELATIVE CHANGE IN CARBONATE CHEMISTRY

Since the calculation of relative surface ocean pH change based on the planktic B/Ca proxy is complicated over time periods characterised by large and relatively poorly constrained changes in surface ocean DIC, which are likely to have occurred during the Late Paleocene–Early Eocene, I focus on describing the mixed layer planktic B/Ca data in terms of relative change in carbonate chemistry (borate ion/DIC ratio; $\frac{[\mathrm{B(OH)_4}^-]}{\mathrm{DIC}}$). A decrease in $\frac{[\mathrm{B(OH)_4}^-]}{\mathrm{DIC}}$ indicates a decrease in borate ion and/or an increase in DIC, suggestive of increasing CO_2 in the surface ocean (and by inference, the ocean-atmosphere system), and a likely decrease in pH. This method is only qualitative however, and the magnitude of CO_2 or pH change cannot be quantified by this technique. The Paleocene calibration of Haynes et al. (2017) was employed, which is based on the modern species *Orbulina universa* cultured under simulated Paleocene seawater conditions:

$$B/Ca_{test} = 1147(\pm 284) \times \frac{[B(OH)_4^-]}{DIC} + 33.7(\pm 4.0) \qquad \textit{[Eq. 17]}$$

which can be rearranged to give:

$$\frac{[\mathrm{B(OH)_4}^-]}{\mathrm{DIC}} = \frac{B/Ca_{test} - 33.7(\pm 4.0)}{1147(\pm 284)} \qquad \textit{[Eq. 18]}$$

6.4.8. CONVERSION OF BENTHIC B/CA TO RELATIVE CHANGE IN CARBONATE SATURATION STATE

Benthic B/Ca can be converted to relative change in carbonate saturation state ($\Delta[CO_3^{2-}]$) of the intermediate waters of the low latitude northern Indian Ocean from the Late Paleocene (peak of the PCIM) to Early Eocene. $\Delta[CO_3^{2-}]$ controls the depths of the lysocline (carbonate saturation horizon) and CCD (depth below which carbonates are not preserved on the seafloor), such that if $\Delta[CO_3^{2-}]$ falls due to a rapid transient injection of CO_2 (i.e., ocean acidification), the depths of the lysocline and CCD will shoal and dissolution of calcium carbonate will take place, raising $\Delta[CO_3^{2-}]$ back to steady state conditions. To calculate $\Delta[CO_3^{2-}]$ from benthic B/Ca data, the modern calibration of Brown et al. (2011) for *Nuttallides umbonifera* was modified to take into account the different $[B]_{sw}$ of Paleogene seawater relative to the modern. Paleogene $[B]_{sw}$ has been modelled to range from ~4.38 ppm during the peak of the PCIM (Late Paleocene; ~58 Ma), to ~4.42 ppm during the PETM, and ~4.47 ppm during the Early Eocene (~53 Ma; Lemarchand et al., 2000), which equates to 0.971, 0.980 and 0.991 times the modern value (4.51 ppm; Lemarchand et al., 2000), respectively. These three values of 0.971 for the Late Paleocene, 0.980 for the PETM, and 0.991 for the Early Eocene are therefore added into the equation of Brown et al. (2011) as an "r" value (after Kender et al., 2014):

$$B/Ca_{test} = r \times 1.23(\pm 0.15) \times \Delta\left[{CO_3}^{2-}\right] + \mathrm{r} \times 133.4(\pm 2.7) \qquad \textit{[Eq. 19]}$$

which can be re-arranged to give:

$$\Delta\left[{CO_3}^{2-}\right] = \frac{B/Ca_{test} - r \times 133.4(\pm 2.7)}{r \times 1.23(\pm 0.15)} \qquad \textit{[Eq. 20]}$$

6.4.9. AGE MODEL FOR IODP SITE U1443 AND ODP SITE 758

The Late Paleocene portion of the trace metal records from the northern Indian Ocean, presented in this chapter, has been placed onto an orbitally-tuned age model generated using the larger 100-kyr paced carbon cycle perturbations observed in the $\delta^{13}C_{bulk}$ record as tie points. The ages of these events were derived from the orbitally-tuned high-resolution $\delta^{13}C_{benthic}$ record from ODP Site

1262 (**Chapter 3**), correlated to the La2010b orbital solution of Laskar et al. (2011a). Ages of the two samples encompassing the PETM were derived by correlating the $\delta^{13}C_{planktic}$ data from IODP Site U1443 to the high-resolution PETM $\delta^{13}C_{planktic}$ record from ODP Site 1209, located at a similar palaeo-latitude and open ocean setting within the northern Hemisphere during this time. This comparison, combined with planktic foraminiferal biostratigraphy suggesting the absence of Zone E1 (comprising the bulk of the onset and core of the PETM), allows the two samples encompassing the PETM at IODP Site U1443 to be placed in the PETM recovery phase and is illustrated in **Section 6.7.1** later in this chapter. Within the condensed Early Eocene portion of the record, where the identification of specific carbon cycle perturbations becomes more ambiguous, global nannoplankton biostratigraphic datums were used alongside the ETM-2 and H2 events. The key tie points used to create the orbitally-tuned age model for the splice between IODP Hole U1443A and ODP Hole 758A are listed in Table 14 below.

Table 14

Event	**Depth in Hole U1443A (CSF-A) and Hole 758A (mbsf)**	**Age (Ma)**
Peak PCIM	259.14	58.030
“A”	256.04	57.493
“B1”	254.66	57.333
“B2”	254.26/264.48	57.220
“C1”	261.19	56.951
“C2”	260.38	56.861
“D1”	257.72	56.485
Onset PETM	248.76	55.930
PETM recovery 1	248.63	55.835
PETM recovery 2	248.60	55.800
Base CP9a (LO *D. diastypus*)	248.15	54.873
ETM-2/H1	246.50	54.051
H2	246.21	53.958
Base NP12 (LO *D. lodoensis*)	245.06	52.944

Chemostratigraphic and biostratigraphic tie points used to create the age model for the trace metal records from IODP Site U1443 and ODP Site 758 presented in this chapter. Depth points from IODP Site U1443 are listed in black, and those from ODP Site 758 are listed in red.

6.4.10. INTEGRATION OF PUBLISHED PALAEOCLIMATE PROXY DATA

To compare the thermal evolution of the low latitude Indian Ocean with the low-latitude Pacific and Atlantic during the Late Paleocene–Early Eocene, the

new trace metal data presented in this chapter from IODP Site U1443 and ODP Site 758 were compared to other published proxy records for mixed layer and sea surface temperature (based on Mg/Ca, $\delta^{18}O$, and TEX_{86}^{H}). With the exception of data from ODP Site 1209, these datasets were initially aligned temporally using the age model of Cramwinckel et al. (2018), which is based on the Geological Time Scale 2012 (GTS2012; Gradstein et al., 2012). However, since GTS2012 places the onset of the PETM (hence the Paleocene/Eocene boundary) at 56 Ma, as opposed to 55.93 Ma in our orbitally-tuned age model (Westerhold et al., 2007; **Chapter 3**), the ages published by Cramwinckel et al. (2018) were shifted by 70 kyr to align with our age model. Data from ODP Site 1209 were temporally aligned using the updated orbitally-tuned age model presented in Westerhold et al. (2018), which is consistent with our age model. Benthic Mg/Ca data from ODP Site 690 were aligned using the published age model in Lear et al. (2015), which was temporally shifted to a PETM age of 55.93 Ma. Additional published data from open ocean sites, incorporated to compare the evolution of temperature and carbonate chemistry across the PETM, were aligned temporally relative to the CIE onset using planktic carbon isotope stratigraphy and a comparison to the most complete PETM carbon isotope curve from ODP Site 1209 (Zachos et al., 2003).

6.5. DATA ATTRIBUTION

I devised the sampling strategy and requested the samples from the Kochi Core Center (KCC) for both IODP Site U1443 and ODP Site 758, dried, sieved and disaggregated the samples, prepared and weighed samples for bulk carbonate stable isotope ($\delta^{13}C_{bulk}$) analysis, and picked and weighed all of the foraminifera. I cleaned the foraminifera and generated the trace metal data from the IODP Site U1443 samples at the University of California Santa Cruz (UCSC), under the supervision of Mr. Dustin Harper and Prof. James Zachos (UCSC). I also generated the absolute temperature estimates, relative temperature and salinity changes from the Mg/Ca and $\delta^{18}O_{planktic}$ data, changes in mixed layer carbonate chemistry from the planktic B/Ca data, and relative changes in carbonate saturation state from the benthic B/Ca data. I compiled all of the published palaeoclimate proxy data presented in this chapter. Dr. Kate Littler and other members of the shipboard scientific party sampled the IODP Site U1443

core, whilst the ODP Site 758 core was sampled by KCC staff. Mr. Dustin Harper (UCSC) cleaned the foraminifera and generated the trace metal data from the ODP Site 758 samples at UCSC, from samples picked and weighed by myself. Dr. Michael Henehan (Yale University) cleaned the foraminifera and generated the trace metal data from the ODP Site 758 samples at the Yale Metal Geochemistry Centre (YMGC), Yale University, from samples picked and weighed by myself. Dr. Leah LeVay (Texas A&M University) generated the calcareous nannoplankton biostratigraphy for these sites from samples prepared by myself. Dr. Kirsty Edgar (University of Birmingham) generated the planktic foraminifera biostratigraphy and funded the planktic stable isotope data, which were generated at Cardiff University with the technical assistance of Dr. Sandra Nederbragt. A portion of the $\delta^{13}C_{bulk}$ data were funded and generated by the NERC Isotope Geosciences Facility under the supervision of Prof. Melanie Leng (IODP Site U1443, 244.945–258.655 m CSF-A), whilst the rest of the $\delta^{13}C_{bulk}$ data were generated at the Camborne School of Mines (University of Exeter), with the assistance of Dr. Clemens Ullmann. The new IODP Site U1443 trace metal records generated at UCSC were funded by grants from the European Consortium for Ocean Research Drilling (ECORD; €2000) and from the International Association of Sedimentologists (IAS; €1000). The new trace metal records from ODP Site 758 generated at Yale University were funded by Dr. Michael Henehan. The bulk carbonate carbon isotope data sets from IODP/ODP Sites U1443 and 758 are included in **Appendix 9** and **10** respectively, the planktic stable isotope data sets from IODP/ODP Sites U1443 and 758 in **Appendix 11** and **12** respectively, and the complete trace metal data sets in **Appendix 13–30**.

6.6. RESULTS AND DISCUSSION

6.6.1. LATE PALEOCENE–EARLY EOCENE STRATIGRAPHY RECOVERED BY THE IODP/ODP SITES U1443/758 SPLICE

As shown in Figure 55 and Figue 56, a significant portion of the Late Paleocene–Early Eocene stratigraphy from the peak of the PCIM to the Early Eocene (~59.4–53.0 Ma) was recovered by the splice between IODP Hole U1443A and ODP Hole 758A, including a partial PETM. The stratigraphic interval covered by the trace metal (Mg/Ca and B/Ca) records spans ~58–53 Ma (Figure

56). The two cores have been correlated based on bulk carbonate stable carbon isotope stratigraphy ($\delta^{13}C_{bulk}$) and calcareous nannoplankton biostratigraphy, with additional control from low-resolution planktic foraminifera biostratigraphy. The highest occurrence (HO) of *Discoaster okadai* forms a key biostratigraphic tiepoint between the two cores (Figure 55). At the reference site, ODP Site 1262 in the South Atlantic, this event occurs during the "B2" event (Agnini et al., 2007; Figure 56), allowing a confident assignment of this event within the IODP/ODP Holes U1443A/758A splice (Figure 55). The lowest occurrence (LO) of *Fasciculithus alanii* occurs during the "C1" event at ODP Site 1262 (Agnini et al., 2007; Figure 56), allowing a confident identification of the "C1" and "C2" events within the ODP Hole 758A stratigraphy (Figure 55). The presence of "D1" can also be inferred as the following negative carbon isotope perturbation upsection. However, a section of the latest Paleocene stratigraphy is still missing in the splice, encompassing the "D2" event (Figure 55). Based on a comparison of the IODP/ODP Holes U1443A/758A $\delta^{13}C_{bulk}$ record to the complete Late Paleocene–Early Eocene $\delta^{13}C_{bulk}$ record from ODP Site 1262 (Zachos et al., 2010; Littler et al., 2014; **Chapter 3**), this interval of missing stratigraphy is likely to encompass no more than ~400 kyr (Figure 56).

The PETM has been identified at 248.63 metres depth (CSF-A) in IODP Hole U1443A by an abrupt ~–0.75‰ excursion in $\delta^{13}C_{bulk}$ and presence of the *Fasciculithus/Zygrhablithus* cross over (Figure 55). The PETM excursion has only been captured in the $\delta^{13}C_{bulk}$ record by two data points, and since it typically attains a magnitude of ~–2.5–3‰ in marine carbonates (e.g., McInerney & Wing, 2011), it is likely that approximately one third of the total magnitude of the PETM excursion has been recovered and the peak of the excursion is missing. Planktic foraminifera Zone E1, encompassing the bulk of the PETM, could also not be confidently defined, further supporting this interpretation (Figure 55). Similarly, the magnitude of the C1, C2 and D1 excursions are also smaller within the ODP Site 758 $\delta^{13}C_{bulk}$ record compared to the ODP Site 1262 $\delta^{13}C_{bulk}$ record (~–0.2‰ at ODP Site 758 vs. ~–0.3–0.4‰ at ODP Site 1262; Figure 56), suggesting that the complete magnitude of these events has also not been captured in the biscuited ODP Hole 758A core.

Based on the carbon isotope stratigraphy and biostratigraphic data, the Early Eocene portion of the record in IODP Hole U1443A appears to be significantly more condensed compared to the Late Paleocene, with a decrease in sedimentation rate from ~0.4–1.2 cm/kyr during the Late Paleocene to ~0.05–0.3 cm/kyr during the Early Eocene (Figure 57). As a result, the correlation of specific carbon cycle perturbations to the ODP Site 1262 $\delta^{13}C_{bulk}$ curve becomes rather more ambiguous in the Early Eocene part of the record, with the exception of the ETM-2 and H2 events. Climate and carbon cycle events within this part of this record are therefore assigned at a lower confidence level (Figure 55; Figure 57).

*Figure 55 (next page). Bulk carbonate carbon isotope ($\delta^{13}C_{bulk}$) stratigraphy, calcareous nannoplankton biostratigraphy and planktic foraminifera biostratigraphy of the Indian Ocean Ninetyeast Ridge IODP/ODP Sites U1443A/758A splice spanning the Late Paleocene–Early Eocene. $\delta^{13}C_{bulk}$ data from IODP Hole U1443A are illustrated as grey-black curves and $\delta^{13}C_{bulk}$ data from ODP Hole 758A are illustrated as a red curve. Core sections from which the data are derived are labelled. Carbon isotopic events and calcareous nannoplankton events from IODP Hole U1443A are labelled in black, from ODP Hole 758A are labelled in red, and critical tie points occurring in both Holes U1443A and 758A are labelled in purple. Carbon isotope events identified at low confidence are labelled in pale grey with a question mark. Calcareous nannoplankton events and biozone boundaries assigned at high confidence are defined by a solid line, and those at low confidence with a dashed line. Stratigraphic sections within IODP Hole U1443A studied for planktic foraminifera biostratigraphy are shaded in grey and bounded by dashed lines. Long (405-kyr) Late Paleocene eccentricity maxima within the La2010b orbital solution (Laskar et al., 2011a), as defined in the orbitally-tuned stable isotope records from ODP Site 1262 (**Chapter 3**), are indicated in red above the carbon isotope curve. Eccentricity maxima are labelled following the nomenclature of Dinarès-Turell et al. (2014). Core gaps and condensed intervals are indicated by vertical grey bands. The stratigraphic interval covered by the trace metal (Mg/Ca & B/Ca) records, from the peak of the PCIM to the Early Eocene, is indicated by a horizontal purple bar. PCIM = Paleocene Carbon Isotope Maximum. ELPE = Early Late Paleocene Event. PETM = Paleocene-Eocene Thermal Maximum. E. robusta = Ericsonia robusta. F. clinatus = Fasciculithus clinatus. D. mohleri = Discoaster mohleri. H. kleinpelli = Heliolithus kleinpelli. D. nobilis = Discoaster nobilis. D. backmanii = Discoaster backmanii. D. okadai = Discoaster okadai. D. delicatus = Discoaster delicatus. D. multiradiatus = Discoaster multiradiatus. F. alanii = Fasciculithus alanii. D. diastypus = Discoaster diastypus. S. radians = Sphenolithus radians. D. lodoensis = Discoaster lodoensis. HO = Highest occurrence. HCO = Highest common occurrence. LO = Lowest occurrence. LCO = Lowest common occurrence. CO = Cross over. CSF-A = Core depth below sea floor. Mbsf = Metres below sea floor.*

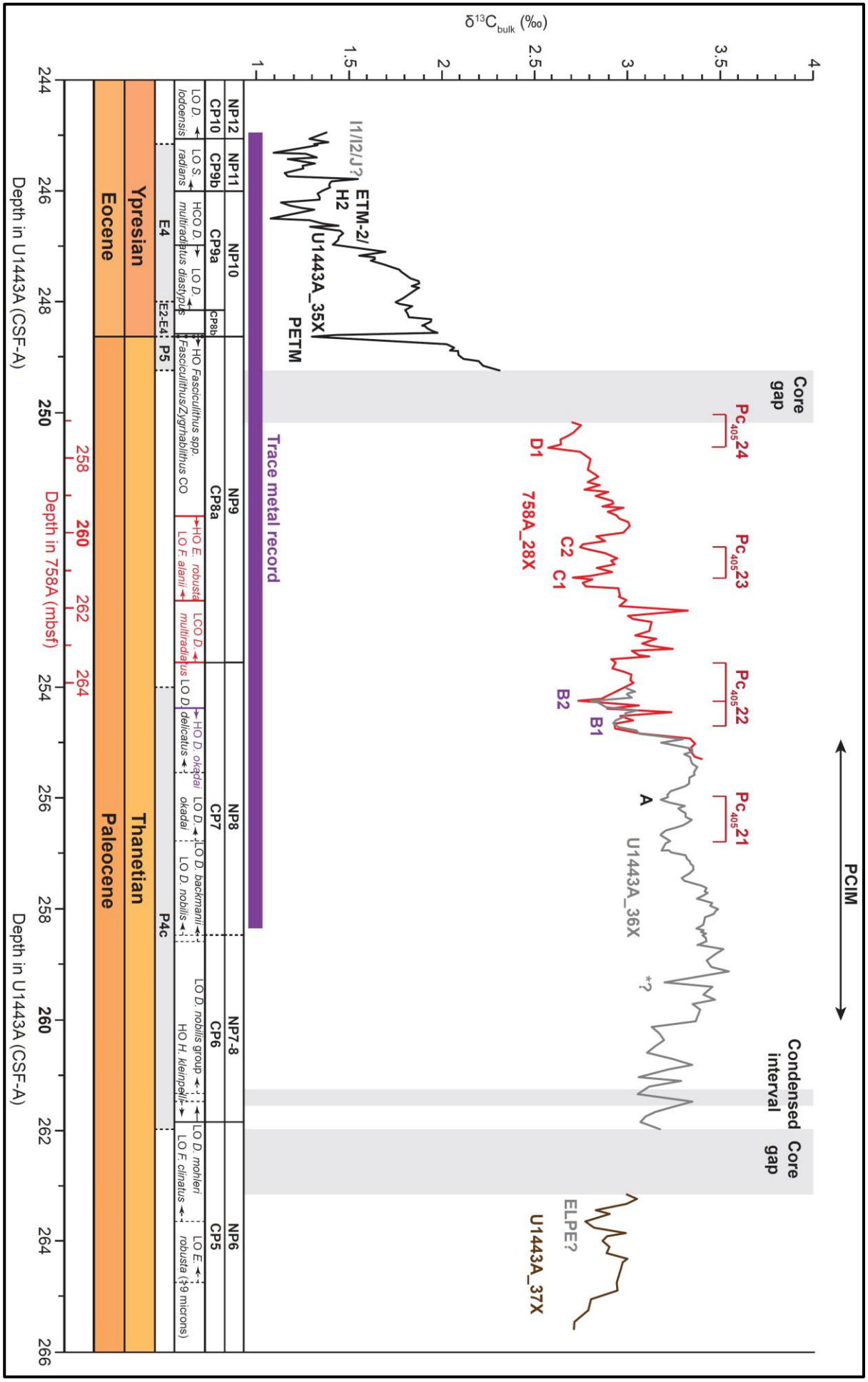
$\delta^{13}C_{bulk}$ (‰)
PCIM
Core gap
Condensed interval
Core gap
Trace metal record
ETM-2/ H2
I1/I2/J?
U1443A_35X
PETM
Pc_{405}24
Pc_{405}23
Pc_{405}22
Pc_{405}21
D1
758A_28X
C2
C1
B2
B1
A
U1443A_36X
*?
ELPE?
U1443A_37X
NP12
NP11
NP10
NP9
NP8
NP7-8
NP6
CP10
CP9b
CP9a
CP8b
CP8a
CP7
CP6
CP5
E4
E2-E4
P5
P4c
Ypresian
Thanetian
Eocene
Paleocene
Depth in U1443A (CSF-A)
Depth in 758A (mbsf)
Depth in U1443A (CSF-A)

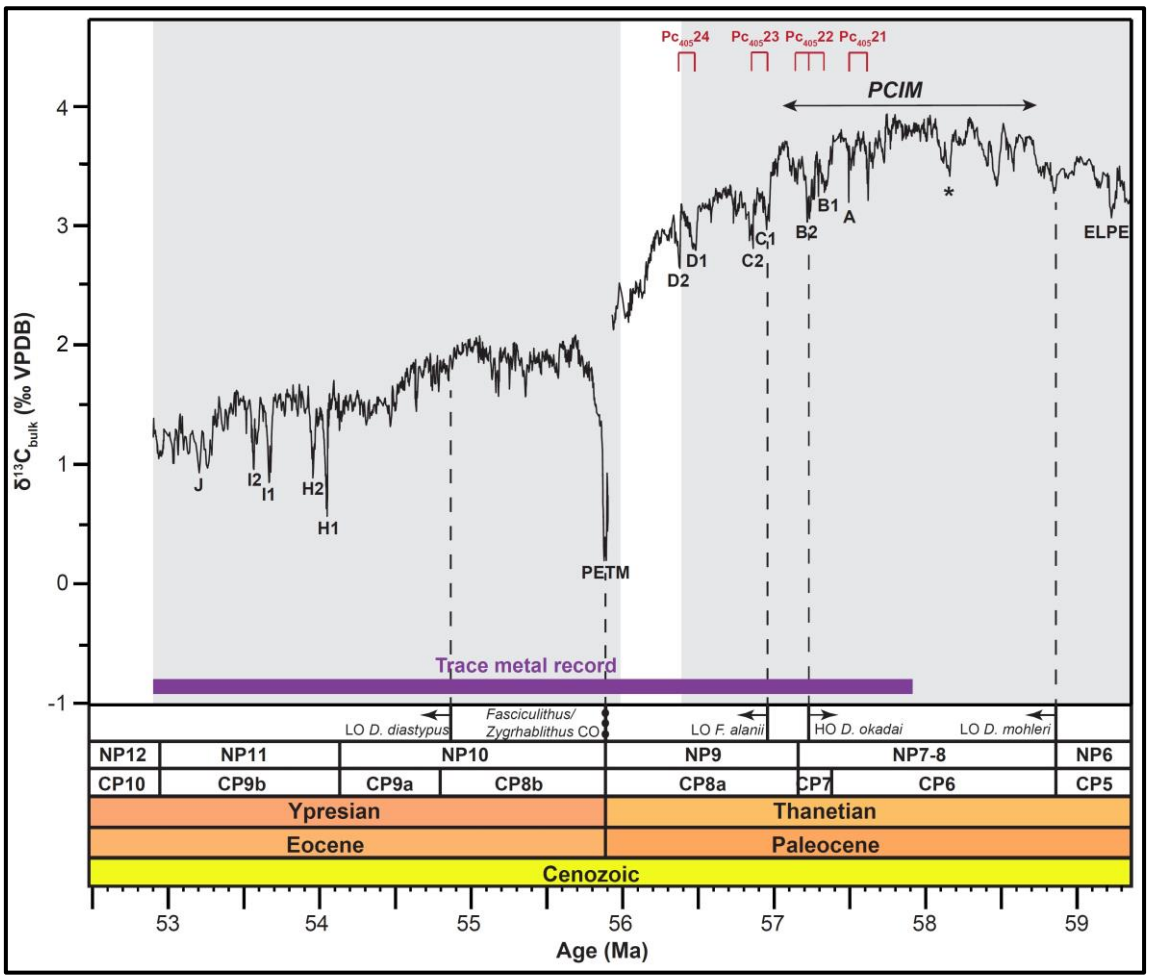

Figure 56. The "reference" bulk carbonate carbon isotope ($\delta^{13}C_{bulk}$) record from South Atlantic Walvis Ridge ODP Site 1262 (Zachos et al., 2010; Littler et al., 2014) spanning the Late Paleocene–Early Eocene, plotted against the updated orbitally-tuned age model presented in this thesis (see ***Chapter 3*** *for the complete $\delta^{13}C_{bulk}$ record from ODP Site 1262 and further details on the age model). Grey shaded areas represent the stratigraphy recovered in the Indian Ocean IODP/ODP Sites U1443/758 splice (Figure 55), spanning ~59.4–53.0 Ma. The stratigraphic interval covered by the trace metal (Mg/Ca and B/Ca) record is illustrated by a purple bar, spanning ~58–53 Ma. Key biostratigraphic datums used to correlate specific events and portions of the stratigraphy between ODP Site 1262 and IODP Site U1443/ODP Site 758 are illustrated by dashed lines. Long (405-kyr) Late Paleocene eccentricity maxima within the La2010b orbital solution (Laskar et al., 2011a) are indicated in red above the carbon isotope curve. Biostratigraphic data is from Agnini et al. (2007). Key carbon cycle events are labelled: ELPE = Early Late Paleocene Event; PCIM = Paleocene Carbon Isotope Maximum; PETM = Paleocene-Eocene Thermal Maximum. D. mohleri = Discoaster mohleri. D. okadai = Discoaster okadai. F. alanii = Fasciculithus alanii. D. diastypus = Discoaster diastypus. HO = Highest occurrence. LO = Lowest occurrence. CO = Cross over.*

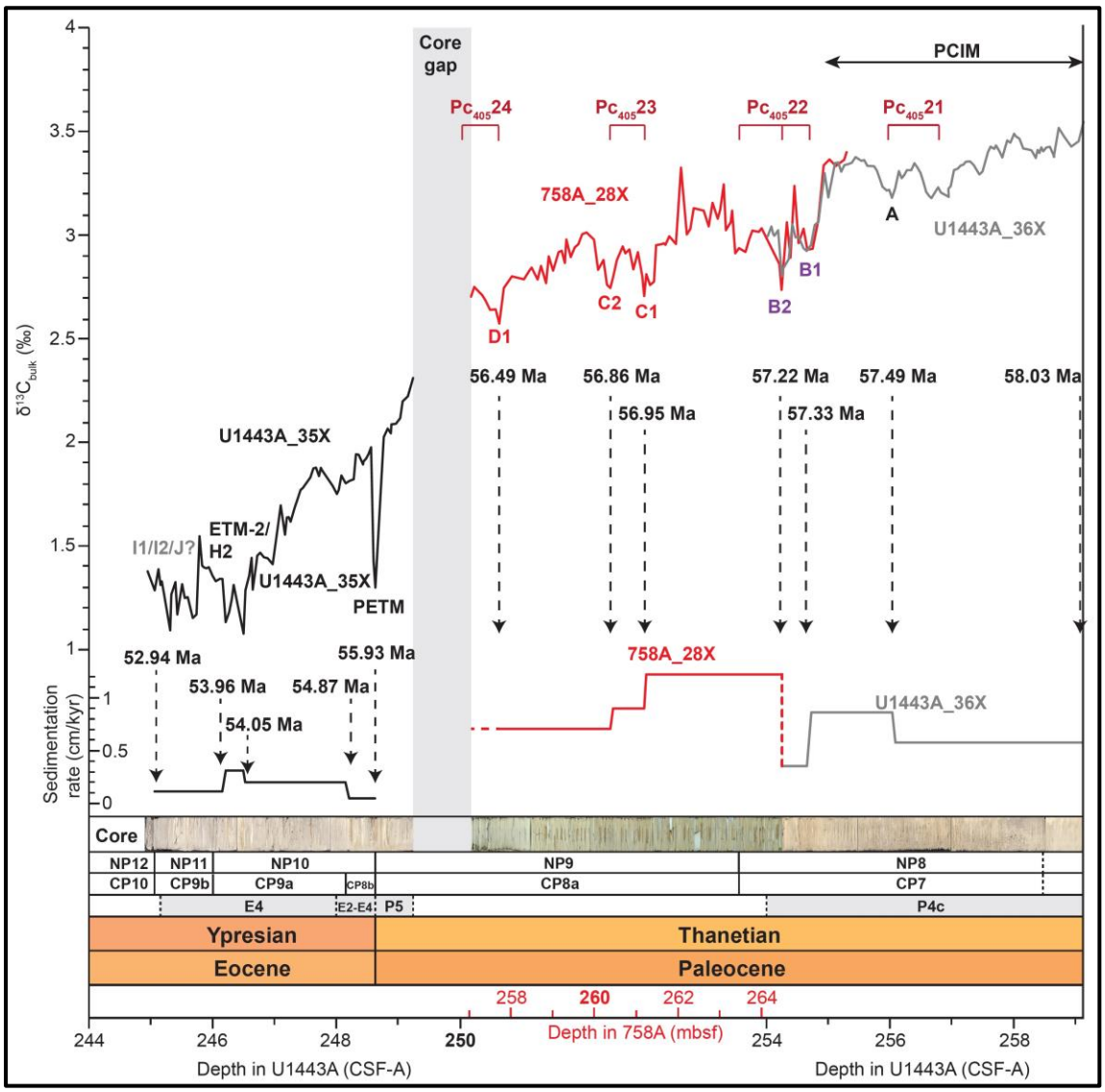

Figure 57. Bulk carbonate carbon isotope ($\delta^{13}C_{bulk}$) stratigraphy plotted against sedimentation rates for IODP Site U1443 (in grey) and ODP Site 758 (in red), and the spliced core image for both sites. Sedimentation rates were calculated using the indicated chemostratigraphic and biostratigraphic age model tie points (listed in Table 14), with ages of the specific carbon cycle and biostratigraphic events based on integration of their stratigraphic position at ODP Site 1262 with the orbitally-tuned age model generated for that site during this study (Agnini et al., 2007; ***Chapter 3****). The core image for the IODP Site U1443 cores is from the LIMS Online Report (LORE) portal website: http://web.iodp.tamu.edu/LORE/, whilst the core image for the ODP Site 758 core is from the Kochi Core Center website: http://www.kochi-core.jp/en/. The apparent colour difference between the two cores is an artefact of different lighting conditions and not a genuine difference in core colour between sites.*

6.6.2. PLANKTIC FORAMINIFERAL PRESERVATION

A subset of planktic foraminifera specimens were selected for imaging using a Field Emission Gun Scanning Electron Microscope (FEG-SEM) at the University of Exeter, to assess the preservation of primary planktic foraminiferal calcite across the record. Whole specimens, test walls on crushed specimens, and pore structures were imaged to assess the degree of diagenetic recrystallisation of test surfaces and walls from three stratigraphic intervals corresponding to the peak of the PCIM within IODP Core U1443-36X (257.815–256.67 m CSF-A; Figure 58), the Late Paleocene within ODP Core 758A-28X (264.0–260.215 mbsf; Figure 59), and the Early Eocene within IODP Core U1443A-35X (248.31–245.31 m CSF-A; Figure 60). Although there is little evidence for infilling of the tests, or major infilling of the pores, there is evidence of some diagenetic recrystallisation of test walls and pores at all three stratigraphic levels. The foraminifera therefore would not be classified as well-preserved with a glassy texture according to Pearson and Burgess (2008), probably due to the predominance of carbonate and limited terrigenous clay within the Late Paleocene–Early Eocene stratigraphies of the Indian Ocean sites (Shipboard Scientific Party, 1989, 2006; see **Chapter 2 Section 2.2.2**). However, as the degree of recrystallisation does not appear to change substantially across the record, the effects on the calculation of relative temperature shifts from the Late Paleocene to the Early Eocene should be relatively small. It should be noted, however, that this recrystallisation may bias absolute temperature estimates, especially of the mixed layer *Morozovella* specimens which exhibit the greatest amount of recrystallisation, visible within the SEM images (Figure 58a; Figure 59a; Figure 60a) as well as under optical light microscopy. This recrystallisation forms the visible spikey or crusty appearance due to the growth of blades of diagenetic calcite over pustules surrounding the keel and on the raised umbilical shoulders of the specimens. This recrystallisation may also have the potential to dampen calculated relative temperature shifts within the mixed layer, as well as bias the interpretation of temperature gradients between the mixed layer and thermocline or intermediate waters. It should be noted, however, that preservation of these planktic foraminifera is at least as good, and in some cases much better, than samples from other low-latitude Paleocene–Eocene sites such as ODP Site 1209 (e.g., Zachos et al., 2003) and ODP Site 865 (e.g., Bralower

et al., 1995). Therefore, it can be assumed that absolute temperatures calculated from the IODP Site U1443/ODP Site 758 Mg/Ca data have not been significantly biased relative to published Mg/Ca data from other low latitude deep-sea sites and are therefore comparable.

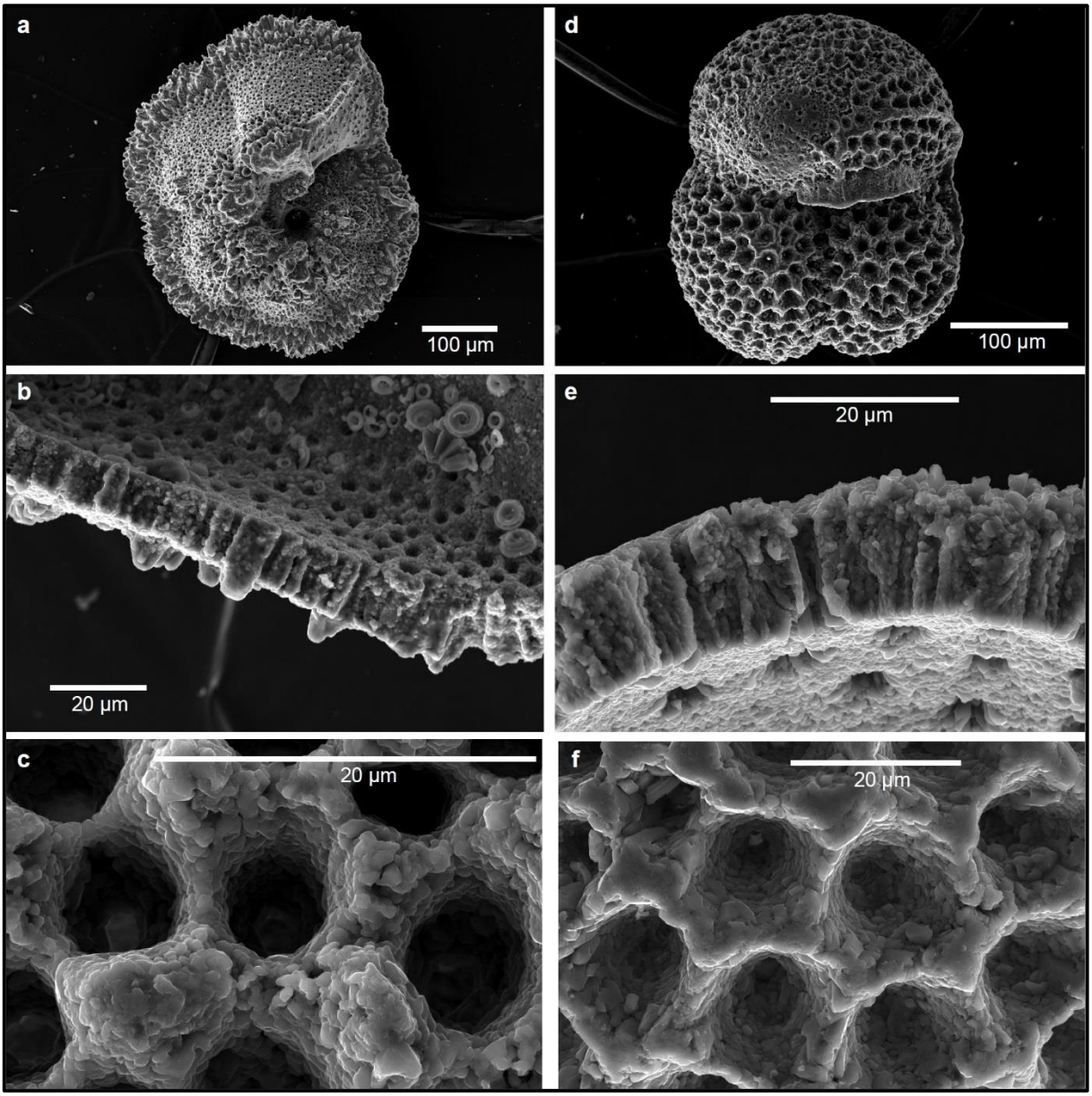

*Figure 58. Scanning Electron Microscope (SEM) images of planktic foraminifera specimens from the peak of the Paleocene Carbon Isotope Maximum (PCIM; 257.815–256.67 m CSF-A; ~57.8–57.6 Ma) in IODP Core U1443A-36X. (**a**-**c**) Morozovella velascoensis, illustrating whole specimen umbilical view (**a**), cross section of test wall (**b**), and pore structure (**c**). (**d**-**f**) Subbotina velascoensis, illustrating whole specimen umbilical view (**d**), cross-section of test wall (**e**), and pore structure (**f**).*

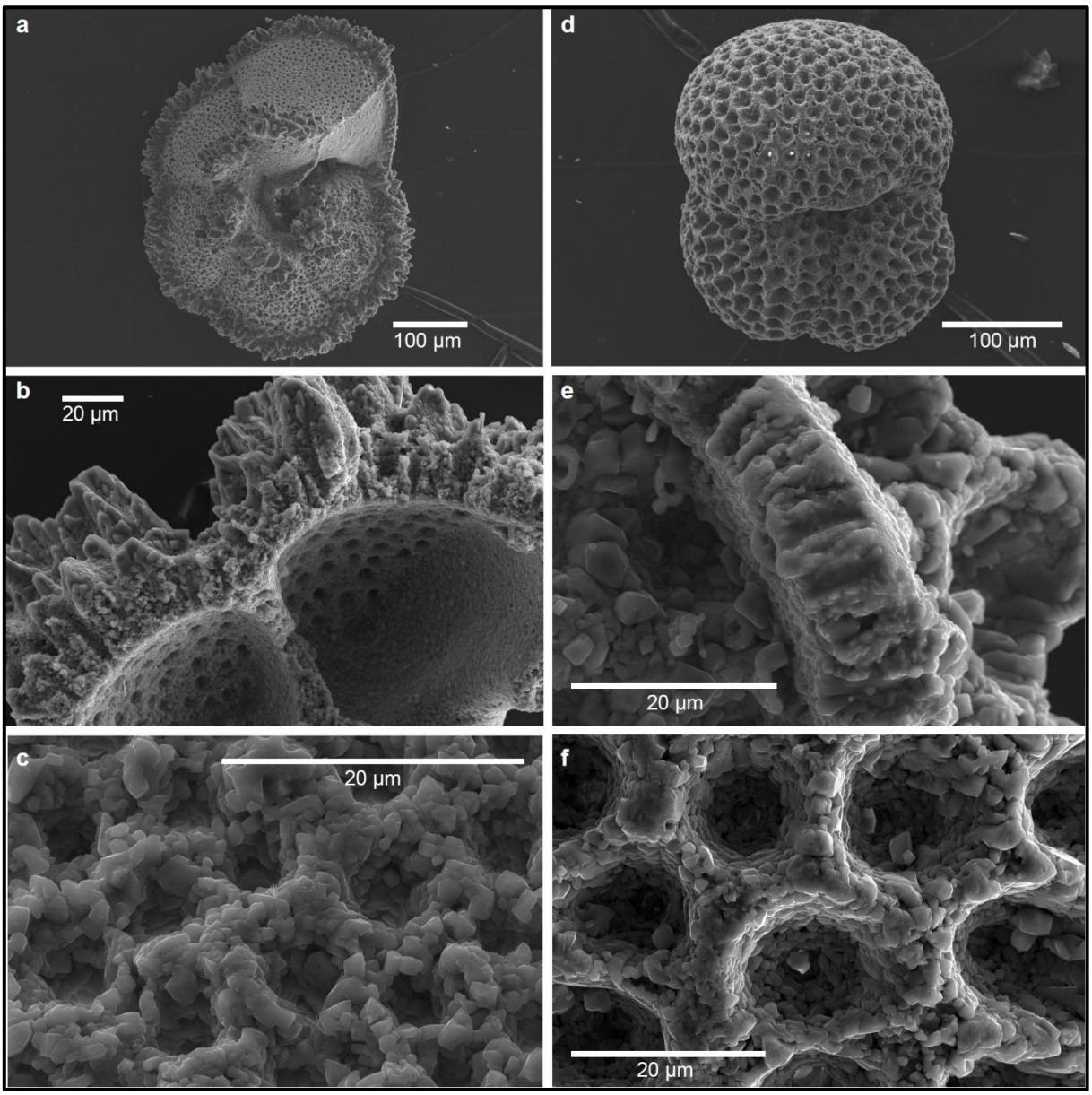

*Figure 59. Scanning Electron Microscope (SEM) images of planktic foraminifera specimens from the Late Paleocene (264.0–260.215 mbsf; ~57.2–56.8 Ma) in ODP Core 758A-28X. (**a**-**c**) Morozovella velascoensis, illustrating whole specimen umbilical view (**a**), cross section of test wall (**b**), and pore structure (**c**). (**d**-**f**) Subbotina velascoensis, illustrating whole specimen umbilical view (**d**), cross-section of test wall (**e**), and pore structure (**f**).*

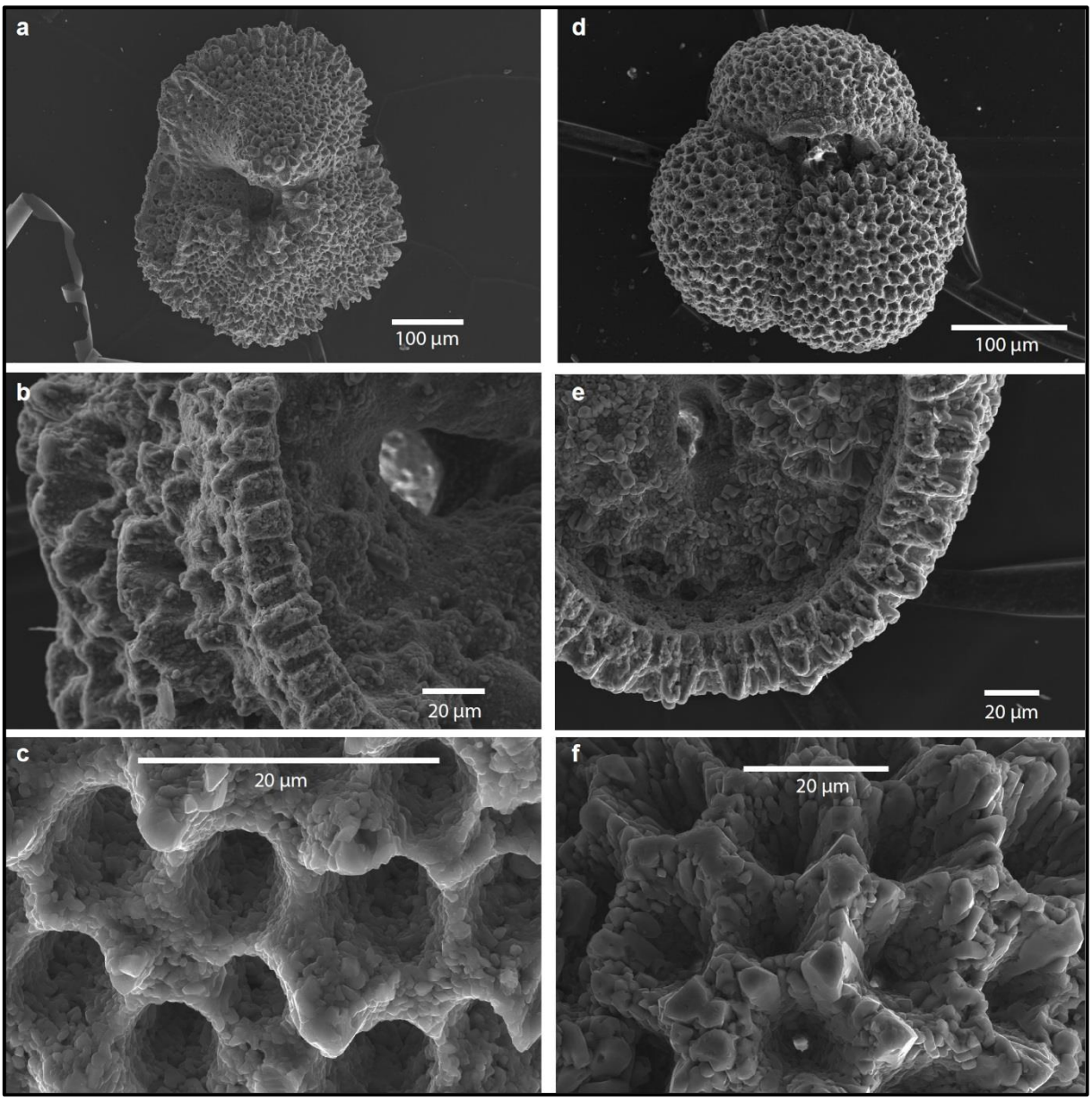

*Figure 60. Scanning Electron Microscope (SEM) images of planktic foraminifera specimens from the Early Eocene (248.31–245.31 m CSF-A; ~55.2–53.2 Ma) in IODP Core U1443A-35X. (**a**-**c**) Morozovella subbotinae-marginodentata plexus, illustrating whole specimen umbilical view (**a**), cross-section of test wall (**b**), and pore structure (**c**). (**d**-**f**) Subbotina hornibrooki, illustrating whole specimen umbilical view (**d**), cross-section of test wall (**e**), and pore structure (**f**).*

6.6.3. CHANGES IN MIXED LAYER CARBONATE CHEMISTRY AND TEMPERATURE DURING THE LATE PALEOCENE–EARLY EOCENE

The mixed layer (*Morozovella*) planktic Mg/Ca and B/Ca records, presented in Figure 61 and Figure 62, respectively, illustrate a coupled long-term increase in Mg/Ca (from ~3.0 mmol/mol to ~3.8 mmol/mol) and decrease in B/Ca (from ~70–80 µmol/mol to ~40–50 µmol/mol) during the Late Paleocene–Early

Eocene (~58–53 Ma). Temperatures have been calculated from the Mg/Ca data assuming Mg/Ca_{sw} = 1.5 mol/mol (based on older modelling studies; Stanley & Hardie, 1998; Demicco et al., 2005) or Mg/Ca_{sw} = 2.5 mol/mol, based on Early Eocene proxy data and considered the most robust (Evans et al., 2018). The assumption of constant Mg/Ca_{sw} during this 5 million year time interval is likely to be an oversimplification, however, no Mg/Ca_{sw} proxy data from the Late Paleocene are currently available to accurately correct for the secular variation in Mg/Ca_{sw} from the Late Paleocene to Early Eocene. Significant shifts in Mg/Ca_{sw} could amplify, dampen, or overprint genuine temperature changes during this time interval. Therefore, future work to generate estimates for Late Paleocene Mg/Ca_{sw} could lead to a refinement of the mixed layer temperature interpretations provided here based on the planktic Mg/Ca data.

Although characterised by comparable trends, an apparent offset in absolute values is visible in *Morozovella* Mg/Ca and B/Ca values between the two laboratories that generated the data from ODP Site 758, UCSC and Yale University (Figure 61c; Figure 62c). However, this offset does not affect the interpretation of the long-term trends discussed here based on the data generated at UCSC, which are still robust if the Late Paleocene data analysed at Yale are removed, nor does it complicate the identification or discussion of the PETM, as all of this data was generated at the same lab (UCSC). We speculate that differing pre-run cleaning and analytical procedures between the two labs may have introduced this offset. As a result, the Yale data has been excluded from subsequent compilations of mixed layer temperature records throughout this chapter.

The decrease in B/Ca (corresponding to a drop in $\frac{[B(OH)_4^-]}{DIC}$ of ~–0.02–0.03) suggests a fall in surface $[B(OH)_4^-]$ (i.e., decrease in surface ocean pH) and/or an increase in surface ocean DIC during the Late Paleocene–Early Eocene (Figure 62c), consistent with the general trend of increasing atmospheric pCO_2 during this time interval as indicated by proxy data (Royer, 2014; **Chapter 3**; Figure 12a). Rising foraminiferal Mg/Ca ratios suggest a concurrent long-term increase in temperature of the mixed layer of the low latitude northern Indian Ocean, from ~29.5 (±1.4)°C during the peak of the PCIM, to ~32.0 (±1.4)°C during the Early Eocene (Figure 61c). This long-term rise in temperature may serve to dampen

the long-term fall observed in the planktic B/Ca record during the Late Paleocene–Early Eocene, suggesting that the calculated decrease in $\frac{[B(OH)_4^-]}{DIC}$ of ~–0.02–0.03 during this time may be a minimum estimate. A step change to generally warmer baseline temperatures was also established in the mixed layer during the Early Eocene following the PETM, suggesting a long lasting change in the temperature of the mixed layer following this enigmatic hyperthermal event (Figure 61c). However, superimposed on this long-term warming trend is an apparent short-term gradual cooling trend of ~–1°C, evident in the mixed layer Mg/Ca data during the latest Paleocene from ~57.4–56.4 Ma, which is also manifested in the $\delta^{18}O_{planktic}$ data by a decrease of ~–0.4‰. A significant decrease in Mg/Ca_{sw} across this latest Paleocene interval could also conceivably explain the temporary fall in mixed layer Mg/Ca, especially if the magnitude of warming across this time interval was negligible, however no data are currently available on secular changes in Mg/Ca_{sw} during the Late Paleocene to test this hypothesis. On the other hand, Mg/Ca_{sw} data from the Early-Middle Eocene suggest a decrease in Mg/Ca_{sw} during that time (Evans et al., 2018), which may dampen the apparent magnitude of warming within the Early Eocene (post-PETM) portion of the planktic Mg/Ca record.

The long-term rise in mixed layer temperature suggested by the Mg/Ca data is not clearly replicated by the $\delta^{18}O_{planktic}$ data, however, which instead show no significant long-term trends from the Paleocene to the Eocene (Figure 61d). Assuming the $\delta^{18}O_{planktic}$ data have not been significantly biased by diagenesis, a long-term rise in planktic foraminiferal Mg/Ca accompanied by a negligible shift in $\delta^{18}O_{planktic}$ could be interpreted to reflect rising Mg/Ca_{sw} across this time interval. Although no Mg/Ca_{sw} data exists for the Late Paleocene, Evans et al. (2018) present an Early Eocene Mg/Ca_{sw} record which suggests decreasing Mg/Ca_{sw} values during this time, confirming that the rise in planktic foraminiferal Mg/Ca represents a temperature signal. The rather stable $\delta^{18}O_{planktic}$ values are therefore interpreted to reflect a positive shift in $\delta^{18}O_{sw}$ from the Late Paleocene to Early Eocene (Figure 61e). A notable positive shift in $\delta^{18}O_{sw}$ occurs during the PETM, with generally higher $\delta^{18}O_{sw}$ values for much of the Early Eocene compared to the Paleocene. This step change at the PETM is interpreted to reflect a rise in sea surface salinity due to higher net evaporation of the surface

ocean of the low latitude Indian Ocean during this hyperthermal event. A similar rise in sea surface salinity during the PETM has been interpreted from combined Mg/Ca and $\delta^{18}O_{planktic}$ analyses from other open ocean sites at comparable subtropical latitudes in the Pacific and Atlantic, such as ODP Site 1209 and DSDP Site 527 (Zachos et al., 2003; Tripati & Elderfield, 2004). Furthermore, a change to a more evaporative regime within the subtropical Indian, Atlantic and Pacific oceans has also been simulated by global climate models, suggesting this surface ocean salinity increase was characteristic of the subtropical surface ocean globally during the PETM (Carmichael et al., 2017). The $\delta^{18}O_{sw}$ record presented here, however, also suggests that the Early Eocene as a whole was generally characterised by higher surface ocean salinity compared to the Late Paleocene, which is likely to be the result of higher net evaporation at subtropical latitudes during the generally warmer background climate.

The resolution of the mixed layer trace element record is sufficiently high in the Paleocene part of the record to allow orbital (eccentricity) -scale variability to be discerned. Long (405-kyr) eccentricity maxima of the Late Paleocene are associated with bottom water warming (of typically ~+1–2°C) and negative excursions in $\delta^{13}C$ at ODP Site 1262, suggesting a global warming and release of isotopically light carbon (CO_2 or CH_4) as a positive feedback response (see **Chapter 3**). The expressions of the $Pc_{405}21$, $Pc_{405}22$ and $Pc_{405}23$ Late Paleocene 405-kyr eccentricity maxima are superimposed on the decreasing long-term trend in planktic B/Ca, resulting in a number of resolvable transient perturbations associated with the B1/B2 ($Pc_{405}22$) and C1/C2 ($Pc_{405}23$) events (Figure 62c). A transient drop in B/Ca of ~12 µmol/mol, followed by a return to pre-excursion conditions, characterises the B1/B2 events in this new record. The corresponding decrease in $\frac{[B(OH)_4^-]}{DIC}$ of ~–0.01, almost half of the magnitude of decrease across the entire record, suggests that this event was associated with a significant transient fall in pH and/or increase in surface DIC, consistent with the transient release of isotopically light carbon and spikes in Fe intensity during these events (suggesting dissolution of $CaCO_3$) observed at ODP Site 1262 in the South Atlantic (see **Chapter 3**; Figure 12f). Although the magnitude of the negative excursions in planktic B/Ca during the B1/B2 events is resolvable beyond analytical error, the comparatively larger magnitude of the B2 excursion in

$\delta^{13}C_{planktic}$ (~–0.7‰ vs. ~–0.3‰ during B1; Figure 62b), in agreement with the $\delta^{13}C_{bulk}$ record from IODP/ODP Sites U1443/758 (Figure 62b) and ODP Site 1262 (Figure 56), is not resolvable in the B/Ca record. Similarly, the B/Ca data exhibit a decrease of ~5 µmol/mol (from ~58.7 to ~53.7 µmol/mol) across the $Pc_{405}23$ eccentricity maximum, however, based on the magnitude of the negative excursions in $\delta^{13}C_{bulk}$ and $\delta^{13}C_{planktic}$ during the C1/C2 events, it is likely that only a portion of the total magnitude of these events has been captured in the ODP Site 758 B/Ca record. The mixed layer response to the PETM is discussed separately in **Section 6.7**.

Any orbitally-paced variations in Late Paleocene mixed layer temperature appear to be less pronounced within the planktic Mg/Ca record than in the paired B/Ca record (Figure 61c), suggesting a negligible temperature effect on the large orbitally-paced excursions observed in the planktic B/Ca record. Rising Mg/Ca values suggest a rise in temperature during the “A”, “C1” and “D1” events, although the magnitude of change falls within analytical uncertainty. However, Mg/Ca-derived temperatures appear to fall during the B1/B2 events, which are characterised by warming bottom water temperatures in the South Atlantic at ODP Site 1262 (Littler et al., 2014), and large negative shifts in planktic B/Ca at the Indian Ocean sites. This may be related to the fact that changes in low latitude mixed layer temperature during these comparatively small Late Paleocene orbital cycles may fall within analytical uncertainty of the Mg/Ca measurements (±0.3°C), especially as it is likely that the total magnitude of these events has not been captured by the Late Paleocene sample resolution (~4–28 kyr) of the IODP Site U1443/ODP Site 758 splice, based on the age model presented herein. Alternatively, diagenetic recrystallisation of the *Morozovella* specimens (Figure 58a; Figure 59a; Figure 60a), may lead to partial homogenisation of the calcite, precluding the ability to resolve smaller temperature perturbations within the mixed layer planktic Mg/Ca record. Lastly, selective minor dissolution of the more soluble high-Mg calcite during these small orbitally-paced climatic events may also have artificially dampened the magnitude of apparent temperature change at orbital timescales within the planktic Mg/Ca record. A rise in mixed layer temperature during the PETM is resolvable beyond analytical uncertainty and discussed further in **Section 6.7.**

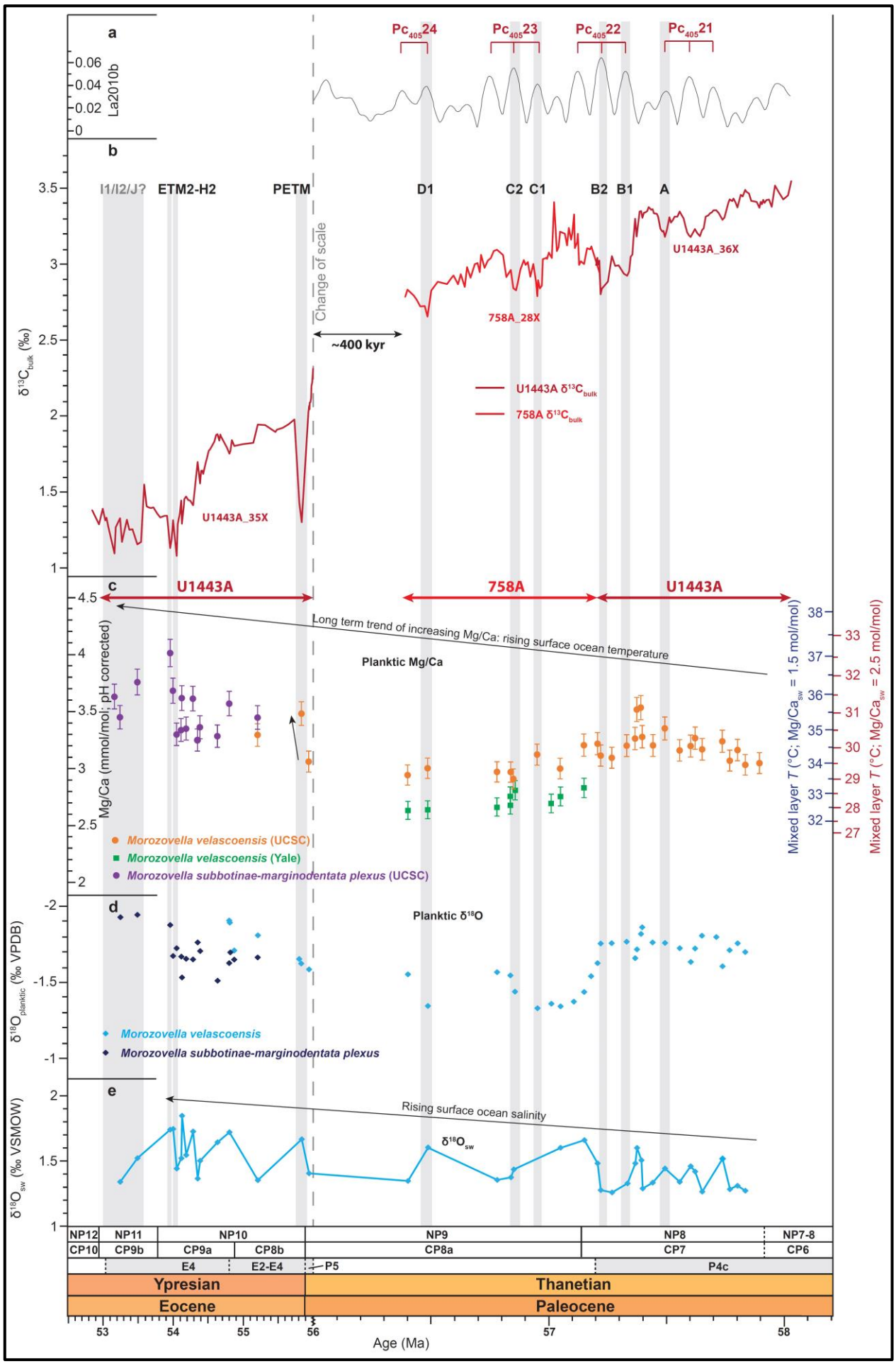
a
La2010b
0.06
0.04
0.02
0
Pc405 24
Pc405 23
Pc405 22
Pc405 21
b
I1/I2/J?
ETM2-H2
PETM
D1
C2 C1
B2 B1
A
Change of scale
~400 kyr
U1443A_36X
758A_28X
U1443A_35X
U1443A δ13Cbulk
758A δ13Cbulk
δ13Cbulk (‰)
c
U1443A
758A
U1443A
Long term trend of increasing Mg/Ca: rising surface ocean temperature
Planktic Mg/Ca
Mg/Ca (mmol/mol; pH corrected)
Morozovella velascoensis (UCSC)
Morozovella velascoensis (Yale)
Morozovella subbotinae-marginodentata plexus (UCSC)
Mixed layer T (°C; Mg/Casw = 1.5 mol/mol)
Mixed layer T (°C; Mg/Casw = 2.5 mol/mol)
d
Planktic δ18O
δ18Oplanktic (‰ VPDB)
Morozovella velascoensis
Morozovella subbotinae-marginodentata plexus
e
Rising surface ocean salinity
δ18Osw
δ18Osw (‰ VSMOW)
NP12
NP11
NP10
NP9
NP8
NP7-8
CP10
CP9b
CP9a
CP8b
CP8a
CP7
CP6
E4
E2-E4
P5
P4c
Ypresian
Thanetian
Eocene
Paleocene
Age (Ma)

Figure 61 (previous page). Mixed layer planktic foraminiferal Mg/Ca, oxygen isotope ($\delta^{18}O_{planktic}$), and bulk carbonate carbon isotope ($\delta^{13}C_{bulk}$) records from IODP/ODP Sites U1443/758, spanning the Late Paleocene–Early Eocene (~58–53 Ma) and calibrated to an orbitally-tuned age model generated during this study. A corresponding figure with the data presented against depth (CSF-A/mbsf) is included in ***Appendix 32****. (**a**) La2010b orbital solution of Laskar et al. (2011a) for the Late Paleocene. Long (405-kyr) eccentricity maxima are labelled following the nomenclature of Dinarès-Turell et al. (2014). (**b**) Bulk carbonate carbon isotope ($\delta^{13}C_{bulk}$) record. Core sections from which the data are derived are labelled. (**c**) Mg/Ca record with values corrected for pH, assuming a background surface ocean pH of 7.7 and PETM pH of 7.6. Absolute mixed layer temperature estimates are calculated using modelled Paleogene Mg/Ca_{sw} values of 1.5 mol/mol (blue scale) and 2.5 mol/mol (red scale), which bracket the potential range of early Paleogene Mg/Ca_{sw} based on modelling (~1.5 mol/mol) and proxy (~2.5 mol/mol) studies and produce an absolute temperature offset of ~4.5°C. Temperatures calculated using Mg/Ca_{sw} = 2.5 mol/mol are considered the most robust. Samples analysed at UCSC are indicated by filled circles, coloured in orange for Morozovella velascoensis samples and purple for Morozovella subbotinae-marginodentata plexus samples. A subset of Late Paleocene samples indicated by filled green squares were analysed at Yale University, but note an offset to lower Mg/Ca values compared to samples analysed at UCSC. The illustrated error bars of ±3% on the Mg/Ca measurements (±0.3°C) represent analytical uncertainty and are based on the long-term reproducibility of internal consistency standards. Absolute temperature values are also associated with a calibration error of ±1.13°C (Anand et al., 2003), giving a total uncertainty of ±1.4°C. Additional sources of uncertainty, which cannot be constrained, include the evolution of Mg/Ca_{sw}, surface ocean pH, and salinity across this time interval. Horizontal bars above the Mg/Ca data indicate the splice between Holes U1443A and 758A used to generate the record. (**d**) Planktic $\delta^{18}O$ record. (**e**) Surface ocean $\delta^{18}O_{sw}$ record, calculated using absolute temperatures with modelled Mg/Ca_{sw} = 2.5 mol/mol and the $\delta^{18}O_{planktic}$ data. The offset Mg/Ca data generated at Yale University were excluded from the $\delta^{18}O_{sw}$ calculations. Hyperthermals and smaller climatic and carbon cycle perturbations are labelled at the top of the figure and correlated across the record as grey vertical bars. PETM = Paleocene-Eocene Thermal Maximum. CSF-A = Core depth below sea floor. Mbsf = Metres below sea floor. VPDB = Vienna Pee Dee Belemnite. VSMOW = Vienna Standard Mean Ocean Water.*

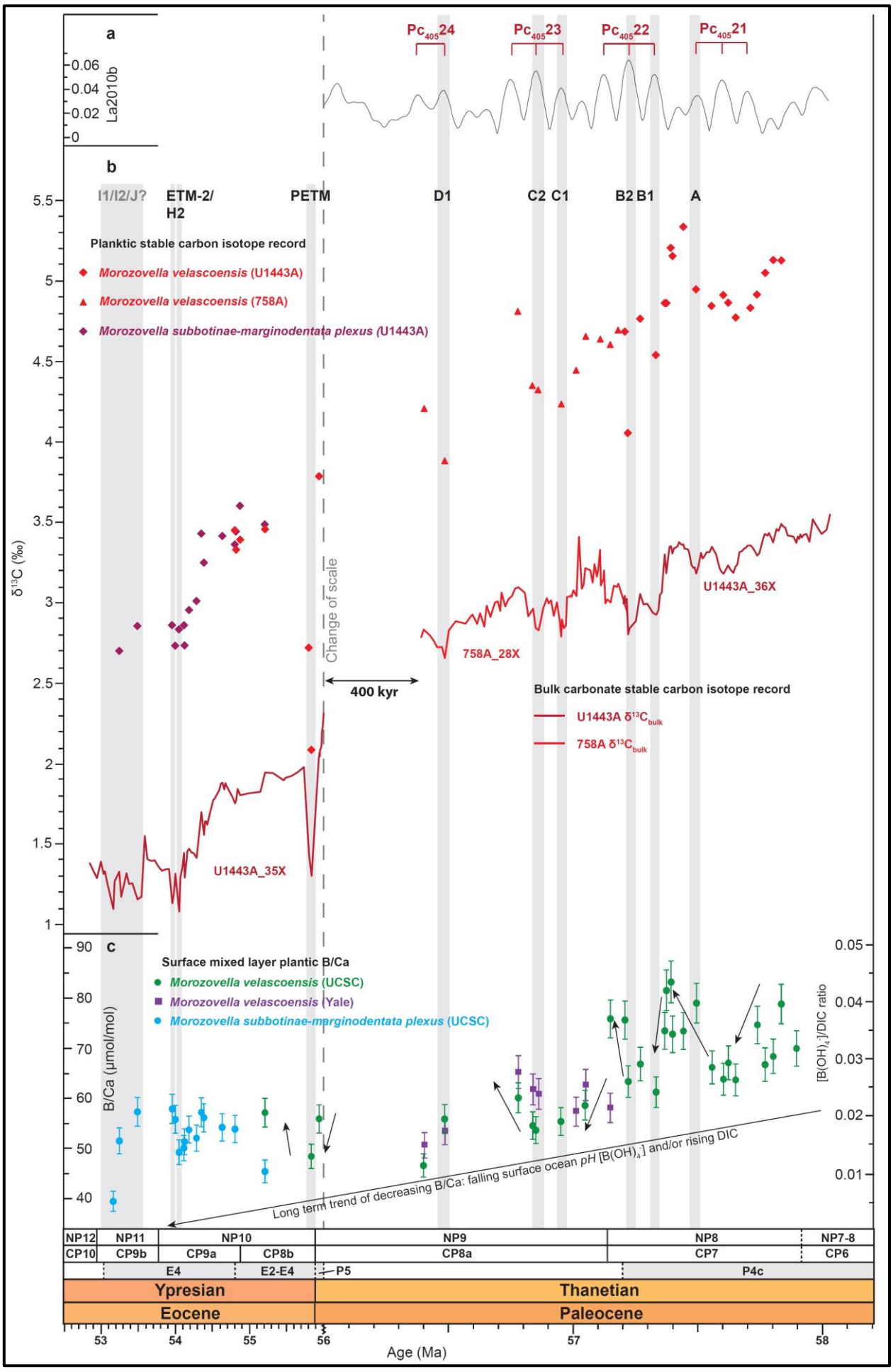
a
La2010b
0.06
0.04
0.02
0
Pc405 24
Pc405 23
Pc405 22
Pc405 21
b
I1/I2/J?
ETM-2/ H2
PETM
D1
C2 C1
B2 B1
A
Planktic stable carbon isotope record
Morozovella velascoensis (U1443A)
Morozovella velascoensis (758A)
Morozovella subbotinae-marginodentata plexus (U1443A)
δ13C (‰)
Change of scale
400 kyr
U1443A_35X
758A_28X
U1443A_36X
Bulk carbonate stable carbon isotope record
U1443A δ13Cbulk
758A δ13Cbulk
c
Surface mixed layer plantic B/Ca
Morozovella velascoensis (UCSC)
Morozovella velascoensis (Yale)
Morozovella subbotinae-marginodentata plexus (UCSC)
B/Ca (µmol/mol)
[B(OH)4]/DIC ratio
Long term trend of decreasing B/Ca: falling surface ocean pH [B(OH)4] and/or rising DIC
NP12 NP11 NP10 NP9 NP8 NP7-8
CP10 CP9b CP9a CP8b CP8a CP7 CP6
E4 E2-E4 P5 P4c
Ypresian Thanetian
Eocene Paleocene
Age (Ma)

Figure 62 (previous page). Mixed layer planktic foraminiferal carbon isotope ($\delta^{13}C_{planktic}$), bulk carbonate carbon isotope ($\delta^{13}C_{bulk}$), and B/Ca records from Indian Ocean IODP/ODP Sites U1443/758, spanning the Late Paleocene–Early Eocene (~58–53 Ma) and calibrated to an orbitally-tuned age model generated during this study. A corresponding figure with the data presented against depth (CSF-A/mbsf) is included in ***Appendix 33****. (**a**) La2010b orbital solution of Laskar et al. (2011a) for the Late Paleocene. Long (405-kyr) eccentricity maxima are labelled following the nomenclature of Dinarès-Turell et al. (2014). (**b**) $\delta^{13}C_{planktic}$ and $\delta^{13}C_{bulk}$ records. $\delta^{13}C_{planktic}$ samples analysed from IODP Hole U1443A are indicated by filled diamonds and samples from ODP Hole 758A are indicated by filled triangles, coloured in pale red for Morozovella velascoensis samples and dark red for Morozovella subbotinae-marginodentata plexus samples. (**c**) B/Ca record with borate/dissolved inorganic carbon ($\frac{[B(OH)_4^-]}{DIC}$) ratios calculated using the Paleocene calibration curve of Haynes et al. (2017). Samples analysed at UCSC are indicated by filled circles, coloured in green for Morozovella velascoensis samples and blue for Morozovella subbotinae-marginodentata plexus samples. A subset of Late Paleocene samples indicated by filled purple squares were analysed at Yale University, but note an offset to generally higher B/Ca values compared to samples analysed at UCSC. Error bars of ±5% are based on the long-term reproducibility of internal consistency standards. Hyperthermals and smaller climatic and carbon cycle perturbations are labelled at the top of the figure and correlated across the record as grey vertical bars. PETM = Paleocene-Eocene Thermal Maximum. CSF-A = Core depth below seafloor. Mbsf = Metres below sea floor.*

6.6.4. COMPARISON BETWEEN THE SURFACE OCEAN THERMAL HISTORY OF THE LOW LATITUDE INDIAN OCEAN AND THE LOW LATITUDES GLOBALLY

To determine if the mixed layer temperatures of the Late Paleocene–Early Eocene low latitude Indian Ocean were characteristic of the low latitudes globally during this time, or whether they were anomalous, the new Mg/Ca-derived temperature data from IODP Site U1443 and ODP Site 758 are plotted with available published surface ocean temperature data against latitude for the Late Paleocene in Figure 63 and the Early Eocene (post-PETM) in Figure 64. The majority of the published low latitude palaeo-temperature proxy data is derived from the equatorial Atlantic and Pacific (see Figure 54), therefore this comparison also highlights how temperatures in the mixed layer of the low latitude Indian Ocean compare to the other two major basins of the world ocean during this time. Temperatures derived from published Mg/Ca data have been recalibrated using the methods employed in this thesis and assuming Mg/Ca_{sw} = 2.5 mol/mol, to facilitate a direct comparison, whilst temperature estimates based on the other proxies remain unchanged from the literature.

These plots illustrate that temperatures within the mixed layer of the low latitude Indian Ocean are characteristic of the low latitudes globally and conform to the general latitudinal surface ocean temperature gradients of the Late Paleocene–Early Eocene, as determined by available temperature proxy data (Figure 63; Figure 64). Mean Late Paleocene mixed layer temperatures of ~29.9°C at IODP Site U1443/ODP Site 758 sit within the lower end of the range of surface ocean temperatures in equatorial regions based on the $\mathrm{TEX}_{86}^{\mathrm{H}}$, Mg/Ca and $\delta^{18}O_{planktic}$ palaeotemperature proxies (~28–34°C), and are consistent with a modelled SST of ~30°C at a paleolatitude of ~29°S based on the National Center for Atmospheric Research (NCAR) Community Earth System Model (CESM1) (Frieling et al., 2017; Figure 63). Similarly, mean Early Eocene mixed layer temperatures of ~31°C at IODP Site U1443 fall within the lower end of the range of temperature estimates in the equatorial Atlantic and Pacific (~30–34°C), based on the $\mathrm{TEX}_{86}^{\mathrm{H}}$, Mg/Ca and clumped isotope proxies (Figure 64). These equatorial temperatures are significantly cooler than estimates of low latitude temperature in the FAMOUS global climate model simulation, representing an example of a model output which struggles to replicate the Early Eocene equator-pole temperature gradient as suggested by proxy data (Sagoo et al., 2013). Late Paleocene–Early Eocene temperature estimates for the surface ocean of the low latitude Indian Ocean are significantly warmer than both modern mean annual temperatures (~15–25°C) and modern maximum summer sea surface temperatures (~25–27°C) at a latitude of ~29°S (Locarnini et al., 2013; Figure 63; Figure 64). These new Mg/Ca-derived temperature estimates from the low latitude Indian Ocean therefore fill a major geographic gap in temperature proxy data for this crucial interval of climate evolution and will represent invaluable data to input into future global climate models.

The surface ocean temperature proxy data compilations in Figure 63 and Figure 64 suggest a significantly lower equator-pole temperature gradient during the Late Paleocene–Early Eocene compared to the modern, suggesting significant amplification of warming in the high-latitudes compared to the low latitudes during this time. However, $\mathrm{TEX}_{86}^{\mathrm{H}}$-derived SST reconstructions from the Arctic Ocean (~18–21°C; Sluijs et al., 2006, 2008) are significantly higher than Mg/Ca-derived mean temperatures of intermediate depth Indian Ocean waters (~10.5–13°C; this study) and $\delta^{18}O_{benthic}$-derived temperatures of deep South

Atlantic waters (~9.5–12°C; Littler et al., 2014; Lauretano et al., 2015). These intermediate water and deep ocean temperatures are consistent with $\delta^{18}O_{planktic}$-derived mixed layer temperatures of the Southern Ocean (~11–11.5°C; Kennett & Stott, 1991; Thomas et al., 2002), which is considered to be the primary source of deep water formation for the Atlantic and Indian Oceans during this time (e.g., Thomas et al., 2003; Hollis et al., 2012). The TEX_{86}^{H}-derived temperature data may be seasonally biased and predominantly record maximum summer temperatures, whilst modelling studies by Hollis et al. (2012) suggest that deep-water formation in the Southern Ocean may have predominantly taken place in winter, therefore biasing deep water temperatures to cooler values than the annual mean. As a result, mean annual early Paleogene temperatures in the polar regions are likely to fall somewhere between the upper end member recorded by the TEX_{86}^{H} proxy data in the Arctic, and the temperature of global ocean bottom waters. Regardless, the difference in mean Late Paleocene–Early Eocene temperature between South Atlantic deep waters and the tropics (~20°C) is still significantly lower than the difference in modern mean annual temperature between the high latitudes and the tropics (~30°C), suggesting significant polar amplification of early Paleogene greenhouse warming in the high latitudes.

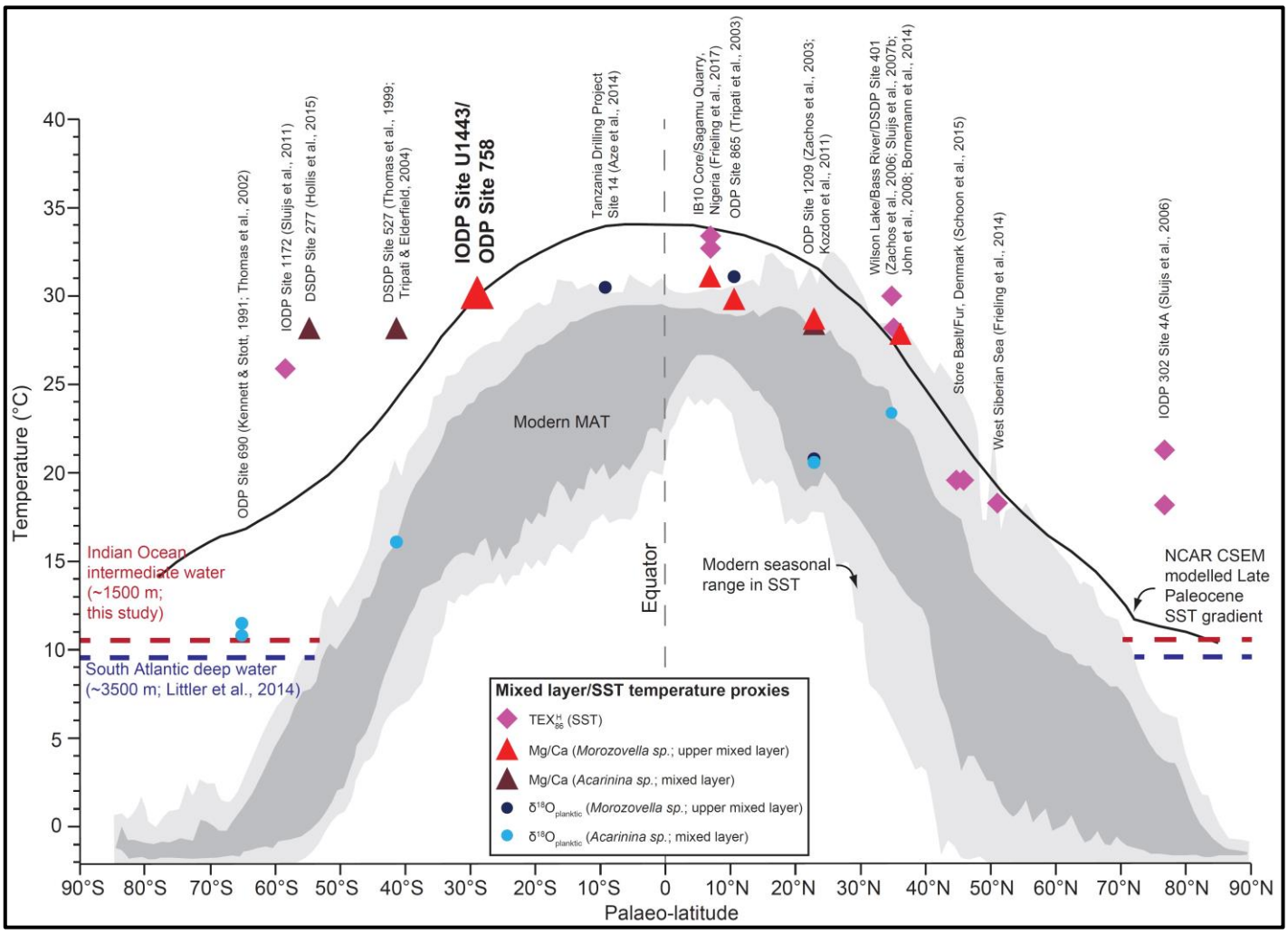

*Figure 63. Proxy data for Late Paleocene sea surface temperature (SST) and mixed layer temperature plotted against palaeo-latitude, including data based on TEX_{86}^{H} (diamonds), Mg/Ca (triangles) and $\delta^{18}O_{planktic}$ (circles). All temperatures derived from published planktic foraminiferal Mg/Ca data have been recalibrated using the methods employed in this thesis and assuming Mg/Ca_{sw} = 2.5 mol/mol. All temperature estimates based on the TEX_{86}^{H} and $\delta^{18}O_{planktic}$ proxies remain unchanged from the original literature source. The dashed red line represents the mean Late Paleocene temperature of Indian Ocean IODP Site U1443/ODP Site 758 intermediate waters based on benthic Mg/Ca (~1500m depth; this study) and the dashed blue line represents the mean temperature of South Atlantic ODP Site 1262 deep waters based on $\delta^{18}O_{benthic}$ (~3500m depth; Littler et al., 2014; see **Chapter 3**). Palaeo-latitudes for the sites during the Late Paleocene were computed relative to the palaeomagnetic reference frame of Torsvik et al. (2012) using Version 2.1 of the model from paleolatitude.org (van Hinsbergen et al., 2015). The black line indicates modelled SST based on the National Center for Atmospheric Research Community Earth System Model (NCAR CESM1; Frieling et al., 2017), assuming a radiative forcing equivalent to 2240 ppm CO_2. Note that this modelled CO_2 value is significantly higher than Late Paleocene proxy estimates (**Chapter 3**; Figure 12a). New data from IODP Site U1443/ODP Site 758 are indicated by an enlarged red triangle. These new data are consistent with the CESM1 model output and other low-latitude temperature proxy data, suggesting that the low-latitude Indian Ocean conforms to the general latitudinal SST gradient of the Late Paleocene. Modern mean annual temperature (MAT) and modern seasonal range in SST are also shown for comparison (Locarnini et al., 2013).*

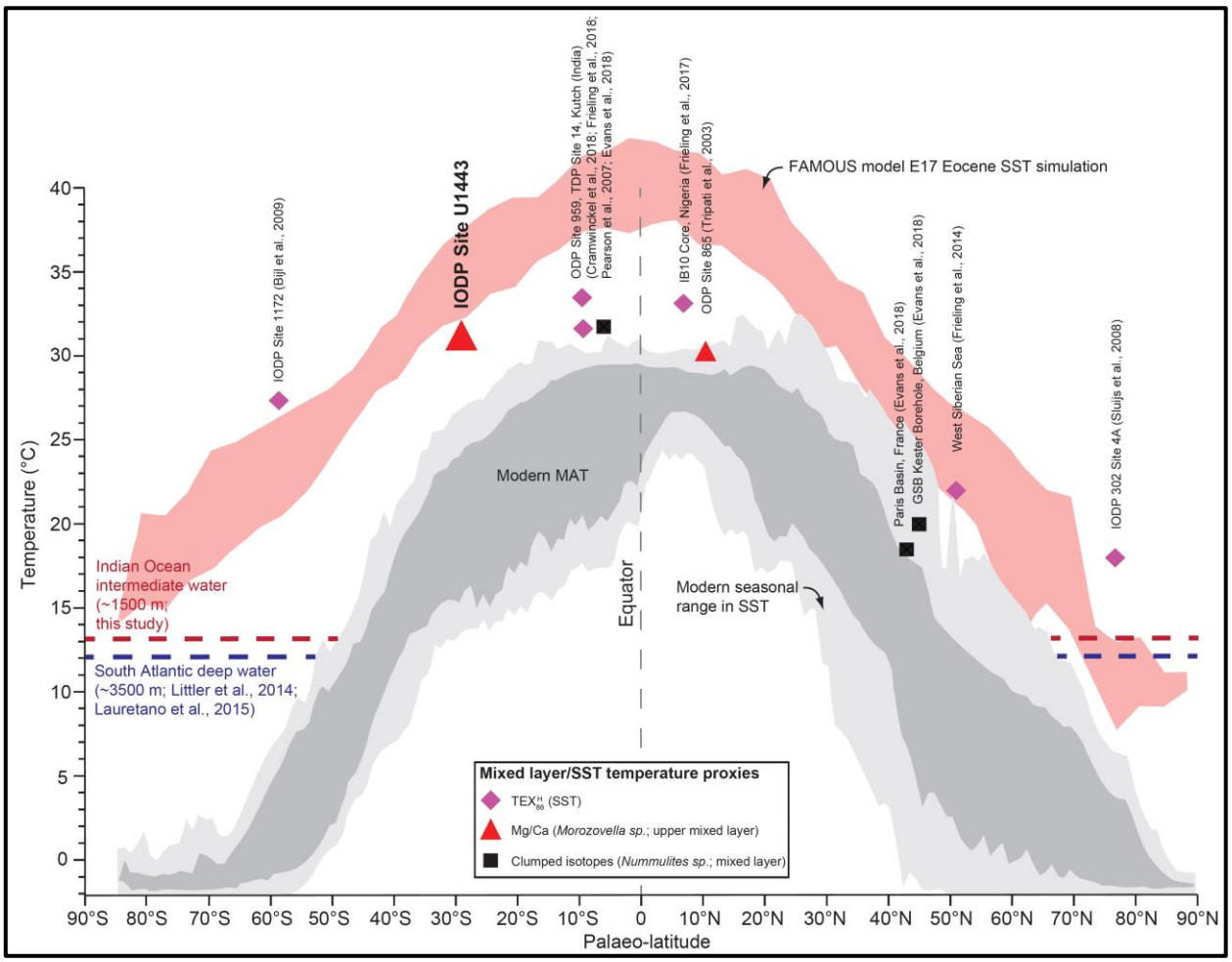

*Figure 64. Proxy data for Early Eocene (post-PETM) sea surface temperature (SST) and mixed layer temperature plotted against palaeo-latitude, including data based on TEX_{86}^{H} (diamonds), Mg/Ca (triangles) and clumped isotopes of large benthic foraminifera (squares). All temperatures derived from published planktic foraminiferal Mg/Ca data have been recalibrated using the methods employed in this thesis and assuming Mg/Ca_{sw} = 2.5 mol/mol. All temperature estimates based on TEX_{86}^{H} and clumped isotopes remain unchanged from the original literature source. The dashed red line represents the mean Early Eocene temperature of Indian Ocean IODP Site U1443 intermediate waters based on benthic Mg/Ca (~1500m depth; this study) and the dashed blue line represents the mean temperature of South Atlantic ODP Site 1262 deep waters based on $\delta^{18}O_{benthic}$ (~3500m depth; Littler et al., 2014; see **Chapter 3**). The FAMOUS Model E17 simulation for SST is also shown (Sagoo et al., 2013), assuming a radiative forcing equivalent to 560 ppm CO_2, representing an example of a model output which captures polar amplification of warming but also predicts significantly higher low latitude temperatures than suggested by proxy data. Palaeo-latitudes for the sites during the Early Eocene were computed relative to the palaeomagnetic reference frame of Torsvik et al. (2012) using Version 2.1 of the model from paleolatitude.org (van Hinsbergen et al., 2015). New data from IODP Site U1443 are indicated by an enlarged red triangle. These new data are consistent with other low-latitude temperature proxy data, suggesting that the low-latitude Indian Ocean conforms to the general latitudinal SST gradient of the Early Eocene. Modern mean annual temperature (MAT) and modern seasonal range in SST are also shown for comparison (Locarnini et al., 2013).*

In order to understand if the thermal evolution of the surface ocean is also comparable between the low latitude Indian Ocean and the low latitude Pacific and Atlantic from the Late Paleocene to Early Eocene, the new Mg/Ca-derived temperature data are also plotted up with a compilation of available published low latitude temperature records across this time interval. Firstly, a comparison between the new Late Paleocene–Early Eocene mixed layer (*Morozovella*) Mg/Ca record from IODP/ODP Sites U1443/758 (palaeolatitude ~29°S) with the only other published long-term planktic Mg/Ca record across this time interval, from the equatorial Pacific Allison Guyot ODP Site 865 (palaeolatitude ~10°N; Tripati et al., 2003), is illustrated in Figure 65. Based on whole-specimen SEM images from ODP Site 865, foraminiferal preservation at both sites appears to be comparable (Bralower et al., 1995). However, Bralower et al. (1995) do not present close-up SEM images of pore structures or cross sections through test walls, therefore foraminiferal preservation at ODP Site 865 at the microscale is challenging to verify. A degree of diagenetic influence on one or both of the records cannot, therefore, be discounted. The correlation highlights the superior resolution of the Indian Ocean Mg/Ca record presented in this thesis compared to the equatorial Pacific record. As a consequence of the lower sample resolution, orbital-scale temperature variability cannot be observed in the ODP Site 865 record. Despite an increase in sample resolution across the PETM (Tripati & Elderfield, 2004), a comparable magnitude of warming at both ODP Site 865 and IODP Site U1443 suggests that the core of this enigmatic hyperthermal event has not been completely resolved in either low latitude Mg/Ca record. Nonetheless, both records appear to be characterised by similar background latest Paleocene and Early Eocene post-recovery mixed layer temperatures. The PETM is discussed further in **Section 6.7** later in this chapter.

Despite differences in sample resolution, and possibly foraminiferal preservation, the long-term thermal histories of the low latitude Indian and Pacific oceans appear to be coupled (Figure 65). This is clear both in the trends and the absolute temperatures of the mixed layer in both records, as both are characterised by a progressive warming from ~29–30.5°C during the Late Paleocene to ~29–32°C during the Early Eocene. Due to the lower resolution of the ODP Site 865 record, however, it is not possible to confirm whether the period

of apparent surface ocean cooling identified between ~57.4–56.4 Ma in the Indian Ocean is also replicated in the equatorial Pacific.

By comparing the long-term Mg/Ca-derived temperature records from the low latitude Indian and Pacific oceans to other proxy temperature estimates from the low latitudes, it is evident that a long-term warming trend within both the mixed layer (based on Mg/Ca, $\delta^{18}O_{planktic}$ and clumped isotopes) and at the sea surface (based on TEX_{86}^{H}), from the Late Paleocene to the start of the Eocene, is characteristic of the low latitudes globally (Figure 66). Interestingly, the apparent period of short-term surface ocean cooling identified between ~57.4–56.4 Ma within the Indian Ocean mixed layer Mg/Ca data is also evident and of a similar magnitude (~–1°C) within the TEX_{86}^{H} and $\delta^{18}O_{planktic}$ proxy data from the eastern Atlantic, suggesting that a genuine surface ocean cooling took place during this time and is characteristic of the low latitudes globally.

The continuation of the warming trend into the Early Eocene is only supported by the mixed layer Mg/Ca-derived temperature data from the low latitude Indian Ocean (this study) and the equatorial Pacific (Tripati et al., 2003). Since there is evidence for decreasing Mg/Ca_{sw} during the Early–Middle Eocene (Evans et al., 2018), the magnitude of the warming trend based on planktic Mg/Ca may be artificially dampened during this time. This data compilation therefore highlights the importance of the new Early Eocene low latitude Indian Ocean Mg/Ca-derived mixed layer temperature record presented herein for describing the evolution of Early Eocene climate in the low latitudes, but also underscores the need for future work focusing on whether this trend is also replicated in other sea surface and mixed layer temperature proxies (e.g., TEX_{86}^{H}, $\delta^{18}O_{planktic}$ and clumped isotopes), as well as within the mixed layer of the low latitude Atlantic Ocean.

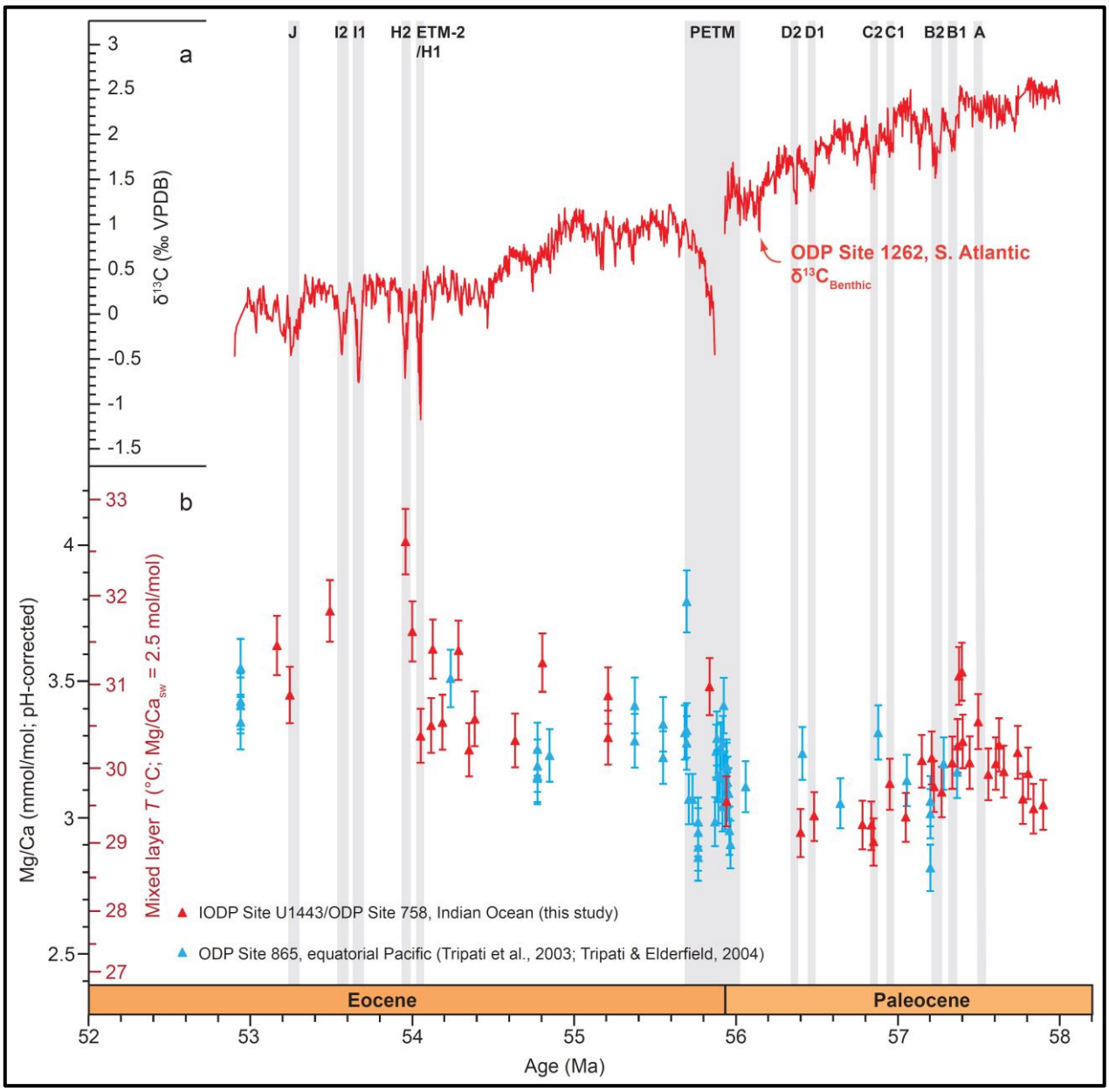

Figure 65. Comparison between mixed layer Mg/Ca data from Indian Ocean IODP/ODP Sites U1443/758 (palaeolatitude ~29°S; this study) and Mg/Ca data from the equatorial Pacific Allison Guyot ODP Site 865 (palaeolatitude ~10°N; Tripati et al., 2003; Tripati & Elderfield, 2004). Both datasets are based on analysis of Morozovella velascoensis/M. subbotinae-marginodentata plexus and both have been pH-corrected assuming an ambient Late Paleocene–Early Eocene pH of 7.7 and PETM pH of 7.6 (assuming the PETM stratigraphy is incomplete at both sites). Absolute mixed layer temperature estimates are calculated using a modelled Paleogene Mg/Ca_{sw} value of 2.5 mol/mol (red scale), which is based on Early Eocene proxy data (Evans et al., 2018). Error bars of ±3% (Indian Ocean data) and ±2.7% (Pacific Ocean data; Tripati et al., 2003; Tripati & Elderfield, 2004) on the Mg/Ca measurements (±0.3°C) represent analytical uncertainty and are based on the long-term reproducibility of consistency standards. Absolute temperature values are also associated with a calibration error of ±1.13°C (Anand et al., 2003), giving a total uncertainty of ±1.4°C. Additional sources of uncertainty, which cannot be constrained, include the evolution of Mg/Ca_{sw}, surface ocean pH, and salinity across this time interval.

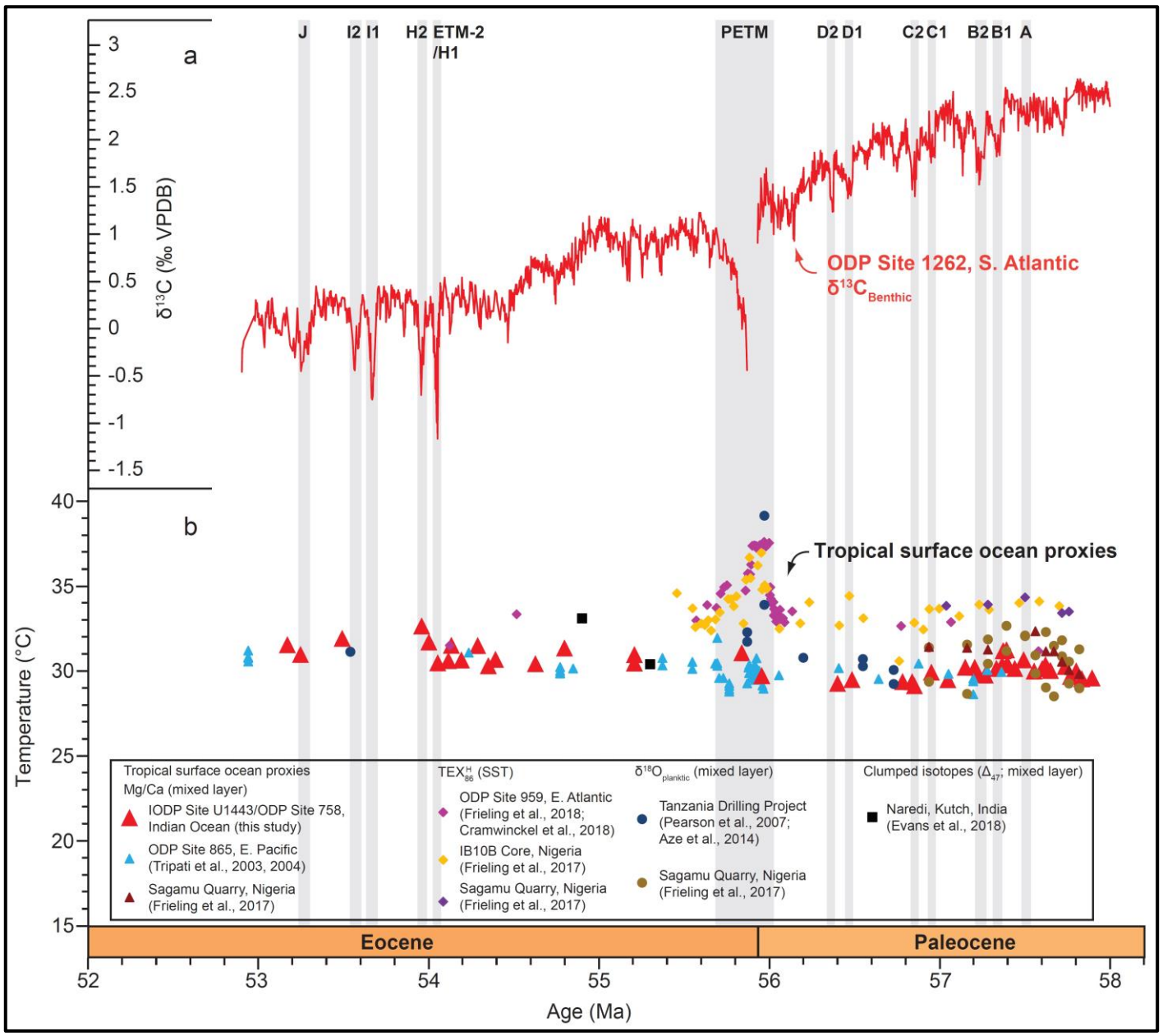

*Figure 66. Compilation of palaeo-temperature proxy data focusing on the thermal evolution of the surface ocean in the low latitudes (tropics) during the Late Paleocene–Early Eocene, calibrated to the orbitally-tuned age model presented in this thesis (**Chapter 3**). (**a**) $\delta^{13}C_{benthic}$ data from ODP Site 1262 (see **Chapter 3**; Littler et al., 2014; Lauretano et al., 2015), with carbon cycle events highlighted and correlated across the figure as vertical grey bars. (**b**) Compilation of low latitude surface ocean temperature proxy data, based on TEX_{86}^{H} (sea surface temperature; coloured diamonds), Mg/Ca (mixed layer; coloured triangles), $\delta^{18}O_{planktic}$ (mixed layer; coloured circles), and clumped isotopes (mixed layer; black squares). Published Mg/Ca-derived temperature estimates have been recalibrated using the methodology employed in this thesis. All Mg/Ca-derived temperature estimates have been calculated assuming Mg/Ca_{sw} = 2.5 mol/mol, consistent with Early Eocene proxy data. All other temperature proxy estimates remain unchanged from the original literature source.*

6.6.5. CHANGES IN THERMOCLINE CARBONATE CHEMISTRY AND TEMPERATURE DURING THE LATE PALEOCENE–EARLY EOCENE

The thermocline (*Subbotina sp.*) planktic B/Ca and Mg/Ca records spanning the Late Paleocene–Early Eocene (~58–53 Ma) are presented in Figure 67. A similar apparent offset is also evident in the thermocline Mg/Ca and B/Ca data between duplicate samples analysed at UCSC and Yale from ODP Site 758, however this offset does not affect the discussion of the long-term trends presented here based on the UCSC data. Comparable to temperature trends within the mixed layer (based on *Morozovella sp*.), there is a long-term rise in Mg/Ca (from ~2.3 to ~3.3 mmol/mol) from the Late Paleocene–Early Eocene, representing an estimated rise in absolute temperature from ~26.5 (±1.4)°C to ~30.0 (±1.4)°C (assuming Mg/Ca_{sw} = 2.5 mol/mol; Figure 67d). However, in contrast to the mixed layer data, there is a negligible long-term shift in B/Ca during this time interval, suggesting that thermocline depths may have been relatively buffered against the long-term fall in pH and/or increase in DIC experienced by the mixed layer during this time. Transient drops in B/Ca are, however, evident during “B1”, “C1”, the PETM, and carbon isotope excursions of the Early Eocene, suggesting that only the larger transient climate and carbon cycle events of this time period appear to have a noticeable expression within the carbonate chemistry at deeper thermocline depths (Figure 67c).

As with the mixed layer, Late Paleocene orbitally-paced excursions in temperature are generally not resolvable within the thermocline Mg/Ca record, with the exception of the PETM and largest events of the Early Eocene (Figure 67d). The temperature response at the thermocline during the PETM is discussed separately in **Section 6.7** below.

Comparable to the mixed layer record (Figure 61c), the long-term Late Paleocene–Early Eocene warming at thermocline depths appears to be interrupted by a transient period of cooling during the latest Paleocene (Figure 67d). However this cooling trend appears to commence later in the thermocline record (~57 Ma as opposed to ~57.4 Ma in the mixed layer record), although it is of a similar magnitude (~–1°C; Figure 61c; Figure 67d). As in the mixed layer Mg/Ca record, this apparent cooling trend in the thermocline Mg/Ca data could

alternatively be explained by a significant fall in Mg/Ca_{sw} across this latest Paleocene time slice, however no Mg/Ca_{sw} proxy data from the Late Paleocene are currently available to test this hypothesis.

Although a step change to warmer baseline temperatures is also evident in the mixed layer Mg/Ca data after the PETM (by ~+1°C; Figure 61c), this step change is significantly greater at thermocline depths (~+2°C), suggesting amplified warming within the thermocline during the PETM and Early Eocene compared to the mixed layer. As a consequence, thermocline temperatures do not fully recover to pre-excursion conditions following transient warming during the PETM. As in the mixed layer, the apparent magnitude of warming during the Early Eocene (post-PETM) portion of the thermocline record may be artificially dampened by a decrease in Mg/Ca_{sw} from the Early to Middle Eocene (Evans et al., 2018).

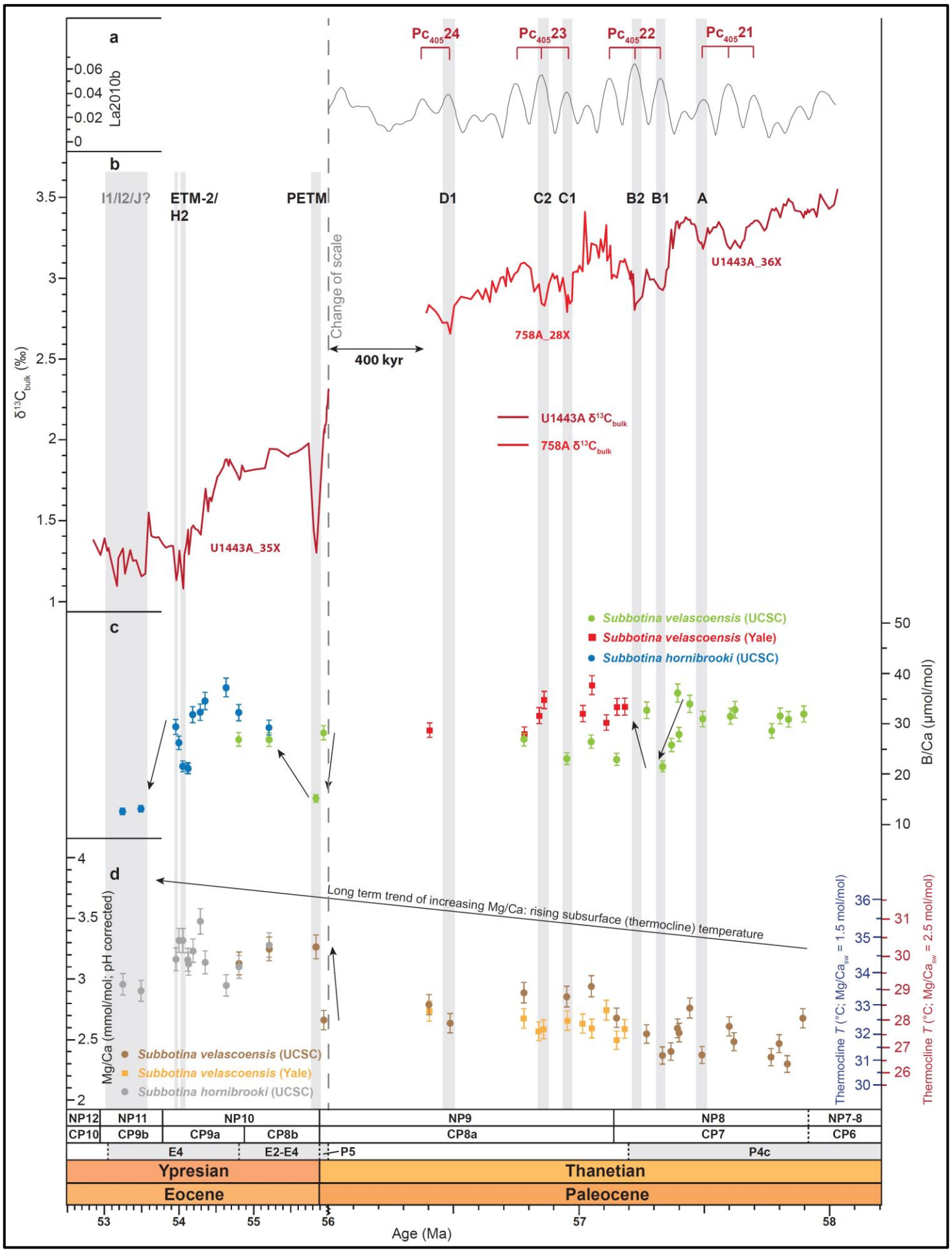
a
La2010b
0.06
0.04
0.02
0
Pc405 24
Pc405 23
Pc405 22
Pc405 21
b
I1/I2/J?
ETM-2/ H2
PETM
D1
C2 C1
B2 B1
A
Change of scale
400 kyr
U1443A_36X
758A_28X
U1443A_35X
U1443A δ13Cbulk
758A δ13Cbulk
δ13Cbulk (‰)
c
Subbotina velascoensis (UCSC)
Subbotina velascoensis (Yale)
Subbotina hornibrooki (UCSC)
B/Ca (µmol/mol)
d
Long term trend of increasing Mg/Ca: rising subsurface (thermocline) temperature
Mg/Ca (mmol/mol; pH corrected)
Thermocline T (°C; Mg/Casw = 1.5 mol/mol)
Thermocline T (°C; Mg/Casw = 2.5 mol/mol)
NP12
NP11
NP10
NP9
NP8
NP7-8
CP10
CP9b
CP9a
CP8b
CP8a
CP7
CP6
E4
E2-E4
P5
P4c
Ypresian
Thanetian
Eocene
Paleocene
Age (Ma)

Figure 67 (previous page). Thermocline planktic foraminiferal B/Ca and Mg/Ca records from Indian Ocean Ninetyeast Ridge IODP Site U1443/ODP Site 758, spanning the Late Paleocene–Early Eocene (~58–53 Ma) and calibrated to an orbitally-tuned age model generated during this study. A corresponding figure with the data presented against depth (CSF-A/mbsf) is included in ***Appendix 34****. (**a**) La2010b orbital solution of Laskar et al. (2011a) for the Late Paleocene. Long (405-kyr) eccentricity maxima are labelled following the nomenclature of Dinarès-Turell et al. (2014). (**b**) Bulk carbonate carbon isotope ($\delta^{13}C_{bulk}$) record. Core sections from which the data are derived are labelled. (**c**) B/Ca record. Samples analysed at UCSC are indicated by filled circles, coloured in green for Subbotina velascoensis samples and blue for Subbotina hornibrooki samples. A subset of Late Paleocene samples indicated by filled red squares were analysed at Yale University, but note an offset to higher B/Ca values compared to samples analysed at UCSC. Error bars of ±5% are based on the long-term reproducibility of internal consistency standards. (**d**) Mg/Ca record with values corrected for pH, assuming a background surface ocean pH of 7.7 and PETM pH of 7.6. Absolute thermocline temperature (T) estimates are calculated using modelled Paleogene Mg/Ca_{sw} values of 1.5 mol/mol (blue scale) and 2.5 mol/mol (red scale), which bracket the potential range of early Paleogene Mg/Ca_{sw} based on modelling (~1.5 mol/mol) and proxy (~2.5 mol/mol) studies and produce an absolute temperature offset of ~4.5°C. Temperatures calculated using Mg/Ca_{sw} = 2.5 mol/mol are considered the most robust. Samples analysed at UCSC are indicated by filled circles, coloured in brown for Subbotina velascoensis samples and grey for Subbotina hornibrooki samples. A subset of Late Paleocene samples indicated by filled orange squares were analysed at Yale University, but note an offset to lower Mg/Ca values compared to samples analysed at UCSC. The illustrated error bars of ±3% on the Mg/Ca measurements (±0.3°C) represent analytical uncertainty and are based on the long-term reproducibility of internal consistency standards. Absolute temperature values are also associated with a calibration error of ±1.13°C (Anand et al., 2003), giving a total uncertainty of ±1.4°C. Additional sources of uncertainty, which cannot be constrained, include the evolution of Mg/Ca_{sw}, surface ocean pH, and salinity across this time interval. Hyperthermals and smaller climatic and carbon cycle perturbations are labelled at the top of the figure and correlated across the records as grey vertical bars. PETM = Paleocene-Eocene Thermal Maximum. CSF-A = Core depth below seafloor. Mbsf = Metres below sea floor.*

6.6.6. RELATIVE CHANGES IN INTERMEDIATE WATER CARBONATE SATURATION STATE AND TEMPERATURE DURING THE LATE PALEOCENE–EARLY EOCENE

Benthic B/Ca and Mg/Ca records spanning the Late Paleocene–Early Eocene (~58–53 Ma), based on analysis of *Nuttallides truempyi* and *Oridorsalis umbonatus*, respectively, are presented in Figure 68. Examination of the data suggests that a laboratory offset also exists between benthic Mg/Ca and B/Ca data generated at UCSC and Yale from ODP Site 758, however, this offset does

not affect the interpretation of the long-term trends discussed here based on the UCSC data.

Benthic (*N. truempyi*) B/Ca values are within analytical error of one another across the PCIM and at the start of the Eocene, however exhibit a rather enigmatic pronounced decrease between ~57.4–56.4 Ma. This temporary fall in benthic B/Ca may suggest a temporary decrease in carbonate saturation state of the intermediate water mass bathing the Indian Ocean sites during the latest Paleocene, before recovery to a comparable carbonate saturation state to the PCIM by the end of the Paleocene (Figure 68c). Dissolution proxies (i.e., Fe intensity) from the deeper South Atlantic ODP Site 1262 suggest a deep and relatively stable background lysocline located below ODP Site 1262 (palaeo-depth ~3500 m) during the Late Paleocene–Early Eocene, except during hyperthermal events (see **Chapter 3**; Figure 12f; Littler et al., 2014). The new benthic B/Ca data presented here, however, provide evidence for a potential decrease in carbonate saturation state of the intermediate water mass in the Indian Ocean during the latest Paleocene.

Whilst the PETM has a pronounced expression within the benthic B/Ca record (discussed further in **Section 6.7**), there appears to be a muted response to the the smaller orbitally-paced climatic perturbations of the Late Paleocene within the benthic B/Ca data, with a pronounced decrease only during the “D1” event. This muted response suggests that intermediate waters (~1500m palaeo-depth) were relatively buffered against the smaller orbitally-paced carbon cycle perturbations of the Late Paleocene (Figure 68c).

A significant step-wise drop in B/Ca of ~–16.5 µmol/mol occurred over ~1 million years during the Early Eocene from ~54.5 Ma, to some of the lowest background values within the record by ~53.5 Ma (~107 µmol/mol; Figure 68c). This drop in B/Ca equates to a decrease in $\Delta[CO_3^{2-}]$ of ~–13.5 µmol/kg, suggesting a significant decrease in background carbonate saturation state during this time, accompanied by a fall in $\delta^{13}C_{bulk}$ to the lightest values preserved within the record. This finding appears to contradict previous proxy studies from deeper water depths on the Ninetyeast Ridge (~3000–3500 m paleo-depth), which based on %$CaCO_3$, suggest that rapid shoaling of the CCD did not occur

until ~52 Ma (Slotnick et al., 2015). However, the new B/Ca data presented here record relative changes in carbonate saturation state of an intermediate depth water mass (~1500 m palaeo-depth), therefore may not be representative of changes in carbonate saturation state within deep bottom waters of the global ocean (i.e., controlling the fluctuating depth of the CCD). These data therefore appear to record a precursor drop in carbonate saturation state of the intermediate depth water mass bathing the low latitude Indian Ocean Ninetyeast Ridge IODP Site U1443, preceding global shoaling of the CCD during EECO, as recorded in proxy data and predicted by modelling studies of the Atlantic and Pacific (Komar et al., 2013; Slotnick et al., 2015), by ~2.5 million years.

In agreement with the mixed layer and thermocline, intermediate waters bathing IODP/ODP Sites U1443/758 exhibit a long-term warming trend from ~9.5–11.5 (±1.8)°C during the Late Paleocene to ~12.5–14.0 (±1.8)°C during the Early Eocene (Figure 68d). A stabilisation or small decrease in intermediate water temperatures is also evident during the latest Paleocene between ~57.4–56.4 Ma, corresponding to the short period of cooling observed within the mixed layer. The argument for a short period of cooling during this latest Paleocene time slice is further strengthened by the low sensitivity of *Oridorsalis umbonatus* Mg/Ca to changing Mg/Ca_{sw} (Lear et al., 2015). A stabilisation of temperatures or gradual cooling during the latest Paleocene therefore appears to be a characteristic feature of all depths within the water column of the Indian Ocean above the Ninetyeast Ridge, interrupting an overall long-term warming trend from the Late Paleocene to the Early Eocene.

The PETM is manifested as an abrupt warming event followed by partial recovery and the establishment of warmer baseline intermediate water temperatures during the Early Eocene (Figure 68d). A more detailed exploration of the intermediate and deep water response to the PETM is discussed separately in **Section 6.7** below. This temperature pattern of gradual Late Paleocene warming, a subsequent latest Paleocene cooling, followed by an abrupt warming to warmer baseline temperatures established during the PETM, is comparable to the temperature pattern observed within the thermocline and mixed layer data (Figure 67d). The magnitude of the step change to warmer baseline temperatures during the Early Eocene is of a comparable magnitude to

that observed at thermocline depths (~+2°C) and greater than the magnitude observed in the mixed layer (~+1°C).

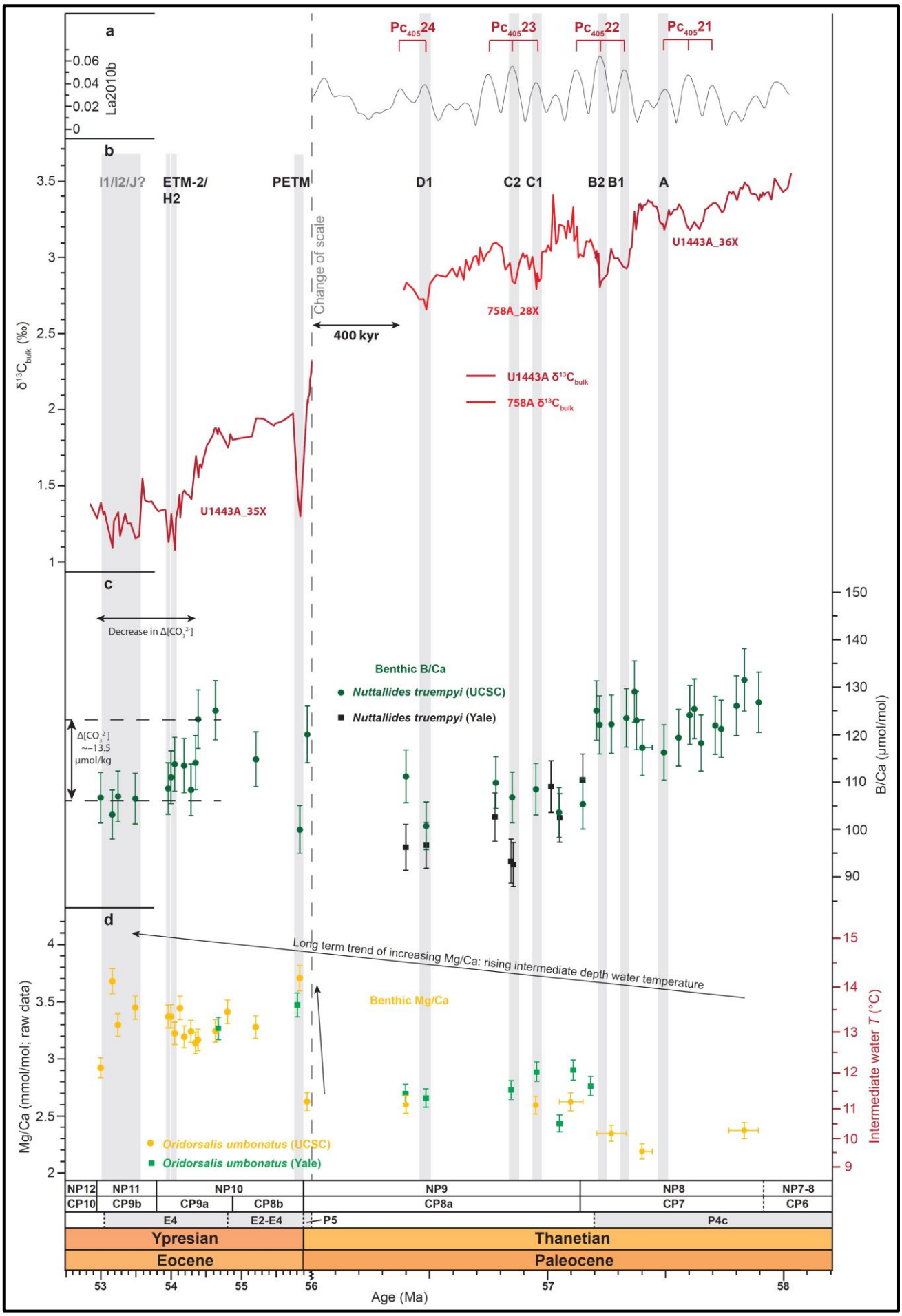
a
La2010b
0.06
0.04
0.02
0
Pc405 24
Pc405 23
Pc405 22
Pc405 21
b
I1/I2/J?
ETM-2/
H2
PETM
D1
C2 C1
B2 B1
A
Change of scale
400 kyr
U1443A_36X
758A_28X
U1443A_35X
U1443A δ13Cbulk
758A δ13Cbulk
δ13Cbulk (‰)
c
Decrease in Δ[CO3 2-]
Δ[CO3 2-]
~–13.5
µmol/kg
Benthic B/Ca
Nuttallides truempyi (UCSC)
Nuttallides truempyi (Yale)
B/Ca (µmol/mol)
d
Long term trend of increasing Mg/Ca: rising intermediate depth water temperature
Benthic Mg/Ca
Oridorsalis umbonatus (UCSC)
Oridorsalis umbonatus (Yale)
Mg/Ca (mmol/mol; raw data)
Intermediate water T (°C)
NP12
NP11
NP10
NP9
NP8
NP7-8
CP10
CP9b
CP9a
CP8b
CP8a
CP7
CP6
E4
E2-E4
P5
P4c
Ypresian
Thanetian
Eocene
Paleocene
Age (Ma)

Figure 68 (previous page). Benthic foraminiferal B/Ca and Mg/Ca records from Indian Ocean IODP/ODP Sites U1443/758 (~1500m palaeo-depth), spanning the Late Paleocene–Early Eocene (~58–53 Ma) and calibrated to an orbitally-tuned age model generated during this study. A corresponding figure with the data presented against depth (CSF-A/mbsf) is included in ***Appendix 35****. (**a**) La2010b orbital solution of Laskar et al. (2011a) for the Late Paleocene. Long (405-kyr) eccentricity maxima are labelled following the nomenclature of Dinarès-Turell et al. (2014). (**b**) Bulk carbonate carbon isotope ($\delta^{13}C_{bulk}$) record. Core sections from which the data are derived are labelled. (**c**) Benthic B/Ca record. Relative changes in carbonate saturation state ($\Delta[CO_3^{2-}]$) were calculated using the calibration developed for Nuttallides umbonifera and modified to take into account the different boron concentration of Paleogene seawater in comparison to the modern. Samples analysed at UCSC are indicated by filled green circles and samples analysed at Yale University by filled black squares. Note an offset of the Yale data to generally lower B/Ca values compared to data from UCSC. Error bars of ±5% are based on the long-term reproducibility of consistency standards. (**d**) Benthic Mg/Ca. Due to the apparent low sensitivity of Oridorsalis umbonatus Mg/Ca to changing Mg/Ca_{sw} (Lear et al., 2015), absolute intermediate water temperature (T) estimates are calculated using Paleogene Mg/Ca_{sw} = 2.5 mol/mol only, consistent with Early Eocene proxy data. Samples analysed at UCSC are indicated by filled orange circles and samples analysed at Yale University by filled green squares. Samples analysed from the same Early Eocene stratigraphic interval at both UCSC and Yale suggest negligible offset between laboratories in the benthic Mg/Ca data. The illustrated error bars of ±3% on the Mg/Ca measurements (±0.3°C) represent analytical uncertainty and are based on the long-term reproducibility of internal consistency standards. Absolute temperature values are also associated with a calibration error of ±1.5°C, derived from error bars associated with the constants used in the temperature calibration equation (Lear et al., 2015), giving a total uncertainty of ±1.8°C. Hyperthermals and smaller climatic and carbon cycle perturbations are labelled at the top of the figure and correlated across the records as grey vertical bars. PETM = Paleocene-Eocene Thermal Maximum. CSF-A = Core depth below seafloor. Mbsf = Metres below sea floor.*

6.6.7. COMPARISON BETWEEN THE THERMAL EVOLUTION OF INDIAN OCEAN INTERMEDIATE WATERS AND INTERMEDIATE-DEEP WATERS OF THE ATLANTIC AND PACIFIC DURING THE LATE PALEOCENE TO EARLY EOCENE

A comparison between Mg/Ca-derived temperatures from intermediate water depths of the Indian Ocean (~1500 m depth) with deep waters from the equatorial Pacific (~2500 m depth), South Atlantic (~3500 m depth) and Southern Ocean (~2500 m depth), is illustrated in Figure 69. Intermediate to deep waters within all ocean basins show a long-term warming trend from the Late Paleocene to Early Eocene, suggesting significant warming within the high-latitude sources of intermediate to deep water formation during this time. However, whilst the

temperature records from ODP Sites 1209, 1262 and 690 suggest comparable absolute temperatures and magnitudes of warming in the deep equatorial Pacific, South Atlantic and Southern Ocean, respectively, the Mg/Ca-derived temperature record from the intermediate waters of the Indian Ocean is generally offset to warmer temperatures by ~+0.5–1.5°C, likely due to the shallower palaeo-depth. Interestingly, the Indian Ocean temperature record appears to converge with the Atlantic, Pacific and Southern Ocean records during the Early Eocene after ETM-2, which may suggest a greater magnitude of warming within the deep equatorial Pacific, South Atlantic and Southern Ocean during the Early Eocene due to polar amplification of Early Eocene greenhouse warming (see Figure 63 and Figure 64). Alternatively, this apparent convergence may be an artefact of poor age control on this portion of the Indian Ocean record after ETM-2 (see **Section 6.6.1.**). The period of apparent latest Paleocene cooling in the Indian Ocean records at ~57.4–56.4 Ma is also expressed as a stabilisation in temperature or gradual cooling, superimposed on an overall long-term warming trend in the high-resolution $\delta^{18}O_{benthic}$ records from the deep Atlantic and Pacific, suggesting that this gradual cooling trend is global in nature.

The Mg/Ca-derived temperature record from the deep equatorial Pacific ODP Site 1209 (Dutton et al., 2005a) exhibits negligible warming from the Late Paleocene to the Early Eocene, in contrast to the $\delta^{18}O_{benthic}$ record from the same site (Westerhold et al., 2011; 2018; Figure 69). This is likely to be due to the fact that the Mg/Ca data were derived from the epifaunal species *Nuttallides truempyi* and normalised to the shallow infaunal species *Oridorsalis umbonatus* based on a limited subset of overlap samples. Benthic Mg/Ca data based on *Nuttallides truempyi* from IODP Site U1443 and ODP Site 758 also exhibit little change across this time interval, and do not record the long-term warming or step-change to significantly warmer baseline temperatures during the Early Eocene, as recorded by data based on analysis of *Oridorsalis umbonatus* (Figure 70). The comparison in Figure 70 therefore highlights the importance of using a shallow infaunal species with a well-developed temperature calibration for benthic Mg/Ca-derived temperature estimates, buffered against low and changing intermediate-deep water pH. The temperature trend inferred from the ODP Site 1209 benthic Mg/Ca record should therefore be treated with caution.

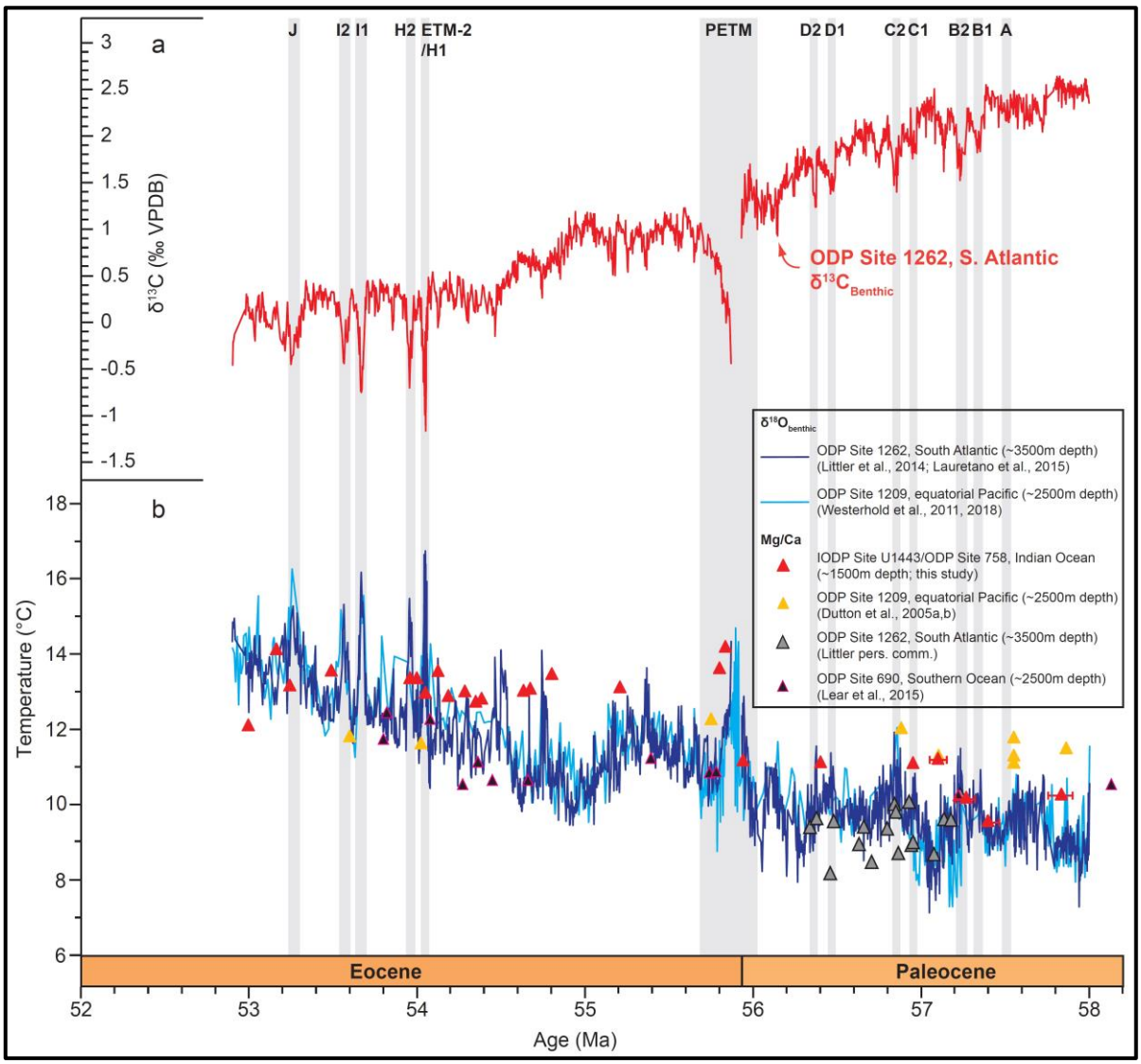

*Figure 69. Thermal evolution of intermediate-deep waters in the Indian, Pacfic and Atlantic oceans during the Late Paleocene–Early Eocene, calibrated to the updated orbitally-tuned age model presented in this thesis. (**a**) $\delta^{13}C_{benthic}$ data from ODP Site 1262 (see **Chapter 3**), with carbon cycle events highlighted and correlated across the figure as vertical grey bars. (**b**) Compilation of intermediate-deep water temperature proxy data, including Mg/Ca-derived temperatures from the Indian Ocean IODP Site U1443 (~1500 m depth; this study), Mg/Ca-derived temperatures from the Southern Ocean ODP Site 690 (~2500 m depth; Lear et al., 2015); Mg/Ca-derived and $\delta^{18}O_{benthic}$-derived temperatures from equatorial Pacific ODP Site 1209 (~2500 m depth; Dutton et al., 2005a, 2005b; Westerhold et al., 2011, 2018), and Mg/Ca-derived and $\delta^{18}O_{benthic}$-derived temperatures from South Atlantic ODP Site 1262 (~3500 m depth; Littler et al., 2014; Lauretano et al., 2015; Littler, pers. comm.). Mg/Ca data from ODP Site 1209, based on analysis of Nuttallides truempyi, were normalised to Oridorsalis umbonatus by applying a correction to account for the mean offset calculated from overlap samples, then temperatures were calculated using the methodologies employed in this thesis for IODP Site U1443 samples. All Mg/Ca-derived temperature estimates reported here were calculated assuming Mg/Ca_{sw} = 2.5 mol/mol, consistent with Early Eocene proxy data. Temperatures were calculated from $\delta^{18}O_{benthic}$ data using the temperature calibration of Kim & O'Neil (1997) for inorganic calcite, modified by Bemis et al. (1998; Equation 1).*

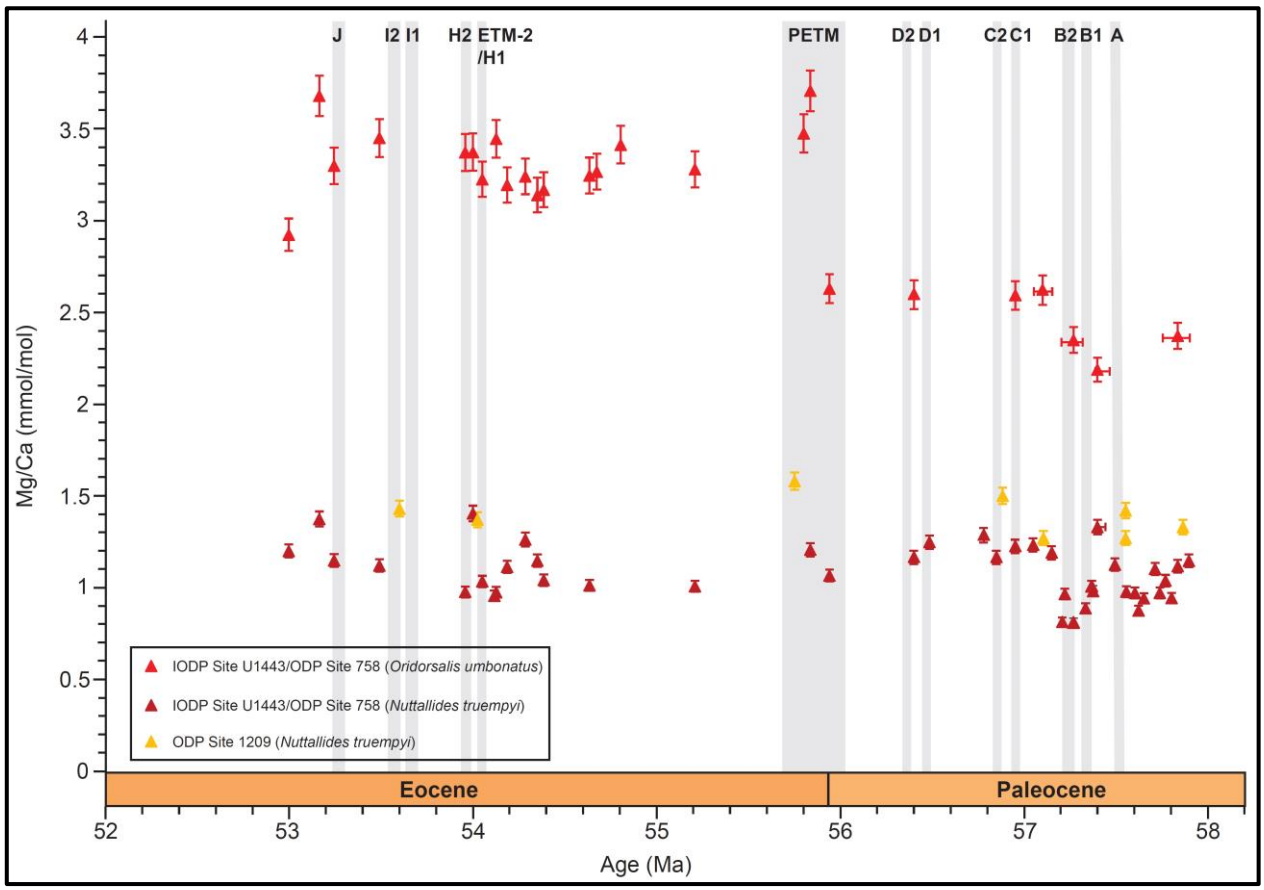

Figure 70. Comparison between raw Mg/Ca data generated from analysis of the shallow infaunal benthic foraminifera species Oridorsalis umbonatus and the epifaunal species Nuttallides truempyi from IODP Site U1443 and ODP Site 758. Benthic Mg/Ca data generated from analysis of Nuttallides truempyi at ODP Site 1209 (Dutton et al., 2005a,b) are also shown for comparison. Both datasets based on Nuttallides truempyi fail to show a significant rise in Mg/Ca from the Late Paleocene to Early Eocene, or replicate the step change to warmer intermediate waters during the Early Eocene, as illustrated by the Oridorsalis umbonatus data. Benthic Mg/Ca data based on analysis of Nuttallides truempyi therefore cannot be used to constrain the long-term pattern and magnitude of temperature change of intermediate to deep waters during the early Paleogene. Error bars of ±3% represent analytical uncertainty.

6.6.8. COMPARISON BETWEEN THE LATE PALEOCENE–EARLY EOCENE TEMPERATURE EVOLUTION IN THE LOW AND HIGH LATITUDES

A comparison between the Late Paleocene–Early Eocene evolution of temperature within the low latitudes and at intermediate-deep water depths in the Indian, Pacific, Atlantic and Southern oceans is presented in Figure 71. Since intermediate-deep water masses record a minimum estimate of surface ocean temperature in their high-latitude region of formation, due to formation predominantly during the winter months, the temperature of deep water masses

can be used to track high latitude temperature evolution and a direct comparison can be made to the evolution of temperature in the low latitudes.

As shown in Figure 71, both low latitude surface ocean and intermediate-deep waters exhibit a long-term warming trend from the Late Paleocene–Early Eocene, confirming that long-term warming of the background climate during this time was global in scale. However, the magnitude of warming of the background climate within the intermediate-deep waters (~+5°C) is more than double the magnitude of warming within the low latitudes (~+1.5–2°C) during this time. This differential magnitude of warming creates a reduction in the temperature gradient between the low latitude mixed layer and global ocean intermediate-bottom waters from ~21°C during the Late Paleocene at ~58 Ma, to ~17°C during the Early Eocene ~53 Ma (Figure 71), implying significant polar amplification of greenhouse warming from the Late Paleocene to Early Eocene (Cramwinckel et al., 2018; see Figure 63 and Figure 64). However, a portion of this apparently muted warming of the low latitude surface ocean could also be explained by decreasing Mg/Ca_{sw} during the Early Eocene, which could selectively bias mixed layer but not benthic Mg/Ca-derived temperature estimates, due to the low sensitivity of *Oridorsalis umbonatus* to changing Mg/Ca_{sw}. Nonetheless, this global nature of the pattern and character of long-term warming within both the low latitudes and the polar regions is consistent with greenhouse gas forcing being the dominant driver of early Paleogene global warming rather than significant changes in thermohaline circulation (Cramwinckel et al., 2018). Changes in thermohaline circulation, such as the opening and closing of ocean gateways, can have significant impacts on climate at the local and regional scale, especially in high-latitude regions characterised by low levels of solar insolation. For example, opening of the Drake Passage at the Eocene/Oligocene boundary and the consequent thermal isolation of Antarctica may have played a secondary role in the onset of widespread Antarctic glaciation ~34 Ma, although declining atmospheric pCO_2 levels below a critical threshold may still have been the controlling factor (e.g., DeConto & Pollard, 2003). Such tectonic reorganisation cannot conceivably explain synchronous temperature rise within both the surface ocean of the low latitudes and the polar regions. The pivotal role of greenhouse gas forcing on synchronising temperature trends in low and high latitude climates has been emphasised for the Plio-Pleistocene by Herbert et al. (2010). However,

as demonstrated by the atmospheric pCO_2 compilation in **Chapter 3** Figure 12a, although there is proxy evidence for generally rising background atmospheric pCO_2 levels during the Paleocene–Early Eocene, the wide range of estimates derived from the array of different proxies means that absolute pCO_2 levels and the magnitude of change cannot be constrained with the currently available proxy database. Therefore, correlating the magnitude of synchronous equatorial and polar warming with the magnitude of atmospheric pCO_2 change, and hence accurately quantifying the magnitude of warming we may expect in our anthropogenically warmer future world under varying fossil fuel emission scenarios, is difficult to constrain with the currently available proxy data.

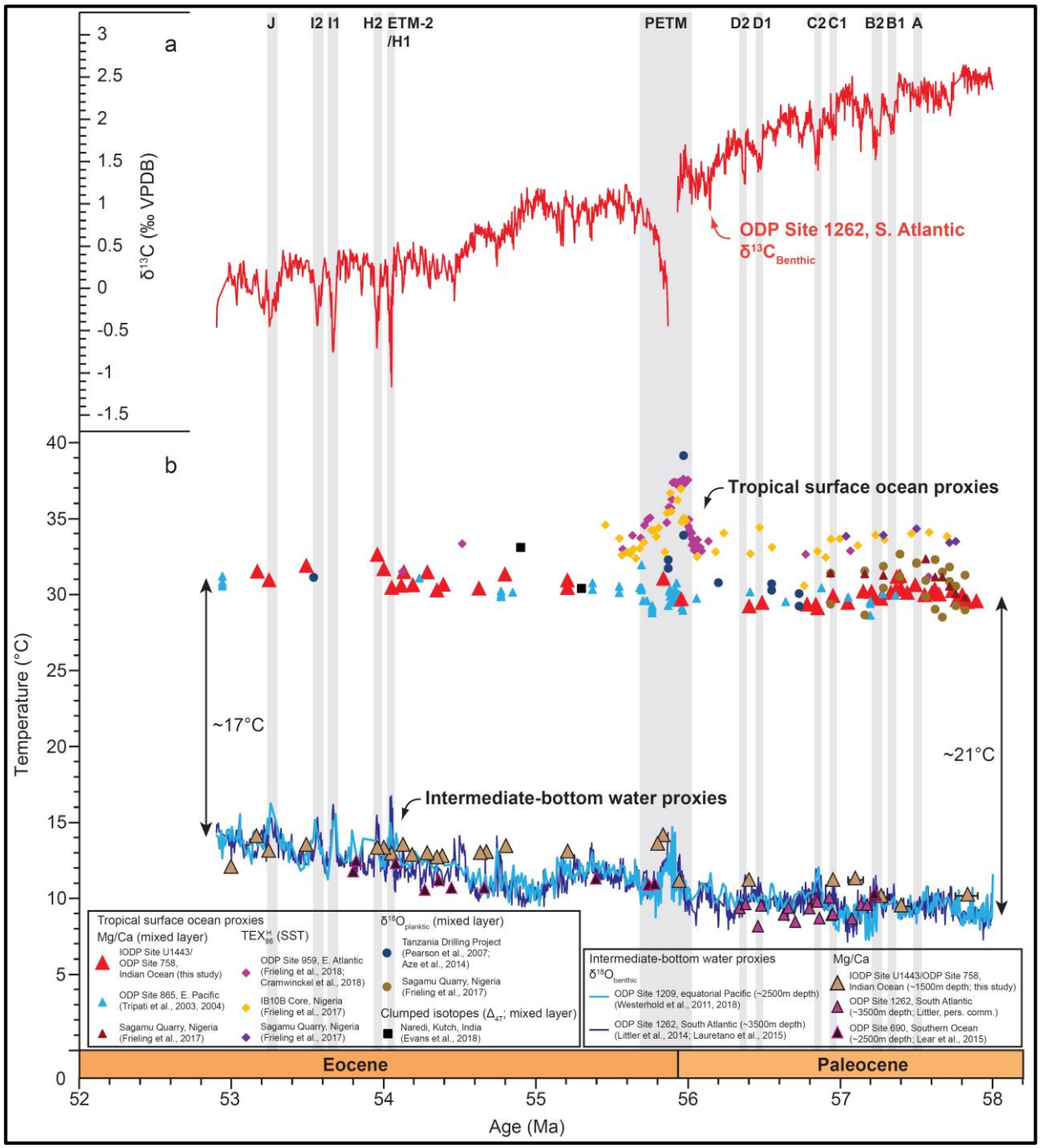

*Figure 71 (previous page). Comparison between the magnitude of warming within the low latitude surface ocean and within global intermediate-deep waters during the Late Paleocene–Early Eocene, calibrated to the updated orbitally-tuned age model presented in this thesis. (**a**) $\delta^{13}C_{benthic}$ data from ODP Site 1262 (see **Chapter 3**; Littler et al., 2014; Lauretano et al., 2015), with carbon cycle events highlighted and correlated across the figure as vertical grey bars. (**b**) Compilation of proxy data from the low latitude surface ocean and the intermediate-deep waters of the Pacific, Atlantic, Southern and Indian oceans. All published Mg/Ca-derived temperature estimates have been recalibrated following the methods employed in this thesis and assuming Mg/Ca_{sw} = 2.5 mol/mol. Temperatures were calculated from published $\delta^{18}O_{benthic}$ data using the temperature calibration of Kim & O'Neil (1997) for inorganic calcite, modified by Bemis et al. (1998; Equation 1). All other temperature proxy estimates remain unchanged from the original literature source. The temperature gradient between the low latitude mixed layer and ocean bottom waters during the Late Paleocene (~58 Ma) and Early Eocene (~53 Ma) are indicated for comparison, highlighting the amplification of bottom water (hence polar surface ocean) warming.*

6.6.9. RELATIVE TEMPERATURE CHANGE FROM THE LATE PALEOCENE TO EARLY EOCENE AT IODP/ODP SITES U1443/758

To circumvent some of the inherent uncertainties in the calculation of absolute temperature estimates during the early Paleogene, relative changes in temperature within the mixed layer, thermocline, and intermediate waters of the northern Indian Ocean from the peak of the PCIM to the Early Eocene (~58–53 Ma) have also been calculated to better illustrate temperature trends (Figure 72). Relative temperature changes from a baseline of 0 for peak PCIM (~58 Ma) conditions have been modelled for three different values for the exponential constant "A" for mixed layer and thermocline data, encompassing the range of potential values for Paleogene seawater. A value of 0.075 for "A" is consistent with the majority of modelling studies at a Paleogene Mg/Ca_{sw} value of ~2.5 mol/mol (Evans et al., 2016a), therefore is considered the most likely scenario and will be discussed as such in the following section. Owing to the lower sensitivity of the infaunal benthic foraminifera *Oridorsalis umbonatus* to changing Mg/Ca_{sw} (Lear et al., 2015), only one value for the exponential constant (A = 0.114) has been modelled for the benthic data.

Excluding anomalous transient warming associated with the ETM2 and H2 events, a long-term warming trend from the peak of the PCIM (~58 Ma) to the Early Eocene (~53 Ma) is observed throughout the water column, equating to ~+2°C in the mixed layer (Figure 72b), ~+4°C at thermocline depths (Figure 72c), and ~+3°C at intermediate water depths (Figure 72d). This long-term warming

trend is interrupted by a ~1 million year long period of cooling during the latest Paleocene, which is most pronounced within the mixed layer and thermocline. The more pronounced latest Paleocene Mg/Ca decrease in the planktic records (and inferred temperature decrease), compared to the benthic records, could be related to a decrease in Mg/Ca_{sw} during this time interval. A change in Mg/Ca_{sw} could account for differential signals between planktic and benthic foraminiferal calcite, both in terms of magnitude and the direction of change, due to the low sensitivity of *Oridorsalis umbonatus* Mg/Ca to changing Mg/Ca_{sw}. However, the magnitude of latest Paleocene cooling in the mixed layer record is consistent with that from other independent temperature proxies from the low latitudes, suggesting that the magnitude of cooling in the mixed layer Mg/Ca record from the Indian Ocean may be a genuine signal. The low resolution of the Late Paleocene benthic Mg/Ca record may also obscure a comparable magnitude of cooling within the intermediate waters of the northern Indian Ocean between ~57.4–56.4 Ma. Decreasing Mg/Ca_{sw} during the Early Eocene could also have the potential to dampen the magnitude of relative temperature change calculated from the mixed layer and thermocline planktic Mg/Ca data within the younger part of the record, after the PETM.

The step-change to warmer baseline temperatures during the Early Eocene following the PETM, especially pronounced at thermocline and intermediate water depths, is clearly evident on the relative temperature plots (Figure 72c,d). Since there is evidence for rising surface ocean salinity (based on more positive $\delta^{18}O_{sw}$ values) during the PETM and Early Eocene above IODP/ODP Sites U1443/758 (Figure 61e), amplified warming at thermocline depths during the PETM and into the Early Eocene may be related to the downwelling of warmer and significantly saltier (hence denser) waters from the mixed layer, resulting in a deepening of the mixed layer. This scenario has also been hypothesised for other low latitude sites such as ODP Site 865, where thermocline temperatures also do not appear to recover after the PETM but instead remain consistently warmer than pre-excursion temperatures by ~+1.5°C (Tripati & Elderfield, 2004). This thermal evolution of the mixed layer and thermocline at ODP Site 865 appears to be comparable to the temperature evolution in the northern Indian Ocean (Figure 72c), suggesting that the thermal response of the low latitude Indian and Pacific oceans to Early Eocene

greenhouse warming may be comparable. Relative temperature change during the PETM and during the PETM recovery is discussed further in **Section 6.7**. There is, however, also the potential for the mixed layer data to be biased by preferential recrystallisation of the *Morozovella* specimens (see Figure 58a; Figure 59a; Figure 60a), although since the northern Indian Ocean Mg/Ca-derived temperature estimates are consistent with those from other sites in the low latitudes (Figure 63; Figure 64), any potential effects of recrystallisation are expected to be small.

The uncertainty introduced by the effect of significantly lower Paleogene Mg/Ca_{sw} relative to the modern on determining the value of the exponential constant "A" is shown by modelling a value of 0.05 (representing the lowest possible model output at Paleogene Mg/Ca_{sw} of ~1.5–2.5 mol/mol; Evans et al., 2016a), and a value of 0.09 (representing the value from a modern multi-species calibration; Anand et al., 2003), for calculations of relative temperature change from planktic foraminiferal data in Figure 72b,c. Modelling a value of 0.05 for "A" produces significantly larger Late Paleocene–Early Eocene relative temperature shifts of ~+3°C and ~+6–7°C within the mixed layer and at thermocline depths respectively (Figure 72b,c). A surface ocean temperature shift of ~+3°C is larger than the magnitude of temperature change during this time interval suggested by any other published low latitude surface ocean temperature proxy data (~+1.5–2°C; Figure 71), therefore A = 0.05 is likely to be an underestimate. If a modern-day value of 0.09 for "A" is modelled, smaller relative temperature shifts of ~+1.5°C and ~+3.5°C are computed within the mixed layer and thermocline respectively across this time interval (Figure 72b,c).

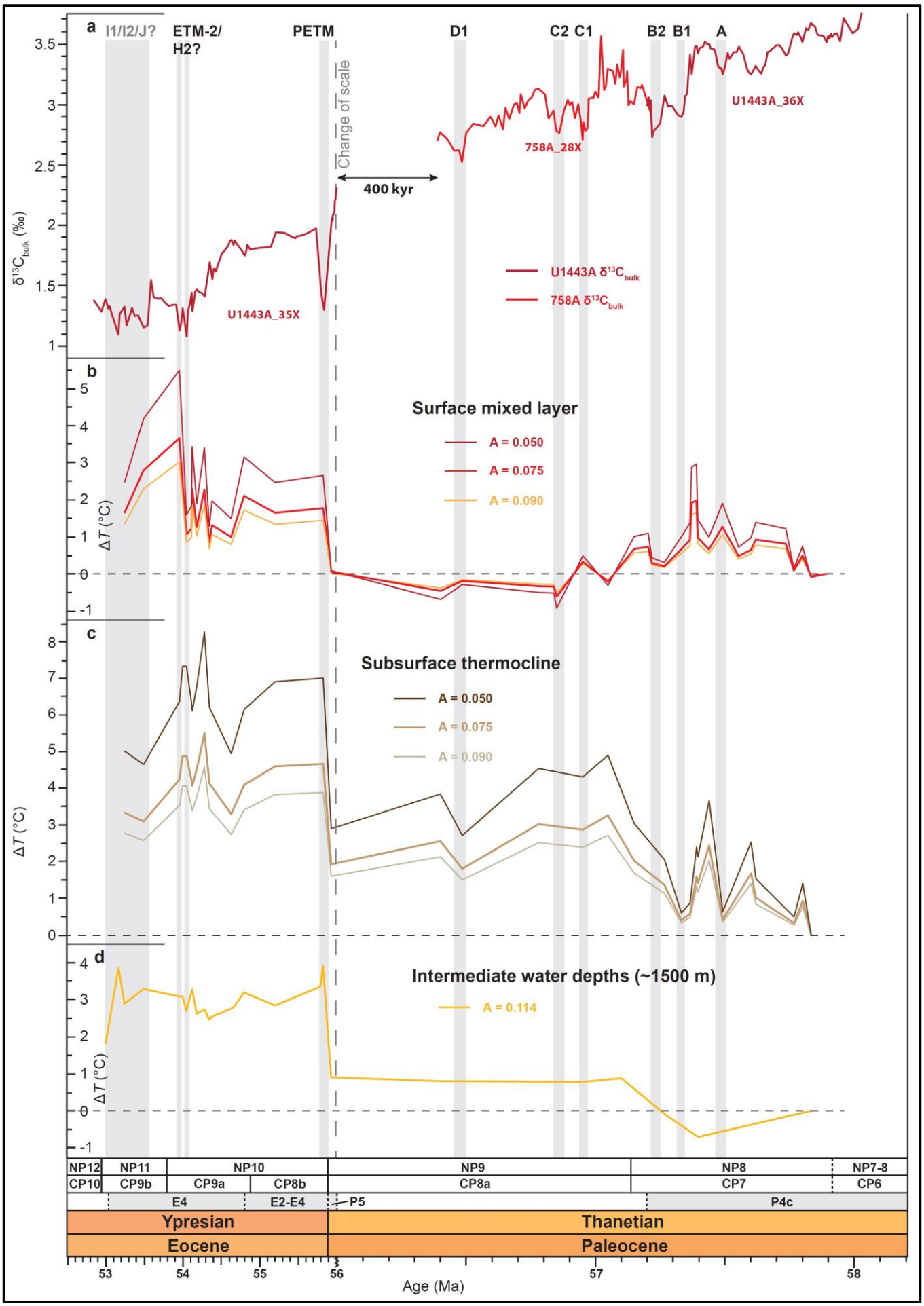
a
I1/I2/J?
ETM-2/
H2?
PETM
D1
C2 C1
B2 B1
A
Change of scale
400 kyr
U1443A_36X
758A_28X
U1443A_35X
U1443A δ13Cbulk
758A δ13Cbulk
δ13Cbulk (‰)
b
Surface mixed layer
A = 0.050
A = 0.075
A = 0.090
ΔT (°C)
c
Subsurface thermocline
A = 0.050
A = 0.075
A = 0.090
ΔT (°C)
d
Intermediate water depths (~1500 m)
A = 0.114
ΔT (°C)
NP12
NP11
NP10
NP9
NP8
NP7-8
CP10
CP9b
CP9a
CP8b
CP8a
CP7
CP6
E4
E2-E4
P5
P4c
Ypresian
Thanetian
Eocene
Paleocene
Age (Ma)

*Figure 72 (previous page). Relative temperature change within the mixed layer, thermocline and intermediate waters (~1500m palaeo-depth) of Indian Ocean Ninetyeast Ridge IODP Site U1443/ODP Site 758, from the peak of the Paleocene Carbon Isotope Maximum (PCIM; Late Paleocene) to the Early Eocene (~58–53 Ma). Temperature change is calculated relative to a baseline of 0 for peak PCIM (~58 Ma) conditions. Hyperthermals and smaller climatic perturbations are labelled and correlated across the records as vertical grey bands. PETM = Paleocene-Eocene Thermal Maximum. (**a**) Bulk carbonate carbon isotope ($\delta^{13}C_{bulk}$) record, with core sections labelled. (**b**) Relative temperature change (ΔT) within the mixed layer, modelled with three different values for the exponential constant "A" encompassing the range of possible values for Paleogene seawater. A value of 0.075 is consistent with the majority of model predictions for Paleogene seawater with Mg/Ca_{sw} of 1.5–2.5 mol/mol (Evans et al., 2016a), and is therefore considered to be the most likely scenario. Mg/Ca data were pH corrected assuming an ambient pH of 7.7 and PETM pH of 7.6. (**c**) Relative temperature change (ΔT) within the thermocline, modelled with three different values for the exponential constant "A" encompassing the range of possible values for Paleogene seawater. A value of 0.075 is consistent with the majority of model predictions for Paleogene seawater with Mg/Ca_{sw} of 1.5–2.5 mol/mol (Evans et al., 2016a), and is therefore considered to be the most likely scenario. Mg/Ca data were pH corrected assuming an ambient pH of 7.7 and PETM pH of 7.6. (**d**) Relative temperature change (ΔT) at intermediate water depths (~1500m palaeo-depth) of the Ninetyeast Ridge.*

6.6.10. LATE PALEOCENE–EARLY EOCENE MIXED LAYER TO THERMOCLINE AND SURFACE-TO-DEEP TEMPERATURE GRADIENTS AT IODP/ODP SITES U1443 AND 758

Temperature gradients between the mixed layer and the thermocline ($\Delta T_{thermocline}$) and mixed layer and intermediate waters ($\Delta T_{benthic}$; palaeo-depth ~1500m) at IODP/ODP Sites U1443 and 758 are illustrated in Figure 73 and Figure 74, respectively. A marked decrease in both $\Delta T_{thermocline}$ and $\Delta T_{benthic}$ commences ~57.5–57.0 Ma during the Late Paleocene, with a further abrupt decrease during the PETM and into the Early Eocene, before temporarily recovering during H2 (Figure 73b; Figure 74c). The Late Paleocene decrease in the $\Delta T_{thermocline}$ and $\Delta T_{benthic}$ gradients is related to a delayed onset of gradual latest Paleocene cooling at thermocline and intermediate water depths (Figure 73a; Figure 74a,b). The further decrease in both gradients during the PETM is a result of a greater magnitude of warming at thermocline and intermediate water depths (Figure 72c,d). The $\Delta T_{thermocline}$ gradient decreases from typical values of ~+1.5–3.5°C during the Late Paleocene (around the PCIM) to ~+0.5–1.5°C during the Early Eocene between the PETM and H2 (Figure 73b), whilst the

$\Delta T_{benthic}$ gradient decreases from Late Paleocene (PCIM) values of ~+19–21°C to ~+17–18.5°C between the PETM and H2 (Figure 74c). These records therefore suggest a significant and relatively long-lasting change in the thermal structure of the low latitude Indian Ocean above IODP/ODP Sites U1443/758 during and following the PETM, which persisted for ~2 million years into the Early Eocene. The amplification of thermocline warming and reduction in the $\Delta T_{thermocline}$ gradient may be related to the downwelling of warm saline mixed layer waters during Early Eocene global warming, expanding the thickness of the mixed layer and permeating warmth to greater water depths. Based on the structure of the $\Delta T_{thermocline}$ gradient, this process occurred until ETM-2, characterised by another decrease in the $\Delta T_{thermocline}$ gradient. A similar reduction in the $\Delta T_{thermocline}$ gradient during and after the PETM was also observed at equatorial Pacific ODP Site 865, suggesting a similar long-lasting response of the global low latitude surface ocean to warming during the PETM (Tripati & Elderfield, 2004). Mixed layer and thermocline warming during the PETM is discussed in further detail in **Section 6.7** below. The amplification of intermediate water warming and reduction of the $\Delta T_{benthic}$ gradient is likely to be related to polar amplification of surface ocean warming within the high-latitude region of intermediate water formation, most likely in the Southern Ocean (Figure 63; Figure 64), although a portion of the decrease in the $\Delta T_{benthic}$ gradient could also be explained by decreasing Mg/Ca_{sw} during the Early Eocene, post-PETM (Evans et al., 2018).

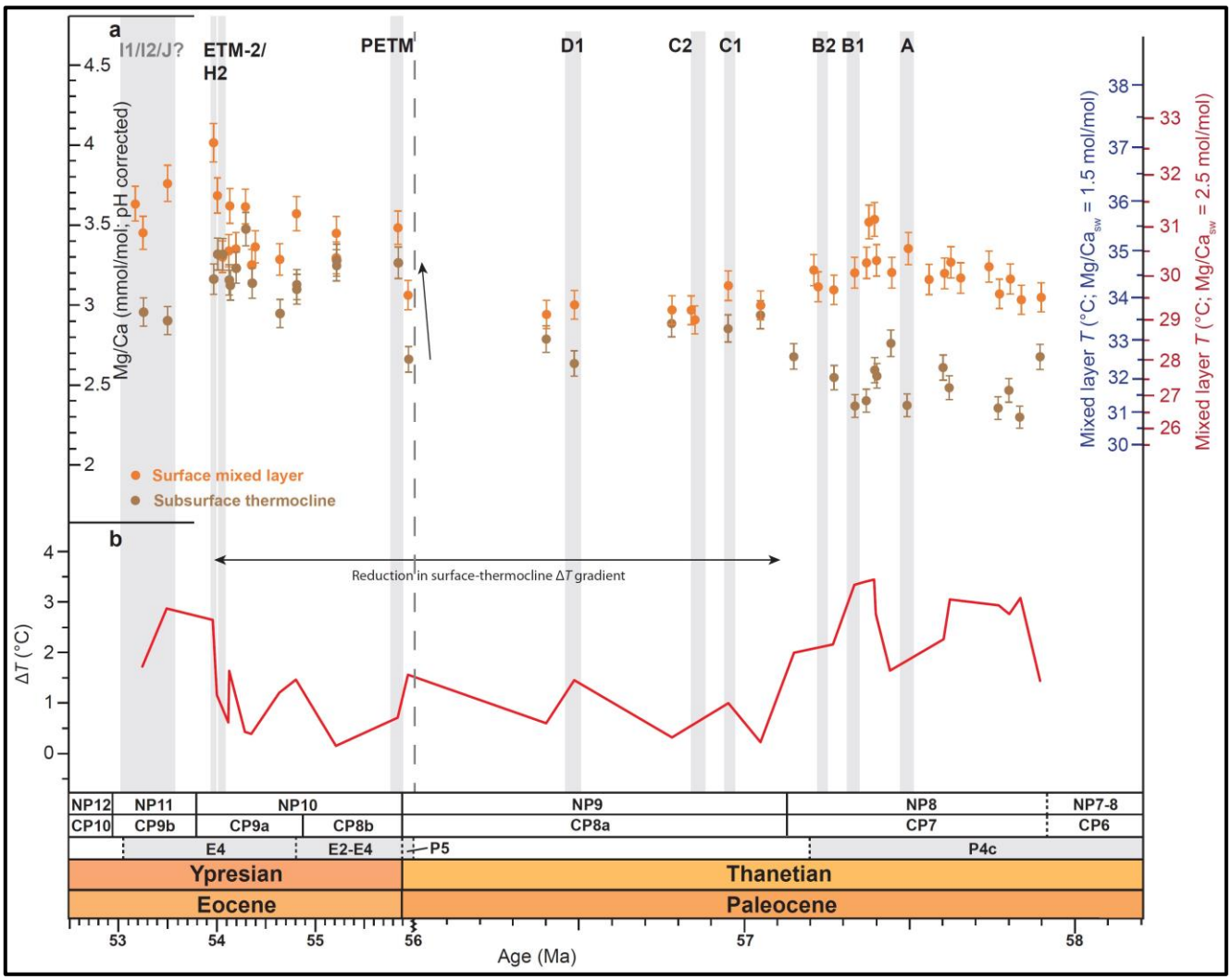

*Figure 73. Mixed layer to thermocline temperature gradient (ΔT) based on the difference between mixed layer and thermocline foraminiferal Mg/Ca ratios from Indian Ocean Ninetyeast Ridge IODP Site U1443/ODP Site 758, spanning the Late Paleocene–Early Eocene (~58–53 Ma). (**a**) Mixed layer and thermocline Mg/Ca records with values corrected for pH, assuming a background surface ocean pH of 7.7 and PETM pH of 7.6. Absolute temperature (T) estimates are calculated using modelled Paleogene Mg/Ca$_{sw}$ values of 1.5 mol/mol (blue scale) and 2.5 mol/mol (red scale), which bracket the potential range of early Paleogene Mg/Ca$_{sw}$ based on modelling (~1.5 mol/mol) and proxy (~2.5 mol/mol) studies and produce an absolute temperature offset of ~4.5°C. Temperatures calculated using Mg/Ca$_{sw}$ = 2.5 mol/mol are considered the most robust. Mixed layer Mg/Ca data (from Morozovella velascoensis/M. subbotinae-marginodentata plexus) are indicated by filled orange circles and and thermocline data (from Subbotina velascoensis/S. hornibrooki) are indicated by brown circles. Error bars of ±3% represent analytical error and are based on the long-term reproducibility of consistency standards. (**b**) Mixed layer to thermocline gradient (ΔT).*

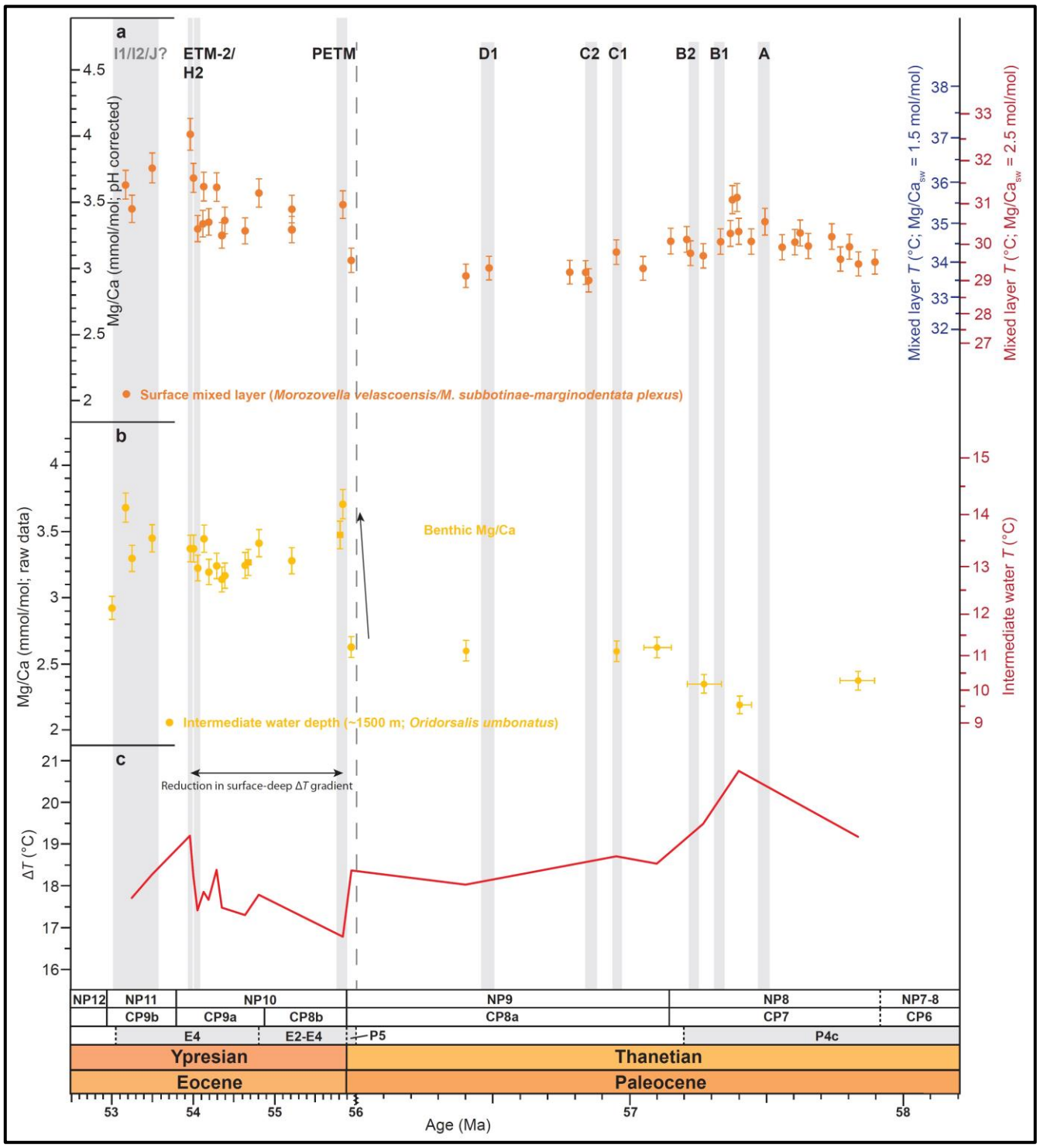

*Figure 74. Surface to intermediate water temperature gradient (ΔT) based on the difference between mixed layer and benthic foraminiferal Mg/Ca ratios from Indian Ocean IODP Site U1443/ODP Site 758 (palaeo-depth ~1500m), spanning the Late Paleocene–Early Eocene (~58–53 Ma). (**a**) Mixed layer Mg/Ca records with values corrected for pH, assuming a background surface ocean pH of 7.7 and PETM pH of 7.6. Absolute surface temperature (T) estimates are calculated using modelled Paleogene Mg/Ca$_{sw}$ values of 1.5 mol/mol (blue scale) and 2.5 mol/mol (red scale), which bracket the potential range of early Paleogene Mg/Ca$_{sw}$ based on modelling (~1.5 mol/mol) and proxy (~2.5 mol/mol) studies and produce an absolute temperature offset of*

*~4.5°C. Temperatures calculated using Mg/Ca$_{sw}$ = 2.5 mol/mol are considered the most robust. Error bars of ±3% represent analytical error and are based on the long-term reproducibility of consistency standards. (**b**) Benthic Mg/Ca. Due to the apparent low sensitivity of Oridorsalis umbonatus Mg/Ca to changing Mg/Ca$_{sw}$ (Lear et al., 2015), absolute intermediate water temperature (T) estimates are calculated using Paleogene Mg/Ca$_{sw}$ = 2.5 mol/mol only, consistent with Early Eocene proxy data. Error bars of ±3% represent analytical error and are based on the long-term reproducibility of consistency standards. (**c**) Surface to deep temperature gradient (ΔT).*

6.7. EXPRESSION OF THE PETM IN THE LOW LATITUDE INDIAN OCEAN

6.7.1. PORTION OF THE PETM STRATIGRAPHY CAPTURED AT IODP SITE U1443

Based on calcareous nannoplankton and planktic foraminiferal biostratigraphy, a portion of the PETM has been captured by 2 samples at 248.63 and 248.60 metres depth (CSF-A) in IODP Hole U1443A, manifested as a transient negative excursion in $\delta^{13}C_{bulk}$ of ~–0.75‰ (see Figure 55). This snapshot of the PETM provides the first insight into the magnitude of change in temperature and carbonate chemistry during this enigmatic event in the low latitude Indian Ocean. To identify which portion of the PETM stratigraphy has been captured, the $\delta^{13}C_{planktic}$ and raw Mg/Ca data from IODP Site U1443 across the latest Paleocene and PETM time interval (both generated from analysis of *Morozovella velascoensis*) have been plotted against the more complete corresponding data from ODP Site 1209 in Figure 75, located at a similar palaeo-latitude within the northern Hemisphere and calibrated to an orbitally-tuned age model (Zachos et al., 2003).

Based on a correlation of absolute $\delta^{13}C_{planktic}$ values from the two data points encompassing the PETM at IODP Site U1443 with the more complete PETM $\delta^{13}C_{planktic}$ curve from ODP Site 1209 (Zachos et al., 2003), the IODP Site U1443 record appears to capture a portion of either the onset or recovery phase of the PETM, whilst the main core of the carbon isotope excursion is missing (Figure 75a). Since the planktic foraminifera species *Acarinina sibaiyaensis*, which defines planktic foraminifera biozone E1 encompassing the majority of the onset and core of the PETM excursion (Wade et al., 2011), was not identified within samples from 248.63 or 248.60 metres depth, it is likely that both samples

sit within the PETM recovery phase. Using the orbitally-tuned age model from ODP Site 1209, the two data points capturing the PETM recovery phase from IODP Site U1443 appear to sit ~95 kyr and ~130 kyr after the onset of the CIE. Although only the data point at ~95 kyr after the CIE onset has been analysed for planktic Mg/Ca, a comparison of the raw planktic Mg/Ca data between the two sites is also consistent with a position of this data point at ~95 kyr after the CIE onset and in the recovery phase (Figure 75b). The age of the latest Paleocene data point relative to the CIE onset has been estimated based on a mean latest Paleocene sedimentation rate of ~0.7 cm/kyr (see Figure 57), however it cannot be further constrained by the ODP Site 1209 carbon isotope data. Nonetheless, this data point estimated at ~100 kyr before the CIE onset, represents an important reference for “pre-excursion” conditions, to which the magnitude of change in temperature and carbonate chemistry during the PETM recovery can be compared.

The magnitude of the negative excursion in $\delta^{13}C_{planktic}$ from IODP Site U1443 (~–1.7 ‰) equates to approximately half the magnitude of the corresponding excursion in the more complete PETM section from ODP Site 1209 (~–3.3 ‰), therefore the apparent magnitudes of temperature and carbonate chemistry change during the PETM in the low latitude Indian Ocean based on the samples from IODP Site U1443 should be treated as conservative minimum estimates.

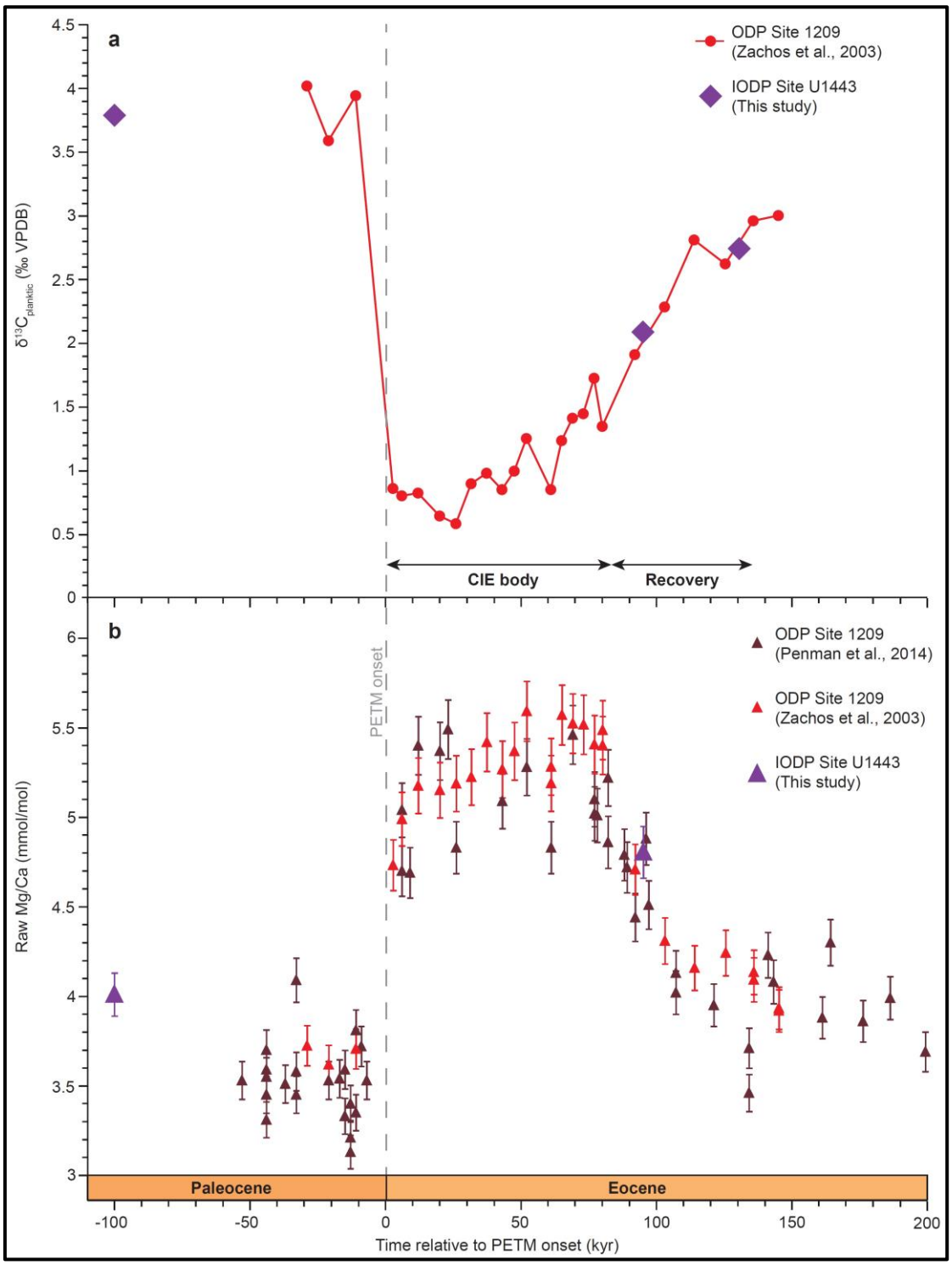

*Figure 75. Comparison between planktic stable carbon isotope ($\delta^{13}C_{planktic}$) and raw Mg/Ca data from Indian Ocean IODP Site U1443 (palaeo-latitude ~29°S) and equatorial Pacific ODP Site 1209 (palaeo-latitude ~23°N) across the Paleocene-Eocene Thermal Maximum (PETM). Both sets of data are based on analysis of Morozovella velascoensis, enabling a direct comparison to be made. (**a**) $\delta^{13}C_{planktic}$ data, with data from IODP Site U1443 clearly sitting in the recovery phase. (**b**) Raw planktic Mg/Ca data, with the older sample from IODP Site U1443 fitting into the trend represented by the recovery phase in the ODP Site 1209 data. The sample within the younger part of the recovery has only been analysed for benthic Mg/Ca.*

6.7.2. RELATIVE TEMPERATURE CHANGE DURING THE PETM AT IODP SITE U1443

Relative changes in temperature within the mixed layer, thermocline, and intermediate waters of the northern Indian Ocean during the PETM (~55.93 Ma) and earliest Eocene are illustrated in Figure 76. Temperature changes are calculated relative to a baseline of 0 for latest Paleocene conditions and have been modelled for three different values for the exponential constant "A" (with A = 0.075 considered the most likely), and also for a fall from ambient pH of 7.7 to 7.6 (solid lines) and to 7.5 (dashed lines) during the PETM. Since the magnitudes of the excursions recorded in $\delta^{13}C_{bulk}$ and $\delta^{13}C_{planktic}$ from IODP Site U1443 suggest that approximately a third or a half of the total magnitude of the PETM has been captured, respectively, a pH decrease of 0.1 units to 7.6 (representing a third of the total magnitude of pH fall during the PETM of ~0.3 units; Penman et al., 2014) is considered the most likely scenario.

A transient warming is observed throughout the upper water column during the portion of the PETM captured within the Mg/Ca record from IODP Site U1443, ranging from ~+1.7°C in the mixed layer to ~+2.7°C at thermocline depths ("most likely" scenario assuming A = 0.075; PETM pH = 7.6; Figure 76b,d). These magnitudes of change within the mixed layer and thermocline of the low latitude Indian Ocean are broadly comparable to the magnitudes of temperature change within the mixed layer (~+1.3°C) and thermocline (~+3.3°C) of the equatorial Pacific above ODP Site 865, where only the PETM recovery phase also appears to have been resolved, suggesting that the muted surface ocean temperature response and amplified warming at thermocline depths in the low latitude Indian Ocean may be characteristic of the low latitudes globally (Figure 77). By changing the value of the exponential constant "A", the magnitude of warming ranges from ~+2.6°C and +4.1°C within the mixed layer and at thermocline depths respectively (A = 0.05; PETM pH = 7.6), to ~+1.4°C and ~+2.3°C within the mixed layer and at thermocline depths respectively (A = 0.09; PETM pH = 7.6; Figure 76b,d). Modelling a decrease in pH to 7.5 during the PETM results in a decrease in the magnitude of relative temperature change within the mixed layer and at thermocline depths by between a quarter and a third, as well as eliminating the partial recovery towards pre-excursion temperatures, therefore is likely to be an

overcorrection (Figure 76c,e). Acquiring a sound knowledge of the relative change in surface ocean pH, for example by generating high-resolution $\delta^{11}B$ data (e.g., Penman et al., 2014), is therefore vital for producing accurate reconstructions of absolute surface ocean temperature, as well as the magnitude of temperature change, during hyperthermal events.

Intermediate water depths on the Ninetyeast Ridge are characterised by the greatest magnitude of warming during the PETM of ~+3.0°C, almost double the magnitude of warming experienced by the mixed layer, suggesting significant polar amplification of surface ocean warming during the PETM (Figure 76f). Furthermore, modelling studies have suggested a significant amplification of intermediate water warming during the PETM within the Atlantic Ocean, due to a decrease in the volume of deep-water production in the Southern Ocean as polar surface ocean waters warmed and their density decreased (Lunt et al., 2010). The new data across the PETM from IODP Site U1443 provides the first evidence for amplified intermediate water warming from the Indian Ocean, supporting evidence from neodymium isotope data that intermediate-deep waters of both the Atlantic and Indian oceans were principally sourced from the Southern Ocean (e.g., Thomas et al., 2003; Figure 54). Furthermore, amplified warming of intermediate-deep waters in both the Atlantic and Indian oceans lends support to the methane hydrate hypothesis as a contributory causal mechanism for the PETM, opening up vast areas of the seafloor to the potential thermal destabilisation and catastrophic release of methane hydrates (e.g., Dickens, 2003, 2011). Since only the recovery phase of the PETM has been captured in the IODP Site U1443 record, the true magnitude of intermediate water warming during the PETM in the northern Indian Ocean may have been significantly larger, and the +3.0°C calculated here should therefore be treated as a conservative minimum estimate.

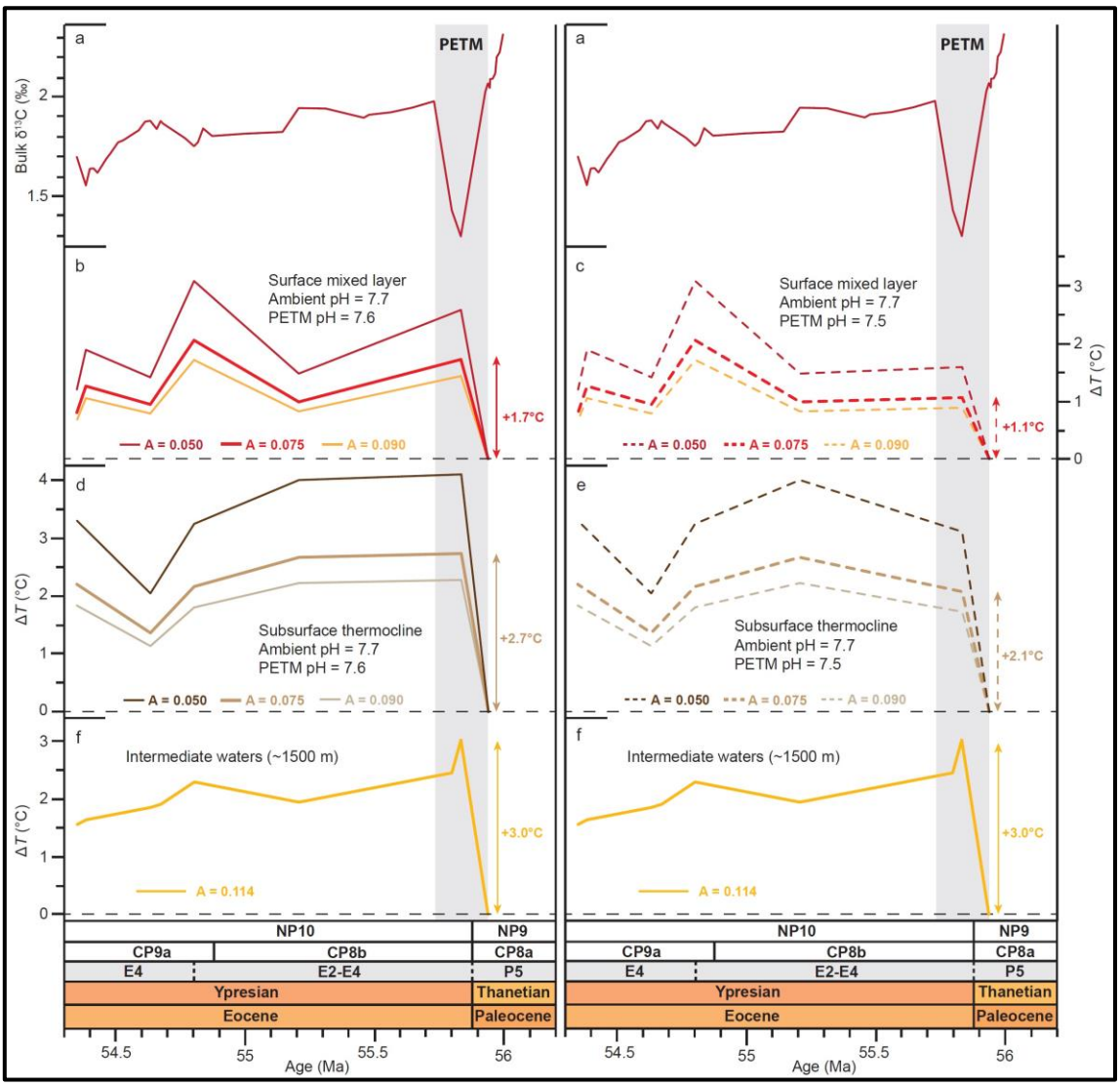

*Figure 76. Relative temperature change within the mixed layer, thermocline and intermediate waters (~1500m palaeo-depth) of Indian Ocean Ninetyeast Ridge IODP Site U1443 during the Paleocene-Eocene Thermal Maximum (PETM; ~55.93 Ma) and earliest Eocene. Temperature change is calculated relative to a baseline of 0 for latest Paleocene conditions. Three different values for the exponential constant "A" have been modelled for the surface and subsurface planktic records, encompassing the range of possible values for Paleogene seawater (Evans et al., 2016a). A = 0.075 is consistent with the majority of modelling studies at typical Paleogene Mg/Ca_{sw} of 2.5 mol/mol and is therefore considered the most likely scenario. The PETM is correlated across the records as a vertical grey bar. (**a**) Bulk carbonate carbon isotope ($\delta^{13}C_{bulk}$) record. (**b**) Relative temperature change (ΔT) within the mixed layer, with raw Mg/Ca data pH-corrected assuming an ambient pH of 7.7 and PETM pH of 7.6. (**c**) Relative temperature change (ΔT) within the mixed layer, with raw Mg/Ca data pH-corrected assuming an ambient pH of 7.7 and PETM pH of 7.5. (**d**) Relative temperature change (ΔT) within the thermocline, with raw Mg/Ca data pH-corrected assuming an ambient pH of 7.7 and PETM pH of 7.6. (**e**) Relative temperature change (ΔT) within the thermocline, with raw Mg/Ca data pH-corrected assuming an ambient pH of 7.7 and PETM pH of 7.5. (**f**) Relative temperature change (ΔT) at intermediate water depths (~1500m palaeo-depth) at IODP Site U1443.*

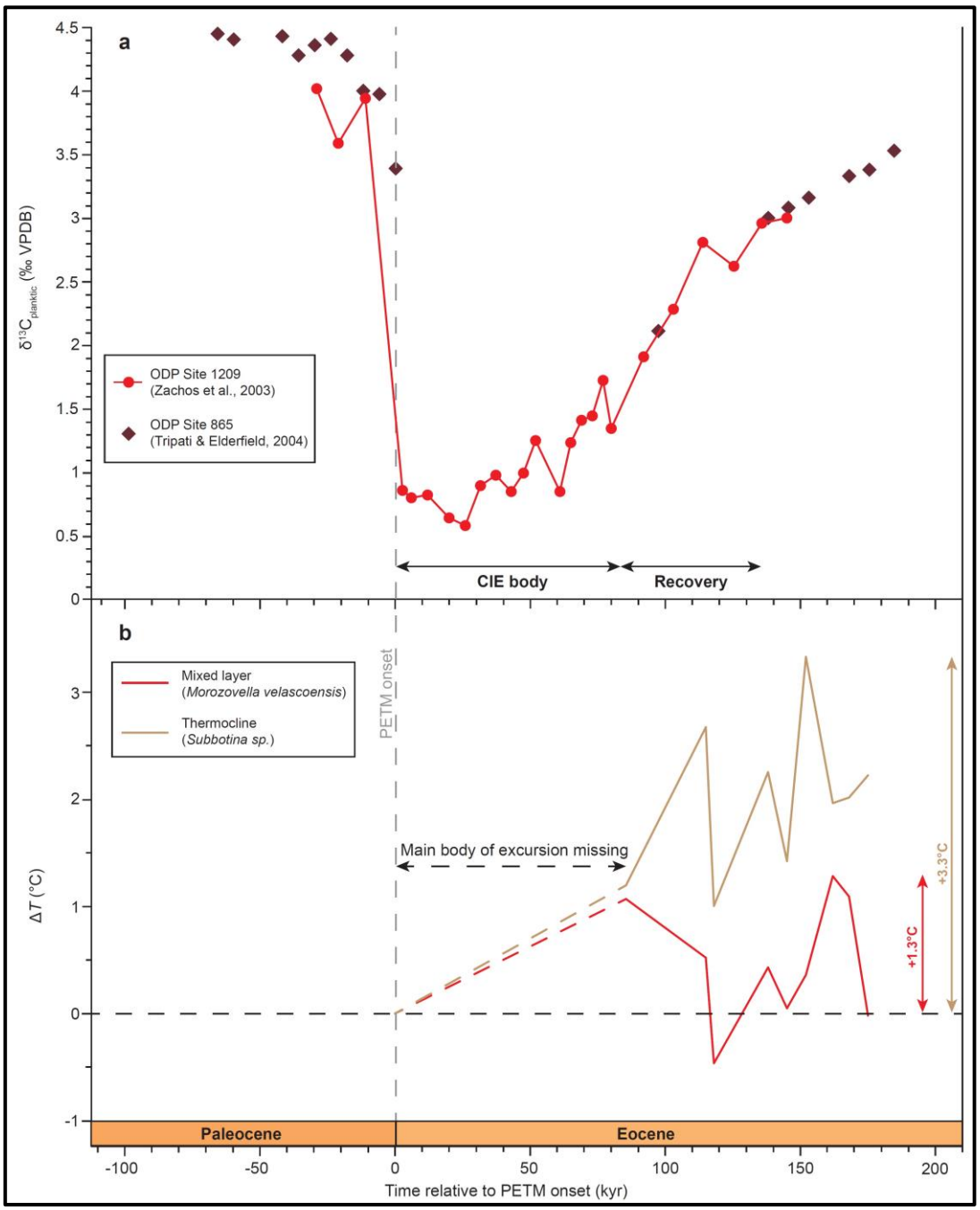

*Figure 77. Relative temperature change within the mixed layer and thermocline of the equatorial Pacific ODP Site 865 during the Paleocene-Eocene Thermal Maximum (PETM). (**a**) $\delta^{13}C_{planktic}$ data from ODP Site 1209 (Zachos et al., 2003) and ODP Site 865 (Tripati & Elderfield, 2004). Both datasets were generated from analysis of Morozovella velascoensis, enabling a direct comparison to be made. The $\delta^{13}C_{planktic}$ data from ODP Site 865 suggest that all samples sit within the recovery phase, analogous to the stratigraphic position of samples from IODP Site U1443 (Figure 75). (**b**) Relative temperature change (ΔT) within the mixed layer and thermocline, with raw Mg/Ca data pH-corrected assuming an ambient pH of 7.7 and PETM recovery pH (~85–150 kyr after CIE onset) of 7.6 (after Penman et al., 2014). Temperature change is calculated relative to a baseline of 0 for latest Paleocene conditions. ΔT has been calculated with A = 0.075, consistent with the majority of modelling studies at typical Paleogene Mg/Ca_{sw} of 2.5 mol/mol. Raw Mg/Ca data are from Tripati & Elderfield (2004).*

6.7.3. COMPARISON OF THE MAGNITUDE OF SURFACE OCEAN TEMPERATURE AND CARBONATE CHEMISTRY CHANGE DURING THE PETM AT IODP SITE U1443 TO PUBLISHED RECORDS

The new Mg/Ca data across the PETM from IODP Site U1443 is plotted up with a compilation of published planktic Mg/Ca data in Figure 78 to illustrate how the magnitude of warming and absolute temperatures compare to Mg/Ca-derived mixed layer temperatures from other low latitude sites. The magnitude of warming at IODP Site U1443 of ~+1.5°C, from ~29.5 (±1.4)°C during the latest Paleocene to ~31.0 (±1.4)°C during the PETM recovery, equates to less than half of the total magnitude of warming (~+4°C) recorded at ODP Site 1209 (Zachos et al., 2003; Penman et al., 2014; Figure 78b). Similarly, the absolute temperature of ~31.0 (±1.4)°C recorded during the PETM recovery at IODP Site U1443 is lower than the peak temperature of ~32.1 (±1.4)°C recorded at ODP Site 1209 (Figure 78b), confirming that the core of the PETM has not been sampled at IODP Site U1443 (Figure 78a).

Based on a comparison to the $\delta^{13}C_{planktic}$ curve from ODP Site 1209, the Mg/Ca records from ODP Site 865 and DSDP Site 527 also appear to be incomplete and only capture the pre-excursion and recovery phases (Tripati & Elderfield, 2004; Figure 78a). Recovery temperatures at ODP Site 865 [~30.8 (±1.4)°C] appear to be very comparable to IODP Site U1443 [~31.0 (±1.4)°C] and equatorial Pacific ODP Site 1209 [~30.5–31.0 (±1.4)°C], although ODP Site 865 is characterised by generally warmer temperatures (by ~+1°C) during the latest Paleocene and recovery interval, perhaps due to its lower palaeo-latitude (~10°N vs. ~23°N at ODP Site 1209 and ~29°S at IODP Site U1443). Whilst latest Paleocene temperatures between DSDP Site 527 and ODP Site 1209 appear to be comparable, temperatures during the recovery phase at DSDP Site 527 appear to be ~–1–2°C cooler than at ODP Site 1209, suggestive of a muted response to PETM warming in the subtropical South Atlantic. However, whilst planktic foraminiferal preservation is generally good above and below the PETM interval, the core of the PETM is characterised by severe carbonate dissolution at DSDP Site 527 due to the deep palaeo-depth of the site (~3400m; Thomas et al., 1999). The core of the PETM has not been resolved in the Mg/Ca record due to the scarcity of preserved foraminifera within the clay-rich interval almost devoid

of carbonate comprising the main body of the PETM excursion, analogous to the sedimentological expression of the PETM at ODP Site 1262, located at a comparable palaeo-depth on Walvis Ridge (Thomas et al., 1999; Zachos et al., 2005; see **Chapter 2**, Figure 6). Carbonate dissolution selectively removes the most impure high-Mg calcite and would therefore bias Mg/Ca-derived temperature estimates to cooler values across the PETM interval affected by dissolution (e.g., Dekens et al., 2002; Regenburg et al., 2006, 2014), providing an explanation for the apparently muted mixed layer temperature excursion during the PETM recovery at DSDP Site 527. Latest Paleocene temperature estimates, unaffected by PETM dissolution and characterised by comparable foraminiferal preservation to IODP Site U1443, appear to be very similar to ODP Site 1209, suggesting at least comparable temperatures between the low latitude South Atlantic (~41°S) and equatorial Pacific (~23°N) before the onset of PETM warming.

By contrast, the anomalously low temperatures calculated from planktic Mg/Ca data from Bass River are from an expanded PETM section characterised by very good foraminiferal preservation (Babila et al., 2016), therefore are unlikely to be biased by diagenesis. Bass River is instead located in a shelfal environment, in contrast to the open ocean setting of the other sites presented in Figure 78, which has the potential to be characterised by significant transient changes in salinity. The anomalously low Mg/Ca-derived temperatures may therefore instead be related to a pulse of freshwater input from the adjacent American continent and significant reduction in salinity of the mixed layer above the New Jersey Shelf during the PETM. This conclusion is in agreement with modelling studies suggesting an intensified hydrological cycle and higher precipitation and freshwater runoff rates across eastern North America during the PETM, as well as high sedimentation rates recorded during the PETM interval across the New Jersey shelf (Zachos et al., 2006; Carmichael et al., 2017). A significant decrease in salinity could serve to lower Mg/Ca ratios and partially counteract an increase in Mg/Ca due to rising temperature, potentially biasing Mg/Ca values and associated temperature calculations to lower values during this event.

The compilation of published mixed layer planktic Mg/Ca data in Figure 78 therefore highlights the paucity of complete stratigraphic sections from open ocean sites across the PETM, characterised by sufficiently good foraminiferal preservation for reliable Mg/Ca-derived absolute temperature reconstructions. Although the PETM section from IODP Site U1443 is clearly much more poorly resolved than the other open ocean sites presented in Figure 78, the generally good preservation of foraminifera enable an important minimum constraint of the magnitude of warming and absolute temperature to be made from the poorly studied Indian Ocean, for which a complete lack of data exists to date. By comparison to the more complete Mg/Ca record from ODP Site 1209, which appears to be characterised by comparable temperatures ~95 kyr after the PETM onset to IODP Site U1443, a tentative prediction of a similar thermal history of the mixed layer between the equatorial Pacific and the low latitude Indian Ocean could be inferred during the PETM.

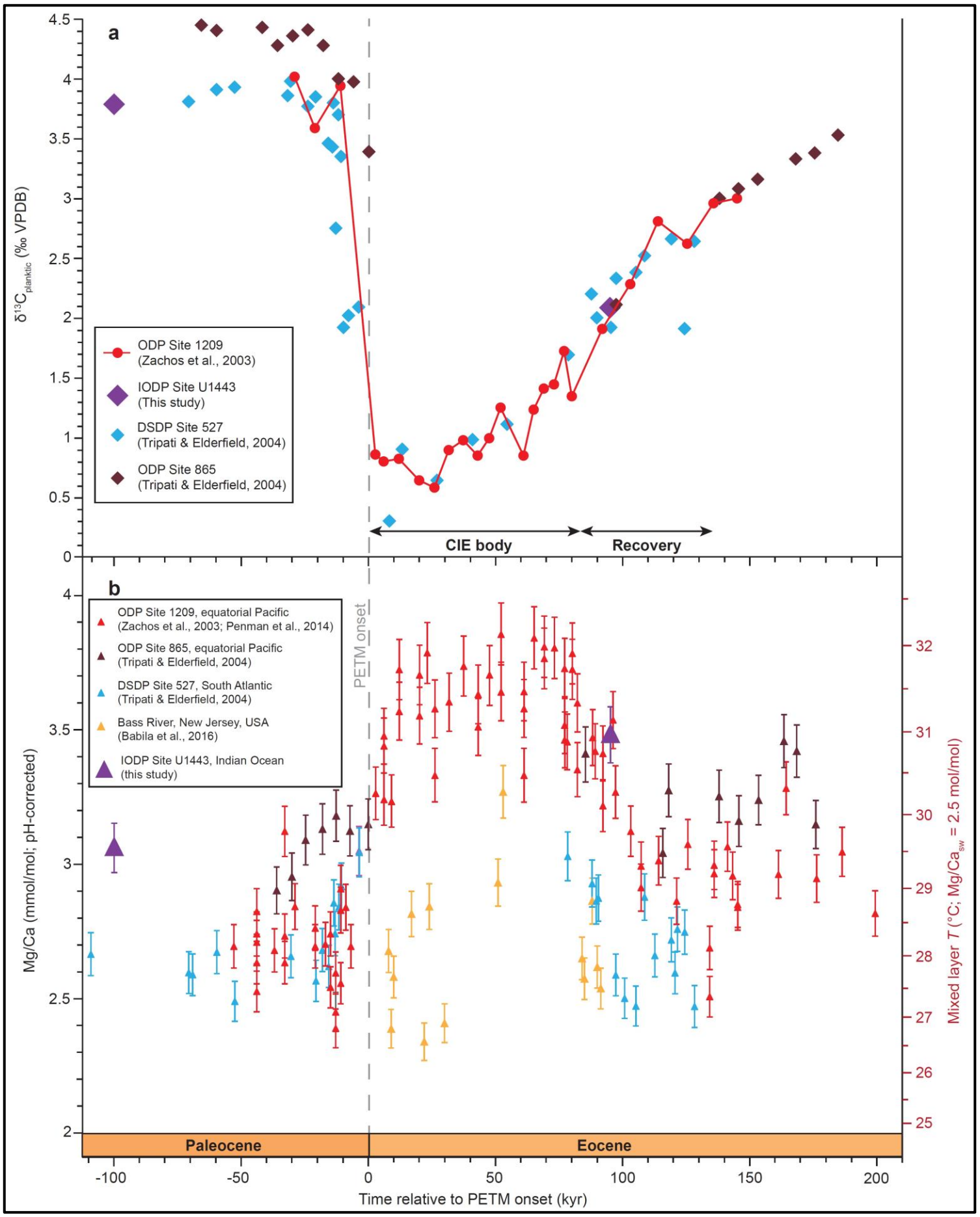
a
$\delta^{13}C_{planktic}$ (‰ VPDB)
ODP Site 1209
(Zachos et al., 2003)
IODP Site U1443
(This study)
DSDP Site 527
(Tripati & Elderfield, 2004)
ODP Site 865
(Tripati & Elderfield, 2004)
CIE body
Recovery
b
ODP Site 1209, equatorial Pacific
(Zachos et al., 2003; Penman et al., 2014)
ODP Site 865, equatorial Pacific
(Tripati & Elderfield, 2004)
DSDP Site 527, South Atlantic
(Tripati & Elderfield, 2004)
Bass River, New Jersey, USA
(Babila et al., 2016)
IODP Site U1443, Indian Ocean
(this study)
PETM onset
Mg/Ca (mmol/mol; pH-corrected)
Mixed layer T (°C; Mg/Ca_{sw} = 2.5 mol/mol)
Paleocene
Eocene
Time relative to PETM onset (kyr)

*Figure 78 (previous page). Comparison between mixed layer planktic Mg/Ca data from IODP Site U1443 and published mixed layer planktic Mg/Ca records from the Pacific and Atlantic across the Paleocene-Eocene Thermal Maximum (PETM). All data from IODP Site U1443, ODP Site 1209, ODP Site 865 and Bass River are based on analysis of Morozovella species, but data from DSDP Site 527 are based on analysis of Acarinina species. (**a**) Comparison of planktic $\delta^{13}C$ data ($\delta^{13}C_{planktic}$) from ODP Site 1209 (Zachos et al., 2003), ODP Site 865 (Tripati & Elderfield, 2004), DSDP Site 527 (Tripati & Elderfield, 2004) and IODP Site U1443 (this study), illustrating the stratigraphic position of samples and enabling the construction of a single age model to facilitate comparison of planktic Mg/Ca data from these sites (in panel **b**). $\delta^{13}C_{planktic}$ data from DSDP Site 527, based on analysis of Acarinina sp., were adjusted by +0.2 ‰, representing the mean offset between $\delta^{13}C_{planktic}$ data generated from Acarinina and Morozovella species in overlap samples at ODP Site 865 (Tripati & Elderfield, 2004). The age model presented in Babila et al. (2018), consistent with the ODP Site 1209 age model presented here, was used to compare Mg/Ca data from Bass River in panel **b**. (**b**) Mixed layer planktic Mg/Ca data from Indian Ocean IODP Site U1443 (purple triangles; palaeo-latitude ~29°S; this study), equatorial Pacific ODP Site 1209 (red triangles; palaeo-latitude ~23°N; Zachos et al., 2003; Penman et al., 2014), equatorial Pacific ODP Site 865 (purple triangles; palaeo-latitude ~10°N; Tripati & Elderfield, 2004), South Atlantic DSDP Site 527 (light blue triangles; palaeo-latitude ~41°S Tripati & Elderfield, 2004), and Bass River, New Jersey, USA (navy blue triangles; palaeo-latitude ~35°N; Babila et al., 2016). A variable pH correction has been applied to the published Mg/Ca data to account for ocean acidification during the PETM, with a modelled pH of 7.5 during the CIE core (~0–85 kyr after CIE onset), modelled pH of 7.6 during the CIE recovery (~85–150 kyr after CIE onset), and modelled ambient pH of 7.7, broadly following Penman et al. (2014). Modelling a pH of 7.4 during the peak of the PETM, consistent with Penman et al. (2014), produces temperatures during the core of the event which are comparable to or cooler than temperatures during the recovery phase, therefore is likely to be an overcorrection. All Mg/Ca-derived temperature estimates are calculated assuming Mg/Ca_{sw} = 2.5 mol/mol, consistent with Early Eocene proxy data.*

The mixed layer B/Ca data from IODP Site U1443 across the PETM is plotted up with a compilation of published B/Ca data across this interval in Figure 79, to illustrate how the magnitude of the B/Ca excursion at IODP Site U1443 compares to the complete magnitude of the B/Ca excursion across the PETM preserved at other sites. The magnitude of decrease in B/Ca of ~–7.5 µmol/mol, from ~56 µmol/mol during the latest Paleocene to ~48.5 µmol/mol during the PETM recovery, equates to between a quarter and a third of the magnitude of the B/Ca excursion within more complete records from the equatorial Pacific and Southern Ocean (~–25–30 µmol/mol; Penman et al., 2014; Babila et al., 2018; Figure 79b). Absolute B/Ca values during the recovery phase at IODP Site U1443 (~48.5 µmol/mol) fall within the range of ~40–60 µmol/mol measured within the PETM recovery from the Southern Ocean, equatorial Pacific and North Atlantic margin, however latest Paleocene values are more characteristic of the Southern

Ocean than the equatorial Pacific (Penman et al., 2014; Babila et al., 2018; Figure 79b). This Southern Ocean signature within the B/Ca data from the surface Indian Ocean is discussed further in **Section 6.7.4** below. Nonetheless, the B/Ca excursion in the mixed layer above IODP Site U1443 confirms that surface ocean acidification, resulting from the massive release of carbon into the exogenic carbon cycle, occurred in the Atlantic, Pacific, Indian and Southern oceans during the PETM and was therefore global in scale.

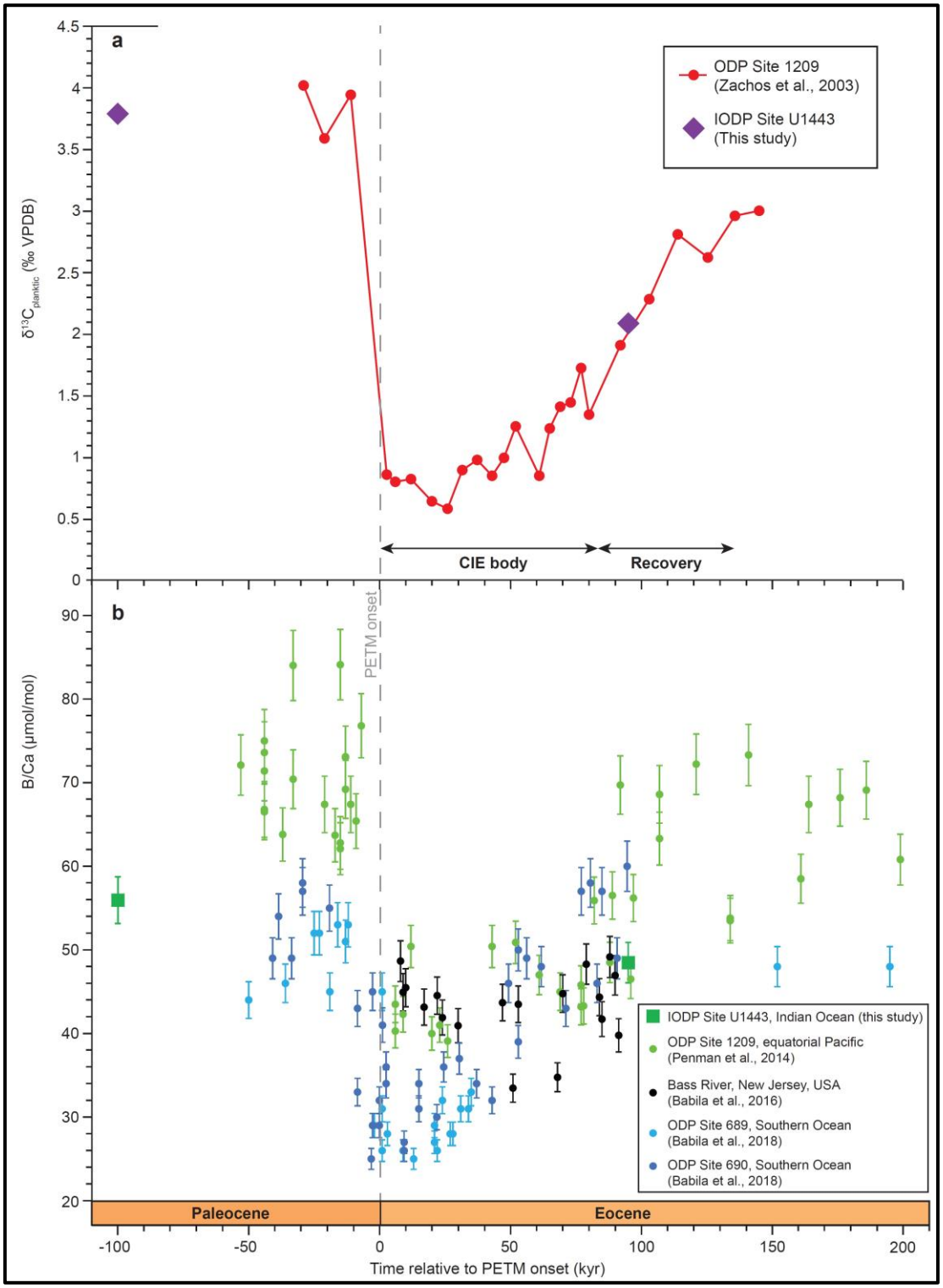

*Figure 79 (previous page). Comparison between mixed layer planktic B/Ca data from IODP Site U1443 and published mixed layer planktic B/Ca records from the Pacific, Atlantic and Southern oceans across the Paleocene-Eocene Thermal Maximum (PETM). All data are based on analysis of Morozovella species, with the exception of data from the Southern Ocean ODP Sites 689 and 690, which are based on analysis of Acarinina soldadoensis. (**a**) Planktic $\delta^{13}C$ data ($\delta^{13}C_{planktic}$) from ODP Site 1209 (Zachos et al., 2003), illustrating the stratigraphic position of samples from IODP Site U1443 on the PETM carbon isotope curve. The age model presented in Babila et al. (2018), consistent with the ODP Site 1209 age model presented here, was used to compare published B/Ca data from the other sites in panel **b**. (**b**) Mixed layer planktic B/Ca data from Indian Ocean IODP Site U1443 (green squares; palaeo-latitude ~29°S; this study), equatorial Pacific ODP Site 1209 (green circles; palaeo-latitude ~23°N; Penman et al., 2014), Southern Ocean ODP Site 689 (light blue circles; palaeo-latitude ~71°S; Babila et al., 2018), Southern Ocean ODP Site 690 (navy blue circles; palaeo-latitude ~73°S; Babila et al., 2018), and Bass River, New Jersey, USA (black circles; palaeo-latitude ~35°N; Babila et al., 2016).*

6.7.4. COMPARISON OF THE MAGNITUDE OF TEMPERATURE AND CARBONATE CHEMISTRY CHANGE AT THE THERMOCLINE DURING THE PETM AT IODP SITE U1443 TO PUBLISHED RECORDS

The thermocline Mg/Ca data generated from IODP Site U1443 and presented in this chapter are compared to other published thermocline Mg/Ca records in Figure 80. The magnitude of thermocline warming at IODP Site U1443 (~+2.3°C), from ~28.0 (±1.4)°C during the latest Paleocene to ~30.3 (±1.4)°C during the PETM recovery, equates to approximately a half of the magnitude of temperature rise recorded in the more complete PETM records from the equatorial Pacific ODP Site 1209 (~+5°C; Penman et al., 2014) and on the low latitude North Atlantic New Jersey shelf (~+4°C; Babila et al., 2016). The stratigraphic positions of the IODP Site U1443 samples places them on the temperature trend exhibited by the thermocline at equatorial Pacific ODP Sites 1209 and 865, with the more complete record from ODP Site 1209 attaining temperatures of ~31.5 (±1.4)°C during the peak of the PETM (Tripati & Elderfield, 2004; Penman et al., 2014; Figure 80b). The temperatures throughout this time interval are generally ~–1–2°C cooler at Bass River compared to ODP Site 1209, which is likely to be related to lower salinity of the thermocline waters due to freshwater input from the adjacent American continent and the higher palaeo-latitude of the site (~35°N). Thermocline temperatures do not recover to pre-excursion values following the PETM recovery at either ODP Site 865 or ODP

Site 1209, remaining ~+1.5°C warmer at both sites (Tripati & Elderfield, 2004; Penman et al., 2014; Figure 80b). This pattern of thermal evolution is comparable to the thermocline waters above the low latitude Indian Ocean IODP Site U1443, which exhibit a step change to warmer thermocline temperatures during the PETM and which is maintained for ~2 million years into the Early Eocene (see Figure 72). Abrupt warming during the PETM, involving a potential deepening of the mixed layer due to downwelling of saline surface ocean waters, appears to have resulted in a long-lasting change to the thermal structure of the upper water column within both the low-latitude Indian and Pacific oceans, and therefore perhaps the low latitudes globally.

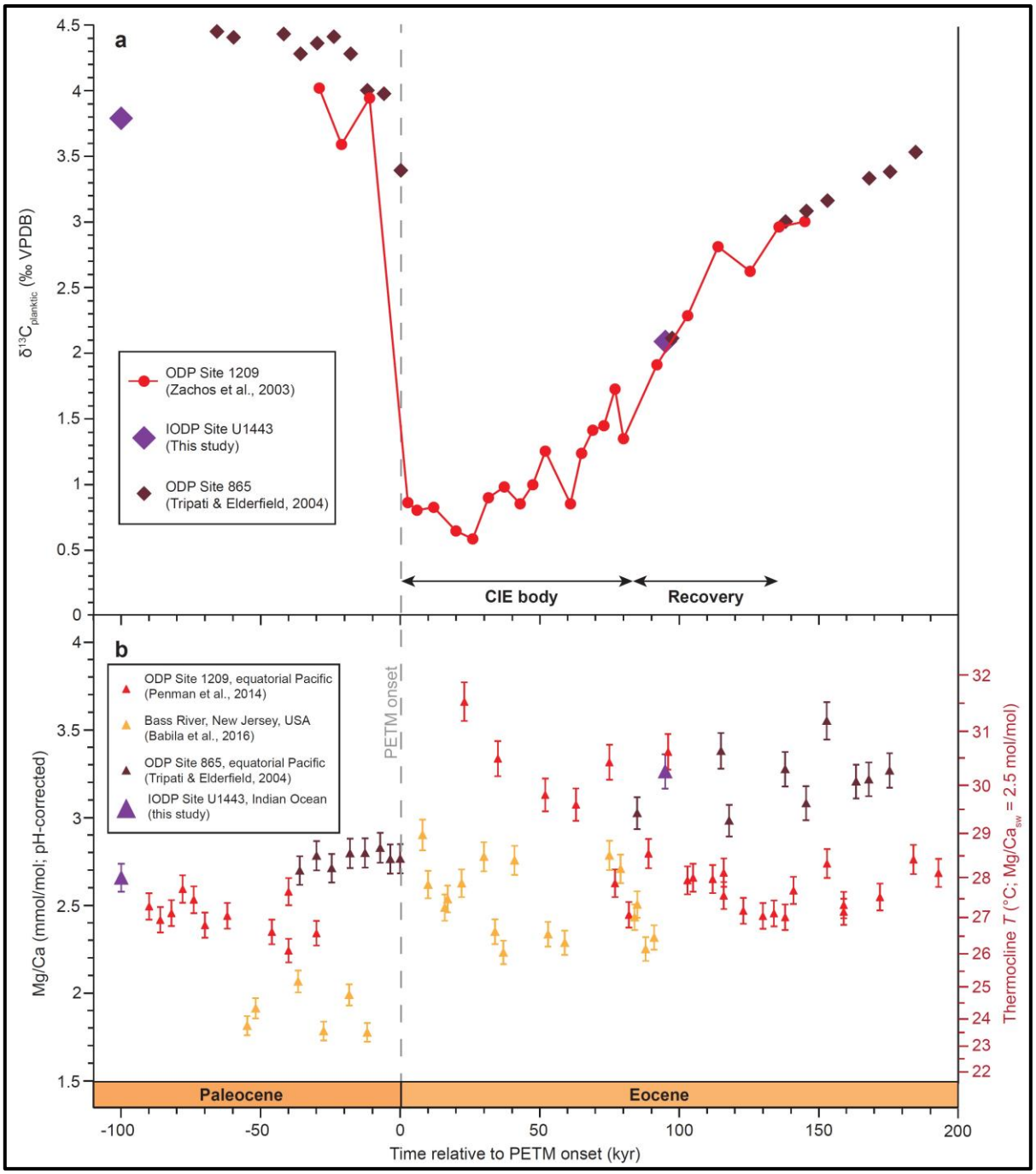

*Figure 80 (previous page). Comparison between thermocline Mg/Ca data from IODP Site U1443 and published thermocline Mg/Ca records from the equatorial Pacific and North Atlantic across the Paleocene-Eocene Thermal Maximum (PETM). All data are based on analysis of Subbotina species. (**a**) Planktic $\delta^{13}C$ data ($\delta^{13}C_{planktic}$) from ODP Site 1209 (Zachos et al., 2003), illustrating the stratigraphic position of samples from IODP Site U1443 and ODP Site 865 on the PETM carbon isotope curve. The age model presented in Babila et al. (2018), consistent with the ODP Site 1209 age model presented here, was used to compare published Mg/Ca data from Bass River with the other sites in panel **b**. (**b**) Thermocline Mg/Ca data from Indian Ocean IODP Site U1443 (purple triangles; palaeo-latitude ~29°S; this study), equatorial Pacific ODP Site 1209 (red triangles; palaeo-latitude ~23°N; Penman et al., 2014), equatorial Pacific ODP Site 865 (purple triangles; palaeo-latitude ~10°N; Tripati & Elderfield, 2004), and Bass River, New Jersey, USA (navy blue triangles; palaeo-latitude ~35°N; Babila et al., 2016). A variable pH correction has been applied to the published Mg/Ca data to account for ocean acidification during the PETM, with a modelled pH of 7.5 during the CIE core (~0–85 kyr after CIE onset), modelled pH of 7.6 during the CIE recovery (~85–150 kyr after CIE onset), and modelled ambient pH of 7.7, broadly following Penman et al. (2014). All Mg/Ca-derived temperature estimates are calculated assuming Mg/Ca_{sw} = 2.5 mol/mol, consistent with Early Eocene proxy data.*

Latest Paleocene and PETM B/Ca ratios of thermocline-dwelling *Subbotina* at IODP Site U1443 are offset to much lower values than data from the equatorial Pacific, North Atlantic, or Southern Ocean, suggestive of comparatively more corrosive thermocline waters within the northern Indian Ocean (Penman et al., 2014; Babila et al., 2016, 2018; Figure 81). B/Ca values decrease by ~–13 µmol/mol, from latest Paleocene values of ~28.3 µmol/mol to ~15.2 µmol/mol within the PETM recovery, lower than minimum values from the Southern Ocean during the core of the PETM excursion (Babila et al., 2018; Figure 81b). The mechanism behind the generation of potentially more corrosive thermocline waters in the northern Indian Ocean during the early Paleogene is somewhat enigmatic. Upwelling of deep older intermediate or bottom waters could bring more corrosive waters up to thermocline depths, however, amplified warming within the thermocline during the PETM and lack of evidence for significant differences in surface ocean productivity between IODP Site U1443 and ODP Site 1209 (based on comparable latest Paleocene $\delta^{13}C_{planktic}$ values; Figure 81a), strongly suggest that upwelling did not occur at IODP Site U1443. Furthermore, higher B/Ca values have been described from planktic foraminifera in upwelling regions due to a positive correlation between B/Ca values and nutrient levels, especially PO_4^{3-} (e.g., Naik & Naidu, 2004; Henehan et al., 2015).

Although there is no evidence for upwelling at IODP Site U1443 itself, it is important to note that thermocline B/Ca values at IODP Site U1443 are most comparable to values from the Southern Ocean, the likely source for intermediate-deep waters within the Indian Ocean based on neodymium isotope data from DSDP Site 213 (e.g., Thomas et al., 2003, 2008). Based on neodymium isotope evidence, deep water production in the central Pacific operated in a bi-modal nature, sourced from both the North Pacific and South Pacific during the early Paleogene, with no connection to Southern Ocean-sourced deep water masses in the Atlantic and Indian oceans (e.g., Thomas et al., 2003, 2008). Since the Indian and Pacific deep water masses appear to be unconnected during this time, upwelling of Southern Ocean-sourced intermediate or deep waters may have occurred within the equatorial portion of the northern Indian Ocean, perhaps along the margins of India or Eurasia at the northern termination of this branch of thermohaline circulation, with surface currents returning this corrosive water back to the Southern Ocean as part of a thermohaline circulation cell in the Indian Ocean (Figure 82). The potential occurrence of old and corrosive Southern Ocean-sourced thermocline waters above IODP Site U1443 could explain the lower absolute B/Ca values relative to the equatorial Pacific. Latest Paleocene mixed layer B/Ca values are also more comparable to Southern Ocean mixed layer values than the equatorial Pacific, supporting a Southern Ocean source for thermocline and mixed layer water masses in the low latitude Indian Ocean above IODP Site U1443.

The magnitude of the B/Ca excursion in the Indian Ocean is comparable to the complete magnitude of the excursion in the Southern Ocean, equatorial Pacific and North Atlantic (Penman et al., 2014; Babila et al., 2016, 2018; Figure 81b). This is consistent with the trend of a smaller and more gradual decrease in B/Ca during the CIE onset, longer duration of the main core of the excursion, and longer recovery phase exhibited by the more complete PETM thermocline records from ODP Site 1209 and Bass River, compared to the mixed layer B/Ca records from these sites (compared Figure 79b and Figure 81b). This trend and character of the excursion suggests that deeper waters at thermocline depths were comparatively buffered against significant transient falls in pH and/or increases in DIC experienced by the mixed layer during the PETM, and responded in a slower and more prolonged fashion to ocean acidification. As a

result, minimum thermocline B/Ca values of ~15.2 µmol/mol from within the CIE recovery phase at IODP Site U1443 are likely to be analogous to B/Ca values from the peak of the CIE within the thermocline of the low latitude Indian Ocean.

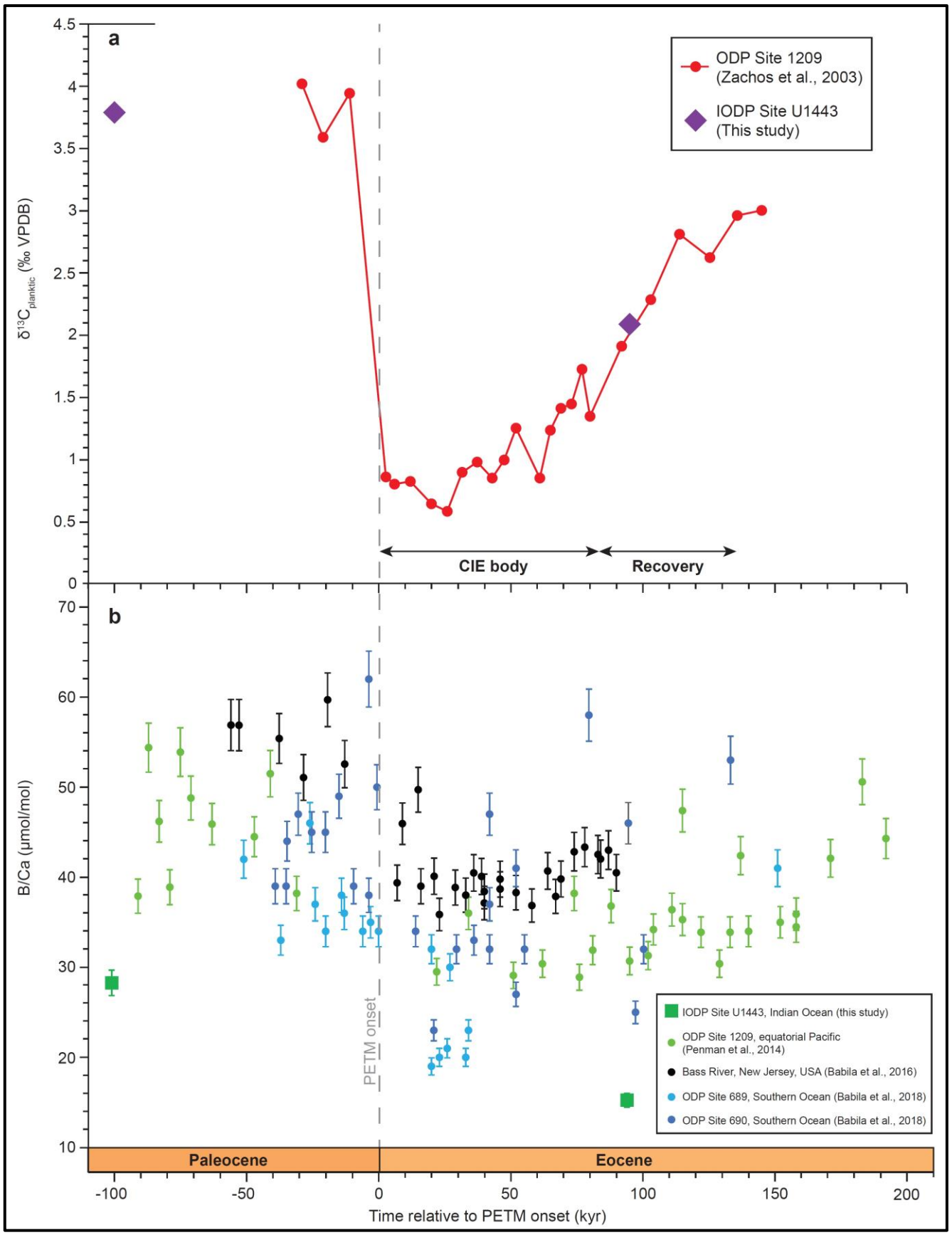

*Figure 81 (previous page). Comparison between thermocline B/Ca data from IODP Site U1443 and published thermocline B/Ca records from the Pacific, Atlantic and Southern oceans across the Paleocene-Eocene Thermal Maximum (PETM). All data are based on analysis of Subbotina species. (**a**) Planktic $\delta^{13}C$ data ($\delta^{13}C_{planktic}$) from ODP Site 1209 (Zachos et al., 2003), illustrating the stratigraphic position of samples from IODP Site U1443 on the PETM carbon isotope curve. The age model presented in Babila et al. (2018), consistent with the ODP Site 1209 age model presented here, was used to compare published B/Ca data from the other sites in panel **b**. (**b**) Thermocline B/Ca data from Indian Ocean IODP Site U1443 (green squares; palaeo-latitude ~29°S; this study), equatorial Pacific ODP Site 1209 (green circles; palaeo-latitude ~23°N; Penman et al., 2014), Southern Ocean ODP Site 689 (light blue circles; palaeo-latitude ~71°S; Babila et al., 2018), Southern Ocean ODP Site 690 (navy blue circles; palaeo-latitude ~73°S; Babila et al., 2018), and Bass River, New Jersey, USA (black circles; palaeo-latitude ~35°N; Babila et al., 2016).*

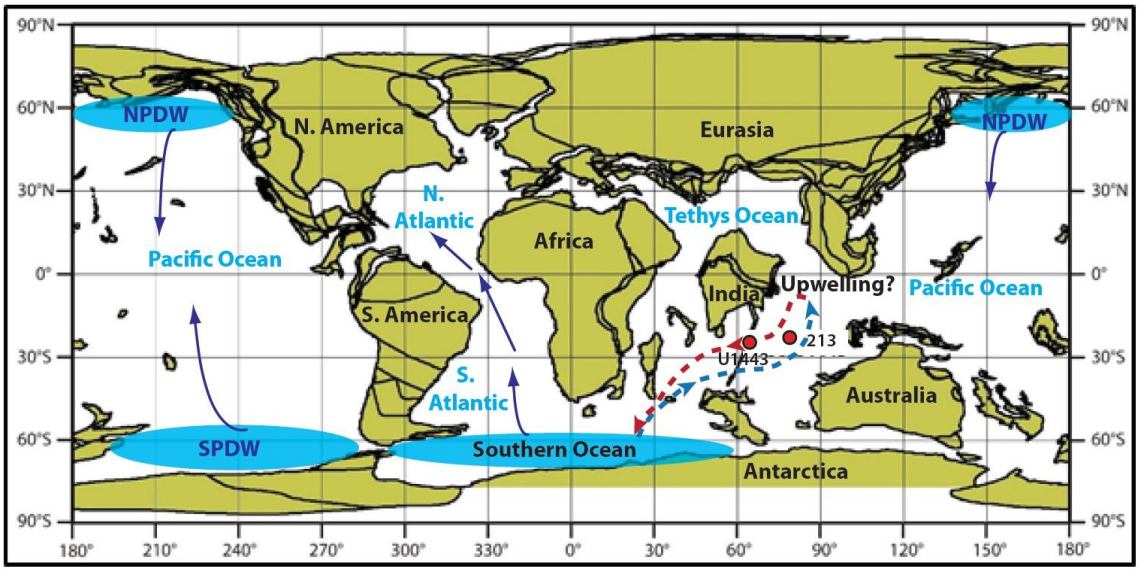

Figure 82. Schematic model for thermohaline circulation within the Indian Ocean which could explain the lower B/Ca values and more corrosive mixed layer and thermocline waters above IODP Site U1443 compared to the equatorial Pacific. The modelled pathway of intermediate-deep water is indicated by a dashed blue line and of surface ocean currents by the dashed red line. Southern Ocean sourced deep water has been identified in the Indian Ocean based on neodymium isotope evidence from DSDP Site 213 (Thomas et al., 2003). A zone of upwelling of Southern Ocean-sourced deep water has been modelled in equatorial regions of the northern Indian Ocean or along the margins of India/Eurasia. Atlantic deep waters were also sourced from the Southern Ocean, whilst Pacific deep waters were sourced from both the North Pacific (North Pacific Deep Water; NPDW) and South Pacific (South Pacific; SPDW), and were unconnected to Atlantic and Indian Ocean deep waters during this time (Thomas et al., 2003).

6.7.5. COMPARISON OF THE MAGNITUDE OF TEMPERATURE CHANGE AT INTERMEDIATE TO DEEP WATER DEPTHS AT IODP SITE U1443 DURING THE PETM TO PUBLISHED RECORDS

The intermediate depth Mg/Ca data generated from IODP Site U1443 and presented in this chapter are compared to other published intermediate to deep water Mg/Ca records from the equatorial Pacific and South Atlantic in Figure 83. Despite different absolute temperatures due to palaeo-depths ranging from ~1300–1500 m at the warmest site, ODP Site 865, to ~3400 m at the coolest site, DSDP Site 527, the thermal trends between the sites and the magnitude of temperature change (~+2.5–3°C) from the latest Paleocene to the PETM recovery phase appear to be comparable (Tripati & Elderfield, 2005; Figure 83b). Therefore, despite incomplete records and absence of the core of the PETM excursion from all but the ODP Site 1209 record, a comparable thermal evolution within intermediate-deep waters of the Indian, Pacific and Atlantic oceans can be inferred during the PETM.

Intermediate water temperatures at IODP Site U1443 rise by ~+3°C from ~11.2 (±1.8)°C during the latest Paleocene to ~14.2 (±1.8)°C during the PETM recovery, ~95 kyr after the onset, then fall to ~13.6 (±1.8)°C by ~130 kyr after onset. These PETM recovery temperatures at IODP Site U1443 sit within the lower range of temperature estimates from the slightly shallower ODP Site 865 (~13.0–15.5 (±1.8)°C; Tripati & Elderfield, 2005), suggesting the thermal evolution of intermediate depth waters in the low latitude Indian and Pacific oceans during the PETM was comparable. Peak temperatures of ~16.5–17.5 (±1.8)°C at ODP Site 865 may correspond to the end of the core of the PETM excursion and represent an analogue for maximum PETM temperatures in the equatorial Pacific intermediate waters.

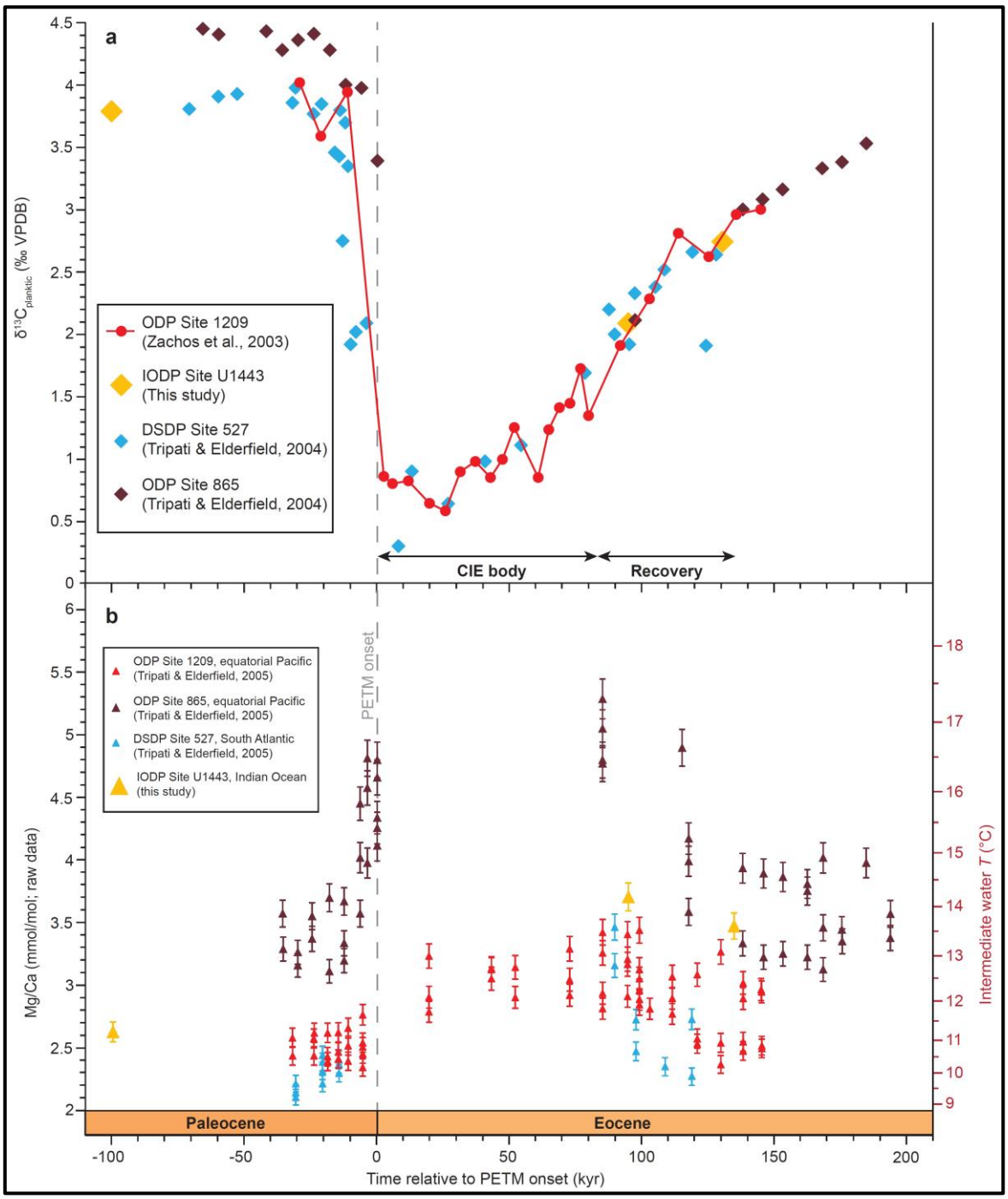

*Figure 83. Comparison between benthic Mg/Ca data from IODP Site U1443 and published benthic Mg/Ca records from the equatorial Pacific and North Atlantic across the Paleocene-Eocene Thermal Maximum (PETM). All data are based on analysis of Oridorsalis umbonatus. (**a**) Planktic δ¹³C data ($\delta^{13}C_{planktic}$) from ODP Site 1209 (Zachos et al., 2003), illustrating the stratigraphic position of samples from IODP Site U1443, ODP Site 865, and DSDP Site 527 on the PETM carbon isotope curve. (**b**) Benthic Mg/Ca data from Indian Ocean IODP Site U1443 (orange triangles; palaeo-depth ~1500m; this study), equatorial Pacific ODP Site 1209 (red triangles; palaeo-depth ~2500m; Tripati & Elderfield, 2005), equatorial Pacific ODP Site 865 (purple triangles; palaeo-depth ~1300–1500m; Tripati & Elderfield, 2005), and South Atlantic DSDP Site 527 (blue triangles; palaeo-depth ~3400m; Tripati & Elderfield, 2005). All Mg/Ca-derived temperature estimates are calculated assuming Mg/Ca_{sw} = 2.5 mol/mol, consistent with Early Eocene proxy data.*

6.7.6. THE RELATIVE CHANGE IN CARBONATE SATURATION STATE AT INTERMEDIATE WATER DEPTHS IN THE LOW LATITUDE INDIAN OCEAN DURING THE PETM

Since there are no other currently published benthic B/Ca records across the PETM, the benthic B/Ca data from IODP Site U1443 presented in Figure 84 represent the first of their kind across this enigmatic hyperthermal event and offer an important insight into changes in carbonate saturation state ($\Delta[CO_3^{2-}]$) at intermediate water depths of the northern Indian Ocean. The PETM is characterised by a transient B/Ca excursion of ~–20 µmol/mol to one of the lowest values recorded in the Late Paleocene–Early Eocene record (~100 µmol/mol; see Figure 68), which equates to a decrease in $\Delta[CO_3^{2-}]$ of ~–17.5 µmol/kg (Figure 84b). This finding is consistent with other proxy data from the Atlantic and Pacific, along with global modelling studies, which suggest a transient decrease in carbonate saturation state and rapid shoaling of the lysocline and CCD during the PETM, consistent with the injection of a large mass of ^{12}C-enriched carbon into the exogenic carbon cycle (e.g., Zachos et al., 2005; Slotnick et al., 2015). These data from IODP Site U1443 confirm a transient decrease in carbonate saturation state within intermediate waters of the Indian Ocean, confirming the global nature of decreasing carbonate saturation states at intermediate to deep water depths of the World ocean during the PETM.

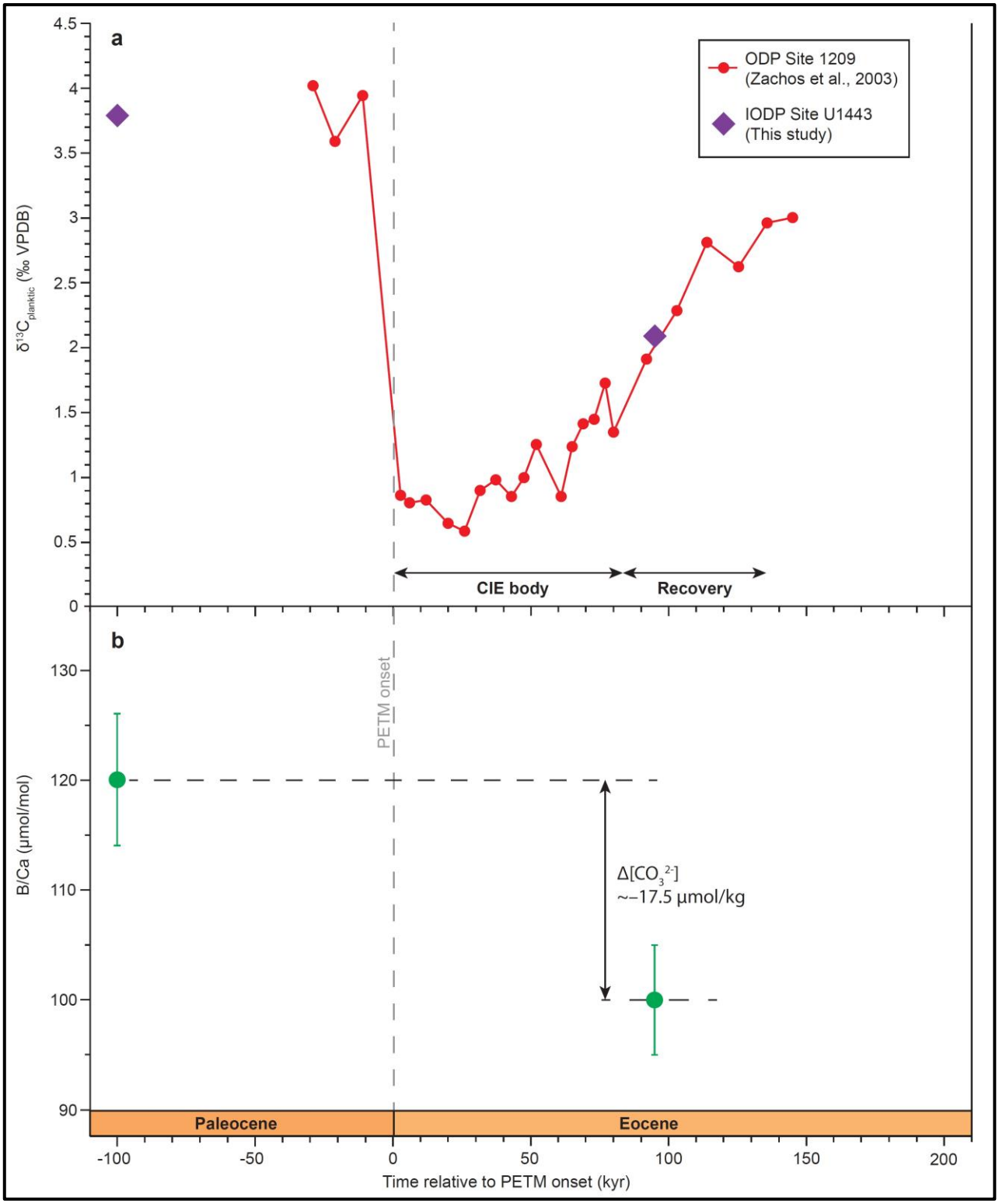

*Figure 84. Benthic B/Ca data across the PETM from IODP Site U1443. (**a**) Planktic $\delta^{13}C$ data ($\delta^{13}C_{planktic}$) from ODP Site 1209 (Zachos et al., 2003), illustrating the stratigraphic position of samples from IODP Site U1443 on the PETM carbon isotope curve. (**b**) Benthic B/Ca data. Relative changes in carbonate saturation state ($\Delta[CO_3^{2-}]$) were calculated using the calibration developed for Nuttallides umbonifera and modified to take into account the different boron concentration of Paleogene seawater in comparison to the modern. Error bars of ±5% are based on the long-term reproducibility of consistency standards.*

6.8. CONCLUSIONS

In this chapter, I have presented the first long-term (~5 myr), orbital-resolution (~14–42 kyr), paired foraminiferal Mg/Ca and B/Ca records spanning the Late Paleocene–Early Eocene (~58–53 Ma) from the mixed layer (~0–30 m), thermocline (~50–200 m), and intermediate water depths (~1500 m) of the low latitude (palaeo-latitude ~29°S) Indian Ocean IODP/ODP Sites U1443 and 758. I have used these records to elucidate the long-term temperature evolution across a depth transect through the water column, the evolution of surface ocean carbonate chemistry (related to pH and DIC), and relative changes in carbonate saturation state at ~1500 m palaeo-depth. By comparing this new Mg/Ca-derived temperature record to other published low latitude surface ocean and intermediate-deep water temperature proxy records, I have shown that the thermal history and absolute temperatures of the northern Indian Ocean surface and intermediate waters are characteristic of the low latitudes globally. A partial PETM record is also captured within IODP Hole U1443A, allowing an investigation of the magnitude of change in temperature, carbonate chemistry and carbonate saturation state for the first time during this event in the low latitude Indian Ocean. I have compared the new planktic stable isotope and trace metal data to more complete published PETM records, to identify which portion of the PETM is captured at IODP Site U1443 and to compare the magnitude of temperature and carbonate chemistry change in the northern Indian Ocean to more complete records from the Pacific, Atlantic, and Southern Ocean. The main conclusions from this chapter are as follows:

- Within the mixed layer, a relative temperature rise of ~+2°C from ~58 Ma to ~53 Ma, along with mean absolute temperatures of ~30 (±1.4)°C during the Late Paleocene and ~31 (±1.4)°C during the Early Eocene, are comparable to absolute temperatures and the magnitude of warming at other low latitude sites in the equatorial Pacific and Atlantic based on the $\mathrm{TEX}_{86}^{\mathrm{H}}$, Mg/Ca, $\delta^{18}O_{planktic}$, and clumped isotope temperature proxies. This long-term warming trend appears to be interrupted by a short-term cooling of ~–1°C during the latest Paleocene in the Indian Ocean and eastern Atlantic. These similarities suggest a coupled thermal evolution across the low latitudes globally,

although the magnitude of temperature rise determined from planktic Mg/Ca during the Early Eocene may be dampened by decreasing Mg/Ca_{sw} during this time.

- Amplified warming of ~+4°C is observed at thermocline depths, with a particularly pronounced step change to warmer temperatures during the PETM and Early Eocene, accompanied by a consequent reduction in the mixed layer-thermocline temperature gradient. This amplified warming may be related to downwelling of increasingly saline warm mixed layer waters and deepening of the mixed layer, as net evaporation exceeded net precipitation within subtropical regions during Early Eocene greenhouse warming, consistent with the outputs from global climate modelling studies (e.g., Carmichael et al., 2017).

- Amplified warming within intermediate waters of the Indian Ocean relative to the low latitude surface ocean (~+3°C), as well as within deep ocean waters globally (~+5°C), is likely to be related to polar amplification of Early Eocene greenhouse warming within high latitude deep water source regions (e.g., the Southern Ocean). However, a portion of this apparent discrepancy in the magnitude of warming between the surface and deep ocean may also be explained by a decrease in Mg/Ca_{sw} during this time.

- This warming is accompanied by steadily decreasing mixed layer planktic foraminiferal B/Ca ratios, suggesting falling pH and/or increasing DIC, consistent with proxy data for increasing atmospheric pCO_2 levels and global warming during this time.

- A pronounced fall in carbonate saturation state of intermediate waters on the Ninetyeast Ridge occurred during the latest Paleocene and again from ~54.5 Ma during the Early Eocene, preceding global CCD shoaling during EECO by ~2.5 million years.

- A portion of the PETM recovery phase is also resolved within the trace metal record from IODP Site U1443, suggesting a warming of ~+1.7°C to temperatures of ~31.0 (±1.4)°C within the mixed layer, ~+2.7°C to

temperatures of ~30.3 (±1.4)°C within the thermocline, and ~+3.0°C to temperatures of ~14.2 (±1.8)°C at intermediate water depths. These absolute temperatures and magnitudes of change are comparable to those from the recovery phase at equatorial Pacific ODP Site 1209, suggesting that a third to a half of the complete magnitude of the PETM has been captured within the new Indian Ocean record.

- The PETM is also characterised by pronounced falls in B/Ca at all depths in the water column, consistent with the injection of a large mass of carbon into the exogenic carbon cycle, resulting in a decrease in pH and carbonate saturation state of the water column. Lower absolute mixed layer and thermocline B/Ca values within the northern Indian Ocean, compared to the equatorial Pacific, suggest a source from the Southern Ocean, potentially from upwelling of intermediate or deep waters in the northern Indian Ocean to the north of IODP Site U1443.

- Synchronous warming within both the low and high-latitudes during the Late Paleocene–Early Eocene suggests that global climate was controlled by greenhouse gas forcing during this time. Although the general trend exhibited by atmospheric pCO_2 proxy data and falling mixed layer B/Ca values provides evidence for generally rising background atmospheric pCO_2, the magnitude of change and absolute concentrations cannot be accurately constrained with the currently available proxy dataset (see **Chapter 3**, Figure 12a). As we gain a better understanding of the evolution of global temperatures during early Paleogene greenhouse climates, future work should focus on providing tighter constraints on the evolution of atmospheric pCO_2 to aid climate predictions of our future anthropogenic world.

7. CONCLUSIONS AND FUTURE WORK

7.1. THESIS SUMMARY

This thesis aims to further our understanding of the interactions between the climate and carbon cycle from the Late Maastrichtian to the Early Eocene (~67–52 Ma), with a focus on both long-term trends and orbitally-paced variability. This enigmatic time period was the most recent in Earth's history to experience sustained global greenhouse warmth coupled with a dynamic carbon cycle, and can offer a crucial insight into the nature of our anthropogenically-warmer future world. To this end, I have applied a diverse suite of geochemical proxies to sedimentary core samples from the South Atlantic (ODP Site 1262) and the Indian Ocean (IODP Site U1443 and ODP Site 758), producing both the longest orbital-resolution, single-site, benthic stable isotope record outside of the Pacific, and the first multi-million year orbital-resolution trace metal (Mg/Ca and B/Ca) records for the Late Paleocene–Early Eocene.

This thesis aims to answer the following overarching questions:

- How did the "background" climate and carbon cycle of both the low and high latitudes evolve during the build-up to the warmest climates of the Cenozoic during EECO?

- What were the responses of the climate and carbon cycle to orbital forcing during the Late Maastrichtian–early Paleogene?

- Did LIP volcanism (i.e., non-orbital forcing mechanisms) impact the climate and carbon cycle dynamics during this time period?

- What were the nature, magnitude and scale of the hitherto poorly studied smaller climatic perturbations of the Early–Middle Paleocene, and can they be classified as global "hyperthermal" events?

A new insight into the long-term evolution of the background climate and carbon cycle during the Late Maastrichtian–early Paleogene, at unprecedented resolution, can be gained from an examination of the new South Atlantic Walvis Ridge ODP Site 1262 benthic stable isotope records, generated and compiled during this project. The orbital-resolution (~1.5–4 kyr), stratigraphic completeness, and duration (~14.75 Myr) of these single-species $\delta^{13}C_{benthic}$ and $\delta^{18}O_{benthic}$ records make them extremely valuable as "reference" records, to which future stable isotope records generated from other deep-sea sites and ocean basins across the globe can be correlated and compared. These records can be compared to the published lower resolution benthic stable isotope records encompassing this time interval from the central Pacific (Westerhold et al., 2011, 2018), and the orbital-resolution trace metal records from the Indian Ocean Ninetyeast Ridge IODP/ODP Sites U1443 and 758, generated during this project for the specific Late Paleocene–Early Eocene time slice. These comparisons can be used to elucidate whether the long-term trends in climate and carbon cycle identified from the South Atlantic Walvis Ridge are also replicated within the other two principle basins of the world ocean, and hence whether they are global in scale.

The broad trends of long-term warming from the Late Maastrichtian until the Early Paleocene at ~63 Ma, followed by a longer-term cooling until ~59 Ma, accompanied by rising $\delta^{13}C_{benthic}$ values to the most positive carbon isotope values of the Cenozoic during the PCIM (~58 Ma), are replicated within both the Atlantic and Pacific records. The Pacific Ocean $\delta^{13}C_{benthic}$ record is generally offset to lighter values compared to the South Atlantic, suggesting an older water mass was bathing the central Pacific site. This is consistent with bi-modal deep water production in the North Pacific and South Pacific for central Pacific bottom waters, and a single source from the Southern Ocean for bottom waters of the South Atlantic. A transient collapse in this gradient in the immediate aftermath of the K/Pg boundary is likely to be primarily related to partial collapse of the biological pump following the K/Pg mass extinction, although a switch between the dominance of North Pacific versus South Pacific deep water sources in the Pacific Ocean may also have played a role during this time.

A long-term warming trend then commenced from the Late Paleocene (~59 Ma) through to the Early Eocene in the South Atlantic, Pacific and Indian Ocean records. A comparable magnitude of ~+3–5°C warming at deep to intermediate water depths (~1500–3500 m) in all three ocean basins, from the peak of the PCIM until the Early Eocene (at ~53 Ma), indicates a very similar thermal evolution of deep to intermediate waters throughout the world ocean during this period of major long-term warming towards EECO. This pattern of long-term warming is also replicated within the surface ocean of the low latitude Indian Ocean, as well as the low latitudes globally, suggesting a synchroneity in climatic trends between the low and high latitudes during the early Paleogene. However, the magnitude of long-term warming in the low latitudes is comparatively muted (~+1.5–2°C), suggesting a significant polar amplification of warming in the high latitudes from the Late Paleocene to the Early Eocene, although a portion of this muted response in planktic Mg/Ca-derived temperature reconstructions may also be explained by decreasing Mg/Ca_{sw} during the Early Eocene.

Within the subtropical Indian Ocean, long-term Late Paleocene–Early Eocene warming appears to be amplified at thermocline depths (~+4°C) compared to the mixed layer (~+2°C). Temperatures at the thermocline also exhibit a particularly pronounced step-change to warmer baseline values during and after the PETM, suggesting a long-lasting change in the thermal structure of the Indian Ocean following this enigmatic hyperthermal event. A similar pattern and character of thermocline warming has been observed at other sites in the subtropical Pacific and Atlantic, suggesting a significant and long-lasting restructuring of the thermal gradient within the upper water column of the subtropical oceans during the PETM. This restructuring may have been initiated by an increase in salinity of surface waters, as net evaporation exceeded net precipitation in the subtropics, resulting in downwelling and a progressive deepening of the mixed layer to thermocline depths.

Accompanying this long-term warming trend, there is also evidence for a long-term rise in background atmospheric CO_2 levels from ~100–500 ppm during the Early Paleocene to ~100–750 ppm during the Early Eocene based on proxy data. A long-term decrease in B/Ca ratios of mixed layer planktic foraminifera

above the Indian Ocean IODP/ODP Sites U1443/758 suggests an accompanied decrease in pH and/or increase in surface ocean DIC from the Late Paleocene to the Early Eocene, supporting the idea of increasing greenhouse gas concentrations within the ocean-atmosphere system during this time. Deeper thermocline and intermediate water depths appear to have been relatively buffered against these long-term changes in surface ocean carbonate chemistry, however, with evidence for a significant long-term drop in B/Ca (and hence decrease in carbonate saturation state) only during the Early Eocene at ~54.5 Ma. The synchroneity of long-term warming trends between the high and low latitudes during the early Paleogene also favours rising atmospheric CO_2 concentrations as the primary modulator of global climate during this time.

These long-term climate and carbon cycle trends are superimposed by a strong imprint of orbital cyclicity throughout the Late Maastrichtian–early Paleogene. Spectral analysis of the complete Late Maastrichtian–Early Eocene benthic stable isotope records from the South Atlantic ODP Site 1262 document pacing of the climate and carbon cycle during this time by long (405-kyr) and short (100-kyr) eccentricity, through the modulation of precession. Phasing between the carbon and oxygen isotope records suggests that perturbations to the global carbon cycle lag changes to global climate throughout this time period, implying that isotopically light carbon was released from temperature- or climate-sensitive reservoirs as a positive feedback to an initial warming induced by changes in orbital configuration. By placing all known hyperthermals of this time period into an orbital cyclostratigraphic framework from a single deep-sea site, I have identified that the majority occur during maxima in the long (405-kyr) eccentricity cycle and appear to be orbitally-paced. The Late Paleocene orbitally-paced excursions in the carbon cycle also have a pronounced expression in the mixed layer carbon isotope and B/Ca records from the Indian Ocean IODP Site U1443 and ODP Site 758, confirming their global extent. Furthermore, the B/Ca perturbations also suggest a significant change in surface ocean carbonate chemistry as a result of a decrease in surface ocean pH and/or an increase in DIC concentration, consistent with the transient orbitally-paced input of CO_2 into the exogenic carbon cycle during these events. By contrast, orbitally-paced climate excursions of the Late Paleocene are generally unresolved within the planktic Mg/Ca records from Indian Ocean IODP/ODP Sites U1443/758,

suggesting that the magnitude of temperature change falls within analytical uncertainty of the measurements in the surface ocean of the subtropical Indian Ocean, the complete magnitudes of the climatic perturbations have not been sampled within the trace metal record, and/or the primary planktic Mg/Ca values have been lowered by minor dissolution of high-Mg calcite during these events.

Two of the largest perturbations to the climate and carbon cycle during this time period, the LMWE and the PETM, do not occur during maxima in the 405-kyr eccentricity cycle and are both likely to have been triggered or augmented by LIP volcanism. The timing of inception of the LMWE coincides, within uncertainty, with the onset of the main phase of Deccan Traps LIP volcanism on the Indian sub-continent, strongly suggesting a causal link. Furthermore, inception of the event during a minimum in the 405-kyr eccentricity cycle and the lack of a major perturbation to the isotopic composition of the global carbon pool, suggest that orbital forcing alone is unlikely to have played a major role in the timing of the event, further supporting volcanogenic mantle-derived CO_2 (with a more positive $\delta^{13}C$ signature of ~–7‰) as the trigger. Similarly, the timing of the PETM correlates with the second phase of NAIP volcanism in the North Atlantic. Unlike the LMWE, the PETM is characterised by a major perturbation to the isotopic composition of the carbon cycle, suggesting the coupled release of an isotopically light carbon source (e.g., thermogenic or biogenic methane) in addition to volcanogenic CO_2. The longer duration and slower rate of warming (and CO_2 release) during the LMWE resulted in a less severe impact on marine and terrestrial biota compared to the PETM, with the lack of evidence for major global extinction events associated with the LMWE suggesting that it did not play a major role in the severity of the subsequent K/Pg mass extinction ~66 Ma.

Based on the magnitude of the carbon isotope excursion recorded in bulk and planktic foraminiferal carbonate, the samples analysed to generate the trace metal records from the Indian Ocean IODP/ODP Sites U1443/758 during this project capture approximately one third to one half of the total magnitude of the PETM. Nonetheless, these records allow us to calculate the first ever conservative minimum estimates of absolute temperatures, magnitude of warming, and carbonate chemistry change across a depth transect through the low latitude Indian Ocean during this archetypal hyperthermal event. These data

represent the first trace metal proxy data encompassing the PETM from the Indian Ocean as a whole, filling a noticeable geographic void in data coverage for a climatic event which arguably represents the best geological analogue for current anthropogenic global warming. This enigmatic hyperthermal event is characterised by a warming of ~+1.7°C to absolute temperatures of ~31.0 (±1.4)°C within the mixed layer, a warming of ~+2.7°C to absolute temperatures of ~30.3 (±1.4)°C within the thermocline, and a warming of ~+3.0°C to absolute intermediate water depth (~1500m) temperatures of ~14.2 (±1.8)°C at IODP Site U1443 (palaeolatitude ~29°S). Temperatures within the mixed layer, thermocline and at intermediate water depths during the PETM recovery at IODP Site U1443 are comparable to those from the subtropical Pacific, suggesting a comparable thermal evolution between the low latitude Indian and Pacific oceans during the PETM, even though the Indian Ocean record is poorly resolved. The PETM is also characterised by pronounced drops in B/Ca at all depths in the water column, supporting the global nature of ocean acidification during the event, resulting from the injection of a significant mass of carbon into the exogenic carbon cycle. Absolute B/Ca values from the mixed layer and thermocline of the Indian Ocean indicate a strong Southern Ocean fingerprint and are very distinct from Pacific Ocean values, confirming different deep water sources within the two ocean basins and a lack of connectivity during the early Paleogene.

By integrating the new orbital-resolution benthic stable isotope record generated from ODP Site 1262 with published palaeoclimate proxy data, the nature, magnitude and scale of the poorly studied climatic events of the Early–Middle Paleocene, including the Dan-C2 event (~65.9–65.7 Ma), Latest Danian Event (LDE; ~62.1–62.0 Ma) and Danian/Selandian Transition Event (D/STE; ~61.4–61.2 Ma), can be more fully evaluated. This evaluation can be used to determine if these events can be classified as typical hyperthermals analogous to those of the Early Eocene such as ETM-2/H2. Global hyperthermal events are characterised by the massive injection of greenhouse gases into the ocean-atmosphere system, significant transient global warming within the terrestrial realm, surface and deep ocean, shoaling of the global deep-ocean lysocline and CCD, and many have a pacing determined by orbital forcing.

The LDE appears to satisfy these criteria, including a pronounced bottom water warming of ~+2–2.5°C within the South Atlantic, central Pacific and Indian Ocean, surface water warming within the central Pacific, and deep-sea carbonate dissolution within the Atlantic and Pacific. The double-spiked nature of the event, as well as its occurrence during two 100-kyr eccentricity maxima which were amplified during the $Pc_{405}10$ (405-kyr) eccentricity maximum, also confirms its pacing by orbital forcing. The expression and character of the event in the ODP Site 1262 benthic stable isotope records are analogous to the double-spiked better-studied hyperthermals of the Early Eocene, such as ETM-2/H2 and I1/I2, albeit with a bottom water warming of around half the magnitude.

Classification of the Dan-C2 and D/STE as hyperthermals is rather more problematic, however, as they exhibit some but not all of the characteristics typical of a global hyperthermal. Whilst possible evidence exists for a significant transient warming event of up to ~+6°C within the terrestrial realm and surface ocean during Dan-C2, along with evidence for an orbitally-paced excursion to the carbon cycle, the lack of a temperature response within the deep South Atlantic and central Pacific suggests that this event cannot be classified as a typical hyperthermal. The Dan-C2 event is interpreted to reflect the first 405-kyr eccentricity maximum of the Paleocene, with a magnified expression within bulk and planktic carbon isotope records due to partial collapse of the biological pump and extreme vital effects within opportunistic planktic foraminifera taxa following the K/Pg mass extinction, as well as ongoing Deccan Traps volcanism. Similarly, whilst the D/STE appears to be characterised by a pronounced carbon cycle perturbation and warming of ~+2°C within the deep South Atlantic, the lack of a temperature response within the deep central Pacific suggests that the climatic response observed from the South Atlantic during this event may not be global in scale. Further studies are therefore required to elucidate the nature, magnitude and scale of environmental change which occurred during Dan-C2 and the D/STE, to better identify their causal mechanisms and potential impacts.

7.2. FUTURE WORK

7.2.1. MODELLING STUDIES

The benthic stable isotope records generated and compiled during this study (**Chapter 3**) detail both long-term and transient orbitally-paced perturbations to the climate and carbon cycle at unprecedented resolution from the Late Maastrichtian–Early Eocene. Due to the paucity of palaeoclimate records encompassing the Early–Middle Paleocene, the new orbital-resolution ODP Site 1262 records will serve as a particularly valuable source of data input into climate and carbon cycle models such as LOSCAR (Zeebe et al., 2017), enhancing our understanding of climate and carbon cycle dynamics during this enigmatic greenhouse period, and extending previous modelling studies back further into deep time from the Late Paleocene to the Late Maastrichtian.

Similarly, the Late Paleocene–Early Eocene long-term, orbital-resolution trace metal records, presented in **Chapter 6** of this thesis, represent the first of their kind to be generated from this time period and the first from the poorly studied Indian Ocean. These data will be valuable for future palaeoclimate modelling studies focused on this time period, in particular for the "Late Paleocene background" timeslice of the Deep-Time Model Intercomparison Project (DeepMIP; https://www.deepmip.org/), where there is currently a real paucity of data compared to the subsequent flagship hyperthermal events such as the PETM and ETM-2. Although the complete magnitude of the event has not been resolved, this trace metal record also captures a portion of the PETM, providing the first ever minimum constraint on absolute temperatures and the magnitude of warming within the low latitude Indian Ocean. These data will therefore prove invaluable for increasing the spatial coverage of data input into climate modelling studies focussed on the largest hyperthermal event of the Paleogene Period.

7.2.2. BIOTIC RESPONSE TO DECCAN VOLCANISM

Whilst I present robust evidence for a causal link between the onset of Deccan Traps volcanism and global environmental change associated with the

LMWE in **Chapter 4**, the paucity of orbital-resolution biotic data still hampers the development of a robust correlation between Deccan-induced environmental change and latest Maastrichtian biotic events. As a consequence, the precise role of Deccan Traps volcanism in the K/Pg mass extinction continues to be shrouded in controversy and remains a heavily debated topic (e.g., Schulte et al., 2010; Keller et al., 2016). Now that the climatic effects of Deccan volcanism have been more precisely constrained at orbital resolution, future work should focus on evaluating the response within marine and terrestrial biota to these environmental changes at orbital resolution with the same rigour. Core material recovered from ODP Site 1262, or shallower sites on the Walvis Ridge, would represent ideal opportunities for high-resolution studies on the impact of marine biota to Deccan-induced environmental change. These studies could build on earlier lower resolution studies by Thibault et al. (2007) from the shallower DSDP Site 525, with easy correlation to the latest Maastrichtian climate and carbon cycle records generated during this study.

7.2.3. GLOBAL ENVIRONMENTAL CHANGE DURING THE DAN-C2 EVENT

Although the results presented in **Chapter 5** suggest that the Dan-C2 event cannot be classified as a typical hyperthermal, the apparent magnitudes of climatic warming in the terrestrial realm and surface ocean, based on sparse published proxy datasets, are difficult to reconcile with the lack of temperature change in the deep waters of the global ocean. The Dan-C2 event has mainly been recognised and described from shallow marine continental shelf settings based on bulk carbonate isotope data (e.g., Coccioni et al., 2010; Punekar et al., 2014b), therefore the apparent magnitude of climatic change during the event in these records may have been biased by diagenesis. Future work should focus on constraining the geographic variability and magnitude of climatic warming in the terrestrial realm and surface waters during Dan-C2, to more fully evaluate the scale and nature of global environmental change that characterised this event. To achieve this aim, the generation of paired palaeoclimate proxy records such as coupled single-species mixed layer planktic stable isotope and Mg/Ca data, as generated for samples from the Indian Ocean Ninetyeast Ridge in **Chapter 6** of this thesis, would yield more robust estimates of the magnitude of surface ocean temperature change during Dan-C2.

7.2.4. GLOBAL ENVIRONMENTAL CHANGE DURING THE DANIAN/SELANDIAN TRANSITION EVENT

Despite evidence for a transient bottom water warming and carbon cycle perturbation within the new South Atlantic Walvis Ridge benthic stable isotope records generated during this study (**Chapter 3**), the lack of a temperature response within the $\delta^{18}O_{benthic}$ record from the central Pacific suggests that the D/STE is not a typical hyperthermal. Whilst the LDE, which pre-dates the D/STE by ~800 kyr, has recently become the focus for a number of palaeoclimate proxy studies (e.g., Jehle et al., 2015; Deprez et al., 2017), the D/STE has been comparatively poorly studied to date, with a paucity of palaeoclimate proxy data characterising environmental change during this event from the surface ocean and terrestrial realms. As a result, the nature of environmental change during the D/STE, and how this environmental change compares to the LDE in terms of magnitude, remain poorly understood. To more fully understand the nature of the D/STE, high-resolution palaeoclimate proxy data (e.g., Mg/Ca, $\mathrm{TEX}_{86}^{\mathrm{H}}$, clumped isotopes) from terrestrial and shallow marine environments are urgently required. By supplementing the planktic stable isotope data generated across the event from ODP Site 1262 during this study with planktic Mg/Ca data, the magnitude of temperature change within the mixed layer above ODP Site 1262 could be quantified and compared to the magnitude of deep sea warming inferred from the coupled $\delta^{18}O_{benthic}$ record.

7.2.5. QUANTITATIVE ESTIMATION OF pH AND *p*CO_2

The trace metal proxy records presented in **Chapter 6** quantify the evolution of temperature, carbonate chemistry (related to pH), and relative changes in bottom water carbonate saturation state within the low latitude Indian Ocean. However, for the quantitative estimation of absolute pH and the evolution of atmospheric *p*CO_2, boron isotope ($\delta^{11}B$) data are required. For the generation of $\delta^{11}B$ data, a large mass of foraminiferal sample is required (1,000–3,000 µg; Foster, 2008), which often precludes the use of this proxy from many marine cores characterised by terrigenous clay dilution or carbonate dissolution. However, the abundant planktic foraminifera within the Paleogene nannofossil and calcareous chalks of the shallow palaeo-depth sites on the Ninetyeast Ridge

would facilitate the application of the $\delta^{11}B$ proxy to these cores. The splice between IODP Site U1443 and ODP Site 758 presented herein is based on carbon isotope stratigraphy, calcareous nannofossil biostratigraphy, and planktic foraminifera biostratigraphy, and therefore provides a robust temporal framework for future work focused on the Late Paleocene–Early Eocene at these sites. Due to the paucity of atmospheric pCO_2 and surface ocean pH data for the "background" climate of the Paleocene–Early Eocene, outside of the larger hyperthermal events of the Early Eocene (e.g., Royer, 2014; **Chapter 3**), the generation of $\delta^{11}B$ data from the Ninetyeast Ridge sites would significantly aid our understanding of the evolution of atmospheric pCO_2 during the build up to peak greenhouse climates of the Cenozoic, and improve model simulations for our future warmer anthropogenic world. In addition, a better understanding of the evolution of ambient surface ocean pH during the early Paleogene could also be used to apply a variable pH correction to the planktic Mg/Ca data presented in this thesis (rather than assuming a single ambient pH of 7.7), thereby reducing uncertainty associated with the calculation of absolute mixed layer temperatures and the magnitude of temperature change from the Late Paleocene to Early Eocene.

7.2.6. CONSTRAINING THE EVOLUTION OF LATE PALEOCENE–EARLY EOCENE MG/CA$_{SW}$

One of the largest uncertainties associated with calculating absolute temperatures and the magnitude of relative temperature changes on multi-million year timescales during the early Paleogene from planktic Mg/Ca data, is the secular variation in Mg/Ca_{sw}. Whilst Mg/Ca_{sw} proxy data have recently been published for the Early Eocene, suggesting values of ~2.5 mol/mol and decreasing towards the Middle Eocene (Evans et al., 2018; the value adopted in this thesis), the evolution of Mg/Ca_{sw} during the Late Paleocene is currently unconstrained by proxy data (e.g., Evans & Müller, 2012). A significant shift in Mg/Ca_{sw} has the potential to mask or modify long-term temperature trends and absolute temperature values interpreted from Mg/Ca data. The generation of Mg/Ca_{sw} estimates for the Late Paleocene could be achieved by using an independent temperature proxy such as clumped isotopes on the same foraminiferal sample analysed for Mg/Ca, to isolate the temperature and Mg/Ca_{sw}

components recorded by the Mg/Ca proxy. A sound understanding of the evolution of Mg/Ca_{sw} during this poorly studied time slice could further reduce uncertainty associated with the calculation of absolute temperatures and magnitudes of relative temperature change from the Late Paleocene to Early Eocene presented in this thesis.

8. APPENDIX

Appendix 1. Definitions and abbreviations used in this thesis.

$\delta^{11}B$	Stable boron isotopes: $^{11}B/^{10}B$ of the sample relative to that of the NIST SRM 951 boric acid standard
$\delta^{13}C$	Stable carbon isotope data: $^{13}C/^{12}C$ of the sample relative to that of the VPDB standard
$\delta^{13}C_{bulk}$	Stable carbon isotope composition of bulk carbonate material
$\delta^{13}C_{planktic}$	Stable carbon isotope composition of planktic foraminifera
$\delta^{13}C_{benthic}$	Stable carbon isotope composition of benthic foraminifera
$\delta^{13}C_{org}$	Stable carbon isotope composition of organic matter
$\delta^{18}O$	Stable oxygen isotope data: $^{18}O/^{16}O$ of the sample relative to that of the VPDB standard
$\delta^{18}O_{bulk}$	Stable oxygen isotope composition of bulk carbonate material
$\delta^{18}O_{planktic}$	Stable oxygen isotope composition of planktic foraminifera
$\delta^{18}O_{benthic}$	Stable oxygen isotope composition of benthic foraminifera
$\delta^{18}O_c$	Stable oxygen isotope composition of carbonate (generic)
$\delta^{18}O_{cib}$	Stable oxygen isotope composition of *Cibicidoides* tests
$\delta^{18}O_{Nutt}$	Stable oxygen isotope composition of *Nuttallides truempyi* tests
$\delta^{18}O_{sw}$	Stable oxygen isotope composition of seawater
Δ_{47}	Carbonate clumped isotope thermometry data
$\Delta^{13}C$	Carbon isotope gradient
$\Delta[CO_3^{2-}]$	Relative change in carbonate saturation state
ΔT	Temperature gradient or relative change in temperature
$[B]_{sw}$	Boron concentration in seawater
[Ca]	Calcium concentration
$[CO_3^{2-}]$	Carbonate ion concentration

$\frac{[B(OH)_4^-]}{DIC}$	Ratio of borate ion [$B(OH)_4^-$] to dissolved inorganic carbon (DIC)
%CF	Percentage coarse fraction
$\%CaCO_3$	Percentage calcium carbonate
‰	Parts per thousand (permil)
µm	Micrometre (0.001 mm)
µg	Microgram (0.000001 g)
µmol	Micromol (0.000001 mol)
µl	Microlitre (0.000001 l)
B/Ca	Ratio of boron (^{11}B) to calcium (^{43}Ca)
$B(OH)_3$	Boric acid
$B(OH)_4^-$	Borate ion
BWT	Bottom water temperature
$CaCO_3$	Calcium carbonate
cc	Cubic centimetre; cm^3
CCD	Calcite Compensation Depth
CH_4	Methane gas
CIE	Carbon isotope excursion
CO	Cross over
CO_3^{2-}	Carbonate ion
CO_2	Carbon dioxide gas
CSF-A	Core depth below sea floor (allowing overlap at Cored Interval and Section boundaries)
Dan-C2	Dan-C2 event
DC1	Dan-C2 carbon isotope excursion 1: oldest Dan-C2 carbon isotope excursion (~65.83 Ma)

DC2	Dan-C2 carbon isotope excursion 2: youngest Dan-C2 carbon isotope excursion (~65.71 Ma)
DIC	Dissolved Inorganic Carbon, mainly comprising bicarbonate ion (HCO_3^-) and carbonate ion (CO_3^{2-})
DSDP	Deep Sea Drilling Project
D/STE	Danian/Selandian Transition Event
Ecc_{405}	Long (405-kyr) eccentricity
Ecc_{100}	Short (100-kyr) eccentricity
EECO	Early Eocene Climatic Optimum
ELPE	Early Late Paleocene Event
ETM-2	Eocene Thermal Maximum 2
ETM-3	Eocene Thermal Maximum 3
FEG-SEM	Field Emission Gun-Scanning Electron Microscope
HCO	Highest common occurrence
HCO_3^-	Bicarbonate ion
HO	Highest occurrence
ICP-MS	Inductively-Coupled Plasma-Mass Spectrometer
IODP	International Ocean Discovery Program
K/Pg	Cretaceous/Paleogene boundary
kyr	Thousands of years
L. C29n	Lower Chron 29n event
L. C26r	Lower Chron 26r event
La2010b	Orbital solution “b” from Laskar et al. (2011a)
LCO	Lowest common occurrence
LDE	Latest Danian Event

LDE1	Latest Danian Event carbon isotope excursion 1: oldest LDE excursion (~62.1 Ma)
LDE2	Latest Danian Event carbon isotope excursion 2: youngest LDE excursion (~62.0 Ma)
LIP	Large igneous province
LMWE	Late Maastrichtian warming event
LO	Lowest occurrence
M. C27r	Middle Chron 27r event
Ma	Million years ago
mbsf	Metres below sea floor
mcd	Metres composite depth
Mg/Ca	Ratio of magnesium (^{24}Mg and ^{25}Mg) to calcium (^{43}Ca)
Mg/Ca_{sw}	Magnesium to calcium ratio in seawater
mg	Milligram (0.001 g)
ml	Millilitre (0.001 l)
mmol	Millimol (0.001 mol)
mol	Mole
MTM	Multi-Taper Method
myr	Millions of years
NERC	Natural Environment Research Council
ODP	Ocean Drilling Program
PCIM	Paleocene Carbon Isotope Maximum
pCO_2	Partial pressure of carbon dioxide
PETM	Paleocene-Eocene Thermal Maximum
PO_4^{3-}	Phosphate ion
ppm	Parts per million

ppmv	Parts per million by volume
$Prec_{21}$	21-kyr precession
SEM	Scanning Electron Microscope
SST	Sea surface temperature
S_z	Soil-respired CO_2 concentration
T	Temperature
TEX_{86}^{H}	Organic paleothermometer proxy
UCSC	University of California Santa Cruz
VPDB	Vienna Pee Dee Belemnite
VSMOW	Vienna Standard Mean Ocean Water
XRF	X-Ray Fluorescence

*Appendix 2. Manuscript published in Geology (Geological Society of America) in December 2017 (Barnet et al., 2017), forming the basis for **Chapter 4**.*

THE GEOLOGICAL SOCIETY OF AMERICA®

A new high-resolution chronology for the late Maastrichtian warming event: Establishing robust temporal links with the onset of Deccan volcanism

James S.K. Barnet[1], Kate Littler[1], Dick Kroon[2], Melanie J. Leng[3,4], Thomas Westerhold[5], Ursula Röhl[5], and James C. Zachos[6]

[1]Camborne School of Mines & Environment and Sustainability Institute, University of Exeter, Penryn Campus, Cornwall TR10 9FE, UK
[2]School of GeoSciences, University of Edinburgh, Edinburgh EH8 9XP, UK
[3]Natural Environment Research Council (NERC) Isotope Geosciences Facility, British Geological Survey, Nottingham NG12 5GG, UK
[4]Centre for Environmental Geochemistry, School of Biosciences, Sutton Bonington Campus, University of Nottingham, Loughborough LE12 5RD, UK
[5]MARUM, University of Bremen, Leobener Strasse, 28359 Bremen, Germany
[6]Department of Earth and Planetary Sciences, University of California Santa Cruz, Santa Cruz, California 95064, USA

ABSTRACT

The late Maastrichtian warming event was defined by a global temperature increase of ~2.5–5 °C that occurred ~150–300 k.y. before the Cretaceous-Paleogene (K-Pg) mass extinction. This transient warming event has traditionally been associated with a major pulse of Deccan Traps (west-central India) volcanism; however, large uncertainties associated with radiogenic dating methods have long hampered a definitive correlation. Here we present a new high-resolution, single species, benthic stable isotope record from the South Atlantic, calibrated to an updated orbitally tuned age model, to provide a revised chronology of the event, which we then correlate to the latest radiogenic dates of the main Deccan Traps eruption phases. Our data reveal that the initiation of deep-sea warming coincides, within uncertainty, with the onset of the main phase of Deccan volcanism, strongly suggesting a causal link. The onset of deep-sea warming is synchronous with a 405 k.y. eccentricity minimum, excluding a control by orbital forcing alone, although amplified carbon cycle sensitivity to orbital precession is evident during the greenhouse warming. A more precise understanding of Deccan-induced climate change paves the way for future work focusing on the fundamental role of these precursor climate shifts in the K-Pg mass extinction.

INTRODUCTION

A period of rapid climate change, represented initially by a transient global warming event and followed by a global cooling, occurred during the last few hundred thousand years of the Maastrichtian and may have played an ancillary role in the ultimate demise of many terrestrial and marine biota at the Cretaceous-Paleogene (K-Pg) boundary (e.g., Keller et al., 2016). The so-called late Maastrichtian warming event was characterized by a transient global ~2.5–4 °C warming in the marine realm based on benthic $\delta^{18}O$ and organic paleothermometer (TEX^{H}_{86}) data (e.g., Li and Keller, 1998; Woelders et al., 2017), and ~5 °C warming in the terrestrial realm based on pedogenic carbonate $\delta^{18}O$ and proportion of untoothed leaf margins in woody dicot plants (Nordt et al., 2003; Wilf et al., 2003). Enhanced deep-sea carbonate dissolution, most pronounced in the high latitudes (Henehan et al., 2016), and abrupt decreases in vertical temperature and carbon isotope gradients in the marine water column have also been documented (Li and Keller, 1998).

This transient warming event has previously been linked to a major pulse of Deccan Traps volcanism, centered in modern-day western India; however, until recently, the large uncertainties associated with radiogenic dating have hampered a robust correlation (e.g., Chenet et al., 2007). In recent years improvements in precision of radiogenic dating methods have allowed for a more robust correlation between pre-K-Pg climate change and volcanism (e.g., Renne et al., 2015; Schoene et al., 2015). To complement advances in dating of the volcanic sequences, we present the highest resolution (1.5–4 k.y.), complete single species benthic stable isotope record produced to date, calibrated to an updated orbitally tuned age model, for the final million years of the Maastrichtian and the first 500 k.y. of the Danian. This allows us to much more accurately correlate the major climatic shifts of the terminal Maastrichtian with Deccan volcanism, facilitating future work investigating the link between Deccan-induced climate change and the K-Pg mass extinction.

MATERIALS AND METHODS

A stratigraphically continuous late Maastrichtian–early Danian sedimentary section was recovered at Ocean Drilling Program (ODP) Site 1262 (Walvis Ridge, South Atlantic; 27°11.15′S, 1°34.62′E; water depth 4759 m, Maastrichtian water depth ~3000 m; Shipboard Scientific Party, 2004), where the late Maastrichtian is represented by an expanded section of foraminifera-bearing, carbonate-rich nannofossil ooze with a mean sedimentation rate of 1.5–2 cm/k.y. We have constructed an updated orbitally tuned age model for this site based on recognition of the stable 405 k.y. eccentricity cycle in our high-resolution benthic carbon isotope ($\delta^{13}C_{benthic}$) data set, correlated to the La2010b solution of Laskar et al. (2011) and anchored to an astronomical K-Pg boundary age of 66.02 Ma (Dinarès-Turell et al., 2014). The key tie points used to create this age model are listed in Table DR2 in the GSA Data Repository[1]. All published data presented herein have also been migrated over to the same age model for comparison (Figs. 1 and 2; detailed methods are provided in the Data Repository). We generated $\delta^{13}C$ and $\delta^{18}O$ data using the epifaunal benthic foraminifera species *Nuttallides truempyi* on an IsoPrime 100 gas source isotope ratio mass spectrometer in dual inlet mode equipped with a Multiprep device at the Natural Environment Research Council Isotope Geosciences Facility (British Geological Survey). The internal standard KCM, calibrated against the international standard NBS-19, was used to place data on the Vienna Peedee belemnite (VPDB) scale, with average

[1]GSA Data Repository item 2018032, further details on site locations and parameters, age model construction, sample preparation and stable isotope analysis, recalibration of pCO_2 estimates, and calculation of Deccan Traps formation volumes, is available online at http://www.geosociety.org/datarepository/2018/ or on request from editing@geosociety.org.

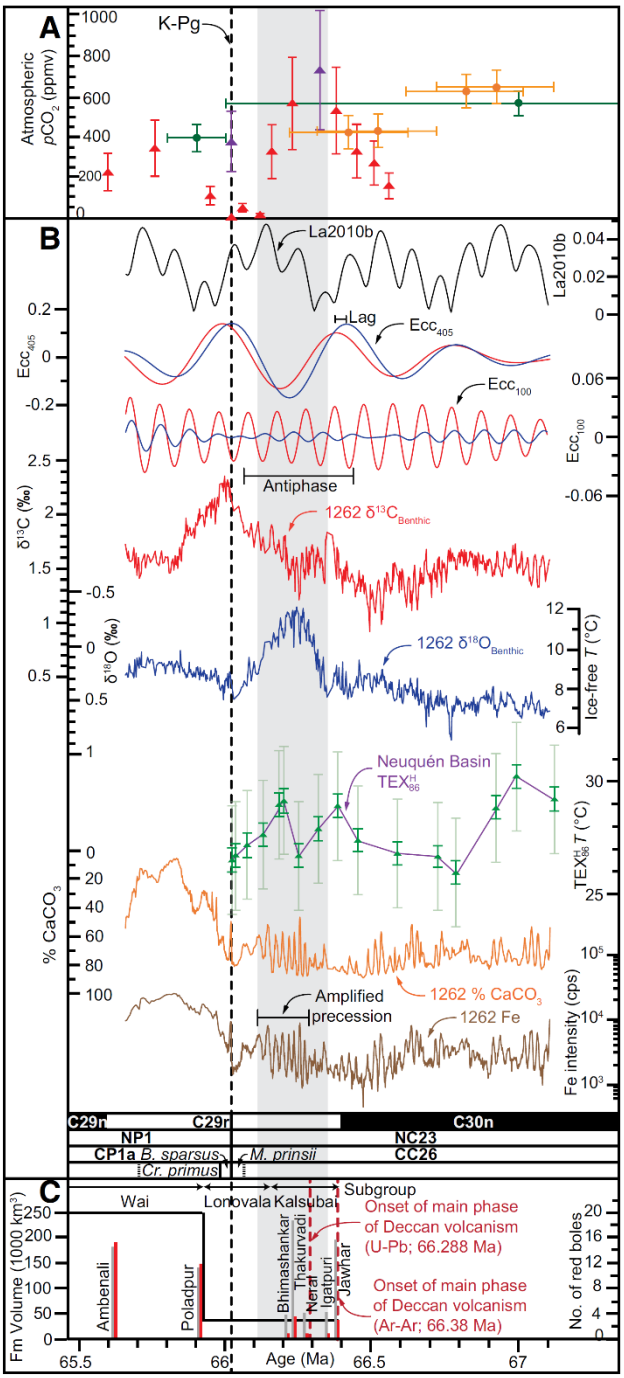

Figure 1. Correlation of environmental proxies to Deccan volcanism and the La2010b orbital solution of Laskar et al. (2011). A: Recalibrated atmospheric pCO_2 estimates based on pedogenic carbonate (purple triangles, raw data from Nordt et al., 2002; red triangles, raw data from Nordt et al., 2003, both recalibrated in this study) and stomatal indices (orange circles, Beerling et al., 2002, recalibrated by Barclay and Wing, 2016; green circles, Steinthorsdottir et al., 2016). K-Pg—Cretaceous-Paleogene boundary. B: New benthic $\delta^{13}C$ and $\delta^{18}O$ data from Ocean Drilling Program Site 1262 and filters at the 405 k.y. and 100 k.y. bands (this study), correlated to the La2010b solution (Laskar et al., 2011), TEX^H_{86} data (Woelders et al., 2017), and Site 1262 Fe and %$CaCO_3$ data (Kroon et al., 2007). Error bars on TEX^H_{86} data represent analytical uncertainty (dark green) and calibration error of absolute temperatures (pale green). Magnetozones are from Bowles (2006) and nannozones are from Shipboard Scientific Party (2004), with high-resolution K-Pg biozones from Bernaola and Monechi (2007). Ecc—eccentricity; *B. sparsus—Biantholithus sparsus*; *M. prinsii—Micula prinsii*; *Cr. primus—Cruciplacolithus primus*. C: Timing of Deccan volcanism, with formation (Fm) volumes calculated by the equal area method (gray), variable area method (red), and red bole distribution illustrated as a black line, using Ar-Ar ages in Renne et al. (2015). U-Pb age data from Schoene et al. (2015) are also shown. Detailed methods are in the Data Repository (see footnote 1).

sample analytical precision (1σ) of 0.03‰ for $\delta^{13}C$ and 0.05‰ for $\delta^{18}O$. The complete benthic stable isotope data set is available online in the PANGAEA database (https://doi.pangaea.de/10.1594/PANGAEA.881019). Bottom-water temperatures were calculated from $\delta^{18}O_{benthic}$ data by converting *N. truempyi* data to *Cibicidoides* values, then using Equation 1 of Bemis et al. (1998). Stable isotope data were graphically detrended in KaleidaGraph 4.0 using a 15% running mean, to remove long-term trends, then bandpass filtering was conducted in AnalySeries 2.0 (Paillard et al., 1996) for 405 k.y. eccentricity at 0.002467 ± 0.000700 cycles/k.y. and 100 k.y. eccentricity at 0.010 ± 0.003 cycles/k.y.

RESULTS

The new stable isotope data show that relatively stable and cool temperatures persisted in the deep South Atlantic Ocean from 67.1 to 66.8 Ma, followed by the onset of a longer term gradual warming (1 °C) and decline in $\delta^{13}C_{benthic}$ values from 66.75 to 66.5 Ma (Fig. 1). The late Maastrichtian warming event initiated at ca. 66.34 Ma, ~300 k.y. before the K-Pg boundary, with peak warming of ~+4 °C ($\delta^{18}O_{benthic}$ excursion of ~0.8‰) attained between ca. 66.27 and 66.18 Ma (Fig. 1). A more gradual, step-wise cooling to pre-excursion temperatures then took place over the next 200 k.y., terminating at the K-Pg boundary (Fig. 1). Conversely, the $\delta^{13}C_{benthic}$ record appears to show a muted response compared to the $\delta^{18}O_{benthic}$ record during the warming event, with only a minor negative excursion of ~0.5‰ noted between 66.3 and 66.2 Ma (Fig. 1). The magnitude and character of the excursions in $\delta^{13}C_{benthic}$ and $\delta^{18}O_{benthic}$ data at Site 1262 are similar to those reported in lower resolution data from Deep Sea Drilling Project (DSDP) Site 525 (Li and Keller, 1998; Fig. DR3), located at a shallower paleodepth of 1–1.5 km on Walvis Ridge, suggesting a similar magnitude of warming in deep and intermediate waters of the South Atlantic. Confirming that these characteristics are global, deep Pacific stable isotope data from ODP Site 1209 also show a coeval but somewhat smaller warming pulse, and a muted response in $\delta^{13}C_{benthic}$ values similar to those observed in the Atlantic (Fig. 2; Westerhold et al., 2011). The minor offset of Pacific $\delta^{13}C_{benthic}$ values by as much as –0.4‰ relative to the South Atlantic, suggests that an older water mass was bathing the equatorial Pacific site, consistent with previously reported Paleocene–Eocene trends (Littler et al., 2014; Fig. 2). The onset of the warming event in the Atlantic corresponds to a 405 k.y. eccentricity minimum, with the peak of the event occurring during a 100 k.y. eccentricity maximum but prior to a 405 k.y. eccentricity maximum. The $\delta^{18}O_{benthic}$ leads $\delta^{13}C_{benthic}$ (i.e., climate leads carbon cycle) by ~30–40 k.y. within the 405 k.y. band, consistent with late Paleocene–early Eocene trends recorded further upsection at this site (Littler et al., 2014). It is interesting that the $\delta^{18}O_{benthic}$ and $\delta^{13}C_{benthic}$ data become antiphase at the 100 k.y. frequency during the warming event, but are in phase with carbon lagging oxygen by ~10 k.y. earlier in the Maastrichtian and by ~5 k.y. during the earliest Danian (Fig. 1).

DISCUSSION

The new high-resolution benthic stable isotope data placed onto our updated orbitally tuned age model demonstrates that the late

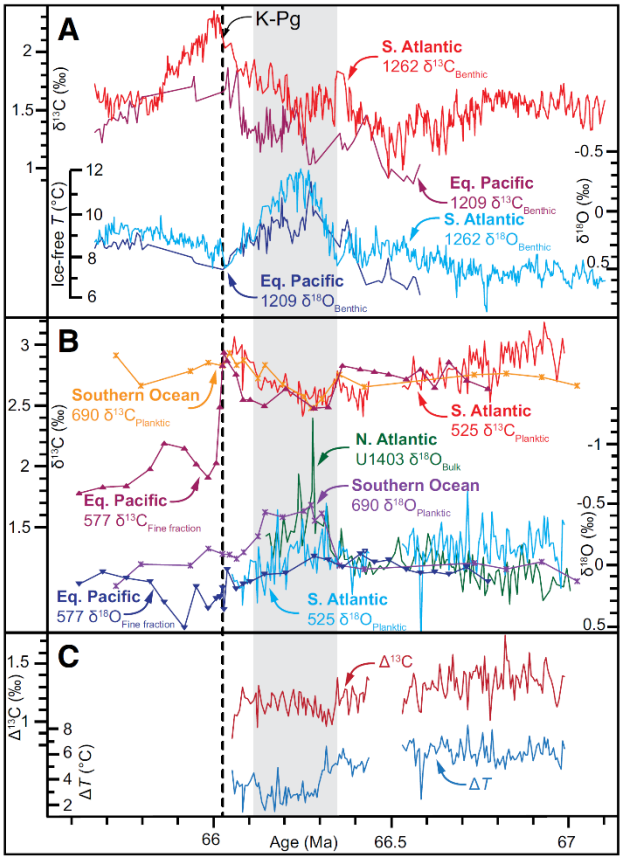

Figure 2. Stable isotope data across the late Maastrichtian event. A: Benthic $\delta^{13}C$ and $\delta^{18}O$ data for Ocean Drilling Program (ODP) Site 1262 (this study) plotted against benthic data from Site 1209 (equatorial Pacific; Westerhold et al., 2011) for comparison. *T*—temperature; S—South; K-Pg—Cretaceous-Paleogene boundary. B: Planktic $\delta^{13}C$ and $\delta^{18}O$ data from Deep Sea Drilling Project (DSDP) Site 577, equatorial (Eq.) Pacific (Zachos et al., 1985), DSDP Site 525, South Atlantic (Li and Keller, 1998), and ODP Site 690, Southern Ocean (Stott and Kennett, 1990). N.—North. Planktic and bulk $\delta^{18}O$ data have been normalized to a baseline of 0‰ for pre-event conditions to compare the magnitude of the warming event by latitude. C: Shallow to deep $\delta^{13}C$ and temperature gradients at Site 525 (Li and Keller, 1998).

Maastrichtian warming event closely coincides with the onset of the main phase of Deccan volcanism, regardless of radiogenic dating technique used, strongly suggesting a causal link (Fig. 1). Furthermore, both the relatively long duration of the warming event and the initiation of the warming during a minimum in the 405 k.y. eccentricity cycle suggest that a control by orbital forcing alone is unlikely, and that Deccan volcanogenic CO_2 emissions were likely to be the primary climate driver over 100 k.y. time scales. Based on the distribution of red boles (weathering horizons) within the Deccan basalts, volcanism of the pre-K-Pg Kalsubai subgroup was characterized by more frequent eruptions of a smaller magnitude, likely leading to a larger cumulative atmospheric pCO_2 increase than post-K-Pg eruptions (Renne et al., 2015; Schoene et al., 2015). By contrast, Danian eruptions had longer hiatuses between large eruptive events, allowing for partial CO_2 sequestration by silicate weathering or organic burial.

Despite strong evidence for climatic warming and some evidence for elevated atmospheric pCO_2 (Barclay and Wing, 2016; Nordt et al., 2002, 2003; Fig. 1), characteristic of many hyperthermals of the early Paleogene such as the Paleocene Eocene Thermal Maximum (e.g., McInerney and Wing, 2011), the C isotope records and lack of evidence for significant ocean acidification at Site 1262 (e.g., reduction in $\%CaCO_3$ or increase in Fe concentration) suggest a relatively minor carbon cycle perturbation (Figs. 1 and 2). Given the comparatively heavy $\delta^{13}C$ signature (–7‰) of volcanogenic CO_2, voluminous Deccan emissions may not have created a major perturbation to the isotope composition of the global $\delta^{13}C$ pool. The absence of a major negative carbon cycle perturbation suggests that sources of isotopically light carbon (e.g., biogenic methane or the oxidation of organic matter), were not destabilized and released in significant quantities during the event. This differential response between the $\delta^{18}O_{benthic}$ and $\delta^{13}C_{benthic}$ records, and the lack of evidence for significant global deep-ocean acidification (Fig. 1), may be due to rates of volcanogenic CO_2 emission and consequent background to peak warming, which occurred rather slowly over ~70–80 k.y. during the late Maastrichtian event, but was much more rapid, ~10–20 k.y., during Paleogene hyperthermals (e.g., McInerney and Wing, 2011; Zeebe et al., 2017). However, evidence for enhanced deep-sea dissolution during this event has been described from the high latitudes in $\%CaCO_3$ records from ODP Site 690 (Henehan et al., 2016) and in orbitally tuned Fe intensity and magnetic susceptibility data from Integrated Ocean Drilling Program Site U1403 on the Newfoundland margin (Batenburg et al., 2017). These deep-sea sites may have been particularly sensitive to smaller carbon cycle perturbations during this time, with Site 690 located in the principle region of deep-water formation in the Southern Ocean and with Site U1403, at a paleodepth of ~4 km, being more sensitive to smaller fluctuations in the Maastrichtian calcite compensation depth than the shallower Site 1262 (Henehan et al., 2016). It is clear that more high-resolution pCO_2 proxy studies are urgently required to more confidently assess Deccan-induced perturbations to the global carbon cycle. The lag between the climate and carbon cycle response within the 405 k.y. band (Fig. 1), as seen throughout the Paleocene–Eocene (Littler et al., 2014), may suggest that small quantities of light carbon were released as a positive feedback to orbitally driven warming. The observed antiphase behavior between $\delta^{13}C$ and $\delta^{18}O$ within the 100 k.y. band during the warming event, but not before or after (Fig. 1), may result from the pulsed release of small amounts of isotopically light carbon superimposed on the longer (300 k.y.) scale warming imparted by the Deccan eruptions. In addition, amplified precession-scale (~21 k.y.) variability visible in the dissolution proxies (Fe and $\%CaCO_3$) and $\delta^{13}C$ records during the event, also suggest increased carbon cycle sensitivity, perhaps due to generally elevated CO_2 levels from Deccan activity (Fig. 1).

The limited available planktic stable isotope data (e.g., ODP Site 690) suggest that significant warming, ~2.5 °C, occurred in the southern high latitudes during the event (Fig. 2; Stott and Kennett, 1990). Organic paleothermometer TEX^H_{86} data from the Neuquén Basin, Argentina, also suggest significant warming of surface waters of ~3 °C in continental shelf settings at mid-latitudes (Fig. 1; Woelders et al., 2017). A negative bulk $\delta^{18}O$ excursion of 1‰ has also been resolved from the Newfoundland margin, suggesting that a pronounced surface-water warming also occurred in the mid-northern latitudes during this time, although bulk $\delta^{18}O$ values cannot reliably be converted into absolute surface-water temperatures (Batenburg et al., 2017). By contrast, there appears to have been very little change in surface-water temperatures at lower latitudes, although this interpretation is tentative based on the availability of only one fine fraction data set from DSDP Site 577 (Fig. 2). A much more significant bottom-water warming at mid-low latitudes created a dramatic reduction in the surface to deep temperature gradient and reduced thermal stratification of the water column (Li and Keller, 1998; Fig. 2). Taken together, these data suggest a possible polar amplification of surface-water warming during the late Maastrichtian warming event; however, more single species planktic isotope records over greater latitudinal coverage are required to fully evaluate latitudinal variations in surface temperature during this event.

CONCLUSIONS

Our revised chronology for the late Maastrichtian warming event, combined with the latest radiogenic dates for Deccan volcanism, point to the synchronous onset of the main phase of Deccan volcanism with the late Maastrichtian warming event ~300 k.y. before the K-Pg boundary. The onset of the warming is unlikely to have been orbitally controlled, further supporting volcanic CO_2 as the trigger. Increased carbon cycle sensitivity to orbital precession is evident during the greenhouse event, suggesting system sensitivity to background temperature conditions. Now that the environmental effects of Deccan volcanism have been more confidently established, future work should focus on evaluating the role of these precursor climatic changes in the K-Pg mass extinction.

ACKNOWLEDGMENTS

The new Ocean Drilling Program Site 1262 $\delta^{13}C$ and $\delta^{18}O$ data were funded by the Natural Environment Research Council Isotope Geosciences Facility at the British Geological Survey (IP-1581–1115); we also thank Hilary Sloane for technical support. We thank the Bremen Core Repository for allowing us to collect the required samples, Gerta Keller for providing the raw stable isotope data from Deep Sea Drilling Project Site 525, and Steve Dworkin for providing the raw pedogenic carbonate data from Texas. Financial support for this research was provided by the Deutsche Forschungsgemeinschaft (DFG) to Ursula Röhl and Thomas Westerhold. We thank Pincelli Hull, Gerta Keller, and an anonymous reviewer for their insightful and constructive reviews, which helped to improve the manuscript.

REFERENCES CITED

Barclay, R.S., and Wing, S.L., 2016, Improving the Ginkgo CO_2 barometer: Implications for the early Cenozoic atmosphere: Earth and Planetary Science Letters, v. 439, p. 158–171, https://doi.org/10.1016/j.epsl.2016.01.012.

Batenburg, S.J., et al., 2017, Late Maastrichtian carbon isotope stratigraphy and cyclostratigraphy of the Newfoundland Margin (Site U1403, IODP Leg 342): Newsletters on Stratigraphy, https://doi.org/10.1127/nos/2017/0398.

Beerling, D.J., Lomax, B.H., Royer, D.L., Upchurch, G.R., and Kump, L.R., 2002, An atmospheric pCO_2 reconstruction across the Cretaceous-Tertiary boundary from leaf megafossils: Proceedings of the National Academy of Sciences of the United States of America, v. 99, p. 7836–7840, https://doi.org/10.1073/pnas.122573099.

Bemis, B.E., Spero, H.J., Bijma, J., and Lea, D.W., 1998, Reevaluation of the oxygen isotopic composition of planktonic foraminifera: Experimental results and revised paleotemperature equations: Paleoceanography, v. 13, p. 150–160, https://doi.org/10.1029/98PA00070.

Bernaola, G., and Monechi, S., 2007, Calcareous nannofossil extinction and survivorship across the Cretaceous-Paleogene boundary at Walvis Ridge (ODP Hole 1262C, South Atlantic Ocean): Palaeogeography, Palaeoclimatology, Palaeoecology, v. 255, p. 132–156, https://doi.org/10.1016/j.palaeo.2007.02.045.

Bowles, J., 2006, Data report: Revised magnetostratigraphy and magnetic mineralogy of sediments from Walvis Ridge, Leg 208, *in* Kroon, D., et al., eds., Proceedings of the Ocean Drilling Program, Scientific results, Volume 208: College Station, Texas, Ocean Drilling Program, p. 1–24, https://doi.org/10.2973/odp.proc.sr.208.206.2006.

Chenet, A.L., Quidelleur, X., Fluteau, F., Courtillot, V., and Bajpai, S., 2007, ^{40}K-^{40}Ar dating of the Main Deccan large igneous province: Further evidence of KTB age and short duration: Earth and Planetary Science Letters, v. 263, p. 1–15, https://doi.org/10.1016/j.epsl.2007.07.011.

Dinarès-Turell, J., Westerhold, T., Pujalte, V., Röhl, U., and Kroon, D., 2014, Astronomical calibration of the Danian stage (early Paleocene) revisited: Settling chronologies of sedimentary records across the Atlantic and Pacific Oceans: Earth and Planetary Science Letters, v. 405, p. 119–131, https://doi.org/10.1016/j.epsl.2014.08.027.

Henehan, M.J., Hull, P.M., Penman, D.E., Rae, J.W.B., and Schmidt, D.N., 2016, Biogeochemical significance of pelagic ecosystem function: An end-Cretaceous case study: Royal Society of London Philosophical Transactions, ser. B, v. 371, p. 1–10, https://doi.org/10.1098/rstb.2015.0510.

Keller, G., Punekar, J., and Mateo, P., 2016, Upheavals during the late Maastrichtian: Volcanism, climate and faunal events preceding the end-Cretaceous mass extinction: Palaeogeography, Palaeoclimatology, Palaeoecology, v. 441, p. 137–151, https://doi.org/10.1016/j.palaeo.2015.06.034.

Kroon, D., and Zachos, J.C., and Leg 208 Scientific Party, 2007, Leg 208 Synthesis: Cenozoic climate cycles and excursions, *in* Kroon, D., et al., eds., Proceedings of the Ocean Drilling Program, Scientific results, Volume 208: College Station, Texas, p. 1–55, https://doi.org/10.2973/odp.proc.sr.208.201.2007.

Laskar, J., Fienga, A., Gastineau, M., and Manche, H., 2011, La2010: A new orbital solution for the long-term motion: Astronomy & Astrophysics, v. 532, p. 1–15, https://doi.org/10.1051/0004-6361/201116836.

Li, L., and Keller, G., 1998, Abrupt deep-sea warming at the end of the Cretaceous: Geology, v. 26, p. 995–998, https://doi.org/10.1130/0091-7613(1998)026<0995:ADSWAT>2.3.CO;2.

Littler, K., Röhl, U., Westerhold, T., and Zachos, J.C., 2014, A high-resolution benthic stable-isotope record for the South Atlantic: Implications for orbital-scale changes in late Paleocene–early Eocene climate and carbon cycling: Earth and Planetary Science Letters, v. 401, p. 18–30, https://doi.org/10.1016/j.epsl.2014.05.054.

McInerney, F.A., and Wing, S.L., 2011, The Paleocene-Eocene Thermal Maximum: A perturbation of carbon cycle, climate, and biosphere with implications for the future: Annual Review of Earth and Planetary Sciences, v. 39, p. 489–516, https://doi.org/10.1146/annurev-earth-040610-133431.

Nordt, L., Atchley, S., and Dworkin, S.I., 2002, Paleosol barometer indicates extreme fluctuations in atmospheric CO_2 across the Cretaceous-Tertiary boundary: Geology, v. 30, p. 703–706, https://doi.org/10.1130/0091-7613(2002)030<0703:PBIEFI>2.0.CO;2.

Nordt, L., Atchley, S., and Dworkin, S., 2003, Terrestrial evidence for two greenhouse events in the latest Cretaceous: GSA Today, v. 13, p. 4–9, https://doi.org/10.1130/1052-5173(2003)013<4:TEFTGE>2.0.CO;2.

Paillard, D., Labeyrie, L., and Yiou, P., 1996, Macintosh program performs time-series analysis: EOS (Transactions, American Geophysical Union) v. 77, p. 379, https://doi.org/10.1029/96EO00259.

Renne, P.R., Sprain, C.J., Richards, M.A., Self, S., Vanderkluysen, L., and Pande, K., 2015, State shift in Deccan volcanism at the Cretaceous-Paleogene boundary, possibly induced by impact: Science, v. 350, p. 76–78, https://doi.org/10.1126/science.aac7549.

Schoene, B., Samperton, K.M., Eddy, M.P., Keller, G., Adatte, T., Bowring, S.A., Khadri, S.F.R., and Gertsch, B., 2015, U-Pb geochronology of the Deccan Traps and relation to the end-Cretaceous mass extinction: Science, v. 347, p. 182–184, https://doi.org/10.1126/science.aaa0118.

Shipboard Scientific Party, 2004, Site 1262, *in* Zachos, J.C., et al., Proceedings of the Ocean Drilling Program, Initial reports, Volume 208: College Station, Texas, Ocean Drilling Program, p. 1–92, https://doi.org/10.2973/odp.proc.ir.208.103.2004.

Steinthorsdottir, M., Vajda, V., and Pole, M., 2016, Global trends of pCO_2 across the Cretaceous-Paleogene boundary supported by the first Southern Hemisphere stomatal proxy-based pCO_2 reconstruction: Palaeogeography, Palaeoclimatology, Palaeoecology, v. 464, p. 143–152, https://doi.org/10.1016/j.palaeo.2016.04.033.

Stott, L.D., and Kennett, J.P., 1990, The paleoceanographic and paleoclimatic signature of the Cretaceous/Paleogene boundary in the Antarctic : Stable isotopic results from ODP Leg 113, *in* Barker, P.F., et al., Proceedings of the Ocean Drilling Program, Scientific results, Volume 113: College Station, Texas, Ocean Drilling Program, p. 829–848, https://doi.org/10.2973/odp.proc.sr.113.158.1990.

Westerhold, T., Röhl, U., Donner, B., Mccarren, H.K., and Zachos, J.C., 2011, A complete high-resolution Paleocene benthic stable isotope record for the central Pacific (ODP Site 1209): Paleoceanography, v. 26, p. 1–13, https://doi.org/10.1029/2010PA002092.

Wilf, P., Johnson, K.R., and Huber, B.T., 2003, Correlated terrestrial and marine evidence for global climate changes before mass extinction at the Cretaceous-Paleogene boundary: Proceedings of the National Academy of Sciences of the United States of America, v. 100, p. 599–604, https://doi.org/10.1073/pnas.0234701100.

Woelders, L., et al., 2017, Latest Cretaceous climatic and environmental change in the South Atlantic region: Paleoceanography, v. 32, p. 466–483, https://doi.org/10.1002/2016PA003007.

Zachos, J.C., Arthur, M.A., Thunell, R.C., Williams, D.F., and Tappa, E.J., 1985, Stable isotope and trace element geochemistry of carbonate sediments across the Cretaceous/Tertiary Boundary at Deep Sea Drilling Project Hole 577, Leg 86, *in* Heath, D.R., et al., Initial reports of the Deep Sea Drilling Project, Volume 86: Washington, D.C., U.S. Government Printing Office, p. 513–532, https://doi.org/10.2973/dsdp.proc.86.120.1985.

Zeebe, R.E., Westerhold, T., Littler, K., and Zachos, J.C., 2017, Orbital forcing of the Paleocene and Eocene carbon cycle: Paleoceanography, v. 32, p. 440–465, https://doi.org/10.1002/2016PA003054.

Manuscript received 3 July 2017
Revised manuscript received 13 November 2017
Manuscript accepted 17 November 2017

Printed in USA

Appendix 3. Age model tie points for the updated orbitally-tuned Late Maastrichtian–Early Eocene age model generated for South Atlantic ODP Site 1262 during this study, modified to the La2010b orbital solution (Laskar et al., 2011a) from the original cited literature source. This age model is utilised within ***Chapters 3, 4*** *and* ***5****.*

Depth (mcd)	Age (Ma; La2010b)	Original literature source	Modifications
103.92	52.361	Littler et al. (2014)	Updated to La2010b
104.58	52.461	Littler et al. (2014)	Updated to La2010b
106.50	52.743	Littler et al. (2014)	Updated to La2010b
107.20	52.843	Littler et al. (2014)	Updated to La2010b
107.78	52.967	Littler et al. (2014)	Updated to La2010b
108.36	53.044	Littler et al. (2014)	Updated to La2010b
109.04	53.106	Littler et al. (2014)	Updated to La2010b
109.76	53.276	Littler et al. (2014)	Updated to La2010b
113.43	53.671	Westerhold et al. (2008)	Updated to La2010b
116.12	53.949	Westerhold et al. (2008)	Updated to La2010b
116.53	53.984	Westerhold et al. (2008)	Updated to La2010b
116.78	54.012	Westerhold et al. (2008)	Updated to La2010b
117.03	54.039	Westerhold et al. (2008)	Updated to La2010b
117.18	54.053	Westerhold et al. (2008)	Updated to La2010b
118.86	54.184	Westerhold et al. (2008)	Updated to La2010b
119.46	54.233	Westerhold et al. (2008)	Updated to La2010b
120.39	54.302	Westerhold et al. (2008)	Updated to La2010b
121.59	54.449	Westerhold et al. (2008)	Updated to La2010b
125.91	54.759	Westerhold et al. (2008)	Updated to La2010b
127.43	54.871	Westerhold et al. (2008)	Updated to La2010b
128.68	54.970	Westerhold et al. (2008)	Updated to La2010b
130.41	55.113	Westerhold et al. (2008)	Updated to La2010b
131.16	55.178	Westerhold et al. (2008)	Updated to La2010b
132.34	55.269	Westerhold et al. (2008)	Updated to La2010b
133.54	55.356	Westerhold et al. (2008)	Updated to La2010b
134.84	55.459	Westerhold et al. (2008)	Updated to La2010b
136.09	55.549	Westerhold et al. (2008)	Updated to La2010b
137.27	55.647	Westerhold et al. (2008)	Updated to La2010b
138.39	55.714	Westerhold et al. (2008)	Updated to La2010b
139.18	55.779	Westerhold et al. (2008)	Updated to La2010b
140.14	55.930	Onset of the PETM (Westerhold et al., 2007)	Updated to La2010b
140.84	56.039	Westerhold et al. (2008)	Updated to La2010b
141.92	56.142	Westerhold et al. (2008)	Updated to La2010b
144.60	56.375	Westerhold et al. (2008)	Updated to La2010b
145.99	56.477	Westerhold et al. (2008)	Updated to La2010b
146.87	56.582	Westerhold et al. (2008)	Updated to La2010b
149.37	56.751	Westerhold et al. (2008)	Updated to La2010b
150.54	56.856	Westerhold et al. (2008)	Updated to La2010b
151.89	56.960	Westerhold et al. (2008)	Updated to La2010b
154.01	57.136	Westerhold et al. (2008)	Updated to La2010b

155.59	57.236	Westerhold et al. (2008)	Updated to La2010b
157.09	57.350	Westerhold et al. (2008)	Updated to La2010b
158.66	57.520	Westerhold et al. (2008)	Updated to La2010b
159.79	57.620	Westerhold et al. (2008)	Updated to La2010b
160.96	57.724	Westerhold et al. (2008)	Updated to La2010b
164.46	58.003	Westerhold et al. (2008)	Updated to La2010b
168.60	58.474	Westerhold et al. (2008)	Updated to La2010b
169.53	58.581	Westerhold et al. (2008)	Updated to La2010b
170.70	58.750	Westerhold et al. (2008)	Updated to La2010b
171.47	58.854	Westerhold et al. (2008)	Updated to La2010b
171.95	58.958	Westerhold et al. (2008)	Updated to La2010b
173.03	59.139	Westerhold et al. (2008)	Updated to La2010b
173.51	59.238	Westerhold et al. (2008)	Updated to La2010b
175.25	59.619	Westerhold et al. (2008)	Updated to La2010b
176.06	59.725	Westerhold et al. (2008)	Updated to La2010b
177.77	60.007	Westerhold et al. (2008)	Updated to La2010b
178.34	60.106	Westerhold et al. (2008)	Updated to La2010b
179.99	60.293	Westerhold et al. (2008)	Updated to La2010b
180.78	60.380	Westerhold et al. (2008)	Updated to La2010b
181.68	60.478	Westerhold et al. (2008)	Updated to La2010b
184.44	60.855	Westerhold et al. (2008)	Updated to La2010b
185.47	60.960	Westerhold et al. (2008)	Updated to La2010b
187.92	61.243	Westerhold et al. (2008)	Updated to La2010b
188.64	61.346	Westerhold et al. (2008)	Updated to La2010b
191.26	61.620	Dinarès-Turell et al. (2014)	Updated to La2010b
192.04	61.722	Dinarès-Turell et al. (2014)	Updated to La2010b
194.44	62.005	Dinarès-Turell et al. (2014)	Updated to La2010b
195.31	62.107	Dinarès-Turell et al. (2014)	Updated to La2010b
196.77	62.301	Dinarès-Turell et al. (2014)	Updated to La2010b
198.96	62.586	Dinarès-Turell et al. (2014)	Updated to La2010b
200.73	62.851	Dinarès-Turell et al. (2014)	Updated to La2010b
201.57	62.957	Dinarès-Turell et al. (2014)	Updated to La2010b
203.22	63.240	Dinarès-Turell et al. (2014)	Updated to La2010b
203.73	63.348	Dinarès-Turell et al. (2014)	Updated to La2010b
205.38	63.720	Dinarès-Turell et al. (2014)	Updated to La2010b
206.70	64.003	Dinarès-Turell et al. (2014)	Updated to La2010b
207.18	64.103	Dinarès-Turell et al. (2014)	Updated to La2010b
208.20	64.307	Dinarès-Turell et al. (2014)	Updated to La2010b
208.83	64.411	Dinarès-Turell et al. (2014)	Updated to La2010b
210.81	64.834	Dinarès-Turell et al. (2014)	Updated to La2010b
211.36	64.942	Dinarès-Turell et al. (2014)	Updated to La2010b
211.77	65.035	Dinarès-Turell et al. (2014)	Updated to La2010b
212.39	65.132	Dinarès-Turell et al. (2014)	Updated to La2010b
213.05	65.225	Dinarès-Turell et al. (2014)	Updated to La2010b
213.31	65.329	Dinarès-Turell et al. (2014)	Updated to La2010b
213.91	65.434	Dinarès-Turell et al. (2014)	Updated to La2010b

214.37	65.527	Dinarès-Turell et al. (2014)	Updated to La2010b
214.79	65.611	Dinarès-Turell et al. (2014)	Updated to La2010b
215.21	65.721	Dinarès-Turell et al. (2014)	Updated to La2010b
215.46	65.828	Dinarès-Turell et al. (2014)	Updated to La2010b
215.93	65.930	Dinarès-Turell et al. (2014)	Updated to La2010b
216.28	65.994	Dinarès-Turell et al. (2014)	Updated to La2010b
216.71	66.0225	K/Pg boundary (Dinarès-Turell et al., 2014)	Updated to La2010b
218.26	66.142	Dinarès-Turell et al. (2014)	Updated to La2010b
220.69	66.253	Dinarès-Turell et al. (2014)	Updated to La2010b
223.03	66.338	Westerhold et al. (2008)	Updated to La2010b
226.68	66.530	Westerhold et al. (2008)	Updated to La2010b
228.76	66.635	Westerhold et al. (2008)	Updated to La2010b
230.86	66.734	Westerhold et al. (2008)	Updated to La2010b
233.74	66.935	Westerhold et al. (2008)	Updated to La2010b
235.20	67.040	Westerhold et al. (2008)	Updated to La2010b

*Appendix 4. Raw Late Maastrichtian–Middle Paleocene benthic foraminiferal stable carbon isotope ($\delta^{13}C_{benthic}$) and benthic foraminiferal stable oxygen isotope ($\delta^{18}O_{benthic}$) data based on analysis of Nuttallides truempyi from South Atlantic Walvis Ridge ODP Site 1262. These data were generated on an Isoprime 100 Gas Source Isotope Ratio Mass Spectrometer in dual inlet model equipped with a Multiprep device at the NERC Isotope Geosciences Facility, with long-term analytical error of 0.03 ‰ for $\delta^{13}C$ and 0.05 ‰ for $\delta^{18}O$ (1σ). These data form the basis of **Chapters 3**, **4**, and **5**. Ages (in Ma) are based on the updated orbitally-tuned age model generated during this study. Also shown are the converted $\delta^{18}O_{benthic}$ data to Cibicidoides values ($\delta^{18}O_{benthic(cib)}$) and the temperatures calculated from $\delta^{18}O_{benthic(cib)}$ using the calibration of Kim & O'Neil (1997) modified by Bemis et al. (1998; Equation 1), assuming $\delta^{18}O_{sw}$ = –1.27 ‰ VSMOW.*

Site_Hole_Core_Type_Section_ Top Depth (cm)_Bottom Depth (cm)_Top Depth (mbsf)	Depth (mcd)	Age (Ma)	$\delta^{13}C_{benthic}$ (‰ VPDB)	$\delta^{18}O_{benthic}$ (‰ VPDB)	$\delta^{18}O_{benthic(cib)}$	Temperature (°C)
1262_B_19_H_5_56_57_168.96	185.05	60.9177	1.52	0.31	0.46	8.33
1262_B_19_H_5_68_69_169.08	185.18	60.9299	1.52	0.25	0.39	8.65
1262_B_19_H_5_71_72_169.11	185.21	60.9330	1.50	0.38	0.54	8.00
1262_B_19_H_5_77_78_169.17	185.27	60.9391	1.50	0.37	0.53	8.04
1262_B_19_H_5_80_81_169.2	185.30	60.9422	1.59	0.44	0.61	7.71
1262_B_19_H_5_83_84_169.23	185.33	60.9452	1.51	0.50	0.67	7.44
1262_B_19_H_5_89_90_169.29	185.38	60.9513	1.41	0.38	0.54	7.98
1262_B_19_H_5_92_93_169.32	185.41	60.9544	1.59	0.37	0.52	8.06
1262_B_19_H_5_98_99_169.38	185.48	60.9606	1.52	0.44	0.61	7.71
1262_C_10_H_2_110_111_170.6	185.52	60.9664	1.67	0.44	0.61	7.70
1262_C_10_H_2_113_114_170.63	185.55	60.9698	1.60	0.46	0.63	7.59
1262_C_10_H_2_116_117_170.66	185.59	60.9733	1.51	0.33	0.49	8.23
1262_C_10_H_2_122_123_170.72	185.65	60.9802	1.57	0.27	0.41	8.56
1262_C_10_H_2_128_129_170.78	185.71	60.9871	1.60	0.34	0.49	8.22
1262_C_10_H_2_134_135_170.84	185.77	60.9941	1.69	0.42	0.59	7.79
1262_C_10_H_2_137_138_170.87	185.80	60.9975	1.66	0.53	0.71	7.27
1262_C_10_H_2_140_141_170.9	185.83	61.0010	1.69	0.56	0.74	7.12
1262_C_10_H_2_143_144_170.93	185.86	61.0045	1.72	0.54	0.72	7.23
1262_C_10_H_2_146_147_170.96	185.88	61.0079	1.68	0.61	0.80	6.88
1262_C_10_H_2_149_150_170.99	185.91	61.0114	1.61	0.46	0.63	7.60
1262_C_10_H_3_2_3_171.02	185.95	61.0149	1.56	0.42	0.59	7.79
1262_C_10_H_3_5_6_171.05	185.98	61.0183	1.62	0.46	0.63	7.61
1262_C_10_H_3_8_9_171.08	186.01	61.0218	1.61	0.58	0.77	7.03
1262_C_10_H_3_11_12_171.11	186.04	61.0253	1.54	0.52	0.69	7.34
1262_C_10_H_3_14_15_171.14	186.07	61.0287	1.60	0.54	0.71	7.24
1262_C_10_H_3_18_19_171.18	186.11	61.0333	1.48	0.33	0.48	8.25
1262_C_10_H_3_20_21_171.2	186.13	61.0357	1.58	0.25	0.40	8.61
1262_C_10_H_3_32_33_171.32	186.25	61.0495	1.46	0.33	0.49	8.23
1262_C_10_H_3_38_39_171.38	186.30	61.0565	1.63	0.48	0.65	7.53
1262_C_10_H_3_41_42_171.41	186.34	61.0599	1.59	0.30	0.45	8.39
1262_C_10_H_3_44_45_171.44	186.37	61.0634	1.58	0.33	0.48	8.26
1262_C_10_H_3_47_48_171.47	186.40	61.0668	1.59	0.29	0.44	8.43
1262_C_10_H_3_50_51_171.5	186.43	61.0703	1.70	0.56	0.74	7.15
1262_C_10_H_3_54_55_171.54	186.47	61.0749	1.61	0.60	0.78	6.95
1262_C_10_H_3_56_57_171.56	186.49	61.0772	1.57	0.34	0.50	8.19
1262_C_10_H_3_59_60_171.59	186.52	61.0807	1.64	0.43	0.59	7.77
1262_C_10_H_3_62_63_171.62	186.55	61.0842	1.60	0.42	0.59	7.78
1262_C_10_H_3_65_66_171.65	186.58	61.0876	1.69	0.51	0.68	7.37
1262_C_10_H_3_68_69_171.68	186.61	61.0911	1.70	0.55	0.73	7.19
1262_C_10_H_3_74_75_171.74	186.66	61.0980	1.57	0.48	0.66	7.49

1262_C_10_H_3_77_78_171.77	186.70	61.1015	1.62	0.59	0.78	6.98
1262_C_10_H_3_80_81_171.8	186.73	61.1050	1.37	0.34	0.49	8.20
1262_C_10_H_3_83_84_171.83	186.76	61.1084	1.54	0.49	0.66	7.47
1262_C_10_H_3_89_90_171.89	186.82	61.1154	1.40	0.33	0.48	8.26
1262_C_10_H_3_92_93_171.92	186.85	61.1188	1.54	0.56	0.74	7.12
1262_C_10_H_3_95_96_171.95	186.88	61.1223	1.45	0.57	0.75	7.10
1262_C_10_H_3_98_99_171.98	186.91	61.1258	1.44	0.41	0.58	7.84
1262_C_10_H_3_101_102_172.01	186.94	61.1292	1.36	0.47	0.64	7.57
1262_C_10_H_3_107_108_172.07	187.00	61.1362	1.41	0.42	0.58	7.81
1262_C_10_H_3_110_111_172.1	187.02	61.1396	1.32	0.27	0.41	8.54
1262_C_10_H_3_113_114_172.13	187.05	61.1431	1.33	0.38	0.54	7.99
1262_C_10_H_3_116_117_172.16	187.09	61.1465	1.31	0.40	0.56	7.90
1262_C_10_H_3_122_123_172.22	187.15	61.1535	1.32	0.44	0.61	7.71
1262_C_10_H_3_125_126_172.25	187.18	61.1569	1.24	0.34	0.49	8.21
1262_C_10_H_3_128_129_172.28	187.21	61.1604	1.30	0.37	0.52	8.07
1262_C_10_H_3_134_135_172.34	187.27	61.1673	1.11	0.20	0.34	8.86
1262_C_10_H_3_143_144_172.43	187.36	61.1777	1.11	0.38	0.54	7.98
1262_C_10_H_3_146_147_172.46	187.38	61.1812	1.11	0.38	0.54	7.99
1262_C_10_H_3_149_150_172.49	187.41	61.1847	1.12	0.31	0.47	8.32
1262_C_10_H_4_2_3_172.52	187.45	61.1881	1.15	0.36	0.52	8.08
1262_C_10_H_4_5_6_172.55	187.48	61.1916	1.22	0.40	0.56	7.90
1262_C_10_H_4_8_9_172.58	187.51	61.1951	1.26	0.46	0.63	7.59
1262_C_10_H_4_11_12_172.61	187.54	61.1985	1.04	0.50	0.68	7.41
1262_C_10_H_4_14_15_172.64	187.57	61.2020	1.15	0.39	0.55	7.94
1262_C_10_H_4_17_18_172.67	187.60	61.2055	1.10	0.33	0.48	8.24
1262_C_10_H_4_20_21_172.7	187.63	61.2089	1.13	0.37	0.52	8.07
1262_C_10_H_4_23_24_172.73	187.66	61.2124	1.25	0.41	0.58	7.84
1262_C_10_H_4_26_27_172.76	187.69	61.2159	1.16	0.38	0.54	8.00
1262_C_10_H_4_29_30_172.79	187.72	61.2193	1.05	0.33	0.48	8.24
1262_C_10_H_4_32_33_172.82	187.75	61.2228	1.13	0.30	0.45	8.39
1262_C_10_H_4_35_36_172.85	187.77	61.2263	1.10	0.39	0.55	7.94
1262_C_10_H_4_38_39_172.88	187.80	61.2297	1.08	0.27	0.42	8.53
1262_C_10_H_4_47_48_172.97	187.90	61.2401	0.88	0.28	0.42	8.49
1262_C_10_H_4_59_60_173.09	188.02	61.2566	0.86	–0.07	0.03	10.22
1262_C_10_H_4_65_66_173.15	188.08	61.2652	0.87	0.01	0.12	9.83
1262_C_10_H_4_74_75_173.24	188.16	61.2780	0.79	–0.15	–0.05	10.59
1262_C_10_H_4_77_78_173.27	188.20	61.2823	1.06	–0.01	0.11	9.89
1262_C_10_H_4_83_84_173.33	188.26	61.2909	0.90	0.14	0.27	9.19
1262_C_10_H_4_86_87_173.36	188.29	61.2952	1.14	0.20	0.33	8.89
1262_C_10_H_4_89_90_173.39	188.32	61.2995	0.88	–0.08	0.02	10.27
1262_C_10_H_4_92_93_173.42	188.35	61.3038	0.88	–0.05	0.06	10.11
1262_C_10_H_4_95_96_173.45	188.38	61.3081	1.00	0.03	0.15	9.69
1262_C_10_H_4_101_102_173.51	188.44	61.3167	0.84	–0.18	–0.09	10.75
1262_C_10_H_4_104_105_173.54	188.47	61.3210	0.91	–0.15	–0.06	10.60
1262_C_10_H_4_110_111_173.6	188.52	61.3295	1.01	–0.07	0.03	10.23
1262_C_10_H_4_113_114_173.63	188.55	61.3338	1.07	0.16	0.29	9.07
1262_C_10_H_4_119_120_173.69	188.62	61.3424	0.92	–0.05	0.05	10.12
1262_C_10_H_4_122_123_173.72	188.65	61.3465	1.10	0.07	0.19	9.52
1262_C_10_H_4_125_126_173.75	188.68	61.3497	0.88	–0.12	–0.02	10.46
1262_C_10_H_4_134_135_173.84	188.77	61.3591	1.04	–0.04	0.07	10.05
1262_C_10_H_4_140_141_173.9	188.83	61.3653	0.83	–0.26	–0.18	11.17
1262_C_10_H_4_149_150_173.99	188.91	61.3748	1.03	0.02	0.13	9.77
1262_C_10_H_5_8_9_174.08	189.01	61.3842	1.19	–0.15	–0.05	10.58
1262_C_10_H_5_11_12_174.11	189.04	61.3873	1.36	0.04	0.16	9.65
1262_C_10_H_5_17_18_174.17	189.10	61.3936	1.14	–0.15	–0.06	10.62
1262_C_10_H_5_20_21_174.2	189.13	61.3967	1.26	0.00	0.11	9.87
1262_C_10_H_5_23_24_174.23	189.16	61.3999	1.25	0.17	0.30	9.03
1262_C_10_H_5_26_27_174.26	189.19	61.4030	1.32	0.29	0.44	8.42
1262_C_10_H_5_29_30_174.29	189.22	61.4061	1.28	0.20	0.34	8.87
1262_C_10_H_5_32_33_174.32	189.25	61.4093	1.46	0.28	0.43	8.47

1262_C_10_H_5_38_39_174.38	189.30	61.4155	1.45	0.33	0.49	8.23
1262_C_10_H_5_41_42_174.41	189.34	61.4187	1.49	0.27	0.41	8.55
1262_C_10_H_5_44_45_174.44	189.37	61.4218	1.46	0.37	0.52	8.07
1262_C_10_H_5_47_48_174.47	189.40	61.4250	1.33	0.20	0.34	8.85
1262_C_10_H_5_50_51_174.5	189.43	61.4281	1.48	0.35	0.51	8.13
1262_C_10_H_5_56_57_174.56	189.49	61.4344	1.41	0.31	0.46	8.32
1262_C_10_H_5_62_63_174.62	189.55	61.4406	1.44	0.37	0.53	8.03
1262_C_10_H_5_65_66_174.65	189.58	61.4438	1.41	0.29	0.43	8.45
1262_C_10_H_5_68_69_174.68	189.61	61.4469	1.41	0.37	0.53	8.03
1262_C_10_H_5_74_75_174.74	189.66	61.4532	1.50	0.33	0.49	8.22
1262_C_10_H_5_80_81_174.8	189.73	61.4595	1.51	0.41	0.57	7.86
1262_C_10_H_5_83_84_174.83	189.76	61.4626	1.44	0.29	0.44	8.44
1262_C_10_H_5_86_87_174.86	189.79	61.4657	1.49	0.28	0.43	8.48
1262_C_10_H_5_89_90_174.89	189.82	61.4689	1.37	0.38	0.54	7.98
1262_C_10_H_5_95_96_174.95	189.88	61.4752	1.32	0.19	0.33	8.92
1262_C_10_H_5_98_99_174.98	189.91	61.4783	1.36	0.29	0.44	8.43
1262_C_10_H_5_101_102_175.01	189.94	61.4814	1.43	0.45	0.61	7.68
1262_C_10_H_5_104_105_175.04	189.97	61.4846	1.28	0.26	0.40	8.61
1262_C_10_H_5_119_120_175.19	190.12	61.5003	1.19	0.26	0.40	8.59
1262_C_10_H_5_122_123_175.22	190.15	61.5034	1.20	0.33	0.48	8.26
1262_C_10_H_5_125_126_175.25	190.18	61.5065	1.28	0.36	0.52	8.10
1262_C_10_H_5_134_135_175.34	190.27	61.5159	1.03	0.24	0.38	8.69
1262_C_10_H_5_137_138_175.37	190.30	61.5191	1.06	0.27	0.41	8.55
1262_C_10_H_5_144_145_175.44	190.37	61.5264	1.03	0.16	0.30	9.05
1262_C_10_H_5_149_150_175.49	190.41	61.5316	1.21	0.44	0.61	7.70
1262_C_10_H_6_11_12_175.61	190.54	61.5442	1.45	0.54	0.71	7.25
1262_C_10_H_6_16_17_175.66	190.59	61.5494	1.40	0.50	0.67	7.43
1262_C_10_H_6_17_18_175.67	190.60	61.5505	1.47	0.52	0.70	7.32
1262_C_10_H_6_20_21_175.7	190.63	61.5536	1.37	0.40	0.57	7.89
1262_C_10_H_6_23_24_175.73	190.66	61.5567	1.46	0.49	0.66	7.46
1262_C_10_H_6_29_30_175.79	190.72	61.5630	1.32	0.45	0.62	7.67
1262_C_10_H_6_32_33_175.82	190.75	61.5661	1.31	0.41	0.57	7.86
1262_C_10_H_6_35_36_175.85	190.77	61.5693	1.28	0.29	0.44	8.42
1262_C_10_H_6_38_39_175.88	190.80	61.5724	1.40	0.42	0.59	7.80
1262_C_10_H_6_41_42_175.91	190.84	61.5756	1.28	0.47	0.64	7.56
1262_C_10_H_6_44_45_175.94	190.87	61.5787	1.24	0.22	0.36	8.79
1262_C_10_H_6_47_48_175.97	190.90	61.5818	1.26	0.24	0.38	8.69
1262_C_10_H_6_50_51_176	190.93	61.5850	1.25	0.37	0.53	8.03
1262_C_10_H_6_53_54_176.03	190.96	61.5881	1.24	0.36	0.52	8.08
1262_C_10_H_6_56_57_176.06	190.99	61.5912	1.18	0.44	0.61	7.71
1262_C_10_H_6_59_60_176.09	191.02	61.5944	1.14	0.30	0.45	8.39
1262_C_10_H_6_68_69_176.18	191.11	61.6038	1.25	0.30	0.45	8.39
1262_B_20_H_2_50_51_173.9	191.24	61.6174	1.11	0.23	0.37	8.71
1262_B_20_H_2_56_57_173.96	191.30	61.6246	1.12	0.26	0.40	8.59
1262_B_20_H_2_68_69_174.08	191.41	61.6403	1.09	0.19	0.33	8.90
1262_B_20_H_2_71_72_174.11	191.45	61.6442	1.21	0.26	0.41	8.56
1262_B_20_H_2_74_75_174.14	191.48	61.6481	1.13	0.19	0.32	8.94
1262_B_20_H_2_77_78_174.17	191.51	61.6520	1.17	0.25	0.40	8.62
1262_B_20_H_2_81_82_174.21	191.55	61.6573	1.11	0.39	0.55	7.94
1262_B_20_H_2_87_88_174.27	191.61	61.6651	1.19	0.34	0.49	8.21
1262_B_20_H_2_90_91_174.3	191.63	61.6690	1.27	0.39	0.55	7.94
1262_B_20_H_2_93_94_174.33	191.66	61.6730	1.20	0.38	0.54	8.00
1262_B_20_H_2_96_97_174.36	191.70	61.6769	1.17	0.36	0.52	8.08
1262_B_20_H_2_99_100_174.39	191.73	61.6808	1.16	0.34	0.50	8.18
1262_B_20_H_2_102_103_174.42	191.76	61.6847	1.10	0.33	0.48	8.25
1262_B_20_H_2_108_109_174.48	191.82	61.6926	1.04	0.29	0.43	8.46
1262_B_20_H_2_111_112_174.51	191.85	61.6965	1.05	0.12	0.25	9.26
1262_B_20_H_2_113_114_174.53	191.87	61.6991	0.97	0.23	0.37	8.75
1262_B_20_H_2_116_117_174.56	191.90	61.7030	1.01	0.25	0.39	8.62
1262_B_20_H_2_119_120_174.59	191.93	61.7070	1.06	0.26	0.41	8.57

1262_B_20_H_2_123_124_174.63	191.97	61.7122	0.97	0.20	0.33	8.89
1262_B_20_H_2_126_127_174.66	192.00	61.7161	1.02	0.30	0.45	8.38
1262_B_20_H_2_129_130_174.69	192.02	61.7200	1.05	0.37	0.52	8.07
1262_B_20_H_2_132_133_174.72	192.05	61.7238	0.98	0.28	0.43	8.48
1262_B_20_H_2_134_135_174.74	192.08	61.7261	0.78	–0.07	0.04	10.18
1262_B_20_H_2_138_139_174.78	192.12	61.7308	0.84	0.10	0.23	9.35
1262_B_20_H_2_141_142_174.81	192.15	61.7344	0.69	0.29	0.43	8.46
1262_B_20_H_2_144_145_174.84	192.18	61.7379	1.04	0.31	0.46	8.35
1262_B_20_H_2_147_148_174.87	192.21	61.7415	0.84	0.08	0.20	9.48
1262_B_20_H_2_149_150_174.89	192.23	61.7438	0.82	0.09	0.21	9.42
1262_B_20_H_3_1_2_174.91	192.25	61.7462	0.99	0.05	0.17	9.59
1262_B_20_H_3_9_10_174.99	192.33	61.7556	1.17	0.30	0.45	8.39
1262_B_20_H_3_12_13_175.02	192.36	61.7591	0.88	0.36	0.51	8.12
1262_B_20_H_3_16_17_175.06	192.40	61.7639	1.04	0.23	0.37	8.74
1262_B_20_H_3_18_19_175.08	192.41	61.7662	1.13	0.35	0.50	8.17
1262_B_20_H_3_21_22_175.11	192.45	61.7698	1.12	0.38	0.54	7.99
1262_B_20_H_3_25_26_175.15	192.49	61.7745	1.19	0.45	0.62	7.66
1262_B_20_H_3_27_28_175.17	192.51	61.7768	1.17	0.37	0.53	8.04
1262_B_20_H_3_31_32_175.21	192.55	61.7815	1.21	0.48	0.65	7.52
1262_B_20_H_3_33_34_175.23	192.57	61.7839	1.10	0.47	0.65	7.54
1262_B_20_H_3_35_36_175.25	192.59	61.7863	1.30	0.41	0.57	7.85
1262_B_20_H_3_39_40_175.29	192.63	61.7910	1.15	0.42	0.58	7.81
1262_B_20_H_3_41_42_175.31	192.65	61.7933	1.24	0.31	0.46	8.35
1262_B_20_H_3_48_49_175.38	192.72	61.8016	0.98	0.34	0.49	8.20
1262_B_20_H_3_51_52_175.41	192.75	61.8051	1.06	0.36	0.52	8.09
1262_B_20_H_3_54_55_175.44	192.77	61.8087	0.90	0.32	0.48	8.27
1262_B_20_H_3_57_58_175.47	192.80	61.8122	1.09	0.39	0.55	7.96
1262_B_20_H_3_60_61_175.5	192.84	61.8157	1.11	0.41	0.58	7.85
1262_B_20_H_3_63_64_175.53	192.87	61.8193	1.02	0.32	0.47	8.30
1262_B_20_H_3_66_67_175.56	192.90	61.8228	1.09	0.46	0.63	7.60
1262_B_20_H_3_69_70_175.59	192.93	61.8264	1.23	0.39	0.55	7.96
1262_B_20_H_3_71_72_175.61	192.95	61.8287	1.00	0.32	0.47	8.28
1262_B_20_H_3_81_82_175.71	193.05	61.8405	1.01	0.32	0.47	8.31
1262_B_20_H_3_84_85_175.74	193.08	61.8440	1.04	0.32	0.47	8.29
1262_B_20_H_3_87_88_175.77	193.11	61.8476	1.05	0.32	0.47	8.29
1262_B_20_H_3_90_91_175.8	193.13	61.8511	1.10	0.44	0.60	7.72
1262_B_20_H_3_94_95_175.84	193.18	61.8558	1.06	0.38	0.54	7.99
1262_B_20_H_3_98_99_175.88	193.22	61.8606	1.23	0.28	0.43	8.47
1262_B_20_H_3_101_102_175.91	193.25	61.8641	1.25	0.37	0.53	8.06
1262_B_20_H_3_106_107_175.96	193.30	61.8700	1.17	0.47	0.64	7.58
1262_B_20_H_3_107_108_175.97	193.30	61.8712	1.24	0.29	0.43	8.46
1262_B_20_H_3_110_111_176	193.34	61.8747	1.14	0.34	0.50	8.19
1262_B_20_H_3_116_117_176.06	193.40	61.8818	1.14	0.30	0.45	8.39
1262_B_20_H_3_119_120_176.09	193.43	61.8853	1.32	0.42	0.58	7.83
1262_B_20_H_3_122_123_176.12	193.46	61.8889	1.13	0.28	0.43	8.48
1262_B_20_H_3_125_126_176.15	193.49	61.8924	1.18	0.24	0.38	8.68
1262_B_20_H_3_129_130_176.19	193.52	61.8971	1.02	0.33	0.48	8.25
1262_B_20_H_3_131_132_176.21	193.55	61.8995	1.22	0.36	0.52	8.09
1262_B_20_H_3_134_135_176.24	193.58	61.9030	1.15	0.30	0.44	8.41
1262_B_20_H_3_137_138_176.27	193.61	61.9065	1.15	0.29	0.44	8.43
1262_B_20_H_3_140_141_176.3	193.63	61.9101	1.11	0.19	0.33	8.92
1262_B_20_H_3_143_144_176.33	193.66	61.9136	1.17	0.25	0.39	8.65
1262_B_20_H_3_146_147_176.36	193.70	61.9172	1.26	0.38	0.54	8.01
1262_B_20_H_3_149_150_176.39	193.73	61.9207	1.11	0.37	0.53	8.03
1262_B_20_H_4_2_3_176.42	193.76	61.9242	1.25	0.52	0.70	7.31
1262_B_20_H_4_5_6_176.45	193.79	61.9278	1.23	0.39	0.55	7.95
1262_B_20_H_4_8_9_176.48	193.82	61.9313	1.17	0.40	0.57	7.88
1262_B_20_H_4_11_12_176.51	193.85	61.9348	1.19	0.48	0.65	7.52
1262_B_20_H_4_14_15_176.54	193.88	61.9384	1.36	0.46	0.63	7.59
1262_B_20_H_4_17_18_176.57	193.91	61.9419	1.18	0.37	0.53	8.04

1262_B_20_H_4_20_21_176.6	193.94	61.9455	1.19	0.46	0.62	7.64
1262_B_20_H_4_23_24_176.63	193.97	61.9490	1.33	0.42	0.58	7.81
1262_B_20_H_4_26_27_176.66	194.00	61.9525	1.27	0.57	0.76	7.07
1262_B_20_H_4_29_30_176.69	194.02	61.9561	1.19	0.31	0.46	8.35
1262_B_20_H_4_32_33_176.72	194.05	61.9596	1.21	0.25	0.39	8.63
1262_B_20_H_4_35_36_176.75	194.09	61.9631	1.20	0.31	0.46	8.35
1262_B_20_H_4_38_39_176.78	194.12	61.9667	1.13	0.27	0.42	8.52
1262_B_20_H_4_41_42_176.81	194.15	61.9702	1.18	0.27	0.42	8.53
1262_B_20_H_4_45_46_176.85	194.19	61.9749	1.03	0.39	0.55	7.97
1262_B_20_H_4_47_48_176.87	194.21	61.9773	1.11	0.36	0.52	8.07
1262_B_20_H_4_50_51_176.9	194.24	61.9808	1.04	0.45	0.62	7.64
1262_B_20_H_4_53_54_176.93	194.27	61.9844	1.12	0.22	0.36	8.77
1262_B_20_H_4_56_57_176.96	194.30	61.9879	1.17	0.33	0.48	8.24
1262_B_20_H_4_59_60_176.99	194.33	61.9914	0.93	0.19	0.33	8.90
1262_B_20_H_4_65_66_177.05	194.38	61.9985	0.85	0.15	0.28	9.12
1262_B_20_H_4_69_70_177.09	194.43	62.0032	0.57	0.09	0.21	9.42
1262_B_20_H_4_71_72_177.11	194.45	62.0056	0.72	–0.03	0.08	10.00
1262_B_20_H_4_74_75_177.14	194.48	62.0091	0.80	0.02	0.13	9.76
1262_B_20_H_4_77_78_177.17	194.51	62.0126	0.65	0.09	0.21	9.43
1262_B_20_H_4_80_81_177.2	194.54	62.0161	0.54	–0.07	0.03	10.21
1262_B_20_H_4_83_84_177.23	194.57	62.0197	0.73	0.04	0.16	9.66
1262_B_20_H_4_86_87_177.26	194.60	62.0232	0.60	–0.11	–0.02	10.42
1262_B_20_H_4_92_93_177.32	194.66	62.0302	0.80	0.14	0.27	9.19
1262_B_20_H_4_95_96_177.35	194.69	62.0337	0.85	0.28	0.43	8.47
1262_B_20_H_4_98_99_177.38	194.72	62.0372	0.84	0.08	0.20	9.47
1262_B_20_H_4_101_102_177.41	194.75	62.0408	0.95	0.18	0.32	8.95
1262_B_20_H_4_104_105_177.44	194.77	62.0443	0.94	0.08	0.21	9.44
1262_B_20_H_4_111_112_177.51	194.85	62.0525	0.94	0.39	0.55	7.94
1262_B_20_H_4_113_114_177.53	194.87	62.0548	1.03	0.24	0.38	8.67
1262_B_20_H_4_116_117_177.56	194.90	62.0583	1.05	0.37	0.53	8.06
1262_B_20_H_4_119_120_177.59	194.93	62.0619	1.06	0.29	0.44	8.43
1262_B_20_H_4_122_123_177.62	194.96	62.0654	1.05	0.21	0.34	8.85
1262_B_20_H_4_125_126_177.65	194.99	62.0689	0.98	0.32	0.47	8.31
1262_B_20_H_4_128_129_177.68	195.02	62.0724	1.06	0.25	0.40	8.62
1262_B_20_H_4_131_132_177.71	195.05	62.0759	0.96	0.31	0.46	8.33
1262_B_20_H_4_134_135_177.74	195.08	62.0794	0.79	0.19	0.32	8.93
1262_B_20_H_4_140_141_177.8	195.13	62.0865	0.74	0.13	0.26	9.21
1262_B_20_H_4_143_144_177.83	195.16	62.0900	0.65	0.02	0.14	9.74
1262_B_20_H_4_149_150_177.89	195.23	62.0970	0.65	0.05	0.17	9.59
1262_B_20_H_5_2_3_177.92	195.26	62.1006	0.41	–0.07	0.03	10.20
1262_B_20_H_5_5_6_177.95	195.29	62.1041	0.48	0.02	0.14	9.75
1262_B_20_H_5_8_9_177.98	195.32	62.1077	0.79	0.17	0.30	9.03
1262_B_20_H_5_11_12_178.01	195.35	62.1116	0.53	0.00	0.11	9.85
1262_B_20_H_5_14_15_178.04	195.38	62.1156	0.52	–0.04	0.07	10.06
1262_B_20_H_5_17_18_178.07	195.41	62.1196	0.75	0.15	0.28	9.12
1262_B_20_H_5_20_21_178.1	195.44	62.1236	0.57	–0.08	0.02	10.27
1262_B_20_H_5_23_24_178.13	195.47	62.1276	0.72	0.05	0.17	9.60
1262_B_20_H_5_26_27_178.16	195.50	62.1316	0.50	–0.08	0.02	10.24
1262_B_20_H_5_29_30_178.19	195.52	62.1356	0.88	0.08	0.21	9.44
1262_B_20_H_5_32_33_178.22	195.55	62.1396	0.88	0.06	0.18	9.58
1262_B_20_H_5_35_36_178.25	195.59	62.1435	1.17	0.40	0.57	7.88
1262_B_20_H_5_41_42_178.31	195.65	62.1515	1.18	0.37	0.53	8.04
1262_B_20_H_5_44_45_178.34	195.68	62.1555	1.29	0.42	0.58	7.81
1262_B_20_H_5_47_48_178.37	195.71	62.1595	1.30	0.49	0.66	7.46
1262_B_20_H_5_50_51_178.4	195.74	62.1635	1.36	0.55	0.73	7.19
1262_C_11_H_2_23_24_179.23	195.76	62.1661	1.14	0.39	0.55	7.94
1262_C_11_H_2_26_27_179.26	195.79	62.1701	1.36	0.46	0.63	7.61
1262_C_11_H_2_29_30_179.29	195.82	62.1741	1.33	0.53	0.71	7.29
1262_C_11_H_2_32_33_179.32	195.85	62.1781	1.33	0.47	0.64	7.55
1262_C_11_H_2_35_36_179.35	195.88	62.1821	1.32	0.48	0.65	7.52

1262_C_11_H_2_38_39_179.38	195.91	62.1861	1.42	0.47	0.64	7.59
1262_C_11_H_2_41_42_179.41	195.94	62.1900	1.37	0.52	0.70	7.31
1262_C_11_H_2_44_45_179.44	195.97	62.1940	1.29	0.47	0.65	7.54
1262_C_11_H_2_47_48_179.47	196.00	62.1980	1.38	0.53	0.71	7.27
1262_C_11_H_2_50_51_179.5	196.02	62.2020	1.36	0.56	0.74	7.13
1262_C_11_H_2_53_54_179.53	196.05	62.2060	1.38	0.52	0.70	7.32
1262_C_11_H_2_57_58_179.57	196.10	62.2113	1.15	0.45	0.62	7.66
1262_C_11_H_2_59_60_179.59	196.12	62.2140	1.37	0.53	0.71	7.28
1262_C_11_H_2_62_63_179.62	196.15	62.2180	1.35	0.49	0.67	7.45
1262_C_11_H_2_65_66_179.65	196.18	62.2219	1.39	0.48	0.65	7.53
1262_C_11_H_2_68_69_179.68	196.21	62.2259	1.50	0.50	0.67	7.44
1262_C_11_H_2_71_72_179.71	196.24	62.2299	1.49	0.56	0.74	7.14
1262_C_11_H_2_74_75_179.74	196.27	62.2339	1.45	0.53	0.71	7.25
1262_C_11_H_2_80_81_179.8	196.33	62.2419	1.41	0.51	0.69	7.35
1262_C_11_H_2_83_84_179.83	196.36	62.2459	1.33	0.57	0.75	7.09
1262_C_11_H_2_86_87_179.86	196.38	62.2498	1.41	0.54	0.72	7.24
1262_C_11_H_2_89_90_179.89	196.41	62.2538	1.32	0.41	0.58	7.83
1262_C_11_H_2_91_92_179.91	196.44	62.2565	1.27	0.53	0.71	7.27
1262_C_11_H_2_96_97_179.96	196.49	62.2631	1.18	0.62	0.81	6.86
1262_C_11_H_2_99_100_179.99	196.52	62.2671	1.30	0.59	0.78	6.98
1262_C_11_H_2_102_103_180.02	196.55	62.2711	1.22	0.56	0.74	7.15
1262_C_11_H_2_105_106_180.05	196.58	62.2751	1.29	0.66	0.85	6.66
1262_C_11_H_2_108_109_180.08	196.61	62.2791	1.27	0.61	0.80	6.87
1262_C_11_H_2_109_110_180.09	196.62	62.2804	1.26	0.53	0.71	7.26
1262_C_11_H_2_114_115_180.14	196.66	62.2870	1.22	0.60	0.79	6.94
1262_C_11_H_2_117_118_180.17	196.70	62.2910	1.21	0.62	0.81	6.85
1262_C_11_H_2_120_121_180.2	196.73	62.2950	1.14	0.49	0.66	7.47
1262_C_11_H_2_123_124_180.23	196.76	62.2990	1.19	0.50	0.67	7.42
1262_C_11_H_2_126_127_180.26	196.79	62.3030	1.08	0.38	0.54	7.99
1262_C_11_H_2_129_130_180.29	196.82	62.3069	1.15	0.41	0.58	7.84
1262_C_11_H_2_131_132_180.31	196.84	62.3095	1.10	0.36	0.52	8.08
1262_C_11_H_2_135_136_180.35	196.88	62.3147	1.27	0.53	0.71	7.26
1262_C_11_H_2_138_139_180.38	196.91	62.3186	1.22	0.48	0.66	7.50
1262_C_11_H_2_141_142_180.41	196.94	62.3225	1.27	0.36	0.52	8.09
1262_C_11_H_2_144_145_180.44	196.97	62.3264	1.16	0.38	0.54	7.99
1262_C_11_H_2_147_148_180.47	197.00	62.3303	1.21	0.44	0.61	7.69
1262_C_11_H_2_149_150_180.49	197.02	62.3329	1.18	0.39	0.55	7.97
1262_C_11_H_3_2_3_180.52	197.05	62.3368	1.30	0.40	0.56	7.90
1262_C_11_H_3_5_6_180.55	197.08	62.3407	1.16	0.39	0.55	7.95
1262_C_11_H_3_9_10_180.59	197.12	62.3459	1.19	0.49	0.66	7.48
1262_C_11_H_3_12_13_180.62	197.15	62.3498	1.08	0.34	0.50	8.18
1262_C_11_H_3_15_16_180.65	197.18	62.3537	1.12	0.35	0.51	8.14
1262_C_11_H_3_18_19_180.68	197.21	62.3576	1.17	0.46	0.63	7.62
1262_C_11_H_3_21_22_180.71	197.24	62.3615	1.10	0.37	0.52	8.06
1262_C_11_H_3_22_23_180.72	197.25	62.3628	1.06	0.35	0.50	8.16
1262_C_11_H_3_27_28_180.77	197.30	62.3693	1.12	0.36	0.51	8.12
1262_C_11_H_3_28_29_180.78	197.30	62.3706	1.08	0.44	0.61	7.70
1262_C_11_H_3_31_32_180.81	197.34	62.3745	1.03	0.49	0.66	7.47
1262_C_11_H_3_33_34_180.83	197.36	62.3771	1.08	0.35	0.50	8.16
1262_C_11_H_3_36_37_180.86	197.38	62.3810	1.18	0.43	0.60	7.74
1262_C_11_H_3_38_39_180.88	197.41	62.3836	0.97	0.35	0.50	8.15
1262_C_11_H_3_39_40_180.89	197.41	62.3849	0.98	0.41	0.57	7.85
1262_C_11_H_3_44_45_180.94	197.47	62.3914	0.84	0.33	0.48	8.26
1262_C_11_H_3_45_46_180.95	197.48	62.3927	1.02	0.40	0.57	7.89
1262_C_11_H_3_48_49_180.98	197.51	62.3966	1.00	0.42	0.58	7.83
1262_C_11_H_3_53_54_181.03	197.55	62.4032	1.02	0.37	0.53	8.05
1262_C_11_H_3_56_57_181.06	197.59	62.4071	1.10	0.39	0.55	7.96
1262_C_11_H_3_59_60_181.09	197.62	62.4110	1.06	0.39	0.55	7.94
1262_C_11_H_3_62_63_181.12	197.65	62.4149	0.83	0.19	0.32	8.93
1262_C_11_H_3_65_66_181.15	197.68	62.4188	1.03	0.35	0.50	8.15

1262_C_11_H_3_68_69_181.18	197.71	62.4227	1.04	0.22	0.36	8.76
1262_C_11_H_3_74_75_181.24	197.77	62.4305	1.13	0.27	0.42	8.53
1262_C_11_H_3_77_78_181.27	197.80	62.4344	1.05	0.19	0.33	8.92
1262_C_11_H_3_80_81_181.3	197.83	62.4383	0.95	0.34	0.49	8.20
1262_C_11_H_3_83_84_181.33	197.86	62.4422	1.13	0.36	0.52	8.10
1262_C_11_H_3_86_87_181.36	197.88	62.4461	1.09	0.25	0.39	8.63
1262_C_11_H_3_89_90_181.39	197.91	62.4500	1.23	0.31	0.46	8.34
1262_C_11_H_3_92_93_181.42	197.95	62.4539	1.18	0.23	0.37	8.75
1262_C_11_H_3_95_96_181.45	197.98	62.4578	1.17	0.26	0.41	8.57
1262_C_11_H_3_98_99_181.48	198.01	62.4617	1.18	0.29	0.44	8.44
1262_C_11_H_3_101_102_181.51	198.04	62.4656	1.07	0.33	0.48	8.27
1262_C_11_H_3_104_105_181.54	198.07	62.4695	1.14	0.28	0.43	8.48
1262_C_11_H_3_107_108_181.57	198.10	62.4734	1.02	0.33	0.49	8.22
1262_C_11_H_3_110_111_181.6	198.13	62.4773	1.08	0.10	0.23	9.35
1262_C_11_H_3_113_114_181.63	198.16	62.4812	1.13	0.30	0.45	8.40
1262_C_11_H_3_116_117_181.66	198.19	62.4851	1.05	0.33	0.49	8.22
1262_C_11_H_3_119_120_181.69	198.22	62.4890	1.20	0.26	0.40	8.58
1262_C_11_H_3_122_123_181.72	198.25	62.4929	1.17	0.39	0.55	7.97
1262_C_11_H_3_125_126_181.75	198.27	62.4969	1.10	0.32	0.47	8.29
1262_C_11_H_3_128_129_181.78	198.30	62.5008	1.03	0.18	0.31	9.00
1262_C_11_H_3_131_132_181.81	198.34	62.5047	0.95	0.13	0.26	9.21
1262_C_11_H_3_134_135_181.84	198.37	62.5086	1.02	0.20	0.34	8.87
1262_C_11_H_3_137_138_181.87	198.40	62.5125	0.91	–0.07	0.03	10.22
1262_C_11_H_3_140_141_181.9	198.43	62.5164	0.95	0.11	0.23	9.32
1262_C_11_H_3_143_144_181.93	198.46	62.5203	1.03	0.20	0.33	8.89
1262_C_11_H_3_146_147_181.96	198.49	62.5242	0.93	–0.02	0.09	9.96
1262_C_11_H_3_148_149_181.98	198.51	62.5268	0.83	0.04	0.16	9.66
1262_C_11_H_4_2_3_182.02	198.55	62.5320	0.83	0.01	0.12	9.83
1262_C_11_H_4_5_6_182.05	198.58	62.5359	1.00	0.05	0.17	9.61
1262_C_11_H_4_8_9_182.08	198.61	62.5398	1.01	–0.01	0.10	9.92
1262_C_11_H_4_12_13_182.12	198.65	62.5450	0.95	0.22	0.36	8.77
1262_C_11_H_4_17_18_182.17	198.70	62.5515	1.31	0.20	0.33	8.89
1262_C_11_H_4_20_21_182.2	198.73	62.5554	1.09	0.04	0.15	9.68
1262_C_11_H_4_23_24_182.23	198.76	62.5593	1.17	0.34	0.49	8.20
1262_C_11_H_4_26_27_182.26	198.79	62.5632	1.22	0.31	0.46	8.35
1262_C_11_H_4_29_30_182.29	198.82	62.5671	1.12	–0.01	0.10	9.89
1262_C_11_H_4_36_37_182.36	198.88	62.5762	1.07	–0.08	0.02	10.24
1262_C_11_H_4_38_39_182.38	198.91	62.5788	1.14	–0.16	–0.06	10.64
1262_C_11_H_4_41_42_182.41	198.94	62.5827	1.02	–0.10	0.00	10.34
1262_C_11_H_4_44_45_182.44	198.97	62.5867	1.22	0.02	0.14	9.74
1262_C_11_H_4_48_49_182.48	199.01	62.5927	1.18	0.32	0.47	8.30
1262_C_11_H_4_50_51_182.5	199.02	62.5957	1.25	0.14	0.27	9.17
1262_C_11_H_4_53_54_182.53	199.05	62.6002	1.25	0.16	0.29	9.06
1262_C_11_H_4_56_57_182.56	199.09	62.6047	1.32	0.09	0.22	9.41
1262_C_11_H_4_60_61_182.6	199.13	62.6107	1.28	0.36	0.52	8.10
1262_C_11_H_4_62_63_182.62	199.15	62.6137	1.31	0.41	0.58	7.85
1262_C_11_H_4_65_66_182.65	199.18	62.6182	1.44	0.37	0.53	8.03
1262_C_11_H_4_68_69_182.68	199.21	62.6227	1.40	0.22	0.36	8.78
1262_C_11_H_4_70_71_182.7	199.23	62.6257	1.37	0.31	0.46	8.33
1262_C_11_H_4_74_75_182.74	199.27	62.6317	1.36	0.35	0.50	8.15
1262_C_11_H_4_78_79_182.78	199.30	62.6377	1.26	0.40	0.56	7.91
1262_C_11_H_4_80_81_182.8	199.33	62.6406	1.25	0.11	0.23	9.32
1262_C_11_H_4_84_85_182.84	199.37	62.6466	1.22	0.52	0.69	7.34
1262_C_11_H_4_86_87_182.86	199.38	62.6496	1.30	0.02	0.13	9.78
1262_C_11_H_4_89_90_182.89	199.41	62.6541	1.34	0.21	0.35	8.82
1262_C_11_H_4_95_96_182.95	199.48	62.6631	1.35	0.29	0.44	8.42
1262_C_11_H_4_98_99_182.98	199.51	62.6676	1.47	0.49	0.66	7.48
1262_C_11_H_4_101_102_183.01	199.54	62.6721	1.48	0.07	0.19	9.52
1262_C_11_H_4_104_105_183.04	199.57	62.6766	1.21	0.19	0.33	8.91
1262_C_11_H_4_107_108_183.07	199.60	62.6811	1.38	0.30	0.45	8.39

1262_C_11_H_4_110_111_183.1	199.63	62.6856	1.42	0.35	0.51	8.15
1262_C_11_H_4_113_114_183.13	199.66	62.6901	1.32	0.15	0.28	9.14
1262_C_11_H_4_116_117_183.16	199.69	62.6945	1.40	0.21	0.35	8.83
1262_C_11_H_4_120_121_183.2	199.73	62.7005	1.25	0.19	0.33	8.90
1262_C_11_H_4_122_123_183.22	199.75	62.7035	1.42	0.36	0.51	8.11
1262_C_11_H_4_125_126_183.25	199.77	62.7080	1.34	0.24	0.38	8.69
1262_C_11_H_4_128_129_183.28	199.80	62.7125	1.30	0.11	0.24	9.30
1262_C_11_H_4_131_132_183.31	199.84	62.7170	1.41	0.46	0.63	7.63
1262_C_11_H_4_134_135_183.34	199.87	62.7215	1.34	0.37	0.52	8.07
1262_C_11_H_4_137_138_183.37	199.90	62.7260	1.36	0.18	0.32	8.96
1262_C_11_H_4_140_141_183.4	199.93	62.7305	1.23	0.08	0.20	9.48
1262_C_11_H_4_144_145_183.44	199.97	62.7365	1.20	0.14	0.27	9.16
1262_C_11_H_4_146_147_183.46	199.99	62.7395	1.40	0.42	0.58	7.81
1262_C_11_H_4_149_150_183.49	200.02	62.7440	1.37	0.39	0.55	7.96
1262_C_11_H_5_2_3_183.52	200.05	62.7484	1.37	0.50	0.67	7.42
1262_C_11_H_5_6_7_183.56	200.09	62.7544	1.29	0.19	0.32	8.94
1262_C_11_H_5_8_9_183.58	200.11	62.7574	1.47	0.41	0.58	7.84
1262_C_11_H_5_18_19_183.68	200.21	62.7724	1.17	0.12	0.24	9.28
1262_C_11_H_5_20_21_183.7	200.23	62.7754	1.23	0.12	0.25	9.27
1262_C_11_H_5_26_27_183.76	200.29	62.7844	1.32	0.46	0.63	7.61
1262_C_11_H_5_29_30_183.79	200.32	62.7889	1.25	0.32	0.47	8.29
1262_C_11_H_5_32_33_183.82	200.35	62.7934	1.17	0.13	0.26	9.21
1262_C_11_H_5_35_36_183.85	200.38	62.7979	1.37	0.42	0.59	7.79
1262_C_11_H_5_38_39_183.88	200.41	62.8023	1.41	0.33	0.49	8.22
1262_C_11_H_5_41_42_183.91	200.44	62.8068	1.18	0.12	0.25	9.28
1262_C_11_H_5_44_45_183.94	200.47	62.8113	1.27	0.05	0.17	9.59
1262_C_11_H_5_50_51_184	200.52	62.8203	1.18	–0.01	0.10	9.90
1262_C_11_H_5_53_54_184.03	200.55	62.8248	1.10	–0.03	0.08	10.00
1262_C_11_H_5_59_60_184.09	200.62	62.8338	1.19	–0.10	0.00	10.35
1262_C_11_H_5_62_63_184.12	200.65	62.8383	1.08	–0.08	0.03	10.23
1262_C_11_H_5_65_66_184.15	200.68	62.8428	1.16	0.08	0.20	9.47
1262_C_11_H_5_71_72_184.21	200.74	62.8516	1.18	–0.11	–0.02	10.42
1262_C_11_H_5_77_78_184.27	200.80	62.8592	0.97	–0.11	–0.01	10.39
1262_C_11_H_5_83_84_184.33	200.86	62.8668	1.11	–0.17	–0.08	10.71
1262_C_11_H_5_87_88_184.37	200.90	62.8718	1.13	–0.10	0.00	10.34
1262_C_11_H_5_89_90_184.39	200.91	62.8743	1.13	–0.10	–0.01	10.38
1262_C_11_H_5_92_93_184.42	200.95	62.8781	1.20	0.03	0.15	9.69
1262_C_11_H_5_95_96_184.45	200.98	62.8819	1.20	–0.03	0.08	10.01
1262_C_11_H_5_98_99_184.48	201.01	62.8857	1.31	–0.04	0.07	10.06
1262_C_11_H_5_107_108_184.57	201.10	62.8971	1.30	–0.16	–0.06	10.63
1262_C_11_H_5_110_111_184.6	201.13	62.9008	1.32	–0.06	0.04	10.17
1262_C_11_H_5_114_115_184.64	201.16	62.9059	1.15	–0.06	0.05	10.14
1262_C_11_H_5_116_117_184.66	201.19	62.9084	1.31	–0.07	0.04	10.19
1262_C_11_H_5_119_120_184.69	201.22	62.9122	1.20	–0.16	–0.06	10.64
1262_C_11_H_5_122_123_184.72	201.25	62.9160	1.42	0.15	0.28	9.12
1262_C_11_H_5_125_126_184.75	201.27	62.9198	1.24	0.02	0.14	9.75
1262_C_11_H_5_128_129_184.78	201.30	62.9236	1.23	–0.01	0.10	9.89
1262_C_11_H_5_131_132_184.81	201.34	62.9273	1.30	0.10	0.22	9.37
1262_C_11_H_5_134_135_184.84	201.37	62.9311	1.16	–0.03	0.08	10.00
1262_C_11_H_5_137_138_184.87	201.40	62.9349	1.14	0.03	0.15	9.70
1262_C_11_H_6_2_3_185.02	201.55	62.9538	1.17	0.08	0.20	9.49
1262_C_11_H_6_5_6_185.05	201.58	62.9579	1.14	–0.12	–0.02	10.43
1262_C_11_H_6_9_10_185.09	201.62	62.9647	1.06	0.00	0.12	9.83
1262_C_11_H_6_11_12_185.11	201.63	62.9681	1.14	–0.24	–0.15	11.04
1262_C_11_H_6_14_15_185.14	201.66	62.9733	1.14	–0.05	0.05	10.12
1262_C_11_H_6_17_18_185.17	201.70	62.9784	1.16	0.03	0.15	9.71
1262_B_21_H_1_38_39_181.78	201.73	62.9836	1.34	0.22	0.36	8.76
1262_B_21_H_1_41_42_181.84	201.76	62.9887	1.36	–0.06	0.05	10.14
1262_B_21_H_1_44_45_181.87	201.79	62.9939	1.31	0.06	0.19	9.54
1262_B_21_H_1_47_48_181.9	201.82	62.9990	1.32	0.24	0.38	8.69

1262_B_21_H_1_50_51_181.93	201.85	63.0042	1.29	0.13	0.26	9.19
1262_B_21_H_1_53_54_181.96	201.88	63.0093	1.39	0.09	0.21	9.41
1262_B_21_H_1_56_57_181.99	201.91	63.0145	1.30	–0.19	–0.10	10.81
1262_B_21_H_1_59_60_182.02	201.94	63.0196	1.35	0.14	0.27	9.18
1262_B_21_H_1_65_66_182.05	202.00	63.0299	1.46	0.15	0.28	9.14
1262_B_21_H_1_68_69_182.08	202.02	63.0350	1.34	–0.12	–0.02	10.44
1262_B_21_H_1_71_72_182.11	202.05	63.0402	1.39	–0.03	0.08	10.01
1262_B_21_H_1_74_75_182.14	202.09	63.0453	1.27	–0.21	–0.12	10.89
1262_B_21_H_1_77_78_182.17	202.12	63.0505	1.31	–0.02	0.09	9.96
1262_B_21_H_1_80_81_182.2	202.15	63.0556	1.28	–0.28	–0.21	11.27
1262_B_21_H_1_83_84_182.23	202.18	63.0608	1.32	0.13	0.26	9.22
1262_B_21_H_1_86_87_182.26	202.21	63.0659	1.16	–0.06	0.05	10.14
1262_B_21_H_1_89_90_182.29	202.24	63.0711	1.35	0.06	0.18	9.55
1262_B_21_H_1_92_93_182.32	202.27	63.0762	1.37	–0.10	0.00	10.34
1262_B_21_H_1_95_96_182.35	202.30	63.0813	1.28	0.05	0.17	9.60
1262_B_21_H_1_98_99_182.38	202.33	63.0865	1.38	0.18	0.31	8.99
1262_B_21_H_1_101_102_182.41	202.36	63.0916	1.37	0.23	0.37	8.75
1262_B_21_H_1_104_105_182.44	202.38	63.0968	1.37	0.25	0.40	8.62
1262_B_21_H_1_107_108_182.47	202.41	63.1019	1.31	0.20	0.34	8.86
1262_B_21_H_1_110_111_182.5	202.45	63.1071	1.26	0.22	0.36	8.78
1262_B_21_H_1_113_114_182.53	202.48	63.1122	1.30	0.23	0.37	8.72
1262_B_21_H_1_116_117_182.56	202.51	63.1174	1.27	0.18	0.31	8.99
1262_B_21_H_1_119_120_182.59	202.54	63.1225	1.29	0.16	0.30	9.06
1262_B_21_H_1_122_123_182.62	202.57	63.1277	1.11	0.16	0.29	9.06
1262_B_21_H_1_125_126_182.65	202.60	63.1328	1.23	0.02	0.13	9.77
1262_B_21_H_1_128_129_182.68	202.63	63.1379	1.20	0.14	0.27	9.15
1262_B_21_H_1_131_132_182.71	202.66	63.1431	1.24	0.12	0.25	9.24
1262_B_21_H_1_134_135_182.74	202.69	63.1482	1.23	0.04	0.15	9.67
1262_B_21_H_1_137_138_182.77	202.72	63.1534	1.11	0.10	0.23	9.35
1262_B_21_H_1_140_141_182.8	202.75	63.1585	1.16	0.07	0.19	9.51
1262_B_21_H_1_143_144_182.83	202.77	63.1637	1.03	–0.06	0.05	10.15
1262_B_21_H_1_146_147_182.86	202.80	63.1688	1.08	0.31	0.46	8.34
1262_B_21_H_1_149_150_182.89	202.84	63.1740	1.31	0.26	0.41	8.56
1262_B_21_H_2_2_3_182.92	202.87	63.1791	1.23	0.21	0.35	8.84
1262_B_21_H_2_5_6_182.95	202.90	63.1843	1.20	–0.01	0.11	9.89
1262_B_21_H_2_8_9_182.98	202.93	63.1894	1.19	0.15	0.28	9.11
1262_B_21_H_2_11_12_183.01	202.96	63.1945	1.12	0.15	0.28	9.14
1262_B_21_H_2_14_15_183.04	202.99	63.1997	1.16	0.09	0.21	9.42
1262_B_21_H_2_17_18_183.07	203.02	63.2048	1.15	0.14	0.27	9.17
1262_B_21_H_2_19_20_183.09	203.04	63.2083	1.09	0.13	0.26	9.21
1262_B_21_H_2_23_24_183.13	203.08	63.2151	1.18	0.01	0.13	9.80
1262_B_21_H_2_26_27_183.16	203.11	63.2203	1.11	0.19	0.32	8.94
1262_B_21_H_2_29_30_183.19	203.13	63.2254	0.94	–0.06	0.05	10.14
1262_B_21_H_2_32_33_183.22	203.16	63.2306	0.93	–0.01	0.11	9.89
1262_B_21_H_2_35_36_183.25	203.20	63.2357	0.96	–0.05	0.05	10.13
1262_B_21_H_2_38_39_183.28	203.23	63.2411	1.02	0.01	0.12	9.82
1262_B_21_H_2_41_42_183.31	203.26	63.2474	0.96	–0.12	–0.02	10.46
1262_B_21_H_2_44_45_183.34	203.29	63.2538	0.94	–0.03	0.08	9.99
1262_B_21_H_2_47_48_183.37	203.32	63.2601	0.99	–0.04	0.07	10.04
1262_B_21_H_2_50_51_183.4	203.35	63.2665	0.97	–0.08	0.03	10.23
1262_B_21_H_2_53_54_183.43	203.38	63.2728	0.99	–0.24	–0.16	11.05
1262_B_21_H_2_57_58_183.47	203.41	63.2813	1.10	0.00	0.12	9.85
1262_B_21_H_2_59_60_183.49	203.44	63.2855	1.18	0.03	0.15	9.71
1262_C_12_H_1_68_69_184.68	203.47	63.2919	1.09	–0.01	0.10	9.92
1262_C_12_H_1_71_72_184.71	203.50	63.2982	1.29	0.04	0.16	9.65
1262_C_12_H_1_74_75_184.74	203.52	63.3046	1.12	0.04	0.16	9.67
1262_C_12_H_1_77_78_184.77	203.55	63.3109	1.16	–0.03	0.07	10.03
1262_C_12_H_1_80_81_184.8	203.59	63.3173	1.14	0.03	0.14	9.73
1262_C_12_H_1_83_84_184.83	203.62	63.3236	1.04	–0.20	–0.12	10.86
1262_C_12_H_1_85_86_184.85	203.63	63.3279	1.01	–0.11	–0.01	10.41

1262_C_12_H_1_89_90_184.89	203.68	63.3364	0.97	–0.05	0.05	10.12
1262_C_12_H_1_92_93_184.92	203.71	63.3427	0.99	–0.14	–0.04	10.53
1262_C_12_H_1_95_96_184.95	203.74	63.3491	0.92	–0.23	–0.14	10.98
1262_C_12_H_1_99_100_184.99	203.77	63.3581	1.01	–0.07	0.03	10.20
1262_C_12_H_1_101_102_185.01	203.80	63.3627	0.92	–0.27	–0.20	11.22
1262_C_12_H_1_104_105_185.04	203.83	63.3694	0.98	–0.20	–0.11	10.86
1262_C_12_H_1_107_108_185.07	203.86	63.3762	1.07	–0.13	–0.04	10.52
1262_C_12_H_1_110_111_185.1	203.88	63.3829	1.11	–0.09	0.01	10.32
1262_C_12_H_1_113_114_185.13	203.91	63.3897	1.10	–0.21	–0.12	10.88
1262_C_12_H_1_116_117_185.16	203.95	63.3965	1.16	–0.10	0.00	10.35
1262_C_12_H_1_122_123_185.22	204.01	63.4100	1.22	–0.12	–0.02	10.43
1262_C_12_H_1_125_126_185.25	204.04	63.4168	1.25	0.24	0.38	8.69
1262_C_12_H_1_128_129_185.28	204.07	63.4235	1.36	0.31	0.46	8.33
1262_C_12_H_1_131_132_185.31	204.10	63.4303	1.19	–0.21	–0.12	10.89
1262_C_12_H_1_134_135_185.34	204.13	63.4371	1.20	0.07	0.19	9.51
1262_C_12_H_1_137_138_185.37	204.16	63.4438	1.25	0.09	0.21	9.43
1262_C_12_H_1_140_141_185.4	204.19	63.4506	1.26	0.35	0.51	8.13
1262_C_12_H_1_143_144_185.43	204.22	63.4573	1.29	0.05	0.17	9.61
1262_C_12_H_1_146_147_185.46	204.25	63.4641	1.19	0.03	0.15	9.70
1262_C_12_H_1_149_150_185.49	204.27	63.4709	1.20	0.00	0.11	9.87
1262_C_12_H_2_2_3_185.52	204.30	63.4776	1.27	0.05	0.17	9.61
1262_C_12_H_2_5_6_185.55	204.34	63.4844	1.17	0.03	0.15	9.71
1262_C_12_H_2_9_10_185.59	204.38	63.4934	1.34	0.21	0.34	8.85
1262_C_12_H_2_11_12_185.61	204.40	63.4979	1.27	–0.35	–0.28	11.59
1262_C_12_H_2_14_15_185.64	204.43	63.5047	1.24	–0.32	–0.24	11.43
1262_C_12_H_2_17_18_185.67	204.46	63.5115	1.32	–0.02	0.09	9.94
1262_C_12_H_2_26_27_185.76	204.55	63.5317	1.21	–0.10	0.00	10.35
1262_C_12_H_2_29_30_185.79	204.58	63.5385	1.25	–0.16	–0.07	10.64
1262_C_12_H_2_33_34_185.83	204.62	63.5475	1.19	–0.15	–0.06	10.62
1262_C_12_H_2_35_36_185.85	204.63	63.5520	1.21	–0.05	0.06	10.10
1262_C_12_H_2_38_39_185.88	204.66	63.5588	1.27	–0.04	0.07	10.06
1262_C_12_H_2_41_42_185.91	204.70	63.5656	1.14	–0.08	0.03	10.24
1262_C_12_H_2_44_45_185.94	204.73	63.5723	1.28	0.01	0.12	9.83
1262_C_12_H_2_47_48_185.97	204.76	63.5791	1.19	–0.07	0.03	10.21
1262_C_12_H_2_50_51_186	204.79	63.5859	1.09	–0.18	–0.09	10.76
1262_C_12_H_2_52_53_186.02	204.80	63.5904	1.14	–0.10	0.00	10.37
1262_C_12_H_2_57_58_186.07	204.86	63.6016	1.00	–0.19	–0.10	10.80
1262_C_12_H_2_59_60_186.09	204.88	63.6061	0.95	–0.24	–0.16	11.04
1262_C_12_H_2_69_70_186.19	204.98	63.6287	1.04	–0.28	–0.20	11.23
1262_C_12_H_2_72_73_186.22	205.01	63.6355	1.15	–0.20	–0.12	10.86
1262_C_12_H_2_74_75_186.24	205.02	63.6400	1.14	–0.29	–0.22	11.31
1262_C_12_H_2_80_81_186.3	205.09	63.6535	1.23	–0.15	–0.05	10.58
1262_C_12_H_2_84_85_186.34	205.13	63.6625	1.22	–0.15	–0.06	10.60
1262_C_12_H_2_86_87_186.36	205.15	63.6670	1.25	–0.09	0.02	10.28
1262_C_12_H_2_89_90_186.39	205.18	63.6738	1.27	–0.16	–0.07	10.66
1262_C_12_H_2_92_93_186.42	205.21	63.6805	1.20	–0.20	–0.11	10.84
1262_C_12_H_2_96_97_186.46	205.25	63.6896	1.05	–0.13	–0.04	10.52
1262_C_12_H_2_98_99_186.48	205.27	63.6941	1.28	0.05	0.17	9.62
1262_C_12_H_2_101_102_186.51	205.30	63.7008	1.07	–0.16	–0.07	10.66
1262_C_12_H_2_104_105_186.54	205.33	63.7076	1.15	–0.13	–0.03	10.49
1262_C_12_H_2_108_109_186.58	205.37	63.7166	1.07	–0.15	–0.06	10.62
1262_C_12_H_2_110_111_186.6	205.38	63.7211	1.19	–0.10	0.00	10.35
1262_C_12_H_2_113_114_186.63	205.41	63.7275	1.12	–0.25	–0.17	11.12
1262_C_12_H_2_116_117_186.66	205.45	63.7339	1.19	–0.20	–0.11	10.85
1262_C_12_H_2_119_120_186.69	205.48	63.7404	1.35	0.06	0.18	9.55
1262_C_12_H_2_122_123_186.72	205.51	63.7468	1.26	–0.03	0.07	10.02
1262_C_12_H_2_125_126_186.75	205.54	63.7532	1.30	0.02	0.13	9.76
1262_C_12_H_2_127_128_186.77	205.55	63.7575	1.34	0.11	0.24	9.31
1262_C_12_H_2_131_132_186.81	205.60	63.7661	1.34	0.02	0.13	9.76
1262_C_12_H_2_133_134_186.83	205.62	63.7704	1.36	0.19	0.33	8.92

1262_C_12_H_2_137_138_186.87	205.66	63.7790	1.33	–0.10	–0.01	10.38
1262_C_12_H_2_140_141_186.9	205.69	63.7854	1.32	0.03	0.15	9.70
1262_C_12_H_2_143_144_186.93	205.72	63.7918	1.46	0.18	0.32	8.96
1262_C_12_H_2_147_148_186.97	205.76	63.8004	1.43	0.27	0.41	8.55
1262_C_12_H_2_149_150_186.99	205.77	63.8047	1.29	–0.19	–0.10	10.80
1262_C_12_H_3_3_4_187.03	205.82	63.8133	1.30	0.03	0.15	9.71
1262_C_12_H_3_9_10_187.09	205.88	63.8261	1.22	–0.13	–0.03	10.48
1262_C_12_H_3_11_12_187.11	205.90	63.8304	1.26	–0.20	–0.11	10.84
1262_C_12_H_3_14_15_187.14	205.93	63.8368	1.34	–0.01	0.10	9.90
1262_C_12_H_3_17_18_187.17	205.96	63.8433	1.18	–0.27	–0.20	11.22
1262_C_12_H_3_20_21_187.2	205.99	63.8497	1.24	–0.23	–0.14	10.99
1262_C_12_H_3_23_24_187.23	206.02	63.8561	1.38	–0.02	0.09	9.95
1262_C_12_H_3_27_28_187.27	206.05	63.8647	1.24	–0.07	0.03	10.21
1262_C_12_H_3_29_30_187.29	206.08	63.8690	1.17	–0.28	–0.20	11.23
1262_C_12_H_3_32_33_187.32	206.11	63.8754	1.31	0.04	0.16	9.64
1262_C_12_H_3_35_36_187.35	206.13	63.8819	1.33	0.05	0.16	9.63
1262_C_12_H_3_39_40_187.39	206.18	63.8904	1.29	0.05	0.17	9.59
1262_C_12_H_3_41_42_187.41	206.20	63.8947	1.29	–0.08	0.02	10.25
1262_C_12_H_3_44_45_187.44	206.23	63.9012	1.35	0.19	0.33	8.92
1262_C_12_H_3_47_48_187.47	206.26	63.9076	1.14	–0.17	–0.08	10.71
1262_C_12_H_3_50_51_187.5	206.29	63.9140	1.14	–0.12	–0.02	10.44
1262_C_12_H_3_56_57_187.56	206.35	63.9269	1.19	–0.18	–0.09	10.75
1262_C_12_H_3_59_60_187.59	206.38	63.9333	1.33	0.08	0.20	9.48
1262_C_12_H_3_63_64_187.63	206.41	63.9419	1.25	0.09	0.21	9.44
1262_C_12_H_3_68_69_187.68	206.47	63.9526	1.05	–0.17	–0.08	10.70
1262_C_12_H_3_72_73_187.72	206.51	63.9612	1.31	0.25	0.39	8.65
1262_C_12_H_3_75_76_187.75	206.54	63.9676	1.34	0.25	0.40	8.62
1262_C_12_H_3_77_78_187.77	206.55	63.9719	1.22	–0.05	0.05	10.12
1262_C_12_H_3_81_82_187.81	206.60	63.9805	1.28	0.22	0.36	8.80
1262_C_12_H_3_83_84_187.83	206.62	63.9848	1.14	–0.01	0.11	9.89
1262_C_12_H_3_85_86_187.85	206.63	63.9891	1.24	0.14	0.27	9.18
1262_C_12_H_3_89_90_187.89	206.68	63.9976	1.28	0.06	0.18	9.56
1262_C_12_H_3_92_93_187.92	206.71	64.0040	1.25	0.09	0.22	9.39
1262_C_12_H_3_95_96_187.95	206.74	64.0103	1.15	–0.13	–0.03	10.50
1262_C_12_H_3_98_99_187.98	206.77	64.0165	1.18	0.02	0.14	9.75
1262_C_12_H_3_101_102_188.01	206.80	64.0228	1.08	–0.22	–0.13	10.94
1262_C_12_H_3_103_104_188.03	206.82	64.0270	1.20	0.07	0.19	9.52
1262_C_12_H_3_107_108_188.07	206.86	64.0353	1.28	0.05	0.17	9.61
1262_C_12_H_3_111_112_188.11	206.90	64.0436	1.28	0.12	0.24	9.29
1262_C_12_H_3_113_114_188.13	206.91	64.0478	1.18	–0.07	0.03	10.21
1262_C_12_H_3_116_117_188.16	206.95	64.0540	1.13	–0.21	–0.12	10.90
1262_C_12_H_3_119_120_188.19	206.98	64.0603	1.14	–0.11	–0.01	10.39
1262_C_12_H_3_125_126_188.25	207.04	64.0728	1.22	–0.03	0.08	10.00
1262_C_12_H_3_128_129_188.28	207.07	64.0790	1.13	–0.15	–0.06	10.62
1262_C_12_H_3_131_132_188.31	207.10	64.0853	1.16	–0.01	0.10	9.91
1262_C_12_H_3_135_136_188.35	207.13	64.0936	1.22	–0.02	0.09	9.94
1262_C_12_H_3_137_138_188.37	207.16	64.0978	1.21	–0.03	0.08	10.01
1262_C_12_H_3_141_142_188.41	207.20	64.1060	1.12	–0.08	0.02	10.27
1262_C_12_H_3_144_145_188.44	207.23	64.1120	1.26	0.11	0.23	9.32
1262_C_12_H_3_146_147_188.46	207.25	64.1160	1.24	0.08	0.20	9.49
1262_C_12_H_3_149_150_188.49	207.27	64.1220	1.19	–0.08	0.02	10.25
1262_C_12_H_4_3_4_188.53	207.32	64.1300	1.18	–0.21	–0.12	10.89
1262_C_12_H_4_13_14_188.63	207.41	64.1500	1.31	0.06	0.18	9.58
1262_C_12_H_4_20_21_188.7	207.49	64.1640	1.28	–0.14	–0.04	10.54
1262_C_12_H_4_26_27_188.76	207.55	64.1760	1.44	0.07	0.19	9.52
1262_C_12_H_4_29_30_188.79	207.58	64.1820	1.47	0.08	0.21	9.44
1262_C_12_H_4_32_33_188.82	207.61	64.1880	1.35	–0.14	–0.05	10.57
1262_C_12_H_4_35_36_188.85	207.63	64.1940	1.52	–0.04	0.07	10.06
1262_C_12_H_4_39_40_188.89	207.68	64.2020	1.46	0.15	0.28	9.11
1262_C_12_H_4_44_45_188.94	207.73	64.2120	1.31	–0.06	0.05	10.15

1262_C_12_H_4_47_48_188.97	207.76	64.2180	1.24	–0.12	–0.02	10.46
1262_C_12_H_4_63_64_189.13	207.91	64.2500	1.41	0.28	0.43	8.48
1262_C_12_H_4_66_67_189.16	207.95	64.2560	1.45	0.10	0.23	9.36
1262_C_12_H_4_68_69_189.18	207.97	64.2600	1.49	0.28	0.43	8.48
1262_C_12_H_4_77_78_189.27	208.05	64.2780	1.50	0.07	0.19	9.50
1262_C_12_H_4_80_81_189.3	208.09	64.2840	1.34	0.01	0.12	9.82
1262_C_12_H_4_83_84_189.33	208.12	64.2900	1.37	–0.14	–0.04	10.53
1262_C_12_H_4_87_88_189.37	208.16	64.2980	1.39	0.18	0.32	8.95
1262_C_12_H_4_89_90_189.39	208.18	64.3020	1.37	–0.07	0.03	10.21
1262_C_12_H_4_92_93_189.42	208.21	64.3078	1.32	0.20	0.33	8.90
1262_C_12_H_4_99_100_189.49	208.27	64.3194	1.40	0.23	0.37	8.73
1262_C_12_H_4_101_102_189.51	208.30	64.3227	1.21	–0.08	0.03	10.24
1262_C_12_H_4_104_105_189.54	208.33	64.3276	1.32	0.00	0.11	9.88
1262_C_12_H_4_111_112_189.61	208.40	64.3392	1.40	–0.03	0.08	10.00
1262_C_12_H_4_113_114_189.63	208.41	64.3425	1.35	–0.03	0.08	10.00
1262_C_12_H_4_116_117_189.66	208.45	64.3474	1.41	0.13	0.26	9.22
1262_C_12_H_4_119_120_189.69	208.48	64.3524	1.40	0.06	0.18	9.54
1262_C_12_H_4_122_123_189.72	208.51	64.3574	1.37	0.19	0.32	8.94
1262_C_12_H_4_125_126_189.75	208.54	64.3623	1.34	0.20	0.34	8.87
1262_C_12_H_4_128_129_189.78	208.57	64.3673	1.46	0.14	0.27	9.19
1262_C_12_H_4_131_132_189.81	208.60	64.3722	1.43	0.15	0.28	9.11
1262_C_12_H_4_133_134_189.83	208.62	64.3755	1.30	0.16	0.29	9.07
1262_C_12_H_4_137_138_189.87	208.66	64.3821	1.27	0.20	0.33	8.89
1262_C_12_H_4_140_141_189.9	208.69	64.3871	1.39	0.23	0.37	8.71
1262_C_12_H_4_143_144_189.93	208.72	64.3920	1.39	0.27	0.42	8.53
1262_C_12_H_4_147_148_189.97	208.76	64.3986	1.23	0.16	0.29	9.07
1262_C_12_H_4_149_150_189.99	208.77	64.4019	1.28	0.09	0.22	9.41
1262_C_12_H_5_2_3_190.02	208.80	64.4069	1.33	0.12	0.25	9.26
1262_C_12_H_5_5_6_190.05	208.84	64.4121	1.33	0.13	0.25	9.24
1262_C_12_H_5_8_9_190.08	208.87	64.4185	1.32	0.14	0.27	9.19
1262_C_12_H_5_11_12_190.11	208.90	64.4249	1.36	0.10	0.22	9.39
1262_C_12_H_5_14_15_190.14	208.93	64.4313	1.32	0.05	0.16	9.63
1262_C_12_H_5_17_18_190.17	208.96	64.4377	1.22	0.14	0.27	9.18
1262_C_12_H_5_21_22_190.21	209.00	64.4463	1.23	0.12	0.25	9.25
1262_C_12_H_5_23_24_190.23	209.02	64.4505	1.10	–0.09	0.01	10.30
1262_C_12_H_5_26_27_190.26	209.05	64.4569	1.16	–0.06	0.04	10.17
1262_C_12_H_5_29_30_190.29	209.08	64.4633	1.18	0.01	0.12	9.81
1262_C_12_H_5_33_34_190.33	209.12	64.4719	1.11	–0.03	0.08	10.02
1262_C_12_H_5_35_36_190.35	209.13	64.4762	1.14	–0.06	0.05	10.15
1262_C_12_H_5_38_39_190.38	209.16	64.4826	1.19	–0.06	0.05	10.14
1262_C_12_H_5_41_42_190.41	209.20	64.4890	1.19	–0.04	0.07	10.05
1262_C_12_H_5_43_44_190.43	209.22	64.4933	1.16	0.02	0.13	9.77
1262_C_12_H_5_47_48_190.47	209.26	64.5018	1.17	–0.09	0.02	10.28
1262_C_12_H_5_50_51_190.5	209.29	64.5082	1.18	–0.05	0.06	10.08
1262_C_12_H_5_53_54_190.53	209.32	64.5146	1.17	–0.07	0.03	10.22
1262_C_12_H_5_57_58_190.57	209.36	64.5232	1.25	0.04	0.16	9.66
1262_C_12_H_5_59_60_190.59	209.38	64.5274	1.29	0.06	0.18	9.56
1262_C_12_H_5_62_63_190.62	209.41	64.5338	1.26	0.00	0.11	9.87
1262_C_12_H_5_65_66_190.65	209.44	64.5403	1.29	0.05	0.16	9.63
1262_C_12_H_5_68_69_190.68	209.47	64.5467	1.19	–0.05	0.06	10.10
1262_C_12_H_5_71_72_190.71	209.50	64.5531	1.25	0.02	0.13	9.77
1262_C_12_H_5_74_75_190.74	209.52	64.5595	1.25	0.03	0.14	9.72
1262_C_12_H_5_77_78_190.77	209.55	64.5659	1.22	–0.05	0.06	10.08
1262_C_12_H_5_79_80_190.79	209.58	64.5702	1.22	0.01	0.12	9.81
1262_C_12_H_5_83_84_190.83	209.62	64.5787	1.13	–0.03	0.08	9.99
1262_C_12_H_5_86_87_190.86	209.65	64.5851	1.15	–0.10	0.00	10.37
1262_C_12_H_5_89_90_190.89	209.68	64.5915	1.18	–0.11	–0.02	10.42
1262_C_12_H_5_93_94_190.93	209.72	64.6001	1.13	–0.11	–0.01	10.39
1262_C_12_H_5_95_96_190.95	209.74	64.6043	1.18	–0.04	0.07	10.04
1262_C_12_H_5_98_99_190.98	209.77	64.6108	1.18	–0.01	0.10	9.91

1262_C_12_H_5_101_102_191.01	209.80	64.6172	1.19	–0.08	0.02	10.28
1262_C_12_H_5_103_104_191.03	209.82	64.6214	1.15	0.03	0.15	9.70
1262_C_12_H_5_107_108_191.07	209.86	64.6300	1.22	–0.02	0.09	9.96
1262_C_12_H_5_110_111_191.1	209.88	64.6364	1.28	–0.06	0.05	10.13
1262_C_12_H_5_113_114_191.13	209.91	64.6428	1.20	–0.03	0.07	10.02
1262_C_12_H_5_116_117_191.16	209.95	64.6492	1.25	0.02	0.13	9.76
1262_C_12_H_5_119_120_191.19	209.98	64.6556	1.30	0.01	0.13	9.80
1262_C_12_H_5_122_123_191.22	210.01	64.6620	1.27	–0.07	0.03	10.21
1262_C_12_H_5_125_126_191.25	210.04	64.6684	1.32	–0.06	0.05	10.14
1262_C_12_H_5_128_129_191.28	210.07	64.6748	1.14	–0.11	–0.01	10.38
1262_C_12_H_5_131_132_191.31	210.10	64.6813	1.31	–0.06	0.04	10.18
1262_C_12_H_5_134_135_191.34	210.13	64.6877	1.29	–0.11	–0.01	10.38
1262_C_12_H_5_137_138_191.37	210.16	64.6941	1.26	–0.06	0.05	10.14
1262_C_12_H_6_1_2_191.51	210.30	64.7240	1.32	–0.02	0.09	9.94
1262_C_12_H_6_5_6_191.55	210.34	64.7325	1.38	0.03	0.15	9.71
1262_C_12_H_6_8_9_191.58	210.37	64.7389	1.38	0.04	0.16	9.65
1262_C_12_H_6_11_12_191.61	210.40	64.7453	1.32	–0.06	0.05	10.14
1262_C_12_H_6_14_15_191.64	210.43	64.7518	1.37	–0.01	0.10	9.90
1262_C_12_H_6_17_18_191.67	210.46	64.7582	1.39	0.08	0.20	9.45
1262_C_12_H_6_20_21_191.7	210.49	64.7646	1.37	0.01	0.12	9.81
1262_C_12_H_6_24_25_191.74	210.52	64.7731	1.49	0.21	0.34	8.85
1262_C_12_H_6_26_27_191.76	210.55	64.7774	1.49	0.09	0.22	9.40
1262_C_12_H_6_29_30_191.79	210.58	64.7838	1.52	0.14	0.27	9.18
1262_C_12_H_6_32_33_191.82	210.61	64.7902	1.47	0.13	0.26	9.21
1262_C_12_H_6_34_35_191.84	210.63	64.7945	1.48	0.13	0.26	9.22
1262_C_12_H_6_38_39_191.88	210.66	64.8030	1.45	0.09	0.22	9.40
1262_C_12_H_6_41_42_191.91	210.70	64.8094	1.47	0.13	0.26	9.23
1262_C_12_H_6_44_45_191.94	210.73	64.8158	1.45	0.03	0.15	9.70
1262_C_12_H_6_47_48_191.97	210.76	64.8223	1.44	0.09	0.22	9.39
1262_C_12_H_6_50_51_192	210.79	64.8287	1.49	0.09	0.21	9.42
1262_C_12_H_6_53_54_192.03	210.82	64.8350	1.41	–0.11	–0.02	10.42
1262_C_12_H_6_56_57_192.06	210.85	64.8409	1.49	0.00	0.11	9.88
1262_C_12_H_6_60_61_192.1	210.88	64.8487	1.37	–0.03	0.08	10.01
1262_C_12_H_6_65_66_192.15	210.94	64.8585	1.43	0.00	0.12	9.84
1262_C_12_H_6_68_69_192.18	210.97	64.8644	1.42	–0.04	0.07	10.05
1262_C_12_H_6_71_72_192.21	211.00	64.8703	1.37	–0.09	0.01	10.30
1262_C_12_H_6_74_75_192.24	211.02	64.8762	1.42	0.01	0.12	9.83
1262_C_12_H_6_77_78_192.27	211.05	64.8821	1.38	–0.01	0.10	9.90
1262_C_12_H_6_80_81_192.3	211.09	64.8880	1.51	0.04	0.16	9.66
1262_C_12_H_6_84_85_192.34	211.13	64.8959	1.38	–0.01	0.10	9.91
1262_C_12_H_6_86_87_192.36	211.15	64.8998	1.46	–0.02	0.09	9.94
1262_C_12_H_6_89_90_192.39	211.18	64.9057	1.31	–0.13	–0.03	10.48
1262_C_12_H_6_92_93_192.42	211.21	64.9116	1.37	–0.14	–0.04	10.55
1262_C_12_H_6_94_95_192.44	211.23	64.9155	1.27	–0.09	0.02	10.28
1262_C_12_H_6_98_99_192.48	211.27	64.9233	1.22	–0.21	–0.12	10.90
1262_C_12_H_7_2_3_192.52	211.30	64.9312	1.21	–0.10	0.00	10.36
1262_C_12_H_7_4_5_192.54	211.33	64.9351	1.20	–0.12	–0.02	10.44
1262_C_12_H_7_9_10_192.59	211.38	64.9454	1.32	–0.09	0.01	10.31
1262_C_12_H_7_11_12_192.61	211.40	64.9499	1.32	–0.07	0.03	10.21
1262_C_12_H_7_14_15_192.64	211.43	64.9567	1.30	–0.13	–0.04	10.51
1262_C_12_H_7_17_18_192.67	211.46	64.9636	1.35	–0.08	0.02	10.27
1262_C_12_H_7_20_21_192.7	211.49	64.9704	1.44	0.06	0.18	9.57
1262_C_12_H_7_23_24_192.73	211.52	64.9772	1.49	0.10	0.22	9.39
1262_C_12_H_7_26_27_192.76	211.55	64.9840	1.51	0.08	0.20	9.46
1262_C_12_H_7_29_30_192.79	211.58	64.9908	1.42	0.05	0.17	9.59
1262_C_12_H_7_31_32_192.81	211.60	64.9953	1.43	0.08	0.20	9.48
1262_C_12_H_7_35_36_192.85	211.63	65.0044	1.47	0.06	0.17	9.58
1262_C_12_H_7_38_39_192.88	211.66	65.0112	1.41	0.01	0.13	9.79
1262_C_12_H_7_41_42_192.91	211.70	65.0180	1.39	0.00	0.11	9.86
1262_C_12_H_7_43_44_192.93	211.72	65.0225	1.41	0.06	0.18	9.58

1262_C_12_H_7_47_48_192.97	211.76	65.0316	1.48	0.03	0.14	9.73
1262_C_12_H_7_50_51_193	211.79	65.0373	1.43	0.02	0.14	9.76
1262_C_12_H_7_53_54_193.03	211.82	65.0420	1.47	0.12	0.25	9.27
1262_C_12_H_7_55_56_193.05	211.84	65.0452	1.42	0.04	0.16	9.66
1262_C_12_H_7_59_60_193.09	211.88	65.0514	1.44	0.02	0.13	9.76
1262_C_12_H_7_62_63_193.12	211.91	65.0561	1.50	0.06	0.18	9.54
1262_C_12_H_7_65_66_193.15	211.94	65.0608	1.42	0.00	0.11	9.86
1262_B_22_H_1_8_9_190.98	211.98	65.0671	1.55	0.02	0.13	9.76
1262_B_22_H_1_11_12_191.01	212.01	65.0718	1.52	–0.10	0.00	10.35
1262_B_22_H_1_14_15_191.04	212.04	65.0765	1.53	–0.01	0.10	9.92
1262_B_22_H_1_16_17_191.06	212.05	65.0796	1.42	–0.12	–0.02	10.44
1262_B_22_H_1_19_20_191.09	212.09	65.0843	1.50	–0.03	0.08	10.00
1262_B_22_H_1_23_24_191.13	212.13	65.0905	1.45	–0.15	–0.05	10.59
1262_B_22_H_1_26_27_191.16	212.16	65.0952	1.39	–0.12	–0.02	10.44
1262_B_22_H_1_29_30_191.19	212.19	65.0999	1.45	0.02	0.14	9.74
1262_B_22_H_1_33_34_191.23	212.23	65.1062	1.39	0.01	0.12	9.82
1262_B_22_H_1_35_36_191.25	212.25	65.1093	1.22	–0.13	–0.04	10.51
1262_B_22_H_1_38_39_191.28	212.27	65.1140	1.18	–0.12	–0.02	10.46
1262_B_22_H_1_41_42_191.31	212.30	65.1187	1.20	–0.08	0.02	10.26
1262_B_22_H_1_44_45_191.34	212.34	65.1234	1.19	–0.15	–0.06	10.61
1262_B_22_H_1_47_48_191.37	212.37	65.1281	1.23	–0.14	–0.04	10.54
1262_B_22_H_1_50_51_191.4	212.40	65.1327	1.29	–0.17	–0.07	10.68
1262_B_22_H_1_53_54_191.43	212.43	65.1369	1.32	–0.14	–0.04	10.55
1262_B_22_H_1_55_56_191.45	212.45	65.1398	1.21	–0.12	–0.02	10.46
1262_B_22_H_1_62_63_191.52	212.52	65.1496	1.22	–0.11	–0.01	10.40
1262_B_22_H_1_65_66_191.55	212.55	65.1538	1.10	–0.13	–0.03	10.49
1262_B_22_H_1_67_68_191.57	212.57	65.1567	1.32	–0.08	0.03	10.23
1262_B_22_H_1_71_72_191.61	212.61	65.1623	1.37	–0.06	0.04	10.17
1262_B_22_H_1_74_75_191.64	212.63	65.1665	1.43	–0.09	0.01	10.30
1262_B_22_H_1_77_78_191.67	212.66	65.1708	1.38	–0.09	0.01	10.30
1262_B_22_H_1_79_80_191.69	212.69	65.1736	1.39	–0.14	–0.04	10.53
1262_B_22_H_1_83_84_191.73	212.73	65.1792	1.35	–0.12	–0.02	10.46
1262_B_22_H_1_86_87_191.76	212.76	65.1834	1.31	–0.10	0.00	10.35
1262_B_22_H_1_89_90_191.79	212.79	65.1877	1.34	–0.09	0.01	10.31
1262_B_22_H_1_93_94_191.83	212.83	65.1933	1.28	–0.05	0.05	10.12
1262_B_22_H_1_95_96_191.85	212.85	65.1961	1.29	–0.13	–0.03	10.49
1262_B_22_H_1_98_99_191.88	212.88	65.2003	1.30	–0.11	–0.02	10.42
1262_B_22_H_2_2_3_191.92	212.91	65.2060	1.19	–0.13	–0.04	10.52
1262_B_22_H_2_6_7_191.96	212.96	65.2116	1.20	–0.13	–0.03	10.50
1262_B_22_H_2_11_12_192.01	213.01	65.2187	1.01	–0.05	0.05	10.12
1262_B_22_H_2_14_15_192.04	213.04	65.2229	1.06	–0.03	0.08	9.98
1262_B_22_H_2_19_20_192.09	213.09	65.2390	1.03	–0.10	0.00	10.35
1262_B_22_H_2_20_21_192.1	213.10	65.2430	0.96	–0.14	–0.05	10.57
1262_B_22_H_2_23_24_192.13	213.13	65.2550	1.02	–0.05	0.05	10.12
1262_B_22_H_2_26_27_192.16	213.16	65.2670	1.17	–0.07	0.04	10.19
1262_B_22_H_2_28_29_192.18	213.18	65.2750	1.12	0.00	0.11	9.88
1262_B_22_H_2_32_33_192.22	213.22	65.2910	1.18	–0.01	0.10	9.92
1262_B_22_H_2_35_36_192.25	213.25	65.3030	1.10	–0.02	0.09	9.97
1262_B_22_H_2_39_40_192.29	213.29	65.3190	1.01	–0.03	0.08	10.00
1262_B_22_H_2_44_45_192.34	213.34	65.3334	0.84	–0.13	–0.04	10.51
1262_B_22_H_2_50_51_192.4	213.40	65.3439	1.18	–0.13	–0.04	10.52
1262_B_22_H_2_52_53_192.42	213.41	65.3474	1.15	–0.10	0.00	10.33
1262_B_22_H_2_56_57_192.46	213.46	65.3544	1.28	–0.04	0.07	10.06
1262_B_22_H_2_59_60_192.49	213.49	65.3596	1.43	–0.01	0.10	9.91
1262_B_22_H_2_62_63_192.52	213.52	65.3649	1.36	0.07	0.19	9.53
1262_B_22_H_2_63_64_192.53	213.52	65.3666	1.36	0.02	0.14	9.76
1262_B_22_H_2_68_69_192.58	213.58	65.3754	1.42	0.04	0.16	9.64
1262_B_22_H_3_2_3_192.68	213.68	65.3929	1.20	–0.16	–0.06	10.63
1262_B_22_H_3_5_6_192.71	213.71	65.3981	1.26	–0.10	0.00	10.34
1262_B_22_H_3_8_9_192.74	213.74	65.4034	1.30	–0.02	0.10	9.93

1262_B_22_H_3_16_17_192.82	213.82	65.4174	1.30	–0.03	0.08	10.01
1262_B_22_H_3_17_18_192.83	213.83	65.4191	1.34	–0.10	0.00	10.37
1262_B_22_H_3_29_30_192.95	213.95	65.4411	1.30	–0.10	0.01	10.33
1262_B_22_H_3_32_33_192.98	213.98	65.4471	1.33	0.00	0.12	9.83
1262_B_22_H_3_35_36_193.01	214.01	65.4532	1.42	0.01	0.13	9.79
1262_B_22_H_3_38_39_193.04	214.04	65.4593	1.36	–0.01	0.10	9.92
1262_B_22_H_3_41_42_193.07	214.07	65.4653	1.35	–0.12	–0.02	10.44
1262_B_22_H_3_44_45_193.1	214.10	65.4714	1.39	0.07	0.19	9.53
1262_B_22_H_3_47_48_193.13	214.13	65.4775	1.35	0.04	0.16	9.67
1262_B_22_H_3_50_51_193.16	214.16	65.4835	1.39	0.03	0.14	9.72
1262_B_22_H_3_53_54_193.19	214.19	65.4896	1.38	–0.01	0.10	9.90
1262_B_22_H_3_56_57_193.22	214.22	65.4957	1.38	0.02	0.14	9.75
1262_B_22_H_3_65_66_193.31	214.30	65.5139	1.28	–0.07	0.03	10.20
1262_B_22_H_3_68_69_193.34	214.34	65.5199	1.26	0.04	0.15	9.68
1262_B_22_H_3_71_72_193.37	214.37	65.5260	1.43	0.03	0.15	9.69
1262_B_22_H_3_76_77_193.42	214.41	65.5360	1.42	0.04	0.16	9.67
1262_B_22_H_3_77_78_193.43	214.43	65.5380	1.45	0.07	0.19	9.52
1262_C_13_H_1_0_1_193.5	214.44	65.5418	1.28	–0.01	0.10	9.91
1262_C_13_H_1_1_2_193.51	214.45	65.5438	1.19	–0.11	–0.01	10.40
1262_B_22_H_3_80_81_193.46	214.46	65.5440	1.45	0.06	0.18	9.57
1262_C_13_H_1_2_3_193.52	214.46	65.5458	1.19	–0.10	–0.01	10.38
1262_C_13_H_1_4_5_193.54	214.48	65.5498	1.34	–0.04	0.07	10.05
1262_B_22_H_3_83_84_193.49	214.49	65.5500	1.48	–0.01	0.10	9.93
1262_C_13_H_1_5_6_193.55	214.49	65.5518	1.44	0.03	0.14	9.72
1262_B_22_H_3_86_87_193.52	214.52	65.5560	1.52	0.06	0.18	9.58
1262_C_13_H_1_8_9_193.58	214.52	65.5578	1.49	0.08	0.20	9.49
1262_C_13_H_1_11_12_193.61	214.57	65.5662	1.44	0.08	0.20	9.48
1262_B_22_H_3_92_93_193.58	214.58	65.5680	1.49	0.00	0.12	9.84
1262_B_22_H_3_95_96_193.61	214.61	65.5740	1.54	0.05	0.17	9.59
1262_C_13_H_1_15_16_193.65	214.64	65.5804	1.26	0.09	0.21	9.44
1262_C_13_H_1_16_17_193.66	214.66	65.5840	1.37	0.05	0.17	9.61
1262_B_22_H_3_101_102_193.67	214.66	65.5860	1.41	0.01	0.12	9.81
1262_C_13_H_1_19_20_193.69	214.71	65.5948	1.38	–0.15	–0.05	10.59
1262_B_22_H_3_107_108_193.73	214.73	65.5980	1.41	–0.03	0.08	9.99
1262_C_13_H_1_20_21_193.7	214.73	65.5984	1.41	–0.02	0.09	9.94
1262_C_13_H_1_21_22_193.71	214.75	65.6020	1.39	–0.16	–0.07	10.67
1262_B_22_H_3_113_114_193.79	214.79	65.6100	1.35	–0.09	0.01	10.32
1262_C_13_H_1_25_26_193.75	214.80	65.6147	1.48	0.03	0.15	9.71
1262_C_13_H_1_26_27_193.76	214.81	65.6173	1.49	0.13	0.26	9.22
1262_C_13_H_1_29_30_193.79	214.84	65.6251	1.56	0.03	0.15	9.70
1262_B_22_H_3_119_120_193.85	214.85	65.6254	1.40	0.03	0.15	9.70
1262_C_13_H_1_32_33_193.82	214.87	65.6330	1.50	0.03	0.15	9.71
1262_B_22_H_3_122_123_193.88	214.88	65.6333	1.51	0.08	0.20	9.48
1262_C_13_H_1_34_35_193.84	214.89	65.6382	1.53	0.07	0.19	9.52
1262_C_13_H_1_35_36_193.85	214.90	65.6409	1.56	0.05	0.17	9.63
1262_B_22_H_3_125_126_193.91	214.91	65.6411	1.60	0.02	0.13	9.77
1262_C_13_H_1_37_38_193.87	214.92	65.6461	1.54	–0.02	0.09	9.96
1262_C_13_H_1_38_39_193.88	214.93	65.6487	1.51	–0.09	0.01	10.32
1262_B_22_H_3_128_129_193.94	214.94	65.6490	1.63	0.08	0.20	9.46
1262_C_13_H_1_40_41_193.9	214.95	65.6540	1.58	–0.02	0.09	9.94
1262_B_22_H_3_131_132_193.97	214.97	65.6568	1.42	–0.13	–0.04	10.52
1262_C_13_H_1_43_44_193.93	214.98	65.6618	1.58	–0.07	0.03	10.23
1262_C_13_H_1_44_45_193.94	214.99	65.6644	1.37	–0.08	0.02	10.27
1262_B_22_H_3_134_135_194	215.00	65.6647	1.72	0.27	0.41	8.55
1262_C_13_H_1_46_47_193.96	215.01	65.6697	1.64	0.25	0.39	8.65
1262_C_13_H_1_47_48_193.97	215.02	65.6723	1.59	0.29	0.43	8.45
1262_C_13_H_1_48_49_193.98	215.03	65.6749	1.66	0.28	0.43	8.46
1262_C_13_H_1_49_50_193.99	215.04	65.6775	1.57	0.16	0.29	9.06
1262_C_13_H_1_51_52_194.01	215.06	65.6828	1.56	0.24	0.39	8.66
1262_C_13_H_1_53_54_194.03	215.08	65.6880	1.58	0.25	0.39	8.64

1262_C_13_H_1_55_56_194.05	215.10	65.6932	1.69	0.29	0.44	8.43
1262_B_22_H_3_146_147_194.12	215.12	65.6961	1.51	0.12	0.25	9.25
1262_C_13_H_1_58_59_194.08	215.13	65.7011	1.64	0.28	0.43	8.46
1262_B_22_H_3_149_150_194.15	215.15	65.7040	1.44	0.11	0.24	9.32
1262_C_13_H_1_61_62_194.11	215.16	65.7090	1.60	0.18	0.32	8.97
1262_C_13_H_1_62_63_194.12	215.17	65.7116	1.52	0.20	0.34	8.86
1262_B_22_H_4_2_3_194.18	215.18	65.7118	1.41	0.10	0.23	9.35
1262_C_13_H_1_64_65_194.14	215.19	65.7168	1.44	0.18	0.31	8.99
1262_C_13_H_1_65_66_194.15	215.20	65.7194	1.48	0.05	0.17	9.60
1262_B_22_H_4_5_6_194.21	215.21	65.7197	1.55	0.19	0.32	8.93
1262_C_13_H_1_68_69_194.18	215.23	65.7291	1.63	0.20	0.33	8.90
1262_C_13_H_1_69_70_194.19	215.24	65.7330	1.51	0.20	0.34	8.88
1262_C_13_H_1_71_72_194.21	215.26	65.7403	1.63	0.10	0.23	9.36
1262_B_22_H_4_11_12_194.27	215.27	65.7463	1.60	0.16	0.29	9.08
1262_C_13_H_1_73_74_194.23	215.27	65.7488	1.56	0.13	0.25	9.24
1262_C_13_H_1_75_76_194.25	215.30	65.7574	1.59	0.12	0.25	9.25
1262_C_13_H_1_77_78_194.27	215.32	65.7659	1.66	0.27	0.42	8.53
1262_C_13_H_1_78_79_194.28	215.33	65.7702	1.55	0.18	0.31	8.99
1262_C_13_H_1_80_81_194.3	215.35	65.7788	1.53	0.15	0.28	9.12
1262_C_13_H_1_81_82_194.31	215.36	65.7831	1.60	0.16	0.29	9.08
1262_C_13_H_1_82_83_194.32	215.37	65.7873	1.66	0.15	0.28	9.12
1262_C_13_H_1_83_84_194.33	215.38	65.7916	1.55	0.18	0.32	8.96
1262_C_13_H_1_84_85_194.34	215.38	65.7959	1.56	0.16	0.29	9.07
1262_C_13_H_1_85_86_194.35	215.40	65.8002	1.61	0.26	0.40	8.60
1262_C_13_H_1_86_87_194.36	215.41	65.8045	1.60	0.17	0.31	9.00
1262_C_13_H_1_87_88_194.37	215.41	65.8087	1.61	0.18	0.31	8.98
1262_C_13_H_1_88_89_194.38	215.43	65.8130	1.46	0.14	0.27	9.17
1262_C_13_H_1_89_90_194.39	215.44	65.8173	1.46	0.17	0.31	9.00
1262_C_13_H_1_90_91_194.4	215.45	65.8216	1.56	0.14	0.27	9.18
1262_C_13_H_1_91_92_194.41	215.46	65.8259	1.59	0.21	0.35	8.84
1262_C_13_H_1_92_93_194.42	215.47	65.8291	1.48	0.25	0.40	8.61
1262_C_13_H_1_93_94_194.43	215.48	65.8313	1.55	0.17	0.30	9.04
1262_C_13_H_1_94_95_194.44	215.49	65.8334	1.62	0.19	0.33	8.90
1262_C_13_H_1_95_96_194.45	215.50	65.8356	1.54	0.16	0.30	9.05
1262_C_13_H_1_96_97_194.46	215.51	65.8378	1.53	0.14	0.27	9.19
1262_C_13_H_1_97_98_194.47	215.52	65.8399	1.61	0.14	0.27	9.16
1262_C_13_H_1_98_99_194.48	215.52	65.8421	1.50	0.16	0.29	9.09
1262_C_13_H_1_99_100_194.49	215.54	65.8443	1.61	0.20	0.33	8.90
1262_C_13_H_1_100_101_194.5	215.55	65.8464	1.58	0.18	0.32	8.96
1262_C_13_H_1_101_102_194.51	215.55	65.8486	1.70	0.25	0.39	8.65
1262_C_13_H_1_102_103_194.52	215.57	65.8508	1.67	0.04	0.16	9.66
1262_C_13_H_1_103_104_194.53	215.58	65.8530	1.58	0.14	0.27	9.15
1262_C_13_H_1_104_105_194.54	215.59	65.8551	1.57	0.19	0.32	8.94
1262_C_13_H_1_105_106_194.55	215.60	65.8573	1.74	0.20	0.33	8.89
1262_C_13_H_1_106_107_194.56	215.61	65.8595	1.72	0.23	0.37	8.72
1262_C_13_H_1_107_108_194.57	215.62	65.8616	1.71	0.24	0.38	8.70
1262_C_13_H_1_108_109_194.58	215.63	65.8638	1.80	0.21	0.35	8.83
1262_C_13_H_1_109_110_194.59	215.63	65.8660	1.82	0.26	0.40	8.58
1262_C_13_H_1_110_111_194.6	215.65	65.8682	1.78	0.24	0.39	8.66
1262_C_13_H_1_111_112_194.61	215.66	65.8703	1.97	0.29	0.44	8.43
1262_C_13_H_1_112_113_194.62	215.66	65.8725	1.84	0.26	0.41	8.58
1262_C_13_H_1_113_114_194.63	215.68	65.8747	1.90	0.29	0.43	8.45
1262_C_13_H_1_114_115_194.64	215.69	65.8768	1.80	0.24	0.39	8.66
1262_C_13_H_1_115_116_194.65	215.70	65.8790	1.85	0.24	0.39	8.66
1262_C_13_H_1_116_117_194.66	215.71	65.8812	1.85	0.15	0.28	9.13
1262_C_13_H_1_117_118_194.67	215.72	65.8833	1.88	0.24	0.38	8.68
1262_C_13_H_1_118_119_194.68	215.73	65.8855	1.83	0.21	0.35	8.80
1262_C_13_H_1_119_120_194.69	215.74	65.8877	1.80	0.26	0.41	8.56
1262_C_13_H_1_120_121_194.7	215.75	65.8899	1.81	0.25	0.40	8.62
1262_C_13_H_1_121_122_194.71	215.76	65.8920	1.83	0.29	0.44	8.45

1262_C_13_H_1_122_123_194.72	215.77	65.8942	1.84	0.27	0.42	8.51
1262_C_13_H_1_123_124_194.73	215.77	65.8964	1.87	0.24	0.38	8.70
1262_C_13_H_1_124_125_194.74	215.79	65.8985	1.78	0.28	0.43	8.48
1262_C_13_H_1_125_126_194.75	215.80	65.9007	1.81	0.25	0.39	8.63
1262_C_13_H_1_126_127_194.76	215.80	65.9029	1.93	0.29	0.44	8.44
1262_C_13_H_1_127_128_194.77	215.82	65.9050	1.91	0.20	0.33	8.89
1262_C_13_H_1_128_129_194.78	215.83	65.9072	1.90	0.22	0.36	8.77
1262_C_13_H_1_129_130_194.79	215.84	65.9094	1.90	0.19	0.32	8.93
1262_C_13_H_1_130_131_194.8	215.85	65.9116	2.00	0.26	0.41	8.57
1262_C_13_H_1_131_132_194.81	215.86	65.9137	1.94	0.24	0.39	8.67
1262_C_13_H_1_132_133_194.82	215.87	65.9159	2.05	0.31	0.46	8.33
1262_C_13_H_1_133_134_194.83	215.88	65.9181	1.96	0.20	0.34	8.88
1262_C_13_H_1_134_135_194.84	215.88	65.9202	1.99	0.25	0.39	8.63
1262_C_13_H_1_135_136_194.85	215.90	65.9224	1.99	0.28	0.42	8.50
1262_C_13_H_1_137_138_194.87	215.91	65.9267	1.99	0.24	0.38	8.68
1262_C_13_H_1_138_139_194.88	215.93	65.9289	1.98	0.28	0.43	8.48
1262_C_13_H_1_139_140_194.89	215.94	65.9309	1.92	0.22	0.36	8.77
1262_C_13_H_1_140_141_194.9	215.95	65.9327	1.89	0.25	0.39	8.63
1262_C_13_H_1_141_142_194.91	215.96	65.9346	1.93	0.25	0.40	8.62
1262_C_13_H_1_142_143_194.92	215.97	65.9364	1.98	0.29	0.44	8.43
1262_C_13_H_1_143_144_194.93	215.98	65.9382	2.08	0.33	0.48	8.26
1262_C_13_H_1_144_145_194.94	215.99	65.9401	1.98	0.26	0.41	8.58
1262_C_13_H_1_146_147_194.96	216.01	65.9437	2.07	0.30	0.45	8.37
1262_C_13_H_2_0_1_195	216.05	65.9510	2.11	0.32	0.47	8.30
1262_C_13_H_2_1_2_195.01	216.05	65.9529	2.09	0.26	0.41	8.56
1262_C_13_H_2_2_3_195.02	216.07	65.9547	1.97	0.22	0.36	8.76
1262_C_13_H_2_3_4_195.03	216.08	65.9565	2.11	0.27	0.42	8.54
1262_C_13_H_2_4_5_195.04	216.09	65.9583	2.14	0.31	0.46	8.36
1262_C_13_H_2_5_6_195.05	216.10	65.9602	2.09	0.28	0.43	8.47
1262_C_13_H_2_6_7_195.06	216.11	65.9620	2.04	0.28	0.42	8.50
1262_C_13_H_2_8_9_195.08	216.13	65.9657	2.11	0.26	0.40	8.60
1262_C_13_H_2_9_10_195.09	216.13	65.9675	2.15	0.29	0.43	8.46
1262_C_13_H_2_10_11_195.1	216.15	65.9693	1.91	0.20	0.34	8.86
1262_C_13_H_2_12_13_195.12	216.16	65.9730	2.06	0.24	0.38	8.69
1262_C_13_H_2_14_15_195.14	216.19	65.9766	2.16	0.35	0.51	8.15
1262_C_13_H_2_16_17_195.16	216.21	65.9803	2.07	0.27	0.42	8.54
1262_C_13_H_2_18_19_195.18	216.23	65.9839	2.28	0.39	0.55	7.95
1262_C_13_H_2_20_21_195.2	216.25	65.9876	2.28	0.41	0.57	7.85
1262_C_13_H_2_22_23_195.22	216.27	65.9913	2.29	0.37	0.52	8.07
1262_C_13_H_2_24_25_195.24	216.29	65.9943	2.25	0.36	0.51	8.11
1262_C_13_H_2_26_27_195.26	216.30	65.9956	2.29	0.43	0.59	7.77
1262_C_13_H_2_28_29_195.28	216.33	65.9969	2.21	0.50	0.67	7.44
1262_C_13_H_2_30_31_195.3	216.35	65.9982	2.27	0.44	0.60	7.73
1262_C_13_H_2_32_33_195.32	216.37	65.9995	2.31	0.37	0.52	8.07
1262_C_13_H_2_34_35_195.34	216.38	66.0008	2.35	0.43	0.59	7.76
1262_C_13_H_2_36_37_195.36	216.41	66.0021	2.25	0.32	0.47	8.31
1262_C_13_H_2_38_39_195.38	216.43	66.0034	2.22	0.32	0.48	8.28
1262_C_13_H_2_42_43_195.42	216.47	66.0060	2.12	0.30	0.45	8.40
1262_C_13_H_2_44_45_195.44	216.49	66.0074	2.29	0.30	0.45	8.37
1262_C_13_H_2_47_48_195.47	216.52	66.0093	2.30	0.33	0.48	8.24
1262_C_13_H_2_49_50_195.49	216.54	66.0106	2.32	0.37	0.53	8.06
1262_C_13_H_2_51_52_195.51	216.55	66.0119	2.26	0.25	0.40	8.62
1262_C_13_H_2_54_55_195.54	216.59	66.0139	2.28	0.39	0.55	7.96
1262_C_13_H_2_56_57_195.56	216.61	66.0152	2.29	0.33	0.49	8.22
1262_C_13_H_2_58_59_195.58	216.63	66.0165	2.23	0.30	0.45	8.40
1262_C_13_H_2_60_61_195.6	216.65	66.0178	2.16	0.24	0.38	8.69
1262_C_13_H_2_61_62_195.61	216.66	66.0184	2.25	0.24	0.38	8.69
1262_C_13_H_2_69_70_195.69	216.74	66.0239	2.13	0.34	0.50	8.17
1262_C_13_H_2_78_79_195.78	216.83	66.0309	2.04	0.47	0.65	7.54
1262_C_13_H_2_79_80_195.79	216.84	66.0317	2.03	0.49	0.67	7.46

1262_C_13_H_2_101_102_196.01	217.05	66.0487	2.08	0.44	0.61	7.69
1262_C_13_H_2_107_108_196.07	217.12	66.0534	2.01	0.42	0.58	7.80
1262_C_13_H_2_113_114_196.13	217.18	66.0580	1.94	0.38	0.54	8.00
1262_C_13_H_2_119_120_196.19	217.24	66.0626	1.92	0.37	0.53	8.03
1262_C_13_H_2_125_126_196.25	217.30	66.0673	1.83	0.32	0.47	8.28
1262_C_13_H_2_137_138_196.37	217.41	66.0766	1.86	0.37	0.53	8.05
1262_C_13_H_2_146_147_196.46	217.51	66.0835	1.79	0.10	0.23	9.35
1262_C_13_H_3_6_7_196.56	217.61	66.0913	1.92	0.32	0.48	8.28
1262_C_13_H_3_18_19_196.68	217.73	66.1006	1.70	0.14	0.27	9.17
1262_C_13_H_3_24_25_196.74	217.79	66.1052	1.81	0.24	0.39	8.67
1262_C_13_H_3_30_31_196.8	217.85	66.1099	1.86	0.26	0.41	8.58
1262_C_13_H_3_36_37_196.86	217.91	66.1145	1.93	0.26	0.40	8.60
1262_C_13_H_3_48_49_196.98	218.02	66.1238	1.67	0.14	0.26	9.19
1262_C_13_H_3_57_58_197.07	218.12	66.1308	1.79	0.10	0.23	9.36
1262_C_13_H_3_66_67_197.16	218.21	66.1377	1.64	–0.04	0.07	10.04
1262_C_13_H_3_96_97_197.46	218.51	66.1532	1.70	–0.04	0.06	10.08
1262_C_13_H_3_102_103_197.52	218.57	66.1559	1.85	–0.03	0.07	10.02
1262_C_13_H_3_111_112_197.61	218.66	66.1600	1.91	0.03	0.14	9.72
1262_C_13_H_3_120_121_197.7	218.75	66.1642	1.87	–0.07	0.03	10.20
1262_C_13_H_3_126_127_197.76	218.80	66.1669	1.77	–0.12	–0.03	10.47
1262_C_13_H_3_132_133_197.82	218.87	66.1696	1.68	–0.09	0.01	10.31
1262_C_13_H_3_138_139_197.88	218.93	66.1724	1.68	–0.04	0.07	10.05
1262_C_13_H_3_141_142_197.91	218.96	66.1737	1.64	–0.06	0.05	10.14
1262_C_13_H_4_3_4_198.03	219.08	66.1792	1.67	–0.09	0.01	10.29
1262_C_13_H_4_6_7_198.06	219.11	66.1806	1.72	–0.08	0.02	10.27
1262_C_13_H_4_12_13_198.12	219.16	66.1833	1.70	0.01	0.12	9.82
1262_C_13_H_4_15_16_198.15	219.20	66.1847	1.77	–0.15	–0.05	10.59
1262_C_13_H_4_21_22_198.21	219.26	66.1874	1.69	–0.18	–0.09	10.74
1262_C_13_H_4_27_28_198.27	219.32	66.1902	1.63	–0.26	–0.18	11.16
1262_C_13_H_4_36_37_198.36	219.41	66.1943	1.56	–0.15	–0.05	10.58
1262_C_13_H_4_42_43_198.42	219.47	66.1970	1.59	–0.17	–0.07	10.68
1262_C_13_H_4_45_46_198.45	219.50	66.1984	1.58	–0.10	0.00	10.36
1262_C_13_H_4_51_52_198.51	219.55	66.2012	1.79	–0.07	0.03	10.22
1262_C_13_H_4_57_58_198.57	219.62	66.2039	1.80	–0.11	–0.01	10.40
1262_C_13_H_4_63_64_198.63	219.68	66.2066	1.81	–0.15	–0.05	10.59
1262_C_13_H_4_66_67_198.66	219.71	66.2080	1.50	–0.29	–0.21	11.28
1262_C_13_H_4_72_73_198.72	219.77	66.2107	1.69	–0.27	–0.19	11.21
1262_C_13_H_4_78_79_198.78	219.83	66.2135	1.60	–0.32	–0.24	11.42
1262_C_13_H_4_87_88_198.87	219.91	66.2176	1.39	–0.30	–0.23	11.37
1262_C_13_H_4_93_94_198.93	219.98	66.2203	1.50	–0.27	–0.19	11.21
1262_C_13_H_4_99_100_198.99	220.04	66.2231	1.48	–0.26	–0.18	11.14
1262_C_13_H_4_102_103_199.02	220.07	66.2244	1.44	–0.20	–0.11	10.84
1262_C_13_H_4_108_109_199.08	220.13	66.2272	1.50	–0.16	–0.07	10.67
1262_C_13_H_4_111_112_199.11	220.16	66.2286	1.59	–0.26	–0.18	11.16
1262_C_13_H_4_117_118_199.17	220.22	66.2313	1.59	–0.33	–0.26	11.50
1262_C_13_H_4_120_121_199.2	220.25	66.2327	1.53	–0.32	–0.25	11.47
1262_C_13_H_4_123_124_199.23	220.27	66.2340	1.61	–0.20	–0.11	10.85
1262_C_13_H_4_126_127_199.26	220.30	66.2354	1.49	0.01	0.12	9.81
1262_C_13_H_4_132_133_199.32	220.37	66.2382	1.47	–0.31	–0.23	11.38
1262_C_13_H_4_135_136_199.35	220.40	66.2395	1.29	–0.33	–0.26	11.49
1262_C_13_H_4_138_139_199.38	220.43	66.2409	1.51	–0.28	–0.20	11.26
1262_C_13_H_4_147_148_199.47	220.52	66.2450	1.60	–0.36	–0.30	11.67
1262_C_13_H_5_0_1_199.5	220.55	66.2464	1.56	–0.33	–0.26	11.51
1262_C_13_H_5_12_13_199.62	220.66	66.2519	1.36	–0.30	–0.22	11.33
1262_C_13_H_5_15_16_199.65	220.70	66.2532	1.21	–0.15	–0.06	10.62
1262_C_13_H_5_18_19_199.68	220.73	66.2543	1.26	–0.10	0.00	10.35
1262_C_13_H_5_27_28_199.77	220.82	66.2575	1.27	–0.02	0.09	9.96
1262_C_13_H_5_30_31_199.8	220.85	66.2586	1.48	–0.17	–0.08	10.72
1262_C_13_H_5_33_34_199.83	220.88	66.2597	1.54	–0.28	–0.20	11.24
1262_C_13_H_5_39_40_199.89	220.94	66.2619	1.64	–0.24	–0.15	11.04

1262_C_13_H_5_45_46_199.95	221.00	66.2641	1.64	–0.22	–0.13	10.94
1262_C_13_H_5_48_49_199.98	221.02	66.2652	1.64	–0.31	–0.23	11.38
1262_C_13_H_5_54_55_200.04	221.09	66.2673	1.52	–0.35	–0.28	11.60
1262_C_13_H_5_57_58_200.07	221.12	66.2684	1.47	–0.26	–0.18	11.17
1262_C_13_H_5_60_61_200.1	221.15	66.2695	1.49	–0.31	–0.24	11.41
1262_C_13_H_5_63_64_200.13	221.18	66.2706	1.42	–0.17	–0.08	10.72
1262_C_13_H_5_69_70_200.19	221.24	66.2728	1.40	–0.14	–0.05	10.56
1262_C_13_H_5_75_76_200.25	221.30	66.2750	1.50	–0.12	–0.03	10.48
1262_C_13_H_5_78_79_200.28	221.33	66.2761	1.44	–0.15	–0.06	10.61
1262_C_13_H_5_84_85_200.34	221.38	66.2782	1.70	–0.05	0.06	10.10
1262_C_13_H_5_90_91_200.4	221.45	66.2804	1.61	–0.18	–0.09	10.74
1262_C_13_H_5_93_94_200.43	221.48	66.2815	1.57	–0.22	–0.13	10.94
1262_C_13_H_5_99_100_200.49	221.54	66.2837	1.46	–0.22	–0.14	10.95
1262_C_13_H_5_105_106_200.55	221.60	66.2859	1.44	–0.25	–0.16	11.07
1262_C_13_H_5_108_109_200.58	221.63	66.2870	1.66	–0.05	0.06	10.08
1262_C_13_H_5_114_115_200.64	221.69	66.2891	1.53	–0.09	0.02	10.28
1262_C_13_H_5_117_118_200.67	221.72	66.2902	1.50	–0.10	0.00	10.34
1262_C_13_H_5_120_121_200.7	221.75	66.2913	1.61	–0.08	0.03	10.24
1262_C_13_H_5_123_124_200.73	221.77	66.2924	1.64	–0.04	0.07	10.05
1262_C_13_H_5_129_130_200.79	221.84	66.2946	1.63	–0.04	0.07	10.05
1262_C_13_H_5_132_133_200.82	221.87	66.2957	1.70	–0.03	0.08	10.01
1262_C_13_H_5_138_139_200.88	221.93	66.2979	1.72	0.00	0.12	9.84
1262_C_13_H_5_144_145_200.94	221.99	66.3000	1.66	–0.04	0.06	10.07
1262_C_13_H_5_147_148_200.97	222.02	66.3011	1.68	–0.09	0.01	10.31
1262_C_13_H_6_0_1_201	222.05	66.3022	1.66	–0.08	0.02	10.27
1262_C_13_H_6_3_4_201.03	222.08	66.3033	1.55	–0.11	–0.01	10.42
1262_C_13_H_6_9_10_201.09	222.13	66.3055	1.49	0.04	0.15	9.68
1262_C_13_H_6_12_13_201.12	222.16	66.3066	1.42	0.05	0.17	9.60
1262_C_13_H_6_18_19_201.18	222.23	66.3088	1.49	0.09	0.21	9.43
1262_C_13_H_6_24_25_201.24	222.29	66.3109	1.62	0.16	0.29	9.09
1262_C_13_H_6_27_28_201.27	222.32	66.3120	1.61	0.22	0.35	8.80
1262_C_13_H_6_30_31_201.3	222.35	66.3131	1.56	0.07	0.19	9.53
1262_C_13_H_6_36_37_201.36	222.41	66.3153	1.70	0.16	0.29	9.06
1262_C_13_H_6_39_40_201.39	222.44	66.3164	1.61	0.03	0.15	9.71
1262_C_13_H_6_42_43_201.42	222.47	66.3175	1.67	0.23	0.37	8.72
1262_C_13_H_6_51_52_201.51	222.55	66.3207	1.60	0.14	0.27	9.15
1262_C_13_H_6_54_55_201.54	222.59	66.3218	1.57	0.12	0.25	9.27
1262_C_13_H_6_57_58_201.57	222.62	66.3229	1.57	0.19	0.33	8.91
1262_C_13_H_6_60_61_201.6	222.65	66.3240	1.51	0.19	0.32	8.94
1262_C_13_H_6_66_67_201.66	222.71	66.3262	1.60	0.39	0.55	7.97
1262_C_13_H_6_75_76_201.75	222.80	66.3295	1.60	0.30	0.44	8.41
1262_C_13_H_6_81_82_201.81	222.86	66.3316	1.55	0.18	0.32	8.97
1262_C_13_H_6_87_88_201.87	222.91	66.3338	1.51	0.19	0.33	8.93
1262_C_13_H_6_90_91_201.9	222.95	66.3349	1.41	0.10	0.23	9.36
1262_C_13_H_6_96_97_201.96	223.01	66.3371	1.39	0.25	0.39	8.64
1262_C_13_H_6_102_103_202.02	223.07	66.3398	1.36	0.41	0.57	7.85
1262_C_13_H_6_108_109_202.08	223.13	66.3430	1.77	0.42	0.58	7.82
1262_C_13_H_6_111_112_202.11	223.16	66.3446	1.76	0.36	0.52	8.08
1262_C_13_H_6_117_118_202.17	223.22	66.3477	1.83	0.47	0.64	7.56
1262_C_13_H_7_32_33_202.52	223.57	66.3661	1.81	0.38	0.53	8.02
1262_C_13_H_7_38_39_202.58	223.63	66.3693	1.74	0.33	0.49	8.22
1262_C_13_H_7_44_45_202.64	223.69	66.3725	1.68	0.25	0.39	8.64
1262_C_13_H_7_47_48_202.67	223.72	66.3740	1.59	0.28	0.42	8.50
1262_C_13_H_7_56_57_202.76	223.80	66.3788	1.44	0.22	0.36	8.77
1262_C_13_H_7_59_60_202.79	223.84	66.3803	1.40	0.18	0.31	8.99
1262_C_13_H_7_62_63_202.82	223.87	66.3819	1.70	0.36	0.52	8.08
1262_C_13_H_7_71_72_202.91	223.96	66.3867	1.64	0.32	0.47	8.30
1262_C_13_H_7_74_75_202.94	223.99	66.3882	1.41	0.20	0.33	8.89
1262_C_13_H_7_77_78_202.97	224.02	66.3898	1.48	0.31	0.46	8.32
1262_C_13_H_7_83_84_203.03	224.08	66.3930	1.50	0.39	0.55	7.93

1262_C_13_H_7_92_93_203.12	224.16	66.3977	1.44	0.41	0.57	7.88
1262_C_13_H_7_98_99_203.18	224.23	66.4009	1.27	0.15	0.28	9.14
1262_C_13_H_7_101_102_203.21	224.26	66.4024	1.44	0.42	0.59	7.80
1262_C_13_H_7_104_105_203.24	224.29	66.4040	1.49	0.45	0.61	7.68
1262_C_13_H_7_110_111_203.3	224.35	66.4072	1.38	0.44	0.61	7.70
1262_C_13_H_7_113_114_203.33	224.38	66.4087	1.51	0.38	0.54	8.00
1262_C_13_H_7_116_117_203.36	224.41	66.4103	1.52	0.36	0.52	8.10
1262_C_13_H_7_119_120_203.39	224.44	66.4119	1.38	0.23	0.38	8.71
1262_B_23_H_1_89_90_201.29	224.48	66.4140	1.57	0.36	0.51	8.11
1262_B_23_H_1_95_96_201.35	224.54	66.4172	1.50	0.45	0.62	7.64
1262_B_23_H_1_98_99_201.38	224.57	66.4187	1.43	0.49	0.66	7.47
1262_B_23_H_1_104_105_201.44	224.63	66.4219	1.39	0.42	0.59	7.79
1262_B_23_H_1_110_111_201.5	224.69	66.4251	1.37	0.35	0.50	8.16
1262_B_23_H_1_119_120_201.59	224.77	66.4298	1.43	0.47	0.64	7.56
1262_B_23_H_1_125_126_201.65	224.84	66.4329	1.45	0.46	0.63	7.63
1262_B_23_H_1_134_135_201.74	224.93	66.4377	1.38	0.38	0.54	8.00
1262_B_23_H_1_140_141_201.8	224.99	66.4408	1.38	0.38	0.54	7.98
1262_B_23_H_1_146_147_201.86	225.05	66.4440	1.24	0.35	0.51	8.13
1262_B_23_H_2_2_3_201.92	225.11	66.4471	1.31	0.31	0.46	8.33
1262_B_23_H_2_5_6_201.95	225.13	66.4487	1.29	0.28	0.43	8.48
1262_B_23_H_2_8_9_201.98	225.16	66.4503	1.36	0.35	0.51	8.13
1262_B_23_H_2_14_15_202.04	225.23	66.4535	1.34	0.39	0.55	7.96
1262_B_23_H_2_20_21_202.1	225.29	66.4566	1.48	0.13	0.26	9.23
1262_B_23_H_2_29_30_202.19	225.38	66.4614	1.29	0.27	0.41	8.56
1262_B_23_H_2_35_36_202.25	225.44	66.4645	1.40	0.31	0.47	8.32
1262_B_23_H_2_38_39_202.28	225.47	66.4661	1.33	0.36	0.51	8.11
1262_B_23_H_2_44_45_202.34	225.52	66.4692	1.44	0.37	0.53	8.03
1262_B_23_H_2_47_48_202.37	225.55	66.4708	1.43	0.41	0.58	7.84
1262_B_23_H_2_53_54_202.43	225.62	66.4740	1.27	0.27	0.42	8.53
1262_B_23_H_2_59_60_202.49	225.68	66.4771	1.37	0.28	0.42	8.50
1262_B_23_H_2_68_69_202.58	225.77	66.4819	1.25	0.30	0.45	8.37
1262_B_23_H_2_74_75_202.64	225.83	66.4850	1.17	0.26	0.40	8.60
1262_B_23_H_2_80_81_202.7	225.88	66.4882	1.14	0.25	0.40	8.62
1262_B_23_H_2_89_90_202.79	225.98	66.4929	0.92	0.26	0.40	8.60
1262_B_23_H_2_92_93_202.82	226.01	66.4945	1.35	0.37	0.53	8.05
1262_B_23_H_2_95_96_202.85	226.04	66.4961	1.22	0.38	0.54	8.01
1262_B_23_H_2_101_102_202.91	226.10	66.4992	1.23	0.40	0.56	7.91
1262_B_23_H_2_104_105_202.94	226.13	66.5008	1.30	0.43	0.60	7.75
1262_B_23_H_2_110_111_203	226.19	66.5040	1.23	0.33	0.49	8.22
1262_B_23_H_2_116_117_203.06	226.25	66.5071	1.15	0.27	0.42	8.51
1262_B_23_H_2_125_126_203.15	226.34	66.5119	1.09	0.31	0.46	8.34
1262_B_23_H_2_131_132_203.21	226.40	66.5150	1.22	0.38	0.54	8.01
1262_B_23_H_2_134_135_203.24	226.43	66.5166	1.26	0.25	0.39	8.63
1262_B_23_H_2_140_141_203.3	226.49	66.5197	1.37	0.34	0.49	8.19
1262_B_23_H_2_146_147_203.36	226.55	66.5229	1.39	0.33	0.49	8.23
1262_B_23_H_2_149_150_203.39	226.58	66.5245	1.35	0.35	0.51	8.13
1262_B_23_H_3_2_3_203.42	226.61	66.5261	1.32	0.31	0.46	8.34
1262_B_23_H_3_5_6_203.45	226.63	66.5276	1.28	0.30	0.45	8.38
1262_B_23_H_3_11_12_203.51	226.70	66.5308	1.08	0.27	0.41	8.55
1262_B_23_H_3_14_15_203.54	226.73	66.5323	0.98	0.32	0.47	8.28
1262_B_23_H_3_17_18_203.57	226.76	66.5338	1.10	0.22	0.36	8.78
1262_B_23_H_3_20_21_203.6	226.79	66.5353	1.03	0.22	0.35	8.80
1262_B_23_H_3_29_30_203.69	226.88	66.5398	1.23	0.31	0.47	8.32
1262_B_23_H_3_35_36_203.75	226.94	66.5429	1.41	0.28	0.43	8.48
1262_B_23_H_3_38_39_203.78	226.97	66.5444	1.39	0.38	0.54	7.98
1262_B_23_H_3_41_42_203.81	227.00	66.5462	1.38	0.32	0.47	8.29
1262_C_14_H_1_62_63_203.62	227.05	66.5484	1.29	0.34	0.50	8.18
1262_C_14_H_1_65_66_203.65	227.08	66.5499	1.46	0.41	0.57	7.85
1262_C_14_H_1_71_72_203.71	227.13	66.5530	1.45	0.44	0.60	7.72
1262_C_14_H_1_77_78_203.77	227.20	66.5560	1.40	0.43	0.59	7.77

1262_C_14_H_1_80_81_203.8	227.23	66.5575	1.36	0.35	0.50	8.16
1262_C_14_H_1_86_87_203.86	227.29	66.5605	1.33	0.39	0.55	7.94
1262_C_14_H_1_92_93_203.92	227.35	66.5636	1.27	0.33	0.48	8.26
1262_C_14_H_1_95_96_203.95	227.38	66.5651	1.33	0.41	0.57	7.87
1262_C_14_H_1_101_102_204.01	227.44	66.5681	1.30	0.33	0.48	8.24
1262_C_14_H_1_107_108_204.07	227.50	66.5711	1.55	0.44	0.61	7.70
1262_C_14_H_1_110_111_204.1	227.52	66.5727	1.38	0.47	0.64	7.56
1262_C_14_H_1_116_117_204.16	227.59	66.5757	1.52	0.50	0.67	7.43
1262_C_14_H_1_119_120_204.19	227.62	66.5772	1.55	0.51	0.68	7.38
1262_C_14_H_1_122_123_204.22	227.65	66.5787	1.54	0.50	0.67	7.44
1262_C_14_H_1_131_132_204.31	227.74	66.5833	1.49	0.49	0.66	7.46
1262_C_14_H_1_134_135_204.34	227.77	66.5848	1.45	0.47	0.64	7.58
1262_C_14_H_1_140_141_204.4	227.83	66.5878	1.44	0.39	0.55	7.94
1262_C_14_H_1_146_147_204.46	227.88	66.5908	1.43	0.40	0.56	7.90
1262_C_14_H_1_149_150_204.49	227.91	66.5923	1.28	0.31	0.46	8.34
1262_C_14_H_2_2_3_204.52	227.95	66.5939	1.48	0.47	0.64	7.55
1262_C_14_H_2_5_6_204.55	227.98	66.5954	1.40	0.45	0.62	7.67
1262_C_14_H_2_11_12_204.61	228.04	66.5984	1.46	0.47	0.64	7.55
1262_C_14_H_2_14_15_204.64	228.07	66.5999	1.30	0.38	0.54	7.99
1262_C_14_H_2_17_18_204.67	228.10	66.6014	1.50	0.51	0.68	7.38
1262_C_14_H_2_23_24_204.73	228.16	66.6045	1.47	0.53	0.71	7.27
1262_C_14_H_2_30_31_204.8	228.23	66.6080	1.36	0.47	0.64	7.58
1262_C_14_H_2_33_34_204.83	228.26	66.6095	1.33	0.36	0.51	8.10
1262_C_14_H_2_39_40_204.89	228.32	66.6125	1.24	0.35	0.51	8.12
1262_C_14_H_2_45_46_204.95	228.38	66.6156	1.19	0.41	0.57	7.86
1262_C_14_H_2_48_49_204.98	228.41	66.6171	1.14	0.40	0.56	7.91
1262_C_14_H_2_54_55_205.04	228.47	66.6201	1.27	0.45	0.62	7.66
1262_C_14_H_2_57_58_205.07	228.50	66.6216	1.37	0.40	0.56	7.92
1262_C_14_H_2_63_64_205.13	228.55	66.6247	1.42	0.43	0.59	7.78
1262_C_14_H_2_69_70_205.19	228.62	66.6277	1.40	0.36	0.52	8.08
1262_C_14_H_2_72_73_205.22	228.65	66.6292	1.19	0.37	0.53	8.05
1262_C_14_H_2_75_76_205.25	228.68	66.6307	1.18	0.30	0.45	8.41
1262_C_14_H_2_78_79_205.28	228.71	66.6322	1.29	0.37	0.52	8.06
1262_C_14_H_2_84_85_205.34	228.77	66.6352	1.11	0.34	0.50	8.18
1262_C_14_H_2_87_88_205.37	228.80	66.6367	1.25	0.38	0.54	7.98
1262_C_14_H_2_90_91_205.4	228.83	66.6381	1.26	0.46	0.63	7.63
1262_C_14_H_2_93_94_205.43	228.86	66.6395	1.29	0.40	0.56	7.90
1262_C_14_H_2_99_100_205.49	228.91	66.6423	1.47	0.41	0.58	7.84
1262_C_14_H_2_104_105_205.54	228.97	66.6447	1.53	0.46	0.63	7.60
1262_C_14_H_2_109_110_205.59	229.02	66.6470	1.40	0.49	0.66	7.47
1262_C_14_H_2_115_116_205.65	229.08	66.6499	1.26	0.39	0.55	7.97
1262_C_14_H_2_121_122_205.71	229.13	66.6527	1.17	0.47	0.64	7.58
1262_C_14_H_2_124_125_205.74	229.16	66.6541	1.12	0.30	0.44	8.41
1262_C_14_H_2_127_128_205.77	229.20	66.6555	1.20	0.50	0.68	7.40
1262_C_14_H_2_130_131_205.8	229.23	66.6569	1.21	0.44	0.61	7.70
1262_C_14_H_2_133_134_205.83	229.26	66.6583	1.36	0.54	0.72	7.22
1262_C_14_H_2_136_137_205.86	229.29	66.6598	1.33	0.54	0.72	7.20
1262_C_14_H_2_142_143_205.92	229.35	66.6626	1.44	0.50	0.67	7.43
1262_C_14_H_2_145_146_205.95	229.38	66.6640	1.51	0.48	0.65	7.51
1262_C_14_H_2_148_149_205.98	229.41	66.6654	1.36	0.40	0.56	7.90
1262_C_14_H_3_2_3_206.02	229.45	66.6673	1.37	0.42	0.58	7.82
1262_C_14_H_3_5_6_206.05	229.48	66.6687	1.46	0.53	0.70	7.29
1262_C_14_H_3_8_9_206.08	229.51	66.6701	1.38	0.47	0.64	7.58
1262_C_14_H_3_14_15_206.14	229.57	66.6730	1.35	0.43	0.59	7.77
1262_C_14_H_3_17_18_206.17	229.60	66.6744	1.42	0.45	0.62	7.67
1262_C_14_H_3_20_21_206.2	229.63	66.6758	1.36	0.42	0.58	7.81
1262_C_14_H_3_23_24_206.23	229.66	66.6772	1.54	0.52	0.70	7.31
1262_C_14_H_3_26_27_206.26	229.69	66.6786	1.57	0.53	0.71	7.27
1262_C_14_H_3_32_33_206.32	229.75	66.6814	1.57	0.59	0.78	6.98
1262_C_14_H_3_38_39_206.38	229.80	66.6843	1.68	0.75	0.95	6.24

1262_C_14_H_3_41_42_206.41	229.84	66.6857	1.49	0.55	0.73	7.18
1262_C_14_H_3_44_45_206.44	229.87	66.6871	1.47	0.57	0.76	7.06
1262_C_14_H_3_50_51_206.5	229.93	66.6899	1.45	0.44	0.61	7.71
1262_C_14_H_3_53_54_206.53	229.96	66.6913	1.44	0.46	0.62	7.63
1262_C_14_H_3_56_57_206.56	229.99	66.6928	1.45	0.65	0.84	6.70
1262_C_14_H_3_62_63_206.62	230.05	66.6956	1.40	0.48	0.65	7.51
1262_C_14_H_3_65_66_206.65	230.08	66.6970	1.37	0.48	0.66	7.49
1262_C_14_H_3_68_69_206.68	230.11	66.6984	1.46	0.46	0.63	7.63
1262_C_14_H_3_71_72_206.71	230.13	66.6998	1.43	0.41	0.57	7.85
1262_C_14_H_3_74_75_206.74	230.16	66.7012	1.29	0.52	0.70	7.31
1262_C_14_H_3_77_78_206.77	230.20	66.7027	1.23	0.56	0.74	7.13
1262_C_14_H_3_80_81_206.8	230.23	66.7041	1.43	0.54	0.72	7.23
1262_C_14_H_3_86_87_206.86	230.29	66.7069	1.48	0.59	0.77	6.99
1262_C_14_H_3_89_90_206.89	230.32	66.7083	1.50	0.57	0.76	7.07
1262_C_14_H_3_92_93_206.92	230.35	66.7097	1.47	0.59	0.77	6.99
1262_C_14_H_3_95_96_206.95	230.38	66.7111	1.55	0.56	0.74	7.12
1262_C_14_H_3_98_99_206.98	230.41	66.7126	1.44	0.55	0.72	7.20
1262_C_14_H_3_101_102_207.01	230.44	66.7140	1.40	0.51	0.69	7.37
1262_C_14_H_3_104_105_207.04	230.47	66.7154	1.47	0.50	0.68	7.40
1262_C_14_H_3_110_111_207.1	230.52	66.7182	1.38	0.47	0.64	7.58
1262_C_14_H_3_113_114_207.13	230.55	66.7196	1.43	0.54	0.72	7.21
1262_C_14_H_3_116_117_207.16	230.59	66.7210	1.33	0.46	0.63	7.62
1262_C_14_H_3_119_120_207.19	230.62	66.7225	1.58	0.51	0.69	7.36
1262_C_14_H_3_122_123_207.22	230.65	66.7239	1.49	0.41	0.57	7.86
1262_C_14_H_3_125_126_207.25	230.68	66.7253	1.60	0.56	0.74	7.15
1262_C_14_H_3_128_129_207.28	230.71	66.7267	1.50	0.54	0.72	7.21
1262_C_14_H_3_131_132_207.31	230.74	66.7281	1.61	0.52	0.70	7.32
1262_C_14_H_3_134_135_207.34	230.77	66.7295	1.51	0.55	0.73	7.16
1262_C_14_H_3_140_141_207.4	230.83	66.7324	1.44	0.41	0.57	7.86
1262_C_14_H_3_143_144_207.43	230.86	66.7338	1.47	0.47	0.64	7.58
1262_C_14_H_3_146_147_207.46	230.88	66.7357	1.28	0.51	0.69	7.37
1262_C_14_H_3_149_150_207.49	230.91	66.7378	1.57	0.54	0.72	7.23
1262_C_14_H_4_2_3_207.52	230.95	66.7399	1.53	0.48	0.65	7.51
1262_C_14_H_4_5_6_207.55	230.98	66.7420	1.50	0.51	0.68	7.38
1262_C_14_H_4_8_9_207.58	231.01	66.7441	1.55	0.55	0.73	7.17
1262_C_14_H_4_11_12_207.61	231.04	66.7462	1.53	0.52	0.70	7.32
1262_C_14_H_4_14_15_207.64	231.07	66.7483	1.49	0.48	0.65	7.53
1262_C_14_H_4_20_21_207.7	231.13	66.7525	1.37	0.46	0.63	7.62
1262_C_14_H_4_23_24_207.73	231.16	66.7546	1.48	0.55	0.74	7.16
1262_C_14_H_4_29_30_207.79	231.22	66.7588	1.67	0.63	0.82	6.80
1262_C_14_H_4_32_33_207.82	231.25	66.7609	1.66	0.61	0.80	6.88
1262_C_14_H_4_35_36_207.85	231.27	66.7630	1.56	0.81	1.03	5.92
1262_C_14_H_4_38_39_207.88	231.30	66.7651	1.69	0.81	1.02	5.93
1262_C_14_H_4_44_45_207.94	231.37	66.7692	1.57	0.87	1.09	5.66
1262_C_14_H_4_47_48_207.97	231.40	66.7713	1.62	0.55	0.73	7.17
1262_C_14_H_4_50_51_208	231.43	66.7734	1.64	0.65	0.84	6.70
1262_C_14_H_4_56_57_208.06	231.49	66.7776	1.57	0.55	0.73	7.20
1262_C_14_H_4_59_60_208.09	231.52	66.7797	1.60	0.60	0.78	6.95
1262_C_14_H_4_62_63_208.12	231.55	66.7818	1.58	0.55	0.73	7.19
1262_C_14_H_4_65_66_208.15	231.58	66.7839	1.49	0.54	0.72	7.23
1262_C_14_H_4_68_69_208.18	231.61	66.7860	1.52	0.46	0.63	7.60
1262_C_14_H_4_71_72_208.21	231.63	66.7881	1.49	0.51	0.68	7.38
1262_C_14_H_4_74_75_208.24	231.66	66.7902	1.58	0.54	0.72	7.21
1262_C_14_H_4_77_78_208.27	231.70	66.7923	1.60	0.48	0.66	7.49
1262_C_14_H_4_80_81_208.3	231.73	66.7944	1.63	0.54	0.72	7.23
1262_C_14_H_4_83_84_208.33	231.76	66.7965	1.65	0.53	0.71	7.27
1262_C_14_H_4_86_87_208.36	231.79	66.7986	1.55	0.50	0.68	7.40
1262_C_14_H_4_92_93_208.42	231.85	66.8027	1.67	0.57	0.75	7.10
1262_C_14_H_4_95_96_208.45	231.88	66.8048	1.61	0.60	0.79	6.93
1262_C_14_H_4_98_99_208.48	231.91	66.8069	1.66	0.60	0.79	6.94

1262_C_14_H_4_101_102_208.51	231.94	66.8090	1.58	0.59	0.77	7.00
1262_C_14_H_4_104_105_208.54	231.97	66.8111	1.52	0.57	0.76	7.07
1262_C_14_H_4_107_108_208.57	232.00	66.8132	1.67	0.63	0.82	6.82
1262_C_14_H_4_110_111_208.6	232.02	66.8153	1.55	0.52	0.69	7.34
1262_C_14_H_4_113_114_208.63	232.05	66.8174	1.58	0.53	0.70	7.30
1262_C_14_H_4_116_117_208.66	232.09	66.8195	1.65	0.56	0.74	7.13
1262_C_14_H_4_119_120_208.69	232.12	66.8216	1.54	0.55	0.74	7.16
1262_C_14_H_4_122_123_208.72	232.15	66.8237	1.52	0.54	0.72	7.21
1262_C_14_H_4_125_126_208.75	232.18	66.8258	1.56	0.56	0.74	7.15
1262_C_14_H_4_128_129_208.78	232.21	66.8279	1.57	0.53	0.70	7.29
1262_C_14_H_4_131_132_208.81	232.24	66.8300	1.58	0.58	0.77	7.02
1262_C_14_H_4_134_135_208.84	232.27	66.8321	1.65	0.57	0.75	7.08
1262_C_14_H_4_137_138_208.87	232.30	66.8342	1.66	0.54	0.72	7.21
1262_C_14_H_4_140_141_208.9	232.33	66.8362	1.62	0.51	0.69	7.35
1262_C_14_H_4_143_144_208.93	232.36	66.8383	1.60	0.52	0.70	7.32
1262_C_14_H_4_146_147_208.96	232.38	66.8404	1.64	0.59	0.78	6.96
1262_C_14_H_4_149_150_208.99	232.41	66.8425	1.58	0.53	0.71	7.27
1262_C_14_H_5_2_3_209.02	232.45	66.8446	1.51	0.47	0.64	7.56
1262_C_14_H_5_8_9_209.08	232.51	66.8488	1.62	0.61	0.80	6.89
1262_C_14_H_5_11_12_209.11	232.54	66.8509	1.48	0.54	0.72	7.24
1262_C_14_H_5_14_15_209.14	232.57	66.8530	1.61	0.65	0.84	6.72
1262_C_14_H_5_17_18_209.17	232.60	66.8551	1.58	0.57	0.75	7.09
1262_C_14_H_5_20_21_209.2	232.63	66.8572	1.44	0.52	0.69	7.34
1262_C_14_H_5_23_24_209.23	232.66	66.8593	1.65	0.62	0.81	6.85
1262_C_14_H_5_26_27_209.26	232.69	66.8614	1.63	0.58	0.77	7.02
1262_C_14_H_5_29_30_209.29	232.72	66.8635	1.61	0.52	0.70	7.32
1262_C_14_H_5_32_33_209.32	232.75	66.8656	1.54	0.51	0.68	7.40
1262_C_14_H_5_38_39_209.38	232.80	66.8697	1.57	0.47	0.65	7.54
1262_C_14_H_5_44_45_209.44	232.87	66.8739	1.54	0.48	0.65	7.53
1262_C_14_H_5_47_48_209.47	232.90	66.8760	1.63	0.47	0.64	7.56
1262_C_14_H_5_50_51_209.5	232.93	66.8781	1.56	0.48	0.65	7.52
1262_C_14_H_5_53_54_209.53	232.96	66.8802	1.57	0.45	0.62	7.64
1262_C_14_H_5_56_57_209.56	232.99	66.8823	1.49	0.49	0.66	7.47
1262_C_14_H_5_59_60_209.59	233.02	66.8844	1.55	0.50	0.67	7.43
1262_C_14_H_5_62_63_209.62	233.05	66.8865	1.46	0.46	0.63	7.61
1262_C_14_H_5_65_66_209.65	233.08	66.8886	1.50	0.41	0.57	7.86
1262_C_14_H_5_68_69_209.68	233.11	66.8907	1.58	0.50	0.67	7.42
1262_C_14_H_5_71_72_209.71	233.13	66.8928	1.53	0.53	0.71	7.28
1262_C_14_H_5_74_75_209.74	233.16	66.8949	1.53	0.44	0.61	7.70
1262_C_14_H_5_77_78_209.77	233.20	66.8970	1.59	0.47	0.64	7.58
1262_C_14_H_5_80_81_209.8	233.23	66.8991	1.59	0.47	0.65	7.54
1262_C_14_H_5_86_87_209.86	233.29	66.9032	1.56	0.54	0.71	7.25
1262_C_14_H_5_89_90_209.89	233.32	66.9053	1.52	0.50	0.68	7.41
1262_C_14_H_5_92_93_209.92	233.35	66.9074	1.44	0.43	0.60	7.74
1262_C_14_H_5_95_96_209.95	233.38	66.9095	1.43	0.38	0.53	8.02
1262_C_14_H_5_98_99_209.98	233.41	66.9116	1.46	0.37	0.53	8.03
1262_C_14_H_5_101_102_210.01	233.44	66.9137	1.49	0.58	0.77	7.01
1262_C_14_H_5_104_105_210.04	233.47	66.9158	1.44	0.55	0.73	7.17
1262_C_14_H_5_107_108_210.07	233.50	66.9179	1.55	0.54	0.72	7.22
1262_C_14_H_5_110_111_210.1	233.52	66.9200	1.50	0.59	0.78	6.98
1262_C_14_H_5_113_114_210.13	233.55	66.9221	1.60	0.59	0.77	6.99
1262_C_14_H_5_116_117_210.16	233.59	66.9242	1.66	0.66	0.85	6.65
1262_C_14_H_5_119_120_210.19	233.62	66.9263	1.65	0.58	0.77	7.03
1262_C_14_H_5_122_123_210.22	233.65	66.9284	1.52	0.60	0.79	6.94
1262_C_14_H_5_125_126_210.25	233.68	66.9305	1.52	0.56	0.74	7.14
1262_C_14_H_5_128_129_210.28	233.71	66.9326	1.50	0.53	0.71	7.27
1262_C_14_H_5_131_132_210.31	233.74	66.9346	1.49	0.52	0.70	7.31
1262_C_14_H_5_134_135_210.34	233.77	66.9368	1.45	0.42	0.59	7.80
1262_C_14_H_5_140_141_210.4	233.83	66.9411	1.42	0.51	0.69	7.37
1262_C_14_H_5_143_144_210.43	233.86	66.9433	1.48	0.50	0.67	7.42

1262_C_14_H_5_146_147_210.46	233.88	66.9454	1.53	0.52	0.70	7.31
1262_C_14_H_6_2_3_210.52	233.95	66.9497	1.65	0.56	0.74	7.12
1262_C_14_H_6_5_6_210.55	233.98	66.9519	1.62	0.52	0.70	7.32
1262_C_14_H_6_8_9_210.58	234.01	66.9541	1.60	0.56	0.74	7.14
1262_C_14_H_6_11_12_210.61	234.04	66.9562	1.59	0.54	0.72	7.24
1262_C_14_H_6_14_15_210.64	234.07	66.9584	1.54	0.43	0.59	7.78
1262_C_14_H_6_23_24_210.73	234.16	66.9648	1.50	0.46	0.63	7.61
1262_C_14_H_6_26_27_210.76	234.19	66.9670	1.53	0.46	0.63	7.61
1262_C_14_H_6_29_30_210.79	234.22	66.9692	1.59	0.44	0.61	7.69
1262_C_14_H_6_32_33_210.82	234.25	66.9713	1.51	0.48	0.65	7.52
1262_C_14_H_6_38_39_210.88	234.30	66.9756	1.63	0.49	0.66	7.46
1262_C_14_H_6_41_42_210.91	234.34	66.9778	1.71	0.53	0.70	7.29
1262_C_14_H_6_44_45_210.94	234.37	66.9799	1.67	0.52	0.70	7.30
1262_C_14_H_6_47_48_210.97	234.40	66.9821	1.63	0.51	0.68	7.38
1262_C_14_H_6_53_54_211.03	234.46	66.9864	1.73	0.60	0.78	6.95
1262_C_14_H_6_56_57_211.06	234.49	66.9886	1.57	0.59	0.78	6.98
1262_C_14_H_6_59_60_211.09	234.52	66.9907	1.48	0.59	0.77	7.01
1262_C_14_H_6_62_63_211.12	234.55	66.9929	1.45	0.62	0.81	6.84
1262_C_14_H_6_65_66_211.15	234.58	66.9951	1.52	0.63	0.82	6.81
1262_C_14_H_6_71_72_211.21	234.63	66.9994	1.55	0.60	0.79	6.94
1262_C_14_H_6_74_75_211.24	234.66	67.0015	1.50	0.65	0.84	6.70
1262_C_14_H_6_77_78_211.27	234.70	67.0037	1.58	0.64	0.84	6.73
1262_C_14_H_6_83_84_211.33	234.76	67.0080	1.66	0.67	0.86	6.61
1262_C_14_H_6_89_90_211.39	234.82	67.0123	1.44	0.54	0.72	7.24
1262_C_14_H_6_92_93_211.42	234.85	67.0145	1.44	0.55	0.73	7.18
1262_C_14_H_6_95_96_211.45	234.88	67.0166	1.48	0.56	0.74	7.13
1262_C_14_H_6_101_102_211.51	234.94	67.0209	1.51	0.46	0.63	7.59
1262_C_14_H_6_107_108_211.57	235.00	67.0253	1.56	0.53	0.70	7.29
1262_C_14_H_6_110_111_211.6	235.02	67.0274	1.60	0.53	0.71	7.27
1262_C_14_H_6_113_114_211.63	235.05	67.0296	1.58	0.59	0.77	6.99
1262_C_14_H_6_119_120_211.69	235.12	67.0339	1.38	0.55	0.73	7.17
1262_C_14_H_6_122_123_211.72	235.15	67.0360	1.42	0.54	0.71	7.25
1262_C_14_H_6_125_126_211.75	235.18	67.0382	1.37	0.47	0.64	7.55
1262_C_14_H_6_128_129_211.78	235.21	67.0404	1.34	0.42	0.59	7.79
1262_C_14_H_6_134_135_211.84	235.27	67.0447	1.40	0.53	0.71	7.27
1262_C_14_H_6_137_138_211.87	235.30	67.0468	1.47	0.53	0.71	7.28
1262_C_14_H_6_140_141_211.9	235.33	67.0490	1.60	0.55	0.73	7.18
1262_C_14_H_6_146_147_211.96	235.38	67.0533	1.63	0.62	0.81	6.83
1262_C_14_H_6_149_150_211.99	235.41	67.0555	1.58	0.59	0.77	7.01
1262_C_14_H_7_2_3_212.02	235.45	67.0576	1.58	0.59	0.77	7.00
1262_C_14_H_7_5_6_212.05	235.48	67.0598	1.39	0.53	0.71	7.26
1262_C_14_H_7_8_9_212.08	235.51	67.0619	1.33	0.52	0.70	7.32
1262_C_14_H_7_11_12_212.11	235.54	67.0641	1.34	0.51	0.69	7.37
1262_C_14_H_7_14_15_212.14	235.57	67.0663	1.33	0.50	0.67	7.42
1262_C_14_H_7_17_18_212.17	235.60	67.0684	1.52	0.55	0.74	7.16
1262_C_14_H_7_20_21_212.2	235.63	67.0706	1.52	0.63	0.83	6.77
1262_C_14_H_7_23_24_212.23	235.66	67.0727	1.52	0.59	0.78	6.98
1262_C_14_H_7_26_27_212.26	235.69	67.0749	1.58	0.65	0.84	6.72
1262_C_14_H_7_32_33_212.32	235.75	67.0792	1.62	0.58	0.77	7.01
1262_C_14_H_7_35_36_212.35	235.77	67.0814	1.59	0.67	0.86	6.62
1262_C_14_H_7_38_39_212.38	235.80	67.0835	1.56	0.63	0.82	6.80
1262_C_14_H_7_41_42_212.41	235.84	67.0857	1.51	0.62	0.80	6.87
1262_C_14_H_7_44_45_212.44	235.87	67.0878	1.38	0.57	0.75	7.10
1262_C_14_H_7_47_48_212.47	235.90	67.0900	1.42	0.60	0.78	6.96
1262_C_14_H_7_50_51_212.5	235.93	67.0921	1.46	0.58	0.76	7.04
1262_C_14_H_7_53_54_212.53	235.96	67.0943	1.47	0.61	0.80	6.90
1262_C_14_H_7_56_57_212.56	235.99	67.0965	1.52	0.60	0.79	6.93
1262_C_14_H_7_59_60_212.59	236.02	67.0986	1.54	0.60	0.79	6.94
1262_C_14_H_7_62_63_212.62	236.05	67.1008	1.58	0.60	0.79	6.92
1262_C_14_H_7_65_66_212.65	236.08	67.1029	1.58	0.60	0.79	6.94

Appendix 5. Recalibrated estimates for atmospheric pCO_2 based on the pedogenic carbonate proxy, using an updated value of 2500 ppm for the soil respired CO_2 concentration (S_z) parameter in the Cerling palaeobarometer. Also shown are the original estimates for pCO_2 reported in the literature. The literature sources for all original data are shown.

Revised age (Ma; this study)	pCO_2 (ppmV; from literature)	Recalibrated pCO_2 (ppmV; this study)	Recalibrated pCO_2 upper limit (ppmV)	Recalibrated pCO_2 lower limit (ppmV)	Literature source for original data
55.50	820	410	574	246	Koch et al. (1992)
56.50	1070	535	749	321	Koch et al. (1992)
55.50	500	125	175	75	Sinha & Stott (1994)
56.50	500	125	175	75	Sinha & Stott (1994)
54.10	2034	1017	1424	610	Royer et al. (2001)
54.80	577	289	404	173	Royer et al. (2001)
56.10	1152	576	806	346	Royer et al. (2001)
56.40	1217	609	852	365	Royer et al. (2001)
56.60	1448	724	1014	434	Royer et al. (2001)
64.52	999	499	699	300	Nordt et al. (2002)
65.02	833	417	583	250	Nordt et al. (2002)
66.02	759	379	531	228	Nordt et al. (2002)
66.32	1440	720	1008	432	Nordt et al. (2002)
64.67	534	223	312	134	Nordt et al. (2003)
64.76	488	203	285	122	Nordt et al. (2003)
64.89	264	110	154	66	Nordt et al. (2003)
65.13	334	139	195	84	Nordt et al. (2003)
65.29	533	222	311	133	Nordt et al. (2003)
65.43	161	67	94	40	Nordt et al. (2003)
65.60	549	229	320	137	Nordt et al. (2003)
65.76	832	347	485	208	Nordt et al. (2003)
65.95	271	113	158	68	Nordt et al. (2003)
66.02	0	0	0	0	Nordt et al. (2003)
66.06	127	53	74	32	Nordt et al. (2003)
66.12	45	19	26	11	Nordt et al. (2003)
66.16	790	329	461	198	Nordt et al. (2003)
66.23	1358	566	792	340	Nordt et al. (2003)
66.38	1277	532	745	319	Nordt et al. (2003)
66.45	796	332	464	199	Nordt et al. (2003)
66.51	657	274	383	164	Nordt et al. (2003)
66.56	385	160	225	96	Nordt et al. (2003)
63.60	399	212	297	127	Huang et al. (2013)
63.70	341	285	400	171	Huang et al. (2013)
64.60	326	244	342	147	Huang et al. (2013)
64.70	456	430	602	258	Huang et al. (2013)
64.90	286	214	300	129	Huang et al. (2013)
65.00	584	437	612	262	Huang et al. (2013)
65.10	451	352	493	211	Huang et al. (2013)
65.20	569	536	751	322	Huang et al. (2013)
65.40	470	443	620	266	Huang et al. (2013)
66.50	837	442	618	265	Huang et al. (2013)

Appendix 6. Compilation of raw estimates for atmospheric pCO_2 based on stomatal indices, liverworts, phytoplankton, boron isotopes, oxygen isotopes, and C3 plants. Atmospheric pCO_2 estimates remain unchanged from the cited literature source. Estimates based on C3 plants (Cui & Schubert, 2017) are given for the PETM, H1, H2, I1, and I2 events, including pre-event (background) pCO_2 concentrations and peak event concentrations, calculated assuming either a very isotopically light methane (CH_4) or an isotopically heavier organic matter (C_{org}) source of carbon release for these Early Eocene events.

Proxy	Revised age (Ma; this study)	Published pCO_2 (ppmV)	Literature source for original data
Stomatal Indices	54.1	443	Royer et al. (2001), recalibrated by Beerling et al. (2009)
Stomatal Indices	54.2	327	Royer et al. (2001), recalibrated by Beerling et al. (2009)
Stomatal Indices	54.6	378	Royer et al. (2001), recalibrated by Beerling et al. (2009)
Stomatal Indices	55.5	479	Royer et al. (2001), recalibrated by Beerling et al. (2009)
Stomatal Indices	55.8	667	Royer et al. (2001), recalibrated by Beerling et al. (2009)
Stomatal Indices	56.0	307	Royer et al. (2001), recalibrated by Beerling et al. (2009)
Stomatal Indices	56.0	307	Royer et al. (2001), recalibrated by Beerling et al. (2009)
Stomatal Indices	56.0	307	Royer et al. (2001), recalibrated by Beerling et al. (2009)
Stomatal Indices	56.0	520	Royer et al. (2001), recalibrated by Beerling et al. (2009)
Stomatal Indices	56.1	304	Royer et al. (2001), recalibrated by Beerling et al. (2009)
Stomatal Indices	56.3	313	Royer et al. (2001), recalibrated by Beerling et al. (2009)
Stomatal Indices	56.4	316	Royer et al. (2001), recalibrated by Beerling et al. (2009)
Stomatal Indices	56.5	320	Royer et al. (2001), recalibrated by Beerling et al. (2009)
Stomatal Indices	56.6	315	Royer et al. (2001), recalibrated by Beerling et al. (2009)
Stomatal Indices	56.6	318	Royer et al. (2001), recalibrated by Beerling et al. (2009)
Stomatal Indices	56.6	318	Royer et al. (2001), recalibrated by Beerling et al. (2009)
Stomatal Indices	57.1	469	Royer et al. (2001), recalibrated by Beerling et al. (2009)
Stomatal Indices	58.0	447	Royer et al. (2001), recalibrated by Beerling et al. (2009)
Stomatal Indices	60.0	535	Royer et al. (2001), recalibrated by Beerling et al. (2009)
Stomatal Indices	60.0	574	Royer et al. (2001), recalibrated by Beerling et al. (2009)
Stomatal Indices	66.4	423	Beerling et al. (2002), recalibrated by Barclay & Wing (2016)
Stomatal Indices	66.8	628	Beerling et al. (2002), recalibrated by Barclay & Wing (2016)
Stomatal Indices	66.9	648	Beerling et al. (2002), recalibrated by Barclay & Wing (2016)
Stomatal Indices	54.3	326	Royer et al. (2003), recalibrated by Barclay & Wing (2016)
Stomatal Indices	54.4	266	Royer et al. (2003), recalibrated by Barclay & Wing (2016)
Stomatal Indices	54.8	333	Royer et al. (2003), recalibrated by Barclay & Wing (2016)
Stomatal Indices	55.7	376	Royer et al. (2003), recalibrated by Barclay & Wing (2016)
Stomatal Indices	56.0	407	Royer et al. (2003), recalibrated by Barclay & Wing (2016)
Stomatal Indices	56.2	443	Royer et al. (2003), recalibrated by Barclay & Wing (2016)
Stomatal Indices	56.2	176	Royer et al. (2003), recalibrated by Barclay & Wing (2016)
Stomatal Indices	56.2	191	Royer et al. (2003), recalibrated by Barclay & Wing (2016)
Stomatal Indices	56.2	169	Royer et al. (2003), recalibrated by Barclay & Wing (2016)
Stomatal Indices	56.3	175	Royer et al. (2003), recalibrated by Barclay & Wing (2016)
Stomatal Indices	56.5	202	Royer et al. (2003), recalibrated by Barclay & Wing (2016)
Stomatal Indices	56.6	214	Royer et al. (2003), recalibrated by Barclay & Wing (2016)
Stomatal Indices	56.7	243	Royer et al. (2003), recalibrated by Barclay & Wing (2016)
Stomatal Indices	56.8	226	Royer et al. (2003), recalibrated by Barclay & Wing (2016)
Stomatal Indices	56.8	234	Royer et al. (2003), recalibrated by Barclay & Wing (2016)
Stomatal Indices	56.8	205	Royer et al. (2003), recalibrated by Barclay & Wing (2016)
Stomatal Indices	57.3	384	Royer et al. (2003), recalibrated by Barclay & Wing (2016)
Stomatal Indices	58.2	350	Royer et al. (2003), recalibrated by Barclay & Wing (2016)
Stomatal Indices	59.4	543	Royer et al. (2003), recalibrated by Barclay & Wing (2016)
Stomatal Indices	59.4	479	Royer et al. (2003), recalibrated by Barclay & Wing (2016)
Stomatal Indices	62.0	227	Royer et al. (2003), recalibrated by Barclay & Wing (2016)

Stomatal Indices	65.1	287	Royer et al. (2003), recalibrated by Barclay & Wing (2016)
Stomatal Indices	65.5	316	Royer et al. (2003), recalibrated by Barclay & Wing (2016)
Stomatal Indices	65.5	331	Royer et al. (2003), recalibrated by Barclay & Wing (2016)
Stomatal Indices	66.5	432	Royer et al. (2003), recalibrated by Barclay & Wing (2016)
Stomatal Indices	60	311	Steinthorsdottir et al. (2016)
Stomatal Indices	65.5	387	Steinthorsdottir et al. (2016)
Stomatal Indices	65.9	396	Steinthorsdottir et al. (2016)
Stomatal Indices	67	568	Steinthorsdottir et al. (2016)
Liverworts	58.8	583	Fletcher et al. (2008)
Phytoplankton	55.5	500	Stott (1992)
Phytoplankton	56.0	600	Stott (1992)
Boron isotopes	53.2	1400	Anagnostou et al. (2016)
Boron isotopes	53.2	506	Demicco et al. (2003)
Boron isotopes	55.8	939	Demicco et al. (2003)
Boron isotopes	57.1	703	Demicco et al. (2003)
Oxygen isotopes	55.5	630	Gehler et al. (2016); assuming modern gross primary productivity
Oxygen isotopes	55.64	230	Gehler et al. (2016); assuming modern gross primary productivity
Oxygen isotopes	56	440	Gehler et al. (2016); assuming modern gross primary productivity
Oxygen isotopes	56.2	450	Gehler et al. (2016); assuming modern gross primary productivity
Oxygen isotopes	55.5	1450	Gehler et al. (2016); assuming 2.3 times modern gross primary productivity
Oxygen isotopes	55.6	530	Gehler et al. (2016); assuming 2.3 times modern gross primary productivity
Oxygen isotopes	56.0	1010	Gehler et al. (2016); assuming 2.3 times modern gross primary productivity
Oxygen isotopes	56.2	1040	Gehler et al. (2016); assuming 2.3 times modern gross primary productivity
C3 plants	53.0	532	Cui & Schubert (2016)
C3 plants	54.4	395	Cui & Schubert (2016)
C3 plants	55.3	579	Cui & Schubert (2016)
C3 plants	56.0	530	Cui & Schubert (2016)
C3 plants	56.1	552	Cui & Schubert (2016)
C3 plants	56	379	Cui & Schubert (2017); background PETM; CH_4 release scenario
C3 plants	56	456	Cui & Schubert (2017); background PETM; CH_4 release scenario
C3 plants	56	180	Cui & Schubert (2017); background PETM; CH_4 release scenario
C3 plants	56	217	Cui & Schubert (2017); background PETM; CH_4 release scenario
C3 plants	56	202	Cui & Schubert (2017); background PETM; CH_4 release scenario
C3 plants	56	236	Cui & Schubert (2017); background PETM; CH_4 release scenario
C3 plants	56	244	Cui & Schubert (2017); background PETM; CH_4 release scenario
C3 plants	56	286	Cui & Schubert (2017); background PETM; CH_4 release scenario
C3 plants	56	238	Cui & Schubert (2017); background PETM; CH_4 release scenario
C3 plants	56	280	Cui & Schubert (2017); background PETM; CH_4 release scenario
C3 plants	56	538	Cui & Schubert (2017); background PETM; C_{org} release scenario
C3 plants	56	651	Cui & Schubert (2017); background PETM; C_{org} release scenario
C3 plants	56	276	Cui & Schubert (2017); background PETM; C_{org} release scenario
C3 plants	56	336	Cui & Schubert (2017); background PETM; C_{org} release scenario
C3 plants	56	311	Cui & Schubert (2017); background PETM; C_{org} release scenario
C3 plants	56	361	Cui & Schubert (2017); background PETM; C_{org} release scenario
C3 plants	56	363	Cui & Schubert (2017); background PETM; C_{org} release scenario
C3 plants	56	425	Cui & Schubert (2017); background PETM; C_{org} release scenario
C3 plants	56	356	Cui & Schubert (2017); background PETM; C_{org} release scenario
C3 plants	56	416	Cui & Schubert (2017); background PETM; C_{org} release scenario
C3 plants	55.87	959	Cui & Schubert (2017); peak PETM; CH_4 release scenario
C3 plants	55.87	1038	Cui & Schubert (2017); peak PETM; CH_4 release scenario
C3 plants	55.87	479	Cui & Schubert (2017); peak PETM; CH_4 release scenario
C3 plants	55.87	532	Cui & Schubert (2017); peak PETM; CH_4 release scenario
C3 plants	55.87	543	Cui & Schubert (2017); peak PETM; CH_4 release scenario
C3 plants	55.87	577	Cui & Schubert (2017); peak PETM; CH_4 release scenario
C3 plants	55.87	648	Cui & Schubert (2017); peak PETM; CH_4 release scenario
C3 plants	55.87	691	Cui & Schubert (2017); peak PETM; CH_4 release scenario

C3 plants	55.87	632	Cui & Schubert (2017); peak PETM; CH_4 release scenario
C3 plants	55.87	676	Cui & Schubert (2017); peak PETM; CH_4 release scenario
C3 plants	55.87	2001	Cui & Schubert (2017); peak PETM; C_{org} release scenario
C3 plants	55.87	2117	Cui & Schubert (2017); peak PETM; C_{org} release scenario
C3 plants	55.87	951	Cui & Schubert (2017); peak PETM; C_{org} release scenario
C3 plants	55.87	1097	Cui & Schubert (2017); peak PETM; C_{org} release scenario
C3 plants	55.87	1138	Cui & Schubert (2017); peak PETM; C_{org} release scenario
C3 plants	55.87	1188	Cui & Schubert (2017); peak PETM; C_{org} release scenario
C3 plants	55.87	1354	Cui & Schubert (2017); peak PETM; C_{org} release scenario
C3 plants	55.87	1417	Cui & Schubert (2017); peak PETM; C_{org} release scenario
C3 plants	55.87	1326	Cui & Schubert (2017); peak PETM; C_{org} release scenario
C3 plants	55.87	1387	Cui & Schubert (2017); peak PETM; C_{org} release scenario
C3 plants	54.09	339	Cui & Schubert (2017); background H1; CH_4 release scenario
C3 plants	54.09	241	Cui & Schubert (2017); background H1; CH_4 release scenario
C3 plants	54.09	400	Cui & Schubert (2017); background H1; CH_4 release scenario
C3 plants	54.09	289	Cui & Schubert (2017); background H1; CH_4 release scenario
C3 plants	54.09	196	Cui & Schubert (2017); background H1; CH_4 release scenario
C3 plants	54.09	140	Cui & Schubert (2017); background H1; CH_4 release scenario
C3 plants	54.09	205	Cui & Schubert (2017); background H1; CH_4 release scenario
C3 plants	54.09	147	Cui & Schubert (2017); background H1; CH_4 release scenario
C3 plants	54.09	137	Cui & Schubert (2017); background H1; CH_4 release scenario
C3 plants	54.09	94	Cui & Schubert (2017); background H1; CH_4 release scenario
C3 plants	54.09	176	Cui & Schubert (2017); background H1; CH_4 release scenario
C3 plants	54.09	124	Cui & Schubert (2017); background H1; CH_4 release scenario
C3 plants	54.09	228	Cui & Schubert (2017); background H1; CH_4 release scenario
C3 plants	54.09	163	Cui & Schubert (2017); background H1; CH_4 release scenario
C3 plants	54.09	249	Cui & Schubert (2017); background H1; CH_4 release scenario
C3 plants	54.09	179	Cui & Schubert (2017); background H1; CH_4 release scenario
C3 plants	54.09	540	Cui & Schubert (2017); background H1; C_{org} release scenario
C3 plants	54.09	394	Cui & Schubert (2017); background H1; C_{org} release scenario
C3 plants	54.09	609	Cui & Schubert (2017); background H1; C_{org} release scenario
C3 plants	54.09	457	Cui & Schubert (2017); background H1; C_{org} release scenario
C3 plants	54.09	342	Cui & Schubert (2017); background H1; C_{org} release scenario
C3 plants	54.09	257	Cui & Schubert (2017); background H1; C_{org} release scenario
C3 plants	54.09	353	Cui & Schubert (2017); background H1; C_{org} release scenario
C3 plants	54.09	265	Cui & Schubert (2017); background H1; C_{org} release scenario
C3 plants	54.09	261	Cui & Schubert (2017); background H1; C_{org} release scenario
C3 plants	54.09	195	Cui & Schubert (2017); background H1; C_{org} release scenario
C3 plants	54.09	312	Cui & Schubert (2017); background H1; C_{org} release scenario
C3 plants	54.09	236	Cui & Schubert (2017); background H1; C_{org} release scenario
C3 plants	54.09	385	Cui & Schubert (2017); background H1; C_{org} release scenario
C3 plants	54.09	287	Cui & Schubert (2017); background H1; C_{org} release scenario
C3 plants	54.09	416	Cui & Schubert (2017); background H1; C_{org} release scenario
C3 plants	54.09	310	Cui & Schubert (2017); background H1; C_{org} release scenario
C3 plants	54.05	540	Cui & Schubert (2017); peak H1; CH_4 release scenario
C3 plants	54.05	448	Cui & Schubert (2017); peak H1; CH_4 release scenario
C3 plants	54.05	628	Cui & Schubert (2017); peak H1; CH_4 release scenario
C3 plants	54.05	532	Cui & Schubert (2017); peak H1; CH_4 release scenario
C3 plants	54.05	316	Cui & Schubert (2017); peak H1; CH_4 release scenario
C3 plants	54.05	262	Cui & Schubert (2017); peak H1; CH_4 release scenario
C3 plants	54.05	330	Cui & Schubert (2017); peak H1; CH_4 release scenario
C3 plants	54.05	273	Cui & Schubert (2017); peak H1; CH_4 release scenario
C3 plants	54.05	224	Cui & Schubert (2017); peak H1; CH_4 release scenario
C3 plants	54.05	182	Cui & Schubert (2017); peak H1; CH_4 release scenario
C3 plants	54.05	284	Cui & Schubert (2017); peak H1; CH_4 release scenario
C3 plants	54.05	234	Cui & Schubert (2017); peak H1; CH_4 release scenario
C3 plants	54.05	365	Cui & Schubert (2017); peak H1; CH_4 release scenario
C3 plants	54.05	304	Cui & Schubert (2017); peak H1; CH_4 release scenario
C3 plants	54.05	399	Cui & Schubert (2017); peak H1; CH_4 release scenario
C3 plants	54.05	334	Cui & Schubert (2017); peak H1; CH_4 release scenario

C3 plants	54.05	1019	Cui & Schubert (2017); peak H1; C_{org} release scenario
C3 plants	54.05	884	Cui & Schubert (2017); peak H1; C_{org} release scenario
C3 plants	54.05	1124	Cui & Schubert (2017); peak H1; C_{org} release scenario
C3 plants	54.05	1040	Cui & Schubert (2017); peak H1; C_{org} release scenario
C3 plants	54.05	624	Cui & Schubert (2017); peak H1; C_{org} release scenario
C3 plants	54.05	545	Cui & Schubert (2017); peak H1; C_{org} release scenario
C3 plants	54.05	646	Cui & Schubert (2017); peak H1; C_{org} release scenario
C3 plants	54.05	564	Cui & Schubert (2017); peak H1; C_{org} release scenario
C3 plants	54.05	463	Cui & Schubert (2017); peak H1; C_{org} release scenario
C3 plants	54.05	400	Cui & Schubert (2017); peak H1; C_{org} release scenario
C3 plants	54.05	564	Cui & Schubert (2017); peak H1; C_{org} release scenario
C3 plants	54.05	492	Cui & Schubert (2017); peak H1; C_{org} release scenario
C3 plants	54.05	711	Cui & Schubert (2017); peak H1; C_{org} release scenario
C3 plants	54.05	620	Cui & Schubert (2017); peak H1; C_{org} release scenario
C3 plants	54.05	772	Cui & Schubert (2017); peak H1; C_{org} release scenario
C3 plants	54.05	675	Cui & Schubert (2017); peak H1; C_{org} release scenario
C3 plants	54	372	Cui & Schubert (2017); background H2; CH_4 release scenario
C3 plants	54	327	Cui & Schubert (2017); background H2; CH_4 release scenario
C3 plants	54	527	Cui & Schubert (2017); background H2; CH_4 release scenario
C3 plants	54	463	Cui & Schubert (2017); background H2; CH_4 release scenario
C3 plants	54	192	Cui & Schubert (2017); background H2; CH_4 release scenario
C3 plants	54	170	Cui & Schubert (2017); background H2; CH_4 release scenario
C3 plants	54	136	Cui & Schubert (2017); background H2; CH_4 release scenario
C3 plants	54	119	Cui & Schubert (2017); background H2; CH_4 release scenario
C3 plants	54	111	Cui & Schubert (2017); background H2; CH_4 release scenario
C3 plants	54	96	Cui & Schubert (2017); background H2; CH_4 release scenario
C3 plants	54	132	Cui & Schubert (2017); background H2; CH_4 release scenario
C3 plants	54	115	Cui & Schubert (2017); background H2; CH_4 release scenario
C3 plants	54	200	Cui & Schubert (2017); background H2; CH_4 release scenario
C3 plants	54	177	Cui & Schubert (2017); background H2; CH_4 release scenario
C3 plants	54	60	Cui & Schubert (2017); background H2; CH_4 release scenario
C3 plants	54	49	Cui & Schubert (2017); background H2; CH_4 release scenario
C3 plants	54	601	Cui & Schubert (2017); background H2; C_{org} release scenario
C3 plants	54	533	Cui & Schubert (2017); background H2; C_{org} release scenario
C3 plants	54	806	Cui & Schubert (2017); background H2; C_{org} release scenario
C3 plants	54	726	Cui & Schubert (2017); background H2; C_{org} release scenario
C3 plants	54	346	Cui & Schubert (2017); background H2; C_{org} release scenario
C3 plants	54	312	Cui & Schubert (2017); background H2; C_{org} release scenario
C3 plants	54	267	Cui & Schubert (2017); background H2; C_{org} release scenario
C3 plants	54	240	Cui & Schubert (2017); background H2; C_{org} release scenario
C3 plants	54	231	Cui & Schubert (2017); background H2; C_{org} release scenario
C3 plants	54	207	Cui & Schubert (2017); background H2; C_{org} release scenario
C3 plants	54	261	Cui & Schubert (2017); background H2; C_{org} release scenario
C3 plants	54	234	Cui & Schubert (2017); background H2; C_{org} release scenario
C3 plants	54	357	Cui & Schubert (2017); background H2; C_{org} release scenario
C3 plants	54	322	Cui & Schubert (2017); background H2; C_{org} release scenario
C3 plants	54	159	Cui & Schubert (2017); background H2; C_{org} release scenario
C3 plants	54	142	Cui & Schubert (2017); background H2; C_{org} release scenario
C3 plants	53.95	522	Cui & Schubert (2017); peak H2; CH_4 release scenario
C3 plants	53.95	482	Cui & Schubert (2017); peak H2; CH_4 release scenario
C3 plants	53.95	724	Cui & Schubert (2017); peak H2; CH_4 release scenario
C3 plants	53.95	676	Cui & Schubert (2017); peak H2; CH_4 release scenario
C3 plants	53.95	272	Cui & Schubert (2017); peak H2; CH_4 release scenario
C3 plants	53.95	252	Cui & Schubert (2017); peak H2; CH_4 release scenario
C3 plants	53.95	195	Cui & Schubert (2017); peak H2; CH_4 release scenario
C3 plants	53.95	180	Cui & Schubert (2017); peak H2; CH_4 release scenario
C3 plants	53.95	160	Cui & Schubert (2017); peak H2; CH_4 release scenario
C3 plants	53.95	147	Cui & Schubert (2017); peak H2; CH_4 release scenario
C3 plants	53.95	189	Cui & Schubert (2017); peak H2; CH_4 release scenario
C3 plants	53.95	174	Cui & Schubert (2017); peak H2; CH_4 release scenario

C3 plants	53.95	283	Cui & Schubert (2017); peak H2; CH_4 release scenario
C3 plants	53.95	263	Cui & Schubert (2017); peak H2; CH_4 release scenario
C3 plants	53.95	93	Cui & Schubert (2017); peak H2; CH_4 release scenario
C3 plants	53.95	83	Cui & Schubert (2017); peak H2; CH_4 release scenario
C3 plants	53.95	957	Cui & Schubert (2017); peak H2; C_{org} release scenario
C3 plants	53.95	900	Cui & Schubert (2017); peak H2; C_{org} release scenario
C3 plants	53.95	1251	Cui & Schubert (2017); peak H2; C_{org} release scenario
C3 plants	53.95	1241	Cui & Schubert (2017); peak H2; C_{org} release scenario
C3 plants	53.95	534	Cui & Schubert (2017); peak H2; C_{org} release scenario
C3 plants	53.95	505	Cui & Schubert (2017); peak H2; C_{org} release scenario
C3 plants	53.95	404	Cui & Schubert (2017); peak H2; C_{org} release scenario
C3 plants	53.95	381	Cui & Schubert (2017); peak H2; C_{org} release scenario
C3 plants	53.95	346	Cui & Schubert (2017); peak H2; C_{org} release scenario
C3 plants	53.95	327	Cui & Schubert (2017); peak H2; C_{org} release scenario
C3 plants	53.95	394	Cui & Schubert (2017); peak H2; C_{org} release scenario
C3 plants	53.95	372	Cui & Schubert (2017); peak H2; C_{org} release scenario
C3 plants	53.95	551	Cui & Schubert (2017); peak H2; C_{org} release scenario
C3 plants	53.95	523	Cui & Schubert (2017); peak H2; C_{org} release scenario
C3 plants	53.95	236	Cui & Schubert (2017); peak H2; C_{org} release scenario
C3 plants	53.95	221	Cui & Schubert (2017); peak H2; C_{org} release scenario
C3 plants	53.7	292	Cui & Schubert (2017); background I1; CH_4 release scenario
C3 plants	53.7	230	Cui & Schubert (2017); background I1; CH_4 release scenario
C3 plants	53.7	319	Cui & Schubert (2017); background I1; CH_4 release scenario
C3 plants	53.7	257	Cui & Schubert (2017); background I1; CH_4 release scenario
C3 plants	53.7	192	Cui & Schubert (2017); background I1; CH_4 release scenario
C3 plants	53.7	151	Cui & Schubert (2017); background I1; CH_4 release scenario
C3 plants	53.7	183	Cui & Schubert (2017); background I1; CH_4 release scenario
C3 plants	53.7	144	Cui & Schubert (2017); background I1; CH_4 release scenario
C3 plants	53.7	131	Cui & Schubert (2017); background I1; CH_4 release scenario
C3 plants	53.7	99	Cui & Schubert (2017); background I1; CH_4 release scenario
C3 plants	53.7	172	Cui & Schubert (2017); background I1; CH_4 release scenario
C3 plants	53.7	134	Cui & Schubert (2017); background I1; CH_4 release scenario
C3 plants	53.7	58	Cui & Schubert (2017); background I1; CH_4 release scenario
C3 plants	53.7	37	Cui & Schubert (2017); background I1; CH_4 release scenario
C3 plants	53.7	178	Cui & Schubert (2017); background I1; CH_4 release scenario
C3 plants	53.7	141	Cui & Schubert (2017); background I1; CH_4 release scenario
C3 plants	53.7	476	Cui & Schubert (2017); background I1; C_{org} release scenario
C3 plants	53.7	383	Cui & Schubert (2017); background I1; C_{org} release scenario
C3 plants	53.7	503	Cui & Schubert (2017); background I1; C_{org} release scenario
C3 plants	53.7	420	Cui & Schubert (2017); background I1; C_{org} release scenario
C3 plants	53.7	339	Cui & Schubert (2017); background I1; C_{org} release scenario
C3 plants	53.7	276	Cui & Schubert (2017); background I1; C_{org} release scenario
C3 plants	53.7	327	Cui & Schubert (2017); background I1; C_{org} release scenario
C3 plants	53.7	266	Cui & Schubert (2017); background I1; C_{org} release scenario
C3 plants	53.7	253	Cui & Schubert (2017); background I1; C_{org} release scenario
C3 plants	53.7	205	Cui & Schubert (2017); background I1; C_{org} release scenario
C3 plants	53.7	311	Cui & Schubert (2017); background I1; C_{org} release scenario
C3 plants	53.7	253	Cui & Schubert (2017); background I1; C_{org} release scenario
C3 plants	53.7	153	Cui & Schubert (2017); background I1; C_{org} release scenario
C3 plants	53.7	120	Cui & Schubert (2017); background I1; C_{org} release scenario
C3 plants	53.7	323	Cui & Schubert (2017); background I1; C_{org} release scenario
C3 plants	53.7	263	Cui & Schubert (2017); background I1; C_{org} release scenario
C3 plants	53.67	458	Cui & Schubert (2017); peak I1; CH_4 release scenario
C3 plants	53.67	394	Cui & Schubert (2017); peak I1; CH_4 release scenario
C3 plants	53.67	495	Cui & Schubert (2017); peak I1; CH_4 release scenario
C3 plants	53.67	439	Cui & Schubert (2017); peak I1; CH_4 release scenario
C3 plants	53.67	304	Cui & Schubert (2017); peak I1; CH_4 release scenario
C3 plants	53.67	261	Cui & Schubert (2017); peak I1; CH_4 release scenario
C3 plants	53.67	290	Cui & Schubert (2017); peak I1; CH_4 release scenario
C3 plants	53.67	249	Cui & Schubert (2017); peak I1; CH_4 release scenario

C3 plants	53.67	209	Cui & Schubert (2017); peak I1; CH_4 release scenario
C3 plants	53.67	177	Cui & Schubert (2017); peak I1; CH_4 release scenario
C3 plants	53.67	272	Cui & Schubert (2017); peak I1; CH_4 release scenario
C3 plants	53.67	233	Cui & Schubert (2017); peak I1; CH_4 release scenario
C3 plants	53.67	102	Cui & Schubert (2017); peak I1; CH_4 release scenario
C3 plants	53.67	81	Cui & Schubert (2017); peak I1; CH_4 release scenario
C3 plants	53.67	282	Cui & Schubert (2017); peak I1; CH_4 release scenario
C3 plants	53.67	245	Cui & Schubert (2017); peak I1; CH_4 release scenario
C3 plants	53.67	870	Cui & Schubert (2017); peak I1; C_{org} release scenario
C3 plants	53.67	771	Cui & Schubert (2017); peak I1; C_{org} release scenario
C3 plants	53.67	902	Cui & Schubert (2017); peak I1; C_{org} release scenario
C3 plants	53.67	851	Cui & Schubert (2017); peak I1; C_{org} release scenario
C3 plants	53.67	599	Cui & Schubert (2017); peak I1; C_{org} release scenario
C3 plants	53.67	533	Cui & Schubert (2017); peak I1; C_{org} release scenario
C3 plants	53.67	574	Cui & Schubert (2017); peak I1; C_{org} release scenario
C3 plants	53.67	511	Cui & Schubert (2017); peak I1; C_{org} release scenario
C3 plants	53.67	436	Cui & Schubert (2017); peak I1; C_{org} release scenario
C3 plants	53.67	386	Cui & Schubert (2017); peak I1; C_{org} release scenario
C3 plants	53.67	544	Cui & Schubert (2017); peak I1; C_{org} release scenario
C3 plants	53.67	484	Cui & Schubert (2017); peak I1; C_{org} release scenario
C3 plants	53.67	256	Cui & Schubert (2017); peak I1; C_{org} release scenario
C3 plants	53.67	222	Cui & Schubert (2017); peak I1; C_{org} release scenario
C3 plants	53.67	568	Cui & Schubert (2017); peak I1; C_{org} release scenario
C3 plants	53.67	506	Cui & Schubert (2017); peak I1; C_{org} release scenario
C3 plants	53.6	237	Cui & Schubert (2017); background I2; CH_4 release scenario
C3 plants	53.6	237	Cui & Schubert (2017); background I2; CH_4 release scenario
C3 plants	53.6	165	Cui & Schubert (2017); background I2; CH_4 release scenario
C3 plants	53.6	172	Cui & Schubert (2017); background I2; CH_4 release scenario
C3 plants	53.6	40	Cui & Schubert (2017); background I2; CH_4 release scenario
C3 plants	53.6	95	Cui & Schubert (2017); background I2; CH_4 release scenario
C3 plants	53.6	22	Cui & Schubert (2017); background I2; CH_4 release scenario
C3 plants	53.6	403	Cui & Schubert (2017); background I2; C_{org} release scenario
C3 plants	53.6	403	Cui & Schubert (2017); background I2; C_{org} release scenario
C3 plants	53.6	303	Cui & Schubert (2017); background I2; C_{org} release scenario
C3 plants	53.6	312	Cui & Schubert (2017); background I2; C_{org} release scenario
C3 plants	53.6	128	Cui & Schubert (2017); background I2; C_{org} release scenario
C3 plants	53.6	205	Cui & Schubert (2017); background I2; C_{org} release scenario
C3 plants	53.6	102	Cui & Schubert (2017); background I2; C_{org} release scenario
C3 plants	53.565	360	Cui & Schubert (2017); peak I2; CH_4 release scenario
C3 plants	53.565	359	Cui & Schubert (2017); peak I2; CH_4 release scenario
C3 plants	53.565	252	Cui & Schubert (2017); peak I2; CH_4 release scenario
C3 plants	53.565	261	Cui & Schubert (2017); peak I2; CH_4 release scenario
C3 plants	53.565	73	Cui & Schubert (2017); peak I2; CH_4 release scenario
C3 plants	53.565	149	Cui & Schubert (2017); peak I2; CH_4 release scenario
C3 plants	53.565	49	Cui & Schubert (2017); peak I2; CH_4 release scenario
C3 plants	53.565	692	Cui & Schubert (2017); peak I2; C_{org} release scenario
C3 plants	53.565	691	Cui & Schubert (2017); peak I2; C_{org} release scenario
C3 plants	53.565	506	Cui & Schubert (2017); peak I2; C_{org} release scenario
C3 plants	53.565	523	Cui & Schubert (2017); peak I2; C_{org} release scenario
C3 plants	53.565	205	Cui & Schubert (2017); peak I2; C_{org} release scenario
C3 plants	53.565	332	Cui & Schubert (2017); peak I2; C_{org} release scenario
C3 plants	53.565	164	Cui & Schubert (2017); peak I2; C_{org} release scenario

Appendix 7. Planktic foraminiferal stable carbon isotope ($\delta^{13}C_{planktic}$) and planktic foraminiferal stable oxygen isotope ($\delta^{18}O_{planktic}$) data across the Danian/Selandian Transition Event based on analysis of Morozovella conicotruncata from South Atlantic Walvis Ridge ODP Site 1262. These data were generated on a Thermo Electron Delta+ Advantage Isotope Ratio Mass Spectrometer at the Wolfson Laboratory, University of Edinburgh, with analytical error of 0.04 ‰ for both $\delta^{13}C$ and $\delta^{18}O$ (1σ). These data are from ***Chapter 3, Section 3.6.6.*** *Ages (in Ma) are based on the updated orbitally-tuned age model generated for ODP Site 1262 during this study.*

Site_Hole_Core_Type_Section_Top Depth (cm)_Bottom Depth (cm)_Top Depth (mbsf)	Depth (mcd)	Age (Ma)	$\delta^{13}C_{planktic}$ (‰ VPDB)	$\delta^{18}O_{planktic}$ (‰ VPDB)
1262_C_10_H_3_68_69_171.68	186.61	61.0911	3.58	–0.11
1262_C_10_H_3_83_84_171.83	186.76	61.1084	3.49	–0.07
1262_C_10_H_3_101_102_172.01	186.94	61.1292	3.50	–0.15
1262_C_10_H_3_122_123_172.22	187.15	61.1535	3.50	–0.16
1262_C_10_H_3_134_135_172.34	187.27	61.1673	3.39	–0.17
1262_C_10_H_3_149_150_172.49	187.42	61.1847	3.61	–0.35
1262_C_10_H_4_11_12_172.61	187.54	61.1985	3.57	–0.48
1262_C_10_H_4_26_27_172.76	187.69	61.2159	3.35	–0.19
1262_C_10_H_4_38_39_172.88	187.81	61.2297	3.58	–0.44
1262_C_10_H_4_50_51_173.0	187.93	61.2442	3.60	–0.45
1262_C_10_H_4_59_60_173.09	188.02	61.2566	3.40	–0.29
1262_C_10_H_4_62_63_173.12	188.05	61.2609	3.41	–0.37
1262_C_10_H_4_68_69_173.18	188.11	61.2695	3.40	–0.39
1262_C_10_H_4_74_75_173.24	188.17	61.2780	3.33	–0.37
1262_C_10_H_4_77_78_173.27	188.20	61.2823	3.33	–0.36
1262_C_10_H_4_83_84_173.33	188.26	61.2909	3.55	–0.48
1262_C_10_H_4_89_90_173.39	188.32	61.2995	3.45	–0.47
1262_C_10_H_4_95_96_173.45	188.38	61.3081	3.61	–0.54
1262_C_10_H_4_101_102_173.51	188.44	61.3167	3.27	–0.33
1262_C_10_H_4_104_105_173.54	188.47	61.3210	3.32	–0.43
1262_C_10_H_4_110_111_173.6	188.53	61.3295	3.35	–0.30
1262_C_10_H_4_113_114_173.63	188.56	61.3338	3.35	–0.32
1262_C_10_H_4_119_120_173.69	188.62	61.3424	3.45	–0.64
1262_C_10_H_4_125_126_173.75	188.68	61.3497	3.47	–0.52
1262_C_10_H_4_134_135_173.84	188.77	61.3591	3.37	–0.27
1262_C_10_H_4_140_141_173.9	188.83	61.3653	3.48	–0.36
1262_C_10_H_4_149_150_173.99	188.92	61.3748	3.09	–0.56
1262_C_10_H_5_8_9_174.08	189.01	61.3842	3.62	–0.27
1262_C_10_H_5_17_18_174.17	189.10	61.3936	3.64	–0.35
1262_C_10_H_5_32_33_174.32	189.25	61.4093	3.64	–0.26

*Appendix 8. Early Paleocene % coarse fraction (% CF) data across the Dan-C2 event from South Atlantic Walvis Ridge ODP Site 1262. Ages (in Ma) are based on the updated orbitally-tuned age model generated during this study. These data are from **Chapter 5**.*

Site_Hole_Core_Type_Section_Top Depth (cm)_Bottom Depth (cm)_Top Depth (mbsf)	Depth (mcd)	Age (Ma)	Bulk dry sample weight (g)	CF (>63 μm) weight (g)	% CF (>63 μm)
1262_C_13_H_1_55_56_194.05	215.10	65.6932	12.378	0.399	3.223
1262_C_13_H_1_58_59_194.08	215.13	65.7011	14.535	0.383	2.634
1262_C_13_H_1_62_63_194.12	215.17	65.7116	10.492	0.104	0.993
1262_C_13_H_1_65_66_194.15	215.20	65.7194	17.386	0.188	1.082
1262_C_13_H_1_69_70_194.19	215.24	65.7330	9.210	0.098	1.066
1262_C_13_H_1_71_72_194.21	215.26	65.7403	11.987	0.193	1.606
1262_C_13_H_1_73.5_74.5_194.235	215.28	65.7488	9.922	0.191	1.920
1262_C_13_H_1_75_76_194.25	215.30	65.7574	5.006	0.068	1.362
1262_C_13_H_1_77_78_194.27	215.32	65.7659	7.203	0.156	2.166
1262_C_13_H_1_78_79_194.28	215.33	65.7702	12.634	0.219	1.730
1262_C_13_H_1_80_81_194.3	215.35	65.7788	7.334	0.161	2.199
1262_C_13_H_1_81_82_194.31	215.36	65.7831	13.291	0.157	1.179
1262_C_13_H_1_82_83_194.32	215.37	65.7873	9.219	0.127	1.380
1262_C_13_H_1_83_84_194.33	215.38	65.7916	6.968	0.085	1.223
1262_C_13_H_1_84_85_194.34	215.39	65.7959	5.326	0.043	0.807
1262_C_13_H_1_85_86_194.35	215.40	65.8002	10.915	0.070	0.638
1262_C_13_H_1_86_87_194.36	215.41	65.8045	8.487	0.032	0.376
1262_C_13_H_1_87_88_194.37	215.42	65.8087	10.400	0.035	0.340
1262_C_13_H_1_88_89_194.38	215.43	65.8130	4.353	0.013	0.287
1262_C_13_H_1_89_90_194.39	215.44	65.8173	8.569	0.015	0.173
1262_C_13_H_1_90_91_194.4	215.45	65.8216	5.028	0.008	0.159
1262_C_13_H_1_91_92_194.41	215.46	65.8259	5.927	0.011	0.181
1262_C_13_H_1_92_93_194.42	215.47	65.8291	8.272	0.014	0.169
1262_C_13_H_1_93_94_194.43	215.48	65.8313	6.416	0.010	0.154
1262_C_13_H_1_94_95_194.44	215.49	65.8334	9.758	0.013	0.137
1262_C_13_H_1_95_96_194.45	215.50	65.8356	10.773	0.012	0.113
1262_C_13_H_1_96_97_194.46	215.51	65.8378	7.030	0.014	0.195
1262_C_13_H_1_97_98_194.47	215.52	65.8399	3.670	0.004	0.114
1262_C_13_H_1_98_99_194.48	215.53	65.8421	3.761	0.005	0.136
1262_C_13_H_1_99_100_194.49	215.54	65.8443	5.876	0.009	0.153
1262_C_13_H_1_100_101_194.5	215.55	65.8464	4.332	0.002	0.051
1262_C_13_H_1_101_102_194.51	215.56	65.8486	10.213	0.055	0.540
1262_C_13_H_1_102_103_194.52	215.57	65.8508	3.963	0.024	0.598
1262_C_13_H_1_103_104_194.53	215.58	65.8530	5.566	0.072	1.288
1262_C_13_H_1_104_105_194.54	215.59	65.8551	7.020	0.096	1.363
1262_C_13_H_1_105_106_194.55	215.60	65.8573	6.062	0.116	1.910
1262_C_13_H_1_106_107_194.56	215.61	65.8595	6.761	0.132	1.946
1262_C_13_H_1_107_108_194.57	215.62	65.8616	6.114	0.127	2.082
1262_C_13_H_1_108_109_194.58	215.63	65.8638	4.387	0.082	1.862
1262_C_13_H_1_109_110_194.59	215.64	65.8660	6.370	0.166	2.601
1262_C_13_H_1_110_111_194.6	215.65	65.8682	4.051	0.101	2.496
1262_C_13_H_1_111_112_194.61	215.66	65.8703	5.758	0.125	2.166
1262_C_13_H_1_112_113_194.62	215.67	65.8725	4.846	0.122	2.513
1262_C_13_H_1_113_114_194.63	215.68	65.8747	8.275	0.228	2.760
1262_C_13_H_1_114_115_194.64	215.69	65.8768	6.107	0.152	2.492
1262_C_13_H_1_115_116_194.65	215.70	65.8790	6.005	0.167	2.778
1262_C_13_H_1_116_117_194.66	215.71	65.8812	3.395	0.076	2.244
1262_C_13_H_1_117_118_194.67	215.72	65.8833	7.421	0.281	3.788
1262_C_13_H_1_118_119_194.68	215.73	65.8855	4.762	0.169	3.557
1262_C_13_H_1_119_120_194.69	215.74	65.8877	4.665	0.143	3.057
1262_C_13_H_1_120_121_194.7	215.75	65.8899	21.761	0.935	4.299

1262_C_13_H_1_121_122_194.71	215.76	65.8920	6.115	0.194	3.169
1262_C_13_H_1_122_123_194.72	215.77	65.8942	7.149	0.272	3.810
1262_C_13_H_1_123_124_194.73	215.78	65.8964	8.558	0.371	4.331
1262_C_13_H_1_124_125_194.74	215.79	65.8985	5.319	0.221	4.161
1262_C_13_H_1_125_126_194.75	215.80	65.9007	8.605	0.378	4.390
1262_C_13_H_1_126_127_194.76	215.81	65.9029	4.975	0.204	4.103
1262_C_13_H_1_127_128_194.77	215.82	65.9050	8.577	0.395	4.600
1262_C_13_H_1_128_129_194.78	215.83	65.9072	5.788	0.204	3.523
1262_C_13_H_1_129_130_194.79	215.84	65.9094	5.006	0.151	3.018
1262_C_13_H_1_130_131_194.8	215.85	65.9116	4.515	0.123	2.716
1262_C_13_H_1_131_132_194.81	215.86	65.9137	6.344	0.204	3.208
1262_C_13_H_1_132_133_194.82	215.87	65.9159	6.338	0.186	2.930
1262_C_13_H_1_133_134_194.83	215.88	65.9181	12.384	0.530	4.276
1262_C_13_H_1_134_135_194.84	215.89	65.9202	4.047	0.105	2.587
1262_C_13_H_1_135_136_194.85	215.90	65.9224	3.598	0.084	2.326
1262_C_13_H_1_137_138_194.87	215.92	65.9267	5.198	0.109	2.093
1262_C_13_H_1_138_139_194.88	215.93	65.9289	5.568	0.123	2.207
1262_C_13_H_1_139_140_194.89	215.94	65.9309	5.670	0.092	1.623
1262_C_13_H_1_140_141_194.9	215.95	65.9327	4.890	0.121	2.470
1262_C_13_H_1_141_142_194.91	215.96	65.9346	4.385	0.093	2.125
1262_C_13_H_1_142_143_194.92	215.97	65.9364	9.820	0.246	2.509
1262_C_13_H_1_143_144_194.93	215.98	65.9382	6.976	0.142	2.028
1262_C_13_H_1_146_147_194.96	216.01	65.9437	6.385	0.123	1.926
1262_C_13_H_2_0_1_195	216.05	65.9510	2.567	0.075	2.906
1262_C_13_H_2_1_2_195.01	216.06	65.9529	4.393	0.094	2.135
1262_C_13_H_2_2_3_195.02	216.07	65.9547	11.478	0.307	2.678
1262_C_13_H_2_3_4_195.03	216.08	65.9565	7.100	0.171	2.404
1262_C_13_H_2_4_5_195.04	216.09	65.9583	10.081	0.316	3.130
1262_C_13_H_2_5_6_195.05	216.10	65.9602	15.560	0.444	2.852
1262_C_13_H_2_6_7_195.06	216.11	65.9620	4.212	0.111	2.633
1262_C_13_H_2_7_8_195.07	216.12	65.9638	5.101	0.113	2.211
1262_C_13_H_2_8_9_195.08	216.13	65.9657	13.793	0.374	2.711
1262_C_13_H_2_9_10_195.09	216.14	65.9675	9.776	0.269	2.756
1262_C_13_H_2_10_11_195.1	216.15	65.9693	5.491	0.121	2.198
1262_C_13_H_2_14_15_195.14	216.19	65.9766	6.184	0.172	2.775
1262_C_13_H_2_16_17_195.16	216.21	65.9803	4.076	0.122	3.001
1262_C_13_H_2_20_21_195.2	216.25	65.9876	5.068	0.111	2.186
1262_C_13_H_2_22_23_195.22	216.27	65.9913	10.070	0.321	3.187
1262_C_13_H_2_26_27_195.26	216.31	65.9956	7.436	0.229	3.074
1262_C_13_H_2_28_29_195.28	216.33	65.9969	7.432	0.226	3.040
1262_C_13_H_2_30_31_195.3	216.35	65.9982	4.860	0.153	3.142
1262_C_13_H_2_34_35_195.34	216.39	66.0008	6.874	0.128	1.866
1262_C_13_H_2_46_47_195.46	216.51	66.0087	4.871	0.060	1.226

Appendix 9. Bulk carbonate stable carbon isotope ($\delta^{13}C_{bulk}$) data from Indian Ocean Ninetyeast Ridge IODP Site U1443. Data were generated on a VG Optima Dual Inlet Mass Spectrometer at the NERC Isotope Geosciences Facility (NIGF), with analytical error of 0.03 ‰ (1σ), and on a Sercon 20-22 Isotope Ratio Mass Spectrometer at the University of Exeter (UoE), with analytical error of 0.06 ‰ (2σ). Tie points used to generate the age model for this site are highlighted in bold. These data are from ***Chapter 6****.*

Site_Hole_Core_Section_Top Depth (cm)_Bottom Depth (cm)	Depth (mbsf)	Age (Ma)	$\delta^{13}C_{bulk}$ (‰ VPDB)	Mass spectrometer
U1443_A_35_1_4_5	244.95	52.847	1.38	VG Optima Dual Inlet (NIGF)
U1443_A_35_1_15.5_16.5	**245.06**	**52.944**	1.29	VG Optima Dual Inlet (NIGF)
U1443_A_35_1_21.5_22.5	245.12	52.997	1.39	VG Optima Dual Inlet (NIGF)
U1443_A_35_1_25_26	245.16	53.032	1.31	VG Optima Dual Inlet (NIGF)
U1443_A_35_1_27_28	245.18	53.050	1.33	VG Optima Dual Inlet (NIGF)
U1443_A_35_1_30.5_31.5	245.21	53.076	1.27	VG Optima Dual Inlet (NIGF)
U1443_A_35_1_40_41	245.31	53.164	1.09	VG Optima Dual Inlet (NIGF)
U1443_A_35_1_42.5_43.5	245.33	53.182	1.27	VG Optima Dual Inlet (NIGF)
U1443_A_35_1_49_50	245.40	53.244	1.33	VG Optima Dual Inlet (NIGF)
U1443_A_35_1_52_53	245.43	53.270	1.17	VG Optima Dual Inlet (NIGF)
U1443_A_35_1_60_61	245.51	53.341	1.32	VG Optima Dual Inlet (NIGF)
U1443_A_35_1_64_65	245.55	53.376	1.25	VG Optima Dual Inlet (NIGF)
U1443_A_35_1_69_70	245.60	53.420	1.25	VG Optima Dual Inlet (NIGF)
U1443_A_35_1_77_78	245.68	53.491	1.15	VG Optima Dual Inlet (NIGF)
U1443_A_35_1_83_84	245.74	53.544	1.17	VG Optima Dual Inlet (NIGF)
U1443_A_35_1_88_89	245.79	53.588	1.55	VG Optima Dual Inlet (NIGF)
U1443_A_35_1_92_93	245.83	53.623	1.41	VG Optima Dual Inlet (NIGF)
U1443_A_35_1_95_96	245.86	53.649	1.40	VG Optima Dual Inlet (NIGF)
U1443_A_35_1_99_100	245.90	53.685	1.39	VG Optima Dual Inlet (NIGF)
U1443_A_35_1_103_104	245.94	53.720	1.40	VG Optima Dual Inlet (NIGF)
U1443_A_35_1_109_110	246.00	53.773	1.36	VG Optima Dual Inlet (NIGF)
U1443_A_35_1_114_115	246.05	53.817	1.33	VG Optima Dual Inlet (NIGF)
U1443_A_35_1_121_122	246.12	53.879	1.34	VG Optima Dual Inlet (NIGF)
U1443_A_35_1_125_126	246.16	53.914	1.34	VG Optima Dual Inlet (NIGF)
U1443_A_35_1_130_131	**246.21**	**53.958**	1.13	VG Optima Dual Inlet (NIGF)
U1443_A_35_1_136_137	246.27	53.977	1.18	VG Optima Dual Inlet (NIGF)
U1443_A_35_1_140_141	246.31	53.990	1.25	VG Optima Dual Inlet (NIGF)
U1443_A_35_1_143_144	246.34	54.000	1.31	VG Optima Dual Inlet (NIGF)
U1443_A_35_2_9_10	**246.50**	**54.051**	1.08	VG Optima Dual Inlet (NIGF)
U1443_A_35_2_12_13	246.53	54.066	1.29	VG Optima Dual Inlet (NIGF)
U1443_A_35_2_18_19	246.59	54.096	1.36	VG Optima Dual Inlet (NIGF)
U1443_A_35_2_22_23	246.63	54.116	1.44	VG Optima Dual Inlet (NIGF)
U1443_A_35_2_24_25	246.65	54.126	1.29	VG Optima Dual Inlet (NIGF)
U1443_A_35_2_30_31	246.71	54.156	1.42	VG Optima Dual Inlet (NIGF)
U1443_A_35_2_31_32	246.72	54.161	1.45	VG Optima Dual Inlet (NIGF)
U1443_A_35_2_36_37	246.77	54.186	1.47	VG Optima Dual Inlet (NIGF)
U1443_A_35_2_42_43	246.83	54.215	1.45	VG Optima Dual Inlet (NIGF)
U1443_A_35_2_48_49	246.89	54.245	1.44	VG Optima Dual Inlet (NIGF)
U1443_A_35_2_56_57	246.97	54.285	1.41	VG Optima Dual Inlet (NIGF)
U1443_A_35_2_69_70	247.10	54.350	1.70	VG Optima Dual Inlet (NIGF)
U1443_A_35_2_76_77	247.17	54.385	1.56	VG Optima Dual Inlet (NIGF)
U1443_A_35_2_79_80	247.20	54.400	1.64	VG Optima Dual Inlet (NIGF)
U1443_A_35_2_82_83	247.23	54.415	1.64	VG Optima Dual Inlet (NIGF)
U1443_A_35_2_85_86	247.26	54.430	1.62	VG Optima Dual Inlet (NIGF)
U1443_A_35_2_92_93	247.33	54.464	1.69	VG Optima Dual Inlet (NIGF)
U1443_A_35_2_95_96	247.36	54.479	1.72	VG Optima Dual Inlet (NIGF)
U1443_A_35_2_101_102	247.42	54.509	1.77	VG Optima Dual Inlet (NIGF)
U1443_A_35_2_105_106	247.46	54.529	1.78	VG Optima Dual Inlet (NIGF)

U1443_A_35_2_117_118	247.58	54.589	1.83	VG Optima Dual Inlet (NIGF)
U1443_A_35_2_122_123	247.63	54.614	1.87	VG Optima Dual Inlet (NIGF)
U1443_A_35_2_126_127	247.67	54.634	1.88	VG Optima Dual Inlet (NIGF)
U1443_A_35_2_131_132	247.72	54.659	1.84	VG Optima Dual Inlet (NIGF)
U1443_A_35_2_134_135	247.75	54.674	1.88	VG Optima Dual Inlet (NIGF)
U1443_A_35_2_136_137	247.77	54.684	1.86	VG Optima Dual Inlet (NIGF)
U1443_A_35_3_3_4	247.94	54.768	1.79	VG Optima Dual Inlet (NIGF)
U1443_A_35_3_10_11	248.01	54.803	1.75	VG Optima Dual Inlet (NIGF)
U1443_A_35_3_13_14	248.04	54.818	1.77	VG Optima Dual Inlet (NIGF)
U1443_A_35_3_17_18	248.08	54.838	1.84	VG Optima Dual Inlet (NIGF)
U1443_A_35_3_24_25	**248.15**	**54.873**	1.80	VG Optima Dual Inlet (NIGF)
U1443_A_35_3_30_31	248.21	54.999	1.81	VG Optima Dual Inlet (NIGF)
U1443_A_35_3_37_38	248.28	55.145	1.82	VG Optima Dual Inlet (NIGF)
U1443_A_35_3_40.5_41.5	248.31	55.208	1.94	VG Optima Dual Inlet (NIGF)
U1443_A_35_3_45_46	248.36	55.313	1.94	VG Optima Dual Inlet (NIGF)
U1443_A_35_3_52_53	248.43	55.459	1.89	VG Optima Dual Inlet (NIGF)
U1443_A_35_3_53_54	248.44	55.480	1.91	VG Optima Dual Inlet (NIGF)
U1443_A_35_3_57_58	248.48	55.564	1.92	VG Optima Dual Inlet (NIGF)
U1443_A_35_3_61_62	248.52	55.648	1.95	VG Optima Dual Inlet (NIGF)
U1443_A_35_3_65_66	248.56	55.731	1.98	VG Optima Dual Inlet (NIGF)
U1443_A_35_3_69_70	**248.60**	**55.800**	1.43	VG Optima Dual Inlet (NIGF)
U1443_A_35_3_72_73	**248.63**	**55.835**	1.30	VG Optima Dual Inlet (NIGF)
U1443_A_35_3_85.5_86.5	**248.76**	**55.930**	2.03	VG Optima Dual Inlet (NIGF)
U1443_A_35_3_92_93	248.83	55.940	2.07	VG Optima Dual Inlet (NIGF)
U1443_A_35_3_97_98	248.88	55.947	2.04	VG Optima Dual Inlet (NIGF)
U1443_A_35_3_98_99	248.89	55.948	2.09	VG Optima Dual Inlet (NIGF)
U1443_A_35_3_105_106	248.96	55.958	2.09	VG Optima Dual Inlet (NIGF)
U1443_A_35_3_112_113	249.03	55.968	2.12	VG Optima Dual Inlet (NIGF)
U1443_A_35_3_116_117	249.07	55.974	2.20	VG Optima Dual Inlet (NIGF)
U1443_A_35_3_124.5_125.5	249.15	55.985	2.22	VG Optima Dual Inlet (NIGF)
U1443_A_35_3_133_134	249.24	55.998	2.31	VG Optima Dual Inlet (NIGF)
U1443_A_36_1_2_3	254.03	57.201	2.99	VG Optima Dual Inlet (NIGF)
U1443_A_36_1_8_9	254.09	57.206	3.04	VG Optima Dual Inlet (NIGF)
U1443_A_36_1_11_12	254.12	57.209	3.00	VG Optima Dual Inlet (NIGF)
U1443_A_36_1_13_14	254.14	57.210	3.00	VG Optima Dual Inlet (NIGF)
U1443_A_36_1_19_20	254.20	57.215	3.02	VG Optima Dual Inlet (NIGF)
U1443_A_36_1_25_26	**254.26**	**57.220**	2.80	VG Optima Dual Inlet (NIGF)
U1443_A_36_1_27_28	254.28	57.226	2.84	VG Optima Dual Inlet (NIGF)
U1443_A_36_1_36_37	254.37	57.251	2.88	VG Optima Dual Inlet (NIGF)
U1443_A_36_1_42_43	254.43	57.268	3.05	VG Optima Dual Inlet (NIGF)
U1443_A_36_1_47_48	254.48	57.282	2.99	VG Optima Dual Inlet (NIGF)
U1443_A_36_1_52_53	254.53	57.296	2.99	VG Optima Dual Inlet (NIGF)
U1443_A_36_1_60_61	254.61	57.319	2.94	VG Optima Dual Inlet (NIGF)
U1443_A_36_1_65_66	**254.66**	**57.333**	2.92	VG Optima Dual Inlet (NIGF)
U1443_A_36_1_72_73	254.73	57.341	2.95	VG Optima Dual Inlet (NIGF)
U1443_A_36_1_78_79	254.79	57.348	3.05	VG Optima Dual Inlet (NIGF)
U1443_A_36_1_84_85	254.85	57.355	3.06	VG Optima Dual Inlet (NIGF)
U1443_A_36_1_88_89	254.89	57.360	3.16	VG Optima Dual Inlet (NIGF)
U1443_A_36_1_94_95	254.95	57.367	3.30	VG Optima Dual Inlet (NIGF)
U1443_A_36_1_100_101	255.01	57.374	3.18	VG Optima Dual Inlet (NIGF)
U1443_A_36_1_111_112	255.12	57.386	3.35	VG Optima Dual Inlet (NIGF)
U1443_A_36_1_116_117	255.17	57.392	3.35	VG Optima Dual Inlet (NIGF)
U1443_A_36_1_121_122	255.22	57.398	3.31	VG Optima Dual Inlet (NIGF)
U1443_A_36_1_126_127	255.27	57.404	3.34	VG Optima Dual Inlet (NIGF)
U1443_A_36_1_132_133	255.33	57.411	3.34	VG Optima Dual Inlet (NIGF)
U1443_A_36_1_138_139	255.39	57.418	3.35	VG Optima Dual Inlet (NIGF)
U1443_A_36_1_144_145	255.45	57.425	3.38	VG Optima Dual Inlet (NIGF)
U1443_A_36_2_3.5_4.5	255.54	57.435	3.36	VG Optima Dual Inlet (NIGF)
U1443_A_36_2_8_9	255.59	57.441	3.36	VG Optima Dual Inlet (NIGF)
U1443_A_36_2_13_14	255.64	57.447	3.33	VG Optima Dual Inlet (NIGF)

U1443_A_36_2_24_25	255.75	57.459	3.33	VG Optima Dual Inlet (NIGF)
U1443_A_36_2_28.5_29.5	255.79	57.464	3.31	VG Optima Dual Inlet (NIGF)
U1443_A_36_2_33.5_34.5	255.84	57.470	3.27	VG Optima Dual Inlet (NIGF)
U1443_A_36_2_38.5_39.5	255.88	57.474	3.23	VG Optima Dual Inlet (NIGF)
U1443_A_36_2_44.5_45.5	255.95	57.483	3.21	VG Optima Dual Inlet (NIGF)
U1443_A_36_2_48.5_49.5	255.99	57.487	3.22	VG Optima Dual Inlet (NIGF)
U1443_A_36_2_53_54	**256.04**	**57.493**	3.18	VG Optima Dual Inlet (NIGF)
U1443_A_36_2_58_59	256.09	57.502	3.23	VG Optima Dual Inlet (NIGF)
U1443_A_36_2_64_65	256.15	57.512	3.31	VG Optima Dual Inlet (NIGF)
U1443_A_36_2_68.5_69.5	256.19	57.519	3.27	VG Optima Dual Inlet (NIGF)
U1443_A_36_2_72.5_73.5	256.23	57.526	3.29	VG Optima Dual Inlet (NIGF)
U1443_A_36_2_77_78	256.28	57.535	3.31	VG Optima Dual Inlet (NIGF)
U1443_A_36_2_84_85	256.35	57.547	3.31	VG Optima Dual Inlet (NIGF)
U1443_A_36_2_89_90	256.40	57.555	3.35	VG Optima Dual Inlet (NIGF)
U1443_A_36_2_93.5_94.5	256.44	57.562	3.33	VG Optima Dual Inlet (NIGF)
U1443_A_36_2_99_100	256.50	57.573	3.30	VG Optima Dual Inlet (NIGF)
U1443_A_36_2_103.5_104.5	256.54	57.580	3.26	VG Optima Dual Inlet (NIGF)
U1443_A_36_2_108_109	256.59	57.588	3.21	VG Optima Dual Inlet (NIGF)
U1443_A_36_2_112.5_113.5	256.63	57.595	3.19	VG Optima Dual Inlet (NIGF)
U1443_A_36_2_116.5_117.5	256.67	57.602	3.18	VG Optima Dual Inlet (NIGF)
U1443_A_36_2_127.5_128.5	256.78	57.621	3.23	VG Optima Dual Inlet (NIGF)
U1443_A_36_2_132_133	256.83	57.630	3.21	VG Optima Dual Inlet (NIGF)
U1443_A_36_2_139_140	256.90	57.642	3.18	VG Optima Dual Inlet (NIGF)
U1443_A_36_2_144_145	256.95	57.651	3.22	VG Optima Dual Inlet (NIGF)
U1443_A_36_2_148_149	256.99	57.658	3.24	VG Optima Dual Inlet (NIGF)
U1443_A_36_3_3_4	257.04	57.666	3.31	VG Optima Dual Inlet (NIGF)
U1443_A_36_3_9_10	257.10	57.677	3.32	VG Optima Dual Inlet (NIGF)
U1443_A_36_3_14_15	257.15	57.685	3.34	VG Optima Dual Inlet (NIGF)
U1443_A_36_3_18_19	257.19	57.692	3.34	VG Optima Dual Inlet (NIGF)
U1443_A_36_3_22_23	257.23	57.699	3.35	VG Optima Dual Inlet (NIGF)
U1443_A_36_3_29_30	257.30	57.711	3.36	VG Optima Dual Inlet (NIGF)
U1443_A_36_3_35_36	257.36	57.722	3.34	VG Optima Dual Inlet (NIGF)
U1443_A_36_3_44_45	257.45	57.737	3.29	VG Optima Dual Inlet (NIGF)
U1443_A_36_3_49_50	257.50	57.746	3.31	VG Optima Dual Inlet (NIGF)
U1443_A_36_3_58_59	257.59	57.762	3.40	VG Optima Dual Inlet (NIGF)
U1443_A_36_3_62_63	257.63	57.768	3.43	VG Optima Dual Inlet (NIGF)
U1443_A_36_3_68_69	257.69	57.779	3.42	VG Optima Dual Inlet (NIGF)
U1443_A_36_3_71_72	257.72	57.784	3.43	VG Optima Dual Inlet (NIGF)
U1443_A_36_3_76_77	257.77	57.793	3.41	VG Optima Dual Inlet (NIGF)
U1443_A_36_3_81_82	257.82	57.801	3.37	VG Optima Dual Inlet (NIGF)
U1443_A_36_3_89_90	257.90	57.815	3.46	VG Optima Dual Inlet (NIGF)
U1443_A_36_3_94_95	257.95	57.824	3.45	VG Optima Dual Inlet (NIGF)
U1443_A_36_3_100_101	258.01	57.834	3.49	VG Optima Dual Inlet (NIGF)
U1443_A_36_3_103_104	258.04	57.839	3.48	VG Optima Dual Inlet (NIGF)
U1443_A_36_3_109_110	258.10	57.850	3.47	VG Optima Dual Inlet (NIGF)
U1443_A_36_3_115_116	258.16	57.860	3.42	VG Optima Dual Inlet (NIGF)
U1443_A_36_3_124_125	258.25	57.876	3.41	VG Optima Dual Inlet (NIGF)
U1443_A_36_3_128_129	258.29	57.883	3.41	VG Optima Dual Inlet (NIGF)
U1443_A_36_3_132_133	258.33	57.890	3.39	VG Optima Dual Inlet (NIGF)
U1443_A_36_3_135_136	258.36	57.895	3.37	VG Optima Dual Inlet (NIGF)
U1443_A_36_3_138_139	258.39	57.900	3.41	VG Optima Dual Inlet (NIGF)
U1443_A_36_3_141_142	258.42	57.905	3.40	VG Optima Dual Inlet (NIGF)
U1443_A_36_3_144_145	258.45	57.910	3.42	VG Optima Dual Inlet (NIGF)
U1443_A_36_3_147_148	258.48	57.916	3.40	VG Optima Dual Inlet (NIGF)
U1443_A_36_4_2_3	258.53	57.924	3.42	VG Optima Dual Inlet (NIGF)
U1443_A_36_4_8_9	258.59	57.935	3.43	VG Optima Dual Inlet (NIGF)
U1443_A_36_4_15_16	258.66	57.947	3.38	VG Optima Dual Inlet (NIGF)
U1443_A_36_4_23_24	258.74	57.961	3.52	Sercon 20-22 (UoE)
U1443_A_36_4_32_33	258.83	57.976	3.47	Sercon 20-22 (UoE)
U1443_A_36_4_43_44	258.94	57.995	3.43	Sercon 20-22 (UoE)

U1443_A_36_4_55_56	259.06	58.016	3.45	Sercon 20-22 (UoE)
U1443_A_36_4_63_64	**259.14**	**58.030**	3.55	Sercon 20-22 (UoE)
U1443_A_36_4_83_84	259.34	-	3.20	Sercon 20-22 (UoE)
U1443_A_36_4_91_92	259.42	-	3.46	Sercon 20-22 (UoE)
U1443_A_36_4_105_106	259.56	-	3.41	Sercon 20-22 (UoE)
U1443_A_36_4_114_115	259.65	-	3.47	Sercon 20-22 (UoE)
U1443_A_36_4_122_123	259.73	-	3.35	Sercon 20-22 (UoE)
U1443_A_36_4_132_133	259.83	-	3.39	Sercon 20-22 (UoE)
U1443_A_36_5_3_4	260.04	-	3.37	Sercon 20-22 (UoE)
U1443_A_36_5_13_14	260.14	-	3.13	Sercon 20-22 (UoE)
U1443_A_36_5_25_26	260.26	-	3.17	Sercon 20-22 (UoE)
U1443_A_36_5_37_38	260.38	-	3.20	Sercon 20-22 (UoE)
U1443_A_36_5_49_50	260.50	-	3.15	Sercon 20-22 (UoE)
U1443_A_36_5_60_61	260.61	-	3.11	Sercon 20-22 (UoE)
U1443_A_36_5_71_72	260.72	-	3.24	Sercon 20-22 (UoE)
U1443_A_36_5_82_83	260.83	-	3.35	Sercon 20-22 (UoE)
U1443_A_36_5_90_91	260.91	-	3.22	Sercon 20-22 (UoE)
U1443_A_36_5_104_105	261.05	-	3.06	Sercon 20-22 (UoE)
U1443_A_36_5_111_112	261.12	-	3.29	Sercon 20-22 (UoE)
U1443_A_36_5_121_122	261.22	-	3.12	Sercon 20-22 (UoE)
U1443_A_36_5_134.5_135.5	261.35	-	3.06	Sercon 20-22 (UoE)
U1443_A_36_5_148_149	261.49	-	3.35	Sercon 20-22 (UoE)
U1443_A_36_6_10_11	261.61	-	3.22	Sercon 20-22 (UoE)
U1443_A_36_6_17_18	261.68	-	3.15	Sercon 20-22 (UoE)
U1443_A_36_6_25_26	261.76	-	3.10	Sercon 20-22 (UoE)
U1443_A_36_6_35_36	261.86	-	3.07	Sercon 20-22 (UoE)
U1443_A_36_6_48_49	261.99	-	3.18	Sercon 20-22 (UoE)
U1443_A_37_1_16_17	263.17	-	3.00	Sercon 20-22 (UoE)
U1443_A_37_1_24_25	263.25	-	3.05	Sercon 20-22 (UoE)
U1443_A_37_1_33_34	263.34	-	2.99	Sercon 20-22 (UoE)
U1443_A_37_1_44_45	263.45	-	2.83	Sercon 20-22 (UoE)
U1443_A_37_1_51_52	263.52	-	2.90	Sercon 20-22 (UoE)
U1443_A_37_1_64.5_65.5	263.65	-	2.77	Sercon 20-22 (UoE)
U1443_A_37_1_76_77	263.77	-	2.82	Sercon 20-22 (UoE)
U1443_A_37_1_85.5_86.5	263.86	-	2.99	Sercon 20-22 (UoE)
U1443_A_37_1_91_92	263.92	-	2.89	Sercon 20-22 (UoE)
U1443_A_37_1_100_101	264.01	-	2.87	Sercon 20-22 (UoE)
U1443_A_37_1_110.5_111.5	264.11	-	2.90	Sercon 20-22 (UoE)
U1443_A_37_1_122_123	264.23	-	2.89	Sercon 20-22 (UoE)
U1443_A_37_1_132_133	264.33	-	3.00	Sercon 20-22 (UoE)
U1443_A_37_1_138_139	264.39	-	2.97	Sercon 20-22 (UoE)
U1443_A_37_2_1_2	264.52	-	2.96	Sercon 20-22 (UoE)
U1443_A_37_2_25_26	264.76	-	2.94	Sercon 20-22 (UoE)
U1443_A_37_2_39_40	264.90	-	2.95	Sercon 20-22 (UoE)
U1443_A_37_2_55_56	265.06	-	2.80	Sercon 20-22 (UoE)
U1443_A_37_2_75_76	265.26	-	2.79	Sercon 20-22 (UoE)
U1443_A_37_2_96_97	265.47	-	2.71	Sercon 20-22 (UoE)
U1443_A_37_2_109_110	265.60	-	2.71	Sercon 20-22 (UoE)

Appendix 10. Bulk carbonate stable carbon isotope ($\delta^{13}C_{bulk}$) data from Indian Ocean Ninetyeast Ridge ODP Site 758. These data were generated on a Sercon 20-22 Isotope Ratio Mass Spectrometer at the University of Exeter, with analytical error of 0.06 ‰ (2σ). Tie points used to generate the age model for this site are highlighted in bold. These data are from ***Chapter 6****.*

Site_Hole_Core_Section_Top Depth (cm)_Bottom Depth (cm)	Depth (mbsf)	Age (Ma)	$\delta^{13}C_{bulk}$ (‰ VPDB)
758_A_28_1_13_16	257.05	56.390	2.79
758_A_28_1_21_23	257.12	56.400	2.83
758_A_28_1_33_35.5	257.24	56.417	2.81
758_A_28_1_40_42	257.31	56.427	2.79
758_A_28_1_48.5_50.5	257.40	56.440	2.77
758_A_28_1_59_61	257.50	56.454	2.72
758_A_28_1_73_74	257.64	56.474	2.72
758_A_28_1_81.5_82.5	**257.72**	**56.485**	2.66
758_A_28_1_92.5_93.5	257.83	56.501	2.83
758_A_28_1_112_113	258.03	56.529	2.88
758_A_28_1_140.5_141.5	258.31	56.568	2.87
758_A_28_2_4_5	258.45	56.588	2.91
758_A_28_2_9_10	258.50	56.595	2.93
758_A_28_2_22.5_23.5	258.64	56.615	2.87
758_A_28_2_30.5_31.5	258.72	56.626	2.93
758_A_28_2_42_43.5	258.84	56.643	2.85
758_A_28_2_49_50	258.91	56.653	2.98
758_A_28_2_59_60.5	259.01	56.667	2.91
758_A_28_2_72.5_73.5	259.14	56.686	3.00
758_A_28_2_80_81	259.22	56.697	3.01
758_A_28_2_87.5_88.5	259.29	56.707	2.95
758_A_28_2_91_92	259.33	56.713	3.06
758_A_28_2_101.5_102.5	259.43	56.727	2.98
758_A_28_2_111.5_112.5	259.53	56.741	3.02
758_A_28_2_120_121	259.62	56.754	3.04
758_A_28_2_129_130	259.71	56.766	3.09
758_A_28_2_139.5_140.5	259.81	56.780	3.09
758_A_28_3_7_8.5	259.99	56.806	3.06
758_A_28_3_17_18	260.09	56.820	2.91
758_A_28_3_30_31	260.22	56.838	2.96
758_A_28_3_38_39.5	260.30	56.850	2.84
758_A_28_3_46.5_47.5	**260.38**	**56.861**	2.83
758_A_28_3_53_54	260.45	56.869	2.88
758_A_28_3_62_63	260.54	56.879	2.96
758_A_28_3_76_77	260.68	56.894	3.03
758_A_28_3_82.5_83.5	260.74	56.901	2.99
758_A_28_3_92_93	260.83	56.911	3.01
758_A_28_3_101.5_102.5	260.93	56.922	2.92
758_A_28_3_112.5_113.5	261.04	56.934	3.00
758_A_28_3_123_124	261.15	56.947	2.88
758_A_28_3_127.5_128.5	**261.19**	**56.951**	2.79
758_A_28_3_132.5_133.5	261.24	56.955	2.89
758_A_28_3_141.5_142.5	261.33	56.962	2.84
758_A_28_4_1_2	261.43	56.971	2.86
758_A_28_4_6_7	261.48	56.975	3.03
758_A_28_4_19.5_20.5	261.61	56.985	3.04
758_A_28_4_24.5_25.5	261.66	56.989	3.04
758_A_28_4_28.5_29.5	261.70	56.993	3.04
758_A_28_4_37.5_38.5	261.79	57.000	3.08
758_A_28_4_53.5_54.5	261.95	57.013	3.04

758_A_28_4_65.5_66.5	262.07	57.023	3.41
758_A_28_4_79.5_80.5	262.21	57.034	3.09
758_A_28_4_88_89	262.30	57.042	3.11
758_A_28_4_96_97	262.38	57.048	3.21
758_A_28_4_120_121	262.62	57.068	3.20
758_A_28_4_132_133	262.74	57.078	3.12
758_A_28_4_141_142	262.83	57.085	3.24
758_A_28_5_3.5_4.5	262.95	57.095	3.16
758_A_28_5_9.5_10.5	263.01	57.100	3.21
758_A_28_5_18_19	263.10	57.107	3.33
758_A_28_5_23_24	263.15	57.111	3.11
758_A_28_5_34.5_35.5	263.26	57.120	3.14
758_A_28_5_38_39	263.30	57.124	3.20
758_A_28_5_45.5_46.5	263.37	57.129	3.00
758_A_28_5_54.5_55.5	263.46	57.137	3.02
758_A_28_5_70_71	263.62	57.150	3.00
758_A_28_5_79_80	263.71	57.157	3.06
758_A_28_5_86.5_87.5	263.78	57.163	3.10
758_A_28_5_102_103	263.94	57.176	3.10
758_A_28_5_108.5_109.5	264.00	57.181	3.12
758_A_28_6_1_2	264.43	57.216	2.94
758_A_28_6_6.5_7.5	**264.48**	**57.220**	2.82
758_A_28_6_19_20	264.61	57.243	3.14
758_A_28_6_27.5_28.5	264.69	57.257	2.97
758_A_28_6_37_38	264.79	57.275	3.32
758_A_28_6_47_48	264.89	57.293	3.04
758_A_28_6_59_60	265.01	57.314	3.11
758_A_28_6_68_69	**265.10**	**57.333**	3.01
758_A_28_6_80.5_81.5	265.22	57.347	3.02
758_A_28_6_94_95	265.36	57.363	3.15
758_A_28_6_107_108	265.49	57.378	3.42
758_A_28_6_121_122	265.63	57.394	3.45
758_A_28_6_136_137	265.78	57.412	3.42
758_A_28_7_6_7	265.98	57.435	3.45
758_A_28_7_12_13	266.04	57.442	3.48

Appendix 11. Planktic foraminiferal stable carbon isotope ($\delta^{13}C_{planktic}$) and stable oxygen isotope ($\delta^{18}O_{planktic}$) data from Indian Ocean Ninetyeast Ridge IODP Site U1443. These data were generated on a Thermo Finnigan MAT 253 Isotope Ratio Mass Spectrometer equipped with a Kiel IV Carbonate Preparation Device at Cardiff University, with long-term analytical precision of 0.02 ‰ for $\delta^{13}C$ and 0.03 ‰ for $\delta^{18}O$ (1σ). These data are from ***Chapter 6****.*

Site_Hole_Core_Section_Top Depth (cm)_Bottom Depth (cm)	Depth (mbsf)	Age (Ma)	Species	$\delta^{13}C_{planktic}$ (‰ VPDB)	$\delta^{18}O_{planktic}$ (‰ VPDB)
U1443_A_35_1_49_50	245.40	53.244	*Morozovella subbotinae*	2.70	–1.93
U1443_A_35_1_77_78	245.68	53.491	*Morozovella subbotinae*	2.86	–1.94
U1443_A_35_1_130_131	246.21	53.958	*Morozovella subbotinae*	2.86	–1.88
U1443_A_35_1_143_144	246.34	54.000	*Morozovella subbotinae*	2.74	–1.67
U1443_A_35_2_9_10	246.50	54.051	*Morozovella subbotinae*	2.84	–1.72
U1443_A_35_2_22_23	246.63	54.116	*Morozovella subbotinae*	2.86	–1.70
U1443_A_35_2_24_25	246.65	54.126	*Morozovella subbotinae*	2.74	–1.53
U1443_A_35_2_36_37	246.77	54.186	*Morozovella subbotinae*	2.95	–1.65
U1443_A_35_2_56_57	246.97	54.285	*Morozovella subbotinae*	3.01	–1.65
U1443_A_35_2_69_70	247.10	54.350	*Morozovella subbotinae*	3.43	–1.76
U1443_A_35_2_76_77	247.17	54.385	*Morozovella subbotinae*	3.25	–1.71
U1443_A_35_2_126_127	247.67	54.634	*Morozovella subbotinae*	3.42	–1.51
U1443_A_35_3_10_11	248.01	54.803	*Morozovella velascoensis*	3.45	–1.91
U1443_A_35_3_10_11	248.01	54.803	*Morozovella subbotinae*	3.36	–1.63
U1443_A_35_3_13_14	248.04	54.818	*Morozovella velascoensis*	3.33	–1.89
U1443_A_35_3_13_14	248.04	54.818	*Morozovella subbotinae*	3.44	–1.70
U1443_A_35_3_24_25	248.15	54.873	*Morozovella velascoensis*	3.39	–1.71
U1443_A_35_3_24_25	248.15	54.873	*Morozovella subbotinae*	3.60	–1.65
U1443_A_35_3_40.5_41.5	248.31	55.208	*Morozovella velascoensis*	3.46	–1.81
U1443_A_35_3_40.5_41.5	248.31	55.208	*Morozovella subbotinae*	3.49	–1.66
U1443_A_35_3_69_70	248.60	55.800	*Morozovella velascoensis*	2.72	–1.65
U1443_A_35_3_72_73	248.63	55.835	*Morozovella velascoensis*	2.09	–1.62
U1443_A_35_3_92_93	248.83	55.940	*Morozovella velascoensis*	3.79	–1.58
U1443_A_36_1_8_9	254.09	57.206	*Morozovella velascoensis*	4.69	–1.63
U1443_A_36_1_25_26	254.26	57.220	*Morozovella velascoensis*	4.06	–1.76
U1443_A_36_1_42_43	254.43	57.268	*Morozovella velascoensis*	4.77	–1.76
U1443_A_36_1_65_66	254.66	57.333	*Morozovella velascoensis*	4.54	–1.77
U1443_A_36_1_94_95	254.95	57.367	*Morozovella velascoensis*	4.86	–1.66
U1443_A_36_1_100_101	255.01	57.374	*Morozovella velascoensis*	4.86	–1.72
U1443_A_36_1_116_117	255.17	57.392	*Morozovella velascoensis*	5.21	–1.82
U1443_A_36_1_121_122	255.22	57.398	*Morozovella velascoensis*	5.16	–1.86
U1443_A_36_2_8_9	255.59	57.441	*Morozovella velascoensis*	5.34	–1.76
U1443_A_36_2_53_54	256.04	57.493	*Morozovella velascoensis*	4.95	–1.76
U1443_A_36_2_89_90	256.40	57.555	*Morozovella velascoensis*	4.85	–1.72
U1443_A_36_2_116.5_117.5	256.67	57.602	*Morozovella velascoensis*	4.91	–1.63
U1443_A_36_2_127.5_128.5	256.78	57.621	*Morozovella velascoensis*	4.87	–1.72
U1443_A_36_2_139_140	256.95	57.651	*Morozovella velascoensis*	4.78	–1.81
U1443_A_36_3_29_30	257.30	57.711	*Morozovella velascoensis*	4.84	–1.80
U1443_A_36_3_44_45	257.45	57.737	*Morozovella velascoensis*	4.92	–1.61
U1443_A_36_3_62_63	257.63	57.768	*Morozovella velascoensis*	5.05	–1.71
U1443_A_36_3_81_82	257.82	57.801	*Morozovella velascoensis*	5.13	–1.76
U1443_A_36_3_100_101	258.01	57.834	*Morozovella velascoensis*	5.13	–1.70

Appendix 12. Planktic foraminiferal stable carbon isotope ($\delta^{13}C_{planktic}$) and stable oxygen isotope ($\delta^{18}O_{planktic}$) data from Indian Ocean Ninetyeast Ridge ODP Site 758. These data were generated on a Thermo Finnigan MAT 253 Isotope Ratio Mass Spectrometer equipped with a Kiel IV Carbonate Preparation Device at Cardiff University, with long-term analytical precision of 0.02 ‰ for $\delta^{13}C$ and 0.03 ‰ for $\delta^{18}O$ (1σ). These data are from ***Chapter 6****.*

Site_Hole_Core_Section_Top Depth (cm)_Bottom Depth (cm)	Depth (mbsf)	Age (Ma)	Species	$\delta^{13}C_{planktic}$ (‰ VPDB)	$\delta^{18}O_{planktic}$ (‰ VPDB)
758_A_28_1_21_23	257.12	56.400	*Morozovella velascoensis*	4.21	–1.55
758_A_28_1_81.5_82.5	257.72	56.485	*Morozovella velascoensis*	3.88	–1.34
758_A_28_2_139.5_140.5	259.81	56.780	*Morozovella velascoensis*	4.81	–1.57
758_A_28_3_30_31	260.22	56.838	*Morozovella velascoensis*	4.35	–1.55
758_A_28_3_38_39.5	260.30	56.850	*Morozovella velascoensis*	4.32	–1.44
758_A_28_3_132.5_133.5	261.24	56.955	*Morozovella velascoensis*	4.23	–1.33
758_A_28_4_53.5_54.5	261.95	57.013	*Morozovella velascoensis*	4.44	–1.36
758_A_28_4_96_97	262.38	57.048	*Morozovella velascoensis*	4.65	–1.34
758_A_28_5_18_19	263.10	57.107	*Morozovella velascoensis*	4.64	–1.37
758_A_28_5_70_71	263.62	57.150	*Morozovella velascoensis*	4.60	–1.44
758_A_28_5_108.5_109.5	264.00	57.181	*Morozovella velascoensis*	4.69	–1.54

Appendix 13. Mixed layer planktic foraminiferal magnesium/calcium (Mg/Ca) data from Indian Ocean Ninetyeast Ridge IODP Site U1443. These data were generated on a Thermo Finnigan Element XR Inductively-Coupled Plasma-Mass Spectrometer at the University of California Santa Cruz, with long-term analytical precision of <3% (2σ). Raw data and pH corrected data (following the linear correction described in Evans et al., 2016a, assuming ambient pH of 7.7 and a PETM pH of 7.6) are shown. Absolute temperature estimates are calculated assuming a Mg/Ca ratio in Paleogene seawater (Mg/Ca_{sw}) of 1.5 mol/mol (consistent with modelling studies by Stanley & Hardie., 1998 and Demicco et al., 2005) and 2.5 mol/mol (consistent with Early Eocene proxy data in Evans et al., 2018). These data are from ***Chapter 6****.*

Site_Hole_Core_Section_Top Depth (cm)_Bottom Depth (cm)	Depth (CSF-A)	Age (Ma)	Species	Mg/Ca (mmol/mol; raw data)	Mg/Ca (mmol/mol; pH corrected	Temperature (°C; Mg/Ca_{sw} = 1.5 mol/mol)	Temperature (°C; Mg/Ca_{sw} = 2.5 mol/mol)
U1443_A_35_1_49_50	245.40	53.244	*Morozovella subbotinae*	4.52	3.45	35.38	30.89
U1443_A_35_1_77_78	245.68	53.491	*Morozovella subbotinae*	4.92	3.76	36.32	31.84
U1443_A_35_1_130_131	246.21	53.958	*Morozovella subbotinae*	5.26	4.01	37.05	32.57
U1443_A_35_1_143_144	246.34	54.000	*Morozovella subbotinae*	4.83	3.68	36.10	31.62
U1443_A_35_2_9_10	246.50	54.051	*Morozovella subbotinae*	4.32	3.30	34.88	30.40
U1443_A_35_2_22_23	246.63	54.116	*Morozovella subbotinae*	4.37	3.34	35.01	30.53
U1443_A_35_2_24_25	246.65	54.126	*Morozovella subbotinae*	4.74	3.62	35.90	31.42
U1443_A_35_2_36_37	246.77	54.186	*Morozovella subbotinae*	4.39	3.35	35.05	30.57
U1443_A_35_2_56_57	246.97	54.285	*Morozovella subbotinae*	4.74	3.61	35.89	31.41
U1443_A_35_2_69_70	247.10	54.350	*Morozovella subbotinae*	4.26	3.25	34.71	30.22
U1443_A_35_2_76_77	247.17	54.385	*Morozovella subbotinae*	4.41	3.36	35.09	30.60
U1443_A_35_2_126_127	247.67	54.634	*Morozovella subbotinae*	4.30	3.28	34.82	30.34
U1443_A_35_3_10_11	248.01	54.803	*Morozovella subbotinae*	4.68	3.57	35.75	31.27
U1443_A_35_3_40.5_41.5	248.31	55.208	*Morozovella subbotinae*	4.52	3.45	35.37	30.88
U1443_A_35_3_40.5_41.5	248.31	55.208	*Morozovella velascoensis*	4.32	3.29	34.86	30.38
U1443_A_35_3_72_73	248.63	55.835	*Morozovella velascoensis*	4.80	3.48	35.47	30.99
U1443_A_35_3_92_93	248.83	55.940	*Morozovella velascoensis*	4.01	3.06	34.04	29.56
U1443_A_36_1_8_9	254.09	57.206	*Morozovella velascoensis*	4.22	3.22	34.60	30.12
U1443_A_36_1_25_26	254.26	57.220	*Morozovella velascoensis*	4.08	3.11	34.24	29.75
U1443_A_36_1_42_43	254.43	57.268	*Morozovella velascoensis*	4.05	3.10	34.17	29.68
U1443_A_36_1_65_66	254.66	57.333	*Morozovella velascoensis*	4.19	3.20	34.54	30.06

U1443_A_36_1_94_95	254.95	57.367	*Morozovella velascoensis*	4.28	3.26	34.76	30.27
U1443_A_36_1_100_101	255.01	57.374	*Morozovella velascoensis*	4.61	3.52	35.60	31.11
U1443_A_36_1_116_117	255.17	57.392	*Morozovella velascoensis*	4.63	3.54	35.65	31.16
U1443_A_36_1_121_122	255.22	57.398	*Morozovella velascoensis*	4.30	3.28	34.81	30.33
U1443_A_36_2_8_9	255.59	57.441	*Morozovella velascoensis*	4.20	3.20	34.55	30.06
U1443_A_36_2_53_54	256.04	57.493	*Morozovella velascoensis*	4.39	3.35	35.05	30.57
U1443_A_36_2_89_90	256.40	57.555	*Morozovella velascoensis*	4.14	3.16	34.40	29.91
U1443_A_36_2_116.5_117.5	256.67	57.602	*Morozovella velascoensis*	4.19	3.20	34.53	30.05
U1443_A_36_2_127.5_128.5	256.78	57.621	*Morozovella velascoensis*	4.28	3.27	34.77	30.28
U1443_A_36_2_139_140	256.95	57.651	*Morozovella velascoensis*	4.15	3.17	34.43	29.95
U1443_A_36_3_44_45	257.45	57.737	*Morozovella velascoensis*	4.24	3.24	34.67	30.19
U1443_A_36_3_62_63	257.63	57.768	*Morozovella velascoensis*	4.02	3.07	34.08	29.59
U1443_A_36_3_81_82	257.82	57.801	*Morozovella velascoensis*	4.14	3.16	34.41	29.92
U1443_A_36_3_100_101	258.01	57.834	*Morozovella velascoensis*	3.97	3.03	33.94	29.46
U1443_A_36_3_135_136	258.36	57.895	*Morozovella velascoensis*	3.99	3.05	34.00	29.51

Appendix 14. Mixed layer planktic foraminiferal magnesium/calcium (Mg/Ca) data from Indian Ocean Ninetyeast Ridge ODP Site 758. These data were generated on a Thermo Finnigan Element XR Inductively-Coupled Plasma-Mass Spectrometer at the University of California Santa Cruz, with long-term analytical precision of <3% (2σ). Raw data and pH corrected data (following the linear correction described in Evans et al., 2016a, assuming ambient pH of 7.7 and a PETM pH of 7.6) are shown. Absolute temperature estimates are calculated assuming a Mg/Ca ratio in Paleogene seawater (Mg/Ca_{sw}) of 1.5 mol/mol (consistent with modelling studies by Stanley & Hardie., 1998 and Demicco et al., 2005) and 2.5 mol/mol (consistent with Early Eocene proxy data in Evans et al., 2018). These data are from ***Chapter 6****.*

Site_Hole_Core_Section_ Top Depth (cm)_Bottom Depth (cm)	**Depth (mbsf)**	**Age (Ma)**	**Species**	**Mg/Ca (mmol/mol; raw data)**	**Mg/Ca (mmol/mol; pH corrected**	**Temperature (°C; Mg/Ca_{sw} = 1.5 mol/mol)**	**Temperature (°C; Mg/Ca_{sw} = 2.5 mol/mol)**
758_A_28_1_21_23	257.12	56.400	*Morozovella velascoensis*	3.86	2.94	33.61	29.12
758_A_28_1_81.5_82.5	257.72	56.485	*Morozovella velascoensis*	3.93	3.00	33.83	29.35
758_A_28_2_139.5_ 140.5	259.81	56.780	*Morozovella velascoensis*	3.89	2.97	33.71	29.23
758_A_28_3_30_31	260.22	56.838	*Morozovella velascoensis*	3.89	2.97	33.70	29.22
758_A_28_3_38_39.5	260.30	56.850	*Morozovella velascoensis*	3.81	2.91	33.48	28.99
758_A_28_3_127.5_ 128.5	261.19	56.951	*Morozovella velascoensis*	4.09	3.12	34.26	29.78
758_A_28_4_96_97	262.38	57.048	*Morozovella velascoensis*	3.93	3.00	33.82	29.34
758_A_28_5_70_71	263.62	57.150	*Morozovella velascoensis*	4.20	3.21	34.56	30.07

Appendix 15. Mixed layer planktic foraminiferal magnesium/calcium (Mg/Ca) data from Indian Ocean Ninetyeast Ridge ODP Site 758. These data were generated on a Thermo Finnigan Element XR Inductively-Coupled Plasma-Mass Spectrometer at Yale University, with long-term analytical precision of <3% (2σ). Raw data and pH corrected data (following the linear correction described in Evans et al., 2016a, assuming ambient pH of 7.7 and a PETM pH of 7.6) are shown. Absolute temperature estimates are calculated assuming a Mg/Ca ratio in Paleogene seawater (Mg/Ca_{sw}) of 1.5 mol/mol (consistent with modelling studies by Stanley & Hardie., 1998 and Demicco et al., 2005) and 2.5 mol/mol (consistent with Early Eocene proxy data in Evans et al., 2018). These data are from ***Chapter 6****.*

Site_Hole_Core_Section_ Top Depth (cm)_Bottom Depth (cm)	**Depth (mbsf)**	**Age (Ma)**	**Species**	**Mg/Ca (mmol/mol; raw data)**	**Mg/Ca (mmol/mol; pH corrected**	**Temperature (°C; Mg/Ca_{sw} = 1.5 mol/mol)**	**Temperature (°C; Mg/Ca_{sw} = 2.5 mol/mol)**
758_A_28_1_21_23	257.12	56.400	*Morozovella velascoensis*	3.45	2.63	32.36	27.88
758_A_28_1_81.5_82.5	257.72	56.485	*Morozovella velascoensis*	3.46	2.64	32.39	27.91
758_A_28_2_139.5_ 140.5	259.81	56.780	*Morozovella velascoensis*	3.49	2.66	32.50	28.02
758_A_28_2_139.5_ 140.5	259.81	56.780	*Morozovella subbotinae*	3.49	2.66	32.49	28.01
758_A_28_3_30_31	260.22	56.838	*Morozovella velascoensis*	3.61	2.76	32.88	28.40
758_A_28_3_30_31	260.22	56.838	*Morozovella subbotinae*	3.51	2.68	32.57	28.09
758_A_28_3_38_39.5	260.30	56.850	*Morozovella velascoensis*	3.68	2.81	33.09	28.61
758_A_28_4_53.5_54.5	261.95	57.013	*Morozovella velascoensis*	3.53	2.69	32.62	28.14
758_A_28_4_96_97	262.38	57.048	*Morozovella velascoensis*	3.61	2.76	32.88	28.39
758_A_28_5_70_71	263.62	57.150	*Morozovella velascoensis*	3.71	2.83	33.17	28.69

Appendix 16. Mixed layer planktic foraminiferal boron/calcium (B/Ca) data from Indian Ocean Ninetyeast Ridge IODP Site U1443. These data were generated on a Thermo Finnigan Element XR Inductively-Coupled Plasma-Mass Spectrometer at the University of California Santa Cruz, with long-term analytical precision of <5% (2σ). The borate/dissolved inorganic carbon ($\frac{[B(OH)_4^-]}{DIC}$) ratio is calculated using the Paleocene calibration of Haynes et al. (2017). These data are from ***Chapter 6****.*

Site_Hole_Core_Section_Top Depth (cm)_Bottom Depth (cm)	Depth (CSF-A)	Age (Ma)	Species	B/Ca (µmol/mol)	$\frac{[B(OH)_4^-]}{DIC}$
U1443_A_35_1_49_50	245.40	53.244	*Morozovella subbotinae*	51.56	0.016
U1443_A_35_1_77_78	245.68	53.491	*Morozovella subbotinae*	57.34	0.021
U1443_A_35_1_130_131	246.21	53.958	*Morozovella subbotinae*	57.97	0.021
U1443_A_35_1_143_144	246.34	54.000	*Morozovella subbotinae*	55.86	0.019
U1443_A_35_2_9_10	246.50	54.051	*Morozovella subbotinae*	49.26	0.014
U1443_A_35_2_22_23	246.63	54.116	*Morozovella subbotinae*	50.10	0.014
U1443_A_35_2_24_25	246.65	54.126	*Morozovella subbotinae*	51.39	0.015
U1443_A_35_2_36_37	246.77	54.186	*Morozovella subbotinae*	53.80	0.018
U1443_A_35_2_56_57	246.97	54.285	*Morozovella subbotinae*	52.11	0.016
U1443_A_35_2_69_70	247.10	54.350	*Morozovella subbotinae*	57.25	0.021
U1443_A_35_2_76_77	247.17	54.385	*Morozovella subbotinae*	56.16	0.020
U1443_A_35_2_126_127	247.67	54.634	*Morozovella subbotinae*	54.24	0.018
U1443_A_35_3_10_11	248.01	54.803	*Morozovella subbotinae*	53.92	0.018
U1443_A_35_3_40.5_41.5	248.31	55.208	*Morozovella subbotinae*	45.43	0.010
U1443_A_35_3_40.5_41.5	248.31	55.208	*Morozovella velascoensis*	57.17	0.020
U1443_A_35_3_72_73	248.63	55.835	*Morozovella velascoensis*	48.47	0.013
U1443_A_35_3_92_93	248.83	55.940	*Morozovella velascoensis*	55.95	0.019
U1443_A_36_1_8_9	254.09	57.206	*Morozovella velascoensis*	75.65	0.037
U1443_A_36_1_25_26	254.26	57.220	*Morozovella velascoensis*	63.33	0.026
U1443_A_36_1_42_43	254.43	57.268	*Morozovella velascoensis*	66.83	0.029
U1443_A_36_1_65_66	254.66	57.333	*Morozovella velascoensis*	61.30	0.024
U1443_A_36_1_94_95	254.95	57.367	*Morozovella velascoensis*	73.51	0.035
U1443_A_36_1_100_101	255.01	57.374	*Morozovella velascoensis*	81.45	0.042
U1443_A_36_1_116_117	255.17	57.392	*Morozovella velascoensis*	83.17	0.043
U1443_A_36_1_121_122	255.22	57.398	*Morozovella velascoensis*	72.79	0.034
U1443_A_36_2_8_9	255.59	57.441	*Morozovella velascoensis*	73.42	0.035
U1443_A_36_2_53_54	256.04	57.493	*Morozovella velascoensis*	78.97	0.039
U1443_A_36_2_89_90	256.40	57.555	*Morozovella velascoensis*	66.18	0.028
U1443_A_36_2_116.5_117.5	256.67	57.602	*Morozovella velascoensis*	63.85	0.026
U1443_A_36_2_127.5_128.5	256.78	57.621	*Morozovella velascoensis*	67.07	0.029
U1443_A_36_2_139_140	256.95	57.651	*Morozovella velascoensis*	63.66	0.026
U1443_A_36_3_44_45	257.45	57.737	*Morozovella velascoensis*	74.64	0.036
U1443_A_36_3_62_63	257.63	57.768	*Morozovella velascoensis*	66.73	0.029
U1443_A_36_3_81_82	257.82	57.801	*Morozovella velascoensis*	68.34	0.030
U1443_A_36_3_100_101	258.01	57.834	*Morozovella velascoensis*	78.80	0.039
U1443_A_36_3_135_136	258.36	57.895	*Morozovella velascoensis*	69.93	0.032

Appendix 17. Mixed layer planktic foraminiferal boron/calcium (B/Ca) data from Indian Ocean Ninetyeast Ridge ODP Site 758. These data were generated on a Thermo Finnigan Element XR Inductively-Coupled Plasma-Mass Spectrometer at the University of California Santa Cruz, with long-term analytical precision of <5% (2σ). The borate/dissolved inorganic carbon ($\frac{[B(OH)_4^-]}{DIC}$) ratio is calculated using the Paleocene calibration of Haynes et al. (2017). These data are from ***Chapter 6****.*

Site_Hole_Core_Section_Top Depth (cm)_Bottom Depth (cm)	Depth (mbsf)	Age (Ma)	Species	B/Ca (μmol/mol)	$\frac{[B(OH)_4^-]}{DIC}$
758_A_28_1_21_23	257.12	56.400	*Morozovella velascoensis*	46.64	0.0113
758_A_28_1_81.5_82.5	257.72	56.485	*Morozovella velascoensis*	55.96	0.0194
758_A_28_2_139.5_140.5	259.81	56.780	*Morozovella velascoensis*	60.13	0.0230
758_A_28_3_30_31	260.22	56.838	*Morozovella velascoensis*	54.59	0.0182
758_A_28_3_38_39.5	260.30	56.850	*Morozovella velascoensis*	53.66	0.0174
758_A_28_3_127.5_128.5	261.19	56.951	*Morozovella velascoensis*	55.40	0.0189
758_A_28_4_96_97	262.38	57.048	*Morozovella velascoensis*	58.66	0.0218
758_A_28_5_70_71	263.62	57.150	*Morozovella velascoensis*	75.91	0.0368

Appendix 18. Mixed layer planktic foraminiferal boron/calcium (B/Ca) data from Indian Ocean Ninetyeast Ridge ODP Site 758. These data were generated on a Thermo Finnigan Element XR Inductively-Coupled Plasma-Mass Spectrometer at Yale University, with long-term analytical precision of <5% (2σ). The borate/dissolved inorganic carbon ($\frac{[B(OH)_4^-]}{DIC}$) ratio is calculated using the Paleocene calibration of Haynes et al. (2017). These data are from ***Chapter 6****.*

Site_Hole_Core_Section_Top Depth (cm)_Bottom Depth (cm)	Depth (mbsf)	Age (Ma)	Species	B/Ca (μmol/mol)	$\frac{[B(OH)_4^-]}{DIC}$
758_A_28_1_21_23	257.12	56.400	*Morozovella velascoensis*	50.65	0.0148
758_A_28_1_81.5_82.5	257.72	56.485	*Morozovella velascoensis*	53.46	0.0172
758_A_28_2_139.5_140.5	259.81	56.780	*Morozovella velascoensis*	65.17	0.0274
758_A_28_2_139.5_140.5	259.81	56.780	*Morozovella subbotinae*	55.20	0.0187
758_A_28_3_30_31	260.22	56.838	*Morozovella velascoensis*	61.77	0.0245
758_A_28_3_30_31	260.22	56.838	*Morozovella subbotinae*	49.61	0.0139
758_A_28_3_38_39.5	260.30	56.850	*Morozovella velascoensis*	60.87	0.0237
758_A_28_4_53.5_54.5	261.95	57.013	*Morozovella velascoensis*	57.39	0.0207
758_A_28_4_96_97	262.38	57.048	*Morozovella velascoensis*	62.61	0.0252
758_A_28_5_70_71	263.62	57.150	*Morozovella velascoensis*	58.18	0.0213

Appendix 19. Thermocline planktic foraminiferal magnesium/calcium (Mg/Ca) data from Indian Ocean Ninetyeast Ridge IODP Site U1443. These data were generated on a Thermo Finnigan Element XR Inductively-Coupled Plasma-Mass Spectrometer at the University of California Santa Cruz, with long-term analytical precision of <3% (2σ). Raw data and pH corrected data (following the linear correction described in Evans et al., 2016a, assuming ambient pH of 7.7 and a PETM pH of 7.6) are shown. Absolute temperature estimates are calculated assuming a Mg/Ca ratio in Paleogene seawater (Mg/Ca_{sw}) of 1.5 mol/mol (consistent with modelling studies by Stanley & Hardie., 1998 and Demicco et al., 2005) and 2.5 mol/mol (consistent with Early Eocene proxy data in Evans et al., 2018). These data are from ***Chapter 6****.*

Site_Hole_Core_Section_ Top Depth (cm)_Bottom Depth (cm)	Depth (mbsf)	Age (Ma)	Species	Mg/Ca (mmol/mol; raw data)	Mg/Ca (mmol/mol; pH corrected	Temperature (°C; Mg/Ca_{sw} = 1.5 mol/mol)	Temperature (°C; Mg/Ca_{sw} = 2.5 mol/mol)
U1443_A_35_1_49_50	245.40	53.244	*Subbotina hornibrooki*	3.87	2.96	33.65	29.17
U1443_A_35_1_77_78	245.68	53.491	*Subbotina hornibrooki*	3.80	2.90	33.45	28.97
U1443_A_35_1_130_ 131	246.21	53.958	*Subbotina hornibrooki*	4.14	3.16	34.41	29.92
U1443_A_35_1_143_ 144	246.34	54.000	*Subbotina hornibrooki*	4.35	3.32	34.94	30.46
U1443_A_35_2_9_10	246.50	54.051	*Subbotina hornibrooki*	4.35	3.32	34.94	30.45
U1443_A_35_2_22_23	246.63	54.116	*Subbotina hornibrooki*	4.14	3.16	34.39	29.91
U1443_A_35_2_24_25	246.65	54.126	*Subbotina hornibrooki*	4.09	3.12	34.27	29.78
U1443_A_35_2_36_37	246.77	54.186	*Subbotina hornibrooki*	4.24	3.23	34.65	30.17
U1443_A_35_2_56_57	246.97	54.285	*Subbotina hornibrooki*	4.55	3.48	35.46	30.98
U1443_A_35_2_69_70	247.10	54.350	*Subbotina hornibrooki*	4.11	3.14	34.32	29.83
U1443_A_35_2_126_ 127	247.67	54.634	*Subbotina hornibrooki*	3.86	2.95	33.62	29.13
U1443_A_35_3_10_11	248.01	54.803	*Subbotina hornibrooki*	4.06	3.10	34.18	29.70
U1443_A_35_3_10_11	248.01	54.803	*Subbotina velascoensis*	4.10	3.13	34.29	29.80
U1443_A_35_3_40.5_ 41.5	248.31	55.208	*Subbotina hornibrooki*	4.30	3.28	34.81	30.33
U1443_A_35_3_40.5_ 41.5	248.31	55.208	*Subbotina velascoensis*	4.26	3.25	34.71	30.22
U1443_A_35_3_72_73	248.63	55.835	*Subbotina velascoensis*	4.51	3.27	34.76	30.28
U1443_A_35_3_92_93	248.83	55.940	*Subbotina velascoensis*	3.48	2.66	32.48	28.00
U1443_A_36_1_42_43	254.43	57.268	*Subbotina velascoensis*	3.34	2.55	32.01	27.52
U1443_A_36_1_65_66	254.66	57.333	*Subbotina velascoensis*	3.11	2.37	31.20	26.72
U1443_A_36_1_94_95	254.95	57.367	*Subbotina velascoensis*	3.15	2.40	31.36	26.87

U1443_A_36_1_116_117	255.17	57.392	*Subbotina velascoensis*	3.40	2.59	32.20	27.72
U1443_A_36_1_121_122	255.22	57.398	*Subbotina velascoensis*	3.35	2.56	32.05	27.57
U1443_A_36_2_8_9	255.59	57.441	*Subbotina velascoensis*	3.62	2.76	32.91	28.42
U1443_A_36_2_53_54	256.04	57.493	*Subbotina velascoensis*	3.11	2.37	31.22	26.74
U1443_A_36_2_116.5_117.5	256.67	57.602	*Subbotina velascoensis*	3.42	2.61	32.27	27.79
U1443_A_36_2_127.5_128.5	256.78	57.621	*Subbotina velascoensis*	3.25	2.48	31.72	27.23
U1443_A_36_3_62_63	257.63	57.768	*Subbotina velascoensis*	3.09	2.36	31.14	26.66
U1443_A_36_3_81_82	257.82	57.801	*Subbotina velascoensis*	3.23	2.47	31.65	27.16
U1443_A_36_3_100_101	258.01	57.834	*Subbotina velascoensis*	3.01	2.30	30.86	26.38
U1443_A_36_3_135_136	258.36	57.895	*Subbotina velascoensis*	3.51	2.68	32.56	28.07

Appendix 20. Thermocline planktic foraminiferal magnesium/calcium (Mg/Ca) data from Indian Ocean Ninetyeast Ridge ODP Site 758. These data were generated on a Thermo Finnigan Element XR Inductively-Coupled Plasma-Mass Spectrometer at the University of California Santa Cruz, with long-term analytical precision of <3% (2σ). Raw data and pH corrected data (following the linear correction described in Evans et al., 2016a, assuming ambient pH of 7.7 and a PETM pH of 7.6) are shown. Absolute temperature estimates are calculated assuming a Mg/Ca ratio in Paleogene seawater (Mg/Ca_{sw}) of 1.5 mol/mol (consistent with modelling studies by Stanley & Hardie., 1998 and Demicco et al., 2005) and 2.5 mol/mol (consistent with Early Eocene proxy data in Evans et al., 2018). These data are from ***Chapter 6****.*

Site_Hole_Core_Section_ Top Depth (cm)_Bottom Depth (cm)	**Depth (mbsf)**	**Age (Ma)**	**Species**	**Mg/Ca (mmol/mol; raw data)**	**Mg/Ca (mmol/mol; pH corrected**	**Temperature (°C; Mg/Ca_{sw} = 1.5 mol/mol)**	**Temperature (°C; Mg/Ca_{sw} = 2.5 mol/mol)**
758_A_28_1_21_23	257.12	56.400	*Subbotina velascoensis*	3.65	2.79	33.00	28.52
758_A_28_1_81.5_82.5	257.72	56.485	*Subbotina velascoensis*	3.45	2.63	32.38	27.89
758_A_28_2_139.5_ 140.5	259.81	56.780	*Subbotina velascoensis*	3.78	2.89	33.39	28.91
758_A_28_3_127.5_ 128.5	261.19	56.951	*Subbotina velascoensis*	3.74	2.85	33.26	28.78
758_A_28_4_96_97	262.38	57.048	*Subbotina velascoensis*	3.85	2.94	33.59	29.11
758_A_28_5_70_71	263.62	57.150	*Subbotina velascoensis*	3.51	2.68	32.56	28.07

Appendix 21. Thermocline planktic foraminiferal magnesium/calcium (Mg/Ca) data from Indian Ocean Ninetyeast Ridge ODP Site 758. These data were generated on a Thermo Finnigan Element XR Inductively-Coupled Plasma-Mass Spectrometer at Yale University, with long-term analytical precision of <3% (2σ). Raw data and pH corrected data (following the linear correction described in Evans et al., 2016a, assuming ambient pH of 7.7 and a PETM pH of 7.6) are shown. Absolute temperature estimates are calculated assuming a Mg/Ca ratio in Paleogene seawater (Mg/Ca_{sw}) of 1.5 mol/mol (consistent with modelling studies by Stanley & Hardie., 1998 and Demicco et al., 2005) and 2.5 mol/mol (consistent with Early Eocene proxy data in Evans et al., 2018). These data are from ***Chapter 6****.*

Site_Hole_Core_Section_ Top Depth (cm)_Bottom Depth (cm)	**Depth (mbsf)**	**Age (Ma)**	**Species**	**Mg/Ca (mmol/mol; raw data)**	**Mg/Ca (mmol/mol; pH corrected**	**Temperature (°C; Mg/Ca_{sw} = 1.5 mol/mol)**	**Temperature (°C; Mg/Ca_{sw} = 2.5 mol/mol)**
758_A_28_1_21_23	257.12	56.400	*Subbotina velascoensis*	3.59	2.74	32.80	28.32
758_A_28_2_139.5_ 140.5	259.81	56.780	*Subbotina velascoensis*	3.51	2.68	32.55	28.07
758_A_28_3_30_31	260.22	56.838	*Subbotina velascoensis*	3.37	2.57	32.10	27.62
758_A_28_3_38_39.5	260.30	56.850	*Subbotina velascoensis*	3.39	2.59	32.17	27.69
758_A_28_3_132.5_ 133.5	261.24	56.955	*Subbotina velascoensis*	3.48	2.66	32.47	27.99
758_A_28_4_53.5_54.5	261.95	57.013	*Subbotina velascoensis*	3.45	2.63	32.37	27.89
758_A_28_4_96_97	262.38	57.048	*Subbotina velascoensis*	3.40	2.59	32.20	27.72
758_A_28_5_18_19	263.10	57.107	*Subbotina velascoensis*	3.60	2.74	32.83	28.35
758_A_28_5_70_71	263.62	57.150	*Subbotina velascoensis*	3.27	2.50	31.78	27.29
758_A_28_5_108.5_ 109.5	264.00	57.181	*Subbotina velascoensis*	3.39	2.59	32.19	27.70

Appendix 22. Thermocline planktic foraminiferal boron/calcium (B/Ca) data from Indian Ocean Ninetyeast Ridge IODP Site U1443. These data were generated on a Thermo Finnigan Element XR Inductively-Coupled Plasma-Mass Spectrometer at the University of California Santa Cruz, with long-term analytical precision of <5% (2σ). These data are from ***Chapter 6****.*

Site_Hole_Core_Section_Top Depth (cm)_Bottom Depth (cm)	Depth (mbsf)	Age (Ma)	Species	B/Ca (µmol/mol)
U1443_A_35_1_49_50	245.40	53.244	*Subbotina hornibrooki*	12.64
U1443_A_35_1_77_78	245.68	53.491	*Subbotina hornibrooki*	13.15
U1443_A_35_1_130_131	246.21	53.958	*Subbotina hornibrooki*	29.44
U1443_A_35_1_143_144	246.34	54.000	*Subbotina hornibrooki*	26.30
U1443_A_35_2_9_10	246.50	54.051	*Subbotina hornibrooki*	21.58
U1443_A_35_2_22_23	246.63	54.116	*Subbotina hornibrooki*	21.31
U1443_A_35_2_24_25	246.65	54.126	*Subbotina hornibrooki*	21.12
U1443_A_35_2_36_37	246.77	54.186	*Subbotina hornibrooki*	31.87
U1443_A_35_2_56_57	246.97	54.285	*Subbotina hornibrooki*	32.39
U1443_A_35_2_69_70	247.10	54.350	*Subbotina hornibrooki*	34.59
U1443_A_35_2_126_127	247.67	54.634	*Subbotina hornibrooki*	37.26
U1443_A_35_3_10_11	248.01	54.803	*Subbotina hornibrooki*	32.27
U1443_A_35_3_10_11	248.01	54.803	*Subbotina velascoensis*	26.98
U1443_A_35_3_40.5_41.5	248.31	55.208	*Subbotina hornibrooki*	29.32
U1443_A_35_3_40.5_41.5	248.31	55.208	*Subbotina velascoensis*	26.96
U1443_A_35_3_72_73	248.63	55.835	*Subbotina velascoensis*	15.24
U1443_A_35_3_92_93	248.83	55.940	*Subbotina velascoensis*	28.27
U1443_A_36_1_65_66	254.66	57.333	*Subbotina velascoensis*	21.58
U1443_A_36_1_94_95	254.95	57.367	*Subbotina velascoensis*	25.84
U1443_A_36_1_116_117	255.17	57.392	*Subbotina velascoensis*	36.13
U1443_A_36_1_121_122	255.22	57.398	*Subbotina velascoensis*	27.91
U1443_A_36_2_8_9	255.59	57.441	*Subbotina velascoensis*	33.98
U1443_A_36_2_53_54	256.04	57.493	*Subbotina velascoensis*	31.00
U1443_A_36_2_116.5_117.5	256.67	57.602	*Subbotina velascoensis*	31.50
U1443_A_36_2_127.5_128.5	256.78	57.621	*Subbotina velascoensis*	32.85
U1443_A_36_3_62_63	257.63	57.768	*Subbotina velascoensis*	28.65
U1443_A_36_3_81_82	257.82	57.801	*Subbotina velascoensis*	31.58
U1443_A_36_3_100_101	258.01	57.834	*Subbotina velascoensis*	30.91
U1443_A_36_3_135_136	258.36	57.895	*Subbotina velascoensis*	31.98

Appendix 23. Thermocline planktic foraminiferal boron/calcium (B/Ca) data from Indian Ocean Ninetyeast Ridge ODP Site 758. These data were generated on a Thermo Finnigan Element XR Inductively-Coupled Plasma-Mass Spectrometer at the University of California Santa Cruz, with long-term analytical precision of <5% (2σ). These data are from ***Chapter 6****.*

Site_Hole_Core_Section_Top Depth (cm)_Bottom Depth (cm)	**Depth (mbsf)**	**Age (Ma)**	**Species**	**B/Ca (μmol/mol)**
758_A_28_2_139.5_140.5	259.81	56.780	*Subbotina velascoensis*	26.92
758_A_28_3_127.5_128.5	261.19	56.951	*Subbotina velascoensis*	23.11
758_A_28_4_96_97	262.38	57.048	*Subbotina velascoensis*	26.46
758_A_28_5_70_71	263.62	57.150	*Subbotina velascoensis*	22.95

*Appendix 24. Thermocline planktic foraminiferal boron/calcium (B/Ca) data from Indian Ocean Ninetyeast Ridge ODP Site 758. These data were generated on a Thermo Finnigan Element XR Inductively-Coupled Plasma-Mass Spectrometer at Yale University, with long-term analytical precision of <5% (2σ). These data are from **Chapter 6**.*

Site_Hole_Core_Section_Top Depth (cm)_Bottom Depth (cm)	Depth (mbsf)	Age (Ma)	Species	B/Ca (μmol/mol)
758_A_28_1_21_23	257.12	56.400	*Subbotina velascoensis*	28.75
758_A_28_2_139.5_140.5	259.81	56.780	*Subbotina velascoensis*	27.99
758_A_28_3_30_31	260.22	56.838	*Subbotina velascoensis*	31.63
758_A_28_3_38_39.5	260.30	56.850	*Subbotina velascoensis*	34.75
758_A_28_3_132.5_133.5	261.24	56.955	*Subbotina velascoensis*	48.10
758_A_28_4_53.5_54.5	261.95	57.013	*Subbotina velascoensis*	32.08
758_A_28_4_96_97	262.38	57.048	*Subbotina velascoensis*	37.68
758_A_28_5_18_19	263.10	57.107	*Subbotina velascoensis*	30.29
758_A_28_5_70_71	263.62	57.150	*Subbotina velascoensis*	33.40
758_A_28_5_108.5_109.5	264.00	57.181	*Subbotina velascoensis*	33.42

Appendix 25. Benthic foraminiferal magnesium/calcium (Mg/Ca) data from Indian Ocean Ninetyeast Ridge IODP Site U1443. The majority of these data were generated at the University of California Santa Cruz, with the exception of the two data points highlighted in bold, which were generated at Yale University. Both datasets were generated on a Thermo Finnigan Element XR Inductively-Coupled Plasma-Mass Spectrometer, with long-term analytical precision of <3% (2σ). Absolute temperature estimates are calculated for the Oridorsalis umbonatus data assuming a Mg/Ca ratio in Paleogene seawater (Mg/Ca_{sw}) of 2.5 mol/mol (consistent with Early Eocene proxy data in Evans et al., 2018). These data are from ***Chapter 6****.*

Site_Hole_Core_Section_ Top Depth (cm)_Bottom Depth (cm)	**Depth (mbsf)**	**Age (Ma)**	**Species**	**Mg/Ca (mmol/mol; raw data)**	**Temperature (°C; Mg/Ca_{sw} = 2.5 mol/mol)**
U1443_A_35_1_21.5_22.5	245.12	52.997	*Oridorsalis umbonatus*	2.92	12.12
U1443_A_35_1_40_41	245.31	53.164	*Oridorsalis umbonatus*	3.68	14.14
U1443_A_35_1_49_50	245.40	53.244	*Oridorsalis umbonatus*	3.30	13.18
U1443_A_35_1_77_78	245.68	53.491	*Oridorsalis umbonatus*	3.45	13.57
U1443_A_35_1_130_131	246.21	53.958	*Oridorsalis umbonatus*	3.37	13.37
U1443_A_35_1_143_144	246.34	54.000	*Oridorsalis umbonatus*	3.37	13.38
U1443_A_35_2_9_10	246.50	54.051	*Oridorsalis umbonatus*	3.22	12.98
U1443_A_35_2_24_25	246.65	54.126	*Oridorsalis umbonatus*	3.44	13.56
U1443_A_35_2_36_37	246.77	54.186	*Oridorsalis umbonatus*	3.19	12.90
U1443_A_35_2_56_57	246.97	54.285	*Oridorsalis umbonatus*	3.24	13.02
U1443_A_35_2_69_70	247.10	54.350	*Oridorsalis umbonatus*	3.14	12.74
U1443_A_35_2_76_77	247.17	54.385	*Oridorsalis umbonatus*	3.17	12.83
U1443_A_35_2_126_127	247.67	54.634	*Oridorsalis umbonatus*	3.24	13.04
U1443_A_35_2_134_135	**247.75**	**54.674**	***Oridorsalis umbonatus***	**3.27**	**13.09**
U1443_A_35_3_10_11	248.01	54.803	*Oridorsalis umbonatus*	3.41	13.48
U1443_A_35_3_40.5_41.5	248.31	55.208	*Oridorsalis umbonatus*	3.28	13.13
U1443_A_35_3_69_70	**248.60**	**55.800**	***Oridorsalis umbonatus***	**3.47**	**13.64**
U1443_A_35_3_72_73	248.63	55.835	*Oridorsalis umbonatus*	3.71	14.20
U1443_A_35_3_92_93	248.83	55.940	*Oridorsalis umbonatus*	2.63	11.19
U1443_A_36_1_8_9–U1443_A_36_1_65_66	254.09–254.66	57.206–57.333	*Oridorsalis umbonatus*	2.35	10.20
U1443_A_36_1_116_117–U1443_A_36_2_8_9	255.17–255.59	57.392–57.441	*Oridorsalis umbonatus*	2.19	9.58

U1443_A_36_3_62_63–U1443_A_36_3_135_136	257.63–258.36	57.768–57.895	*Oridorsalis umbonatus*	2.37	10.29
U1443_A_35_1_21.5_22.5	245.12	52.997	*Nuttallides truempyi*	1.20	NA
U1443_A_35_1_40_41	245.31	53.164	*Nuttallides truempyi*	1.37	NA
U1443_A_35_1_49_50	245.40	53.244	*Nuttallides truempyi*	1.15	NA
U1443_A_35_1_77_78	245.68	53.491	*Nuttallides truempyi*	1.12	NA
U1443_A_35_1_130_131	246.21	53.958	*Nuttallides truempyi*	0.98	NA
U1443_A_35_1_143_144	246.34	54.000	*Nuttallides truempyi*	1.40	NA
U1443_A_35_2_9_10	246.50	54.051	*Nuttallides truempyi*	1.03	NA
U1443_A_35_2_22_23	246.63	54.116	*Nuttallides truempyi*	0.96	NA
U1443_A_35_2_24_25	246.65	54.126	*Nuttallides truempyi*	0.97	NA
U1443_A_35_2_36_37	246.77	54.186	*Nuttallides truempyi*	1.11	NA
U1443_A_35_2_56_57	246.97	54.285	*Nuttallides truempyi*	1.26	NA
U1443_A_35_2_69_70	247.10	54.350	*Nuttallides truempyi*	1.15	NA
U1443_A_35_2_76_77	247.17	54.385	*Nuttallides truempyi*	1.04	NA
U1443_A_35_2_126_127	247.67	54.634	*Nuttallides truempyi*	1.01	NA
U1443_A_35_3_40.5_41.5	248.31	55.208	*Nuttallides truempyi*	1.01	NA
U1443_A_35_3_72_73	248.63	55.835	*Nuttallides truempyi*	1.21	NA
U1443_A_35_3_92_93	248.83	55.940	*Nuttallides truempyi*	1.07	NA
U1443_A_36_1_8_9	254.09	57.206	*Nuttallides truempyi*	0.81	NA
U1443_A_36_1_25_26	254.26	57.220	*Nuttallides truempyi*	0.96	NA
U1443_A_36_1_42_43	254.43	57.268	*Nuttallides truempyi*	0.81	NA
U1443_A_36_1_65_66	254.66	57.333	*Nuttallides truempyi*	0.89	NA
U1443_A_36_1_94_95	254.95	57.367	*Nuttallides truempyi*	1.01	NA
U1443_A_36_1_100_101	255.01	57.374	*Nuttallides truempyi*	0.98	NA
U1443_A_36_2_8_9–U1443_A_36_1_116_117	255.59–255.17	57.441–57.392	*Nuttallides truempyi*	1.33	NA
U1443_A_36_2_53_54	256.04	57.493	*Nuttallides truempyi*	1.13	NA
U1443_A_36_2_89_90	256.40	57.555	*Nuttallides truempyi*	0.98	NA
U1443_A_36_2_116.5_117.5	256.67	57.602	*Nuttallides truempyi*	0.97	NA
U1443_A_36_2_127.5_128.5	256.78	57.621	*Nuttallides truempyi*	0.88	NA
U1443_A_36_2_139_140	256.95	57.651	*Nuttallides truempyi*	0.94	NA

U1443_A_36_3_29_30	257.30	57.711	*Nuttallides truempyi*	1.10	NA
U1443_A_36_3_44_45	257.45	57.737	*Nuttallides truempyi*	0.97	NA
U1443_A_36_3_62_63	257.63	57.768	*Nuttallides truempyi*	1.04	NA
U1443_A_36_3_81_82	257.82	57.801	*Nuttallides truempyi*	0.94	NA
U1443_A_36_3_100_101	258.01	57.834	*Nuttallides truempyi*	1.12	NA
U1443_A_36_3_135_136	258.36	57.895	*Nuttallides truempyi*	1.15	NA

Appendix 26. Benthic foraminiferal magnesium/calcium (Mg/Ca) data from Indian Ocean Ninetyeast Ridge ODP Site 758. These data were generated at the University of California Santa Cruz on a Thermo Finnigan Element XR Inductively-Coupled Plasma-Mass Spectrometer, with long-term analytical precision of <3% (2σ). Absolute temperature estimates are calculated for the Oridorsalis umbonatus data assuming a Mg/Ca ratio in Paleogene seawater (Mg/Ca_{sw}) of 2.5 mol/mol (consistent with Early Eocene proxy data in Evans et al., 2018). These data are from ***Chapter 6****.*

Site_Hole_Core_Section_Top Depth (cm)_Bottom Depth (cm)	**Depth (mbsf)**	**Age (Ma)**	**Species**	**Mg/Ca (mmol/mol; raw data)**	**Temperature (°C; Mg/Ca_{sw} = 2.5 mol/mol)**
758_A_28_1_23_25	257.14	56.403	*Oridorsalis umbonatus*	2.60	11.09
758_A_28_3_128_129.5	261.20	56.952	*Oridorsalis umbonatus*	2.59	11.07
758_A_28_4_97_98–758_A_28_5_71_72	262.39–263.63	57.049–57.151	*Oridorsalis umbonatus*	2.62	11.17
758_A_28_1_23_25	257.14	56.403	*Nuttallides truempyi*	1.17	NA
758_A_28_1_82.5_83.5	257.73	56.486	*Nuttallides truempyi*	1.25	NA
758_A_28_2_140.5_141.5	259.82	56.782	*Nuttallides truempyi*	1.29	NA
758_A_28_3_39.5_40.5	260.31	56.851	*Nuttallides truempyi*	1.17	NA
758_A_28_3_128_129.5	261.20	56.952	*Nuttallides truempyi*	1.23	NA
758_A_28_4_97_98	262.39	57.049	*Nuttallides truempyi*	1.23	NA
758_A_28_5_71_72	263.63	57.151	*Nuttallides truempyi*	1.19	NA

Appendix 27. Benthic foraminiferal magnesium/calcium (Mg/Ca) data from Indian Ocean Ninetyeast Ridge ODP Site 758. These data were generated at Yale University on a Thermo Finnigan Element XR Inductively-Coupled Plasma-Mass Spectrometer, with long-term analytical precision of <3% (2σ). Absolute temperature estimates are calculated for the Oridorsalis umbonatus data assuming a Mg/Ca ratio in Paleogene seawater (Mg/Ca_{sw}) of 2.5 mol/mol (consistent with Early Eocene proxy data in Evans et al., 2018). These data are from ***Chapter 6****.*

Site_Hole_Core_Section_Top Depth (cm)_Bottom Depth (cm)	**Depth (mbsf)**	**Age (Ma)**	**Species**	**Mg/Ca (mmol/mol; raw data)**	**Temperature (°C; Mg/Ca_{sw} = 2.5 mol/mol)**
758_A_28_1_21_23	257.12	56.400	*Oridorsalis umbonatus*	2.69	11.41
758_A_28_1_81.5_82.5	257.72	56.485	*Oridorsalis umbonatus*	2.66	11.28
758_A_28_3_30_31–758_A_28_3_38_39.5	260.22–260.3	56.838–56.850	*Oridorsalis umbonatus*	2.73	11.51
758_A_28_3_127.5_128.5–758_A_28_3_132.5_133.5	261.19–261.24	56.951–56.955	*Oridorsalis umbonatus*	2.89	12.01
758_A_28_4_96_97	262.38	57.048	*Oridorsalis umbonatus*	2.43	10.52
758_A_28_5_9.5_10.5–758_A_28_5_18_19	263.01–263.10	57.100–57.107	*Oridorsalis umbonatus*	2.90	12.05
758_A_28_5_102_103–758_A_28_5_108.5_109.5	263.94–264.00	57.176–57.181	*Oridorsalis umbonatus*	2.76	11.62
758_A_28_1_21_23	257.12	56.400	*Nuttallides truempyi*	1.18	NA
758_A_28_1_81.5_82.5	257.72	56.485	*Nuttallides truempyi*	1.17	NA
758_A_28_2_139.5_140.5	259.81	56.780	*Nuttallides truempyi*	1.26	NA
758_A_28_3_30_31	260.22	56.838	*Nuttallides truempyi*	1.20	NA
758_A_28_3_38_39.5	260.3	56.850	*Nuttallides truempyi*	1.16	NA
758_A_28_4_53.5_54.5	261.95	57.013	*Nuttallides truempyi*	1.19	NA
758_A_28_4_96_97	262.38	57.048	*Nuttallides truempyi*	1.28	NA
758_A_28_5_70_71	263.62	57.150	*Nuttallides truempyi*	1.17	NA

Appendix 28. Benthic foraminiferal boron/calcium (B/Ca) data from Indian Ocean Ninetyeast Ridge IODP Site U1443. The majority of these data were generated at the University of California Santa Cruz, with the exception of the two data points highlighted in bold, which were generated at Yale University. Both data sets were generated on a Thermo Finnigan Element XR Inductively-Coupled Plasma-Mass Spectrometer, with long-term analytical precision of <5% (2σ). These data are from ***Chapter 6****.*

Site_Hole_Core_Section_Top Depth (cm)_Bottom Depth (cm)	Depth (mbsf)	Age (Ma)	Species	B/Ca (µmol/mol)
U1443_A_35_1_21.5_22.5	245.12	52.997	*Nuttallides truempyi*	106.71
U1443_A_35_1_40_41	245.31	53.164	*Nuttallides truempyi*	103.12
U1443_A_35_1_49_50	245.40	53.244	*Nuttallides truempyi*	106.99
U1443_A_35_1_77_78	245.68	53.491	*Nuttallides truempyi*	106.52
U1443_A_35_1_130_131	246.21	53.958	*Nuttallides truempyi*	108.64
U1443_A_35_1_143_144	246.34	54.000	*Nuttallides truempyi*	111.02
U1443_A_35_2_9_10	246.50	54.051	*Nuttallides truempyi*	113.76
U1443_A_35_2_22_23	246.63	54.116	*Nuttallides truempyi*	136.61
U1443_A_35_2_24_25	246.65	54.126	*Nuttallides truempyi*	139.24
U1443_A_35_2_36_37	246.77	54.186	*Nuttallides truempyi*	113.47
U1443_A_35_2_56_57	246.97	54.285	*Nuttallides truempyi*	108.37
U1443_A_35_2_69_70	247.10	54.350	*Nuttallides truempyi*	114.10
U1443_A_35_2_76_77	247.17	54.385	*Nuttallides truempyi*	123.28
U1443_A_35_2_126_127	247.67	54.634	*Nuttallides truempyi*	125.13
U1443_A_35_3_40.5_41.5	248.31	55.208	*Nuttallides truempyi*	114.82
U1443_A_35_3_72_73	248.63	55.835	*Nuttallides truempyi*	99.99
U1443_A_35_3_92_93	248.83	55.940	*Nuttallides truempyi*	120.06
U1443_A_36_1_8_9	254.09	57.206	*Nuttallides truempyi*	125.02
U1443_A_36_1_25_26	254.26	57.220	*Nuttallides truempyi*	122.04
U1443_A_36_1_42_43	254.43	57.268	*Nuttallides truempyi*	122.16
U1443_A_36_1_65_66	254.66	57.333	*Nuttallides truempyi*	123.48
U1443_A_36_1_94_95	254.95	57.367	*Nuttallides truempyi*	129.06
U1443_A_36_1_100_101	255.01	57.374	*Nuttallides truempyi*	122.95
U1443_A_36_2_8_9–U1443_A_36_1_116_117	255.59–255.17	57.441–57.392	*Nuttallides truempyi*	117.28
U1443_A_36_2_53_54	256.04	57.493	*Nuttallides truempyi*	116.24
U1443_A_36_2_89_90	256.40	57.555	*Nuttallides truempyi*	119.33
U1443_A_36_2_116.5_117.5	256.67	57.602	*Nuttallides truempyi*	124.09
U1443_A_36_2_127.5_128.5	256.78	57.621	*Nuttallides truempyi*	125.41
U1443_A_36_2_139_140	256.95	57.651	*Nuttallides truempyi*	118.24
U1443_A_36_3_29_30	257.30	57.711	*Nuttallides truempyi*	121.95
U1443_A_36_3_44_45	257.45	57.737	*Nuttallides truempyi*	121.22
U1443_A_36_3_62_63	257.63	57.768	*Nuttallides truempyi*	112.84
U1443_A_36_3_81_82	257.82	57.801	*Nuttallides truempyi*	126.10
U1443_A_36_3_100_101	258.01	57.834	*Nuttallides truempyi*	131.50
U1443_A_36_3_135_136	258.36	57.895	*Nuttallides truempyi*	126.80
U1443_A_35_1_40_41	245.31	53.164	*Oridorsalis umbonatus*	12.64
U1443_A_35_1_49_50	245.40	53.244	*Oridorsalis umbonatus*	15.24
U1443_A_35_1_77_78	245.68	53.491	*Oridorsalis umbonatus*	19.59
U1443_A_35_1_130_131	246.21	53.958	*Oridorsalis umbonatus*	15.44
U1443_A_35_1_143_144	246.34	54.000	*Oridorsalis umbonatus*	16.79
U1443_A_35_2_9_10	246.50	54.051	*Oridorsalis umbonatus*	11.28
U1443_A_35_2_24_25	246.65	54.126	*Oridorsalis umbonatus*	15.59
U1443_A_35_2_36_37	246.77	54.186	*Oridorsalis umbonatus*	14.47
U1443_A_35_2_56_57	246.97	54.285	*Oridorsalis umbonatus*	14.38
U1443_A_35_2_69_70	247.10	54.350	*Oridorsalis umbonatus*	16.39
U1443_A_35_2_76_77	247.17	54.385	*Oridorsalis umbonatus*	16.73
U1443_A_35_2_126_127	247.67	54.634	*Oridorsalis umbonatus*	16.41

U1443_A_35_2_134_135	**247.75**	**54.674**	***Oridorsalis umbonatus***	**24.18**
U1443_A_35_3_10_11	248.01	54.803	*Oridorsalis umbonatus*	14.53
U1443_A_35_3_40.5_41.5	248.31	55.208	*Oridorsalis umbonatus*	14.51
U1443_A_35_3_69_70	**248.60**	**55.800**	***Oridorsalis umbonatus***	**19.90**
U1443_A_35_3_72_73	248.63	55.835	*Oridorsalis umbonatus*	11.23
U1443_A_35_3_92_93	248.83	55.940	*Oridorsalis umbonatus*	8.81
U1443_A_36_1_8_9– U1443_A_36_1_65_66	254.09– 254.66	57.206– 57.333	*Oridorsalis umbonatus*	13.14
U1443_A_36_1_116_117– U1443_A_36_2_8_9	255.17– 255.59	57.392– 57.441	*Oridorsalis umbonatus*	5.36
U1443_A_36_3_62_63– U1443_A_36_3_135_136	257.63– 258.36	57.768– 57.895	*Oridorsalis umbonatus*	14.23

Appendix 29. Benthic foraminiferal boron/calcium (B/Ca) data from Indian Ocean Ninetyeast Ridge ODP Site 758. These data were generated at the University of California Santa Cruz on a Thermo Finnigan Element XR Inductively-Coupled Plasma-Mass Spectrometer, with long-term analytical precision of <5% (2σ). These data are from ***Chapter 6****.*

Site_Hole_Core_Section_Top Depth (cm)_Bottom Depth (cm)	Depth (mbsf)	Age (Ma)	Species	B/Ca (µmol/mol)
758_A_28_1_23_25	257.14	56.403	*Nuttallides truempyi*	111.22
758_A_28_1_82.5_83.5	257.73	56.486	*Nuttallides truempyi*	100.78
758_A_28_2_140.5_141.5	259.82	56.782	*Nuttallides truempyi*	109.89
758_A_28_3_39.5_40.5	260.31	56.851	*Nuttallides truempyi*	106.81
758_A_28_3_128_129.5	261.20	56.952	*Nuttallides truempyi*	108.51
758_A_28_4_97_98	262.39	57.049	*Nuttallides truempyi*	103.64
758_A_28_5_71_72	263.63	57.151	*Nuttallides truempyi*	105.38
758_A_28_1_23_25	257.14	56.403	*Oridorsalis umbonatus*	23.71
758_A_28_3_128_129.5	261.20	56.952	*Oridorsalis umbonatus*	22.50

*Appendix 30. Benthic foraminiferal boron/calcium (B/Ca) data from Indian Ocean Ninetyeast Ridge ODP Site 758. These data were generated at Yale University on a Thermo Finnigan Element XR Inductively-Coupled Plasma-Mass Spectrometer, with long-term analytical precision of <5% (2σ). These data are from **Chapter 6**.*

Site_Hole_Core_Section_Top Depth (cm)_Bottom Depth (cm)	Depth (mbsf)	Age (Ma)	Species	B/Ca (µmol/mol)
758_A_28_1_21_23	257.12	56.400	*Nuttallides truempyi*	96.27
758_A_28_1_81.5_82.5	257.72	56.485	*Nuttallides truempyi*	96.70
758_A_28_2_139.5_140.5	259.81	56.780	*Nuttallides truempyi*	102.66
758_A_28_3_30_31	260.22	56.838	*Nuttallides truempyi*	93.34
758_A_28_3_38_39.5	260.30	56.850	*Nuttallides truempyi*	92.64
758_A_28_4_53.5_54.5	261.95	57.013	*Nuttallides truempyi*	109.05
758_A_28_4_96_97	262.38	57.048	*Nuttallides truempyi*	102.45
758_A_28_5_70_71	263.62	57.150	*Nuttallides truempyi*	110.44
758_A_28_1_21_23	257.12	56.400	*Oridorsalis umbonatus*	19.98
758_A_28_1_81.5_82.5	257.72	56.485	*Oridorsalis umbonatus*	10.92
758_A_28_3_30_31–758_A_28_3_38_39.5	260.22–260.30	56.838–56.850	*Oridorsalis umbonatus*	11.76
758_A_28_3_127.5_128.5–758_A_28_3_132.5_133.5	261.19–261.24	56.951–56.955	*Oridorsalis umbonatus*	20.19
758_A_28_4_96_97	262.38	57.048	*Oridorsalis umbonatus*	19.60
758_A_28_5_9.5_10.5–758_A_28_5_18_19	263.01–263.10	57.100–57.107	*Oridorsalis umbonatus*	23.14
758_A_28_5_102_103–758_A_28_5_108.5_109.5	263.94–264.00	57.176–57.181	*Oridorsalis umbonatus*	24.30

Appendix 31. $\delta^{13}C_{bulk}$, $\delta^{13}C_{benthic}$, $\delta^{18}O_{benthic}$ and Fe intensity records from ODP Site 1262 plotted against depth (mcd) and attributed by literature source.

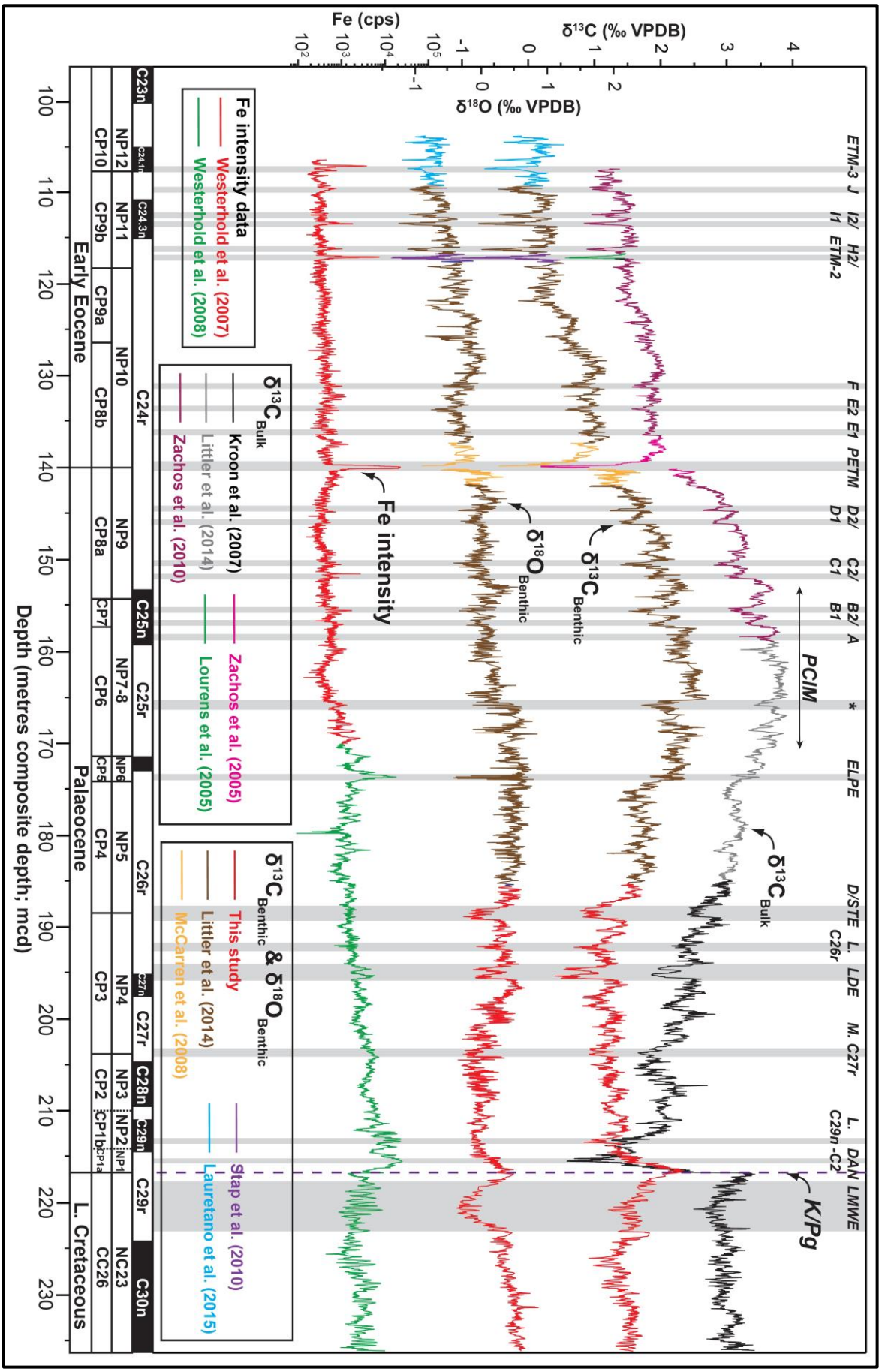

Appendix

*Appendix 32. $\delta^{13}C_{bulk}$ (**a**), mixed layer planktic Mg/Ca (**b**), and $\delta^{18}O_{planktic}$ data (**c**) from IODP Site U1443/ODP Site 758 plotted against depth (CSF-A/mbsf). Only mixed layer planktic Mg/Ca data generated at UCSC are shown.*

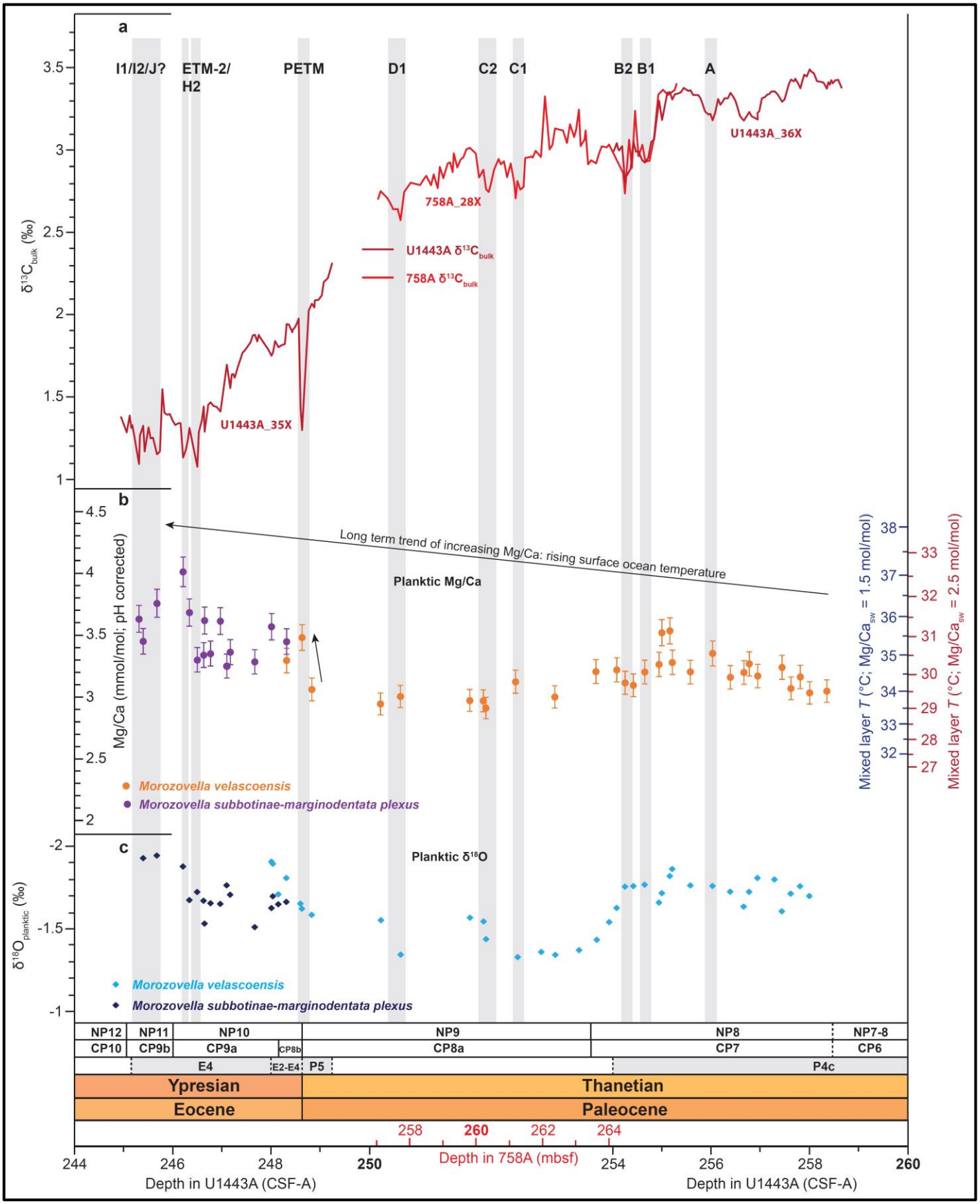

*Appendix 33. $\delta^{13}C_{bulk}$ and $\delta^{13}C_{planktic}$ (**a**) and mixed layer planktic B/Ca (**b**) from IODP Site U1443/ODP Site 758 plotted against depth (CSF-A/mbsf). Only mixed layer planktic B/Ca data generated at UCSC are shown.*

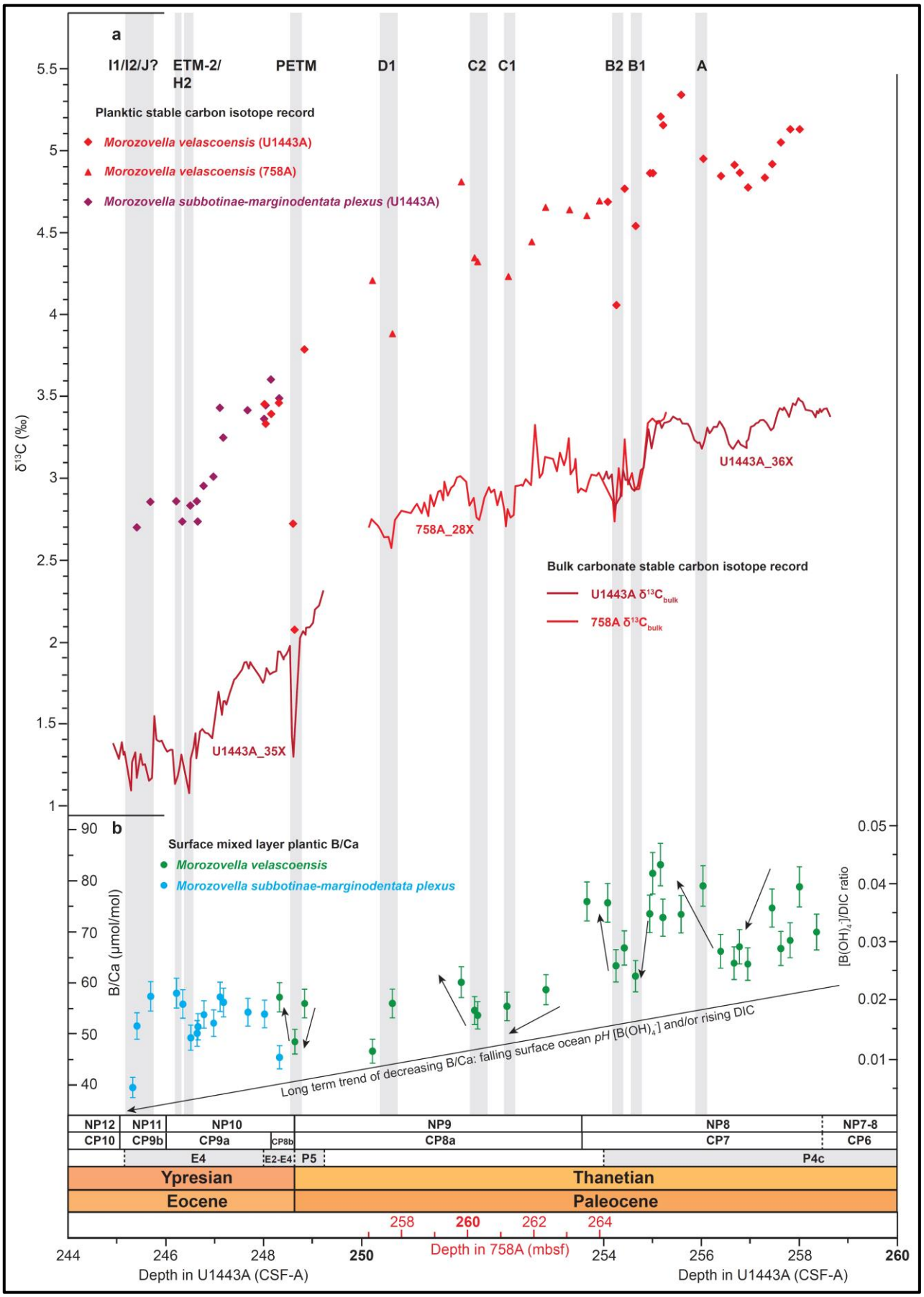

*Appendix 34. $\delta^{13}C_{bulk}$ (**a**), thermocline planktic B/Ca (**b**), and thermocline planktic Mg/Ca (**c**) from IODP Site U1443/ODP Site 758 plotted against depth (CSF-A/mbsf). Only thermocline planktic B/Ca and Mg/Ca data generated at UCSC are shown.*

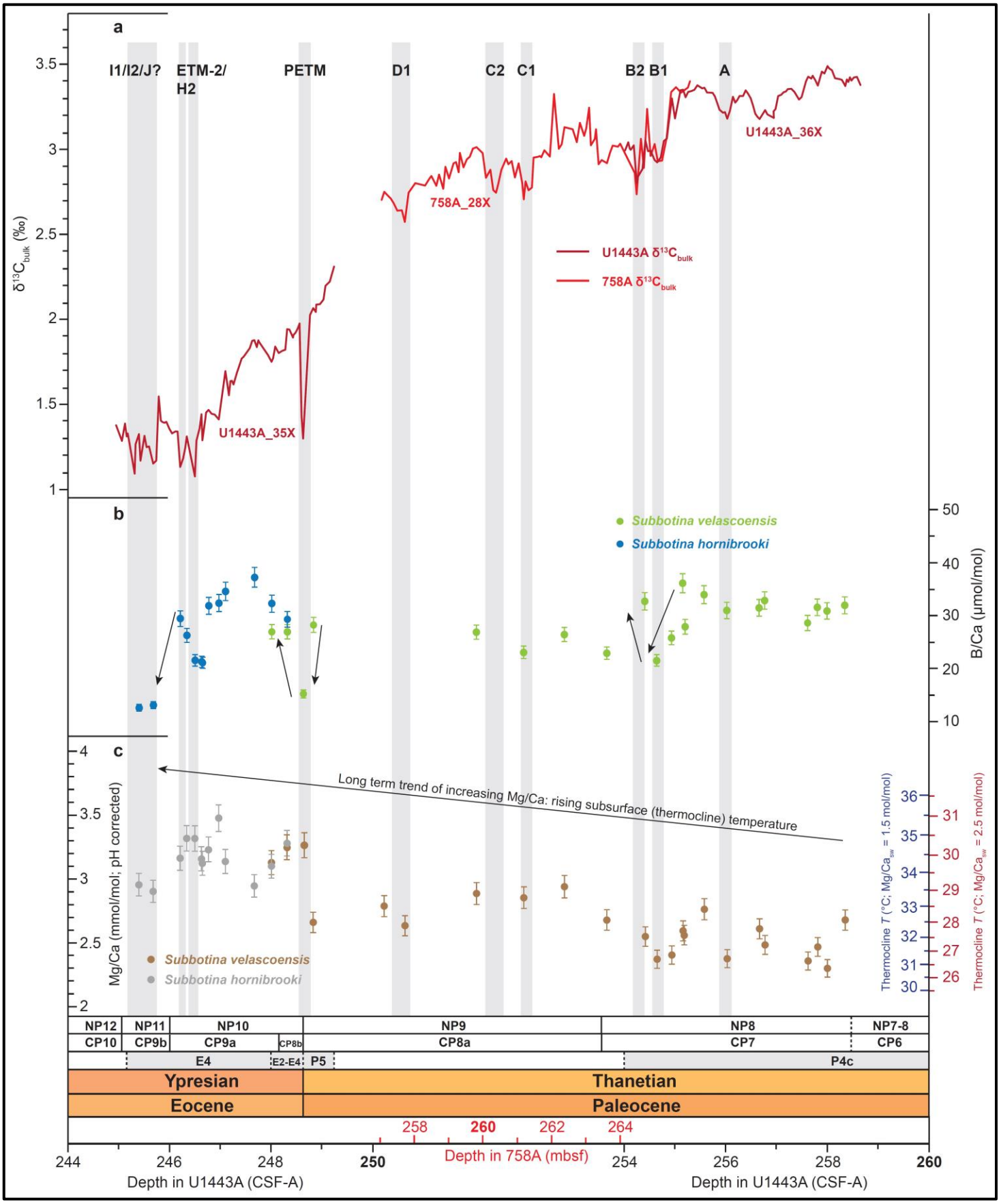

*Appendix 35. $\delta^{13}C_{bulk}$ (**a**), benthic B/Ca (**b**), and benthic Mg/Ca (**c**) from IODP Site U1443/ODP Site 758 plotted against depth (CSF-A/mbsf). Only benthic B/Ca and Mg/Ca data generated at UCSC are shown.*

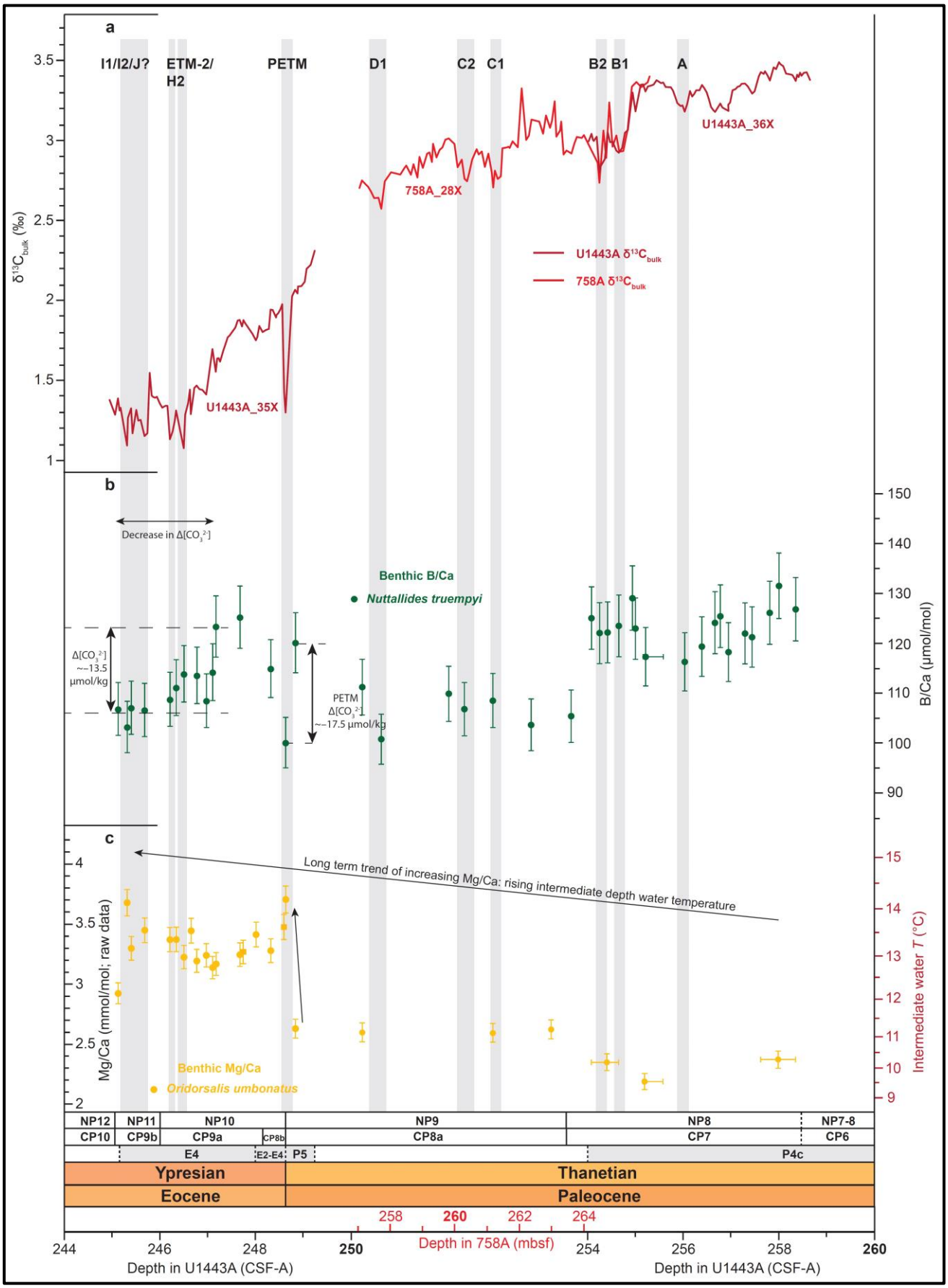

9. BIBLIOGRAPHY

Abramovich, S., and Keller, G., 2002, High stress late Maastrichtian paleoenvironment: inference from planktonic foraminifera in Tunisia: Palaeogeography, Palaeoclimatology, Palaeoecology, v. 178, p. 145–164, doi: 10.1016/S0031-0182(01)00394-7.

Abramovich, S., and Keller, G., 2003, Planktonic foraminiferal response to the latest Maastrichtian abrupt warm event: a case study from South Atlantic DSDP Site 525A: Marine Micropaleontology, v. 48, p. 225–249, doi: 10.1016/S0377-8398(03)00021-5.

Abramovich, S., Yovel-Corem, S., Almogi-Labin, A., and Benjamini, C., 2010, Global climate change and planktic foraminiferal response in the Maastrichtian: Paleoceanography, v. 25, PA2201, doi: 10.1029/2009PA001843.

Agnini, C., Fornaciari, E., Raffi, I., Rio, D., Röhl, U., and Westerhold, T., 2007, High-resolution nannofossil biochronology of middle Paleocene to early Eocene at ODP Site 1262: Implications for calcareous nannoplankton evolution: Marine Micropaleontology, v. 64, p. 215–248, doi: 10.1016/j.marmicro.2007.05.003.

Alegret, L., and Thomas, E., 2001, Upper Cretaceous and Lower Paleogene benthic foraminifera from northeastern Mexico: Micropaleontology, v. 47, p. 269–316.

Alegret, L., and Thomas, E., 2005, Cretaceous/Paleogene boundary bathyal paleo-environments in the central North Pacific (DSDP Site 465), the Northwestern Atlantic (ODP Site 1049), the Gulf of Mexico and the Tethys: The benthic foraminiferal record: Palaeogeography, Palaeoclimatology, Palaeoecology, v. 224, p. 53–82, doi: 10.1016/j.palaeo.2005.03.031.

Alegret, L., and Thomas, E., 2007, Deep-Sea environments across the Cretaceous/Paleogene boundary in the eastern South Atlantic Ocean (ODP Leg 208 ,Walvis Ridge): Marine Micropaleontology, v. 64, p. 1–17, doi: 10.1016/j.marmicro.2006.12.003.

Alegret, L., and Thomas, E., 2009, Food supply to the seafloor in the Pacific Ocean after the Cretaceous/Paleogene boundary event: Marine

Micropaleontology, v. 73, p. 105–116, doi:10.1016/j.marmicro.2009.07.005.

Alegret, L., Thomas, E., and Lohmann, K.C., 2012, End-Cretaceous marine mass extinction not caused by productivity collapse: Proceedings of the National Academy of Sciences of the United States of America, v. 109, p. 728–732, doi: 10.1073/pnas.1110601109.

Allen, K.A., Hönisch, B., Eggins, S.M., Yu, J., Spero, H.J., and Elderfield, H., 2011, Controls on boron incorporation in cultured tests of the planktic foraminifer *Orbulina universa*: Earth and Planetary Science Letters, v. 309, p. 291–301, doi: 10.1016/j.epsl.2011.07.010.

Allen, K.A., and Hönisch, B., 2012, The planktic foraminiferal B/Ca proxy for seawater carbonate chemistry: A critical evaluation: Earth and Planetary Science Letters, v. 345–348, p. 203–211, doi: 10.1016/j.epsl.2012.06.012.

Allen, K.A., Hönisch, B., Eggins, S.M., and Rosenthal, Y., 2012, Environmental controls on B/Ca in calcite tests of the tropical planktic foraminifer species *Globigerinoides ruber* and *Globigerinoides sacculifer*: Earth and Planetary Science Letters, v. 351–352, p. 270–280, doi: 10.1016/j.epsl.2012.07.004.

Anagnostou, E., John, E.H., Edgar, K.M., Foster, G.L., Ridgwell, A., Inglis, G.N., Pancost, R.D., Lunt, D.J., and Pearson, P.N., 2016, Changing atmospheric CO_2 concentration was the primary driver of early Cenozoic climate: Nature, v. 533, p. 380–384, doi: 10.1038/nature17423.

Anand, P., Elderfield, H., and Conte, M.H., 2003, Calibration of Mg/Ca thermometry in planktonic foraminifera from a sediment trap time series: Paleoceanography, v. 18, 1050, doi: 10.1029/2002PA000846.

Arenillas, I., Molina, E., Ortiz, S., and Schmitz, B., 2008, Foraminiferal and $\delta^{13}C$ isotopic event-stratigraphy across the Danian-Selandian transition at Zumaya (northern Spain): Chronostratigraphic implications: Terra Nova, v. 20, p. 38–44, doi: 10.1111/j.1365-3121.2007.00784.x.

Aze, T., Pearson, P.N., Dickson, A.J., Badger, M.P.S., Bown, P.R., Pancost, R.D., Gibbs, S.J., Huber, B.T., Leng, M.J., Coe, A.L., Cohen, A.S., and Foster, G.L., 2014, Extreme warming of tropical waters during the Paleocene-Eocene Thermal Maximum: Geology, v. 42, p. 739–742, doi: 10.1130/G35637.1.

Babila, T.L., Rosenthal, Y., Wright, J.D., and Miller, K.G., 2016, A continental shelf perspective of ocean acidification and temperature evolution during the Paleocene-Eocene Thermal Maximum: Geology, v. 44, p. 275–278, doi: 10.1130/G37522.1.

Babila, T.L., Penman, D.E., Hönisch, B., Kelly, D.C., Bralower, T.J., Rosenthal, Y., and Zachos, J.C., 2018, Capturing the global signature of surface ocean acidification during the Palaeocene–Eocene Thermal Maximum: Philosophical Transactions of the Royal Society A, v. 376, 20170072, doi: 10.1098/rsta.2017.0072.

Barclay, R.S., and Wing, S.L., 2016, Improving the Ginkgo CO_2 barometer: Implications for the early Cenozoic atmosphere: Earth and Planetary Science Letters, v. 439, p. 158–171, doi: 10.1016/j.epsl.2016.01.012.

Barnet, J.S.K., Littler, K., Kroon, D., Leng, M.J., Westerhold, T., Röhl, U., and Zachos, J.C., 2017, A new high-resolution chronology for the late Maastrichtian warming event: Establishing robust temporal links with the onset of Deccan volcanism: Geology, v. 46, p. 147–150, doi: 10.1130/G39771.1.

Barrera, E., and Savin, S.M., 1999, Evolution of late Campanian–Maastrichtian marine climates and oceans, *in* Barrera, E., and Johnson, C.C., Evolution of the Cretaceous ocean-climate system: Boulder, Colorado, Geological Society of America Special Paper 332, p. 245–282.

Batenburg, S.J., Friedrich, O., Moriya, K., Voigt, S., Cournède, C., Möbius, I., Blum, P., Bornemann, A., Fiebig, J., Hasegawa, T., Hull, P.M., Norris, R.D., Röhl, U., Sexton, P.F., Westerhold, T., Wilson, P.A., and the IODP Expedition 342 Scientists, 2017, Late Maastrichtian carbon isotope stratigraphy and cyclostratigraphy of the Newfoundland Margin (Site U1403, IODP Leg 342): Newsletters on Stratigraphy, v. 51, p. 245–260, doi: 10.1127/nos/2017/0398.

Beerling, D.J., Lomax, B.H., Royer, D.L., Upchurch, G.R., and Kump, L.R., 2002, An atmospheric pCO_2 reconstruction across the Cretaceous-Tertiary boundary from leaf megafossils: Proceedings of the National Academy of Sciences, USA, v. 99, p. 7836-7840, doi: 10.1073/pnas.122573099.

Beerling, D.J., Fox, A., and Anderson, C.W., 2009, Quantitative uncertainty analyses of ancient atmospheric CO_2 estimates from fossil leaves: American Journal of Science, v. 309, p. 775-787, doi: 10.2475/09.2009.01.

Bemis, B.E., Spero, H.J., Bijma, J., and Lea, D.W., 1998, Reevaluation of the oxygen isotopic composition of planktonic foraminifera: Experimental results and revised paleotemperature equations: Paleoceanography, v. 13, p. 150–160, doi: 10.1029/98PA00070.

Berner, R.A., 2004, A model for calcium, magnesium and sulfate in seawater over Phanerozoic time: American Journal of Science, v. 304, p. 438–453, doi: 10.2475/ajs.304.5.438.

Bijl, P.K., Schouten, S., Sluijs, A., Reichart, G-J., Zachos, J.C., and Brinkhuis, H., 2009, Early Palaeogene temperature evolution of the southwest Pacific Ocean: Nature, v. 461, p. 776–779.

Birch, H.S., Coxall, H.K., and Pearson, P.N., 2012, Evolutionary ecology of Early Paleocene planktonic foraminifera: size, depth habitat and symbiosis: Paleobiology, v. 38, p. 374–390, doi: 10.1666/11027.1.

Birch, H., Coxall, H.K., Pearson, P.N., Kroon, D., and O'Regan, M., 2013, Planktonic foraminifera stable isotopes and water column structure: Disentangling ecological signals: Marine Micropaleontology, v. 101, p. 127–145, doi: 10.1016/j.marmicro.2013.02.002.

Birch, H.S., Coxall, H.K., Pearson, P.N., Kroon, D., and Schmidt, D.N., 2016, Partial collapse of the marine carbon pump after the Cretaceous-Paleogene boundary: Geology, v. 44, p. 287–290, doi: 10.1130/G37581.1.

Bornemann, A., Schulte, P., Sprong, J., Steurbaut, E., Youssef, M., and Speijer, R.P., 2009, Latest Danian carbon isotope anomaly and associated environmental change in the southern Tethys (Nile Basin, Egypt): Journal of the Geological Society, London, v. 166, p. 1135–1142, doi: 10.1144/0016-76492008-104.

Bornemann, A., Norris, R.D., Lyman, J.A., D'haenens, S., Groeneveld, J., Röhl, U., Farley, K.A., and Speijer, R.P., 2014, Persistent environmental change after the Paleocene–Eocene Thermal Maximum in the eastern North Atlantic: Earth and Planetary Science Letters, v. 394, p. 70–81, doi:

10.1016/j.epsl.2014.03.017.

Bowen, G.J., Maibauer, B.J., Kraus, M.J., Röhl, U., Westerhold, T., Steimke, A., Gingerich, P.D., Wing, S.L., and Clyde, W.C., 2015, Two massive, rapid releases of carbon during the onset of the Palaeocene–Eocene thermal maximum: Nature Geoscience, v. 8, p. 44–47, doi: 10.1038/NGEO2316.

Bowles, J., 2006, Data report: Revised magnetostratigraphy and magnetic mineralogy of sediments from Walvis Ridge, Leg 208, *in* Kroon, D., Zachos, J.C., and Richter, C., Proceedings of the Ocean Drilling Program, Scientific Results, v. 208: College Station, Texas, Ocean Drilling Program, p. 1–24, doi: 10.2973/odp.proc.sr.208.206.2006.

Bown, P.R., Lees, J.A., and Young, J.R., 2004, Calcareous nannoplankton evolution and diversity through time, *in* Thierstein, H.R., Coccolithophores, Springer, Berlin, Heidelberg, p. 481–508, doi: 10.1007/978-3-662-06278-4_18.

Bown, P.R., 2005, Calcareous nannoplankton evolution: a tale of two oceans: Micropaleontology, v. 51, p. 299–308, doi: 10.2113/gsmicropal.51.4.299.

Boyle, E.A., and Keigwin, L.D., 1985/86, Comparison of Atlantic and Pacific paleochemical records for the last 215,000 years: changes in deep ocean circulation and chemical inventories: Earth and Planetary Science Letters, v. 76, p. 135–150, doi: 10.1016/0012-821X(85)90154-2.

Bralower, T.J., Zachos, J.C., Thomas, E., Parrow, M., Paull, C.K., Clay Kelly, D., Premoli Silva, I., Sliter, W.V., and Lohmann, K.C., 1995, Late Paleocene to Eocene paleoceanography of the equatorial Pacific Ocean: Stable isotopes recorded at Ocean Drilling Program Site 865, Allison Guyot: Paleoceanography, v. 10, p. 841–865, doi: 10.1029/95PA01143.

Breecker, D.O., Sharp, Z.D., and McFadden, L.D., 2010, Atmospheric CO_2 concentrations during ancient greenhouse climates were similar to those predicted for A.D. 2100: Proceedings of the National Academy of Sciences of the United States of America, v. 107, p. 576–580, doi: 10.1073/pnas.0902323106.

Broecker, W.S., and Peng, T-H., 1982, Tracers in the sea: Eldigio Press, Lamont-Doherty Geological Observatory, Columbia University, Palisades, New York.

Brown, S.J., and Elderfield, H., 1996, Variations in Mg/Ca and Sr/Ca ratios of planktonic foraminifera caused by postdepositional dissolution: Evidence of shallow Mg-dependent dissolution: Paleoceanography, v. 11, p. 543–551, doi: 10.1029/96PA01491.

Brown, R.E., Anderson, L.D., Thomas, E., and Zachos, J.C., 2011, A core-top calibration of B/Ca in the benthic foraminifers *Nuttallides umbonifera* and *Oridorsalis umbonatus*: A proxy for Cenozoic bottom water carbonate saturation: Earth and Planetary Science Letters, v. 310, p. 360–368, doi: 10.1016/j.epsl.2011.08.023.

Brusatte, S.L., Butler, R.J., Barrett, P.M., Carrano, M.T., Evans, D.C., Lloyd, G.T., Mannion, P.D., Norell, M.A., Peppe, D.J., Upchurch, P., and Williamson, T.E., 2015, The extinction of the dinosaurs: Biological Reviews, v. 90, p. 628–642, doi: 10.1111/brv.12128.

Bryan, S.P., and Marchitto, T.M., 2008, Mg/Ca–temperature proxy in benthic foraminifera: New calibrations from the Florida Straits and a hypothesis regarding Mg/Li: Paleoceanography, v. 23, PA2220, doi: 10.1029/2007PA001553.

Cande, S.C., and Kent, D.V., 1995, Revised calibration of the geomagnetic polarity timescale for the Late Cretaceous and Cenozoic: Journal of Geophysical Research, v. 100, p. 6093–6095, doi: 10.1029/94JB03098.

Carmichael, M.J., Inglis, G.N., Badger, M.P.S., Naafs, B.D.A., Behrooz, L., Remmelzwaal, S., Monteiro, F.M., Rohrssen, M., Farnsworth, A., Buss, H.L., Dickson, A.J., Valdes, P.J., Lunt, D.J., and Pancost, R.D., 2017, Hydrological and associated biogeochemical consequences of rapid global warming during the Paleocene-Eocene Thermal Maximum: Global and Planetary Change, v. 157, p. 114–138, doi: 10.1016/j.gloplacha.2017.07.014.

Cerling, T.E., 1999, Palaeoweathering, palaeosurfaces and related continental deposits, *in* Simon-Coincon, R., Special Publication of the International Association of Sedimentologists, Blackwell, Cambridge, p. 43–60.

Chenet, A.L., Quidelleur, X., Fluteau, F., Courtillot, V., and Bajpai, S., 2007, ^{40}K-^{40}Ar dating of the Main Deccan large igneous province: Further evidence of KTB age and short duration: Earth and Planetary Science Letters, v. 263, p.

1–15, doi: 10.1016/j.epsl.2007.07.011.

Clemmensen, A., and Thomsen, E., 2005, Palaeoenvironmental changes across the Danian–Selandian boundary in the North Sea Basin: Palaeogeography, Palaeoclimatology, Palaeoecology, v. 219, p. 351–394, doi: 10.1016/j.palaeo.2005.01.005.

Coadic, R., Bassinot, F., Dissard, D., Douville, E., Greaves, M., and Michel, E., 2013, A core-top study of dissolution effect on B/Ca in *Globigerinoides sacculifer* from the tropical Atlantic: Potential bias for paleo-reconstruction of seawater carbonate chemistry: Geochemistry, Geophysics, Geosystems, v. 14, p. 1053–1068, doi: 10.1029/2012GC004296.

Coccioni, R., Frontalini, F., Bancalà, G., Fornaciari, E., Jovane, L., and Sprovieri, M., 2010, The Dan-C2 hyperthermal event at Gubbio (Italy): Global implications, environmental effects, and cause(s): Earth and Planetary Science Letters, v. 297, p. 298–305, doi: 10.1016/j.epsl.2010.06.031.

Coccioni, R., Bancalà, G., Catanzarit, R., Fornaciari, E., Frontalini, F., Giusberti, L., Jovane, L., Luciani, V., Savian, J., and Sprovieri, M., 2012, An integrated stratigraphic record of the Palaeocene-lower Eocene at Gubbio (Italy): New insights into the early Palaeogene hyperthermals and carbon isotope excursions: Terra Nova, v. 24, p. 380–386, doi: 10.1111/j.1365-3121.2012.01076.x.

Coggon, R.M., Teagle, D.A.H., Smith-Duque, C.E., Alt, J.C., and Cooper, M.J., 2010, Reconstructing past seawater Mg/Ca and Sr/Ca from mid-ocean ridge flank calcium carbonate veins: Science, v. 327, p. 1114–1117, doi: 10.1126/science.1182252.

Corfield, R.M., 1994, Palaeocene oceans and climate: An isotopic perspective: Earth Science Reviews, v. 37, p. 225–252, doi: 10.1016/0012-8252(94)90030-2.

Courtillot, V., Féraud, G., Maluski, H., Vandamme, D., Moreau, M.G., and Besse, J., 1988, Deccan flood basalts and the Cretaceous/Tertiary boundary: Nature, v. 333, p. 843–846, doi: 10.1038/333843a0.

Courtillot, V., Gallet, Y., Rocchia, R., Féraud, G., Robin, E., Hofmann, C., Bhandari, N., and Ghevariya, Z.G., 2000, Cosmic markers, $^{40}Ar/^{39}Ar$ dating

and paleomagnetism of the KT sections in the Anjar Area of the Deccan large igneous province: Earth and Planetary Science Letters, v. 182, p. 137–156, doi: 10.1016/S0012-821X(00)00238-7.

Cramer, B.S., Wright, J.D., Kent, D.V, and Aubry, M.-P., 2003, Orbital climate forcing of $\delta^{13}C$ excursions in the late Paleocene–early Eocene (chrons C24n–C25n): Paleoceanography, v. 18, 1097, doi: 10.1029/2003PA000909.

Cramer, B.S., Toggweiler, J.R., Wright, J.D., Katz, M.E., and Miller, K.G., 2009, Ocean overturning since the Late Cretaceous: Inferences from a new benthic foraminiferal isotope compilation: Paleoceanography, v. 24, PA4216, doi: 10.1029/2008PA001683.

Cramer, B.S., Miller, K.G., Barrett, P.J., and Wright, J.D., 2011, Late Cretaceous–Neogene trends in deep ocean temperature and continental ice volume: Reconciling records of benthic foraminiferal geochemistry ($\delta^{18}O$ and Mg/Ca) with sea level history: Journal of Geophysical Research, v. 116, C12023, doi: 10.1029/2011JC007255.

Cramwinckel, M.J., Huber, M., Kocken, I.J., Agnini, C., Bijl, P.K., Bohaty, S.M., Frieling, J., Goldner, A., Hilgen, F.J., Kip, E.L., Peterse, F., van der Ploeg, R., Röhl, U., Schouten, S., and Sluijs, A., 2018, Synchronous tropical and polar temperature evolution in the Eocene: Nature, v. 559, p. 382–386, doi: 10.1038/s41586-018-0272-2.

Cubasch, U., Wuebbles, D., Chen, D., Facchini, M.C., Frame, D., Mahowald, N., and Winther, J-G., 2013, Introduction, *in* Stocker, T.F., Qin, D., Plattner, G-K., Tignor, M., Allen, S.K., Boschung, J., Nauels, A., Xia, Y., Bex, V., and Midgley, P.M., Climate change 2013: The physical science basis. Contribution of Working Group I to the Fifth Assessment Report of the Intergovernmental Panel on Climate Change, Cambridge University Press, Cambridge, United Kingdom and New York, NY, USA, p. 119–158.

Cui, Y., and Schubert, B.A., 2016, Quantifying uncertainty of past pCO_2 determined from changes in C_3 plant carbon isotope fractionation: Geochimica et Cosmochimica Acta, v. 172, p. 127–138, doi: 10.1016/j.gca.2015.09.032.

Cui, Y., and Schubert, B.A., 2017, Atmospheric pCO_2 reconstructed across five

early Eocene global warming events: Earth and Planetary Science Letters, v. 478, p. 225–233, doi: 10.1016/j.epsl.2017.08.038.

D'Hondt, S., Zachos, J.C., and Schultz, G., 1994, Stable isotopic signals and photosymbiosis in Late Paleocene planktic foraminifera: Paleobiology, v. 20, p. 391–406, doi: 10.1017/S0094837300012847.

Dameron, S.N., Leckie, R.M., Clark, K., MacLeod, K.G., Thomas, D.J., and Lees, J.A., 2017, Extinction, dissolution, and possible ocean acidification prior to the Cretaceous/Paleogene (K/Pg) boundary in the tropical Pacific: Palaeogeography, Palaeoclimatology, Palaeoecology, v. 485, p. 433–454, doi: 10.1016/j.palaeo.2017.06.032.

DeConto, R.M., and Pollard, D., 2003, A coupled climate–ice sheet modeling approach to the Early Cenozoic history of the Antarctic ice sheet: Palaeogeography, Palaeoclimatology, Palaeoecology, v. 198, p. 39–52, doi: 10.1016/S0031-0182(03)00393-6.

DeConto, R.M., Galeotti, S., Pagani, M., Tracy, D., Schaefer, K., Zhang, T., Pollard, D., and Beerling, D.J., 2012, Past extreme warming events linked to massive carbon release from thawing permafrost: Nature, v. 490, p. 292–292, doi: 10.1038/nature10929.

Dekens, P.S., Lea, D.W., Pak, D.K., and Spero, H.J., 2002, Core top calibration of Mg/Ca in tropical foraminifera: Refining paleotemperature estimation: Geochemistry Geophysics, Geosystems, v. 3, p. 1–29, doi: 10.1029/2001GC000200.

Delaney, M.L., Bé, A.W.H., and Boyle, E.A., 1985, Li, Sr, Mg, and Na in foraminiferal calcite shells from laboratory culture, sediment traps, and sediment cores: Geochimica et Cosmochimica Acta, v. 49, p. 1327–1341, doi: 10.1016/0016-7037(85)90284-4.

Demicco, R.V., Lowenstein, T.K., and Hardie, L.A., 2003, Atmospheric pCO_2 since 60 Ma from records of seawater pH, calcium, and primary carbonate mineralogy: Geology, v. 31, p. 793–796, doi: 10.1130/G19727.1.

Demicco, R.V., Lowenstein, T.K., Hardie, L.A., and Spencer, R.J., 2005, Model of seawater composition for the Phanerozoic: Geology, v. 33, p. 877–880, doi: 10.1130/G21945.1.

Deprez, A., Jehle, S., Bornemann, A.E., and Speijer, R.P., 2017, Differential response at the seafloor during Palaeocene and Eocene ocean warming events at Walvis Ridge, Atlantic Ocean (ODP Site 1262): Terra Nova, v. 29, p. 71–76, doi: 10.1111/ter.12250.

Dickens, G.R., 2003, Rethinking the global carbon cycle with a large, dynamic and microbially mediated gas hydrate capacitor: Earth and Planetary Science Letters, v. 213, p. 169–183, doi: 10.1016/S0012-821X(03)00325-X.

Dickens, G.R., 2011, Down the Rabbit Hole: toward appropriate discussion of methane release from gas hydrate systems during the Paleocene-Eocene thermal maximum and other past hyperthermal events: Climate of the Past, v. 7, p. 831–846, doi: 10.5194/cp-7-831-2011.

Dickson, J.A.D., 2002, Fossil echinoderms as monitor of the Mg/Ca ratio of Phanerozoic oceans: Science, v. 298, p. 1222–1224, doi: 10.1126/science.1075882.

Dickson, J.A.D., 2004, Echinoderm skeletal preservation: calcite-aragonite seas and the Mg/Ca ratio of Phanerozoic oceans: Journal of Sedimentary Research, v. 74, p. 355–365, doi: 10.1306/112203740355.

Dinarès-Turell, J., Westerhold, T., Pujalte, V., Röhl, U., and Kroon, D., 2014, Astronomical calibration of the Danian stage (Early Paleocene) revisited: Settling chronologies of sedimentary records across the Atlantic and Pacific Oceans: Earth and Planetary Science Letters, v. 405, p. 119–131, doi: 10.1016/j.epsl.2014.08.027.

Do Monte Guerra, R., Concheyro, A., Wise, S.W.Jr., Kender, S., and Fauth, G., 2016, New latitude-based nannofossil zonations for the Campanian–Maastrichtian of the South Atlantic Ocean and their paleoceanographic implications: Palaeogeography, Palaeoclimatology, Palaeoecology, v. 452, p. 55–67, doi: 10.1016/j.palaeo.2016.04.010.

Dutton, A., Lohmann, K.C., and Leckie, R.M., 2005a, Insights from the Paleogene tropical Pacific: Foraminiferal stable isotope and elemental results from Site 1209, Shatsky Rise: Paleoceanography, v. 20, PA3004, doi: 10.1029/2004PA001098.

Dutton, A., Lohmann, K.C., and Leckie, R.M., 2005b, Data report: Stable isotope

and Mg/Ca of Paleocene and Eocene foraminifers, ODP Site 1209, Shatsky Rise, *in* Bralower, T.J., Premoli Silva, I., and Malone, M.J., Proceedings of the Ocean Drilling Program, Scientific Results, v. 198: College Station, Texas, Ocean Drilling Program, p. 1–19, doi: 10.2973/odp.proc.sr.198.119.2005.

Eberle, J.J., Gottfried, M.D., Hutchison, J.H., and Brochu, C.A., 2014, First record of Eocene bony fishes and crocodyliforms from Canada's Western Arctic: PLoS One, v. 9, e96079, doi: 10.1371/journal.pone.0096079.

Edgar, K.M., Pälike, H., and Wilson, P.A., 2013, Testing the impact of diagenesis on the $\delta^{18}O$ and $\delta^{13}C$ of benthic foraminiferal calcite from a sediment burial depth transect in the equatorial Pacific: Paleoceanography, v. 28, p. 468–480, doi: 10.1002/palo.20045.

Elderfield, H., and Ganssen, G., 2000, Past temperature and $\delta^{18}O$ of surface ocean waters inferred from foraminiferal Mg/Ca ratios: Nature, v. 405, p. 442–445, doi: 10.1038/35013033.

Elderfield, H., Vautravers, M., and Cooper, M., 2002, The relationship between shell size and Mg/Ca, Sr/Ca, $\delta^{18}O$, and $\delta^{13}C$ of species of planktonic foraminifera: Geochemistry, Geophysics, Geosystems, v. 3, p. 1–13, doi: 10.1029/2001GC000194.

Elderfield, H., Ferretti, P., Greaves, M., Crowhurst, S., McCave, I.N., Hodell, D., and Piotrowski, A.M., 2012, Evolution of ocean temperature and ice volume through the Mid-Pleistocene climate transition: Science, v. 337, p. 704–709, doi: 10.1126/science.1221294.

Erez, J., 2003, The source of ions for biomineralization in foraminifera and their implications for paleoceanographic proxies: Reviews in Mineralogy and Geochemistry, v. 54, p. 115–149, doi: 10.2113/0540115.

Esmeray-Senlet, S., Wright, J.D., Olsson, R.K., Miller, K.G., Browning, J.V., and Quan, T.M., 2015, Evidence for reduced export productivity following the Cretaceous/Paleogene mass extinction: Paleoceanography, v. 30, p. 718–738, doi: 10.1002/2014PA002724.

Evans, D., and Müller, W., 2012, Deep time foraminifera Mg/Ca paleothermometry: Nonlinear correction for secular change in seawater

Mg/Ca: Paleoceanography, v. 27, PA4205, doi: 10.1029/2012PA002315.

Evans, D., Erez, J., Oron, S., and Müller, W., 2015, Mg/Ca-temperature and seawater-test chemistry relationships in the shallow-dwelling large benthic foraminifera *Operculina ammonoides*: Geochimica et Cosmochimica Acta, v. 148, p. 325–342, doi: 10.1016/j.gca.2014.09.039.

Evans, D., Wade, B.S., Henehan, M., Erez, J., and Müller, W., 2016a, Revisiting carbonate chemistry controls on planktic foraminifera Mg/Ca: implications for sea surface temperature and hydrology shifts over the Paleocene–Eocene Thermal Maximum and Eocene–Oligocene transition: Climate of the Past, v. 12, p. 819–835, doi: 10.5194/cp-12-819-2016.

Evans, D., Brierley, C., Raymo, M.R., Erez, J., and Müller, W., 2016b, Planktic foraminifera shell chemistry response to seawater chemistry: Pliocene–Pleistocene seawater Mg/Ca, temperature and sea level change: Earth and Planetary Science Letters, v. 438, p. 139–148, doi: 10.1016/j.epsl.2016.01.013.

Evans, D., Sagoo, N., Renema, W., Cotton, L., Müller, W., Todd, J.A., Saraswati, P.K., Stassen, P., Ziegler, M., Pearson, P.N., Valdes, P.J., and Affek, H.P., 2018, Eocene greenhouse climate revealed by coupled clumped isotope-Mg/Ca thermometry: Proceedings of the National Academy of Sciences of the United States of America, doi: 10.1073/pnas.1714744115 (in press).

Fletcher, B.J., Brentnall, S.J., Anderson, C.W., Berner, R.A., and Beerling, D.J., 2008, Atmospheric carbon dioxide linked with Mesozoic and early Cenozoic climate change: Nature Geoscience, v. 1, p. 43-48, doi: 10.1038/ngeo.2007.29.

Font, E., Adatte, T., Andrade, M., Keller, G., Mbabi, A., Carvallo, C., Ferreira, J., Diogo, Z., and Mirão, J., 2018, Deccan volcanism induced high-stress environment during the Cretaceous–Paleogene transition at Zumaia, Spain: Evidence from magnetic, mineralogical and biostratigraphic records: Earth and Planetary Science Letters, v. 484, p. 53–66, doi: 10.1016/j.epsl.2017.11.055.

Foster, G.L., 2008, Seawater pH, pCO_2 and [CO_3^{2-}] variations in the Caribbean Sea over the last 130 kyr: A boron isotope and B/Ca study of planktic

foraminifera: Earth and Planetary Science Letters, v. 271, p. 254–266, doi: 10.1016/j.epsl.2008.04.015.

Friedrich, O., Schiebel, R., Wilson, P.A., Weldeab, S., Beer, C.J., Cooper, M.J., and Fiebig, J., 2012, Influence of test size, water depth, and ecology on Mg/Ca, Sr/Ca, $\delta^{18}O$ and $\delta^{13}C$ in nine modern species of planktic foraminifers: Earth and Planetary Science Letters, v. 319–320, p. 133–145, doi: 10.1016/j.epsl.2011.12.002.

Frieling, J., Iakovleva, A.I., Reichart, G-J., Aleksandrova, G.N., Gnibidenko, Z.N., Schouten, S., and Sluijs, A., 2014, Paleocene–Eocene warming and biotic response in the epicontinental West Siberian Sea: Geology, v. 42, p. 767–770, doi: 10.1130/G35724.1.

Frieling, J., Gebhardt, H., Huber, M., Adekeye, O.A., Akande, S.O., Reichart, G.-J., Middelburg, J.J., Schouten, S., and Sluijs, A., 2017, Extreme warmth and heat-stressed plankton in the tropics during the Paleocene-Eocene Thermal Maximum: Science Advances, v. 3, e1600891, doi: 10.1126/sciadv.1600891.

Frieling, J., Reichart, G-J., Middelburg, J.J., Röhl, U., Westerhold, T., Bohaty, M., and Sluijs, A., 2018, Tropical Atlantic climate and ecosystem regime shifts during the Paleocene-Eocene Thermal Maximum: Climate of the Past, v. 14, p. 39–55, doi: 10.5194/cp-14-39-2018.

Galeotti, S., Moretti, M., Cappelli, C., Phillips, J., Lanci, L., Littler, K., Monechi, S., Petrizzo, M.R., Premoli Silva, I., and Zachos, J.C., 2015, The Bottaccione section at Gubbio, central Italy: a classical Paleocene Tethyan setting revisited: Newsletters on Stratigraphy, v. 48/3, p. 325–339, doi: 10.1127/nos/2015/0067.

Gehler, A., Gingerich, P.D., and Pack, A., 2016, Temperature and atmospheric CO_2 concentration estimates through the PETM using triple oxygen isotope analysis of mammalian bioapatite: Proceedings of the National Academy of Sciences of the United States of America, v. 113, p. 7739–7744, doi: 10.1073/pnas.1518116113.

Gilmour, I., Gilmour, M., Jolley, D., Kelley, S., Kemp, D., Daly, R., and Watson, J., 2013, A high-resolution nonmarine record of an early Danian hyperthermal event, Boltysh crater, Ukraine: Geology, v. 41, p. 783–786, doi:

10.1130/G34292.1.

Gradstein, F.M., Ogg, J.G., Smith, A.G., Bleeker, W., and Lourens, L.J., 2004, A new Geologic Time Scale, with special reference to Precambrian and Neogene: Episodes, v. 27, p. 83–100.

Gradstein, F.M., Ogg, J.G., Schmitz, M.D., and Ogg, G.M., 2012, The Geologic Time Scale 2012, Elsevier, Amsterdam, 1176p.

Gutjahr, M., Ridgwell, A., Sexton, P.F., Anagnostou, E., Pearson, P.N., Pälike, H., Norris, R.D., Thomas, E., and Foster, G.L., 2017, Very large release of mostly volcanic carbon during the Palaeocene–Eocene Thermal Maximum: Nature, v. 548, p. 573–577, doi: 10.1038/nature23646.

Hancock, H.J.L., Dickens, G.R., Thomas, E., and Blake, K.L., 2006, Reappraisal of early Paleogene CCD curves: foraminiferal assemblages and stable carbon isotopes across the carbonate facies of Perth Abyssal Plain: International Journal of Earth Sciences, v. 96, p. 925–946.

Harding, I.C., Charles, A.J., Marshall, J.E.A., Pälike, H., Roberts, A.P., Wilson, P.A., Jarvis, E., Thorne, R., Morris, E., Moremon, R., Pearce, R.B., and Akbari, S., 2011, Sea-level and salinity fluctuations during the Paleocene–Eocene thermal maximum in Arctic Spitsbergen: Earth and Planetary Science Letters, v. 303, p. 97–107, doi: 10.1016/j.epsl.2010.12.043.

Harper, D.T., Zeebe, R., Hönisch, B., Schrader, C.D., Lourens, L.J., and Zachos, J.C., 2018, Subtropical sea-surface warming and increased salinity during Eocene Thermal Maximum 2: Geology, v. 46, p. 187–190, doi: 10.1130/G39658.1.

Hasiuk, F.J., and Lohmann, K.C., 2010, Application of calcite Mg partitioning functions to the reconstruction of paleocean Mg/Ca: Geochimica et Cosmochimica Acta, v. 74, p. 6751–6763, doi: 10.1016/j.gca.2010.07.030.

Haynes, L.L., Hönisch, B., Dyez, K.A., Holland, K., Rosenthal, Y., Fish, C.R., Subhas, A.V., and Rae, J.W.B., 2017, Calibration of the B/Ca proxy in the planktic foraminifer *Orbulina universa* to Paleocene seawater conditions: Paleoceanography, v. 32, p. 580–599, doi: 10.1002/2016PA003069.

He, M., Xiao, Y., Jin, Z., Liu, W., Ma, Y., Zhang, Y., and Luo, C., 2013,

Quantification of boron incorporation into synthetic calcite under controlled pH and temperature conditions using a differential solubility technique: Chemical Geology, v. 337–338, p. 67–74, doi: 10.1016/j.chemgeo.2012.11.013.

Hemming, N.G., and Hanson, G.N., 1992, Boron isotopic composition and concentration in modern marine carbonates: Geochimica et Cosmochimica Acta, v. 56, p. 537–543, doi: 10.1016/0016-7037(92)90151-8.

Hemming, N.G., Reeder, R.J., and Hanson, G.N., 1995, Mineral-fluid partitioning and isotopic fractionation of boron in synthetic calcium carbonate: Geochimica et Cosmochimica Acta, v. 59, p. 371–379, doi: 10.1016/0016-7037(95)00288-B.

Henehan, M.J., Rae, J.W.B., Foster, G.L., Erez, J., Prentice, K.C., Kucera, M., Bostock, H.C., Martínez-Botí, M.A., Milton, J.A., Wilson, P.A., Marshall, B.J., and Elliott, T., 2013, Calibration of the boron isotope proxy in the planktonic foraminifera *Globigerinoides ruber* for use in palaeo-CO_2 reconstruction: Earth and Planetary Science Letters, v. 364, p. 111–122, doi: 10.1016/j.epsl.2012.12.029.

Henehan, M.J., Foster, G.L., Rae, J.W.B., Prentice, K.C., Erez, J., Bostock, H.C., Marshall, B.J., and Wilson, P.A., 2015, Evaluating the utility of B/Ca ratios in planktic foraminifera as a proxy for the carbonate system: A case study of *Globigerinoides ruber*: Geochemistry, Geophysics, Geosystems, v. 16, p. 1052–1069, doi: 10.1002/2014GC005514.

Henehan, M.J., Foster, G.L., Bostock, H.C., Greenop, R., Marshall, B.J., and Wilson, P.A., 2016a, A new boron isotope-pH calibration for *Orbulina universa*, with implications for understanding and accounting for “vital effects”: Earth and Planetary Science Letters, v. 454, p. 282–292, doi: 10.1016/j.epsl.2016.09.024.

Henehan, M.J., Hull, P.M., Penman, D.E., Rae, J.W.B., and Schmidt, D.N., 2016b, Biogeochemical significance of pelagic ecosystem function: an end-Cretaceous case study: Philosophical Transactions of the Royal Society B, v. 371, 20150510, doi: 10.1098/rstb.2015.0510.

Herbert, T.D., Cleaveland Peterson, L., Lawrence, K.T., and Liu, Z., 2010,

Tropical ocean temperatures over the past 3.5 million years: Science, v. 328, p. 1530–1534, doi: 10.1126/science.1185435.

Higgins, J.A., and Schrag, D.P., 2006, Beyond methane: Towards a theory for the Paleocene–Eocene Thermal Maximum: Earth and Planetary Science Letters, v. 245, p. 523–537, doi: 10.1016/j.epsl.2006.03.009.

Hilting, A.K., Kump, L.R., and Bralower, T.J., 2008, Variations in the oceanic vertical carbon isotope gradient and their implications for the Paleocene-Eocene biological pump: Paleoceanography, v. 23, PA3222, doi: 10.1029/2007PA001458.

Hofmann, C., Féraud, G., and Courtillot, V., 2000, $^{40}Ar/^{39}Ar$ dating of mineral separates and whole rocks from the Western Ghats lava pile: Further constraints on duration and age of the Deccan traps: Earth and Planetary Science Letters, v. 180, p. 13–27, doi: 10.1016/S0012-821X(00)00159-X.

Hollis, C.J., Taylor, K.W.R., Handley, L., Pancost, R.D., Huber, M., Creech, J.B., Hines, B.R., Crouch, E.M., Morgans, H.E.G., Crampton, J.S., Gibbs, S., Pearson, P.N., and Zachos, J.C., 2012, Early Paleogene temperature history of the Southwest Pacific Ocean: Reconciling proxies and models: Earth and Planetary Science Letters, v. 349–350, p. 53–66, doi: 10.1016/j.epsl.2012.06.024.

Hollis, C.J., Hines, B.R., Littler, K., Villasante-Marcos, V., Kulhanek, D.K., Strong, C.P., Zachos, J.C., Eggins, S.M., Northcote, L., and Phillips, A., 2015, The Paleocene-Eocene Thermal Maximum at DSDP Site 277, Campbell Plateau, southern Pacific Ocean: Climate of the Past, v. 11, p. 1009–1025, doi: 10.5194/cp-11-1009-2015.

Hong, S.K., and Lee, Y. Il., 2012, Evaluation of atmospheric carbon dioxide concentrations during the Cretaceous: Earth and Planetary Science Letters, v. 327–328, p. 23–28, doi: 10.1016/j.epsl.2012.01.014.

Hönisch, B., and Hemming, N.G., 2004, Ground-truthing the boron isotope-paleo-pH proxy in planktonic foraminifera shells: Partial dissolution and shell size effects: Paleoceanography, v. 19, PA4010, doi: 10.1029/2004PA001026.

Hönisch, B., Allen, K.A., Lea, D.W., Spero, H.J., Eggins, S.M., Arbuszewski, J., deMenocal, P., Rosenthal, Y., Russell, A.D., and Elderfield, H., 2013, The

influence of salinity on Mg/Ca in planktic foraminifers - Evidence from cultures, core-top sediments and complementary $\delta^{18}O$: Geochimica et Cosmochimica Acta, v. 121, p. 196–213, doi: 10.1016/j.gca.2013.07.028.

Huang, C., Hesselbo, S.P., and Hinnov, L., 2010, Astrochronology of the late Jurassic Kimmeridge Clay (Dorset, England) and implications for Earth system processes: Earth and Planetary Science Letters, v. 289, p. 242–255, doi: 10.1016/j.epsl.2009.11.013.

Huang, C., Retallack, G.J., Wang, C., and Huang, Q., 2013, Paleoatmospheric pCO_2 fluctuations across the Cretaceous–Tertiary boundary recorded from paleosol carbonates in NE China: Palaeogeography, Palaeoclimatology, Palaeoecology, v. 385, p. 95–105, doi: 10.1016/j.palaeo.2013.01.005.

Huber, B.T., MacLeod, K.G., Watkins, D.K., and Coffin, M.F., 2018, The rise and fall of the Cretaceous Hot Greenhouse climate: Global and Planetary Change, v. 167, p. 1–23, doi: 10.1016/j.gloplacha.2018.04.004.

Hunt, J.M., 1996, Petroleum Geochemistry and Geology, W.H. Freeman, San Francisco.

Husson, D., Galbrun, B., Laskar, J., Hinnov, L.A., Thibault, N., Gardin, S., and Locklair, R.E., 2011, Astronomical calibration of the Maastrichtian (Late Cretaceous): Earth and Planetary Science Letters, v. 305, p. 328–340, doi: 10.1016/j.epsl.2011.03.008.

Jay, A.E., and Widdowson, M., 2008, Stratigraphy, structure and volcanology of the SE Deccan continental flood basalt province: implications for eruptive extent and volumes: Journal of the Geological Society, London, v. 165, p. 177–188, doi: 10.1144/0016-76492006-062.

Jehle, S., Bornemann, A., Deprez, A., and Speijer, R.P., 2015, The impact of the Latest Danian Event on planktic foraminiferal faunas at ODP Site 1210 (Shatsky Rise, Pacific Ocean): PLoS ONE, v. 10, p. 1–26, doi: 10.1371/journal.pone.0141644.

John, C.M., Bohaty, S.M., Zachos, J.C., Sluijs, A., Gibbs, S., Brinkhuis, H., and Bralower, T.J., 2008, North American continental margin records of the Paleocene-Eocene thermal maximum: Implications for global carbon and hydrological cycling: Paleoceanography, v. 23, p. PA2217,

10.1029/2007PA001465.

Jolley, D.W., Gilmour, I., Gilmour, M., Kemp, D.B., and Kelley, S.P., 2015, Long-term resilience decline in plant ecosystems across the Danian Dan-C2 hyperthermal event, Boltysh crater, Ukraine: Journal of the Geological Society, London, v. 172, p. 491–498, doi: 10.1144/jgs2014-130.

Kaminski, M.A., and Gradstein, F.M., 2005, Atlas of Paleogene cosmopolitan deep-water agglutinated foraminifera: Grzybowski Foundation Special Publication, v. 10, Grzybowski Foundation, Krakow, Poland, 547p.

Katz, M.E., Katz, D.R., Wright, J.D., Miller, K.G., Pak, D.K., Shackleton, N.J., and Thomas, E., 2003, Early Cenozoic benthic foraminiferal isotopes: Species reliability and interspecies correction factors: Paleoceanography, v. 18, 1024, doi: 10.1029/2002PA000798.

Keller, G., 2001, The end-cretaceous mass extinction in the marine realm: year 2000 assessment: Planetary and Space Science, v. 49, p. 817–830, doi: 10.1016/S0032-0633(01)00032-0.

Keller, G., Adatte, T., Burns, S.J., and Tantawy, A.A., 2002, High-stress paleoenvironment during the late Maastrichtian to early Paleocene in Central Egypt: Palaeogeography, Palaeoclimatology, Palaeoecology, v. 187, p. 35–60, doi: 10.1016/S0031-0182(02)00504-7.

Keller, G., and Abramovich, S., 2009, Lilliput effect in late Maastrichtian planktic foraminifera: Response to environmental stress: Palaeogeography, Palaeoclimatology, Palaeoecology, v. 284, p. 47–62, doi: 10.1016/j.palaeo.2009.08.029.

Keller, G., Adatte, T., Bhowmick, P.K., Upadhyay, H., Dave, A., Reddy, A.N., and Jaiprakash, B.C., 2012, Nature and timing of extinctions in Cretaceous-Tertiary planktic foraminifera preserved in Deccan intertrappean sediments of the Krishna–Godavari Basin, India: Earth and Planetary Science Letters, v. 341–344, p. 211–221, doi: 10.1016/j.epsl.2012.06.021.

Keller, G., Punekar, J., and Mateo, P., 2016, Upheavals during the Late Maastrichtian: Volcanism, climate and faunal events preceding the end-Cretaceous mass extinction: Palaeogeography, Palaeoclimatology, Palaeoecology, v. 441, p. 137–151, doi: 10.1016/j.palaeo.2015.06.034.

Kender, S., Yu, J., and Peck, V.L., 2014, Deep ocean carbonate ion increase during mid Miocene CO_2 decline: Scientific Reports, v. 4, 4187, doi: 10.1038/srep04187.

Kennett, J.P., and Stott, L.D., 1991, Abrupt deep-sea warming, palaeoceanographic changes and benthic extinctions at the end of the Palaeocene: Nature, v. 353, p. 225–229.

Kim, S-T., and O'Neil, J.R., 1997, Equilibrium and nonequilibrium oxygen isotope effects in synthetic carbonates: Geochimica et Cosmochimica Acta, v. 61, p. 3461–3475.

Kirtland Turner, S., Sexton, P.F., Charles, C.D., and Norris, R.D., 2014, Persistence of carbon release events through the peak of early Eocene global warmth: Nature Geoscience, v. 7, p. 8–11, doi: 10.1038/NGEO2240.

Kisakürek, B., Eisenhauer, A., Böhm, F., Garbe-Schönberg, D., and Erez, J., 2008, Controls on shell Mg/Ca and Sr/Ca in cultured planktonic foraminiferan, *Globigerinoides ruber* (white): Earth and Planetary Science Letters, v. 273, p. 260–269, doi: 10.1016/j.epsl.2008.06.026.

Koch, P.L., Zachos, J.C., and Gingerich, P.D., 1992, Correlation between isotope records in marine and continental carbon reservoirs near the Palaeocene/Eocene boundary: Nature, v. 358, p. 319–322, doi: 10.1038/358319a0.

Komar, N., Zeebe, R.E., and Dickens, G.R., 2013, Understanding long-term carbon cycle trends: The late Paleocene through the early Eocene: Paleoceanography, v. 28, p. 650–662, doi: 10.1002/palo.20060.

Kozdon, R., Kelly, D.C., Kita, N.T., Fournelle, J.H., and Valley, J.W., 2011, Planktonic foraminiferal oxygen isotope analysis by ion microprobe technique suggests warm tropical sea surface temperatures during the Early Paleogene: Paleoceanography, v. 26, PA3206, doi: 10.1029/2010PA002056.

Kozdon, R., Kelly, D.C., Kitajima, K., Strickland, A., Fournelle, J.H., and Valley, J.W., 2013, In situ $\delta^{18}O$ and Mg/Ca analyses of diagenetic and planktic foraminiferal calcite preserved in a deep-sea record of the Paleocene-Eocene thermal maximum: Paleoceanography, v. 28, p. 517–528, doi:

10.1002/palo.20048.

Kroon, D., Zachos, J.C., and Leg 208 Scientific Party, 2007, Leg 208 Synthesis: Cenozoic Climate Cycles and Excursions, *in* Kroon, D., Zachos, J.C., and Richter, C., Proceedings of the Ocean Drilling Program, Scientific Results, v. 208: College Station, Texas, Ocean Drilling Program, p. 1–55, doi: 10.2973/odp.proc.sr.208.201.2007.

Kucera, M., and Malmgren, B.A., 1998, Terminal Cretaceous warming event in the mid-latitude South Atlantic Ocean: evidence from poleward migration of *Contusotruncana contusa* (planktonic foraminifera) morphotypes: Palaeogeography, Palaeoclimatology, Palaeoecology, v. 138, p. 1–15, doi: 10.1016/S0031-0182(97)00124-7.

Kuhnt, W., 1990, Agglutinated foraminifera of western Mediterranean Upper Cretaceous pelagic limestones (Umbrian Apennines, Italy, and Betic Cordillera, Southern Spain): Micropaleontology, v. 36, p. 297–330, doi: 10.2307/1485473.

Kump, L.R., 1991, Interpreting carbon-isotope excursions: Strangelove oceans: Geology, v. 19, p. 299–302, doi: 10.1130/0091-7613(1991)019<0299:ICIESO>2.3.CO;2.

Kump, L.R., and Arthur, M.A., 1999, Interpreting carbon-isotope excursions: carbonates and organic matter: Chemical Geology, v. 161, p. 181–198, doi: 10.1016/S0009-2541(99)00086-8.

Kurtz, A.C., Kump, L.R., Arthur, M.A., Zachos, J.C., and Paytan, A., 2003, Early Cenozoic decoupling of the global carbon and sulfur cycles: Paleoceanography, v. 18, 1090, doi: 10.1029/2003PA000908.

Kvenvolden, K.A., 1993, Gas hydrates—geological perspective and global change: Reviews of Geophysics, v. 31, p. 173–187, doi: 10.1029/93RG00268.

Laskar, J., Robutel, P., Joutel, F., Gastineau, M., Correia, A., and Levrard, B., 2004, A long-term numerical solution for the insolation quantities of the Earth: Astronomy and Astrophysics, v. 428, p. 261–285, doi: 10.1051/0004-6361:20041335.

Laskar, J., Fienga, A., Gastineau, M., and Manche, H., 2011a, La2010: a new orbital solution for the long-term motion of the Earth: Astronomy and Astrophysics, v. 532, A89, doi: 10.1051/0004-6361/201116836.

Laskar, J., Gastineau, M., Delisle, J.-B., Farres, A., Fienga, A., 2011b, Strong chaos induced by close encounters with Ceres and Vesta: Astronomy and Astrophysics, v. 532, L4, doi: 10.1051/0004-6361/201117504.

Lauretano, V., Littler, K., Polling, M., Zachos, J.C., and Lourens, L.J., 2015, Frequency, magnitude and character of hyperthermal events at the onset of the Early Eocene Climatic Optimum: Climate of the Past, v. 11, p. 1313–1324, doi: 10.5194/cp-11-1313-2015.

Lea, D.W., Mashiotta, T.A., and Spero, H.J., 1999, Controls on magnesium and strontium uptake in planktonic foraminifera determined by live culturing: Geochimica et Cosmochimica Acta, v. 63, p. 2369–2379, doi: 10.1016/S0016-7037(99)00197-0.

Lea, D.W., Pak, D.K., and Spero, H.J., 2000, Climate impact of Late Quaternary equatorial Pacific sea surface temperature variations: Science, v. 289, p. 1719–1724, doi: 10.1126/science.289.5485.1719.

Lea, D.W., Martin, P.A., Pak, D.K., and Spero, H.J., 2002, Reconstructing a 350 ky history of sea level using planktonic Mg/Ca and oxygen isotope records from a Cocos Ridge core: Quaternary Science Reviews, v. 21, p. 283–293, doi: 10.1016/S0277-3791(01)00081-6.

Lear, C.H., Elderfield, H., and Wilson, P.A., 2000, Cenozoic deep-sea temperatures and global ice volumes from Mg/Ca in benthic foraminiferal calcite: Science, v. 287, p. 269–272, doi: 10.1126/science.287.5451.269.

Lear, C.H., Rosenthal, Y., and Slowey, N., 2002, Benthic foraminiferal Mg/Ca-paleothermometry: A revised core-top calibration: Geochimica et Cosmochimica Acta, v. 66, p. 3375–3387, doi: 10.1016/S0016-7037(02)00941-9.

Lear, C.H., Mawbey, E.M., and Rosenthal, Y., 2010, Cenozoic benthic foraminiferal Mg/Ca and Li/Ca records: Toward unlocking temperatures and saturation states: Paleoceanography, v. 25, PA4215, doi: 10.1029/2009PA001880.

Lear, C.H., Coxall, H.K., Foster, G.L., Lunt, D.J., Mawbey, E.M., Rosenthal, Y., Sosdian, S.M., Thomas, E., and Wilson, P.A., 2015, Neogene ice volume and ocean temperatures: Insights from infaunal foraminiferal Mg/Ca paleothermometry: Paleoceanography, v. 30, p. 1437–1454, doi: 10.1002/2015PA002833.

Lemarchand, D., Gaillardet, J., Lewin, É., Allègre, C.J., 2000, The influence of rivers on marine boron isotopes and implications for reconstructing past ocean pH: Nature, v. 408, p. 951–954, doi: 10.1038/35050058.

Li, L., and Keller, G., 1998, Abrupt deep-sea warming at the end of the Cretaceous: Geology, v. 26, p. 995–998, doi: 10.1130/0091-7613(1998)026<0995:ADSWAT>2.3.CO;2.

Li, L., and Keller, G., 1999, Variability in Late Cretaceous climate and deep waters: evidence from stable isotopes: Marine Geology, v. 161, p. 171–190, doi: 10.1016/S0025-3227(99)00078-X.

Li, Y-H., 1982, A brief discussion on the mean oceanic residence time of elements: Geochimica et Cosmochimica Acta, v. 46, p. 2671–2675, doi: 10.1016/0016-7037(82)90386-6.

Liebrand, D., Beddow, H.M., Lourens, L.J., Pälike, H., Raffi, I., Bohaty, S.M., Hilgen, F.J., Saes, M.J.M., Wilson, P.A., van Dijk, A.E., Hodell, D.A., Kroon, D., Huck, C.E., and Batenburg, S.J., 2016, Cyclostratigraphy and eccentricity tuning of the early Oligocene through early Miocene (30.1–17.1 Ma): *Cibicides mundulus* stable oxygen and carbon isotope records from Walvis Ridge Site 1264: Earth and Planetary Science Letters, v. 450, p. 392–405, doi: 10.1016/j.epsl.2016.06.007.

Lisiecki, L.E., and Raymo, M.E., 2005, A Pliocene-Pleistocene stack of 57 globally distributed benthic $\delta^{18}O$ records: Paleoceanography, v. 20, PA1003, doi: 10.1029/2004PA001071.

Littler, K., Röhl, U., Westerhold, T., and Zachos, J.C., 2014, A high-resolution benthic stable-isotope record for the South Atlantic: Implications for orbital-scale changes in Late Paleocene-Early Eocene climate and carbon cycling: Earth and Planetary Science Letters, v. 401, p. 18–30, doi: 10.1016/j.epsl.2014.05.054.

Locarnini, R.A., Mishonov, A.V., Antonov, J.I., Boyer, T.P., Garcia, H.E., Baranova, O.K., Zweng, M.M., Paver, C.R., Reagan, J.R., Johnson, D.R., Hamilton, M., and Seidov, D., 2013, World Ocean Atlas 2013, Volume 1: Temperature, in Levitus, S., and Mishonov, A., NOAA Atlas NESDIS 73, 40p.

Lourens, L.J., Sluijs, A., Kroon, D., Zachos, J.C., Thomas, E., Röhl, U., Bowles, J., and Raffi, I., 2005, Astronomical pacing of late Palaeocene to early Eocene global warming events: Nature, v. 435, p. 1083–1087, doi: 10.1038/nature03814.

Lunt, D.J., Valdes, P.J., Dunkley Jones, T., Ridgwell, A., Haywood, A.M., Schmidt, D.N., Marsh, R., and Maslin, M., 2010, CO_2-driven ocean circulation changes as an amplifier of Paleocene-Eocene thermal maximum hydrate destabilization: Geology, v. 38, p. 875–878, doi: 10.1130/G31184.1.

Lunt, D.J., Ridgwell, A., Sluijs, A., Zachos, J., Hunter, S., and Haywood, A., 2011, A model for orbital pacing of methane hydrate destabilization during the Palaeogene: Nature Geoscience, v. 4, p. 775–778, doi: 10.1038/ngeo1266.

Manners, H.R., Grimes, S.T., Sutton, P.A., Domingo, L., Leng, M.J., Twitchett, R.J., Hart, M.B., Dunkley Jones, T., Pancost, R.D., Duller, R., and Lopez-Martinez, N., 2013, Magnitude and profile of organic carbon isotope records from the Paleocene–Eocene Thermal Maximum: Evidence from northern Spain: Earth and Planetary Science Letters, v. 376, p. 220–230, doi: 10.1016/j.epsl.2013.06.016.

Martini, E., 1971, Standard Tertiary and Quaternary calcareous nannoplankton zonation, *in* Farinacci, A., Proceedings of the Second Planktonic Conference Roma 1970, v. 2, Edizioni Tecnoscienza, Roma, p. 739–785.

Mashiotta, T.A., Lea, D.W., and Spero, H.J., 1999, Glacial–interglacial changes in Subantarctic sea surface temperature and δ^{18}O-water using foraminiferal Mg: Earth and Planetary Science Letters, v. 170, p. 417–432, doi: 10.1016/S0012-821X(99)00116-8.

McCarren, H., Thomas, E., Hasegawa, T., Röhl, U., and Zachos, J.C., 2008, Depth dependency of the Paleocene-Eocene carbon isotope excursion: Paired benthic and terrestrial biomarker records (Ocean Drilling Program Leg 208, Walvis Ridge): Geochemistry, Geophysics, Geosystems, v. 9, p. 1–

10, doi: 10.1029/2008GC002116.

McConnell, M.C., and Thunell, R.C., 2005, Calibration of the planktonic foraminiferal Mg/Ca paleothermometer: Sediment trap results from the Guaymas Basin, Gulf of California: Paleoceanography, v. 20, PA2016, doi: 10.1029/2004PA001077.

McInerney, F.A., and Wing, S.L., 2011, The Paleocene-Eocene Thermal Maximum: A Perturbation of Carbon Cycle, Climate, and Biosphere with Implications for the Future: Annual Review of Earth and Planetary Sciences, v. 39, p. 489–516, doi: 10.1146/annurev-earth-040610-133431.

Meyers, S.R., 2012, Seeing Red in Cyclic Stratigraphy: Spectral Noise Estimation for Astrochronology: Paleoceanography, v. 27, PA3228, doi: 10.1029/2012PA002307.

Meyers, S.R., 2014, Astrochron: An R Package for Astrochronology. http://cran.rproject.org/package=astrochron

Milkov, A.V., 2005, Molecular and stable isotope compositions of natural gas hydrates: A revised global dataset and basic interpretations in the context of geological settings: Organic Geochemistry, v. 36, p. 681–702, doi: 10.1016/j.orggeochem.2005.01.010.

Mitchell, J.S., Roopnarine, P.D., and Angielczyk, K.D., 2012, Late Cretaceous restructuring of terrestrial communities facilitated the end-Cretaceous mass extinction in North America: Proceedings of the National Academy of Sciences of the United States of America, v. 109, p. 18857–18861, doi: 10.1073/pnas.1202196109.

Monechi, S., Reale, V., Bernaola, G., and Balestra, B., 2013, The Danian/Selandian boundary at Site 1262 (South Atlantic) and in the Tethyan region: Biomagnetostratigraphy, evolutionary trends in fasciculiths and environmental effects of the Latest Danian Event: Marine Micropaleontology, v. 98, p. 28–40, doi: 10.1016/j.marmicro.2012.11.002.

Moore, T.C., and the Expedition 302 Scientists, 2006, Sedimentation and subsidence history of the Lomonosov Ridge, in Backman, J., Moran, K., McInroy, D.B., Mayer, L.A., and the Expedition 302 Scientists, Proceedings of the International Ocean Discovery Program, v. 302: Edinburgh (Integrated

Ocean Drilling Program Management International, Inc.), doi: 10.2204/iodp.proc.302.105.2006.

Murphy, B.H., Farley, K.A., and Zachos, J.C., 2010, An extraterrestrial ^{3}He-based timescale for the Paleocene-Eocene thermal maximum (PETM) from Walvis Ridge, IODP Site 1266: Geochimica et Cosmochimica Acta, v. 74, p. 5098–5108, doi: 10.1016/j.gca.2010.03.039.

Naik, S.S., and Naidu, P.D., 2014, Boron/calcium ratios in *Globigerinoides ruber* from the Arabian Sea: Implications for controls on boron incorporation: Marine Micropaleontology, v. 107, p. 1–7, doi: 10.1016/j.marmicro.2014.01.004.

Nordt, L., Atchley, S., and Dworkin, S.I., 2002, Paleosol barometer indicates extreme fluctuations in atmospheric CO_2 across the Cretaceous-Tertiary boundary: Geology, v. 30, p. 703–706, doi: 10.1130/0091-7613(2002)030<0703:PBIEFI>2.0.CO;2.

Nordt, L., Atchley, S., and Dworkin, S., 2003, Terrestrial evidence for two greenhouse events in the latest Cretaceous: GSA Today, v. 13, p. 4–9, doi: 10.1130/1052-5173(2003)013<4:TEFTGE>2.0.CO;2.

Nunes, F., and Norris, R.D., 2006, Abrupt reversal in ocean overturning during the Palaeocene/Eocene warm period: Nature, v. 439, p. 60–63, doi: 10.1038/nature04386.

Nürnberg, D., 1995, Magnesium in tests of *Neogloboquadrina pachyderma* sinistral from high northern and southern latitudes: Journal of Foraminiferal Research, v. 25, p. 350–368, doi: 10.2113/gsjfr.25.4.350.

Nürnberg, D., Buma, J., and Hemleben, C., 1996, Assessing the reliability of magnesium in foraminiferal calcite as a proxy for water mass temperatures: Geochimica et Cosmochimica Acta, v. 60, p. 803–814, doi: 10.1016/0016-7037(95)00446-7.

Olsson, R.K., Hemleben, C., Berggren, W.A., and Huber, B.T., 1999, Atlas of Paleocene Planktonic Foraminifera: Smithsonian Institution Press, Washington D.C., 258p.

Olsson, R.K., Wright, J.D., and Miller, K.G., 2001, Paleobiogeography of

Pseudotextularia elegans during the latest Maastrichtian global warming event: Journal of Foraminiferal Research, v. 31, p. 275–282, doi: 10.2113/31.3.275.

Oomori, T., Kaneshima, H., Maezato, Y., and Kitano, Y., 1987, Distribution coefficient of Mg^{2+} ions between calcite and solution at 10–50°C: Marine Chemistry, v. 20, p. 327–336, doi: 10.1016/0304-4203(87)90066-1.

Paillard, D., Labeyrie, L., and Yiou, P., 1996, Macintosh program performs time-series analysis: EOS Transactions, v. 77, p. 379, doi: 10.1029/96EO00259.

Panchuk, K., Ridgwell, A., and Kump, L.R., 2008, Sedimentary response to Paleocene-Eocene Thermal Maximum carbon release: A model-data comparison: Geology, v. 36, p. 315–318, doi: 10.1130/G24474A.1.

Pearson, P.N., Olsson, R.K., Huber, B.T., Hemleben, C., Berggren, W.A., and Coxall, H.K., 2006, Chapter 1: Overview of Eocene planktonic foraminiferal taxonomy, paleoecology, phylogeny, and biostratigraphy, *in* Pearson, P.N., Olsson, R.K., Huber, B.T., Hemleben, C., and Berggren, W.A., Atlas of Eocene planktonic foraminifera, Cushman Foundation Special Publication, v. 41, p. 11–28.

Pearson, P.N., van Dongen, B.E., Nicholas, C.J., Pancost, R.D., Schouten, S., Singano, J.M., and Wade, B.S., 2007, Stable warm tropical climate through the Eocene Epoch: Geology, v. 35, p. 211–214, doi: 10.1130/G23175A.1.

Pearson, P.N., and Burgess, C.E., 2008, Foraminifer test preservation and diagenesis: comparison of high latitude Eocene sites: Geological Society, London, Special Publications, v. 303, p. 59–72, doi: 10.1144/SP303.5.

Penman, D.E., Hönisch, B., Zeebe, R.E., Thomas, E., and Zachos, J.C., 2014, Rapid and sustained surface ocean acidification during the Paleocene-Eocene Thermal Maximum: Paleoceanography, v. 29, p. 357–369, doi: 10.1002/2014PA002621.

Pross, J., Contreras, L., Bijl, P.K., Greenwood, D.R., Bohaty, S.M., Schouten, S., Bendle, J.A., Röhl, U., Tauxe, L., Raine, J.I., Huck, C.E., van de Flierdt, T., Jamieson, S.S.R., Stickley, C.E., van de Schootbrugge, B., Escutia, C., Brinkhuis, H., and Integrated Ocean Drilling Program Expedition 318 Scientists, 2012, Persistent near-tropical warmth on the Antarctic continent

during the early Eocene epoch: Nature, v. 488, p. 73–77, doi: 10.1038/nature11300.

Punekar, J., Mateo, P., and Keller, G., 2014a, Effects of Deccan volcanism on paleoenvironment and planktic Foraminifera; a global survey, *in* Keller, G., and Kerr, A.C., Volcanism, Impacts, and Mass Extinctions: Causes and Effects: Geological Society of America Special Paper 505, p. 91–116, doi: 10.1130/2014.2505(04).

Punekar, J., Keller, G., Khozyem, H., Hamming, C., Adatte, T., Tantawy, A.A., and Spangenberg, J.E., 2014b, Late Maastrichtian-early Danian high-stress environments and delayed recovery linked to Deccan volcanism: Cretaceous Research, v. 49, p. 63–82, doi: 10.1016/j.cretres.2014.01.002.

Quillévéré, F., Aubry, M-P., Norris, R.D., and Berggren, W.A., 2002, Paleocene oceanography of the eastern subtropical Indian Ocean: An integrated magnetobiostratigraphic and stable isotope study of ODP Hole 761B (Wombat Plateau): Palaeogeography, Palaeoclimatology, Palaeoecology, v. 184, p. 371–405, doi: 10.1016/S0031-0182(02)00275-4.

Quillévéré, F., Norris, R.D., Kroon, D., and Wilson, P.A., 2008, Transient ocean warming and shifts in carbon reservoirs during the early Danian: Earth and Planetary Science Letters, v. 265, p. 600–615, doi: 10.1016/j.epsl.2007.10.040.

Rae, J.W.B., Foster, G.L., Schmidt, D.N., and Elliott, T., 2011, Boron isotopes and B/Ca in benthic foraminifera: Proxies for the deep ocean carbonate system: Earth and Planetary Science Letters, v. 302, p. 403–413, doi: 10.1016/j.epsl.2010.12.034.

Rathmann, S., Hess, S., Kuhnert, H., and Mulitza, S., 2004, Mg/Ca ratios of the benthic foraminifera *Oridorsalis umbonatus* obtained by laser ablation from core top sediments: Relationship to bottom water temperature: Geochemistry, Geophysics, Geosystems, v. 5, p. 1–10, doi: 10.1029/2004GC000808.

Regenberg, M., Nürnberg, D., Steph, S., Groeneveld, J., Garbe-Schönberg, D., Tiedemann, R., and Dullo, W-C., 2006, Assessing the effect of dissolution on planktonic foraminiferal Mg/Ca ratios: Evidence from Caribbean core

tops: Geochemistry, Geophysics, Geosystems, v. 7, p. 1–23, doi: 10.1029/2005GC001019.

Regenberg, M., Regenberg, A., Garbe-Schönberg, D., and Lea, D.W., 2014, Global dissolution effects on planktonic foraminiferal Mg/Ca ratios controlled by the calcite-saturation state of bottom waters: Paleoceanography, v. 29, p. 127–142, doi: 10.1002/2013PA002492.

Renne, P.R., Deino, A.L., Hilgen, F.J., Kuiper, K.F., Mark, D.F., Mitchell, W.S., Morgan, L.E., Mundil, R., and Smit, J., 2013, Time scales of critical events around the Cretaceous-Paleogene boundary: Science, v. 339, p. 684–687, doi: 10.1126/science.1230492.

Renne, P.R., Sprain, C.J., Richards, M.A., Self, S., Vanderkluysen, L., and Pande, K., 2015, State shift in Deccan volcanism at the Cretaceous-Paleogene boundary, possibly induced by impact: Science, v. 350, p. 76–78, doi: 10.1126/science.aac7549.

Ries, J.B., 2004, Effect of ambient Mg/Ca ratio on Mg fractionation in calcareous marine invertebrates: A record of the oceanic Mg/Ca ratio over the Phanerozoic: Geology, v. 32, p. 981–984, doi: 10.1130/G20851.1.

Röhl, U., Westerhold, T., Bralower, T.J., and Zachos, J.C., 2007, On the duration of the Paleocene-Eocene thermal maximum (PETM): Geochemistry, Geophysics, Geosystems, v. 8, p. 1–13, doi: 10.1029/2007GC001784.

Romein, A.J.T., 1979, Lineages in early Paleogene calcareous nannoplankton: Utrecht Micropaleontological Bulletins, v. 22, p. 1–230.

Rosenthal, Y., and Boyle, E.A., 1993, Factors controlling the fluoride content of planktonic foraminifera: An evaluation of its paleoceanographic applicability: Geochimica et Cosmochimica Acta, v. 57, p. 335–346, doi: 10.1016/0016-7037(93)90435-Y.

Rosenthal, Y., Boyle, E.A., and Slowey, N., 1997, Temperature control on the incorporation of magnesium, strontium, fluorine, and cadmium into benthic foraminiferal shells from Little Bahama Bank: Prospects for thermocline paleoceanography: Geochimica et Cosmochimica Acta, v. 61, p. 3633–3643, doi: 10.1016/S0016-7037(97)00181-6.

Rosenthal, Y., Lohmann, G.P., Lohmann, K.C., and Sherrell, R.M., 2000, Incorporation and preservation of Mg in *Globigerinoides sacculifer*: Implications for reconstructing the temperature and $^{18}O/^{16}O$ of seawater: Paleoceanography, v. 15, p. 135–145, doi: 10.1029/1999PA000415.

Royer, D.L., Wing, S.L., Beerling, D.J., Jolley, D.W., Koch, P.L., Hickey, L.J., and Berner, R.A., 2001, Paleobotanical evidence for near present-day levels of atmospheric CO_2 during part of the Tertiary: Science, v. 292, p. 2310–2313, doi: 10.1126/science.292.5525.2310.

Royer, D.L., 2003, Estimating latest Cretaceous and Tertiary atmospheric CO_2 concentration from stomatal indices, *in* Wing, S.L., Gingerich, P.D., Schmitz, B., and Thomas, E., Causes and Consequences of Globally Warm Climates in the Early Paleogene: Boulder, Colorado, Geological Society of America Special Paper 369, p. 79–93.

Royer, D.L., 2006, CO_2-forced climate thresholds during the Phanerozoic: Geochimica et Cosmochimica Acta, v. 70, p. 5665–5675, doi: 10.1016/j.gca.2005.11.031.

Royer, D.L., 2014, Atmospheric CO_2 and O_2 during the Phanerozoic: tools, patterns, and impacts: Geochemistry Treatise (Second Edition), v. 6, p. 251-267, http://droyer.web.wesleyan.edu/Royer_2014_Treatise.pdf

Russell, A.D., Hönisch, B., Spero, H.J., and Lea, D.W., 2004, Effects of seawater carbonate ion concentration and temperature on shell U, Mg, and Sr in cultured planktonic foraminifera: Geochimica et Cosmochimica Acta, v. 68, p. 4347–4361, doi: 10.1016/j.gca.2004.03.013.

Sagoo, N., Valdes, P., Flecker, R., and Gregoire, L.J., 2013, The Early Eocene equable climate problem: can perturbations of climate model parameters identify possible solutions?: Philosophical Transactions of the Royal Society A, v. 371, p. 1–35, doi: 10.1098/rsta.2013.0123.

Sanyal, A., Nugent, M., Reeder, R.J., and Bijma, J., 2000, Seawater pH control on the boron isotopic composition of calcite: Evidence from inorganic calcite precipitation experiments: Geochimica et Cosmochimica Acta, v. 64, p. 1551–1555, doi: 10.1016/S0016-7037(99)00437-8.

Schoene, B., Samperton, K.M., Eddy, M.P., Keller, G., Adatte, T., Bowring, S.A.,

Khadri, S.F.R., and Gertsch, B., 2015, U-Pb geochronology of the Deccan Traps and relation to the end-Cretaceous mass extinction: Science, v. 347, p. 182–184, doi: 10.1126/science.aaa0118.

Schoon, P.L., Heilmann-Clausen, C., Schultz, B.P., Sinninghe Damste, J.S., and Schouten, S., 2015, Warming and environmental changes in the eastern North Sea Basin during the Palaeocene–Eocene Thermal Maximum as revealed by biomarker lipids: Organic Geochemistry, v. 78, p. 79–88, doi: 10.1016/j.orggeochem.2014.11.003.

Schulte, P., Alegret, L., Arenillas, I., Arz, J.A., Barton, P.J., Bown, P.R., Bralower, T.J., Christeson, G.L., Claeys, P., Cockell, C.S., Collins, G.S., Deutsch, A., Goldin, T.J., Goto, K., et al., 2010, The Chicxulub Asteroid Impact and Mass Extinction at the Cretaceous-Paleogene Boundary: Science, v. 327, p. 1214–1218, doi: 10.1126/science.1177265.

Seilacher, A., 1967, Bathymetry of trace fossils: Marine Geology, v. 5, p. 413–428, doi: 10.1016/0025-3227(67)90051-5.

Self, S., Blake, S., Sharma, K., Widdowson, M., and Sephton, S., 2008, Sulfur and chlorine in Late Cretaceous Deccan magmas and eruptive gas release: Science, v. 319, p. 1654–1657, doi: 10.1126/science.1152830.

Sen Gupta, B.K., and Machain-Castillo, M.L., 1993, Benthic foraminifera in oxygen-poor habitats: Marine Micropaleontology, v. 20, p. 183–201, doi: 10.1016/0377-8398(93)90032-S.

Sexton, P.F., Norris, R.D., Wilson, P.A., Pälike, H., Westerhold, T., Röhl, U., Bolton, C.T., and Gibbs, S., 2011, Eocene global warming events driven by ventilation of oceanic dissolved organic carbon: Nature, v. 471, p. 349–352, doi: 10.1038/nature09826.

Shackleton, N.J., Hall, M.A., and Boersma, A., 1984, Oxygen and carbon isotope data from Leg 74 foraminifers, *in* Moore, T.C., Jr., Rabinowitz, P.D., et al., Initial Reports of the Deep Sea Drilling Project, v. 74, p. 599–612, doi: 10.2973/dsdp.proc.74.115.1984.

Shannon, C.E., and Weaver, W., 1949, The mathematical theory of communication: University of Illinois Press, Urbana.

Sheldon, E., Ineson, J., and Bown, P., 2010, Late Maastrichtian warming in the Boreal Realm: Calcareous nannofossil evidence from Denmark: Palaeogeography, Palaeoclimatology, Palaeoecology, v. 295, p. 55–75, doi: 10.1016/j.palaeo.2010.05.016.

Shipboard Scientific Party, 1975, Site 277, *in* Kennett, J.P., Houtz, R.E., et al., Initial Reports of the Deep Sea Drilling Project, v. 29: Washington (U.S. Government Printing Office), p. 45–120, doi: 10.2973/dsdp.proc.29.104.1975.

Shipboard Scientific Party, 1979, Site 401, *in* Montadert, L., et al., Initial Reports of the Deep Sea Drilling Project, v. 48: Washington (U.S. Government Printing Office), p. 73–123, doi: 10.2973/dsdp.proc.48.104.1979.

Shipboard Scientific Party, 1984a, Site 525, *in* Moore, T.C., Jr., Rabinowitz, P.D., et al., Initial Reports of the Deep Sea Drilling Project, v. 74: Washington (U.S. Government Printing Office), p. 41–306, doi: 10.2973/dsdp.proc.74.102.1984.

Shipboard Scientific Party, 1984b, Site 527, *in* Moore, T.C., Jr., Rabinowitz, P.D., et al., Initial Reports of the Deep Sea Drilling Project, v. 74: Washington (U.S. Government Printing Office), p. 237–160, doi: 10.2973/dsdp.proc.74.104.1984.

Shipboard Scientific Party, 1985, Site 577, *in* Heath, G.R., Burckle, L.H., et al., Initial Reports of the Deep Sea Drilling Project, v. 86: Washington (U.S. Government Printing Office), p. 91–137, doi: 10.2973/dsdp.proc.86.104.1985.

Shipboard Scientific Party, 1988a, Site 689, *in* Barker, P.F., Kennett, J.P., et al., Proceedings of the Ocean Drilling Program, Initial Reports, v. 113: College Station, Texas, Ocean Drilling Program, p. 89–181, doi: /10.2973/odp.proc.ir.113.106.1988.

Shipboard Scientific Party, 1988b, Site 690, *in* Barker, P.F., Kennett, J.P., et al., Proceedings of the Ocean Drilling Program, Initial Reports, v. 113: College Station, Texas, Ocean Drilling Program, p. 183–292, doi: 10.2973/odp.proc.ir.113.107.1988.

Shipboard Scientific Party, 1989, Site 758, *in* Peirce, J., Weissel, J., et al.,

Proceedings of the Ocean Drilling Program, Initial Reports, v. 121: College Station, Texas, Ocean Drilling Program, p. 359–453, doi: 10.2973/odp.proc.ir.121.112.1989.

Shipboard Scientific Party, 1990, Site 761, *in* Haq, B.U., von Rad, U., et al., Proceedings of the Ocean Drilling Program, Initial Reports, v. 122: College Station, Texas, Ocean Drilling Program, p. 161–211, doi: 10.2973/odp.proc.ir.122.107.1990.

Shipboard Scientific Party, 1993, Site 865, *in* Sager, W.W., Winterer, E.L., Firth, J.V., et al., Proceedings of the Ocean Drilling Program, Initial Reports, v. 143: College Station, Texas, Ocean Drilling Program, p. 111–180, doi: 10.2973/odp.proc.ir.143.106.1993.

Shipboard Scientific Party, 1996, Site 959, *in* Mascle, J., Lohmann, G.P., Clift, P.D., et al., Proceedings of the Ocean Drilling Program, Initial Reports, v. 159: College Station, Texas, Ocean Drilling Program, p. 65–150, doi: 10.2973/odp.proc.ir.159.105.1996.

Shipboard Scientific Party, 1998, Site 1049, *in* Norris, R.D., Kroon, D., Klaus, A., et al., Proceedings of the Ocean Drilling Program, Initial Reports, v. 171B: College Station, Texas, Ocean Drilling Program, p. 47–91, doi: 10.2973/odp.proc.ir.171B.103.1998.

Shipboard Scientific Party, 2001, Site 1172, *in* Exon, N.F., Kennett, J.P., Malone, M.J., et al., Proceedings of the Ocean Drilling Program, Initial Reports, v. 189: College Station, Texas, Ocean Drilling Program, p. 1–149, doi: 10.2973/odp.proc.ir.189.107.2001.

Shipboard Scientific Party, 2002a, Site 1209, *in* Bralower, T.J., Premoli Silva, I., Malone, M.J., et al., Proceedings of the Ocean Drilling Program, Initial Reports, v. 198: College Station, Texas, Ocean Drilling Program, p. 1–102, doi: 10.2973/odp.proc.ir.198.105.2002.

Shipboard Scientific Party, 2002b, Site 1210, *in* Bralower, T.J., Premoli Silva, I., Malone, M.J., et al., Proceedings of the Ocean Drilling Program, Initial Reports, v. 198: College Station, Texas, Ocean Drilling Program, p. 1–89, doi: 10.2973/odp.proc.ir.198.106.2002.

Shipboard Scientific Party, 2004a, Site 1262, *in* Zachos, J.C., Kroon, D., Blum,

P., et al., Proceedings of the Ocean Drilling Program, Initial Reports, v. 208: College Station, Texas, Ocean Drilling Program, p. 1–92, doi: 10.2973/odp.proc.ir.208.103.2004.

Shipboard Scientific Party, 2004b, Leg 208 Summary, *in* Zachos, J.C., Kroon, D., Blum, P., et al., Proceedings of the Ocean Drilling Program, Initial Reports, v. 208: College Station, Texas, Ocean Drilling Program, p. 1–112, doi: 10.2973/odp.proc.ir.208.101.2004.

Shipboard Scientific Party, 2004c, Site 1263, *in* Zachos, J.C., Kroon, D., Blum, P., et al., Proceedings of the Ocean Drilling Program, Initial Reports, v. 208: College Station, Texas, Ocean Drilling Program, p. 1–87, doi: 10.2973/odp.proc.ir.208.104.2004.

Shipboard Scientific Party, 2014, Site U1403, *in* Norris, R.D., Wilson, P.A., Blum, P., and the Expedition 342 Scientists, Proceedings of the Integrated Ocean Drilling Program, v. 342: College Station, Texas, Integrated Ocean Drilling Program, p. 1–98, doi: 10.2204/iodp.proc.342.104.2014.

Shipboard Scientific Party, 2016, Site U1443, *in* Clemens, S.C., Kuhnt, W., LeVay, L.J., and the Expedition 353 Scientists, Proceedings of the International Ocean Discovery Program, v. 353: College Station, Texas, International Ocean Discovery Program, p. 1–41, doi: 10.14379/iodp.proc.353.103.2016.

Sinha, A., and Stott, L.D., 1994, New atmospheric pCO_2 estimates from palesols during the late Paleocene/early Eocene global warming interval: Global and Planetary Change, v. 9, p. 297–307, doi: 10.1016/0921-8181(94)00010-7.

Sinton, C.W., and Duncan, R.A., 1998, ^{40}Ar-^{39}Ar ages of lavas from the southeast Greenland margin, ODP Leg 152, and the Rockall Plateau, DSDP Leg 81, *in* Saunders, A.D., Larsen, H.C., and Wise, S.W., Jr., Proceedings of the Ocean Drilling Program, Scientific Results, v. 152: College Station, Texas, Ocean Drilling Program, p. 387–402, doi: 10.2973/odp.proc.sr.152.234.1998.

Slotnick, B.S., Lauretano, V., Backman, J., Dickens, G.R., Sluijs, A., and Lourens, L., 2015, Early Paleogene variations in the calcite compensation depth: new constraints using old borehole sediments from across Ninetyeast Ridge, central Indian Ocean: Climate of the Past, v. 11, p. 473–493, doi: 10.5194/cp-

11-473-2015.

Sluijs, A., Schouten, S., Pagani, M., Woltering, M., Brinkhuis, H., Sinninghe Damsté, J.S., Dickens, G.R., Huber, M., Reichart, G.J., Stein, R., Matthiessen, J., Lourens, L.J., Pedentchouk, N., Backman, J., Moran, K., and the Expedition 302 Scientists, 2006, Subtropical Arctic Ocean temperatures during the Palaeocene/Eocene thermal maximum: Nature, v. 441, p. 610–613, doi: 10.1038/nature04668.

Sluijs, A., Bowen, G.J., Brinkhuis, H., Lourens, L.J., and Thomas, E., 2007a, The Palaeocene–Eocene Thermal Maximum super greenhouse: biotic and geochemical signatures, age models and mechanisms of global change, *in* Williams, H., Haywood, A.M., Gregory, F.J., and Schmidt, D.N., Deep-Time Perspectives on Climate Change: Marrying the Signal from Computer Models and Biological Proxies, The Micropalaeontological Society, Special Publications, The Geological Society, London, p. 323–349.

Sluijs, A., Brinkhuis, H., Schouten, S., Bohaty, S.M., John, C.M., Zachos, J.C., Reichart, G-J., Sinninghe Damsté, J.S., Crouch, E.M., and Dickens, G.R., 2007b, Environmental precursors to rapid light carbon injection at the Palaeocene/Eocene boundary: Nature, v. 450, p. 1218–1221.

Sluijs, A., Röhl, U., Schouten, S., Brumsack, H-J., Sangiorgi, F., Sinninghe Damsté, J.S., and Brinkhuis, H., 2008, Arctic late Paleocene–early Eocene paleoenvironments with special emphasis on the Paleocene-Eocene thermal maximum (Lomonosov Ridge, Integrated Ocean Drilling Program Expedition 302): Paleoceanography, v. 23, PA1S11, doi: 10.1029/2007PA001495.

Sluijs, A., Bijl, P.K., Schouten, S., Röhl, U., Reichart, G-J., and Brinkhuis, H., 2011, Southern ocean warming, sea level and hydrological change during the Paleocene-Eocene thermal maximum: Climate of the Past, v. 7, p. 47–61.

Sosdian, S., and Rosenthal, Y., 2009, Deep-sea temperature and ice volume changes across the Pliocene-Pleistocene climate transitions: Science, v. 325, p. 306–310, doi: 10.1126/science.1169938.

Spivack, A.J., and Edmond, J.M., 1987, Boron isotope exchange between seawater and the oceanic crust: Geochimica et Cosmochimica Acta, v. 51,

p. 1033–1043, doi: 10.1016/0016-7037(87)90198-0.

Stanley, S.M., and Hardie, L.A., 1998, Secular oscillations in the carbonate mineralogy of reef-building and sediment-producing organisms driven by tectonically forced shifts in seawater chemistry: Palaeogeography, Palaeoclimatology, Palaeoecology, v. 144, p. 3–19, doi: 10.1016/S0031-0182(98)00109-6.

Stap, L., Sluijs, A., Thomas, E., and Lourens, L., 2009, Patterns and magnitude of deep sea carbonate dissolution during Eocene Thermal Maximum 2 and H2, Walvis Ridge, southeastern Atlantic Ocean: Paleoceanography, v. 24, PA1211, doi: 10.1029/2008PA001655.

Stap, L., Lourens, L.J., Thomas, E., Sluijs, A., Bohaty, S., and Zachos, J.C., 2010, High-resolution deep-sea carbon and oxygen isotope records of Eocene Thermal Maximum 2 and H2: Geology, v. 38, p. 607–610, doi: 10.1130/G30777.1.

Steinthorsdottir, M., Vajda, V., and Pole, M., 2016, Global trends of pCO_2 across the Cretaceous–Paleogene boundary supported by the first Southern Hemisphere stomatal proxy-based pCO_2 reconstruction: Palaeogeography, Palaeoclimatology, Palaeoecology, v. 464, p. 143–152, doi: 10.1016/j.palaeo.2016.04.033.

Stott, L.D., and Kennett, J.P., 1990, The paleoceanographic and paleoclimatic signature of the Cretaceous/Paleogene boundary in the Antarctic: stable isotopic results from ODP Leg 113, *in* Barker, P.F., Kennett, J.P., et al., Proceedings of the Ocean Drilling Program, Scientific Results, v. 113, p. 829–848, doi: 10.2973/odp.proc.sr.113.158.1990.

Stott, L.D., 1992, Higher temperatures and lower oceanic pCO_2: A climate enigma at the end of the Paleocene Epoch: Paleoceanography, v. 7, p. 395–404, doi: 10.1029/92PA01183.

Stüben, D., Kramar, U., Berner, Z., Stinnesbeck, W., Keller, G., and Adatte, T., 2002, Trace elements, stable isotopes, and clay mineralogy of the Elles II K–T boundary section in Tunisia: indications for sea level fluctuations and primary productivity: Palaeogeography, Palaeoclimatology, Palaeoecology, v. 178, p. 321–345, doi: 10.1016/S0031-0182(01)00401-1.

Stüben, D., Kramar, U., Berner, Z.A., Meudt, M., Keller, G., Abramovich, S., Adatte, T., Hambach, U., and Stinnesbeck, W., 2003, Late Maastrichtian paleoclimatic and paleoceanographic changes inferred from Sr/Ca ratio and stable isotopes: Palaeogeography, Palaeoclimatology, Palaeoecology, v. 199, p. 107–127, doi: 10.1016/S0031-0182(03)00499-1.

Svensen, H., Planke, S., Malthe-Sørenssen, A., Jamtveit, B., Myklebust, R., Rasmussen Eidem, T., and Rey, S.S., 2004, Release of methane from a volcanic basin as a mechanism for initial Eocene global warming: Nature, v. 429, p. 542–545, doi: 10.1038/nature02566.

Tantawy, A.A.A., Keller, G., and Pardo, A., 2009, Late Maastrichtian volcanism in the Indian Ocean: Effects on calcareous nannofossils and planktic foraminifera: Palaeogeography, Palaeoclimatology, Palaeoecology, v. 284, p. 63–87, doi: 10.1016/j.palaeo.2009.08.025.

Tappan, H., and Loeblich, A.R., Jr., 1988, Foraminiferal evolution, diversification, and extinction: Journal of Paleontology, v. 62, p. 695–714.

Thibault, N., and Gardin, S., 2007, The late Maastrichtian nannofossil record of climate change in the South Atlantic DSDP Hole 525A: Marine Micropaleontology, v. 65, p. 163–184, doi: 10.1016/j.marmicro.2007.07.004.

Thomas, D.J., Bralower, T.J., and Zachos, J.C., 1999, New evidence for subtropical warming during the Late Paleocene thermal maximum: Stable isotopes from Deep Sea Drilling Project Site 527, Walvis Ridge: Paleoceanography and Paleoclimatology, v. 14, p. 561–570, doi: 10.1029/1999PA900031.

Thomas, D.J., Zachos, J.C., Bralower, T.J., Thomas, E., and Bohaty, S., 2002, Warming the fuel for the fire: Evidence for the thermal dissociation of methane hydrate during the Paleocene-Eocene thermal maximum: Geology, v. 30, p. 1067–1070, doi: 10.1130/0091-7613(2002)030<1067:WTFFTF>2.0.CO;2.

Thomas, D.J., Bralower. T.J., and Jones, C.E., 2003, Neodymium isotopic reconstruction of late Paleocene–early Eocene thermohaline circulation: Earth and Planetary Science Letters, v. 209, p. 309–322, doi: 10.1016/S0012-821X(03)00096-7.

Thomas, D.J., Lyle, M., Moore, T.C.Jr., and Rea, D.K., 2008, Paleogene deepwater mass composition of the tropical Pacific and implications for thermohaline circulation in a greenhouse world: Geochemistry, Geophysics, Geosystems, v. 9, Q02002, doi: 10.1029/2007GC001748.

Thomas, E., 1998, Biogeography of the Late Paleocene Benthic Foraminifera Extinction, *in* Aubry, M.-P., et al., Late Paleocene–early Eocene biotic and climatic events in the marine and terrestrial records: New York, Columbia University Press, p. 214–243.

Thomas, E., Zachos, J.C., and Bralower, T.J., 2000, Deep-sea environments on a warm Earth: latest Paleocene–early Eocene, *in* Huber, B., MacLeod, K., and Wing, S., Warm Climates in Earth History: Cambridge University Press, Cambridge, UK, p. 132–160.

Thomas, E., 2003, Extinction and food at the seafloor: A high-resolution benthic foraminiferal record across the Initial Eocene Thermal Maximum, Southern Ocean Site 690, *in* Wing, S.L., Gingerich, P.D., Schmitz, B., and Thomas, E., Causes and Consequences of Globally Warm Climates in the Early Paleogene: Boulder, Colorado, Geological Society of America Special Paper 369, p. 319–332.

Tjalsma, R.C., and Lohmann, G.P., 1983, Paleocene-Eocene bathyal and abyssal benthic foraminifera from the Atlantic Ocean: Micropaleontology Special Publication, v. 4.

Tobin, T.S., Ward, P.D., Steig, E.J., Olivero, E.B., Hilburn, I.A., Mitchell, R.N., Diamond, M.R., Raub, T.D., and Kirschvink, J.L., 2012, Extinction patterns, $\delta^{18}O$ trends, and magnetostratigraphy from a southern high-latitude Cretaceous-Paleogene section: Links with Deccan volcanism: Palaeogeography, Palaeoclimatology, Palaeoecology, v. 350–352, p. 180–188, doi: 10.1016/j.palaeo.2012.06.029.

Tobin, T.S., Wilson, G.P., Eiler, J.M., and Hartman, J.H., 2014, Environmental change across a terrestrial Cretaceous-Paleogene boundary section in eastern Montana, USA, constrained by carbonate clumped isotope paleothermometry: Geology, v. 42, p. 351–354, doi: 10.1130/G35262.1.

Torsvik, T.H., Van der Voo, R., Preeden, U., Niocaill, C. Mac, Steinberger, B.,

Doubrovine, P. V., van Hinsbergen, D.J.J., Domeier, M., Gaina, C., Tohver, E., Meert, J.G., McCausland, P.J.A., and Cocks, L.R.M., 2012, Phanerozoic polar wander, palaeogeography and dynamics: Earth-Science Reviews, v. 114, p. 325–368, doi: 10.1016/j.earscirev.2012.06.002.

Tripati, A.K., Delaney, M.L., Zachos, J.C., Anderson, L.D., Kelly, D.C., and Elderfield, H., 2003, Tropical sea-surface temperature reconstruction for the early Paleogene using Mg/Ca ratios of planktonic foraminifera: Paleoceanography, v. 18, 1101, doi: 10.1029/2003PA000937.

Tripati, A.K., and Elderfield, H., 2004, Abrupt hydrographic changes in the equatorial Pacific and subtropical Atlantic from foraminiferal Mg/Ca indicate greenhouse origin for the thermal maximum at the Paleocene-Eocene Boundary: Geochemistry, Geophysics, Geosystems, v. 5, p. 1–11, doi: 10.1029/2003GC000631.

Tripati, A., and Elderfield, H., 2005, Deep-sea temperature and circulation changes at the Paleocene-Eocene Thermal Maximum: Science, v. 308, p. 1894–1898, doi: 10.1126/science.1109202.

Tyrrell, T., and Zeebe, R.E., 2004, History of carbonate ion concentration over the last 100 million years: Geochimica et Cosmochimica Acta, v. 68, p. 3521–3530, doi: 10.1016/j.gca.2004.02.018.

Van Hinsbergen, D.J.J., De Groot, L. V., Van Schaik, S.J., Spakman, W., Bijl, P.K., Sluijs, A., Langereis, C.G., and Brinkhuis, H., 2015, A paleolatitude calculator for paleoclimate studies: PLoS ONE, v. 10, p. 1–21, doi: 10.1371/journal.pone.0126946.

Van Morkhoven, F.P.C., Berggren, W.A., and Edwards, A.S., 1986, Cenozoic cosmopolitan deep-water benthic foraminifera: Elf-Aquitaine, Pau, France.

Vellekoop, J., Esmeray-senlet, S., Miller, K.G., Browning, J.V., Sluijs, A., van de Schootbrugge, B., Damsté, J.S.S., and Brinkhuis, H., 2016, Evidence for Cretaceous-Paleogene boundary bolide “impact winter” conditions from New Jersey, USA: Geology, v. 44, p. 619–622, doi: 10.1130/G37961.1.

Wade, B.S., Pearson, P.N., Berggren, W.A., and Pälike, H., 2011, Review and revision of Cenozoic tropical planktonic foraminiferal biostratigraphy and calibration to the geomagnetic polarity and astronomical time scale: Earth-

Science Reviews, v. 104, p. 111–142, doi: 10.1016/j.earscirev.2010.09.003.

Wade, B.S., Houben, A.J.P., Quaijtaal, W., Schouten, S., Rosenthal, Y., Miller, K.G., Katz, M.E., Wright, J.D., and Brinkhuis, H., 2012, Multiproxy record of abrupt sea-surface cooling across the Eocene-Oligocene transition in the Gulf of Mexico: Geology, v. 40, p. 159–162, doi: 10.1130/G32577.1.

Wara, M.W., Delaney, M.L., Bullen, T.D., and Ravelo, A.C., 2003, Possible roles of pH, temperature, and partial dissolution in determining boron concentration and isotopic composition in planktonic foraminifera: Paleoceanography, v. 18, 1100, doi: 10.1029/2002PA000797.

Westerhold, T., Röhl, U., Laskar, J., Raffi, I., Bowles, J., Lourens, L.J., and Zachos, J.C., 2007, On the duration of magnetochrons C24r and C25n and the timing of early Eocene global warming events: Implications from the Ocean Drilling Program Leg 208 Walvis Ridge depth transect: Paleoceanography, v. 22, PA2201, doi: 10.1029/2006PA001322.

Westerhold, T., Röhl, U., Raffi, I., Fornaciari, E., Monechi, S., Reale, V., Bowles, J., and Evans, H.F., 2008, Astronomical calibration of the Paleocene time: Palaeogeography, Palaeoclimatology, Palaeoecology, v. 257, p. 377–403, doi: 10.1016/j.palaeo.2007.09.016.

Westerhold, T., and Röhl, U., 2009, High resolution cyclostratigraphy of the early Eocene – new insights into the origin of the Cenozoic cooling trend: Climate of the Past, v. 5, p. 309–327, doi: 10.5194/cp-5-309-2009.

Westerhold, T., Röhl, U., McCarren, H.K., and Zachos, J.C., 2009, Latest on the absolute age of the Paleocene–Eocene Thermal Maximum (PETM): New insights from exact stratigraphic position of key ash layers + 19 and – 17: Earth and Planetary Science Letters, v. 287, p. 412–419, doi: 10.1016/j.epsl.2009.08.027.

Westerhold, T., Röhl, U., Donner, B., Mccarren, H.K., and Zachos, J.C., 2011, A complete high-resolution Paleocene benthic stable isotope record for the central Pacific (ODP Site 1209): Paleoceanography, v. 26, PA2216, doi: 10.1029/2010PA002092.

Westerhold, T., Röhl, U., Frederichs, T., Agnini, C., Raffi, I., Zachos, J.C., and Wilkens, R.H., 2017, Astronomical calibration of the Ypresian time scale:

implications for seafloor spreading rates and the chaotic behaviour of the solar system?: Climate of the Past, v. 13, p. 1129–1152, doi: 10.5194/cp-13-1129-2017.

Westerhold, T., Röhl, U., Donner, B., and Zachos, J.C., 2018, Global extent of Early Eocene hyperthermal events – a new Pacific benthic foraminiferal isotope record from Shatsky Rise (ODP Site 1209): Paleoceanography and Paleoclimatology, v. 33, p. 626–642, doi: 10.1029/2017PA003306.

Wilf, P., Johnson, K.R., and Huber, B.T., 2003, Correlated terrestrial and marine evidence for global climate changes before mass extinction at the Cretaceous-Paleogene boundary: Proceedings of the National Academy of Sciences of the United States of America, v. 100, p. 599–604, doi: 10.1073/pnas.0234701100.

Witts, J.D., Bowman, V.C., Wignall, P.B., Crame, J.A., Francis, J.E., and Newton, R.J., 2015, Evolution and extinction of Maastrichtian (Late Cretaceous) cephalopods from the López de Bertodano Formation, Seymour Island, Antarctica: Palaeogeography, Palaeoclimatology, Palaeoecology, v. 418, p. 193–212, doi: 10.1016/j.palaeo.2014.11.002.

Woelders, L., Vellekoop, J., Kroon, D., Smit, J., Casadio, S., Prámparo, M.B., Dinarès-Turell, J., Peterse, F., Sluijs, A., Lenaerts, J.T.M., and Speijer, R.P., 2017, Latest Cretaceous climatic and environmental change in the South Atlantic region: Paleoceanography, v. 32, p. 466–483, doi: 10.1002/2016PA003007.

Yu, J., Elderfield, H., and Hönisch, B., 2007, B/Ca in planktonic foraminifera as a proxy for surface seawater pH: Paleoceanography, v. 22, PA2202, doi: 10.1029/2006PA001347.

Yu, J., Broecker, W.S., Elderfield, H., Jin, Z., McManus, J., and Zhang, F., 2010, Loss of carbon from the deep sea since the Last Glacial Maximum: Science, v. 330, p. 1084–1087, doi: 10.1126/science.1193221.

Zachos, J.C., Arthur, M.A., Thunell, R.C., Williams, D.F., and Tappa, E.J., 1985, Stable isotope and trace element geochemistry of carbonate sediments across the Cretaceous/Tertiary boundary at Deep Sea Drilling Project Hole 577, Leg 86, *in* Heath, G.R., Burckle, L.H., et al., Initial Reports of the Deep

Sea Drilling Project, v. 86: Washington (U.S. Government Printing Office), p. 513–532, doi: 10.2973/dsdp.proc.86.120.1985.

Zachos, J.C., Rea, D.K., Seto, K., Nomura, R., and Niitsuma, N., 1992, Paleogene and Early Neogene deep water paleoceanography of the Indian Ocean as determined from benthic foraminifer stable carbon and oxygen isotope records: Synthesis of Results from Scientific Drilling in the Indian Ocean Geophysical Monograph 70, p. 351–385.

Zachos, J., Pagani, M., Sloan, L., Thomas, E., and Billups, K., 2001, Trends, rhythms, and aberrations in global climate 65 Ma to present: Science, v. 292, p. 686–693, doi: 10.1126/science.1059412.

Zachos, J.C., Wara, M.W., Bohaty, S., Delaney, M.L., Petrizzo, M.R., Brill, A., Bralower, T.J., and Premoli-Silva, I., 2003, A transient rise in tropical sea surface temperature during the Paleocene-Eocene Thermal Maximum: Science, v. 302, p. 1551–1554, doi: 10.1126/science.1090110.

Zachos, J.C., Röhl, U., Schellenberg, S.A., Sluijs, A., Hodell, D.A., Kelly, D.C., Thomas, E., Nicolo, M., Raffi, I., Lourens, L.J., McCarren, H., and Kroon, D., 2005, Rapid acidification of the ocean during the Paleocene-Eocene Thermal Maximum: Science, v. 308, p. 1611–1615, doi: 10.1126/science.1109004.

Zachos, J.C., Schouten, S., Bohaty, S., Quattlebaum, T., Sluijs, A., Brinkhuis, H., Gibbs, S.J., and Bralower, T.J., 2006, Extreme warming of mid-latitude coastal ocean during the Paleocene-Eocene Thermal Maximum: Inferences from TEX86 and isotope data: Geology, v. 34, p. 737–740, doi: 10.1130/G22522.1.

Zachos, J.C., Dickens, G.R., and Zeebe, R.E., 2008, An early Cenozoic perspective on greenhouse warming and carbon-cycle dynamics: Nature, v. 451, p. 279–283, doi: 10.1038/nature06588.

Zachos, J.C., McCarren, H., Murphy, B., Röhl, U., and Westerhold, T., 2010, Tempo and scale of late Paleocene and early Eocene carbon isotope cycles: Implications for the origin of hyperthermals: Earth and Planetary Science Letters, v. 299, p. 242–249, doi: 10.1016/j.epsl.2010.09.004.

Zeebe, R.E., Zachos, J.C., and Dickens, G.R., 2009, Carbon dioxide forcing

alone insufficient to explain Palaeocene–Eocene Thermal Maximum warming: Nature Geoscience, v. 2, p. 576–580, doi: 10.1038/ngeo578.

Zeebe, R.E., Westerhold, T., Littler, K., and Zachos, J.C., 2017, Orbital forcing of the Paleocene and Eocene carbon cycle: Paleoceanography, v. 32, p. 1–26, doi: 10.1002/2016PA003054.

Zhang, L., Wang, C., Wignall, P.B., Kluge, T., Wan, X., Wang, Q., and Gao, Y., 2018, Deccan volcanism caused coupled pCO_2 and terrestrial temperature rises, and pre-impact extinctions in northern China: Geology, v. 46, p. 271–274, doi: 10.1130/G39992.1.